DCU

Ollscoil Chathair
Bhaile Átha Cliath
Dublin City University

DEVELOPMENT AND DEPLOYMENT OF A NOVEL IN SITU MULTIPARAMETER OPTICAL SENSOR FOR MARINE AND FRESHWATER ENVIRONMENTS

Seán Power B.Eng.

Supervisors: Prof. Fiona Regan, Dr. Nigel Kent

School of Chemical Sciences

Dublin City University

Thesis submitted for Degree of Doctor of Philosophy

January 2024

DECLARATION

I hereby certify that this material, which I now submit for assessment on the programme of study leading to the award of Doctor of Philosophy is entirely my own work, and that I have exercised reasonable care to ensure that the work is original, and does not to the best of my knowledge breach any law of copyright, and has not been taken from the work of others save and to the extent that such work has been cited and acknowledged within the text of my work.

Signed: _____ ID No.: _____ Date: _____

"Ritheann uiscí doimhne ciúin."

- seanfhocal gaelach

ACKNOWLEDGEMENTS

Firstly, I would like to thank my supervisors Professor Fiona Regan and Dr Nigel Kent for their consistent support and guidance that they have given me throughout my project and for the many opportunities they have given me. For believing in me and for being great mentors.

I thank the projects that funded my PhD work, the Disruptive Technologies Innovation Fund Advanced Water Monitoring System project, the industry partner TechWorks Marine and their employees who worked on the project as well as the Horizon 2020 Technologies for Ocean Sensing project and all who worked on the project.

I would like to thank everyone in the School of Chemical Sciences in DCU. I would also like to thank everyone in the Water Research Group in DCU. I must say a huge thank you to all the people I worked with along the way who I have had the pleasure of getting to know and who helped me greatly throughout my time in DCU. Thank you to Louis, Ciprian, Adrian, Caroline, Lisa, Fiona Bracken, Conor, Ruth, Weili, Paola, Martin, Dylan, Kristyna, Stef, Adam, and Harry.

I would also like to thank my family, Martina, Colm, Tom, Ellen and the dog Hector for their support and encouragement.

Finally, and most importantly, I would like to thank Chloe for her love, patience, support, and for constantly believing in me. The greatest outcome of this PhD for me, was meeting you.

TABLE OF CONTENTS

LIST OF TABLES

LIST OF FIGURES

LIST OF PUBLICATIONS

Journal Articles

- Power, S; Free L.; Briciu-Burghina, C.; Delgado A.; Richards C.; Gomez E. A.; Kent, N.; Regan F. Novel low-cost plug-and-play multi-spectral LED based fluorometer, with application to chlorophyll detection. Anal. Methods 2023, doi:10.1039/d3ay00991b.

- Briciu-Burghina, C.; Power, S.; Delgado, A.; Regan, F. Sensors for Coastal and Ocean Monitoring. *Annual Review of Analytical Chemistry* 2023, *16* (1), 451–469.

- Delgado, A.; Power, S.; Richards, C.; Daly, P.; Briciu-Burghina, C.; Delauré, Y.; Regan, F. Establishment of an Antifouling Performance Index Derived from the Assessment of Biofouling on Typical Marine Sensor Materials. Science of The Total Environment 2023, 887, 164059.

- Power, S; Free L.; Briciu-Burghina, C.; Delgado A.; Richards C.; Gomez E. A.; Kent, N.; Regan F. Multiparameter Optical Head Design for Marine Environmental Monitoring. Intended for submission to MDPI Journal.

- Power, S; Free L.; Briciu-Burghina, C.; Delgado A.; Richards C.; Gomez E. A.; Kent, N.; Regan F. Method of Scaled-Up In Situ Sensor Prototype Design Production, Validation and Deployment in the Marine Environment. Intended for submission to IEEE Journal.

Conference Proceedings

- Power, S.; Murphy, C.; Guo, W.; Free, L.; Briciu-Burghina, C.; Drago, P.; Richards, C.; Regan, F.; Parle-McDermott, A. A Centrifugal Microfluidic Sensing Platform for the Detection of Contaminants in the Marine Environment. In OCEANS 2023 - Limerick; 2023; pp 1–8.

- Briciu-Burghina, C.; Njongwe, A.; Worthington, A.; Power, S.; Richards, C.; Kent, N.; Regan, F. The 2nd Generation ColiSense System for the Detection of E. Coli in Bathing Waters. In OCEANS 2023 - Limerick; 2023; pp 1–7.

- Guo, W.; Murphy, C.; Free, L.; Power, S.; Briciu-Burghina, C.; Richards, C.; Parle-McDermott, A.; Regan, F. Emerging Ocean Contaminant Sensing Using Antibody-Based Optical Detection. In OCEANS 2023 - Limerick; 2023; pp 1–6.

- Delgado, A.; Richards, C.; Daly, P.; Power, S.; Briciu-Burghina, C.; Delauré, Y.; Regan, F. Assessment of Biofouling on Typical Marine Sensors Materials. In OCEANS 2023 - Limerick; 2023; pp 1–8.

Posters and Presentations

- 30th April 2021 Collaborate to Innovate: Next Generation Sensors for Marine Monitoring , Webinar Event – Oral Presentation.

- 23–28 April 2023 – EGU 2023 (European Geosciences Union) A Low-cost Novel Optical Sensor for In Situ Water Quality Monitoring, Austria Center Vienna (ACV), Vienna, Austria – Oral and Poster Presentation

- 5-8 June 2023 - OCEANS 2023, A Centrifugal Microfluidic Sensing Platform for the Detection of Contaminants in the Marine Environment, University of Limerick, County Limerick, Ireland – Oral Presentation

ABSTRACT

Development and deployment of a novel in situ multiparameter optical sensor for marine and freshwater environments.

Seán Power

Global warming and pollution due to human activities has had a major impact on the world's waterbodies which are vital for sustaining life on this planet. With this rapid escalation of threat to the oceans, seas, lakes, and rivers there has been an increased focus and urgency to monitor these changes to better understand the consequences of our anthropogenic impact. This culminates in a greater need for monitoring technologies to gather real-time data with high temporal and spatial resolutions to provide a holistic understanding of the changes to the waterbodies and inform regulations to protect our waters from further damage. The bridge the technological and research gaps required to sufficiently monitor the aquatic environments the work presented in this thesis aimed to demonstrate the design and development of beyond state of the art in situ optical detection by applying advanced optical and electronic components. A unique and novel design was produced by applying two mini spectrometers, a multispectral LED array light source, a photodiode, and custom electronics for interfacing with the optical system and housing the system in a robust enclosure using advanced manufacturing methods. The finalised system and enclosure design was replicated by manufacturing multiple identical systems as low-cost going beyond what is currently being achieved in the research field. The systems were demonstrated to have superior multispectral and multiparameter optical measurement capabilities when compared to current commercial systems with higher resolution detection of chlorophyll and turbidity as well as the ability to measure other tested analytes of petroleum and dissolved organic matter. The built systems showed robustness through repeated deployments and provided insightful data on the locations of deployment measuring multiple different environmental events while in situ.

1 INTRODUCTION

The oceans, seas and waterbodies on earth are vast, covering nearly 71% of the earth's surface, and play a vital role in the sustaining life on this planet. The health of the oceans and coastal regions are of paramount importance in supporting the worlds natural ecosystems, weather patterns and shaping our climate which due to climate change caused by human activities is rapidly changing [1–4]. The state of the ocean has been significantly altered due to anthropogenic activities which has led to a decline in biodiversity and habitat loss [5–7]. The rapid changes made to the climate due to human activity has caused the warming to accelerate over the past few decades [8] which in turn has caused a decline of the glaciers, ice caps and ice sheets in the polar regions leading to rising sea levels, decrease in primary production and alterations to the ocean stratification [3,9]. Therefore, it is becoming ever more pressing that we monitor and analyse the activity of our oceans with finer detail to understand these significant changes to be able to act to prevent further deterioration to them.

A major challenge is presented in sufficiently monitoring the vastness of all waterbodies in their entirety to obtain a holistic understanding. Oceanography is the study of the physical, chemical, and biological features of the ocean and limnology the equivalent for freshwater bodies. In situ sensors play a vital role in the monitoring of these parameters. Different approaches can be used from the macro to the micro spatial scale of detection (see Figure 1-1). Satellite and aircraft remote sensing cover large expanses (100s of 1000s of km) [10]. Ships of opportunity and research vessels sampling over selected wide areas [11] used in addition to autonomous underwater vehicles (AUVs) with built in sampling and sensing tools to cover moderate areas (1000s of km at 1000s of m depth) [12]. In situ sensors are then utilised for localised and high resolution monitoring of key positions of interest (millimetres to meters) [13]. Each method plays an intrinsic role in providing data to understand the marine and freshwater environments holistically by tracking different parameter of interest at different spatial scales and over different temporal changes in conditions (seconds to decades).

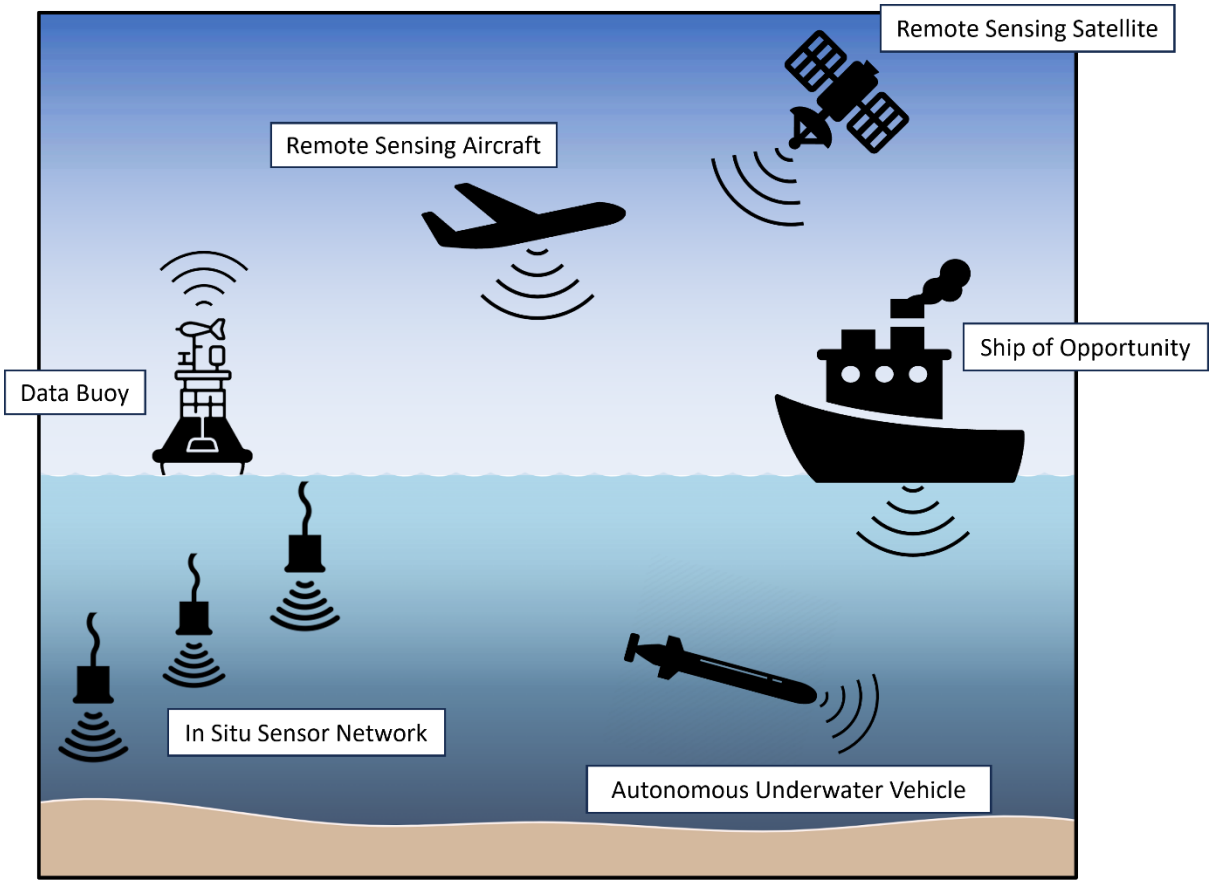

Figure 1-1 Diagram showing currently used methods and technologies at different spatial and temporal scales for monitoring of the world's aquatic environments.

The part that in situ sensors play is to obtain the localised and calibrated information on a target parameter of measurement while being in direct contact with the environmental medium. They are instrumental for oceanographical and limnological monitoring. The incorporation of individual sensors into a larger network allows for larger areas to be monitoring at high spatial and temporal resolutions. Sensor networks are providing, to date, the most promising approach for collecting temporally and vertically resolved observations of biogeochemical processes throughout the ocean [14], real-time data for decision support in coastal areas [15,16], validation of space- and air-borne observations [17] and high frequency data for forecasting models, internet of things (IoT) and big data analytics [18].

In response to the deterioration of the oceans, regional to global scale in situ ocean observing networks have been established to provide better understanding of ocean dynamics which are complex. Examples of such organisations include the Global Ocean Observing System (GOOS) [19], the Ocean Observatories Initiative (OOI) [20], the Export Processes in the Ocean from Remote Sensing (EXPORTS) [21], the Biogeochemical-Argo(BGC-Argo)

program [22] and the U.S Integrated Ocean Observing System(IOOS) [23]. There are many legislative measures for coastal areas currently in place to limit the transport of anthropogenic pollutants to the marine environment such as the Water Frame Directive (WFD, 2000/60/EC) which has a goal of achieving 'good ecological status' [24] and Marine Strategy Framework Directive (MSFD, 2008/56/EC) aiming to achieve 'good environmental status of the EU's marine waters'[25]. With an ever-increasing demand for data on the status of waterbodies by organisations and governments the need for in situ sensor networks is growing.

The next section is a review of state of the art in situ sensors which provides up-to-date information on available in situ technologies that are available, either at the laboratory and prototype stages or commercially, and are suitable for deployment in the aquatic environment. This is then followed by a review of the theory of sensing systems operations and measurement approaches for target analytes along with the investigation of sensing components and their functionality. Finally, a review of the environmental challenges faced by in situ sensors deployed in the marine environment is conducted. This is combined with an investigation of suitable materials, manufacturing methods and antifouling strategies to produce a robust sensor design.

1.1 Review of Current State of the Art In situ Sensors

Sensors operating in the aquatic environments, particularly in the marine environment, are exposed to extreme conditions and must endure long deployments to be cost effective. To withstand the harsh marine environment, sensors have to be robust, power efficient and equipped with suitable antifouling protection [26]. There are many different types of in situ sensors designed to measurement different parameters and multiple parameters simultaneously of the waterbody. The majority of in situ sensors and instruments can be divided into two main categories: sample draw and interface.

The first category of sample drawing sensors operate by transferring an external environmental sample to the internal processing and detection systems within the sensor typically using a pump system. Internalising the measurement steps within the body and using microfluidic technology for wet chemistry sample handling ensures that conditions are stable and controlled for good analytical performance. Sample draw systems fill a gap

in the detection of species and analytes which are challenging for interface-based sensors to detect. For example, certain nutrients, faecal indicator bacterial, eDNA and algal toxins which all require exact chemistry or biological steps to be quantified. Although sample draw sensors provide better accuracy, precision, and resolution they are more complicated in terms of functionality (pumping, filtration, heating systems), require more bulky components than interface-based systems and are more expensive to fabricate. Submersible sensors exist at different TRLs for phosphate [27–29] nitrate [30,31], silicate [32], ammonium and iron [33], nitrate and sulfide [30], and iron and sulfide [34] with more advanced systems performing electrochemical desalination and passive acidification to remove interfering ions [35]. Figure 1-2 shows some examples of commercial and research developed wet based chemistry sensors.

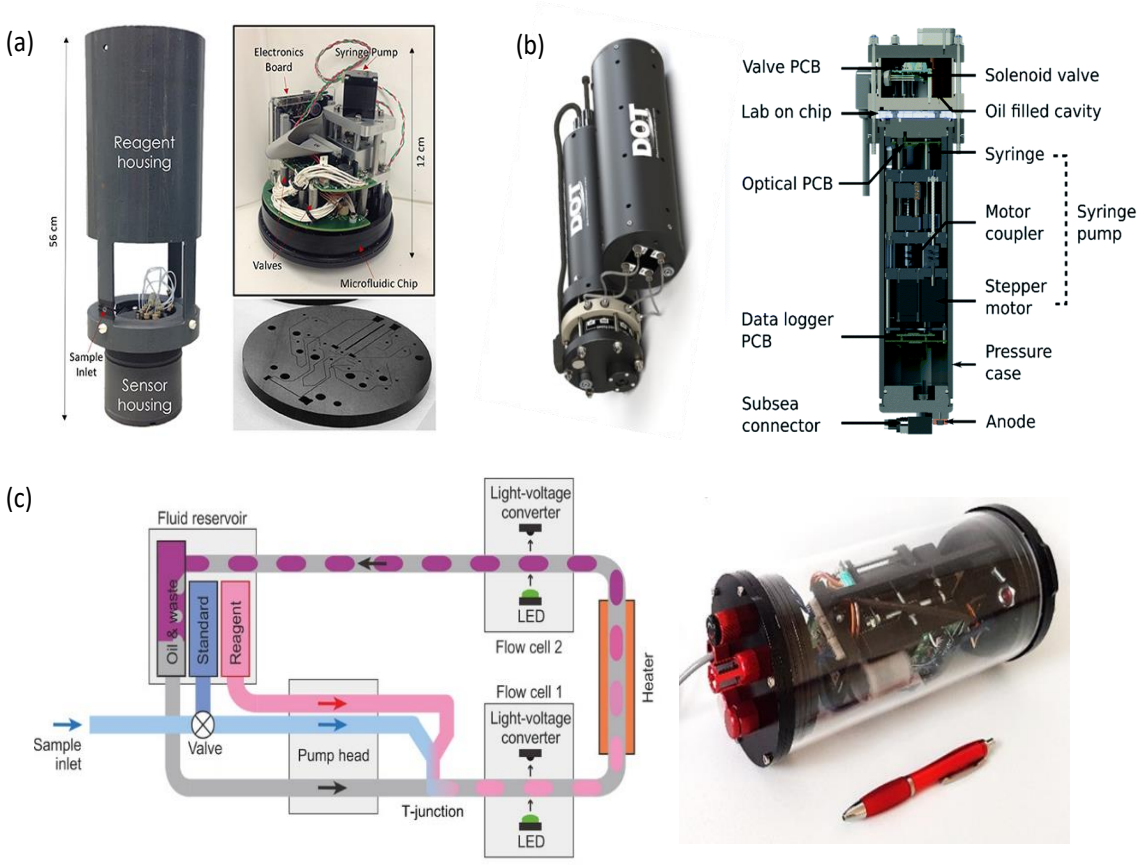

Figure 1-2 Wet-chemistry based sensors; (a) Lab-On-Chip phosphate sensor; (Left) A fully assembled sensor with reagent housing. (Top-right) A LOC sensor prior to placement in the watertight sensor housing. (Bottom) One of the PMMA layers of a phosphate Lab-On-Chip (Sensor 1) showing the micro milled microfluidic channels prior to sealing with the other layers of the microfluidic chip phosphate-based sensors. (b) (Left) Phosphate sensor and reagent canister; (Right) cross section view of the interior of the phosphate sensor. Fluid is pulled and directed into the lab-on-chip by stepper motor-actuated syringes and active solenoid valves. Valve control, data logging and optical control are handled using three separate electronics boards. (c) Nitrate and nitrite sensor. (Left) Schematic showing the fluidics of the sensor and illustrating the mode of operation; (Right) Finished sensor incorporating fluidics, heater, flow cells, and control electronics.

The second category of sensors operate at the interface with the environment to convert the physical, chemical, or biological parameter into an electrical signal which can in turn be measured electrically by circuitry and converted to quantifiable data. Physical and chemical-based sensors units produce a response to a physical change (e.g., change in temperature) or chemical change of concentration in the water medium. Other physical parameters that are commonly measured in waterbodies are conductivity, oxygen levels, pH, and carbon dioxide levels. Multiple physical parameters are frequently required to be measured together. An example of a common multiparameter combination sold commercially is a conductivity, temperature, and depth (CTD) profiling instrument, additional sensors can be included with a CTD to measure auxiliary parameter such as chlorophyll (Chl), turbidity, pH, etc., depending on which specific characteristics are applicable to the environment of interest.

Optical sensors function by introducing an optical signal as a stimulus and detecting the perceived change caused by the target parameter on the stimulus light signal which can be measured by a photodetector and converted to an electrical signal to be analysed. The primary advantage optical sensors have is the simplicity of their principle of measurement which involves the interaction of ultraviolet (UV), the visible spectrum (VIS) and infrared (IR) with the water column or sample being measured. Optical sensors utilize three modes of detection, absorption, fluorescence, and scatter to detect a wide variety of parameters. The optical sensing approach has a broad range of application for the detection of physical, chemical, and biological parameters for example, turbidity which represents the clarity of the water, can be measured optically by a detector by measuring the amount of light being scattered or the level of transmission in the water column by suspended particles. Biological matter can be detected by measuring a fluorescence signal which is emitted by cause of an excitation wavelength acting upon the matter. Measuring the absorption derived from the light attenuation of certain wavelengths passing through the water column from a light source can be used to determine the presence and concentration of target molecules.

The most versatile commercial sensors for environmental monitoring are the multi-parameter sondes which bring together a plethora of different probe options in a modular plug and play format allowing for a wide expanse of customisable setups for the detection of a suite of parameters in a single sensing platform. The base probe on a sonde tends to be

the CTD probe while a wide range of additional optical probes to measure parameters such as turbidity or Chl can be added by the user based on the application. The most advanced sondes commercially available offer the option of adding up to 7 probes with available plug-in ports and can monitor all parameters simultaneously.

There is a clear trend evident from sensor manufacturers and research prototypes towards smaller, smarter, and cheaper sensors with three main characteristics: miniaturisation, use of lower price materials and use of innovative approaches for sensor design, integration, and signal transduction. An example of the lowering of sensor costs is a traditional CTD sensor which would cost in the region of $10k can now be replaced with a new MEMS-based CTD which has a 10 fold reduction in cost while another example would be a typical DO optode which would also cost in the region of $10k can be repackaged using lower cost materials and electronics to reduce the cost by between 5 and 10 fold [36].

There are two primary categories noticeable in the current state of in situ sensors manufacturers. Manufacturers of high specification instrumentation (i.e., YSI, a Xylem brand, Yellow Springs, Ohio, USA and Sea-Bird Scientific, Bellevue, Washington, USA) place the requirements of the end-user at the centre of product design and provide solutions for an extended range of applications. Such sensors are the result of many years of experience, in-house know-how and research and continuous engagement with end-users. The performance of such sensors is in general excellent and takes precedent over cost. The second category is that of the emergence of lower cost- optical based sensors. Significant progress has been made in recent years to advance of optical and electronic components, reducing their size and cost due to better manufacturing methods. This second category of sensor is more suitable to be built and deployed at scale in sensor networks to cover greater areas and provide high spatial and temporal 3D resolutions of the waterbody.

Table 1-1 gives some of the interface sensors single and multiparameter optical instrumentation that are currently available commercially.

There is a clear trend evident from sensor manufacturers and research prototypes towards smaller, smarter, and cheaper sensors with three main characteristics: miniaturisation, use of lower price materials and use of innovative approaches for sensor design, integration, and signal transduction. An example of the lowering of sensor costs is a traditional CTD sensor which would cost in the region of $10k can now be replaced with a new MEMS-based CTD which has a 10 fold reduction in cost while another example would be a typical DO optode which would also cost in the region of $10k can be repackaged using lower cost materials and electronics to reduce the cost by between 5 and 10 fold [36].

There are two primary categories noticeable in the current state of in situ sensors manufacturers. Manufacturers of high specification instrumentation (i.e., YSI, a Xylem brand, Yellow Springs, Ohio, USA and Sea-Bird Scientific, Bellevue, Washington, USA) place the requirements of the end-user at the centre of product design and provide solutions for an extended range of applications. Such sensors are the result of many years of experience, in-house know-how and research and continuous engagement with end-users. The performance of such sensors is in general excellent and takes precedent over cost. The second category is that of the emergence of lower cost- optical based sensors. Significant progress has been made in recent years to advance of optical and electronic components, reducing their size and cost due to better manufacturing methods. This second category of sensor is more suitable to be built and deployed at scale in sensor networks to cover greater areas and provide high spatial and temporal 3D resolutions of the waterbody.

Table 1-1 Commercially available in situ water quality sensors and instrumentation

	Sensor	Parameter	Manufacturer	Reference
Single/multi wavelength absorption, scatter, and fluorescence probes	Spectro::lyser V3	Turbidity, *Chl-a*, TOC, DOC, BOD, Temp	S::can GmbH, Vienna, Austria	https://www.s-can.at/products
	Nitratax Plus SC	NO_3^-	Hack Lange GmbH, Düsseldorf, Germany	https://de.hach.com/
	SUNA V2	NO_3^-	Sea-Bird Scientific, WA, USA	https://www.seabird.com/
	ECO Triplet	*Chl-a*, *f*DOM, Rho, PC, PE		
	SeaOWL UV-A	Crude oil, *Chl-a*		
	ECO NTU, ECO BB9	Turb, OBS		
	VLux series	BGA (PC/PE), Try, *Chl-a*, *b*, *c*, Turb, fDOM, BTEX, PAH,	Chelsea Technologies, Surrey, UK	https://chelsea.co.uk/
	EnviroFLU, matrixFlu VIS, nanoFLU, microFlu V2	*Chl-a*, PC, Rho, CDOM, PAH, Try, PC.	TriOS Mess- und Datentechnik GmbH, Rastede, Germany	https://www.trios.de/en/index.php
	TTurb,	Turb		
	NICO, LISA, OPUS	NO_3^- , NO_2^-, SAC254, TOC etc		
	OBS501	Turb	Campbell Scientific, Logan, UT, USA	https://www.campbellsci.com/
	C3, CP6	T,D, Try, Rho, fDOM, crude and fine oil, PC,PE, *Chl-a* ,	Turner Designs, CA, USA	https://www.turnerdesigns.com/
	PhytoFind	Algae speciation		
	Hyperion series	Turb, *Chl-a*, PC, Rho	Valeport Ltd, Devon, UK	https://www.valeport.co.uk/
	Algal Torch	BGA, *Chl-a*	Bbe Moldaenke GmbH, Germany	https://www.bbe-moldaenke.de/en/
	FluorProbe	Algae speciation, *Chl-a*		
	Turbidity sensor 4296	Turb	Aanderaa, Bergen, Norway	https://www.aanderaa.com/
	The Pixie™	*Chl-a*, PC, PE, fDOM	Dartmounth Ocean, Technologies Inc, Canda	https://dartmouthocean.com/
Multiparameter sondes	YSI EXO-series	C, T, D, pH, ORP, fDOM, BGA, Rho, NO_3^- (optical), *Chl-a*, DO, Turb, NH_4^+	YSI, a Xylem brand, Yellow Springs, OH, USA	https://www.ysi.com
	Sea-Bird HydroCAT-EP	C, T, D, pH, Turb, *Chl-a*, DO	Sea-Bird Scientific, WA, USA	https://www.seabird.com/
	DS5X, HL7	C, T, D, pH, ORP, BGA, Rho, NO_3^- (ISE), *Chl-a*, DO, Turb	Hydrolab, Loveland, CO, USA	https://www.hydrolab.com/
	Eureka Trimeter™	C, T, D, pH, OPR, DO, *Chl-a*, BGA, Rho, Crude & refined oil	Eureka, TX, USA	http://rshydro.ie/eureka-m-20.html
	Proteus	C, T, D, pH, OPR, DO, Crude & refined oil, Try, CDOM	Proteus Instruments Ltd, Worcestershire, UK	https://www.proteus-instruments.com/
	MIDAS CDT+	C, T, D, pH, OPR, DO, *Chl-a*	Valeport Ltd, Devon, UK	https://www.valeport.co.uk/

BGA-blue green algae; Chl-a,b,c- Chlorophyll a,a,b,c; C-conductivity, T-temperature, D-depth (derived from pressure); ORP-oxidation reduction potential; DO – dissolved oxygen, Try – tryptophan, Rho-Rhodamine; CDOM-chromophoric dissolved organic matter; fDOM- fluorescent dissolved organic matter; Turb –turbidity; PC-phycocyanin; PE- phycoerythrin; TOC-total organic carbon; PAH-polycyclic aromatic hydrocarbons; BTEX-benzene, toluene, ethylbenzene and xylene; OBS-optical back scattering, multiple angles; pCO_2 – partial CO_2 pressure

1.2 **Identifying Target Analytes**

The parameters that the sensor will measure are defined by commercial opportunity which in turn is driven by key environmental directives on water quality and monitoring of waterbody health. In Europe, there are frameworks in place such as the Water Framework Directive [37], the Bathing Water Directive [38], the Marine Strategy Framework Directive[25] and the Urban Wastewater Treatment Directive [39] which all acknowledge the marine environment and water in general as heritages which "must be protected, preserved and where practical, restored with the ultimate aim of maintaining biodiversity and providing diverse dynamic oceans and seas which are clean, healthy and productive [25]".

There are many parameters and water quality monitoring requirements outlined in the directives. The Water Framework Directive details how surface waterbodies are assigned an ecological status class of which there are five (High, Good, Moderate, Poor, and Bad). This status is ascertained by the combination of several key biological and physio-chemical parameters. A set of parameters which can be measured optically are chlorophyll (Chl), turbidity, dissolved organic matter (DOM) and oil. This outlines the end goal of the sensor design to be able to target each of these parameters with one single sensing tool using optical measuring approaches. The monitoring of each of these analytes gives a holistic insight into the state of the waters the sensor in placed in highlighting key changes in the environment over different temporal ranges.

The presence of Chl gives an insight into the abundance or lack of dissolved nutrients (particularly of phosphorus and nitrogen) [40,41], dissolved oxygen [42], and state of aquatic ecosystems [43]. Chl measurements can be used as a proxy for phytoplankton biomass [44] which can be related to the state of algal biomass like net primary production [45] and harmful algal blooms (HABs) [46]. Chl can be measured optically by the absorption of particular wavelengths [47] or by the fluorescence signal it emits at certain excitation wavelengths [48].

The measurement of turbidity can provide important data on the health of the water body and the impact human activity has made on it. Turbidity is defined as the reduction in clarity of the water due to light being absorbed, reflected or scattered [49]. Biological turbidity can

indicate the number of microorganisms present in the water column, organisms such as bacteria [50] or species such as phytoplankton which along with Chl measurements can be used to monitor their populations and indicate a pollution event such as agricultural runoff with spikes in population growth. An increase in turbidity can also be caused by dangerous compounds entering the water which results in cloudy water. These compounds can be released by human activity such as water treatments plants discharging, agricultural run off or wastewater from industrial facilities which can damage the environment and ecosystems of the water body. The most common cause of turbidity is physical particles suspended in the water column, suspended sediment concentration (SSC) or total suspended solids (TSS). The suspended solids and sediments can consist of clay or silt which has been disturbed by an external force from the waterbed or from the land. An increase of physical turbidity can indicate disturbances from either human activity such as dredging [51,52] or natural causes such as a storm event [53,54] or run off from the land [55]. The optical properties of turbidity can be measured using both transmittance and scatter [56].

DOM can be found in all-natural aquatic environments and consists of a heterogeneous mixture of decomposed products of plant material, bacteria, and algae [57,58]. There are two main categories of DOM which are: allochthonous derived from terrestrial sources and autochthonous which is derived from within the aquatic ecosystem itself (primary production and processes of decomposition) [57]. The measurement of the amount and composition of DOM precent in the aquatic environment is significant in indicating the health of the ecosystem as it is a major source of bioavailable organic carbon [59]. DOM is a complex soluble organic compound [60] which varies in reactivity [61], ecological role and the important role it plays in nutrient transport [62] and aquatic food web dynamics [63]. The amount of DOM present in the water can also affect the clarity of the water providing protection to organisms from harmful irradiation such as zooplankton [64]. However, in terms of drinking water, the presence of DOM in the water disinfection process can react to form by-products which are harmful to human health [65]. DOM's optical properties of absorption and fluorescence can be used to measure its composition [66].

Oil and hydrocarbon-based pollutants can have significant detrimental effects on the marine environment [67–69]. It is important to respond to an oil spill quickly to reduce the impact on the ecosystem [70,71]. Oil spills are most commonly monitored using remote sensing

methods as outlined in this review by Fingas and Brown, (2018) [72]. However, there are limitations to the detection of oil using remote sensing [72] as they can be difficult to detect from air or satellite. Small pollution oil pollution events can be missed, in rough seas the oil can mix below the surface without a visible slick on the surface [73]. In situ optical detectors can be used in conjunction with remote sensing to fill the gaps in oil detection in marine and coastal environments [73–75]. In sea water, petroleum hydrocarbon compounds in the water column are dispersed as small droplets or dissolved in soluble form [76]. The light aromatic hydrocarbon compounds are the most soluble and are found in crude and refined oil products [77]. These dissolved aromatic hydrocarbons can be detected by an optical sensor [78,79] and used as a proxy for oil detection [80]. Aromatic hydrocarbons can be detected using fluorescence due to a benzene ring structure allowing for surface and subsurface detection [81].

1.3 Optical Detection Methods

In situ optical sensors measure target parameters in the water column by their optical properties. There are two categories of optical properties which can be measured which are inherent optical properties (IOPs) and apparent optical properties (AOPs) [82,83]. The properties differ as IOPs are the optical properties of pure water [84] while AOPs are the optical properties of water including the presence of particles, dissolved organic matter or other materials [83]. IOPs estimate the concentration of particles or dissolved matter in the water by measuring scatter and absorption of light by the water itself independent of the particles or matter present in the water [82]. Using this method, the spectral attenuation coefficient of water can be used to estimate concentrations of particles or dissolved matter which absorb or scatter the light at different wavelengths. Another coefficient of water is the backscatter coefficient which can be used to estimate the concentration of particles that scatter light by detecting the scattered light at various angles relative to a light source. For the detection the presence of CDOM (chromophoric dissolved organic matter) or other absorbing matter in the water column the absorption coefficient of water can be used [84].

To measure the concentrations of particles, dissolved matter or other target parameters directly, AOPs are used as the presence of the target analyte modifies the optical properties of the water can then be measured while also considering the IOPs of the water [83]. The properties which can be measured are light absorbed by the presence of particles such a DOM, light reflected or scattered by particles such as suspended sediment or the fluorescence of matter such as Chl in the water [83,85]. For the calibration of AOP measuring sensors the IOPs of water must be considered. By using the IOPs of water as the baseline, under controlled laboratory conditions an AOP sensors can be calibrated for measurement of the concentration of target analytes in natural waters by accounting for the scatter and absorption properties of the water itself [86].

1.3.1 Transmittance and Absorption

Transmittance is the measurement of the attenuation of light having passed through a sample. Absorption is the measurement of the light absorbed and converted to energy at a specific wavelength, reduced light intensity can also be caused by scattering effects of light due to physical particles in the sample [87]. The measurement of transmittance can be used

to measure turbidity as it can be related to the number of suspended particles in the sample providing the wavelength used as the incident of light is not absorbed by the sample [88,89]. Turbidimetry is the measurement of turbidity by this process using a light source of known intensity and infrared (IR) wavelength emission. IR wavelengths are used to avoid interference from absorbing compounds such as DOM or Chl in the water column [88]. The International Standard ISO 7027–Water Quality–Determination of Turbidity stipulates, that the light source must have a wavelength of 860 nm and spectral bandwidth of no more than 60 nm for the measurement of turbidity [89]. To measure turbidity using transmittance the detector must be placed directly in line with the light source allowing it to measure the reduction of light intensity caused by the level of turbidity in the sample as seen in Figure 1-3.

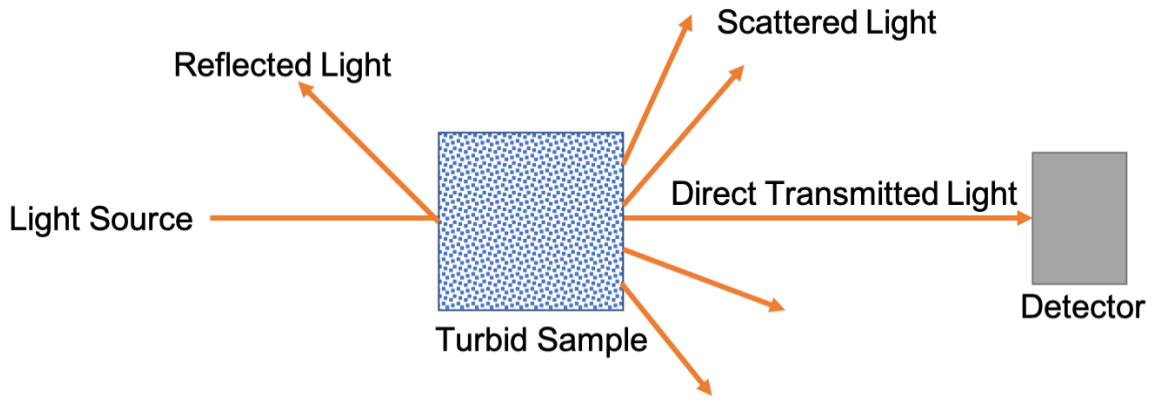

Figure 1-3 Diagram working principle of optical transmission measurement with light source entering turbid sample and detector measuring light directly transmitted through the sample.

The measurement of absorption is a commonly used optical measurement technique used in many scientific fields for ascertaining the concentration of a target analyte in a sample [90–92]. It is the process of energy transfer of light in a medium when photons of a certain wavelength from a light source are absorbed by electrons of a target molecule in the medium while the light passes through the sample. The resulting attenuation of light intensity having passed through the sample can be measured and compared to the initial light intensity entering to sample. The change in initial intensity of incident of light (I_o) and the resulting intensity of transmitted light (I) having passed through the sample as transmittance (T) and is given by Equation 1-1

$$T = \frac{I}{I_o} \qquad 1\text{-}1$$

There is a logarithmic relationship between transmittance and absorbance (A). This relationship is given by the Equation 1-2

$$A = -log_{10}T \qquad 1\text{-}2$$

A linear relationship between absorbance and concentration (c) of a target analyte can be derived using the Beer-Lambert law [93] which takes into account the molar absorptivity constant (ε) which is sample dependent and outlines how strong an absorber a sample is a specific wavelength. The equation also considers the path length (l) which is the distance the light travels through the sample before reaching the detector. The longer the path length the more photons which will be absorbed by the sample. The Beer-Lambert equation (Equation 1-3) can be seen below:

$$A = \varepsilon cl \qquad 1\text{-}3$$

Using the derived linear relationship between absorbance and concentration a calibration curve can be created for a particular target analyte through experimentation using a series of known standard solutions. If experimental conditions are kept constant, the slope of the linear plotted calibration curve can be used to calculate unknown concentrations of the target analyte. Figure 1-4 gives an overview of the working principle used to optically measure transmittance of light through a sample with the sample and detector positioned directly in line with the incident light.

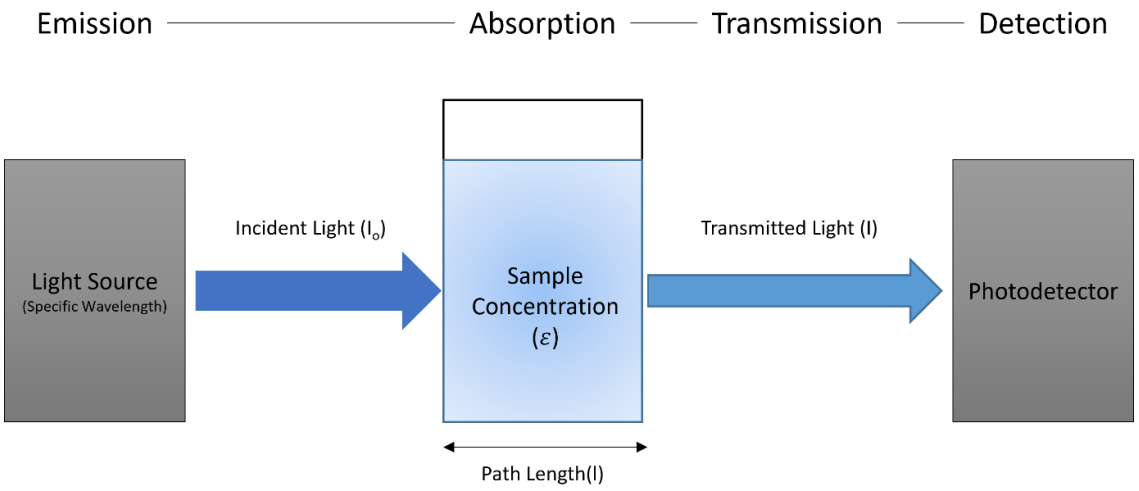

Figure 1-4 Diagram of working principle of optical absorption measurement.

As discussed in Section 1.2, many target analytes of interest in the marine environment can be detected using absorption measurements. Figure 1-5 shows the absorbance spectra of extracted Chl types a and b as well as other organic molecules which indicate the presence of biomaterial (carotene and anthocyanin) in the water column. From Figure 1-5 chlorophyll a (Chl-a) has the highest absorbance of the organic compounds with peak absorbance (λ_{max}) at 428 nm and a secondary peak at 660 nm. For a detector, a light source with emitted wavelength in the region of 428 nm would be the most effective for the detection of Chl-a through absorption.

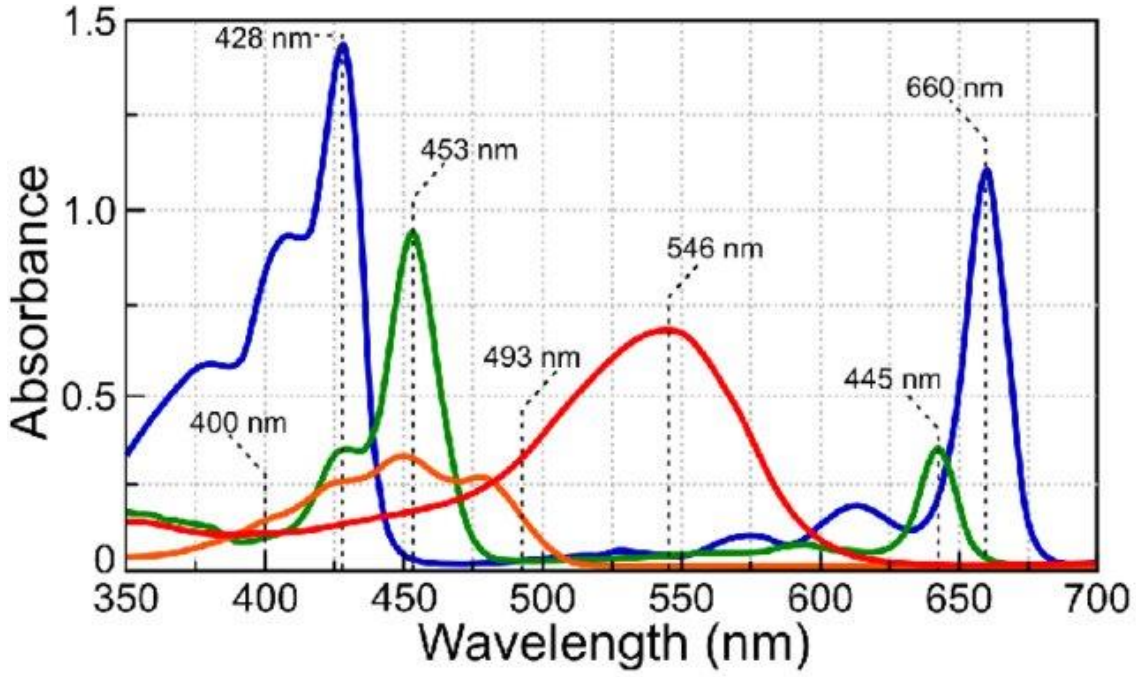

Figure 1-5 Absorption spectra of freshly isolated chlorophyll a (blue), chlorophyll b (green), β-carotene (orange), and anthocyanin with pH 1.0 (red) adapted from a figure by Barragán Campos et al. [94].

DOM, specifically CDOM can be detected using the absorption method [95]. As seen in Figure 1-6, as an example, with CDOM levels measured at different depths in the Atlantic Ocean. CDOM absorbs UV wavelengths very strongly [96] which can be used for the purpose of detection and this study found a distinct shoulder characteristic in the absorption between 410-415 nm using a light source [60,97].

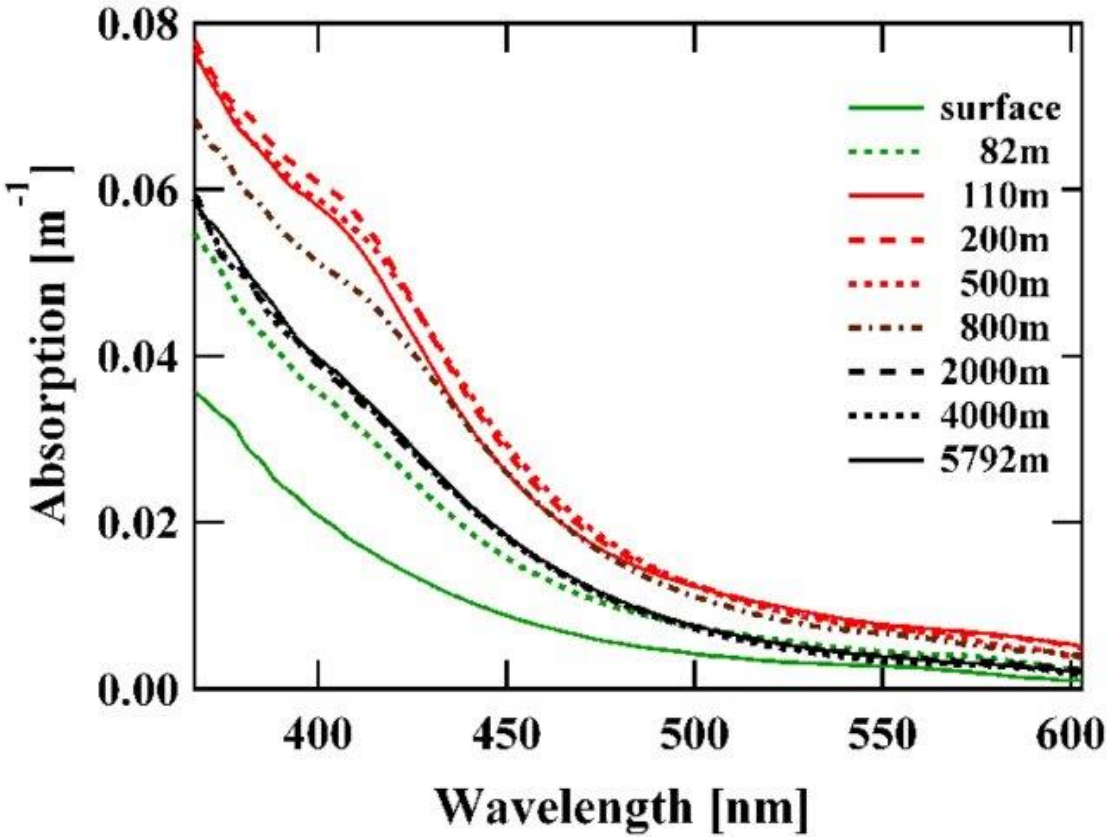

Figure 1-6 Light absorption of CDOM in the tropical Atlantic Ocean sea water samples at different depths, November 2005, the study was conducted by Rottgers and Koch [97].

1.3.2 Scatter

The clarity or turbidity of the water column can be measured based on the level of scattering of light from particles [88,98]. A detector positioned at an angle to the incident of light can measure the light intensity of the scattered light and correlate the signal with the turbidity of the water column [98]. This represents suspended sediment (SSC) or total suspended solids (TSS) [88]. The direction and concentration of light scatters depends on the particle size of the solutes present in the fluid as seen in Figure 1-7 [99].

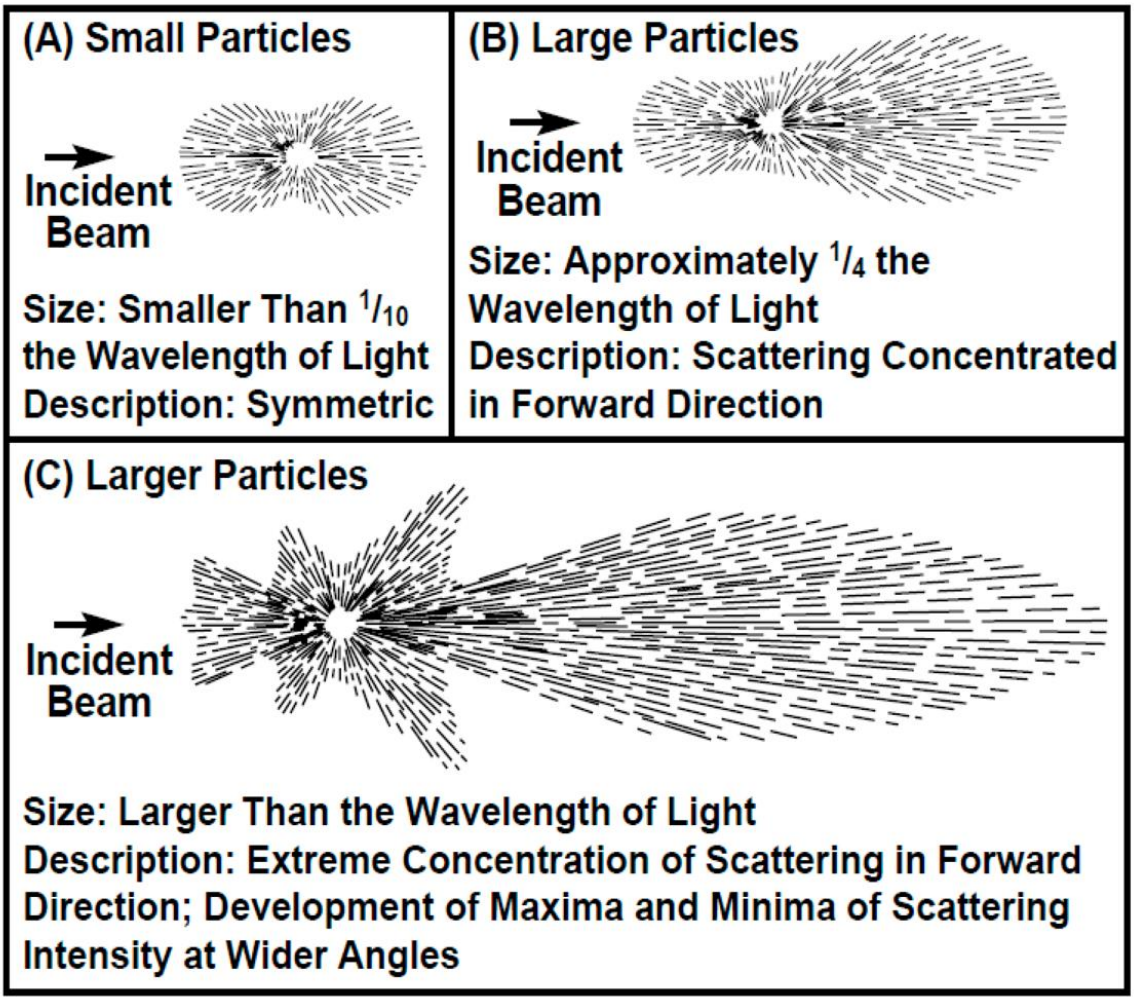

Figure 1-7 Diagram of effect of particle size on light scatter direction relative to the wavelength of the incident of light. (a) shows a symmetrical scattering of the light with particles smaller than 1/10 of the wavelength. (b) shows an increase concentration of scattered light in the forward direction with larger particles ¼ the size of the wavelength. (c) shows an extreme concentration of scattering in the forward direction when particles are larger than the wavelength [100].

The standard position of the detector for the measurement of turbidity in commercial optical sensors is at the 90 degree position as outlined in both ISO7027 [89] and EPA method 180.1 [101]. Additional detectors can be used in conjunction to the side scatter detector to improve turbidity measurement accuracy and limit the effect of particle size, colour and stray light from the light source, these detectors can be positioned in the forward or back scatter positions [99]. However, the position of the forward scatter detector can lead to measurement errors due to interference from transmitted light from the light source caused by its proximity to the 0 degree point of the incident of light [102]. The use of a detector positioned between 0 and 90 degrees relative to the incident of light can be used to measure forward scatter for lower turbidity levels to improve accuracy due to the lower sample volume the light must

pass through and is more effective for the detection of larger particles as can be seen in the higher concentration of forward light caused by larger particles in Figure 1-7c.

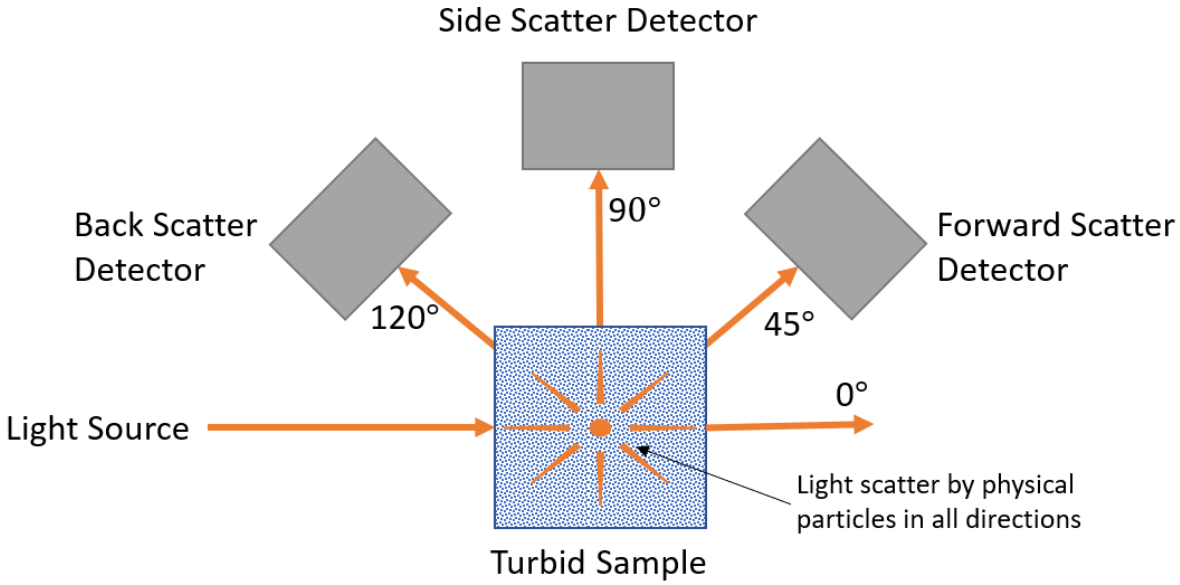

Figure 1-8 Diagram of the working principle of the measurement of scattered light through a turbid sample.

A detector positioned between 90 and 180 degrees in the backscatter position can be used for higher turbidity levels due to the higher sample volume the light must pass through [49]. The greatest intensity of light in the backscatter position for seawater is found to be at the 120 degree angle [103]. However, another study by Maffione and Dana [104] shows 140 degrees to be the highest point of light intensity. The wavelength spectrum emission of the light source used in most commercial turbidimeters are in the infrared (IR) spectrum. The advantage of using a light source with IR wavelength over UV or VIS spectrums emissions is that IR is less affected by colour or turbidity of a sample. The IR region is less lightly to be absorbed by organic matter and is also less affected by ambient light (400-700 nm). Additionally, IR light can penetrate the water column further than lower wavelengths allowing for a higher limit of detection. ISO7027 specifies for the measurement of turbidity that 860 nm wavelength be used while a range of 780 nm to 950 nm is acceptable depending on the application.

1.3.3 **Fluorescence**

Chemical species most commonly absorb shorter wavelengths of light and undergo a radiative process which results in a longer wavelength of light being emitted as fluorescence [105]. The fluorescent molecule absorbs a photon of light and in turn is excited to a higher energy state. The molecule then relaxes quickly, returning to its ground state. A photon of light is emitted as the molecule returns to its ground state at a longer wavelength than the photon which was absorbed. This difference in wavelength between the absorbed photon and the emitted wavelength is known as Stokes shift. The Jablonski diagram (see Figure 1-9) graphically shows this process of the change of energy states of a molecule and how a fluorescence emission is produced.

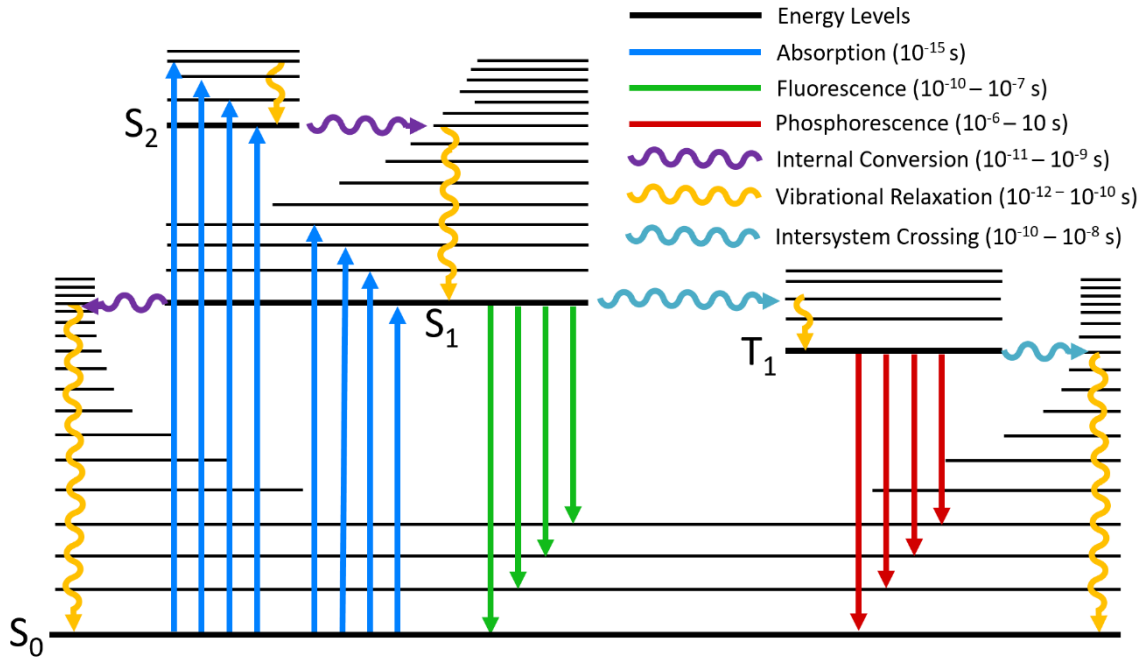

Figure 1-9 Typical Jablonski diagram showing the possible radiative and non-radiative transitions after a molecule has been photoexcited with the quantum energy levels and the corresponding absorption and emission (fluorescence and phosphorescence) processes shown [106].

Fluorescence light is emitted by a molecule isotropically. However, to maximise detection the ideal location of the detector is perpendicular to the incident of light [107]. By placing the detector at 90 degrees to the light source this ensures that the maximum amount of fluorescence is captured while limiting the amount of scattered light from the light source and other ambient light sources. There are two main requirements for fluorescence-based measurement systems each with their own set of challenges to induce and detect

fluorescence accurately. The first requirement is a sufficient light source of the required wavelength and intensity to induce fluorescence in the target fluorescent molecule under investigation. The second is for the detector to have the required sensitivity in the spectral range of the targeted fluorescence signal. This requires a strong light source signal and optical filtration using lenses with a photodetector. Fluorescence measurements allows for the identification and quantification of key analytes based on measuring the signal at the expected wavelength of fluorescence emission of the target analyte when a light source of the excitation wavelength is turned on. Table 1-2 shows the maximum excitation and emission wavelengths of key target analytes based on spectral analytes by previous research characterising the spectral response of the analytes

Table 1-2 Key excitation and emission wavelengths of target analytes based on literature studies on the spectral response.

Target Analyte	Max Excitation Wavelength (nm)	Max Emission Wavelength (nm)	Reference
Chl-a	440	685	[44,48,108]
***f*DOM**	UV Region: 230-275 Blue Region: 300-350 Green Region: 385–420	UV Region: 340 Blue Region: 400-500 Green Region: 470–504	[109,110]
Petroleum Compounds	Petrol: 266 & 355 Diesel/Engine Oil: 266 & 355	Petrol: 320 – 360 Diesel/Engine Oil: 330-395	[111,112]

Chl-a – Chlorophyll a, fDOM – fluorescent dissolved organic matter, UV - ultraviolet

Figure 1-10 shows a fluorescence emission spectrum for both chl-a and chl-b. This is from a study by Israsena Na Ayudhya et al., (2015) [113] characterised the photosynthetic pigments from ferns. This provides a fluorescence spectral emission profile for chl-a and b when excited at 440 nm and 460 nm respectively.

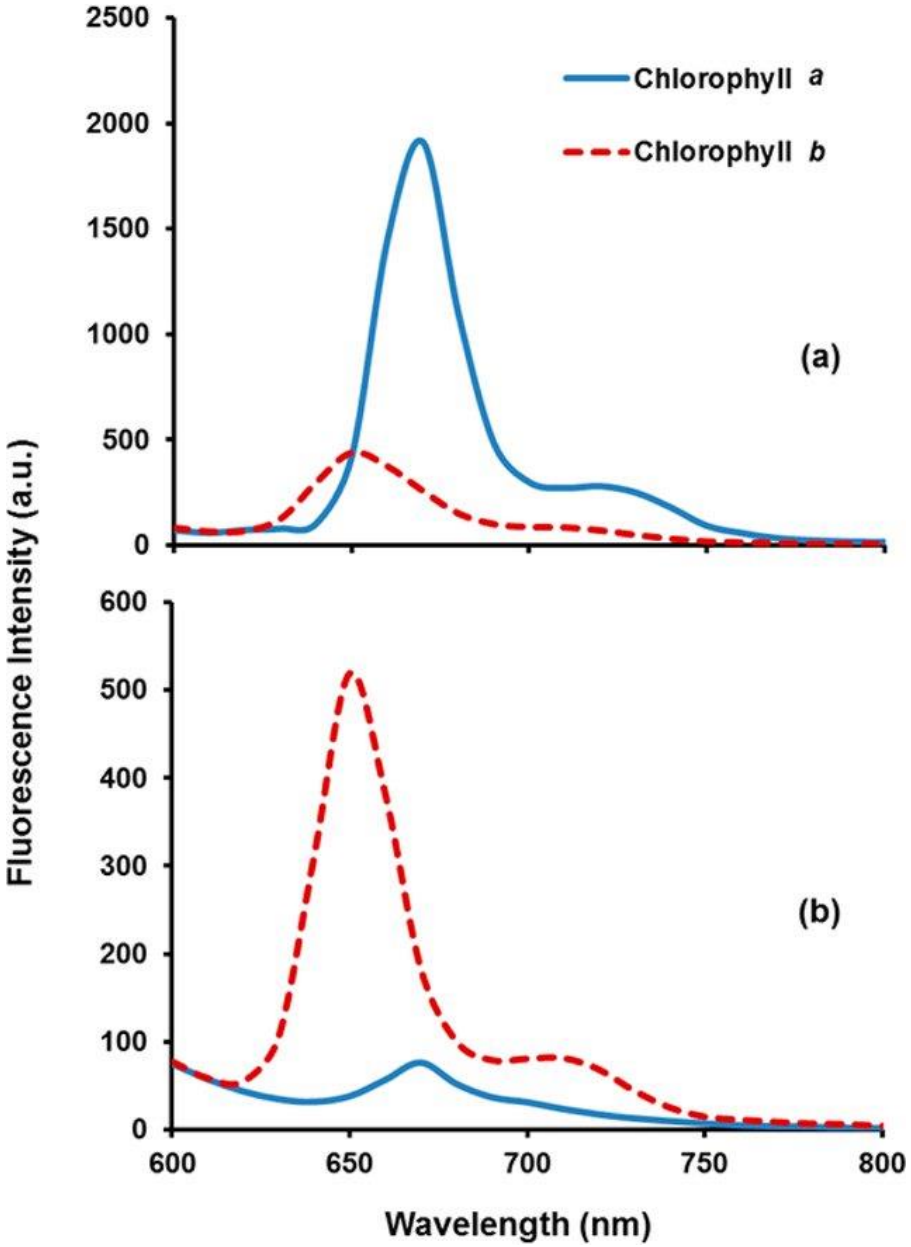

Figure 1-10 Fluorescence spectra of chlorophyll a (Chl-a) (λmax 650 nm) and chlorophyll b (Chl-b) (λmax 670 nm). (a) Fluorescence emission signal from an excitation at 440 nm showing significant fluorescence from Chl-a. (b) Fluorescence emission signal from an excitation at 460 nm showing significant fluorescence from Chl-b. [113]

The results of a study conducted by E.M. Carstea et al., (2020) [109] can be seen in Figure 1-11. This study provides a heat map of the fluorescence excitation and emission spectrums of fDOM (fluorescence dissolved organic matter) types identified in the literature. Key fluorescence regions are highlighted showing the spectral characteristics of dissolved organic matter. The separate regions outline the different potential compositions of the organic matter dissolved in the water column. In the figure, the region marked "T" indicated the UV region ($\lambda_{ex}/\lambda_{em}$ = ~230 & ~275/~340 nm) which can be described as tryptophan-like

with possible microbial contamination. The peak at the region "C" and "C+" in the blue ($\lambda_{ex}/\lambda_{em}$ = 300–350/400–500 nm) and green ($\lambda_{ex}/\lambda_{em}$ = 250 & 385–420/470–504 nm) regions are humic-like or chromophoric DOM. Peaks A ($\lambda_{ex}/\lambda_{em}$ = 260/400–500 nm) and B ($\lambda_{ex}/\lambda_{em}$ = 230 & 275/305 nm) are associated with compounds with two aromatic rings and at least one aromatic ring respectively.

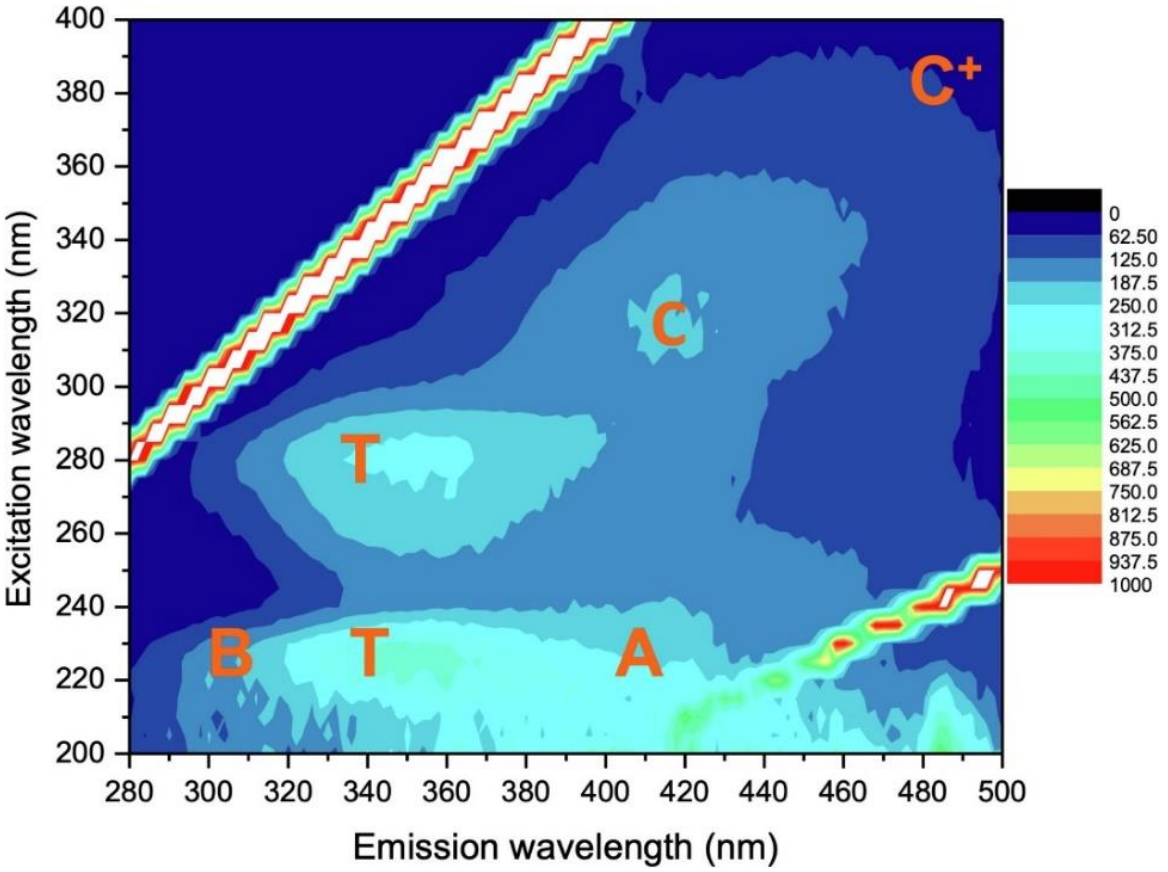

Figure 1-11 Heat map of fluorescence signatures of components of fDOM as identified in literature review by E.M. Carstea et al. [109]. Common fluorescence peaks are highlighted with labels: peak T in UV region, C and C+ in blue and green region, peak B is associated with compounds with a single benzene ring and peak A is a compound with two benzene rings.

The categorisation of fluorescence emission of hydrocarbon compounds is broad with many different compositions effecting the overall spectral characteristics. Figure 1-12 gives a good insight into different hydrocarbon compounds and their fluorescence spectral emissions excitation is provided by a 308 nm laser. Lightly refined hydrocarbon compounds fluoresce strongly in the region of 350 nm while heavier compounds such as diesel and crude oil have weaker fluoresce emission outputs and fluorescence at a longer wavelength. Diesel has a broad spectral emission from 350 nm to 450 nm.

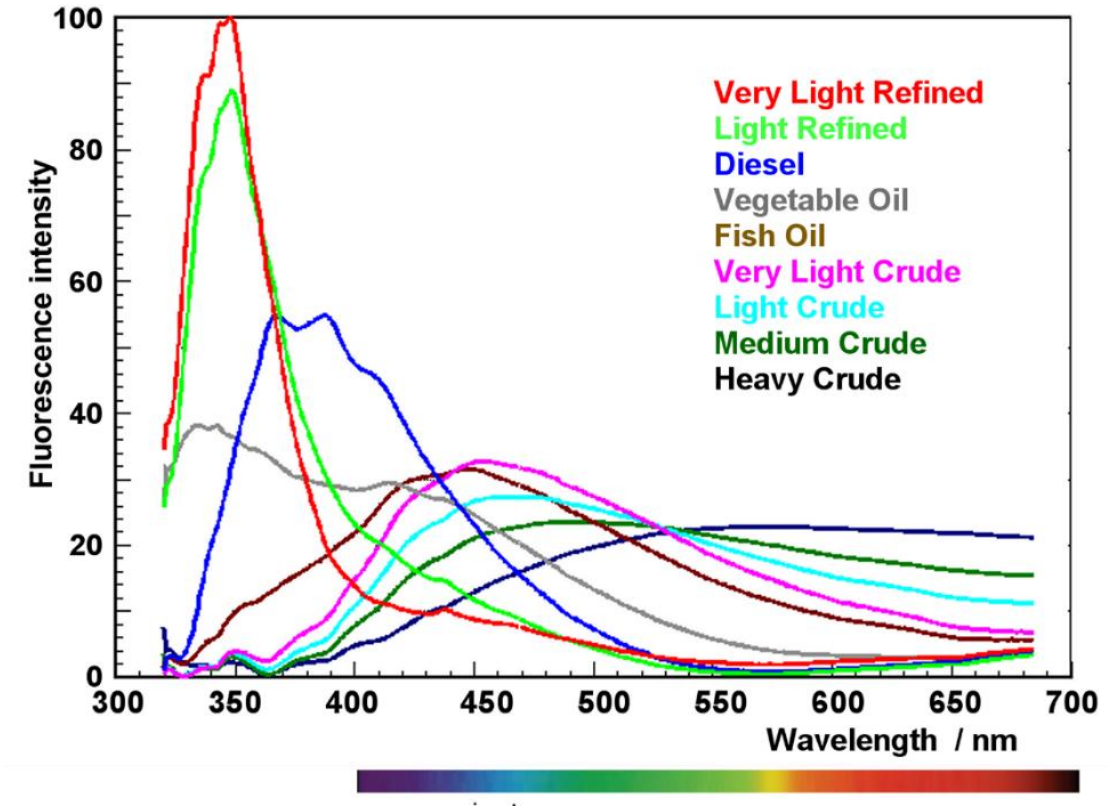

Figure 1-12 Figure from the SEOS EU project [114] gives the fluorescence emission spectral of different oil types excited by a 308nm UV light source. Lighter oil compounds are shown to have a greater fluorescence output signal compared to heavier crude oils.

1.3.4 Temperature

Temperature is a physical property of water which can be measured using a temperature probe or thermistor. Monitoring the change in temperature of the water can give further insight into the condition of the environment along with optical measurements being taken. The temperature of the water can have a direct effect on the optical properties of water and can be used as a correcting factor in optical measurements. For example, with temperature, the density of water changes which in turn alters the refractive index. This change in refractive index can affect accuracy of the measurement by an optical sensor. Additionally, temperature alters the absorption and scatter coefficients of water which can influence the accuracy of the AOP measurements being made by the sensor. The amount of light absorbed by water is temperature dependent. The number of suspended particles in water can also be influenced by the water temperature. The environmental temperature can influence the temperature of the light-related optical elements of the sensor itself. The operation of components such as the light source and the photodetectors are influenced by temperature. Meixia Shi et al., (2022) [115] presents a study on the impact of water temperature on

turbidity values and concludes that with a temperature change greater than 15°C temperature corrections are required and the fundamental factor affecting the detection of turbidity was the temperature of the optical components themselves. In this way, temperature needs to be factored into the calibration of the sensor to account for temperature dependent changes to ensure the measurement of target analytes are accurate.

1.4 Sensing Technology for Optical Detection

As outlined in the previous section, there are key components required by an optical sensor to perform the required measurements. These components include wavelength specific light source or light sources, optical hardware optimise the light source, optical hardware to collect the signal being detected, optical filtration to isolate the signal being detected and photodetectors. These components must then be arranged in a particular geometry with the photodetectors positioned relative to the light source to detect different optical properties of the sample, examples of optical orientations from optical sensor designs can be seen in Figure 1-13.

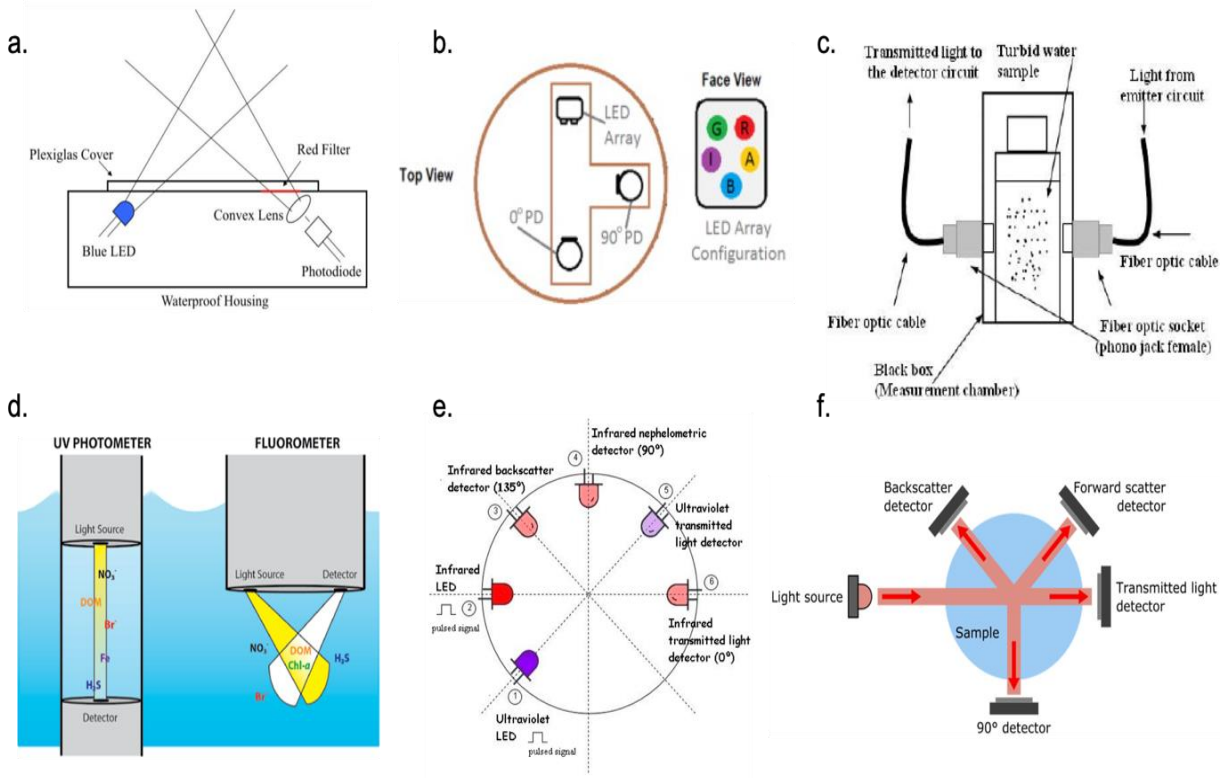

Figure 1-13 Examples of optical orientations and positioning of components for the detection of optical properties and target analytes for water monitoring. (a) A design for Leeuw et al. [116] for measuring the fluorescence emission of phytoplankton using a blue LED , a convex lens and photodiode in a 90 degree orientation. (b) This design uses multiple LEDs of different wavelengths in an LED array configuration for the detection of multiple parameters using two photodiodes positioned at 90 and 0 degrees designed by Heery et al. [117]. (c) Demonstrates the use of fibre optical cables used for the measurement of turbidity in transmittance mode from Omar et al. [98]. (d) Is an example of a UV photometer for measuring the absorption of nutrients and a fluorometer for measuring the fluorescence of nutrients[118]. (e) Is a diagram of a prototype design by Matos et al. [119] for the detection of turbidity and suspended particle matter using multiple LEDs of different wavelength and detectors at different positions for transmittance, scatter and backscatter measurements.) (f) A design from Sullivan et al. [120] on optically measuring turbidity in water with detectors positioned to measure back, forward and side scatter as well as transmitted light.

1.4.1 **Light Source**

In the last decade, light emitting diodes (LEDs) have become cheaper, smaller, and available in a wide spectral emission range (from deep UV (100 nm) to IR (1500 nm)) [121] which has led to an uptake in their use in environmental optical sensors. In Mogensen and Kutter's review [122] they provide a thorough outline of the technological advancements of some LED-based chemical sensing devices including configurations and applications. LEDs are more efficient, brighter and less bulky than alternative light sources, such as argon, xenon, halogen, mercury or incandescent lamps [123,124]. This makes them suitable for use in power limited remote applications such as in situ sensors. LEDs can be used together on the same device to provide multispectral data readings [117,125].

An LED is a solid-state semiconductor allowing unidirectional current flow from the anode to the cathode within a specific voltage range. Two doped materials in the diode form a p-n junction in the diode with the p-side containing additional positive charge (holes) and the n-side having additional negative charge (electrons). Current will flow from the p-side to the n-side when a forward voltage is applied which forces electronics to move from the n to the p side while the holes make the reverse path. The electronics will recombine with the hole as it crosses the depletion layer near the junction and drops from the conduction band to a lower energy level (valence band) which in turn releases energy as a photon (see Figure 1-14). This is a form of electroluminescence as incoherent narrow-spectrum light is emitted. The emitted wavelength of the LED is determined by the junction's materials and the band energy between them [126].

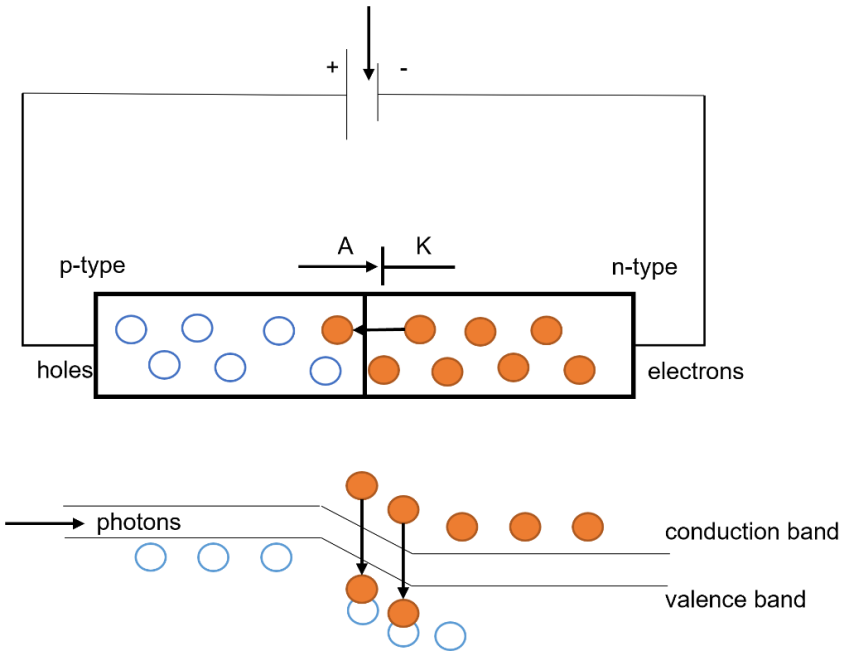

Figure 1-14 Working principle of an LED showing current flow from the p-side to the n-side when a forward voltage is applied.

Epitaxy is the process in which LEDs are manufactured. This involves growing a thin layer of a semiconductor material, such as gallium arsenide, on a substrate material such as silicon. The semiconductor is then doped with impurities to form the p-n junction. Photolithography is a step used to pattern the semiconductor into the desired shape of the chip. A layer of metal is added to form contacts for the anode and cathode. The specific wavelength output obtained by this process is governed by the doping of the semiconductor material, the impurities introduced alter the bandgap energy which in turn, determines the spectral characteristics of the emitted light. For example, the addition of aluminium or indium to gallium arsenide results in a green or yellow light emitted by an LED. Further control of the emitted spectrum of the LED can be introduced using the quantum confinement process. This process involves creating thin layers of the semiconductor material which then restricts the movement of electrons and holes within the material. The confinement alters the bandgap energy of the material resulting in a narrower spectral output for more precise wavelength output.

Light sources with lower wavelength outputs from blue (380 to 490 nm) down to the deep UV ranges (100 to 380 nm) are required by optical detection system to induce fluorescence or measure absorption of target analytes such as Chl, oil or DOM. UV LEDs are also becoming more widely used as a fouling prevention method for marine and water-based

sensors [127]. LEDs are available commercially with these spectral outputs however achieving the lower wavelengths have posed significant manufacturing challenges in the last decade. The first LED with a blue output was only achieved in 1993 by Shuji Nakamura [128], being the last of the primary colours in LEDs to be created.

There are now commercially available LEDs in the UV. They can be separated into three categories: UV-A which has a UV radiation band of between 315 to 380nm, UV-B with a UV radiation band between 280 and 215 nm and UV-C with a UV radiation band of between 100 and 280 nm. The UV emission sources are fabricated by varying doping levels of aluminium gallium indium nitride (AlGaInN) alloy to tune the emission wavelength of the semiconductor (see Figure 1-15) [129]. Blue LEDs have been manufactured using indium gallium nitride (InGaN) [128]. The technology to manufacture these LEDs is advanced and blue LEDs are widely adopted [130]. Commercially they are used for many applications including white LED light sources, LCD displays, optical sensors and medical equipment [130–132]. Semiconductors using AlGaInN are not yet at the level of technological development as InGaN [133]. They suffer from a range of inefficiencies from electrical and optical limitations while also being more expensive to manufacture due to the difficulties of epitaxy process of the required layers [131,135].

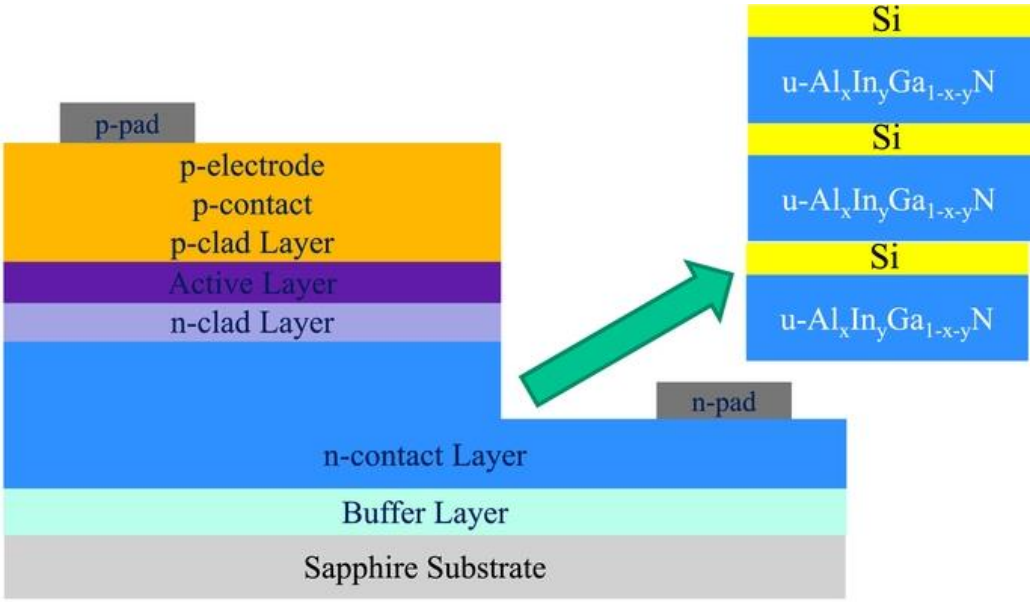

Figure 1-15 A structural diagram of a common UV-LED chip construction highlighting the schematic of silicon (Si) and undoped AlInGaN as created by Yoshihiko Muramoto et al. [129].

LEDs come in two categories of packages, through hole technology (THT) and surface mounted technology (SMT). THT LEDs tend to be larger in size and more expensive when used in a mass-produced product due to difficulties in assembly of components on circuit board. Additional manufacturing steps are required for through hole components which require holes to be drilled and soldering in place. However, devices designed with THT components are characterised as having better interconnection reliability [134]. SMT LEDs are much cheaper, much smaller and lend to automated assembly of printed circuit board making them more suitable to mass production [135].

An LED array is an assembly of LEDs on a single platform which can comprise of multiple different LED packages for a multispectral emission or a single more intense spectral output. The advantage of using a multiple spectral light source are the that a wider range of targets can be detected in a single sensing device [117,136,137]. The smaller size of current LED packages allows for multiple LEDs to be positioned together [138] to form a low profile multispectral led array light source [139]. An example of an LED array developed for multispectral analysis was produced by Brydegaard et al., (2009) [140] to produce a broad band multispectral microscope for transmission spectroscopy imaging as seen in.

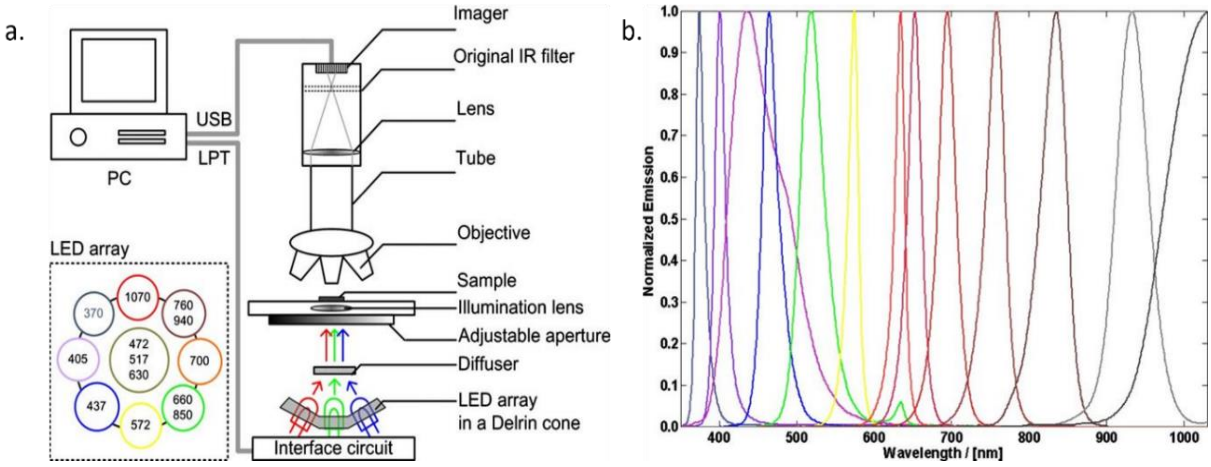

Figure 1-16 Application of a multispectral output LED array developed by Mikkel Brydegaard et al., (2009) [140] for imaging transmission spectroscopy. (a) Diagram of the microscope setup and the arrangement of multiple LEDs of different wavelengths controlled by a PC computer. (b) Figure of the normalised spectral emissions of the different LED sources of the LED array.

As LEDs are semiconductor devices unlike incandescent and discharge lamps, they have a high sensitivity to thermal, photonic, and electrical variations. The implementation of a driver circuit is important to ensure correct operation [141–147]. The driver circuit must

address several features to provide consistent luminous output for accurate optical measurements. An LED's luminous output can vary greatly with a slight change in applies voltage across the LED due to their diode-like V-I characteristic. To avoid this large fluctuation in luminous output the LEDs must be driven from a current source rather than a voltage source. Additionally an LEDs luminous efficacy and colour spectra is temperature dependent with luminous efficacy decreasing with junction temperature [146] which can cause a wavelength shift and would reduce the accuracy of optical measurements [147].

1.4.2 **Photodetector**

Photodetectors are used in optical sensors to convert the observed light into an electrical signal which can be quantified by a microprocessor. Advancements in the development of silicon based electronic components have significantly reduced the price and size of detectors [148,149] making the potential to used multiple detectors in a single sensor more achievable.

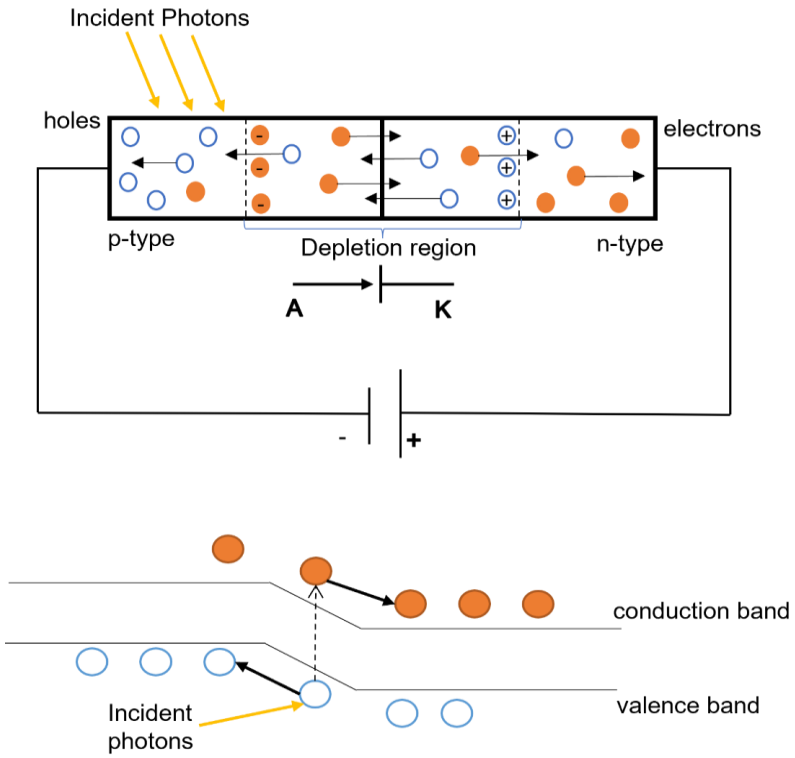

Figure 1-17 Diagram of working principle of a P-N junction photodiode showing the absorption of incident photons by the p-n junction causing current to flow as electron-hole pairs are formed and separated by the electric field in the p-n junction.

Photodiodes are commonly used for optical detection applications [150–153]; they are semiconductors which generate an electrical current from light. They work on the principle of photoelectric effect which is the emission of electronics from a material due to light [154]. Like an LED the photodiode consists of P-N junction. Photons of light are absorbed by the semiconductor when they strike the P-N junction which excites the electrons and creates electron-hole pairs. The electrons and holes are then separated by the electric field present in the P-N junction and they flow towards the opposite sides of the device creating a current flow. The more intense the light signal is the greater the number of electron-hole pairs which are generated which in turn produces a greater amount of current.

Alterations to the P-N junction of a photodiode can be made to alter the characteristics and response of the photodiode to light signals. For example, the addition of an intrinsic layer between the two doped layers, known as a P-I-N photodiode [155]. A P-I-N junction has a high resistance increasing the electric field strength in the photodiode. The benefit of the intrinsic layer is that the depletion region is greatly increased with reduces the photodiodes capacitance allowing the photodiodes frequency response to increase [156]. This has many applications were measurement frequency is high such as fibre optic communication [156,157].

There are different modes of operations a photodiode can be setup to operate in. Photovoltaic mode (unbiased) can be used with standard P-N and PIN photodiodes where no voltage is added across the photodiode junction, this reduces the dark current and is suitable for low light applications. However, without a voltage bias, the photodiodes response time is slow with the photodiode's capacitance at a maximum. A photodiode in photovoltaic mode gives a current response linearly corresponding to the light intensity [157]. Another mode photodiodes can be used in is photoconductive mode. The photodiode is reversed biased with an external voltage applied to the P-N junction. A negative voltage is applied to the anode which is the P layer of the junction and the cathode, the N layer is connected to a positive voltage. In this mode the photodiode operates as a current source with the magnitude of current depending on the intensity of light acting upon it. This mode is more suitable to high sensitivity and larger dynamic ranges but also has a higher dark current with the applied voltage across the junction [158,159]. A photodiode in photoconductive mode does not give a linear response to light intensity. With a good response time (nano to microseconds) and relatively low-cost (€10 - €100) photodiodes are suitable for calibrated in-field optical

measurement. However, single photodiode detectors are limited to just intensity measurements and require optical filtration to isolate the targeted wavelength regions of interest [161,162].

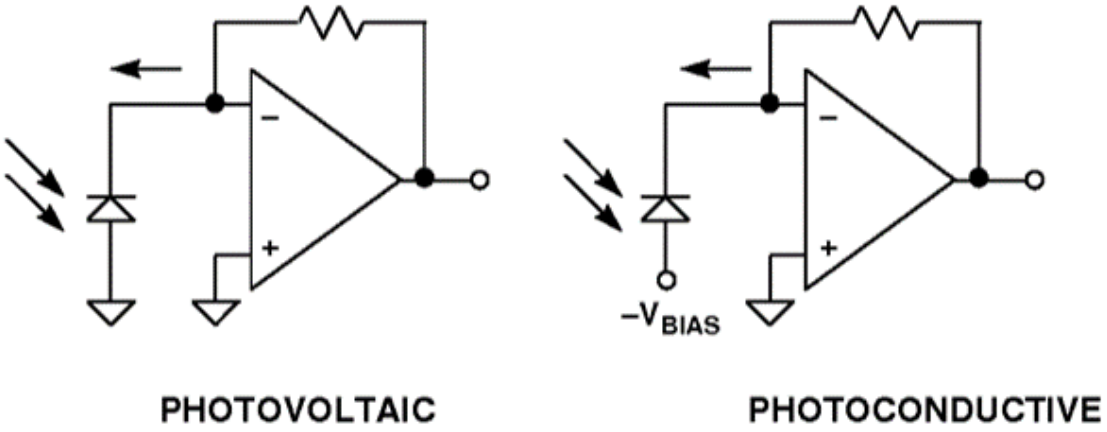

Figure 1-18 Diagram of photodiode circuitry from the Op Amp Handbook by Jung (2005) [160], circuit of a photodiode in photovoltaic mode on the left which provides greater linear operation and photoconductive mode on the right which gives greater switching speeds at the expense of linearity.

Photomultipliers (PMTs) are also used by in situ optical sensors [163–166]. PMTs are highly sensitive to low radiation levels making them suitable for fluorescence detection at very low levels of light [167]. They have a good response time between nano and microseconds but have a higher cost compared to photodiodes ranging between €100 - €1000. A PMT (see Figure 1-19) uses a photocathode, a series of dynodes and an anode. A photon of light strikes the photocathode, ejecting an electron due to the photoelectric effect. The electron accelerates towards the first dynode which is at a high positive voltage. When the first electron strikes the first dynode, several secondary electrons are emitted onto the next dynode and so on the dynodes amplify the signal. The final electrons are collected by the anode at the end producing an electrical signal which can be measured. A disadvantage of a PMT is they require high voltage power supply to operate which is challenging to implement in a deployable in situ sensor [157].

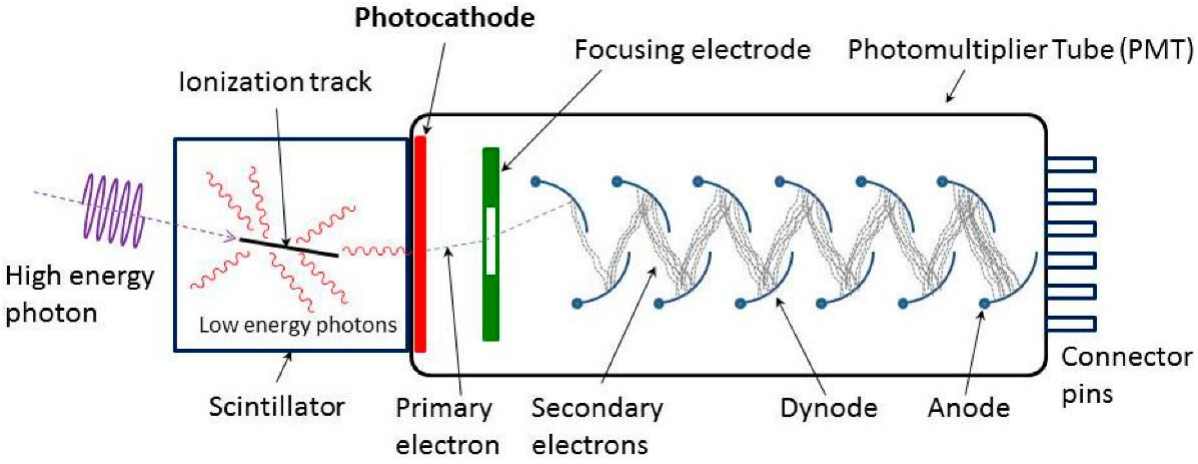

Figure 1-19 Diagram of working principle of a photomultiplier tube [168] showing the entry of a high energy photon (UV,VIS or IR) striking the photocathode via an ionization track and releasing a low energy electron. The primary electron is then multiplied as it is striking the first dynode producing secondary electrons. This multiplication is continued before being measured by the anode due to the electrical charge produced by the electronics produced.

Both photodiodes and photomultipliers give a measurement of the light intensity present at the time of measurement which is ideal when the wavelength region of light being measured is known. However, for some measurement applications, particularly for fluorescence measurements, it is necessary to spectrally resolve a signal from the incident of light as they can be located at two different regions of the spectrum [169]. Spectroscopy, which is the study of the interaction between matter and electromagnetic radiation (in this case light) as a function of wavelength or frequency. A spectrometer is a photodetector instrument which can measure light intensity as a function of wavelength. This capability allows for multiple parameter signals to be measured over a spectral range using a wide range of different light source spectrums [157,169].

A spectrometer works on the principle the dispersion of light (see Figure 1-20). A collimated beam of light can be passed through a prism and due to the refraction or bending of light at different rates which separates the light based on wavelength into its constituent components. Light enters the spectrometer though a narrow aperture called an entrance slit, the slit vignettes the incoming light. A concave mirror is used to collimate the light and a diffraction grating or prism disperses the light into its spectral components which are directed away at slightly different angles. An image sensor or array of photodetectors can be lined up with the respective angles of the dispersed light or a focusing lens or mirror can direct the light to measure the individual components of the light as wavelength regions.

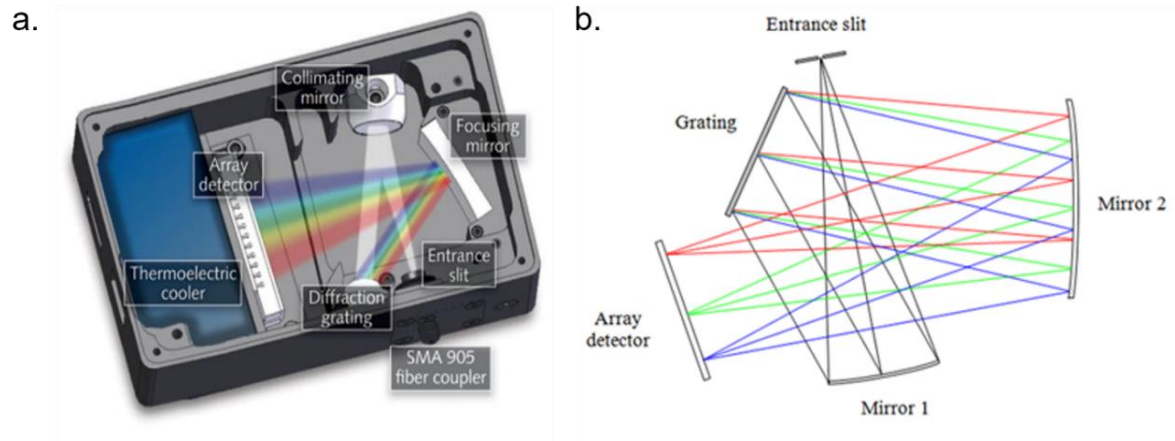

Figure 1-20 Working principle of a spectrometer unit, (a) shows the internal setup of a mini benchtop spectrometer by B&W Tek [170], showing the input of light through a slit, collimation of light, dispersion of light by a diffraction grating and direction of light onto a detector array.. (b) is a diagram of the light path and components of the spectrometer in a Crossed Czerny-Turner configuration.

Traditional lab-based spectrometers are bulky, expensive, and unsuitable for in situ deployable sensors. The use of mini spectrometers in marine/underwater scientific instruments has increased [171,172] given the advancements in technology allowing for more compact spectrometer devices to be manufactured with better resolution. Over the last two decades advancements spectrometer optical design, software, hardware and fabrication techniques has given ultracompact mini-spectrometer systems that maintain an "acceptable" level of performance and a sufficient resolution in the visible range which is adequate for in situ sensors [173–175]. Research projects have begun to use the latest mini-spectrometer components in their prototypes and have shown the potential for applying them as compact benchtop measurements devices with good resolution and have an advantage over photodiodes by providing a full spectral output over a range of wavelengths [176,177].

The key developments which have been made to allow for ultra-compact spectrometer components are the materials and manufacturing of the gratings used to disperse the incoming light as well of the size and pixel density of the image sensors used. The more dispersion of light and higher pixel density of an image sensor results in better resolution of a spectrometer. The factors which would influence the dispersion of the light would be the effectiveness of the grating as well of the pathlength. By making a spectrometer more compact the pathlength must also be decreased which mean the grating used must disperse the light more. Rasmussen [178] demonstrates the design of a compact spectrometer (see

Figure 1-21) by using a transmission grating (with 100% light transmission efficiency) instead of the traditional reflection grating (which are limited by a 90% reflection efficiency of the materials used) to provide greater efficiency allowing the size of the spectrometer to be reduced. The manufacturer Hamamatsu have been able to go even further in reducing the size of their commercial sensor units by using a reflective concave blazed grating (see Figure 1-22) which removes the need for additional alignment components allowing for the spectrometer to be "fingertip" sized (20.1 × 12.5 × 10.1 mm).

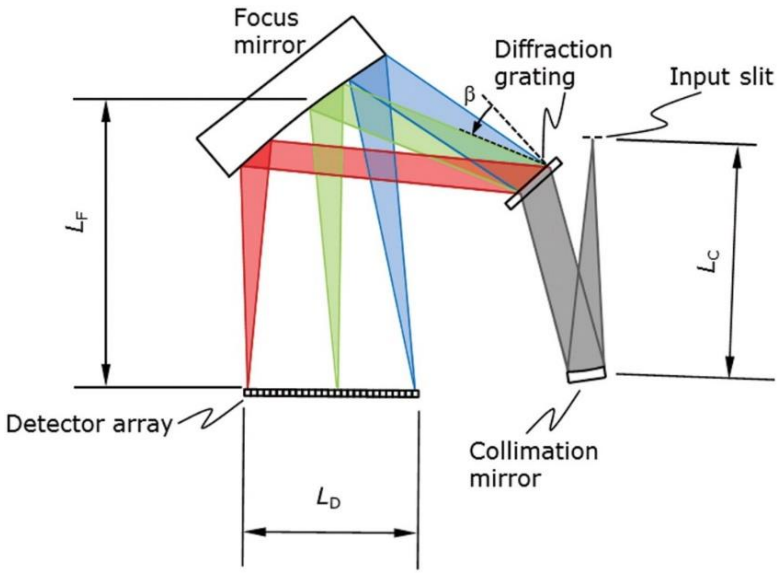

Figure 1-21 Diagram of the spectrometer design from Rasmussen et al., 2016 [178] showing the alignment of components in a compact spectrometer and key parameters, detector length LD and focal lengths LF and LC.

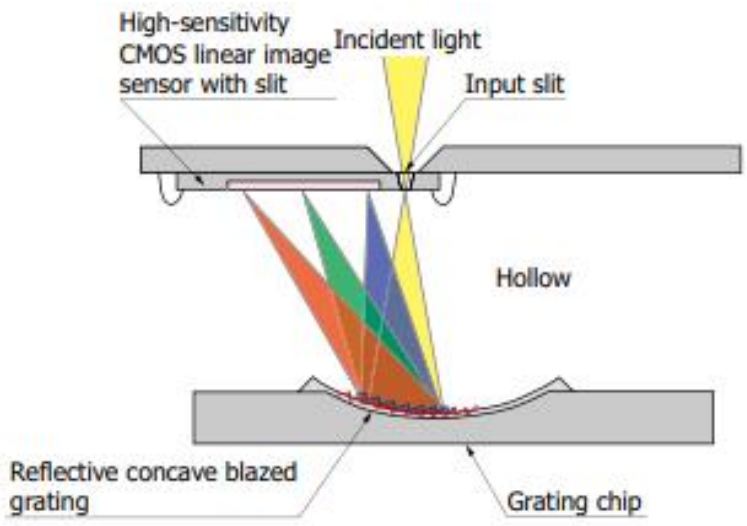

Figure 1-22 Diagram of Hamamatsu ultra-compact mini spectrometer unit [179] using a reflective concave blazed grating.

An array of photodetectors is used to measure the intensity of light aligned with the dispersed light's wavelengths. There are many technologies which can be applied to form the detector utilised in the spectrometer. The most widely used technologies include photodiode arrays (PDAs), charge coupled devices (CCDs), complementary metal-oxide semiconductors (CMOSs) and PMTs [173,180–182]. The optimal technologies for the miniaturisation of spectrometers are the use of CCDs or CMOS devices (see Figure 1-23) [173,181]. The use of CCD detectors in spectroscopy is well established due to their high sensitivity and low noise characteristics for compact spectrometer designs [181]. CCDs consist of an array of light sensitive pixels which convert incoming photons to electrical charge. They require an additional analog to digital (ADC) conversion circuit to be read by a microcontroller. CMOS detectors have become more popular in recent years due to their low power consumption, high integration capabilities and compact size [183]. The CMOS detector consists of an array of active photo pixels each with their own amplifying circuit and ADC making their output as a voltage more suitable for integrating with a microcontroller. They provide good sensitivity, dynamic range and a high-speed readout making them suitable for real-time spectroscopic measurements [184,185]. CMOS detectors have a higher noise level to CCD however due to their faster response and dynamic range capabilities they are more suitable to real time environmental monitoring [185].

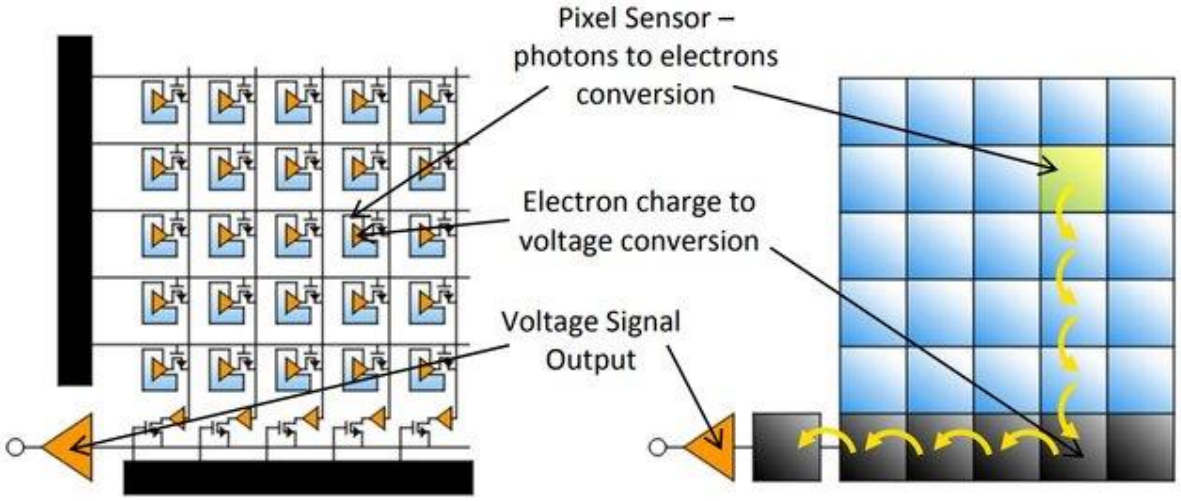

Figure 1-23 The working principle of a CMOS detector (on left) and a CCD detector (on the right). Output signal from a CMOS pixel is a voltage as opposed to the output from a CCD pixel which is as an electrical field [185]

1.4.3 Optics and Component Positioning

Optical lenses, windows and fibre optical cables are needed by in situ optical sensors as the interface between the environment being measured and the optical sensing components. They allow for the emission light source and the response light signal to be measured while not exposing the internal sensing components to the outside environment. Lenses can be incorporated into an optical system to perform optical functions redirecting the light for better measurements purposes. These functions include collimation of a light source when a lens takes an incoming divergent light source and converts the light into a parallel beam by refracting the rays. An aspheric lens is used with the divergent light source entering the lens on a flat surface and exiting via a curved surface with the refraction of light emitting the light at a parallel direction horizontal to the lens. This allows for uniform illumination and beam alignment of the light source entering the water column for measurement. It is a key required for optical turbidity sensing devices to use a collimation lens as per the ISO 7027:2016 [89]. Lenses can also be used to focus the light signal collecting it onto the photodetector to enhance the signal strength which in turn increases the devices limits of detection. A plano-convex or bi-convex shaped lens is used to focus light converging to a point of a distance known as the focal length from the lens. Light is refracted inward by passing through a curved section of the lens. For optimum signal the photodetector must be positioned at the focal length from the lens [186].

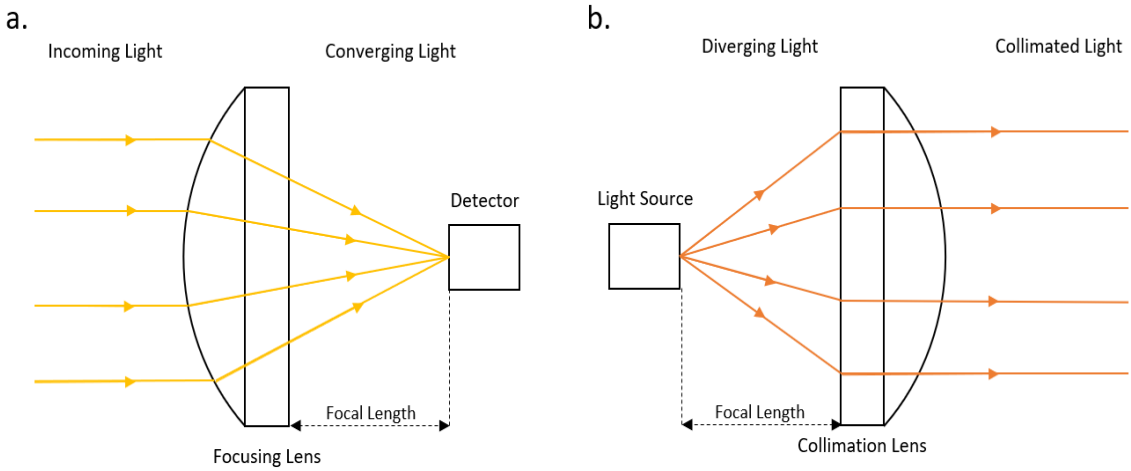

Figure 1-24 Diagram of the working principle of lenses used in optical sensors. (a) shows the changing of incoming light through a focusing lens converging the light to a point at the detector at the focal length. (b) Shows a collimation lens with light source emitted from a point at the focal length distance from the lens and the diverging light being collimated in parallel uniform direction.

Fibre optic cables are commonly used in in situ optical sensors as they allow for light to be transmitted to and from the sensor efficiently provide a light path while the sensing components be placed within the sensor housing. Fibre optical cables work based on total internal reflection. There are many examples of fibre optic cables being incorporated into optical sensor designs, Wang et al., (2022) [187] demonstrates the use of fibre optic cables in the development of a handheld dissolved oxygen sensor capable of measuring a fluorescence signal using an excitation LED and detector with a multi-mode bifurcated fibre coupler. Steiner et al., (2003) [188] have developed a prototype of a mid-IR sensor for the measurement of organic pollutants in ground water using fibre optical cables to join a spectrometer detector with an IR light source in sensor head. A review of optical fibre sensors for the measurement of water turbidity was carried out by Omar et al., (2009) [49] demonstrating their application in developing in situ turbidimeters.

In many cases when measuring an optical signal, it is necessary to block or allow the transmission a particular wavelength range. Optical filters are used to perform such functions allowing for the spectrum of interest to be isolated for detection purposes. A bandpass optical filter allows a narrow wavelength range to pass while blocking higher and lower wavelengths. This allows for the isolation of spectral range of note to be measured by a photodetector. Similar optical filters are long pass and short pass filters which allow longer wavelengths to pass or shorter wavelength to pass respectively. An example of the requirement of these filters would be in fluorescence detection. If the light source used to excite a molecule being measured overlaps or interferes with the emitted fluorescence signal it would block or mask the fluorescence signal to be measured. A long pass filter can be placed in front of a detector to block the noise from the light source. The use of the filter improves the signal to noise ratio giving greater limits of detection.

The material the optical component is made from also must be considered as different material compositions have different spectral transmission ranges (see Figure 1-25) as well as mechanical properties and costs. Fused silica and sapphire glass are used to manufacture lenses and fibre optical cables with a broad spectral allowance including in the UV region [189] and are used in optical marine sensors [190–192]. The optical components used in an aquatic environmental sensor must keep a watertight seal while also withstanding hydrostatic pressure, fouling, abrasion, and impact.

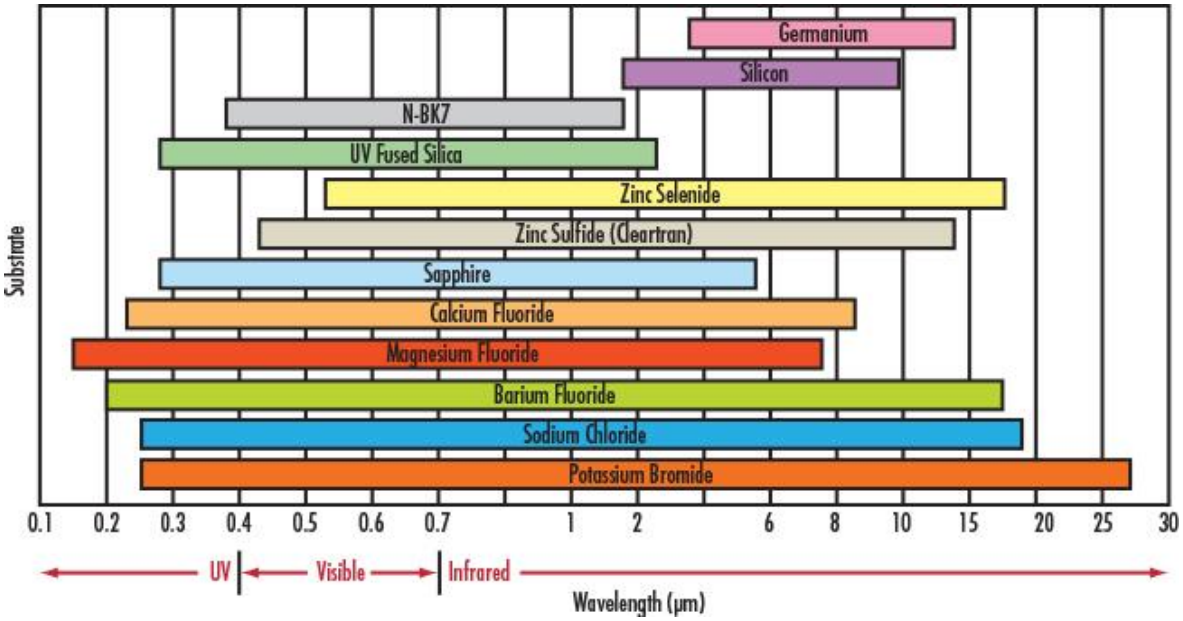

Figure 1-25 Transmission region comparisons of different substrates of optical windows adapted from figure by optical supplier Edmund Optics [193].

1.4.4 Temperature Sensor

There are many different technologies used to measure water temperature implemented in commercial in situ aquatic sensors with varying accuracy, temperature measurement ranges and cost depending on application. The temperature of aquatic environments can vary from frozen lakes, glacial waters (-4 °C to 0 °C) to tropical sea waters and geothermal areas (30 °C to 45 °C) which the temperature sensor must be able to measure accurately. Four of the most used technologies are compared in Table 1-3.

The technologies compared consist of the thermocouple, resistance temperature detector (RTD), thermistor and integrated silicon. A thermocouple works on the principle of two dissimilar metal materials joined together to form a junction. A voltage is generated between the two dissimilar materials which is proportional to the temperature (Seebeck effect) which can be measured [194]. Thermocouples provide the widest range of temperature measurement and are rugged in design [195]. RTD's work based on the principle of the relationship between temperature and the electrical resistance of metal [196]. With a current flow across the RTD, Ohm's Law can be applied to measure the voltage drop which gives the resistance which in turn can be converted to temperature. RTDs provide high levels of accuracy however are prone to breaking [195]. A thermistor uses the same principle as an RTD but uses a ceramic or semiconducting material [196]. Integrated Silicon or Integrated

Circuit (IC) consists of a temperature sensor element such as a diode or a transistor as well are the required circuitry to process and output the temperature readings [197]. The output from the IC can be a voltage, current or a digital communication protocol which makes them ideal for integrating with a microcontroller without the need for additional processing circuitry. An IC temperature sensor also does not need additional conversion for linear response unlike the other three technologies [195].

Table 1-3 Comparison of temperature sensing technologies adapted from [195]. The technologies compared are the thermocouple, the resistance temperature detector (RTD), the thermistor and integrated silicon.

	Thermocouple	**RTD**	**Thermistor**	**Integrated Silicon**
Temperature Range	-270 to 1800 °C	-250 to 900 °C	-100 to 450 °C	-55 to 150 °C
Accuracy	± 0.5 °C	± 0.01 °C	± 0.1 °C	± 1 °C
Linearity	4^{th} order polynomial or equivalent lookup table required	2^{nd} order polynomial or equivalent lookup table required	3^{rd} order polynomial or equivalent lookup table required	No linearization required.
Ruggedness	Larger gauge wires an insultation materials used offer rugged and sturdy design.	Susceptible to damage due to vibration caused by small gauge leads prone to breaking.	Not affected by shock or vibration. Difficult to handle due to glass enclosure.	Very rugged and robust due to integrated circuitry plastic housing.
Responsiveness in stirred oil	Less than 1 s	1 to 10 s	1 to 5 s	4 to 60 s
Excitation	None required	Current Source	Voltage source	Voltage supply
Form of Output	Voltage	Resistance	Resistance	Voltage, current or digital.
Typical Size	Bead diameter = 5 x wire diameter	6 mm x 6 mm	2.5 mm x 2.5 mm	From TO-92 to SMD packages (2 x 2 x 0.5 mm)
Price	€1 to €50	€25 to €100	€2 to €10	€1 to €10

1.5 Review of Marinisation Design, Manufacture and Materials

In the marine environment the expected environmental challenges can be caused by several factors as shown in Table 1-4. The environmental challenges identified from the literature span a wide range of variabilities from mechanical to chemical to biological stresses. These variables must be considered in a design process of the mechanical structure, electronic systems, and material selection to output a sensor which is insensitive to external variables in the environment. Figure 1-26 gives an example of the different components and materials used in commercial marine sensor designs. It can be seen from the figures of the components that an emphasis is placed on simple, mechanically robust design and the use of durable materials.

Table 1-4 Challenges posed by the marine environment for in situ sensors and marine equipment.

	Environmental Challenge	**Description**	**Refs.**
Mechanical	Hydrostatic Pressure, Watertightness and Moisture Damage	A submerged object experiences hydrostatic pressure proportional to the depth. Maintaining structural integrity to resist the external forces while maintaining a watertight seal is critical. Moisture damages internal electronics is exposed.	[198–200]
	Impact	Impact forces on equipment due to collision caused by turbulent movement while deployed can severely damage equipment.	[198,199]
	Abrasion	Abrasive action on material surfaces due to sand, wave action or repeated rubbing with another surface can cause major mechanical stresses.	[199,201]
	Temperature Changes	Fluid temperature changes can cause thermal expansion/compression cycles within the materials resulting in structural stresses.	[198,199,202]
Chemical	Corrosion	Corrosion is a deterioration mechanism cause by high salinity on metallic materials	[203–205]
	Ultraviolet (UV) Radiation	Solar UV radiation due to exposure of the material can deteriorate a material predominantly plastics and wood.	[206,207]
	Alkaline Solution	Exposure of materials to alkaline solutions can cause a degradation of the materials integrity. Primarily polymers and composites are affected.	[198,208]
	Weathering	Due to exposure to air and sea water a deterioration process of weathering can affect materials.	[209,210]
Fouling	Biological Growth	Build-up of biological growth on sensor equipment can damage the structural integrity and affect sensor measurements.	[211,212]
	Sediment Build Up	Sediment particles can build up on equipment causing damage and affecting measurements of sensors.	[212]

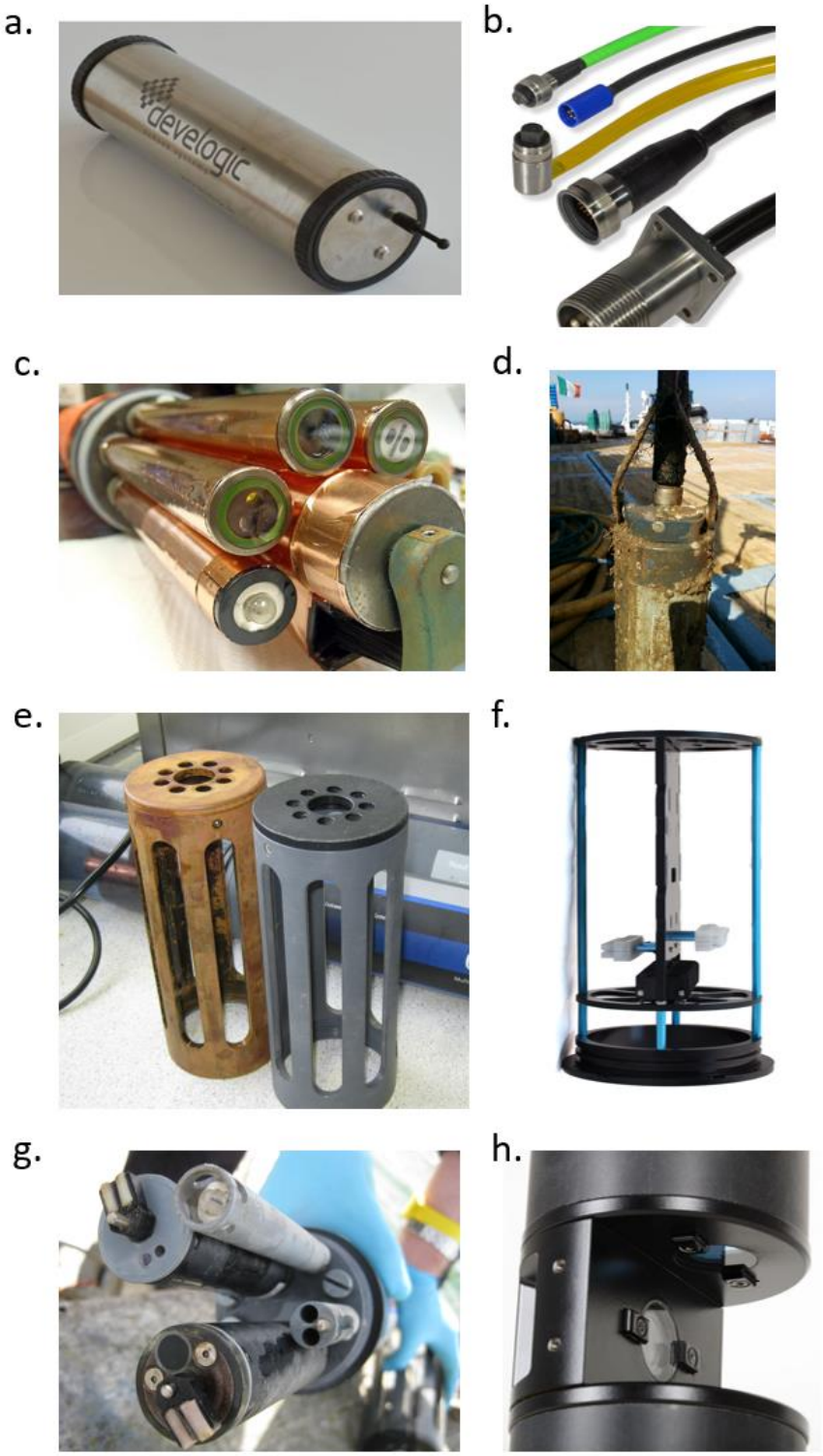

Figure 1-26 Example of Marine Sensor Design. (a) Example of an off-the-shelf titanium sensor enclosure from Develogil; (b) Example of commonly used IP68 rated marine cable connectors: Eaton's subsea connectors and cable assemblies using BurtonTM dry-mate and wet-mate; (c) Example of a probe type sensor head with copper foil by YSI, a Xylem brand, Yellow Springs, OH, USA; (d) Marine cable connected to marine sensor; (e) Example of sensor guard design for YSI V2 6600 Sonde. (f) Example of internal frame structure used on a sensor from Blue Robotics; (g) Example of an optical wiper cleaning system used by probes of the YSI V2 6600 Sonde; (h) Example of optical sensor head set up using optical windows with light source and photodetectors, PhycoProbe manufactured by BBE Moldaenke, Germany.

1.5.1 Materials for the Marine Environment

1.5.1.1 Materials Used by Commercial In-Situ Sensors

Table 1-5 shows examples of common materials being used by commercial marine sensor manufacturers for the construction of the housings of their instrumentation. The table shows that manufacturers commonly use a mix of metal-based and polymer materials for different components. The material of the component is dependent on the function and mechanical performance required. This allows for reduction of costs by only using metal-based materials when required due to their higher costs and weight relative to polymers [213,214].

Table 1-5 Materials used in marine sensor manufacturing.

Metal Based Materials		
Grade	**Material**	**Used In Sensors**
316	Stainless steel alloy (contains molybdenum)	YSI, Seabird, Turner etc
AH36	Carbon Steel	YSI
6061-T6	Aluminium	Blue Robotics ROV
-	Titanium	YSI, Seabird, Chelsea Tech., TriOS, S: CAN, Turner, etc
1.4571/1.4404	Stainless steel	TriOS
-	Copper	Seabird, TriOS, HydroCAT-EP, Chelsea, Turner, Hydrolabs, etc
Polymer Materials		
Grade	**Material**	**Used In Sensors**
Xenoy	Blend/resins	YSI
Lexan	Polycarbonates/thermo plastic	YSI
Victrex PEEK	thermoplastic	Quantum analytical
PPS (Polyphenylene sulfide)	thermoplastic	Chelsea
POM-C	thermoplastic	TriOS
Rigid Polyurethane	thermoplastic/thermoset	Seapoint

Advancements in metallurgy have allowed for superior materials to be developing including corrosion resistant alloys (CRAs) which have specific properties to resist chemical corrosion [215]. There has been a noticeable trend of marine components being manufactured using

titanium alloys due to their corrosion resistance, mechanical properties, and long-life durability [216,217]. However, the trade-off of using titanium is the cost of both raw material but also the machining and manufacturing costs however there have been developments in the manufacturing processes to reduce this cost and make titanium more appealing for sensor applications. Many commercial marine sensors have begun to utilise titanium components due to increasingly competitive prices [218–220]. Other marine grade metals include Stainless Steel A316 which is alloyed with molybdenum to improve its corrosion resistance. Stainless steel has traditionally been used by marine sensors [221,222], however, with the price of titanium becoming more competitive there has been a shift away from stainless steel. Furthermore, another marine grade metal which is cost effective due to its machinability is Aluminium 6061-T6 which is alloyed with both magnesium and silicon.

Polymers used in marine applications are required to withstand the high pressure, salt water, UV radiation and biofouling. A commonly used polymer for marine applications is polyoxymethylene (POM) which is an engineering thermoplastic [265]. There are two variations of POM which are homopolymer (POM-H) and copolymer (POM-C). POM-H is harder and stiffer compared to POM-C which is more flexible [213,223]. POM plastics provide good resistance to wear and is easy to machine to high tolerances. Polyether ether ketone (PEEK) possess good mechanical properties with high resistance to high temperatures and chemical degradation. It is also very durable making it suitable for the harsh environment such as the marine environment. Polyvinyl Chloride (PVC), polypropylene (PP) and polyethylene (PE) are also commonly used for marine components due to their resistance to chemicals, mechanical properties, and high durability [212].

1.5.1.2 Material Degradation under Environmental Conditions

Corrosion proofing is a necessity for all metal-based components which will be exposed to salt water for any period including electronics and components such as fasteners, enclosures etc. Marine corrosion can affect metallic materials in several ways including pitting [256], galvanic [224], stray current [225], and cavitation [203] corrosion. Deterring corrosion is a major requirement for any components used in direct or indirect contact with the marine environment including the external enclosure, fasteners, cables, optical components, and electronic components. ISO 9223 (the international standard for corrosion in metals and alloys) outlines standards for corrosion of metals and alloys, time of wetness (TOW) is

defined as the amount of time a metal surface is remains wet during atmospheric exposure [226].

Additional post processing treatments can also be used on metals to isolate the metal from exposure to the environment [203]. Cathodic protection can be provided to steel components through the use of a sacrificial anode made from zinc or aluminium [227]. This method works on the basis that the material of the anode has a more negative electrochemical potential than the steel in the structure. Creating a physical barrier between the metal component and the water is another effective way of preventing corrosion [203]. Applying paint or grease to metal surfaces can create an isolating layer to keep the metal from corroding[228]. Additionally, anodising which is a chemical process on metal surfaces achieved by using an electrolytic acid bath (highly applicable with aluminium) [229].

To avoid issues of corrosion entirely engineering polymers can be selected for certain external components [230]. Polymer materials are inherently resistance to electrochemical corrosion due to their molecular structure which does not facilitate ion exchange unlike the molecular structure of conductive materials [231]. Engineering polymers are commonly used in marine applications due to their chemical stability, light weight and reduced cost of fabrication [213]. However, as identified in Table 1-4, some polymers are susceptible to deterioration process such as weathering, solar UV radiation and alkaline solution stresses.

1.5.1.3 **Mechanical Properties of Materials**

Table 1-6 shows a comparison of relevant mechanical properties of the selected materials commonly used in marine applications that meet the required performance criteria. Stainless steel 316 is the densest of the materials while the polymers POM-C and PEEK are the least dense. This property informs on the strength to weight ratio when designing the sensor. The yield strength of the material is the point at which the material begins to deform plastically, stainless steel and aluminium 6061 have the highest yield strength while the polymers have the lowest. Stainless steel and titanium have the best young's modulus which is the measurement of a materials ability to resist being deformed elastically when a force is applied which informs the design of stiffer materials such as stainless steel versus more flexible materials such as the polymers.

Table 1-6 Mechanical Properties Comparison of Marine Engineering Materials

Material	Density (g/cc)	Yield Strength (MPa)	Youngs Modulus (GPa)	References
Stainless Steel 316	7.99	290	193	[232,233]
Titanium	4.5	140	116	[233,234]
POM	1.41	59.5	2.65	[214,235]
PEEK	1.3	90-100	3-4	[214,236]
Aluminium 6061-T6	2.70	276	68.9	[237,238]

Mechanical performance of the materials selected are of great importance when it comes to the sensor being able to withstand external loads, wear and hydrostatic pressure while submerged in the marine environment for extended periods of time. The materials selected must be based on the mechanical criteria outlined in Table 1-7.

Table 1-7 Environmental challenges and corresponding ideal material properties

Environmental Challenge	Material Properties
Repeated use in harsh environment	High strength, rigidity, and toughness
Potential for impact while moored at sea	Impact strength, even at low temperatures
Abrasion caused by movement during deployments and while at sea	Wear resistance and sliding properties
Under loaded strain for extended periods of time while moored	Creep resistance
Maintaining watertight seal under varying environmental conditions	High dimensional stability
Exposure to aquatic environment for extended periods of time	Resistance to hydrolysis
Reduce cost of manufacturer	Material cost and machinability

1.5.2 Manufacturing Methods for Marine Applications

1.5.2.1 Traditional Manufacturing Methods

The manufacturing processes required to produce marine sensor housings and enclosures are dependent on the material used. For metal casings such as stainless steel 316 and titanium alloy, stock material such as sheet, block, or tube to be fabricated into the required form using processes such as deep drawing [239], extrusion [240] and rolling [241]. For finer

detailing, drilling, milling and lathe work may be required. The harder metals result in higher manufacturing costs in tool wear and longer manufacturing times [242]. Plastics can be purchased in the form of pellets which can be transformed into any form using manufacturing processes such as injection moulding, extrusion, die casting or blow moulding [223,243]. Material and manufacturing costs are lower due to the higher detail that can be produced in a single step using moulding techniques and buying material in raw form (pellets) [265].

1.5.2.2 **Additive Manufacturing Methods**

Additive manufacturing techniques are now being used widely for prototyping and low scale manufacturing which has previously been used in marine applications [244,245]. A review of 3D-printed sensors was conducted by Ni et al., (2017) [246] showing many different applications of additive manufacturing for sensor development. For rapid prototyping fused deposition modelling (FDM) 3D printing is ideal as a part can be printed in a matter of hours for testing components [247]. The process involves extruding a polymer from a filament and builds a part layer by layer. Designs (see Figure 1-27a). There are a wide variety of filaments available for FDM such a polylactic acid (PLA), acrylonitrile butadiene styrene (ABS), polyethylene terephthalate glycol (PETG) etc. Each printing material has their own properties and applications. Mato et al., (2023) [248] presents a FDM 3D printed approach in developing a low cost in situ optical sensor for the marine environment using PLA, ABS and PLA with copper particles filaments.

There are other additive manufacturing methods which can achieve much higher resolution and structural strength than FDM printing [249]. Stereolithography (SLA) printing with uses UV light to cure resin layer by layer (see Figure 1-27b). Resins made up of photopolymers with different mechanical and thermal properties can be used depending on the application. This printing process results in accurate and high resolution components making it ideal for intricate component geometries [250]. However, SLA printing equipment and materials are more expensive than the FDM printing equipment equivalents [251]. Commonly, FDM printers can produce larger components. The components produced by SLA are less durable and more rigid than components printed on FDM printers [251].

Selective laser sintering (SLS) uses a high-powered laser to fuse polymer powder in layers to form a high-resolution structure (see Figure 1-27c). Common polymers used in SLS printing include nylon or polyamide [250]. Unlike FDM or SLA printing, SLS printing does not require supports which allows for more intricate structures and geometries to be fabricated [252,253]. Due to the sintering process, SLS printed components are robust and suitable for end-use applications [254]. Compared to FDM and SLA printing, SLS equipment and material is cost prohibitive for personal use. SLS printing for small scale prototyping would require outsourcing to larger manufacturing companies.

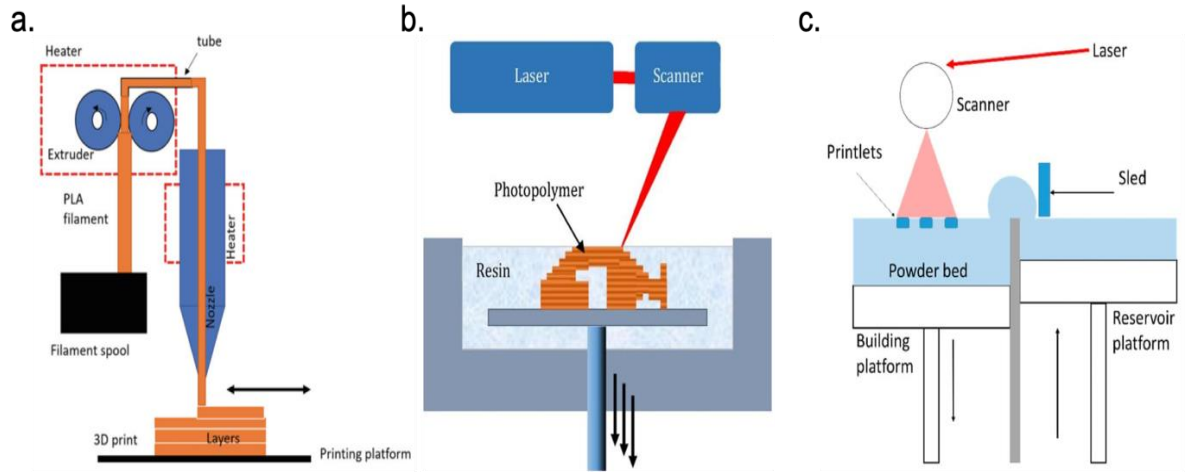

Figure 1-27 Additive manufacturing methods. (a) Fused Deposit Modelling (FDM) 3D printing, diagram modified from Mwema FM et al. [255]. (b) Stereolithography (SLA) 3D printing, diagram modified from Stansbury JW et al. [256]. (c) Selective Laser Sintering (SLA) 3D printing, diagram modified from Gueche, Y.A et al. [252]

1.5.2.3 **Watertight Seals and Interfaces**

Maintaining a watertight seal is of paramount importance for a marine sensor which is intended to be submerged under water for prolonged periods of time. This relates to every section of the sensor and all connection components used. Any join or interface between components that is exposed to the surround water requires a sealing method to prevent any moisture from entering the internal enclosure.

O-Rings are critical components used in sensors and enclosures which are intended to be submerged in water for prolonged periods of time to maintain a watertight seal on the interface between the outside environment and the internal area. The internal areas must remain dry for electronics and components to remain operational without being damaged by

moisture and corrosion effects. For significant joints it is convention for two O-rings to be used with the first primary O-ring maintaining the watertight seal and the second to provide a failsafe backup just in case the primary O-ring is compromised (see Figure 1-28). It is essential to lubricate O-rings when installing as this prevents damage due to pinching, twisting or abrasion [309]. This would reduce the O-rings ability to maintain a complete seal. Silicon grease is commonly used to lubricate O-rings. Other points that need to remain watertight are the optical lenses, O-rings and gaskets can be used to seal the area around the lens as well as using mechanical mounts, adhesives and cements to secure the lens in place [258,259].

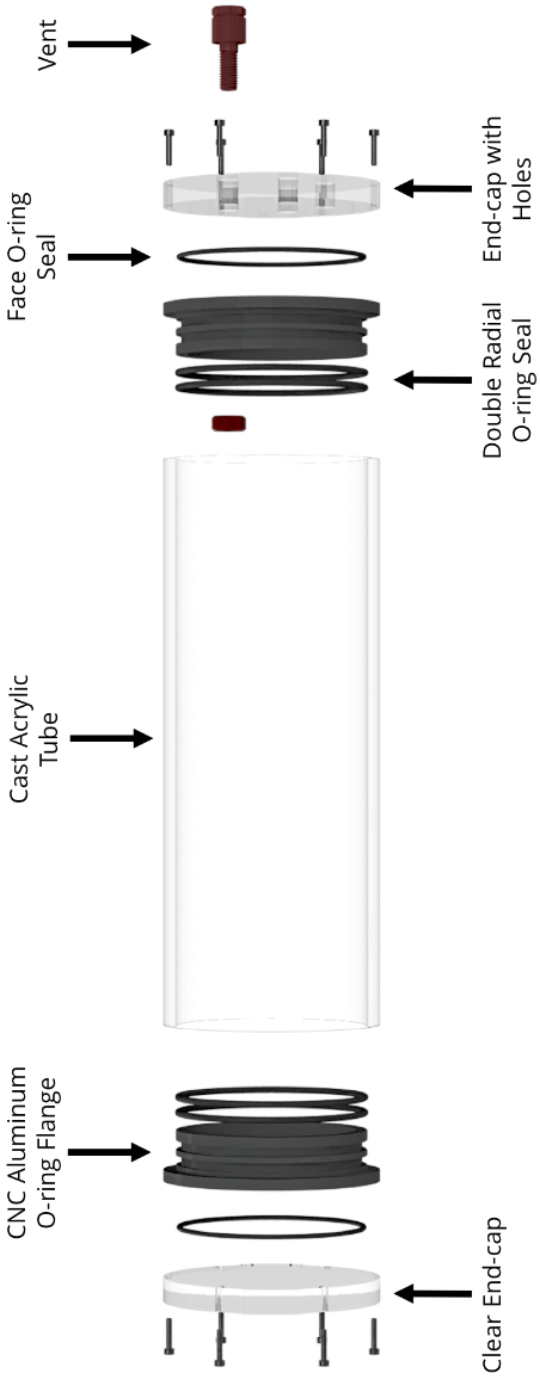

Figure 1-28 Example of watertight enclosure by the use of radial and facial O-rings and flanges, image modified from Blue Robotics (www.bluerobotics.com) [312].

Additive manufacturing lends to more porous surfaces due to the layer by layer method of fabrication [261,262]. This is due to void formation between layers of the material being deposited which limits the bonding between layers causing porosity [263]. Post processing steps can be taken to ensure the printed component is watertight. The use of coatings such as epoxy resins varnishes or sealants can fill the pores on the surface of the component

creating a complete seal [264]. Another technique which is applicable to certain polymer materials such as ABS, is vapor smoothing [265]. Vapor smoothing uses a solvent vapor to partially melt the surface of the component, in turn smoothing and plugging the gaps of the components surface. In industry, infiltration is a common method for reducing porosity [263]. This method involves placing the component into a vacuum chamber and introducing sealant oil. The sealant penetrates the voids of the material which closes the pores on the components surface creating a pressure tight component.

It is standard practice for marine electronic applications is to employ protective coatings on electronics used in marine sensors to guard against moisture damage [200]. During the fabrication and post fabrication processes, prevention steps can be taken to ensure the electronic circuit boards are not vulnerable to moisture which would damage the circuitry. One such approach is the surface finishing of the board at the point of fabrication to cover any exposed copper on the board to reduce exposure to the environment which would cause oxidation of the copper and corrosion [266]. This protects the board and is done before the assembly step. After assembly, a post fabrication step of conformal coating can be done which applies a layer of hydrophobic material to insulate the surfaces of the electronic circuit from the environment as shown in Figure 1-29. This will prevent moisture, dust, other contaminants, and UV exposure [64–66]. Additionally, to reduce moisture levels from the air inside the enclosure, silica gel desiccants can be used which can be sourced in packets of pellets and placed inside the sensor enclosure. The silica gel absorbs the moisture from the air by attracting the water molecules which are then bond to the surface of the silica gel surface [270].

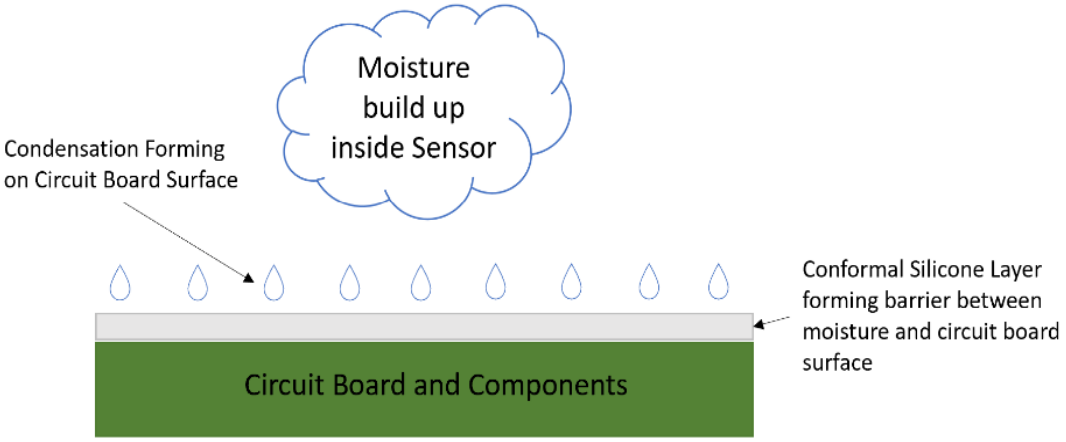

Figure 1-29 Silicon conformal coasting of electronic board surface to provide protections from moisture on the left and diagram of the hydrophobic barrier formed on the right.

1.5.3 **Antifouling Strategies for In Situ Sensors**

Biofouling is the accumulation of unwanted material on any surface submerged in an aquatic environment. Fouling of structures in the marine environment is a major hurdle to long term deployments of marine sensors as the growth of biological matter that can cause damage to the sensor and reduce its performance [271]. This is a concern in particular for optical sensors as any obstruction in front of a lens, light source or detector can skew the data being measured by the sensor and a signal drop would be evident [272]. Figure 1-30, a study conducted by L. Delauney et al., (2010) [273], shows the effects of biofouling on optical sensors. In Figure 1-30b the drift begins as soon as seven days after initial deployment.

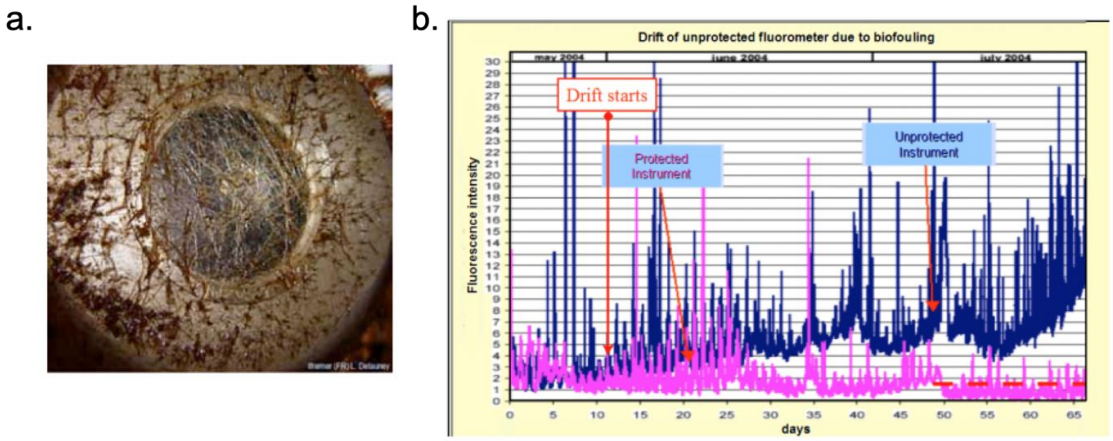

Figure 1-30 The effect of fouling on optical sensor readings (a) Optical window of a transmissometer after 40 day period in Trondheim Harbour (Norway) in summer [273]. (b) The measurement drift on an unprotected fluorometer due to biofouling on optics [273].

1.5.3.1 **Physical Fouling Prevention Methods**

There are many methods used by commercial optical marine sensors to prohibit or reduce fouling. Mechanical cleaners/wipers are the most common method used, using a brush or scrubber driven by a motor to periodically wipe the lenses of the sensor (see Figure 1-31b). However, as the mechanical wiper system involves the use of moving parts underwater which makes the manufacturing and maintenance costs of the system relatively high [273]. Additionally, the power consumption of the motor is relatively high which reduces deployment times [274].

Another solution less frequently used are biocide generation system which inject chemicals such as peracids, halogens and quaternary ammonium compounds into the water column killing off any micro-organisms building up on the sensor surfaces [275]. Examples of this method used by in-situ commercial marine sensors can be seen in Figure 1-31d. This method though is highly toxic to the environment and is also power demanding as the system requires a hydraulic pumping system [26].

1.5.3.2 **Ultraviolet Light Fouling Prevention Method**

Due to the power demands of physical wipers and toxicity of used biocides manufactures have begun to move away from these methods. Deep ultraviolet light (UVC) sources (100 – 280 nm) have become significantly cheaper to manufacture and more widely available in the form of LEDs. The UVC light has a degradation effect on the nucleic acid of cells

therefore destroying any micro-organisms in its direct path [127,276]. This method has very promising applications for optical sensors as the UV LEDs can be used to keep the lens clear of any fouling (see Figure 1-31a) which in turn increases the longevity of a deployment by maintaining good measurement and signal quality (as seen in Figure 1-30b) while using less power than a mechanical wiper system [274].

1.5.3.3 **Material-based and Coatings Fouling Prevention Methods**

Copper in its raw form [277], in an alloy (commonly with nickel) [278] or copper-based paints [279] are frequently used to prevent fouling as they are highly effective at stopping biofilms from developing on surfaces [275]. Ions from the coppers surface are released which degrade the RNA of organic cells acting as a biocide [280]. It creates a constant toxic surface making it difficult for micro-organisms to grow in high numbers to begin the fouling process [70]. Copper structures as in Figure 1-31c, can be used by sensors to create a physical barrier to prevent fouling for effecting the sensing probes. Copper can also be sourced in tape or sprays [277] to cover surfaces to prevent fouling build up.

Other antifouling coatings exists which employ as non-stick approach to deter micro-organisms from gaining a foothold on the surface therefore prohibiting the growth of biofilm [275]. Commonly based on silicones, most commonly using PDMS (polydimethylsiloxane) non-stick coatings are commercially available [279,281]. The benefit of non-stick coatings is they are non-toxic to the marine environment as opposed to the biocide-based approaches [282]. The use of sol-gel based materials offer a non-toxic solution to fouling prevention [283] at lower cost compared to silicone-based paints [284]. Sol-gel coatings can be transparent allowing them to be applied to optical lenses and windows on in-situ optical sensors acting as a benign fouling prevention approach for optical detections in the marine environment [285].

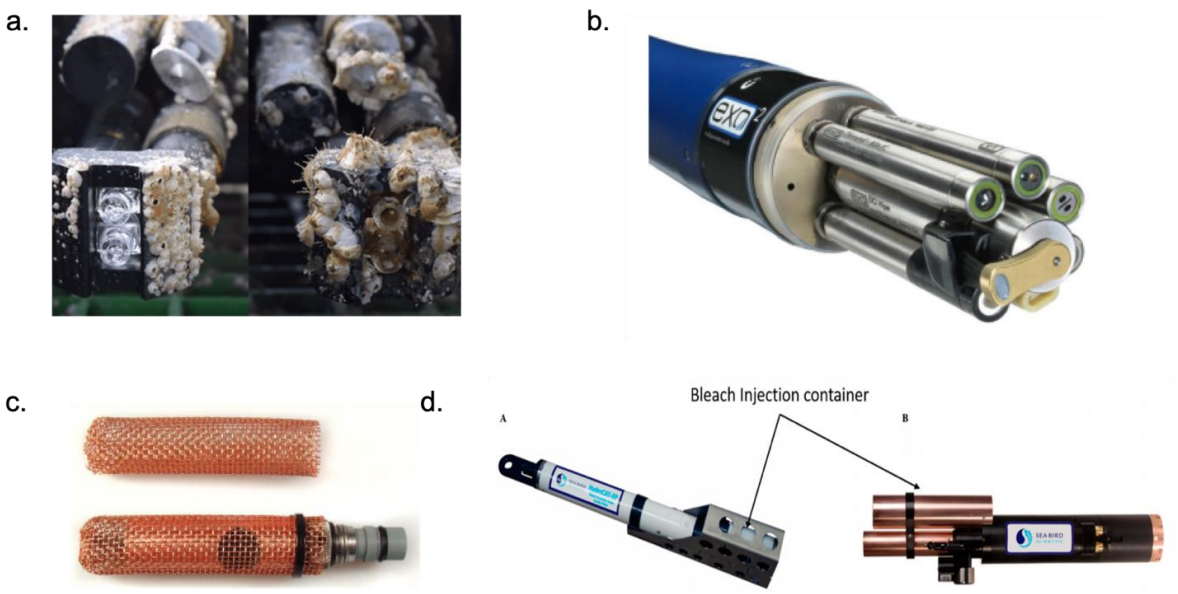

Figure 1-31 Antifouling strategies. (a) the use of UV LEDs to prevent the build-up of fouling on the left, without the UV LEDs operating on the right [286],(b) physical wiper is employed on the YSI sonde for fouling prevention on the optical lenses [287], (c) using copper allow sheathe to prevent fouling build up on probe [287], (d) examples of commercial sensors using bleach injection system to prevent fouling, HydroCAT-EP, Sea-Bird Scientific on the left and Water Quality Monitor (WQM) Wet-Labs and Sea-Bird Scientific sensor on the right, diagram modified from Delgado et al. [212].

1.6 Discussion and Conclusion

In this chapter the key role in situ sensors have in monitoring aquatic environments was outlined. The current trend in in situ water sensing instrumentation was found to be moving away from the expensive traditional sensor to develop more adaptable, lower cost and smarter sensors. The theory of the optical properties both inherent and apparent in water were investigated and how the presence of target analytes can be measured and quantified. There are multiple measurement modes which can be applied that were explored including transmittance/absorption, scattering of light and fluorescence of molecules. Using the literature, the spectral characteristic of key target analytes were highlighted including that of turbidity, suspended particle matter, Chl as an equivalent quantification of phytoplankton and other algae species, dissolved organic matter as well as petroleum compounds. Finally, a thorough review of the challenges which must be overcome in in situ sensor design for robust and low cost sensor enclosures to be deployable in the marine environment was conducted. The outcome of this investigation was the identification of suitable marine grade materials, low cost manufacturing methods and a selection of antifouling strategies which can be applied to in situ enclosure design.

1.6.1 Optical Measurement of Target Analytes

The application of the combination of a light source and a detector these parameters can be optically measured and converted to an electrical signal. The spectral emission of the light source and the measurement of wavelength intensities is important for producing an accurate measurement of a parameter. The required optical measurement spectrums have been tabulated in the Table 1-8.

Table 1-8 Optical characteristic requirements for the measurement of select target analytes.

	Turbidity	**Algae Species/Chlorophyll**	**Dissolved Organic Matter**	**Petroleum Compounds**
Measurement Mode	Trans/Sct	Abs/Flr	Abs/Flr	Flr
Light Source	IR (800-900 nm)	Abs: 400-450 nm & 650-680 nm Flr: 300-450 nm	Abs: 400 – 500 nm Flr: 300 – 420 nm	266 – 355 nm
Detection Region	IR (800-900 nm)	Abs: 400-450 nm & 650-680 nm Flr: 650-680 nm	Abs: 400 – 500 nm Flr: 340 – 500 nm	320 – 395 nm

Trans – Transmittance, Sct – Scatter, Abs – Absorption, Flr – Fluorescence, IR – Infrared

With the optical characteristics identified an investigation of the current technology available was carried out to identify the suitability and novel advancement opportunities which could be applied to developing a more sophisticated and lower cost sensing unit. Starting with the light source, when compared to traditional broadband light sources such as xenon lamps, LEDs provide an advantage in cost, size, and range of spectral emission ranges available to be able to measure multiple different optical characteristics of the water column. The decrease in size (surface mounted components) to power output of an LED was identified to have the potential to allow multiple different LEDs to be combined onto a single light source array for multiparameter measurements and examples of this have been seen in the literature of other water sensing prototypes. LED technology has advanced significantly provide a wide range of low-cost UV models which used prominently for absorption and fluorescence detection methods of analytes. A full analysis of photodetectors available was conducted comparing the advantage and disadvantages of currently available photodetectors which has been tabulated in Table 1-9. This table shows the advantages of using photodiodes which are the most commonly used photodetector in commercial in optical situ sensors due to their size, cost and sensitivity [79,288]. However, the recent advancements made in the miniaturisation of spectrometer technology [173] holds a significant potential for the development of a novel sensor capable of spectrally resolving more complex solutions to analyse the water column in a holistic way providing higher resolution spectral data.

Table 1-9 Table comparing the performance characteristics of three photodetectors, photodiodes, photomultiplier tubes and micro spectrometers.

	Photodiode	**Photomultiplier Tube**	**Compact-Spectrometer**
Spectral Range	200 nm - 1100 nm	185 nm - 900 nm	200 nm - 2500 nm
Sensitivity	Up to 0.1 A/W	Up to 10^6 A/W	Up to 10^4 counts/W
Ruggedness	Moderate	Less rugged	Moderate
Optical Filtering	External filters	External Filters	External filters can be used but not essential
Excitation	Voltage source (voltage bias)	High Voltage source (in kilovolts)	Voltage source
Form of Output	Current or voltage	Current	Digital or analog
Measurement Speed	Nanoseconds to microseconds	Nanoseconds to microseconds	Milliseconds to seconds
Size	1.6 mm x 0.8 mm SMD to 10 mm diameter THT	Compact 25 mm to 50 mm diameter	Compact 11.5 × 4.0 × 3.1 mm to 20.1 × 12.5 × 10.1 mm
Cost	€10 - €100	€100 - €1000	€100 - €1000

The use of compact spectrometers as photodetectors in a multiparameter optical sensors would provide many opportunities as they can be used in multiple different optical modes without the need to swap out optical filters due to their spectral range. The sensitivity of a spectrometer can also be altered by setting its integration time or exposure time. This would allow for fine-tuned sensitivity depending on the optical measurement and light source configuration required. If two spectrometer units were to be incorporated into the design this would achieve four different measurement modes by positioning one in front of the light source (transmission/absorption) and one at 90 degrees (side scatter/fluorescence). To add additional functionality to the design a photodiode can be placed in the backscatter position. This would extend the sensors limits of detection of turbidity in extreme cases producing high turbidity events such as storms or high rates of suspended particle conditions.

The importance of the selection of optical lenses, windows, or fibre optical cables which the optical sensing components are positioned behind has been highlighted in this chapter. For the light source a collimation lens is required to produce a parallel and even beam entering the sample for accurate measurements. To enhance the sensitivity of the sensor overall,

plano-convex, or convex lenses can be used to focus the light signal onto the detectors positioned at the focal point of the lenses. The material of the lenses also has an influence on the measurements as it must allow the transmission of the spectral range being measured. UV fused silica, sapphire and N-BK7 provide low-cost solution with ranges from UV to IR. N-BK7 is limited in the UV spectral range compared to UV fused silica and sapphire. UV fused silica lenses are overall lower cost than sapphire which would make them more suitable to the overall design requirements.

Although not essential to an optical in situ detector, from this investigation the benefit of including a temperature probe in the system has been highlighted. The inclusion of a temperature parameter with the optical data has the advantage of providing additional context of the local surroundings of the sensor adding to a more holistic picture of the water quality being sampled. The temperature data along over different temporal ranges can be insightful showing short- and long-term trends in the aquatic environment which can be used in conjunction with other changes in target analyte measurements. The technologies evaluated included thermistors, thermo couples, RTDs and IC based temperature sensors. From the analysis of each technology, IC based temperature sensors provide a cost-effective solution with suitable temperature measurement ranges and accuracies. The additional advantage of IC temperature sensors is that not additional circuitry is required to provide linear correction and the data can be integrated with a microcontroller over a digital communication protocol without the need for calibration or look up tables.

1.6.2 Robust Design for the Marine Environment

The marine and other aquatic environments post significant design challenges for developing technology intended to be deployed in the environment repeatedly and for extended periods of time. From a review of the literature, the primary considerations in material selection and manufacturing methods are the mechanical robustness of the design, the chemical resistance of the materials and the occurrence for fouling due to biological growth. It can be seen from the review that state of the art commercial sensors typically use a combination of polymers and marine grade metal materials in their design. The materials choice is made on a component to component basis based on the application with the mechanical properties, chemical resistance and fouling prevention properties considered. The use of engineering polymers gives an advantage in cost in both raw material cost and

manufacturing cost while metal components maintain better mechanical properties which needs to be taken into consideration.

Traditional manufacturing methods such as injection moulding and machining are commonly used however there is a major opportunity to take advantage of the advanced manufacturing methods of additive manufacturing which have developed considerably over the last 10 years to be applied to in situ sensor design. The novel application of additive manufacturing can provide advantages in cost, prototyping production speed, allow for more complex geometries to be designed and for scaling of manufacturing to be carried out which will be taken into consideration.

A review of the effects of fouling build up on optical in situ sensors was conducted and the current strategies used by in situ sensor manufacturers to address this challenge was conducted. It was revealed that there are a wide range of approaches from physical wipers, the use biocides, non-stick materials, and UV radiation used. The key factors identified to inform on the strategy or combined strategies applied in an in situ sensor are toxicity informed by environmental regulations, cost of implementation and operational power usage.

1.6.3 Prototype Development Process

An iterative design methodology includes analysis, evaluation, and redesign steps to aid with better decision making [289]. The reasoning for adopting such an approach is to optimise the sensor design cyclically to reduce the need for alterations later in the development life cycle where changes would incur higher costs [290]. Figure 1-32 shows the adopted iterative design process with the design inputs of the initial concept for the sensor design and outline of specific requirements which are fed into an iterative design loop. The ideate stage considers known knowledge and experience from the other steps to restart the cycle for an improved design. Once a new design is conceived it can be built and prototyped using simulation of physical prototyping. The prototype can then be tested under the key performance criteria to assess the suitability of the design for the requirements which can then be fed back into the cycle for another iteration or if deemed to meet the required criteria can be output as the final design.

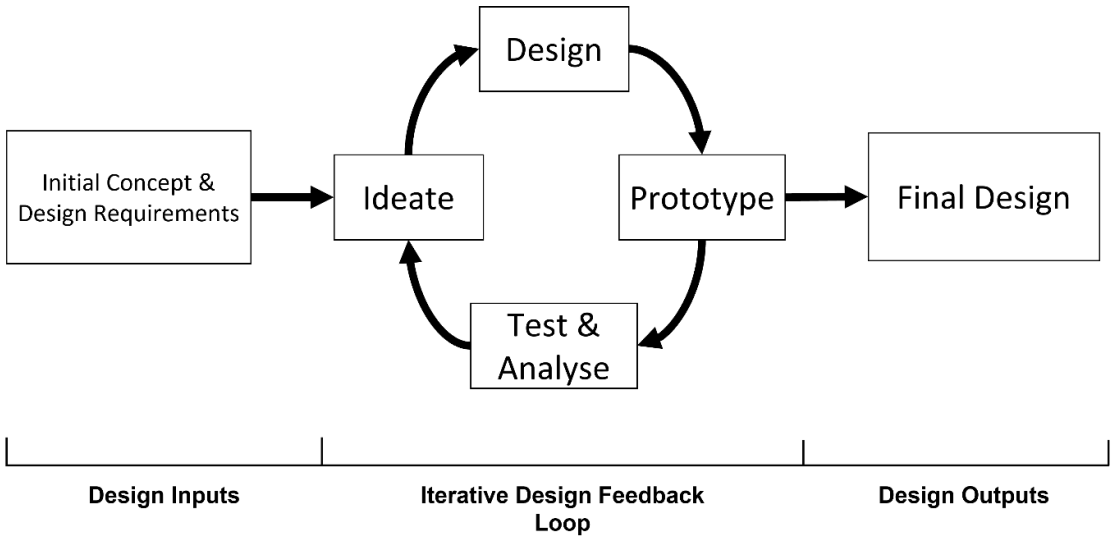

Figure 1-32 Iterative design process from initial concept and requirements being input to the iterative design feedback loop and outputting the final design.

The Technology Readiness Levels rating system was originally developed by NASA. This system has stages from 0 to 9 outlining the readiness of the technology as tabulated in Table 1-10 from international standards protocol ISO 16290:2013 [291]. There is a major crossover in technological challenges between the space industry and the marine industry which is why TRLs have been applied to marine technology development [292]. The use a TRLs is conducive to being able to assess the maturity of the technology being developed. This can then be fed back into the iterative design process to ensure the design fit within the project requirements and advance the technology to a suitable level. The TRL system will be used as a reference throughout the development of the technology as a benchmark of progress for this work. In this chapter alone, TRLs 0 to 2 have been achieved with a formulation of the technology concept and applied identified. The TRL will be factored into the iterative design process to identify the breakout point of the iterative design feedback loop for the required final design output as outlined in Figure 1-32.

Table 1-10 Description of the Technology Readiness Levels (TRLs) for gauging the advancement of the technology being developed.

TRL	Description
0	Unproven idea or concept without any tests performed.
1	Initial research with principles proposed but no experimental proof.
2	Formulation of technology with concept and application identified.
3	Initial applied research is conducted with proof-of-concept tests performed.
4	Small scale prototype built and operated under laboratory conditions.
5	Large scale prototype built and operated in intended environment.
6	Full prototype system tested in intended environment close to expected performance.
7	Demonstration system operating in operation environment at pre-commercial scale.
8	Actual system completed and qualified through test and demonstration.
9	Technology fully qualified and available commercially.

1.7 Aims and Objectives

The aim of this thesis is to develop a novel in situ sensing system for the aquatic environment with advanced multiparameter measurement capability at high resolution and high selectively of environmental parameters to go beyond state of the art and address the research and technological gaps required to produce the next generation of in situ sensors at scale and low cost. The design will incorporate the requirements to meet the environmental challenges requiring robustness, measurement reliability and validation, manufacturability and scalability of the technology developed. This can be done by producing a deployable optical measurement system disruptive to current commercial sensor equivalents currently in use and generate vital methods and research to contribute to the development of the next generation of in situ environmental sensing technologies. To achieve this, aim the following objectives are set out:

1. Advanced Multiparameter Optical Measurement System Design and Testing:

- The selection of the latest advanced technology in compact optical detectors, light sources and arrangement of components are required. This will produce optical measurements over a wide spectral range of multiple target analytes in a compact formfactor which is currently not available in state of the art systems.

- To interface the selected optical measurement components a custom electronic and firmware system must be designed and developed. This will address the challenges of sequencing control and automation, measurement reliability, universal system integration with external hardware and power systems. These challenges have been identified as critical to be addressed by the next generation of in situ sensing technology being deployed.

- For validation of the optical and electronics systems in the lab a modular benchtop system must be designed and built to a TRL 3 level. A modular design with plug and play capabilities will gives a novel approach to the validation of advanced optical measurement systems developed to further the testing of novel designs and components.

2. Robust Deployable Enclosure Design and Marine Grade Materials:

- Design and build a robust and deployable enclosure to house the optical measurement components and electronics and provide protection against environmental challenges. An emphasis is to be placed on suitable material selection, robust mechanical design, and low-cost manufacturing methods. A significant outcome of this work will be to produce a thorough assessment of the ideal materials and manufacturing method to produce the low cost and robust enclosure for marine applications.

- Comprehensive analytical testing of the built sensor design must be conducted to validate the optical measurement capabilities of the system (to a TRL 5 level) to be used for in situ measurements and a performance comparison made with currently available in situ optical sensor systems. This will serve a benchmarking of the systems performance relative to current state of the art systems contributing to the validation methods of in situ prototype systems in contextualizing performance.

3. Scaling and Deployment:

- A scaled-up production of the finalised sensor design must be carried out to produce a total of 10 units. This will require planning of logistics, procurement, fabrication methods and assembly techniques to produce multiple identical robust sensor units. Producing multiple replicant units of a prototype is not currently done in the research field to this scale and new methods are required to be developed which can be applied to the research field for the development of the next generation of in situ sensing technologies.

- New and novel methods are required to be developed for testing, calibration, and ensuring deployment readiness of the multiple sensor units to achieve a TRL level above TR 6. This validation method will be capable of being universally applied to all systems to standardise the response of each system allowing for interchangeability of systems for the deployment as sensor networks. The method

developed will be a contribution to the field as it is currently not demonstrated in research field in the developed of in situ aquatic optical systems.

- Full validation of the sensor units built (to a TRL 7 level) must be conducted through deployments in the intended environment to verify the sensor's design for suitability in the environment and the capabilities of the sensor's optical measurement system for monitoring environmental parameters. Deployment of multiple replicant systems is rarely performed at a research level with this work potentially contributing vital information on the methods and results of scaled and repeated deployments of novel prototype designs.

2 DEVELOPMENT OF AN OPTICAL MULTIPARAMETER PROOF OF CONCEPT BENCHTOP SYSTEM

2.1 Introduction

With increasing environmental pressure due to global climate change, increases in global population and the need for sustainable obtained resources, water resources management is critical [19]. Sensors and instrumentation play a key role in water management, and are becoming smaller, smarter, and more economical. Optical based sensors are receiving great interest due recent advances in photonics and the ability to work in harsh environments [293,294]. Smarter water monitoring sensors and benchtop systems are moving towards integrating multiparameter measurement abilities to decrease the overall sensor's required to gain a greater understanding of the waterbodies holistically [295–297].

For the target selective optical measurements, monochromators, such as a diffraction grating, or optical filters are typically used to select the desired emission wavelength. Once filtered this light is typically directed towards a photo-multiplier tube (PMT) for detection. Using these systems for fluorescence detection are rather bulky and not suitable for in-situ or continuous monitoring of local events. Thus, the majority of environmental sensors, either for fluorescence or scatter measurements employ photodiodes as photodetectors and light emitting diodes (LED) as light sources [48]. Selectivity to target analytes is thus achieved through the use of LEDs with narrow bandwidth emissions, laser diodes and optical filters which in general block or reduce the leaching of incident light into the photodiodes [116,150,151,298–301]. In the race for miniaturisation and field application a range of photodetectors have been demonstrated in the literature for different applications and include: PMTs [163–165] which although have excellent sensitivity require higher voltages to operate, camera sensors [302–304], PDs [150–153] and Cadmium-Sulfide (CdS) photoresistors [301,305].

Due to the low cost, small size, and improved performance these optical components have accelerated the development of in-situ optical sensors [306]. However, limitations still exist due to the complex composition of environmental waters and the overlapping of absorption or emission spectra associated with the presence of different optically active compounds [307,308]. While photodiodes provide poor spectral resolution, array detectors provide multi-spectral resolution which in turn captures multiple spectral emission bands associated with the presence of different constituents. Thus, the higher resolution enables spectral deconvolution and the assigning of emission peaks to environmental constituents.

Miniaturised spectrometers now exist to enable the fabrication of low-cost portable sensors with a recent demonstration for the use of the Hamamatsu C12880MA spectrometer chip for absorbance measurements [304].

For the next generation in situ sensors the capabilities of multiparameter sensing are to be increased to take advantage of technological advancements in LED packaging [123,124], photodetectors [148,309] and electronics [149]. In the last decade electronic components have been miniaturised and their cost has been greatly reduced giving way to a significant opportunity to apply these technologies to a deployable low-cost marine sensor. Components are more practical to integrate into a deployable portable sensor bringing scientific instruments out of the laboratory and into the field [306]. Mass-production of components and materials have led to a reduction in costs making technology more accessible [310]. Other industries, external to the ocean sciences and environmental sensors, are developing technology and reducing sensing component costs which feeds into the environmental sensor technological advancements [311]. Lower cost hobby grade electronics are readily available and new fabrication technologies such as 3D printing make development of sensors much easier, cheaper and faster than ever before [36,312].

The aim of the work presented in this chapter is to develop a proof-of-concept benchtop system which validates the selected optical measurement technologies and optical setup capable of an advanced multiparameter, multispectral and target selective optical measurement approach. This aim will be achieved by the following objectives:

1. The optical sensing technology and components must be selected which allow a wide spectral range and spectral resolution to allow target selectivity for the purpose of multiparameter measurement capabilities.

2. An electronic control system must be developed to interface with the optical sensing components to allow optical measurements to be carried out with operational control over the measurement parameters and the data output for processing.

3. A benchtop test rig must be designed and built to position the optical sensing components and sample in an exact orientation to facilitate multiple optical

measurement modes including absorption, transmittance, scatter, backscatter, and fluorescence. A plug and play system can be implemented to allow different components to be easily swapped in and out for testing and also create adaptability to the design.

4. Proof of concept experiments must be conducted to validate the performance of the optical measurement systems capabilities for multiparameter measurement of lab standards, target analytes and real-world samples.

2.2 Material and Methods

2.2.1 Benchtop System and Experiment Materials

The optical sensing components used are tabulated in Table 2-1. The electronic components used in this study are detailed in Table 4-5.

Table 2-1 Table of optical sensing components used.

Optical Component	Component No	Source
Mini Spectrometer	C12880MA	Hamamatsu Inc
Photodiode	MT03-021	Digikey, Ireland
25 mm UV Fused Silica Collimation Lens	36689	Edmund Optics, UK
12 mm UV Fused Silica Plano-Convex Lens	48668	Edmund Optics, UK
IR 850 nm LED	VSMY1850X01	Mouser Electronics, Ireland
Red 660 nm LED	SML-LXF0805SRC-TR	Mouser Electronics, Ireland
Green 565 nm LED	SML-LX0805SGC-TR	Mouser Electronics, Ireland
Blue 430 nm LED	KP-2012MBC	Farnell, Ireland
UV 385 nm LED	ATS2012UV385	Mouser Electronics, Ireland
UV 365 nm LED	ATS2012UV365	Mouser Electronics, Ireland
UV 310 nm LED	CUD1GF1A	Digikey, Ireland
UV 280 nm LED	XBT-1313-UV-A130-AA280-00	Mouser Electronics, Ireland
25 mm lens mount	CP33/M	ThorLabs Inc

The soldering equipment used consisted of a Weller WS 81 Analogue Soldering Station 80W (Radionics Ltd): Used for soldering of through-hole components to the circuit boards. A reflow oven (RK-10590, Betalayout Ltd) equipped with a temperature profile controller; it facilitated the soldering of surface-mounted components to the circuit boards. A Lulzbot Taz6 3D printer using a 0.5 mm nozzle sourced from Farnell Ireland was used to print the components for the benchtop components. Black polylactic acid (PLA) 2.85 mm diameter filament was used.

The standards, dyes, chemical and algae species used and suppliers for the optical validation experiments of the system are tabulated in Table 2-2.

Table 2-2 Table of standards, dyes, chemicals and algae species and their source which were used in the validation of the optical system experiments.

Category	Item/Chemical	Supplier/Source
Turbidity Standard	Reagecon CRS-4000-100 (4000 NTU)	Reagecon Diagnostics Ltd
Dyes and Chemicals	Fluorescein (CAS: 2321-07-5,)	Sigma Aldrich, Ireland
	Rhodamine B (CAS: 81-88-9)	Thermo Fisher Scientific Inc.
	Basic Blue 3 (CAS: 33203-82-6)	Sigma Aldrich, Ireland
	Quinine Sulfate (CAS: 207671-44-1)	Sigma Aldrich, Ireland
	Cyan Fluorescent Protein (CFP)	Thermo Fisher Scientific Inc.
Algae Species	Diatom Species Nitzschia Ovalis	SAMS Limited, Scotland

Other Equipment

3.5 mL 10 mm × 10 mm four polished faces UV Quartz Cuvettes with a Teflon stop cap (Helma Analytics) were used to hold samples for optical measurements. The Shimadzu UV-1800 UV-Vis Double Beam Spectrophotometer was used for absorbance readings of the tested standards and the for quantifying the extracted Chl-a from the algae diatoms. The Jasco FP-8300 Benchtop Fluorometer was used for fluorescence measurements of tested standards.

2.2.2 Design and Assembly Method of Electronic Control Systems

The electronic systems were designed using ECAD (electronic computer-aided design) software AutoDesk Fusion 360 and Autodesk Eagle. The schematic was drawn up for each of the required circuitry block and the correct components were identified. Once the schematic was captured the printed circuit board (PCB) layout was done and the components placed on the board. The connection traces were then drawn to complete the circuits. The design was then sent to a PCB fabricator (Betalayout Ltd) to manufacture the blank board, the components were procured, and hand assembled using reflow and through hole soldering. The description of the functionality of the circuit blocks implemented is tabulated in Table 2-3. Figure 2-1 gives an overview of the electronic systems designed for the sensor unit. The electronic system design was broken up into two main sections: 1) the control board which interfaced the control electronics, power systems and data output with the optical sensing components, 2) the optical sensing components and the circuitry required to connect them to the control board.

Table 2-3 Description of the circuitry blocks and their function.

Component/Block	**Functionality**
Microcontroller Unit (MCU)	Provides firmware-based control of optical sensing components, automates measurement sequencing, processes data, and outputs data to external devices.
Power regulation and power monitoring	Regulates voltage power rails, measures the system's current draw, and feeds back data to the MCU.
Serial communications	Transmits data output and receives command inputs to/from the MCU. Also converts TTL serial from the MCU to RS-232 protocol for external communication.
LED driver	Switches power to the LEDs at a regulated current and controls pulse width modulation via I2C commands from the MCU.
Analog input and ADC	Processes analog signals from optical measurement components.
Digital I/O and digital communication protocols	Allows the MCU to control pins as high/low and communicates with temperature sensor, current monitor IC, and LED driver using the I2C protocol.
MCU – Microcontroller unit, TTL – transistor-transistor logic, LED – light emitting diode, I2C – inter-integrated circuit, ADC – analog to digital converter, I/O – input/output.	

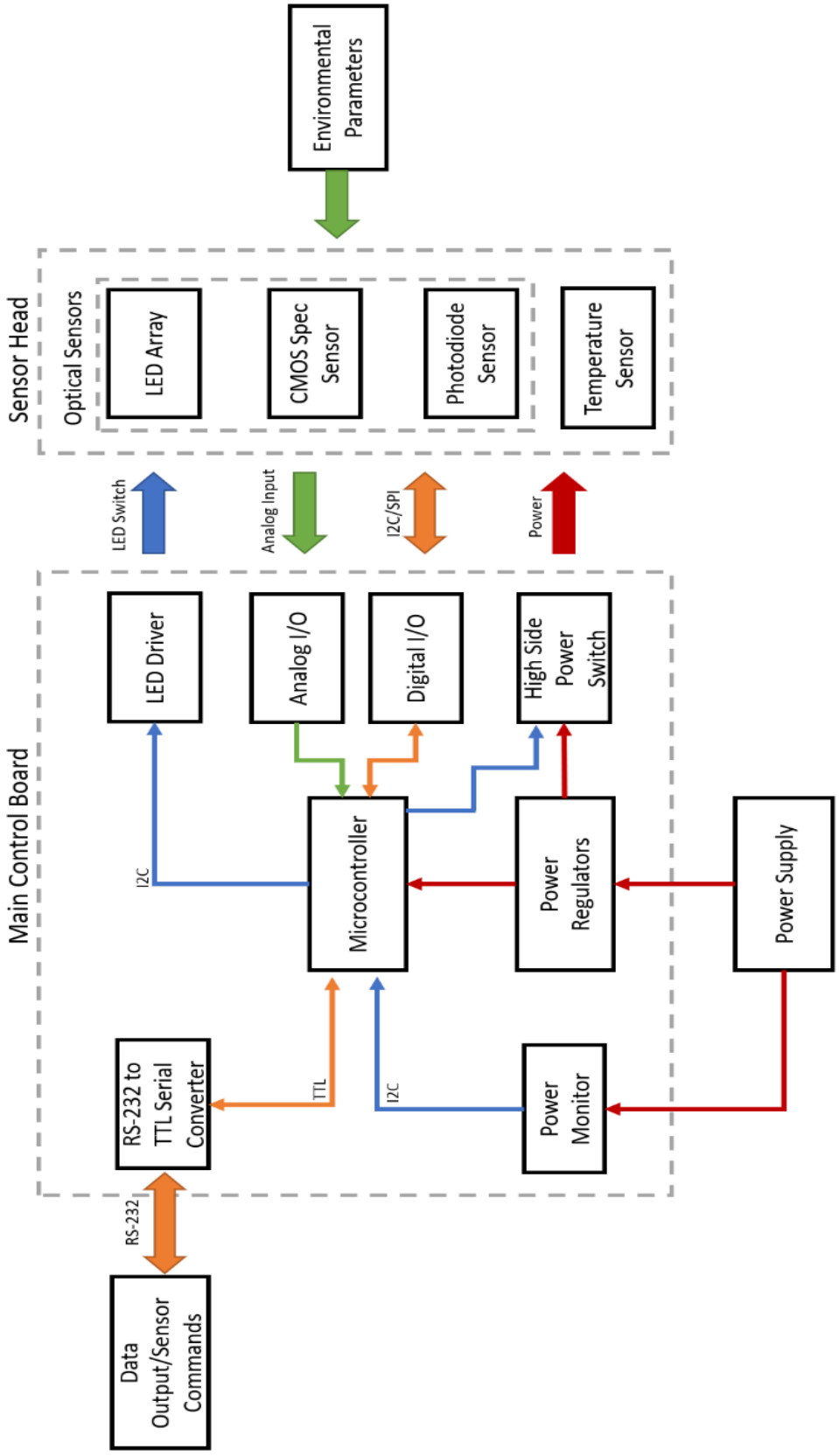

Figure 2-1 Overview diagram of electronic system design to operate the sensor's measurement systems and provide data output to an external controller.

2.2.3 Firmware Development

The firmware was written in the C++ language using the. Arduino integrated development environment (IDE). An additional plugin software called Teensyduino developed by PJRC.com was used with the Arduino IDE to program the Teensy 3.2 board. The firmware was written to test the functionality of the selected optical component and perform measurements functions. Table 2-4 gives the function blocks used and a description of their functionality. Figure 2-2 shows an overview of the overall function blocks and their implementation.

Table 2-4 Description of the circuitry blocks and their function.

Firmware Function Blocks	**Functionality**
System Wake/Polling I/O	Checks the wake status of the system using an external hardware device.
Serial Communication	Provides a link between an external device and the electronic system for command communication and data output.
Event Handler	Allows the system to respond appropriately to input commands or external inputs.
Data Processing	Processes data retrieved from sensor components before transmission to an external device.
Power Management	Monitors the system's power usage for diagnostic purposes.
Multitasking/Timers	Manages the timing of sequences and performs multiple tasks simultaneously for efficient operation.
PWM (Pulse Width Modulation)	Generates PWM signals to modify the duty cycle of the UV LEDs, controlled by the controller's I/O output.
UV LED Control	Controls the UV LEDs used as an antifouling strategy; activation timing is managed by the controller.
LED Sequencing	Times the sequencing of the measurement LEDs to align with corresponding photodetector measurements.
Photodetector Sensors Read	Manages the timing, setup, and data output of the photodetectors during the measurement cycle.
Temperature Sensor Read	Controls the timing, setup, and data output from the temperature sensor during the measurement cycle.

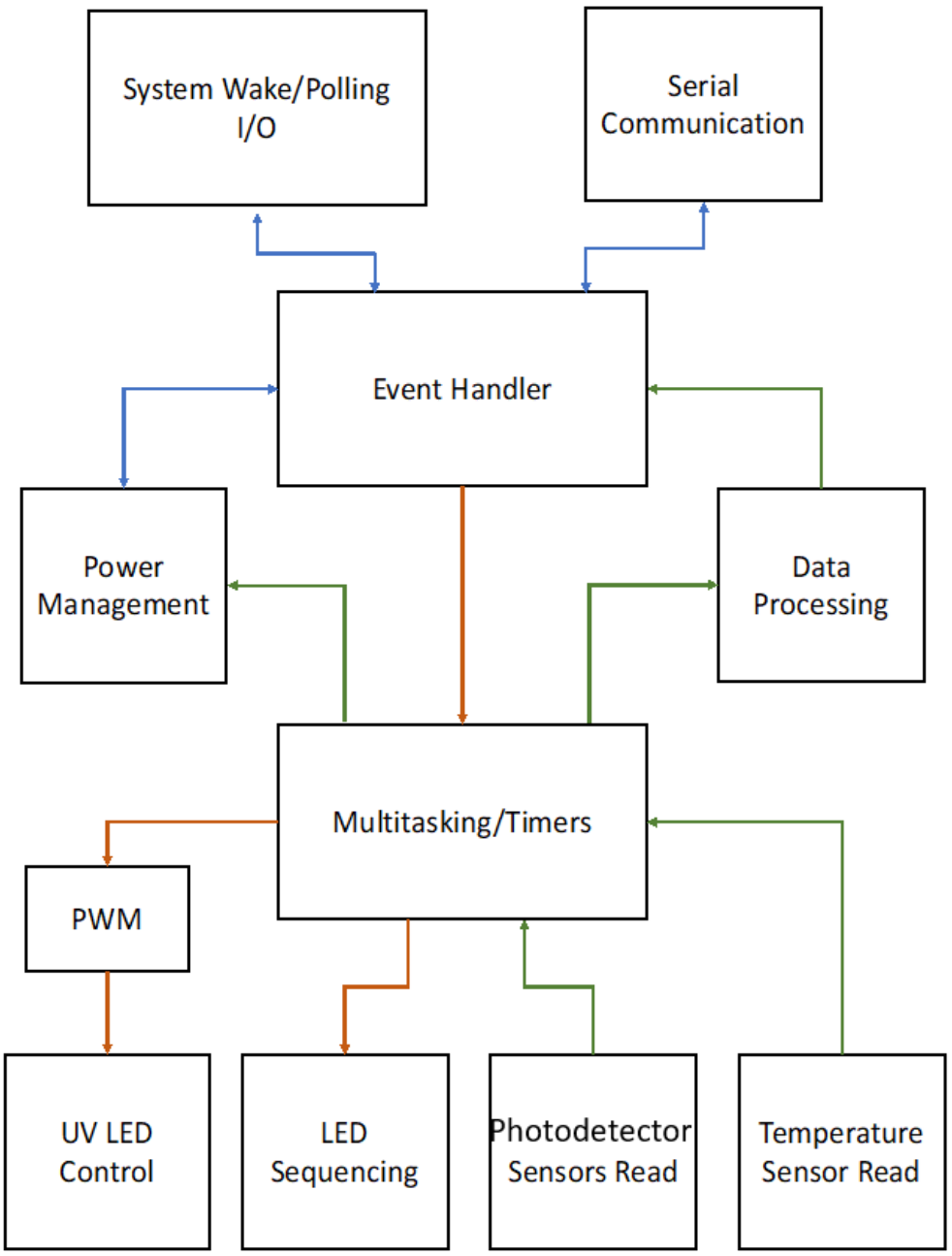

Figure 2-2 Overview flow chart of the structure of the firmware to operate the sensor.

2.2.3.1 **Measurement Cycle Sequence Design**

Figure 2-3 gives an outline of the sampling process the firmware controlled. When the input command to sample was received by the MCU from the user, the sensor started the sequence of measurements. A cycle of LED switching and photodetector readings was done with each photodetector taking a measurement with each specific LED ON as well as a background scan taken with the LED OFF to capture the ambient light without the light source. The background scan was then subtracted from the measurement scan to remove ambient light effects. Additionally, a temperature reading was taken at the end of the measurement cycle.

The data collected was then processed by the MCU and converted to a comma separated variable (CSV) format which allowed the data to be sent as a string and easily deserialised on the other side for additional processing and analysis. The formatted data was then transmitted via the serial port of the MCU to a serial conversion IC (TTL to RS-232) to an external network or via USB.

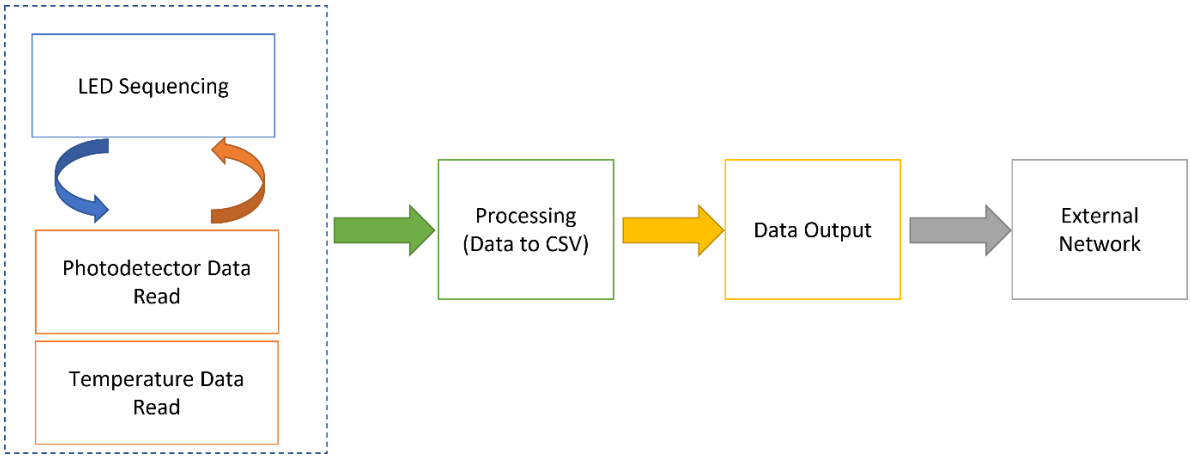

Figure 2-3 Diagram of sensor measurement cycle which uses sequencing between LED switch and sensor measurements in an automated cycle outputting the data to an external receive.

2.2.3.2 **Additional Firmware Libraries Used**

Additional external libraries were used to provide certain functionality to the firmware to interact with different components. To interface with the Hamamatsu CMOS Spectrometer C12880MA a library sourced from GitHub by open-eio "arduino-microspec"[313] was used which provided all required functionality to initialise the sensor, set integration time on as well as retrieve readings. The LED driver used (TLC59116) which is interfaced with the MCU via the I^2C protocol was interfaced using a library sourced from GitHub by Majenko Technologies "TLC59116" [314] which allow for initialising of the IC, switching on/off of channels to the LEDs as well as setting the pulse width modulation (PWM) parameters (duty cycle and frequency). To interface with the current sensor IC, calibrate and retrieve the power readings a library by jarzebski "Arduino-INA226" was used [315]. The library used to interface with the TSYS01 (BlueRobotics_TSYS01_Library) was made by the supplier of the temperature probe BlueRobotics Ltd which allows for communication with the IC over I^2C, to initialise the IC and returns the temperature reading from the probe in degrees Celsius.

2.2.4 Optical Component Performance Tests

2.2.4.1 Optical Setup Evaluation

The selected optical lenses were empirically tested with the LED array light source to identify the optimum positioning. The collimation lens (25 mm UVFS with 25 mm focal length) was tested with the LED array positioned 50 mm from a target. The LED Array was tested with and without the collimation lens positioned 10 mm ahead of it. The dispersion of the light from the eight LEDs was observed. A second test was implemented to test the effectiveness of a plano-convex 12 mm lens for focusing the signal light on the detector and the ideal distance to the detector. Two positions were tested with the LED Array positioned 50 mm ahead of the focusing lens. The target was positioned 15 mm and 30 mm respectively from the focusing lens to observe the concentration of light at different positions. The third optical set up consisted of implementing both the collimation lens and the focusing lens to observe the usability of this system for the benchtop prototype.

2.2.4.2 Output Spectra of Selected LEDs

The output spectrum of the selected LEDs were measured using a benchtop spectrometer unit (Ocean Optics Maya 2000). The Ocean Optics Maya spectrometer has a measurement range of 175 – 1100 nm with an optical resolution of 0.035 nm (FWHM) and a high sensitivity in the UV spectrum.

2.2.4.3 Comparison of Selected Spectrometer with Commercial Spectrometer

To evaluate the performance of the C12280MA spectrometer against a commercial benchtop spectrometer, three of the eight LEDs with wavelengths of 360 nm, 380 nm, and 430 nm were used. Their spectra were recorded by the C12280MA spectrometer and compared with an Ocean Optics Maya spectrometer. The accuracy, spectral resolution and detection ranges of both spectrometers were observed in the context of the difference of component cost and physical size differences for the application of deployable optical detector components.

2.2.5 Design of Benchtop Test Rig

In this section the benchtop unit designs are outlined with different setups. The first design is of a benchtop fluorometer. This design incorporated a C12880MA spectrometer positioned at 90 degrees relative to the light source and three LEDs to induce fluorescence. The second design expands on this first design to incorporate an additional spectrometer

positioned in front of the light source and full suite of LEDs as outlined in are utilised. The third design incorporates plug and play features and furthers the integration of the electronics and sensing technology. In this design the backscatter photodiode and optics are added as well as the interfacing electronics.

2.2.5.1 **Fluorometer Design**

Figure 2-4 shows a labelled exploded view of the fluorescence detection benchtop setup. The collimation lens was positioned in from of the LED light source using ThorLabs SM1L03 (https://www.thorlabs.com/thorproduct.cfm?partnumber=SM1L03) stackable lens tube. The light source holder consists of a ThorLabs CP33/M (https://www.thorlabs.com/thorproduct.cfm?partnumber=CP33/M) threaded optical mount and a FDM 3D printed adapter to hold a through hole LED (as shown in Figure 2-4) or an LED array. Figure 2-5 shows an exploded view of the LED Array mounting to the adapter piece which fits into the CP33/M threaded optical mount. For the detector, a 12 mm UVTFS plano-convex lens with a 10 mm focal length was used to refocus the emitted light from the sample onto the entrance slit of the spectrometer. The mounting structure for the electronic sensing components was designed in the shape of a saddle or bridge to allow easy access to all components as well as positioning the components and the optics in the correct orientation. The sample is held using a 10 mm x 10 mm 3.5 mL UV cuvette which sits at the centre of the setup.

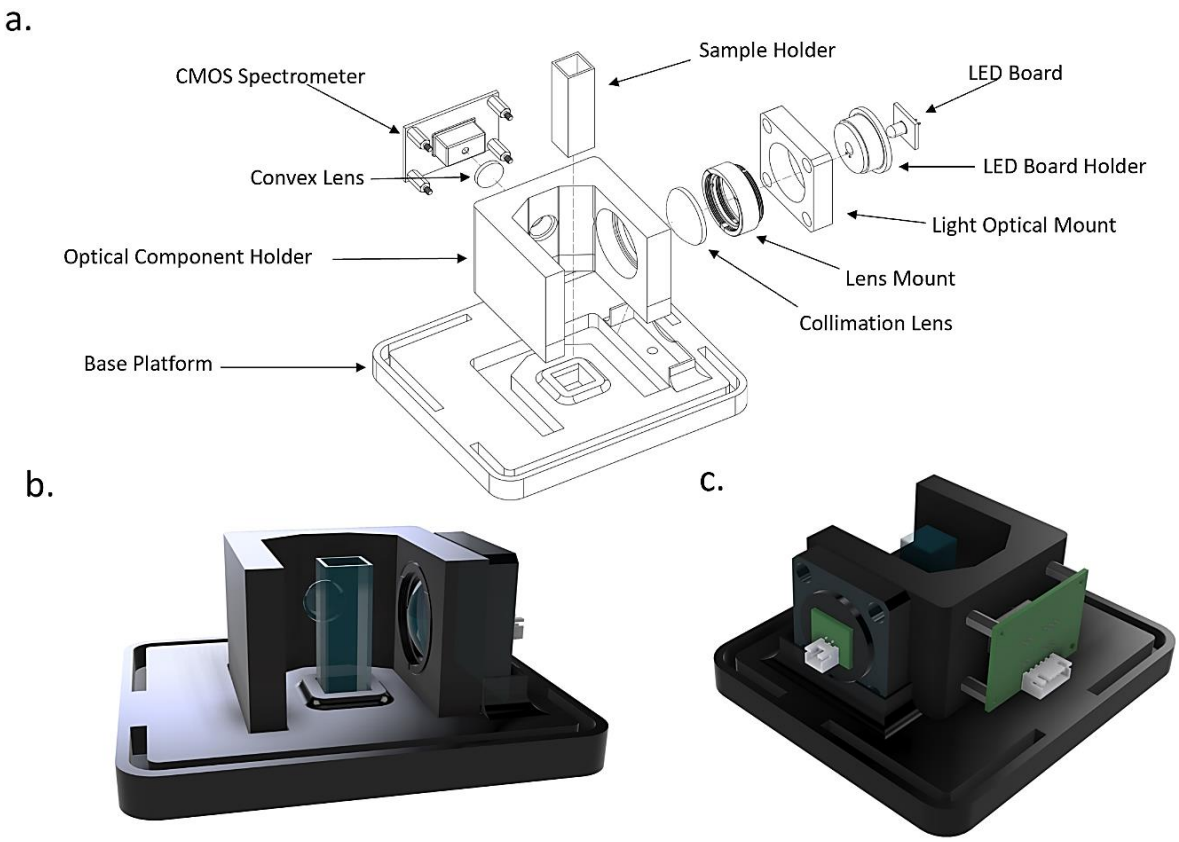

Figure 2-4 The benchtop optical detection system design for fluorescence and scatter measurements (a) An exploded and labelled view of the benchtop design showing components used and assembly. (b) Shows a 3D render view of the optical detection zone and sample holder. (c) Gives a 3D render view of the mounted detection components.

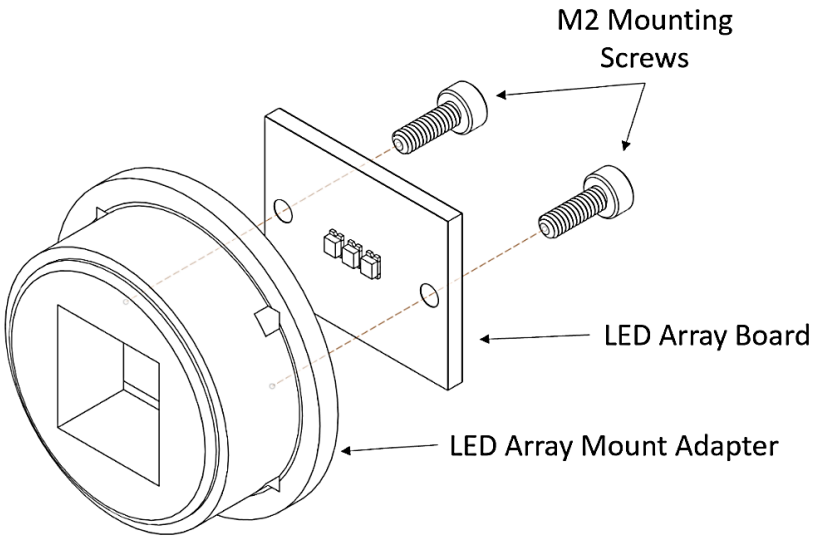

Figure 2-5 Image of mounting system for LED Array using mounting adapter for the CP33/M threaded optical mount.

2.2.5.2 **Multi-Measurement Design**

A second iteration of the benchtop system (see Figure 2-6) was designed which incorporated a second position for a spectrometer to be placed at 0 degrees to the light source to allow all three modes of detection to be tested, absorbance, scatter, and fluorescence. With this version the full suite of LEDs can be used for a wide range of measurements on environmental samples. This gives the capability of testing samples and building up the required hardware and firmware to be able to carry out all functionality of the sensor in one automated sequence.

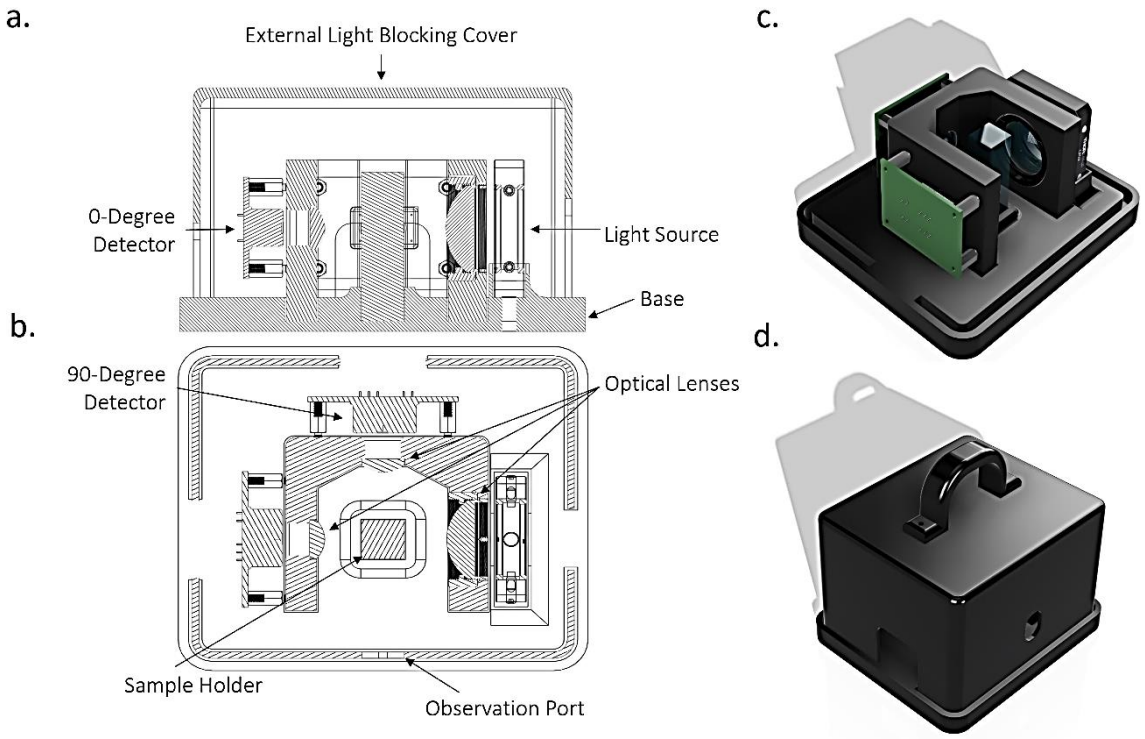

Figure 2-6 Multi-spectrometer benchtop detector design using two spectrometer detectors. (a) Labelled front sectional-view. (b) Labelled top sectional-view. (c) 3D render model render of benchtop detector without light blocking cover. (d) 3D render model render of benchtop detector with light blocking cover.

2.2.5.3 **Full Plug and Play Design**

Figure 2-7 shows the third iteration of the design of the benchtop prototype. In this iteration the electronics were fully integrated and mounted to a saddle structure. Figure 2-7a shows how the electronics mounting tray is positioned onto the benchtop device. The design of the electronics mounting tray is described in Section 3.2.2.1. This design was to allow for different sensor setups to be mounted to the electronics mounting trat and slotted onto the

benchtop device. The photodiode board was positioned at 120 degrees relative to the incident of light to allow for backscatter measurements to be made.

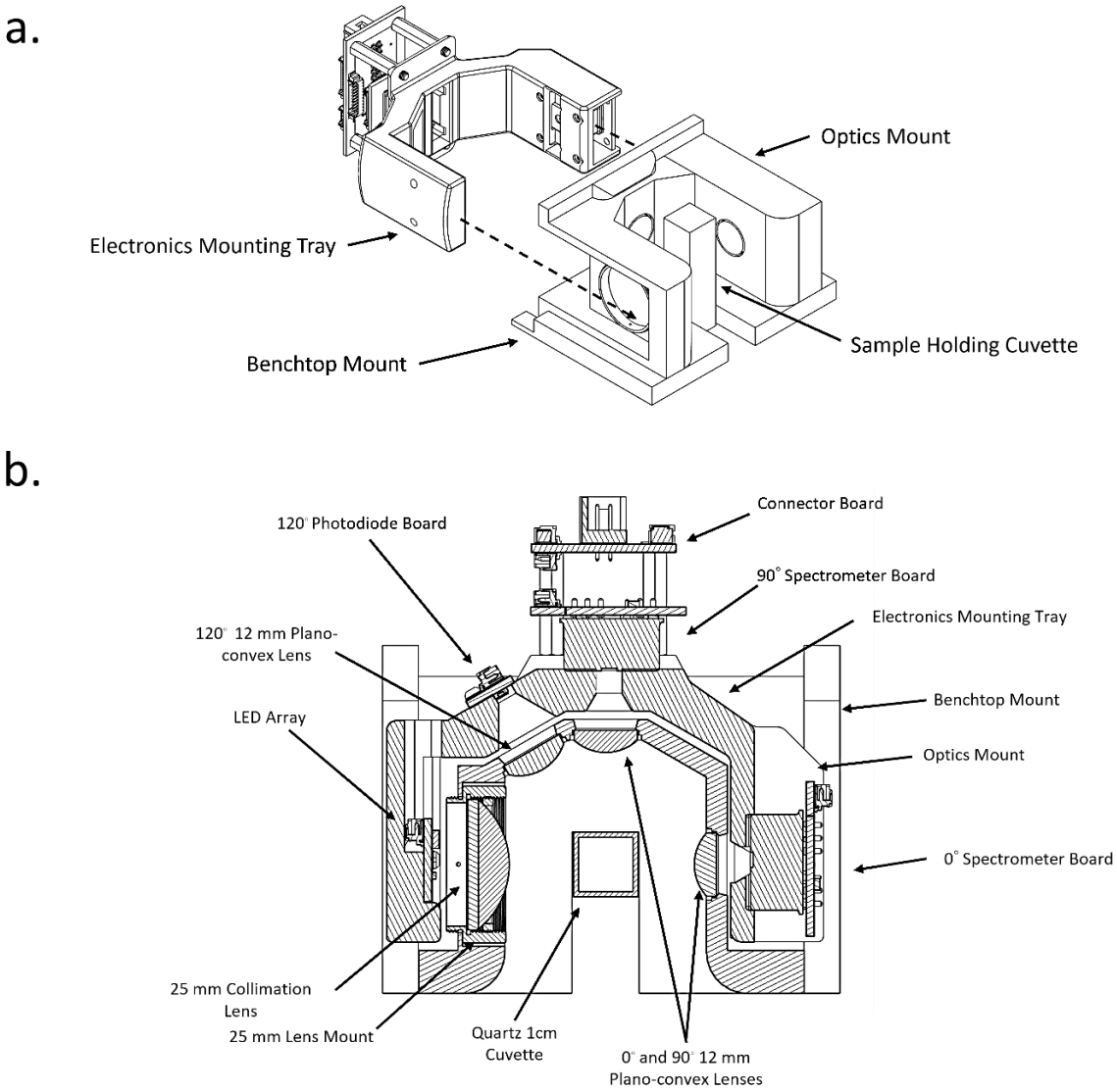

Figure 2-7 Benchtop optical detector design with full plug and play features. Two spectrometers positioned at 0 and 90 degrees to the LED array light source and a photodiode positioned at 120 degrees. (a) Depicts the mounting of the electronics holder onto the benchtop and optics mounts. (b) A labelled cross-sectional view of the benchtop design.

2.2.6 **Proof of Concept Experiments**

The C12880MA spectrometer measured light used 288 pixels which each corresponding to a particular wavelength, given by Equation 2-1.

$$\boldsymbol{\lambda = A_0 + B_1 n + B_2 n^2 + B_3 n^3 + B_4 n^4 + B_5 n^5} \qquad 2\text{-}1$$

where, A_0, B_1, B_2, B_3, B_4 and B_5, were empirically measured constants specific to each spectrometer and n is the pixel number. The integration time of the spectrometer could be controlled and set using serial commands from the user interface, ranging from 11 μs – 4 s. The integration time controls the length of time that the detector of spectrometer is allowed to collect photons before sending the accumulated charge to the microcontroller unit's (MCU's) analog to digital converter (ADC), weaker signals have longer integration times, while more intense signals required shorter integration times. The integration time was established at the start of each experiment by adjusting the integration time such that the intensity of the strongest signal under investigation was approximately 90 % of the maximum and kept constant throughout the experiment.

2.2.6.1 **Absorption Detection**

The systems performance in measuring target analytes analytically by measuring transmission and resulting absorption levels was conducted on the multi-measurement benchtop prototype. The LEDs which were used for this experiment were the Blue (430 nm), Green (565 nm) and Red (660 nm) LEDs in the visible region. The spectrometer positioned at 0^o relative to the incident of light was used to measure the light source transmitted through the sample region. The absorption experiments were conducted with three dyes of different absorption ranges corresponding to each LED emission range. The dyes and LED used for each absorption measurement experiment are outlined in Table 2-5.

Table 2-5 Selected dyes and corresponding LED used for absorption experiments.

LED	Dye
Blue (430 nm)	Fluorescein
Green (565 nm)	Rhodamine B
Red (660 nm)	Basic Blue 3

A stock solution of 10 μgL^{-1} concentration was made for each dye by diluting the dye in deionized (DI) water (18 $M\Omega cm^{-1}$). Using serial dilution with DI water, five concentrations were made for each dye with a total volume of 10 mL. The dilutions are presented in Table 2-6. A 3.5 mL volume of the dye concentration was pipetted into the cuvette of 10 mm path length.

Table 2-6 Dilution volumes of stock 10 µgL^{-1} dye with deionised water for achieved concentrations and 10 mL total volume.

Volume of 10 µgL^{-1} Stock Solution (mL)	Volume of DI water (mL)	Dye Concentration (µgL^{-1})
0	10	0
0.125	9.875	0.125
0.25	9.75	0.25
0.5	9.5	0.5
1	9	1

The integration time used for the Blue LED was 0.0006 s, for the Green LED was 0.003 s and for the Red LED was 0.0001 s. A spectral scan was taken by the spectrometer for each concentration with the LED on and the LED off for a background measurement. The background measurement was subtracted from the LED on measurement to normalise the sensor response. To convert the transmission sensor response to absorption, firstly the light intensity at a selected wavelength was extracting using Equation 2-1 from corresponding pixel value applying the coefficients for the C12280MA unit used. The Equations 1-1 and 1-2 outlined in Section 1.3.1 are applied to the sensor response to calculate the absorption rate. The resulting absorption measurements for each LED and dye concentration were then plotted and analysed for a linear fit. The absorption regions of each dye were measured using the Shimadzu UV 1800 Spectrometer. The LED spectrum measured by the C12280MA spectrometer on the benchtop device was overlayed with the absorption spectrum to observe the overlap with the corresponding dye.

2.2.6.2 Scatter Detection

To test the systems performance for the measurement of scatter an IR 850 nm LED was used as seen in the table of selected LEDs (Table 2-8). The spectrometer positioned at 90 degrees relative to the light source was used to measure the scattered IR light in the sample. The photodiodes positioned at 120 degrees relative to the incident of light was used to measure backscatter. Dilution of the turbidity standard in DI water was performed to generate a range of concentrations from 0 to 78.43 NTU as seen in Table 2-7. A total volume of 10 mL for each turbidity value was produced.

Table 2-7 Dilution volumes of 4000 NTU turbidity standards with deionised water with total end volume of 10 mL.

Volume of 4000 NTU Standard (mL)	Volume of DI water (mL)	Turbidity (NTU)
0.0000	10.0000	0.00
0.0199	9.9801	7.98
0.0398	9.9601	15.94
0.0596	9.9403	23.86
0.0794	9.9206	31.75
0.0990	9.9010	39.60
0.1186	9.8814	47.43
0.1381	9.8619	55.23
0.1575	9.8425	62.99
0.1768	9.8232	70.73
0.1961	9.8039	78.43

An integration time of 0.2 s was used for the spectrometer scatter measurements. The backscatter measurement was taken directly after the scatter measurement. A background measurement was made before each concentration measurement and subtracted from the turbidity measurement. The spectrometers response at 850 nm was retrieved from the corresponding pixel intensity. The photodiode and spectrometer responses were plotted using a scatter plot and their linearity and limits of detection (LODs) were compared.

2.2.6.3 Fluorescence Detection

Proof of Concept Qualitative Experiments

Initially, three high concentration solutions of quinine sulfate, extracted Chl-a and cyan fluorescent protein (CFP) were used for screening system application. An appropriate integration time for each fluorophore was established by turning each LED on and adjusting the integration time until the peak of each fluorescence signal reached approximately 80 – 90 % of the maximum signal. This ensured a high dynamic range without detector saturation.

Analytical Performance with Laboratory Standards

The analytical performance of the device was assessed with laboratory prepared standards of basic blue 3 dye (BB3), and comparison with a Jasco FP-8300 benchtop fluorometer.

Performance Evaluation with Algae Cultures

Laboratory grown algae were used to determine the fluorometers capabilities to detect Chl fluorescence. The diatom species was cultured in filtered artificial seawater water (0.45 μm) supplemented with nutrients to make Guillard's F/2 + Si medium (43). The cultures were grown in batch growth system in 5L Pyrex bottles (15 – 23 ^{o}C, 12:12; light:dark, continuous light of 65 μmoles/m^2/s). The concentration of biomass was calculated by determining the concentration of Chl-a in 25 mL aliquots that were filtered at low pressure (700 mb) through GF/F glass fibre filters (Whatman GF/F, pore size 0.7 μm) kept in the dark at -20 ^{o}C for 12 hrs. Subsequently, 8 mL of 90 % (v/v) acetone was added to each 25 mL filtered aliquot, followed by sonication in an ultrasound bath for 5 min. Extraction was carried out in the dark at 4 ^{o}C for at least three hrs following centrifugation (5000 r.p.m., 10 min) and recovery of the supernatant. Absorbance was read at 665 nm and 750 nm on a Shimadzu UV-1800 UV-Vis double beam spectrophotometer allowing the calculation of Chl-a concentration as outlined in [316] and conversion to μg L^{-1} concentrations.

Environmental Case Study

Environmental samples were used to determine if it was possible for the sensor to be used for in-vivo fluorescence. Samples were collected from Dublin Harbour and can be classified as brackish. Samples were analysed untreated on the bench-top system, with fluorescence scans collected for all three LEDs.

2.3 Results and Discussion

In this section the selected optical and electronic components are discussed and justified. The optical component's performance is analysed to validate their incorporation in the optical detection system. The assembled benchtop designs are reviewed and the analytical measurement performance of the system for multiparameter measurements are analysed.

2.3.1 Selection of Optical Sensing Components

2.3.1.1 Spectrometer Photodetector

The spectrometer chosen for the 0 degree and 90 degree detectors was the C12880MA mini spectrometer manufactured and sourced from Hamamatsu (https://www.hamamatsu.com/eu/en/product/optical-sensors/spectrometers/mini-spectrometer/C12880MA.html). The mini-spectrometer has a spectral response range between 340 – 850 nm with a typical spectral resolution of 12 nm (FWHM) using a high-sensitivity CMOS (complementary metal oxide semiconductor) linear image sensor with 288 pixels.

2.3.1.2 Photodiode Photodetector

For the measurement of backscatter, the detector positioned at 120 degrees relative to the light, a photodiode was selected with a broad sensitivity range. The photodiode selected was the MT03-021 (https://marktechopto.com/pdf/products/datasheet/MT03-021.pdf) manufactured by Marktech Optoelectronics and sourced from Digikey Electronics Ltd. This photodiode was selected due to its broad spectral range (300 nm to 1100 nm) with peak sensitivity in the IR region. The MT03-021 comes in a compact surface mounted package (3 mm x 3 mm x 1.15 mm) making it suitable to integrate into the optical head detector.

2.3.1.3 LED Array Light Source

Table 2-8 shows the selected LEDs with their peak emitted wavelength, spectral bandwidth (FWHM), corresponding target analyte of detection and mode of detection. The measurement type column gives the method and position of the detector to be used for measurement of the light signal. The selected LED component number, package side (all are surface mounted packages), manufacturer and supplier the LEDs were sourced from are given in the following columns. Each LED was selected based on its spectral output corresponding with an identified target analyte for measurement in a particular optical

measurement mode as identified in Section 1.3. The LEDs spectral emission cover the UV, visible and IR ranges to produce a multispectral light source of individually controlled LEDs. This range of different LED emission profiles give a wide range of optical measurement applications. The form factor or package size was also factored in, 0805 smd package size was prioritised due to its small footprint and to allow for potential plug and play of different LED profiles in the future. LEDs 3-8 use this form factor with the LEDs 1 and 2 unavailable in the 0805-package size.

Table 2-8 LEDs Selected for specific analyte detection and surface mounted packages.

LED No.	Peak Wavelength (nm)	FWHM (nm)	Target Analyte	Measurement Type	LED Product Number	LED Package	Name of Manufacturer	Name of Supplier
1	280	10	DOM + Petrol	Flr	XBT-1313-UV-A150-AG270-00	1.3 mm x 1.3 mm	Luminus Devices	Mouser Electronics.
2	310	11	DOM + Petrol	Flr	CUD1GF1A	1414 (3535 Metric)	SETi/Seoul Viosys	Digi-Key Electronics
3	365	10	DOM + Chl A	Flr & Abs	ATS2012UV365	0805(2012 metric)	Kingbright	Mouser Electronics.
4	385	12	DOM + Chl A	Flr & Abs	ATS2012UV385	0805(2012 metric)	Kingbright	Mouser Electronics.
5	430	60	Chl A	Flr & Abs	KP-2012MBC	0805(2012 metric)	Kingbright	Farnell Ireland
6	565	ND	Blue Algae	Abs	SML-LX0805SGC-TR	0805(2012 metric)	Lumex	Mouser Electronics.
7	660	ND	Green Algae	Abs	SML-LXF0805SRC-TR	0805(2012 metric)	Lumex	Mouser Electronics.
8	850	30	Turbidity	Sct & Bsct	VSMY1850X01	0805(2012 metric)	Vishay Semiconductors	Mouser Electronics.

FWHM = Full width at half maximum, Flr = Fluorescence, Abs = Absorption, Sct = Side scatter, Bsct = Back scatter, DOM – Dissolved Organic Matter, Chl A – Chlorophyll A, ND – No Data

2.3.2 Development and Interfacing of Electronic Systems

The resulting full schematic of the control board can be seen in the Figure A-1 Appendix A. The grouped schematic designs of the optical sensing and connector circuit boards can be seen in Figure A-2 Appendix A.

2.3.2.1 Main Control Board Development

Microcontroller Unit and Communication Electronic Systems

The MCU controlled the functionality of the sensor and integrated with the external sensing and communication components. The MCU selected for the sensor was the Teensy 3.2 (https://www.pjrc.com/store/teensy32.html) manufactured by PJRC.com sourced from Digikey Electronics Ltd. The Teensy 3.2 was selected due to its high-resolution ADC at 16 bits, it's numerous I/O pins, processing speed (72MHz) and other additional features which made it ideal for the task of automating and carrying out the required functions for the sensor. To convert the TTL serial output of the sensor to the required RS-232 protocol a converter IC was selected and implemented to carry out this task. The IC selected was the MAX3232 (https://www.ti.com/product/MAX3232) manufactured by Texas Instruments and sourced from Digikey Electronics Ltd. This allowed for data from the sensor to be outputted to the external hardware controller as well as allowing the external controller to send commands to operate the sensor.

System Power Regulation

The system was able to be powered over a defined range of input voltages (rated for 7 V to 35 V input) to power the circuitry in accordance with international standards outlined in ISO 22013 Section 5.9.1 [317]. To do this, three linear drops out (LDO) regulators were used to achieve three separate power rails (7 V, 5 V and 3.3 V) to power specific components. The voltage regulator used to provide a stable 5 V supply was the L7805ACD2T-TR (https://www.st.com/resource/en/datasheet/l78.pdf) manufactured by STMicroelectronics sourced from Digikey Electronics Ltd which outputs 5V with a 1.5 A rating and input voltage range of 5 V to 35 V. The 5 V rail powers the 3.3 V voltage regulator, spectrometers and RS-232 chip. The second regulator used to provide a and adjustable voltage output is the LM317D2TR4G (https://www.mouser.ie/datasheet/2/308/1/LM317_D-2314752.pdf) which has an adjustable voltage output set to 7V using a reference resistor. Rated to up to 40 V input it outputs 1.5 A. The 7 V power rail provides power at a steady voltage to the

LEDs to ensure consistent illumination for the detector. The final regulator is built into the Teensy 3.2 MCU board (LP38691 (https://www.ti.com/product/LP38691)) which received a regulated 5V input voltage and provides the 3.3V logic level voltage rail for the MCU as well as the additional ICs in the circuit.

A current monitoring IC was used to allow the sensor to monitor power draw of the overall system as well as individual components for the purpose of diagnostics and power usage analysis. The IC selected was the INA226AIDGST (https://www.ti.com/product/INA226/part-details/INA226AIDGST) manufactured by Texas Instruments and sourced from Digikey Electronics Ltd which can monitor a voltage range between 0 and 36V. A low ohm current sense resistor (100 mΩ, ±1%, 2W Chip Resistor 2512 (6432 Metric), CSRN2512FTR100 (https://www.seielect.com/catalog/sei-csr_csrn.pdf) source from Digikey Ltd) was used to measure the voltage drop across it and the current monitor IC concerted this to a current draw and power value which was read by the MCU via the I^2C protocol. These power measurements were used to ascertain individual components current draw in the system such as the LEDs and optical head sensors etc. The current draw was taken before and after the component was turned on with the current draw of that component being isolated and measured. This was used for diagnostic purposes to assess if the component was functioning correctly.

A power diode was also included into the power circuitry in series with the positive input of the power supply to prohibit current backflow. This was installed to avoid damage to the system if the sensor were to be connected incorrectly or a short circuit occurred. The power diode selected was the SBR3U30P1-7 (https://www.diodes.com/assets/Datasheets/SBR3U30P1.pdf) manufactured by Diodes Incorporated and sourced from Digikey Electronics Ltd. The power diode can block a reverse voltage of up to 30V at 3A with a forward voltage of 430 mV at 3 A and a reverse leakage of 400 µA at 30 V.

A MOSFET (metal-oxide-semiconductor field-effect transistor) array in an N and P-channel configuration was used to switch power to the sensors powered on the 5V power rail. The NTJD1155LT2G (https://www.onsemi.com/pdf/datasheet/ntjd1155l-d.pdf) manufactured by OnSemi and sourced from Digikey Ltd was used. The P-Channel MOSFET was set up as a high side driver to switch 5 V to the optical head sensors. The N-Channel MOSFET

was used to allow logic level voltages to drive the P-Channel MOSFET gate. High and low signals from an i/o pin of the MCU were used to switch the 5 V to the sensors.

Sensing Components Interfacing with Control Systems

The C12880MA spectrometer, was controlled using a set sequence of pulse cycles to set the integration time and start the measurement. The signals required from the MCU were a steady frequency clock pulse and a start pulse. The integration time was set by the ratio of clock pulses completed during the start pulses up time. The readings from the linear array of the CMOS were read back over a video channel with the analog measurements. The datasheet from the manufacturer recommended using a digital buffer [179] for the clock and start signals. This was to isolate the input of the MCU from the CMOS output signal to avoid additional noise on the input circuit. The digital buffer IC implemented was the MC74VHCT125ADTRG (https://www.onsemi.com/pdf/datasheet/mc74vhct125a-d.pdf) manufactured by OnSemi and sourced from Digikey Electronics Ltd. Additionally, a single ended buffer using an operational amplifier with unity gain was used for the video analog input. This was to ensure that a steady voltage output from the CMOS to the MCU's ADC was maintained. For the operational amplifier, a MCP601 manufactured by Microchip Technology and sourced from Digikey Electronics Ltd was used. The output voltage from the C12880MA at saturation can be up to 4.3V [179] while the Teensy 3.2 ADC input range is 0 to 3.3V [318]. To avoid the input damaging the MCU's ADC, a voltage divider was used to scale the input from 0-4.3V to 0-3.3V.

The MT03-021 photodiode was setup in photovoltaic. This was done by using a transimpedance amplifier to convert the output current from the photodiode to a proportional voltage which was read into the MCU's ADC. The MCP601 (https://www.microchip.com/en-us/product/mcp601) operational amplifier (op amp) was used with a 1 MΩ negative feedback resistor connected to the inverting pin of the op amp to set the gain. A 1 nF ceramic feedback capacitor was placed in parallel with the feedback resistor to limit output drift and unwanted oscillations.

The stability of the LED intensity was important for the optical measurement to produce consistent and reliable readings. To achieve this a dedicated LED driver IC was selected to switch on and off the LEDs while also closely regulating the current to them. The LED

Driver selected was the TLC59116FIPWR (https://www.ti.com/product/TLC59116F/part-details/TLC59116FIPWR) manufactured by Texas Instruments and sourced from Digi-Key Electronics Inc which can drive 16 separate channels with a regulated current set by an external resistor value and can be controlled by the MCU over I^2C digital protocol which reduced the number of output pins needed from the MCU. The IC can regulate the current consistently to keep the output intensity of the LEDs stable without variation and can also output a PWM with programable duty cycle and frequency. PWM allowed for dimming and power saving control. The IC manages the PWM signal automatically which allowed for the MCU to conduct other tasks or go into sleep mode, if necessary.

System Connectors

Two primary connectors were used. The first connector provided serials and power connections between the control board and a marine cable connector. A 6 pin through hole pluggable terminal block (component number: 691382010006) and screwless 6 pin plug (component number: 691381000006) manufactured by Wurth Elektronik were used. Both were sourced from Mouser Electronics. The terminal block plug system allowed for easy removal and plugging of the connecting when disassembling. The second connector made the connection between the control board and the optical head. The connector selected for both the control board and the connector board was a 26 way, 2 row IDC ribbon cable connector (component number: 625-7319). The corresponding 26-way female ribbon connectors (component number: 625-7404) were used. A 26-way 1.27 mm pitch flat ribbon cable was used (component number: 289-9925). The IDC connectors and ribbon cable were manufactured and sourced from Radionics Ltd

Development and Design of the Main Control Board

To test the selected components for control and communication, a prototype board was made. A copper stripboard was used to solder the component to and make wired connections between the components. The systems that were tested were: the power regulation circuitry, the MCU and communication control functions and the interface circuitry with sensing components. Figure 2-8a shows the control board PCB design made in the ECAD software. Figure 2-8b shows the PCB design top layer from the ECAD software. This view shows the component placement, the trace routing and the power planes used. A ground plane was used on the top and bottom layers to minimise the route to ground for signals. Two smaller power planes are positioned beneath the heat sink footprints of the voltage regulators to help

dissipate heat. Figure 2-8c shows the CAD model of the board and board dimensions (110 mm x 82 mm).

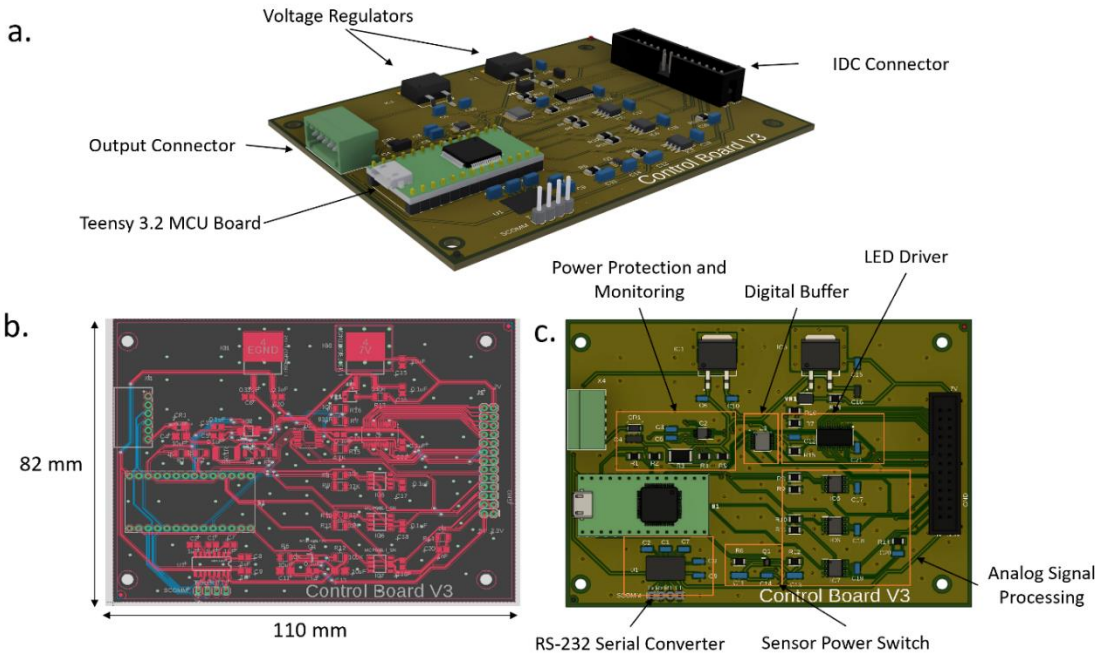

Figure 2-8 Design layout of the control board printed circuit board (PCB). (a) 3D labelled model view of the control board design. (b) Dimensioned PCB layout top layer view showing layout, component placement, trace routing and copper power planes. (c) 3D labelled model top view of PCB showing circuitry blocks for functionality of the system.

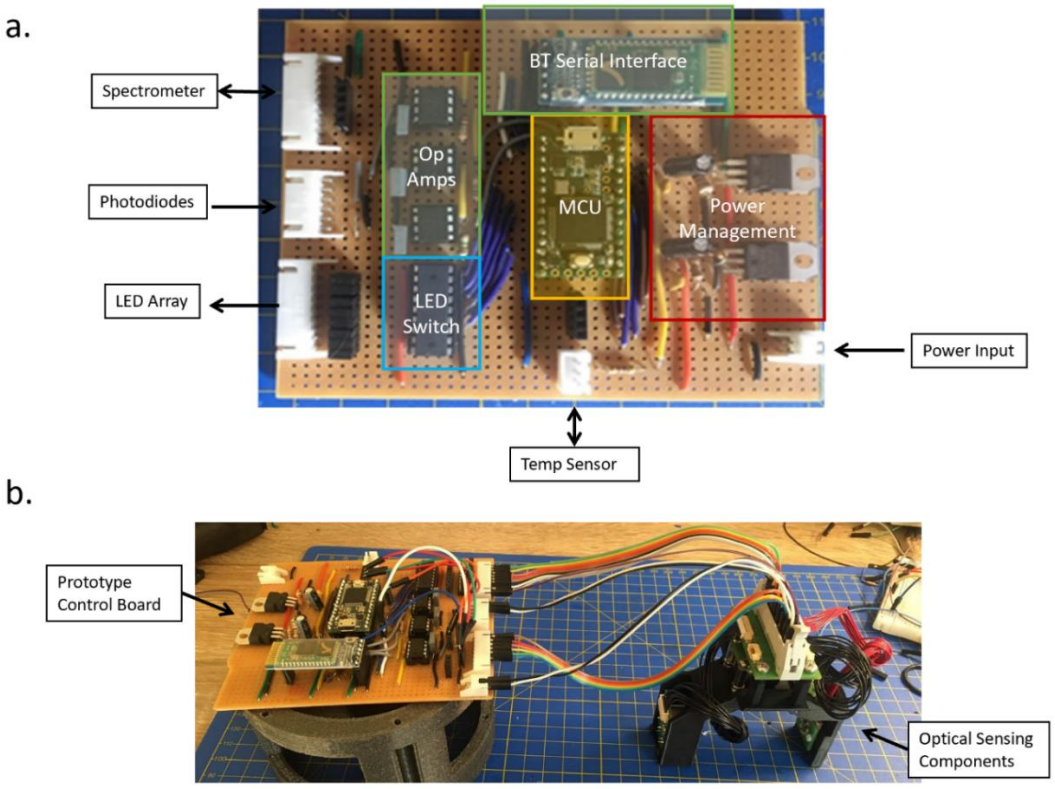

Figure 2-9 Prototype control board using copper strip protoboard (a) Labelled top view of the prototype control board with circuitry blocks and connections highlighted and labelled. (b) Image of the prototype control board interfaced with the optical sensing components for testing.

In Figure 2-9, the first control board prototype can be seen. The development of this first prototype gave insight into the circuitry design for interfacing the MCU with the sensing components and testing the developed firmware. From the testing of the circuitry developed on the prototype board the embedded system was designed. It required three iterations of the control board design in total. The circuitry, component performance and positioning were improved with each iteration following testing of the previous iteration. The three iterations of the assembled control board designs can be seen in Figure 2-10. The first iteration positioned the Teensy 3.2 board to the side of the board which was changed in the second iteration to allow for easier connection when installed in the sensor enclosure from the top. Additionally, a Darlington transistor array and current limiting variable resistors were used to switch LEDs and regulate current. This was revised in the second iteration with the use of a dedicated LED driver with built in current regulation and I^2C connectivity. This change to a dedicated LED driver allowed for more previse current control to the LEDs as well as less i/o pins to be required by the MCU to switch LEDs, reducing the number from 8 outputs to 2 I2C pins which also were used by the current monitor chip and temperature probe with all being controlled on the same communication bus with address specific commands. Another change made between the first and second iterations was the incorporation of a digital buffer for the control signals between the MCU and the spectrometers including the clock pulse signal and the start pulse signal. This was installed to provide more stable signals without voltage drop. Another change made between the first and second iteration was the incorporation of a power switch to turn the sensing components off when not in use. A N-P Mosfet high side Mosfet was installed to allow the MCU to switch the 5V power supply to the sensor components off. The final change made for the second iteration was the incorporation of a dedicated TTL to RS-232 converter to allow the system to communicate over the protocol which was required for data integration of the sensor with external infrastructure. The changes made between the second and third iteration included the removal of the test pins which were no longer required as well as the addition of a plug terminal connector instead of terminal pins to allow for easier connection when installed in the sensor enclosure to the bulkhead connector. Electronic connection issues and component positioning identified in previous iterations were also addressed in the third iteration of the control board.

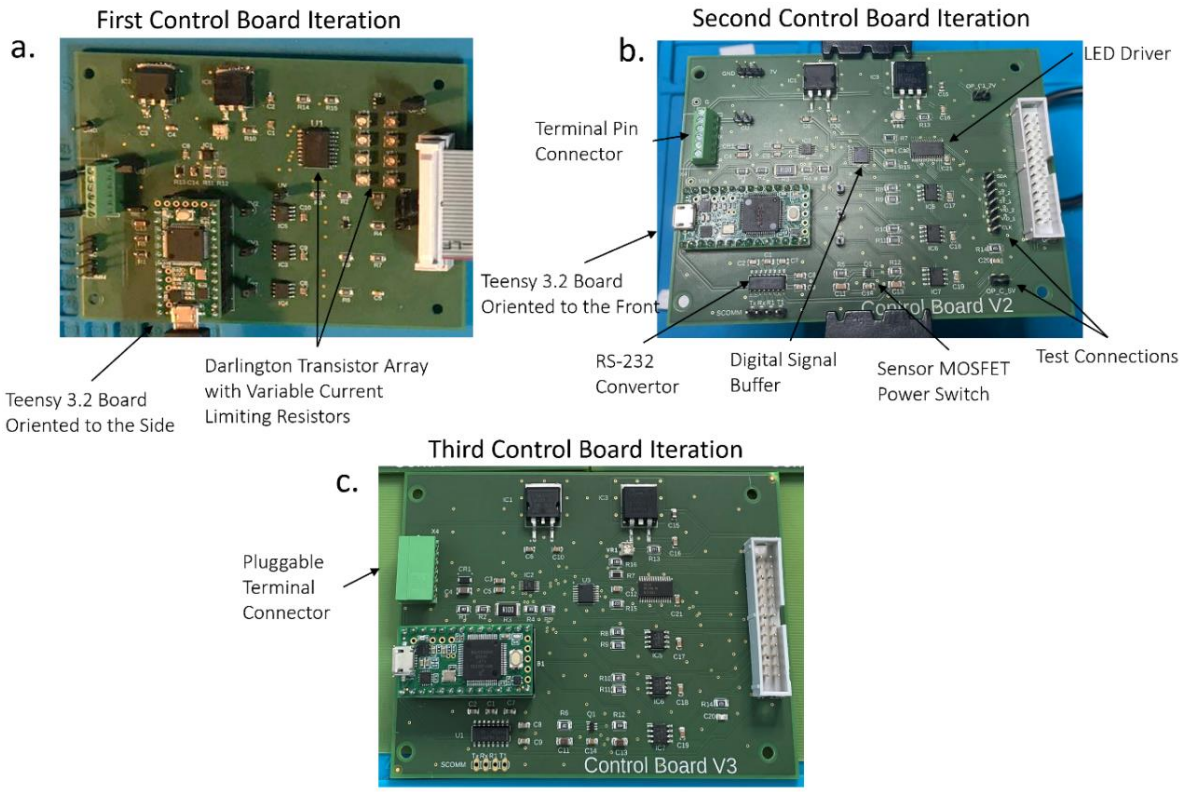

Figure 2-10 Iterations of the assembled control boards designs with changes made labelled. (a) Assembled PCB of first iteration control board. (b) Assembled PCB of second iteration control board. (b) Assembled PCB of third and final iteration of the control board design.

2.3.2.2 **Plug and Play Connector Board Design and Development**

To reduce complexity and implementing a plug at play system to allow interchangeable light sources and detectors a central connector board was designed. This board allowed the LED array and photodetector boards in the optical head to plug in and consolidates all the signals into a single IDC (insulation displacement connector) ribbon cable connector. The IDC connectors required a total of 26 connections to provide power and outputs as well as receive inputs from the optical head electronic system. The IDC connector selected for the connection board was the RS Pro IDC 26-way, 20-row connector (component number: 471-064) sourced from Radionics Ltd. This connector interfaced with the IDC connector and cable used on the main control board but included an ejection latch system to allow for easy disconnect of the ribbon cable connector. The connectors used for all optical head light source and detector boards were Molex PicoBlade 1.25 mm pitch connectors and cables sourced from Radionics Ltd. A total of six 10 contact PicoBlade connectors (component number: 53261-1071) were used for the connections between the LED Array Board and the spectrometer mounting boards to the connector board. Two 100 mm 10-way Picoblade

cables (component number: 15134-1001) were used to connect the LED Array Board and the spectrometer mounting board in the 0-degree position to the connector board. An additional 50 mm 10-way cable (component number: 15134-1000) was used to connect the spectrometer mounting board in the 90-degree position to the connector board. An additional two 4-contact Molex PicoBlade connectors (component number: 53261-0471) and 50 mm connector cable (component number: 15134-0400) were used to connect the photodiode board with the connector board. The only additional connector required was for the temperature probe which came with a preassembled cable and connector, this used the Hirose 4-contact 1.25 mm pitch DF13 connector (component number: DF13-4P-1.25H) source form Radionics Ltd.

Figure 2-11a shows the CAD model of the connector PCB. All connectors are placed on the top layer apart from the spectrometer board in the 90-degree position connector which is placed on the bottom layer. The placement of this connector on the bottom layer was made to reduce board size and provide easier connection to be made. Figure 2-11b shows the ECAD design of the connector board showing the component placements, traced routed and a ground plane placed on the bottom layer to reduce the number of traces needed. Figure 2-11c shows the top view CAD model of the connection board and the board dimensions (48 mm x 28 mm).

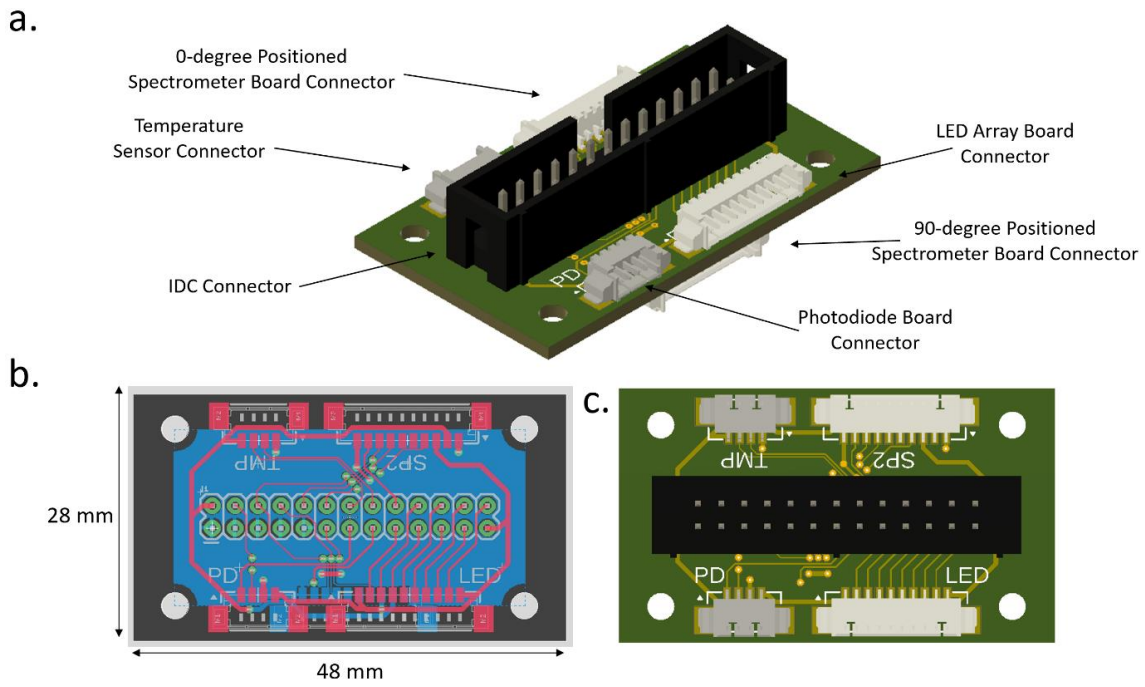

Figure 2-11 Design layout of the connector circuit board. (a) 3D labelled model view of the connector board design. (b) Dimensioned PCB layout top layer view showing layout, component placement, trace routing and copper power planes. (c) 3D model top view of PCB.

In Figure 2-12 the assembled connector board PCB can be seen with surface mounted PicoBlade and Hirose connectors soldered as well as the IDC ribbon cable connector. The connector board offered ease of use to allow the interfacing between the sensing components and the main control board.

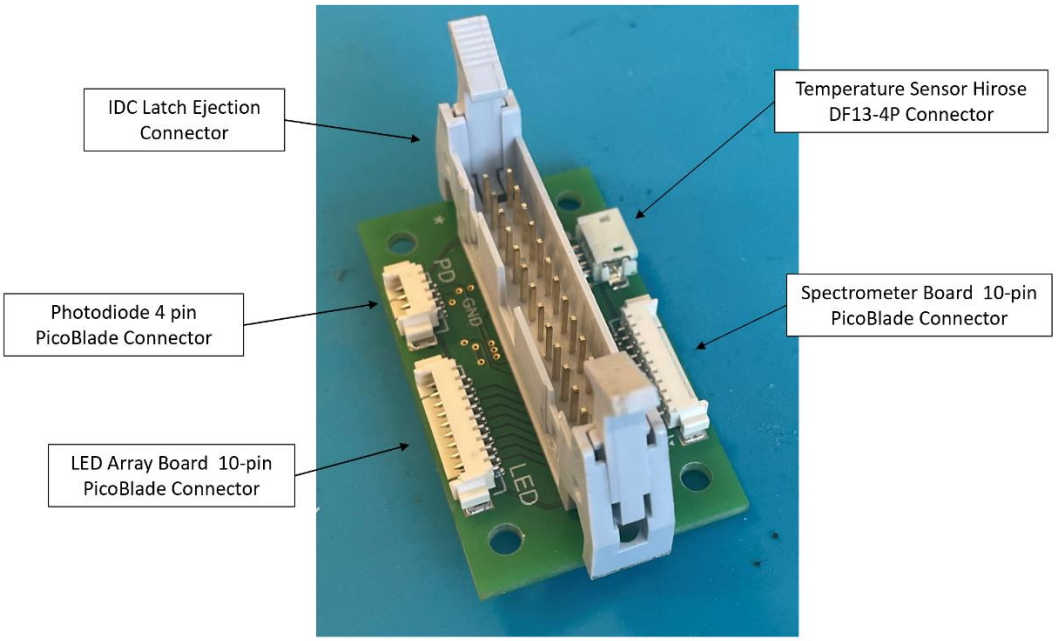

Figure 2-12 Labelled image of the assembled connector board PCB and connectors used to allow for pub and play operation.

2.3.2.3 **Temperature Sensor**

The temperature probe selected was the TSYS01 manufactured by TE Connectivity which has a resolution of ±0.1°C within the range of -5 to 50°C and a digital interface using the I^2C protocol. The IC is incorporated into an attachable watertight probe and penetrator package by Blue Robotics, CELSIUS-SENSOR-R1-RP (https://bluerobotics.com/store/sensors-cameras/sensors/celsius-sensor-r1/) sourced from BlueRov Solutions. The probe came with a preassembled cable with the Hirose 4-pin DF13 connector to connect to the connection board. Figure 2-13a shows the interfacing of the TSYS01 temperature probe with the Teensy 3.2 MCU. The measurement output from the TSYS01 was successfully read by the MCU over the I^2C protocol and output to a PC via USB serial connection. Figure 2-13b shows the data being displayed over the Arduini Serial Monitor in degrees Celsius.

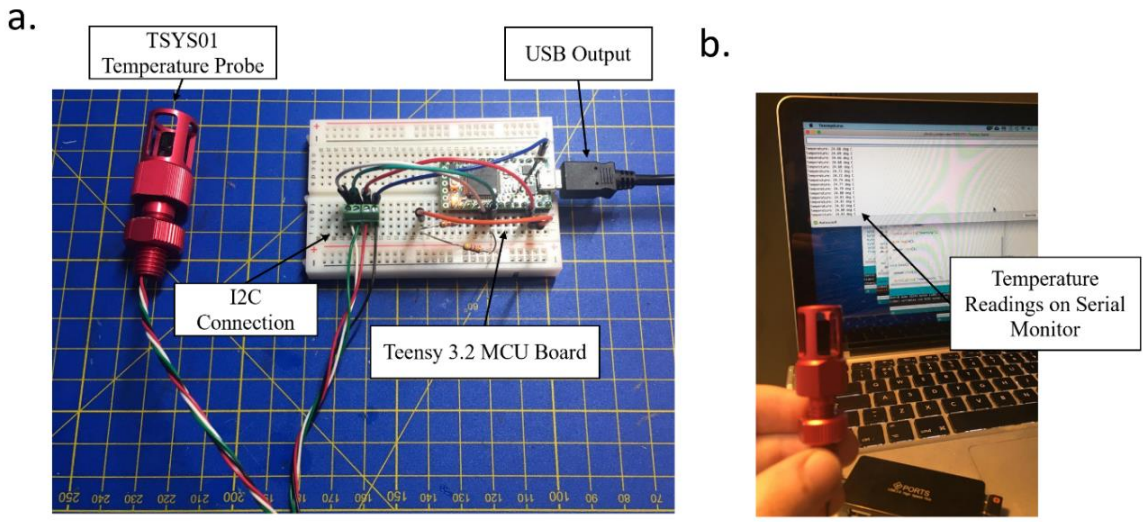

Figure 2-13 TSYS01 temperature probe being tested. (a) The probe interfaced over I^2C protocol with a Teensy 3.2 MCU board and USB connection to a computer. (b) The temperature probe readings being displayed on a serial monitor on the PC.

2.3.2.4 **UV Light Source for Biofouling Prevention**

As is described in Section 3.2.4.2, UV light was selected to prevent biological growth from building up on the optical lenses. This required the UV light source to be positioned behind each optical lens. The UV antifouling LEDs selected were XBT-1313-UV-A150-AG270-00 (https://download.luminus.com/datasheets/Luminus_XBT-1313-UVC_Datasheet.pdf) manufactured by Luminous Devices and sourced from Mouser Electronics Ltd. The LED has a peak wavelength emission of 280 nm. Additionally, they were selected due to their small package size (1.1 mm x 1.3 mm x 1.3 mm), low cost (circa €3) and low power consumption (6mW). The two LEDs were connected in parallel sharing an anode and cathode which allowed the two to be turned on with a single channel of the LED driver. The UV LED pairs are seen implemented in Figure 2-17.

2.3.2.5 **Photodetector Mounting Boards**

Spectrometer Mounting Board Design

Due to the C12880MA's size (20.1 × 12.5 × 10.1 mm), the UV LEDs were placed on a separate board stacked on top of the spectrometer mounting board as shown in Figure 2-14d. This was done to allow the LEDs to be at the same height as the top surface of the spectrometer. This positioned them as close to the optical lens at possible for maximum UV radiation coverage. Figure 2-14 shows the dimensions of the two boards fitted together with a spacer used to position the antifouling board at the correct height (9 mm). For the design

iterations of the spacer, see Section 3.2.2.1. The dimensions of the stacked board at 22 mm width, 30 mm length and 12.16 mm height. When assembled the two LEDs were located approx. 7.5 mm from the entrance slit of the spectrometer (see Figure 2-14a). Two header pins on the spectrometer mounting board (see Figure 2-15a) join with two female pints on the antifouling board. This provided connection of the LED's anode and cathode between the antifouling board and the spectrometer mounting board. A 10 pin Molex PicoBlade connector is used on the bottom layer (see Figure 2-15b and c) of the CMOS board for output connections to the connector board.

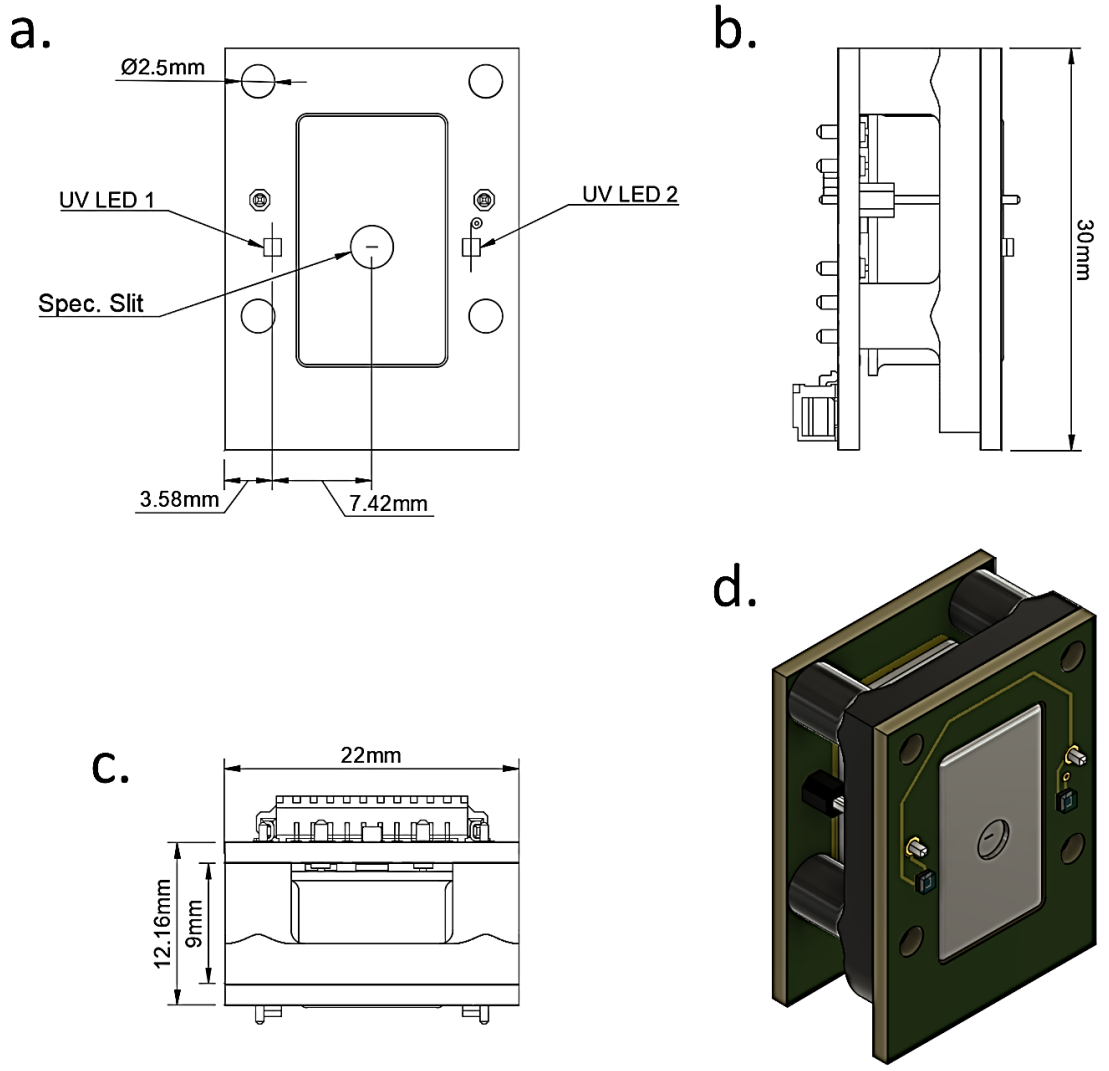

Figure 2-14 C12880MA spectrometer mounting board and stacked ultraviolet (UV) LED board design. (a) Dimensioned top view of board stack with LEDs and spectrometer slit labelled. (b) Dimensioned side view of stacked boards. (c) Dimensioned front view of stacked boards. (d) 3D CAD render of stacked boards assembly.

Figure 2-15 shows in more detail the C12880MA spectrometer mounting board. The design of the PCB allowed for the C12880MA to be seated on three gold plated brass alloy contact

discs (1593-0-57-15-00-00-03-0 (https://www.mill-max.com/products/datasheet/pinsrecs/1593-0-57-15-00-00-03-0) manufactured by Mill-Max Manufacturing Corp. and sourced from Digikey Ltd). The discs have a diameter of 2.36 mm and height of 0.64 mm. The contact discs provided grounded contact points for the metal body of the C12880MA spectrometer when mounted (see Figure 2-15a and b). This was to ensure no build-up of charge occurred within the spectrometer's enclosure during use. PCB pin sockets were used to provide easy insertion of the C12880MA spectrometer onto the PCB (see Figure 2-15a). This approach was used instead of soldering directly to allow for damaged spectrometers to be easily replaced. The PCB sockets used were H3153-05 (https://www.harwin.com/products/H3153-05/) manufactured by Harwin and sourced from Mouser Electronics. The anode and cathode connections of the UV LEDs join the top board using male headers and connect to corresponding female headers on the top board. Figure 2-15c shows the ECAD PCB design of the spectrometer mounting board. A ground plane was positioned on the top and bottom layers underneath the C12880MA position. This was done to shorten the path to ground. A 0.1 µF ceramic decoupling capacitor was used on the input voltage pin of the spectrometer.

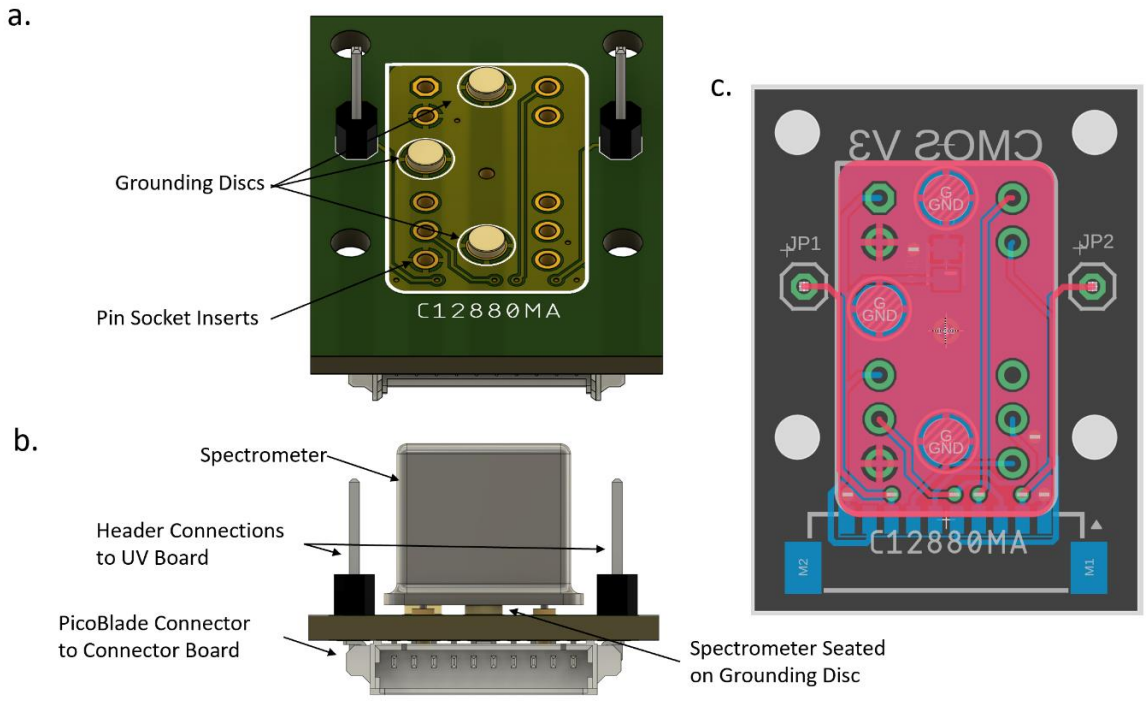

Figure 2-15 C12880MA spectrometer mounting board. (a) Labelled 3D model view of the top side of the spectrometer mounting board showing brass contact mounts and pin sockets (b) Labelled 3D model front view of the spectrometer mounting board showing C12880MA mounted with pin sockets, seated on contact surface mounts and header connectors to UV stacked board. (c) PCB

(printed circuit board) layout view of the top side of the spectrometer mounting PCB showing component position, trace routing and ground place.

Photodiode Board Design

Figure 2-16 shows the PCB design to mount the photodiode and the UV LEDs behind the backscatter lens. The PCB dimensions are 16 mm width and 10 mm height. Figure 2-16a shows the distance of 3 mm of the LEDs relative to the centre of the photodiode. A 4 pin Molex PicoBlade connector on the bottom layer is used for output connection (see Figure 2-16b and c).

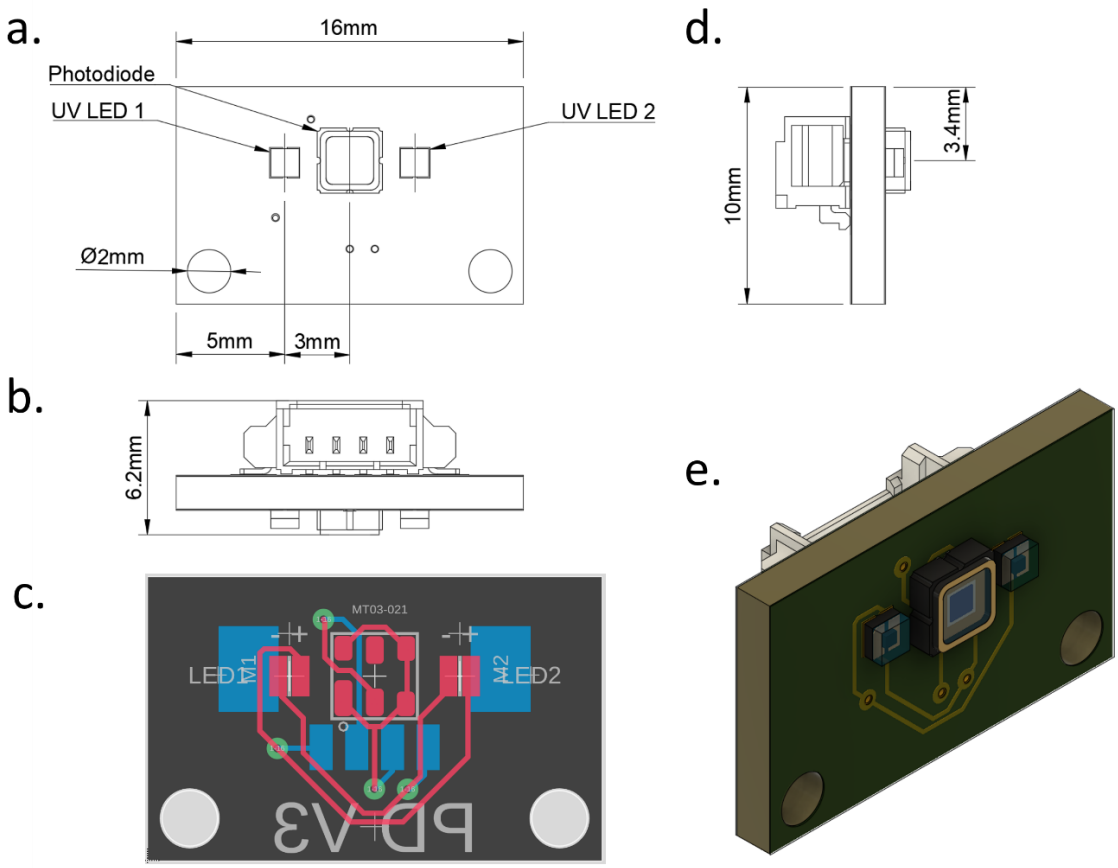

Figure 2-16 MT03-021 Photodiode and UV LED printed circuit board design (PCB). (a) Dimensioned top view of board with labelled LEDs and photodiode. (b) Dimensioned front view of board. (c) Design layout of PCB design top view showing component placement and trace routing. (d) Dimensioned side view of the photodiode board. (e) 3D rendered view of the photodiode and UV LED board.

In Figure 2-17 the assembled PCBs for mounting the photodetectors can be seen. Figure 2-17a shows the stacked PCBs of the spectrometer mounting board and the UV antifouling LEDs. Figure 2-17b shows the assembled photodiode and UV antifouling LED board.

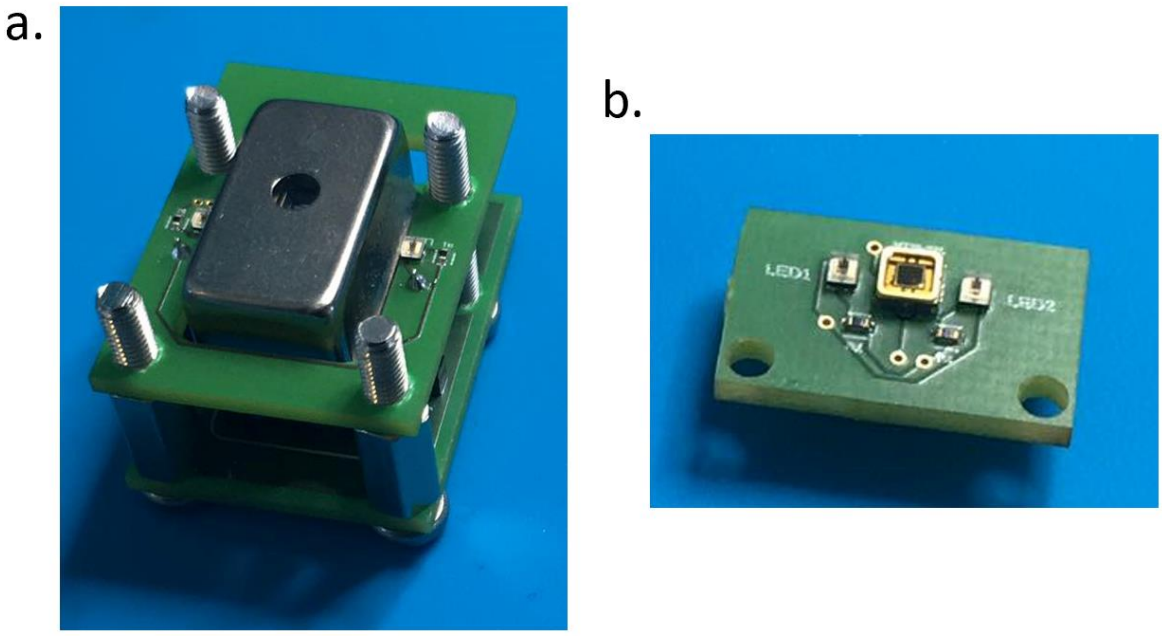

Figure 2-17 Assembled photodetector printed circuit board boards (a) The stacked spectrometer mouting board and UV LED antifouling board. (b) The photodiode and UV antifouling board.

2.3.2.6 **LED Array Design**

An iterative design process was implemented to identify the optimum positioning, configuration, and orientation of the selected LEDs from Table 2-8. A series of test designs and prototypes were made to evaluate the LED array design based on the criteria of compactness and even spectral distribution when used in conjunction with a collimation lens. Figure 2-18 shows the two main designs for the LED array positioning the eight LEDs on a compact 20 mm by 16 mm PCB. Figure 2-18a shows the design concept of positioning the shorter wavelength emitting LEDs on the periphery and the visual/IR spectrum emitters centrally. Figure 2-18b depicts the second design concept of compact circular formation of the smaller LED package sizes around the largest LED package, the 310 nm LED.

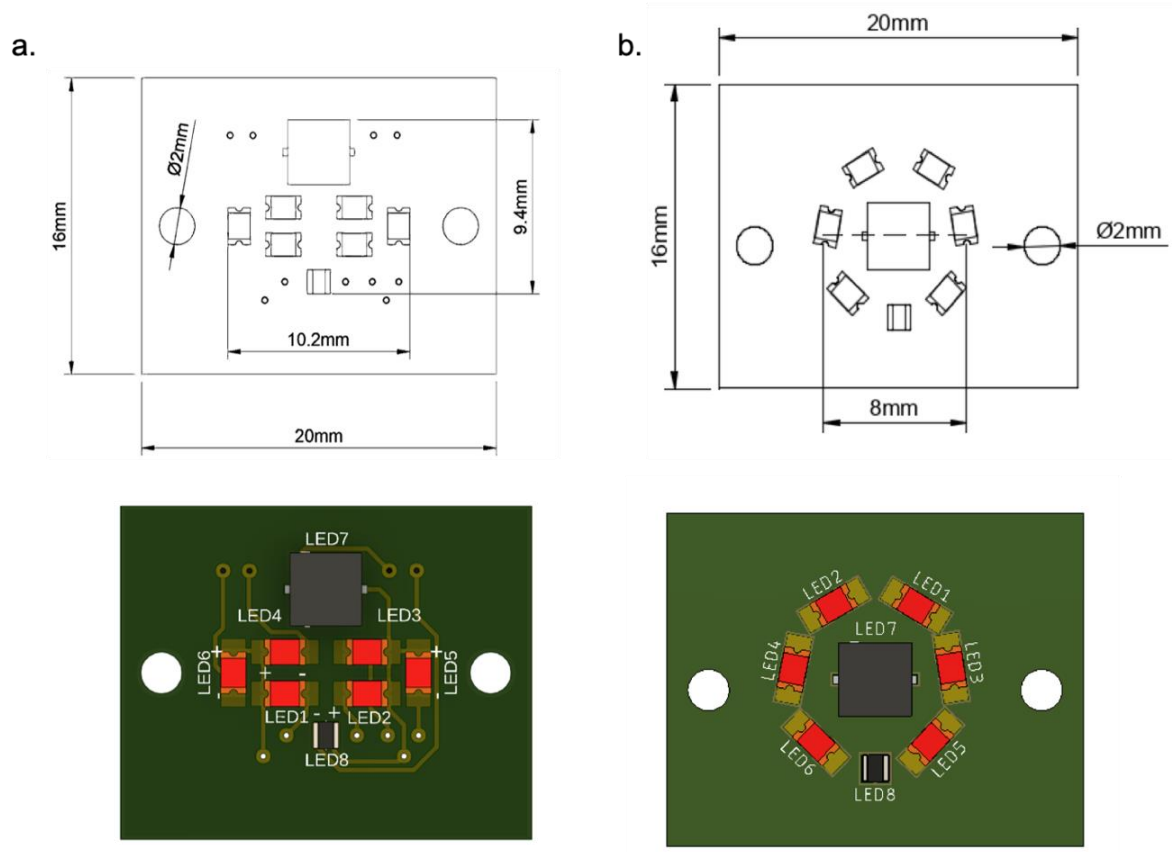

Figure 2-18 LED Array printed circuit board designs. (a) LED placement based on placing the lower wavelength LEDs LED8 to LED 5 (280 nm to 380 nm peak emissions) on the outside peripheral positions and the visible to the IR LEDs on the inside totalling 10.2 mm by 9.4 mm area (b) The second configuration placing LED 7 (310 nm peak LED) at the centre with the remaining LEDs positioned in a circle around LED7 totalling an area with diameter of 8 mm.

Figure 2-19 shows the iterative design progression of the light source for the sensor. Figure 2-19a was the first concept using through hole technology (THT) LED packages placed linearly. This however proved to be both spatially and cost prohibitive as the THT packages for the LEDs were too large and more expensive than their surface mounted (SMD) counterparts. The total size of the array was 83 mm by 33 mm. Figure 2-19b shows the progression from THT to SMD packages of the equivalent wavelength output in a linear array mounted onto a PCB. The total size of the second linear array concept was 38 mm by 19 mm. However, for the application, the width of 38 mm was unsuitable as it remained too wide to place behind conventional collimation lenses without being impractically large to integrate into a deployment unit. Figure 2-19c an array of SMD LEDs in a compact formation to reduce area to allow the LED array to sit behind a 25 mm diameter lens to fit into an optical head design. The use of 0805 SMD component adapters were incorporated to allow copper stripboard to be used as the mounting circuit board.

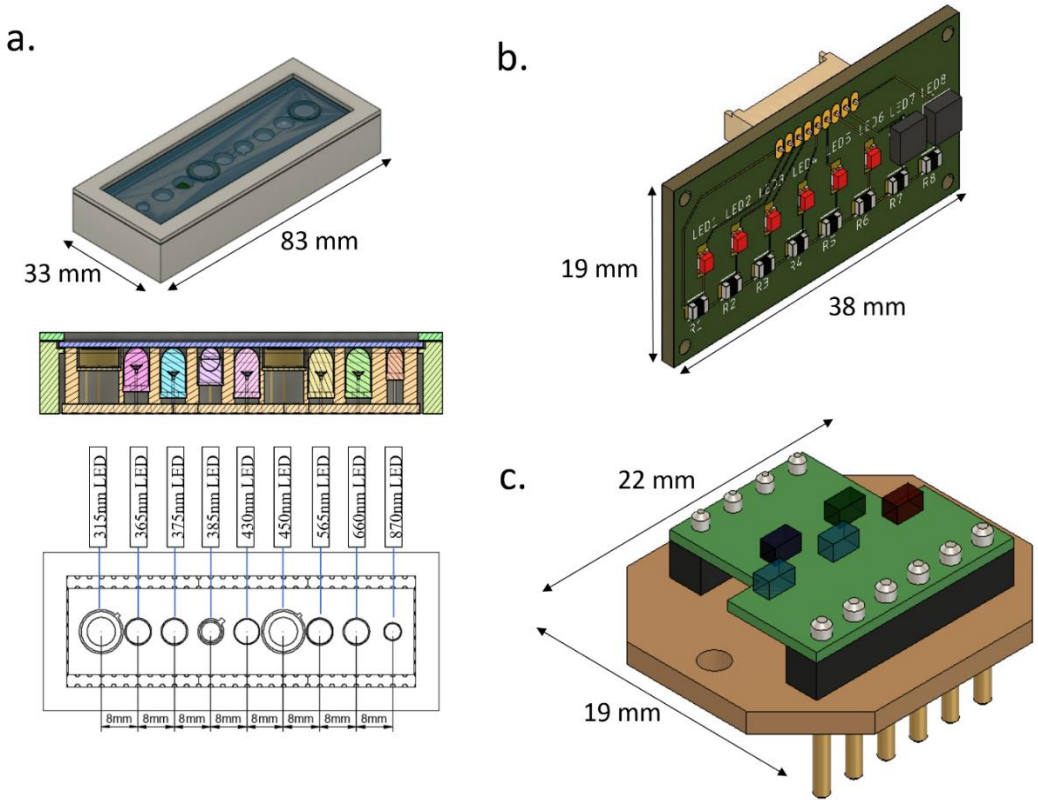

Figure 2-19 Iterative designs for multi-LED array light source. (a) Linear array design using through hole LED packages with a board size of 83 mm x 33 mm (b) Circuit board linear array design using surface mounted LED packages with a board size of 38 mm x 19 mm (c) Compact array using surface mounted LED packages with a board size of 22 mm x 19 mm.

Figure 2-20 shows the assembled compact LED array concept using SMD component adapters and copper strip protoboard. Due to the use of the adapter board all LEDs could not sit on the same board. Two separate boards were assembled as seen in Figure 2-20a and c, to hold the two sets of LEDs for testing. Figure 2-20a shows the compact LED array with the LEDs from the visible regions mounted and Figure 2-20c shows the array with the IR and UV LEDs mounted. Figure 2-20b shows the LED array being tested using resistors to limit to the current to each LED.

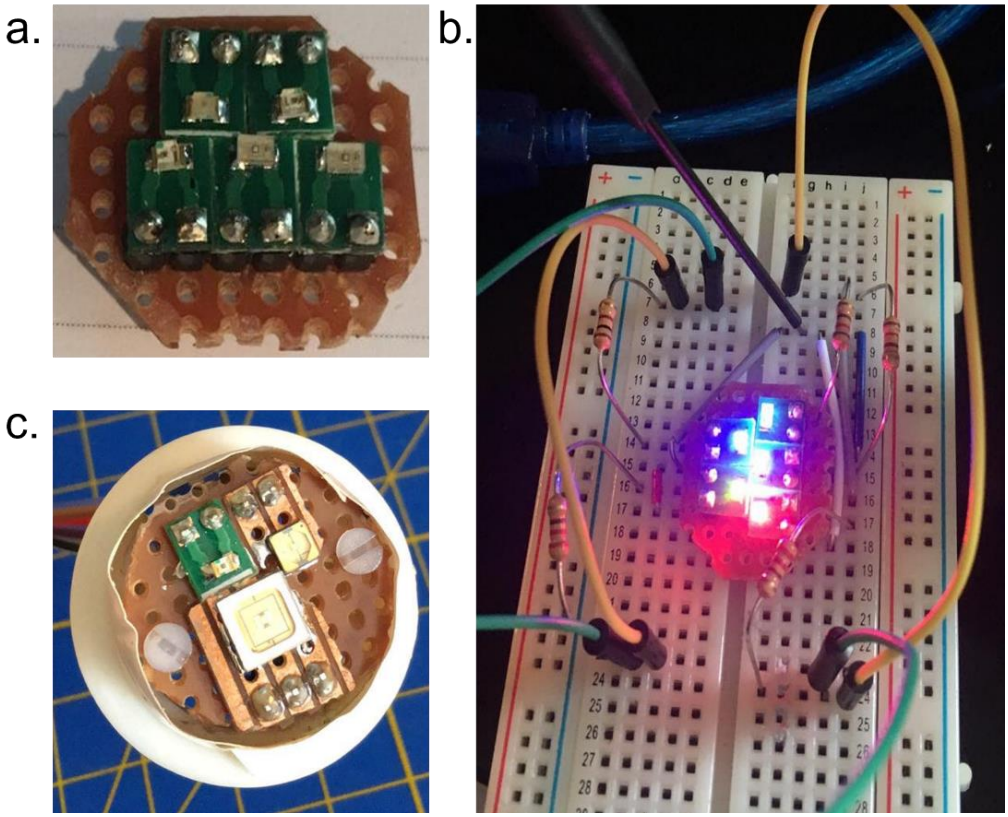

Figure 2-20 LED Array prototypes with LED packages soldered to adapter board for mounting to optical test setup. (a) the adapter board for VIS wavelength LEDs using 0805 adapter boards (b). testing of VIS LEDs board adapter with current limiting resistor (c) the adapter board for the IR and UV LEDs using 0805 adapter board for the IR LED and hand soldered copper strip board adapters for UV LED packages.

The outcome of the iterative design process was a compact LED array which could place the LED packages within a 25 mm diameter to fit behind the selected collimation lens. The two designs which were built to test can be seen in Figure 2-21.

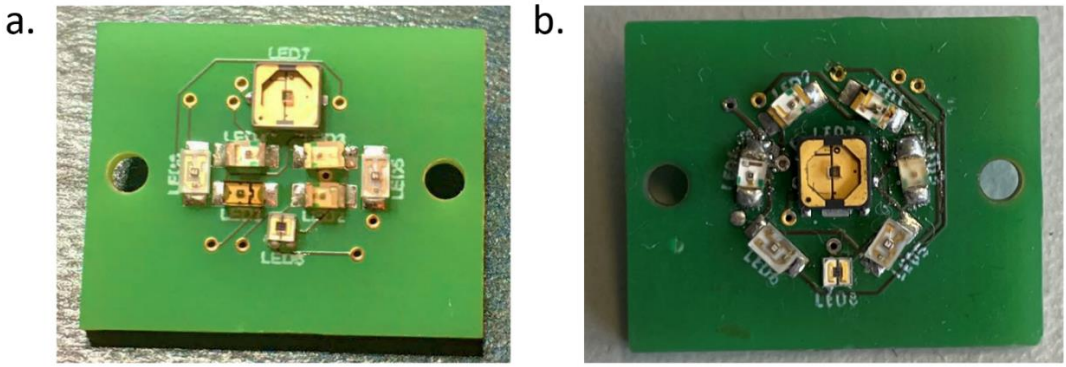

Figure 2-21 Assembled compact LED array designs. (a) Assembled compact LED array with design concept of placing UV LEDs on the periphery. (b) Assembled compact LED array with design concept of placing smaller LED packerage circularly around the largest LED package.

2.3.2.7 **Integration of Full Electronic System**

Figure 2-22 shows the fully assembled first version of the electronics system for the sensor unit including the main control board, cable to connection board, connection board, LED Array, CMOS Detector boards, photodiode board and temperature probe. With this full system developed a series of tests and validation were carried out to find potential improvements that could be made to the hardware performance including component compatibility, power efficiency and functionality.

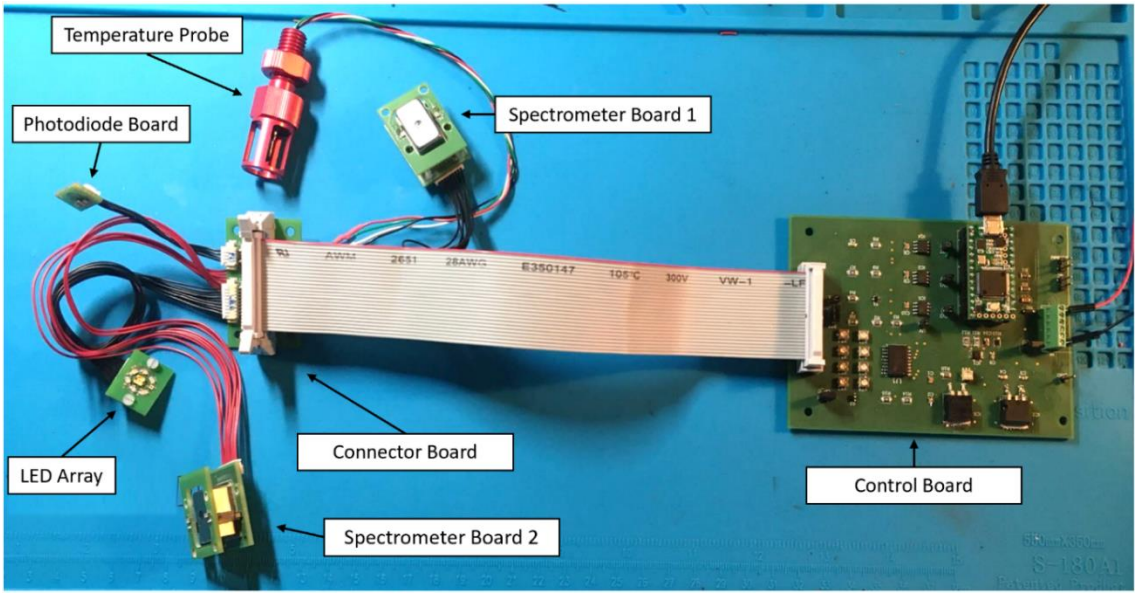

Figure 2-22 Assembled sensor electronic system including control board, two spectrometer and UV LED stacked boards, photodiode and UV LED board, LED Array, connector board and temperature probe.

2.3.2.8 **Firmware Input Commands and Communication**

An initial firmware program developed was to allow for development of firmware functions and testing with the hardware. A simple serial command user interface was developed and is shown in Figure 2-23. The commands are typed into the serial monitor on the Arduino IDE and sent via USB to the microcontroller. This first program could be used to easily implement different functions to iterate through potential modes of operation for the sensor. The firmware written to control the benchtop unit can be seen in Appendix B Section B.1.

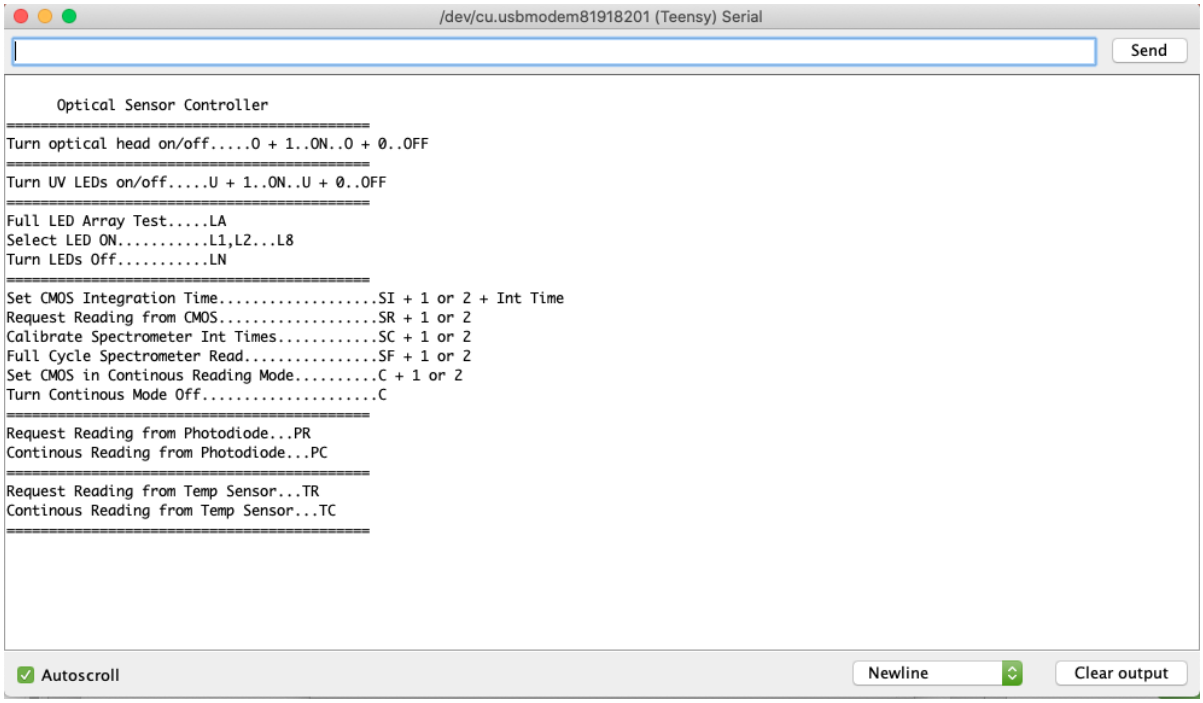

Figure 2-23 Serial command user interface for lab testing showing menu of typed commands to operate the sensor.

2.3.3 Optical Sensing Components Performance

2.3.3.1 Optical Setup

From the investigation carried out in Chapter 1 on optical detection methods and technology, the chosen optical detection system design concept can be seen in Figure 2-24. Based on optical measurement techniques the position of the detectors and their orientation were arranged. A transmittance/absorption measuring spectrometer was positioned at 0 degrees relative to the light source. Adjacent to it, a second spectrometer was situated at 90 degrees to measure side scatter and fluorescence. Further, an additional photodiode was placed at 120 degrees to capture backscatter measurements. A multispectral light source was designed which consisting of surface-mounted LEDs selected to produce the required spectral outputs for the selective measurement of the target analytes. Beyond the primary optical sensing unit design, considerations were made for temperature monitoring; thus, a temperature probe based on integrated circuit (IC) temperature sensing technology was chosen and integrated into the design.

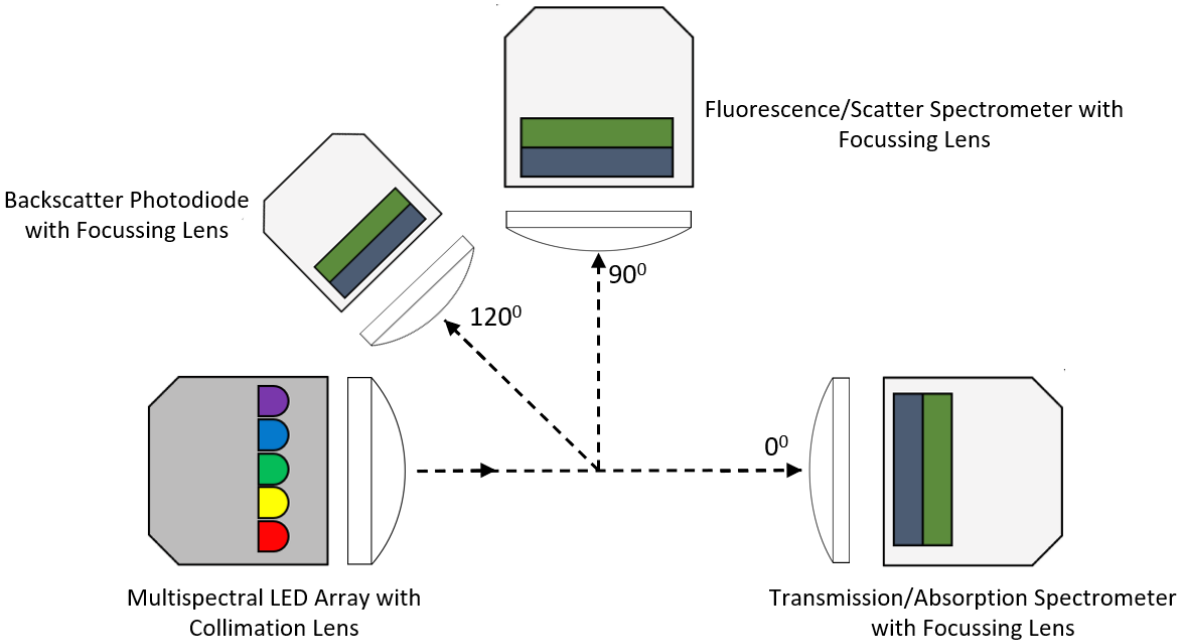

Figure 2-24 Diagram of the optical setup and selected components to build the sensor system for multiparameter sensing using a multispectral LED array light source, two micro spectrometers and a photodiode which is capable of measuring transmission, absorption, fluorescence, side and back scatter in a single sensing unit. A UV fused silica collimation lens is placed in front of the light source and focussing UV fused silica plano-convex lenses used in front of the three detectors.

The application of optical lenses instead of optical windows in an in-situ optical sensor was investigated in Section 1.4.3. The use of lenses for optimising the region sampled in the water column is outlined in Figure 2-25. By using a collimation lens for the light source and a focusing lens with the photodetectors, the region within the water column which is being sampled is maximised. This light source is positioned behind an ultraviolet (UV) transmitting fused silica (UVTFS) collimation lens to ensure parallel distribution of the light entering the sample or water column. UVTFS plan-convex focussing lenses are used to enhance the signal to the detectors to further the limits of the detection of the system.

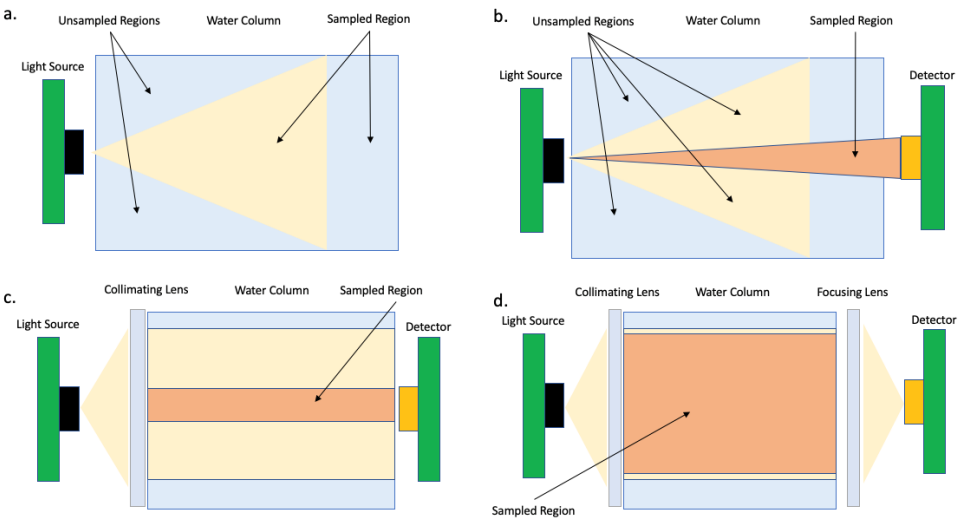

Figure 2-25 The improved optical sampling potential gained by using optical lenses. (a) the outward projection of the light source into the water column. (b) the sampling region of a photodetector positioned Infront of the light source with no lenses. (c) effect of a collimation lens to produces parallel light source into water column. (d) Increased region in water column samples with the use of a focusing lens.

2.3.3.2 **Optical Setup Evaluation Results**

Figure 2-26 shows the comparison between the LED array light output with and without the use of a collimation lens. It can be seen in Figure 2-26a that without the collimation lens the light from the eight LEDs is dispersed at a wide angle. By contrast in Figure 2-26b the emission of light from the LEDs is less dispersed and the output beams are more concentrated in a forward direction.

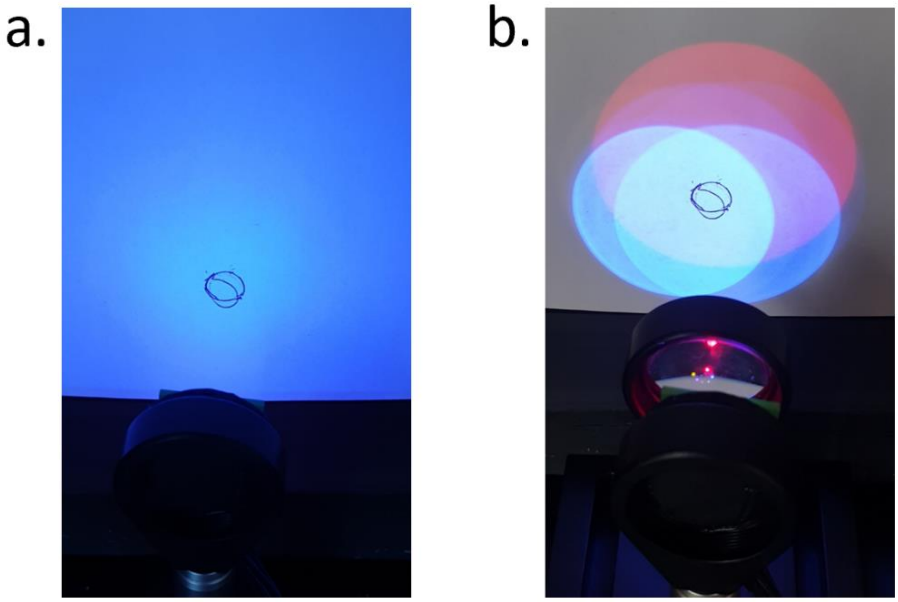

Figure 2-26 Test of the effectiveness of the collimation lens. (a) LED Array with no optics positioned 50 mm from target. (b) LED Array positioned 10 mm behind 25 mm collimation lens and 50 mm from target.

The importance of the positioning of the detector relative to the focusing lens can be seen in Figure 2-27. The 12 mm focussing lens used had a focal length of 10 mm. Positioning of the detector at 15 mm as seen in Figure 2-27a provided an overlap of the LED's beam emission which is centred on the detector. Figure 2-27b presents the optical output at 30 mm from the lens. The output from each LED is dispersed away from the centre of the detector.

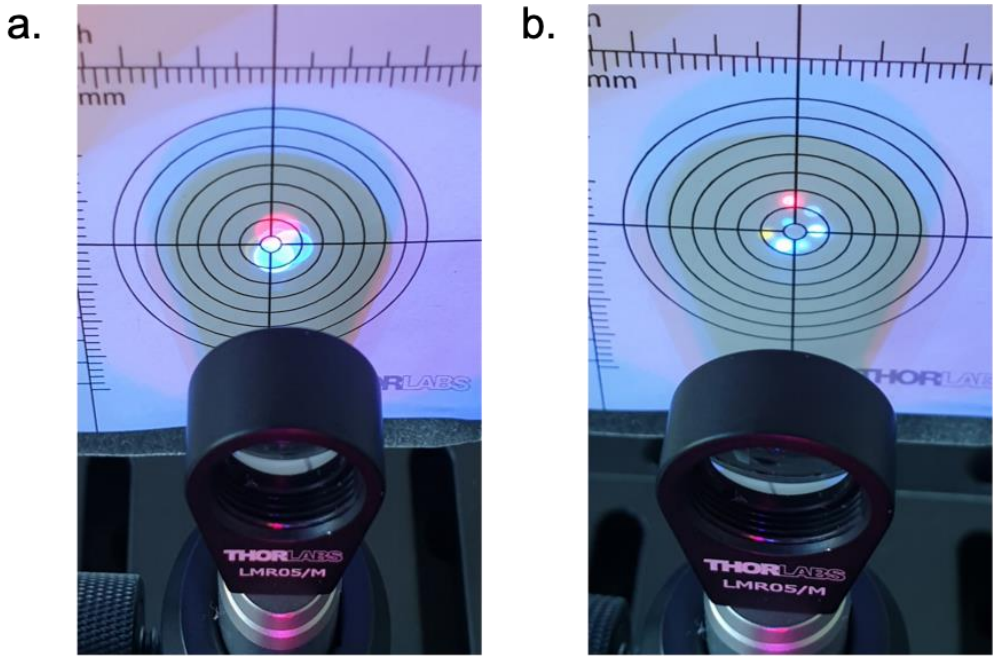

Figure 2-27 Light source with all LEDs on and 12 mm plano-convex focusing lens. (a) Light source positioned 15 mm from lens. (b) Light source positioned 30 mm from lens.

Figure 2-28 shows the effect of combining the collimation lens and the focusing lens. The collimation lens is successful in homogenising the spectral emission from the LED Array and directing the light in a forward path towards the focussing lens. The focusing lens concentrated the light emission to a compact focal area which should increase the signal measured by the photodetector.

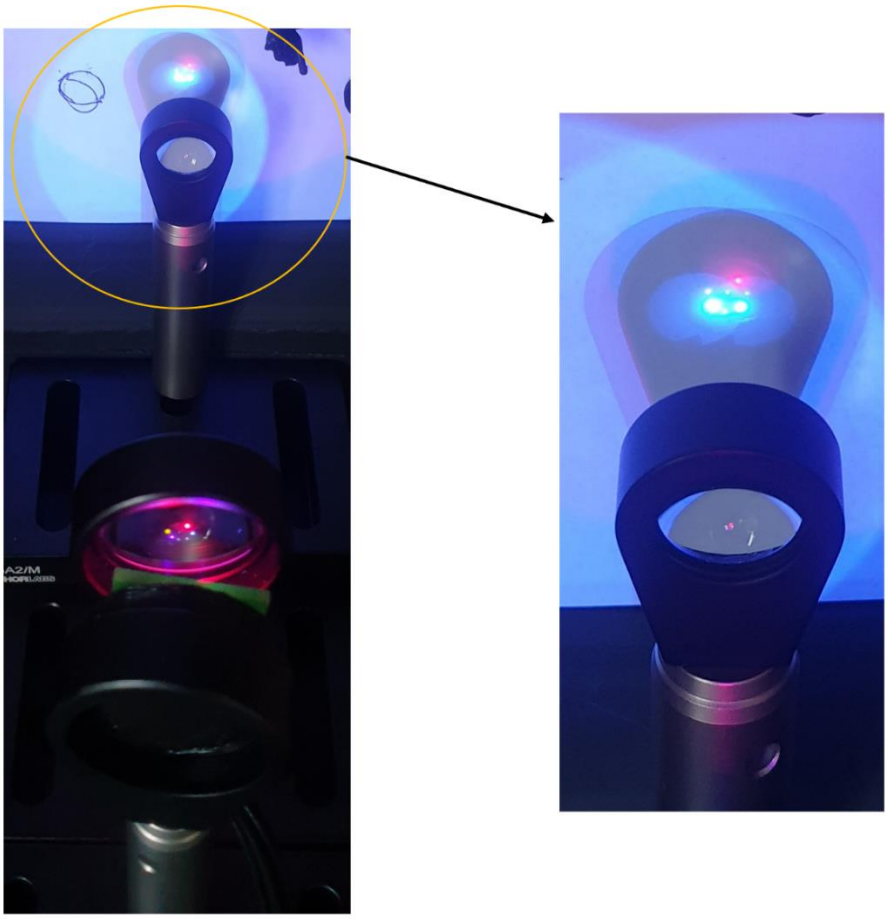

Figure 2-28 Optical test of the combination of the use of a 25 mm collimation lens and 12 mm plano-convex focusing lens. LED Array is positioned 10 mm behind the collimation lens, collimation lens is positioned a 50 mm distance from the focusing lens and a 15 mm distance is between the focusing lens and the target. Close up of the focusing lens and the target are shown on the right.

2.3.3.3 **Output Spectra of Selected LEDs**

Figure 2-29 shows the spectra of the selected LEDs from Table 2-8 to be used in the sensor unit taken by a commercial benchtop spectrometer. The profiles of the LEDs vary in broadness, UV1, UV2, B1, B2 and R have a narrow peak while B3, G and IR have much broader peaks. These profiles will need to be considered during the measurements to understand the signal spectral output of target analytes. The Maya spectrometer uses boxcar averaging to smooth out the spectral output which has caused a jagged distortion of the IR LEDs profile.

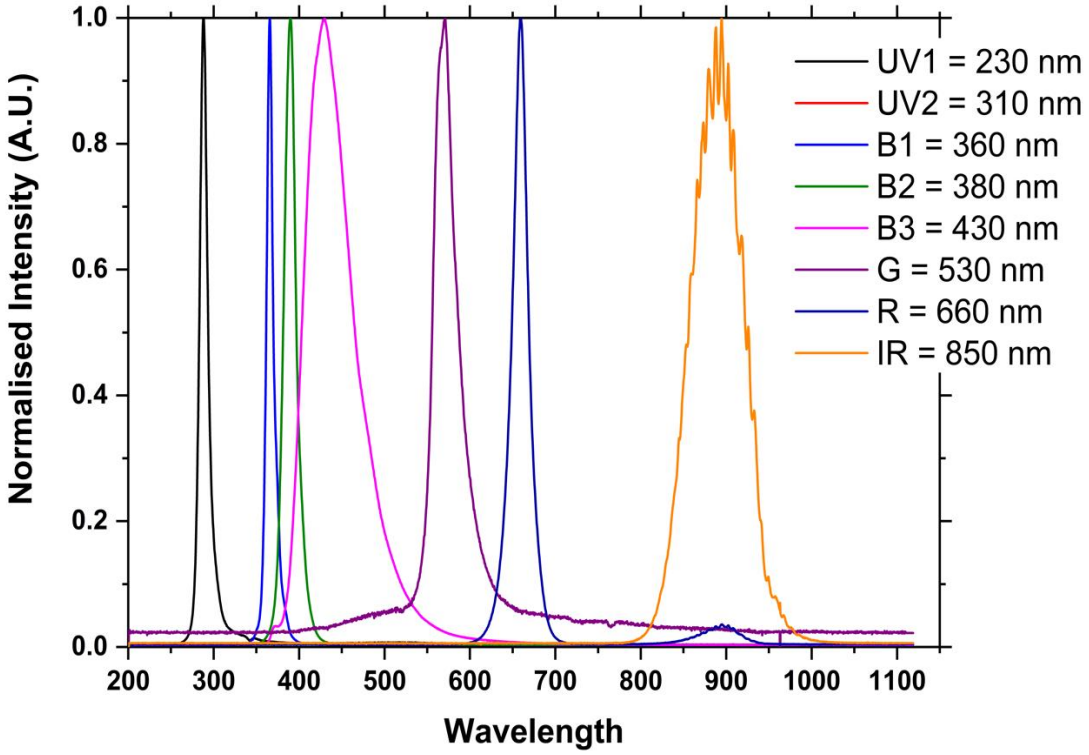

Figure 2-29 Overlay of all eight selected LED emission spectra using the Ocean Optics Maya spectrometer.

2.3.3.4 Comparison of Selected Spectrometer with Commercial Spectrometer

In Figure 2-30 the normalized spectrum of each LED recorded by the C12880MA spectrometer and Ocean Optics Maya benchtop spectrometer. LEDs B1 and B2 have narrow band emissions with a FWHM of 14 nm and 19 nm respectively as recorded on the mini spectrometer and 9 nm and 18 nm on the Maya spectrometer. B3 on the other hand a much broader and asymmetrical spectrum than the other LEDs with a FWHM of 60 nm recorded on the mini-spectrometer and 58 nm on the Maya.

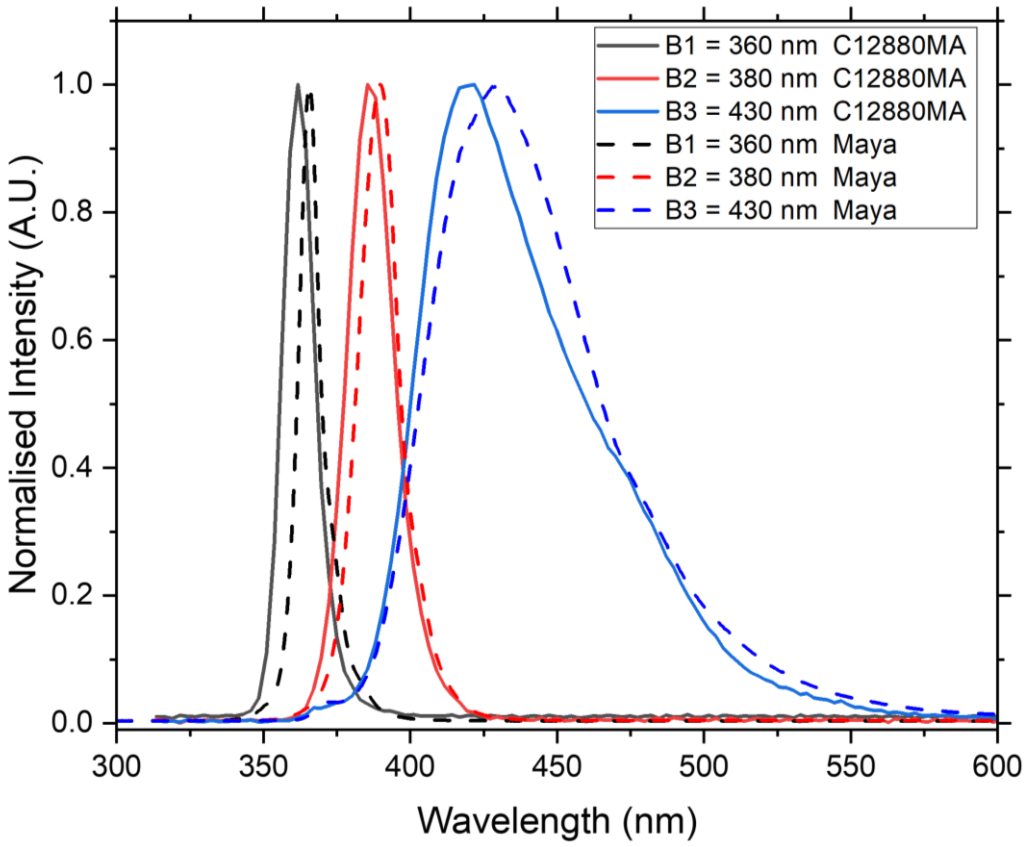

Figure 2-30 Spectrum of each LED as recorded on the Hamamatsu C12880MA mini spectrometer. Overlaid with the spectrum of each LED as recorded on the Ocean Optics Maya spectrometer.

2.3.4 Assembly of Benchtop Detection Systems

Figure 2-31 shows the assembled prototype of the multi-spectrometer benchtop design. This benchtop design was able to make absorption, transmission, scatter, and fluorescence measurements by use of the two spectrometers incorporated and a multispectral LED array. Figure 2-32 shows the third concept iteration for the benchtop measurement system. This design allowed for easier placement of the optical components via the optical mounting tray. The benchtop unit was able to perform multi-measurements including absorption, transmission, scatter, fluorescence, and backscatter.

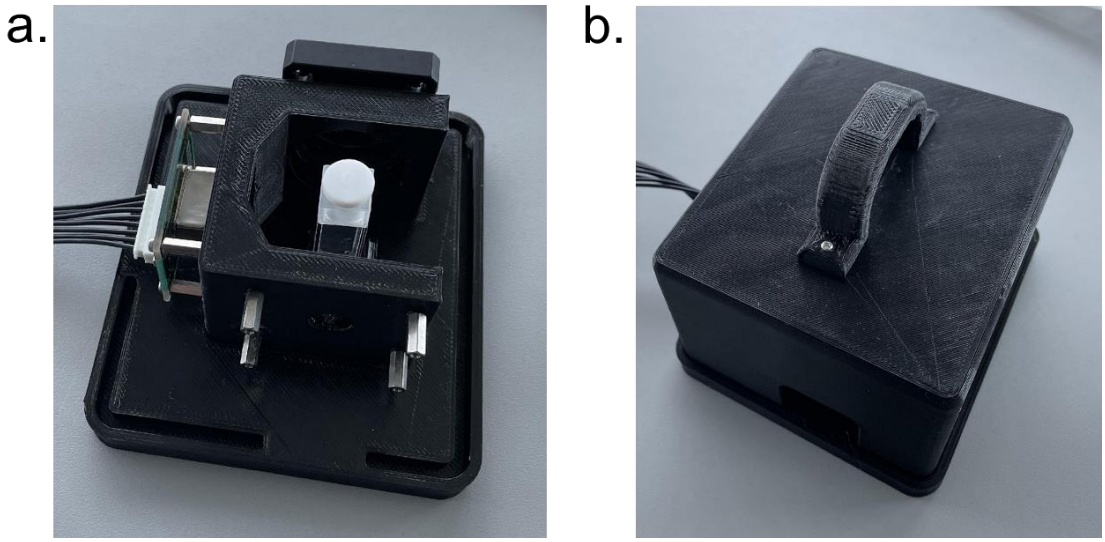

Figure 2-31 Assembled plug and play benchtop optical testing prototype (a) view of internal components with mini spectrometer mounted at the 90-degree position and sample holder (b) view of device with top enclosure on during measurement being taken.

Figure 2-32 Benchtop multi-detector design assembled with incorperated electronic systems.

2.3.5 Proof of Concept Experiment Results

2.3.5.1 Absorption Measurements

Figure 2-33 shows the overlaid measurements of the measured absorption spectrum of Rhodamine and the spectral emission of the 565 nm LED. Rhodamine is shown to have a peak absorption wavelength of 552 nm which is consistent with other studies [22–24]. There is an overlap between the absorption spectral range of rhodamine B and the emission spectrum of the 565 nm LED between 525 nm and 500 nm.

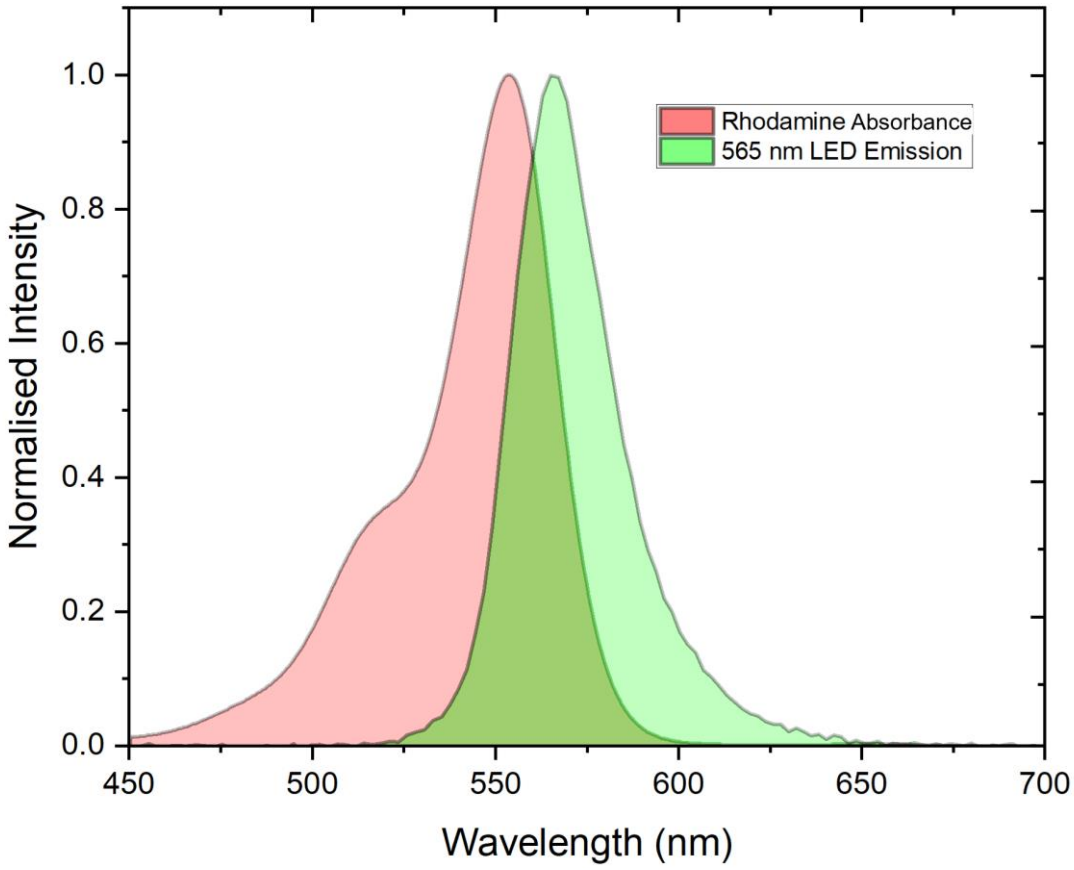

Figure 2-33 Plotted rhodamine absorption and normalised 565 nm LED emission spectra overlap. Rhodamine absorption spectra measured using Shimadzu UV-1800 UV/Visible Scanning Spectrophotometer. 565 nm LED emission measured using the Hamamatsu C12880MA spectrometer.

The spectra measured and the scatter plot of the calculated absorption for rhodamine B are presented in Figure 2-34. A decrease in the transmission of the LED emission is seen to correlate with an increase of concentration of rhodamine B is seen in Figure 2-34a. Figure 2-34b presents the calculated absorption plotted against the concentration. A positive linear trend is seen with a linear fit applied. The given slope from the linear fit is 0.446 with an

intercept of -0.01 and a R^2 value of 0.99322. This shows a good sensitivity in absorption when using the 565 nm LED at the pixel corresponding to 570 nm. A good R^2 value indicates a clear linear correlation. Alternatively, a linear fit using the measured peak absorption wavelength of 552 nm for rhodamine B gives a slope of 0.5 however a corresponding linear fit of 0.9269 from the sensor response. This indicates that the LED overlap is insufficient at that wavelength with very low sensor response at the corresponding pixel. The peak of the LED gives a more substantial signal and in turn a better linear fit for the measurement of rhodamine B absorption while sensitivity is less. A red protein pigment present in red algae, R-Phycoerythrin, is known to absorb peak between 500 and 600 nm and is also present in some species of blue-green algae [322,323]. Measuring the absorption in this region can give insights into the species of algae present and can be used in conjunction with other Chl measurements. The combination of the 565 nm LED and the absorption measurements taken by the spectrometer show this optical measurement could be applied to detect such pigments present in algae species for more accurate determination within a sample.

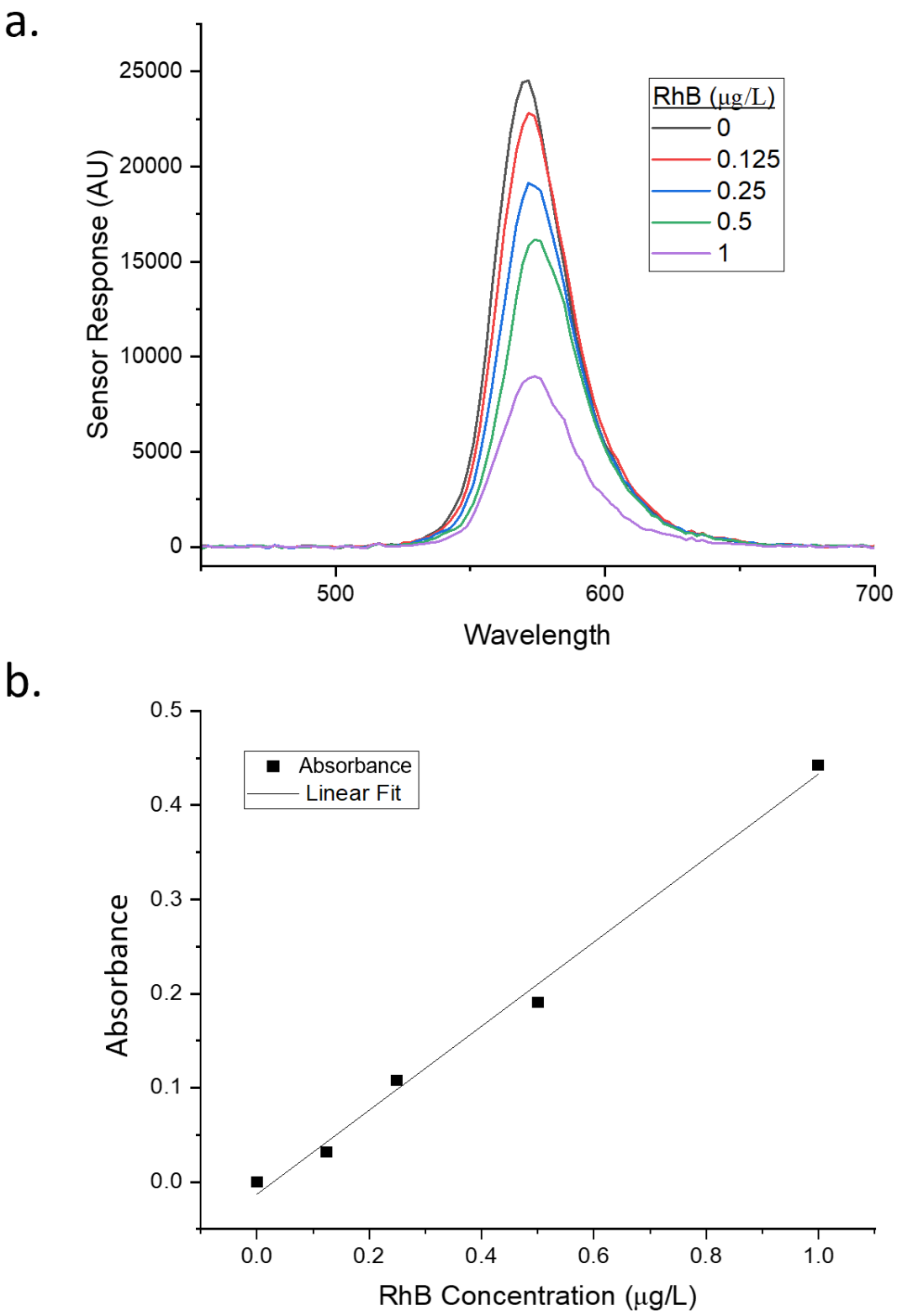

Figure 2-34 Sensor response to increasing concentration of rhodamine B using a 565 nm LED (n =1) (a) Spectral response of the spectrometer to concentration between 0 μgL^{-1} to 1 μgL^{-1} . (b) Scatter plot of the calculated absorption for each concentration at 570 nm and a linear fit applied. The linear slope is 0.446, intercept -0.01 and R^2 value of 0.99322.

In Figure 2-35 the overlaid plots of the measured absorption spectrum of fluorescein and the emission of the 430 nm LED are presented. Fluorescein is measured to have a peak absorption wavelength at 487 nm which is consistent with other literature [324,325]. There is a significant overlap between the 430 nm emission spectrum and the absorption region of fluoresceine between 350 nm and 530 nm.

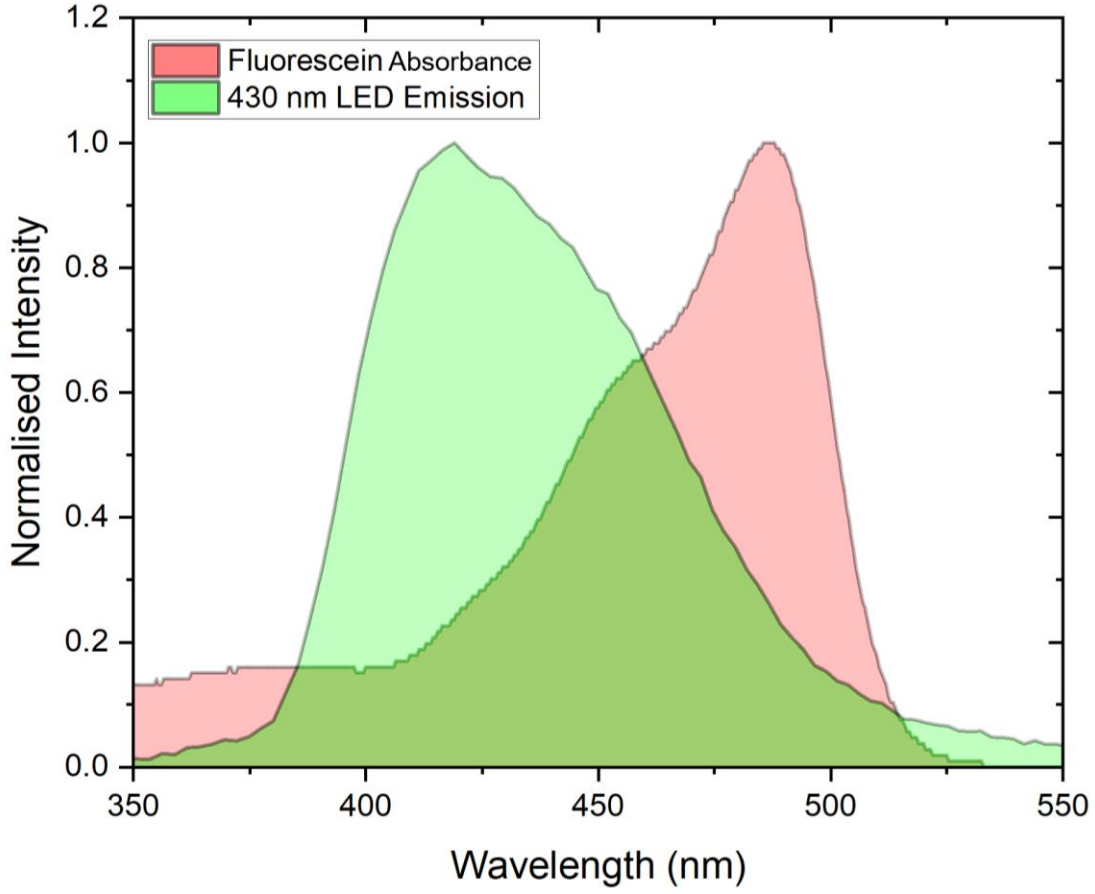

Figure 2-35 Plotted fluorescein absorption and normalised 430 nm LED emission spectra overlap. Fluorescein absorption spectra measured using Shimadzu UV-1800 UV/Visible Scanning Spectrophotometer. 430 nm LED emission measured using the Hamamatsu C12880MA spectrometer.

Figure 2-36 presents the sensor's response to increasing concentrations of fluorescein using the 430 nm LED. In Figure 2-36a, it can be seen from the spectrometer's spectral response that the LED's emission spectrum intensity decreases with each increase of fluorescein concentration. Figure 2-36b presents the calculated absorption at the peak wavelength of the 430 nm LED. This response gives a good linear response with an R^2 value of 0.99871. The sensitivity of the system for the measurement of fluorescein in absorption is given by a slope of 0.51 and an intercept near zero. As noted in the Chapter 1 and in the literature, Chl components such as Chl-a,-b and carotenoids absorb highly in the 400 to 500 nm region

[325,326]. The use of fluorescein and the 430 nm LED present a promising method of calibration for the detection of Chl in water samples by use of the absorption optical measurement method.

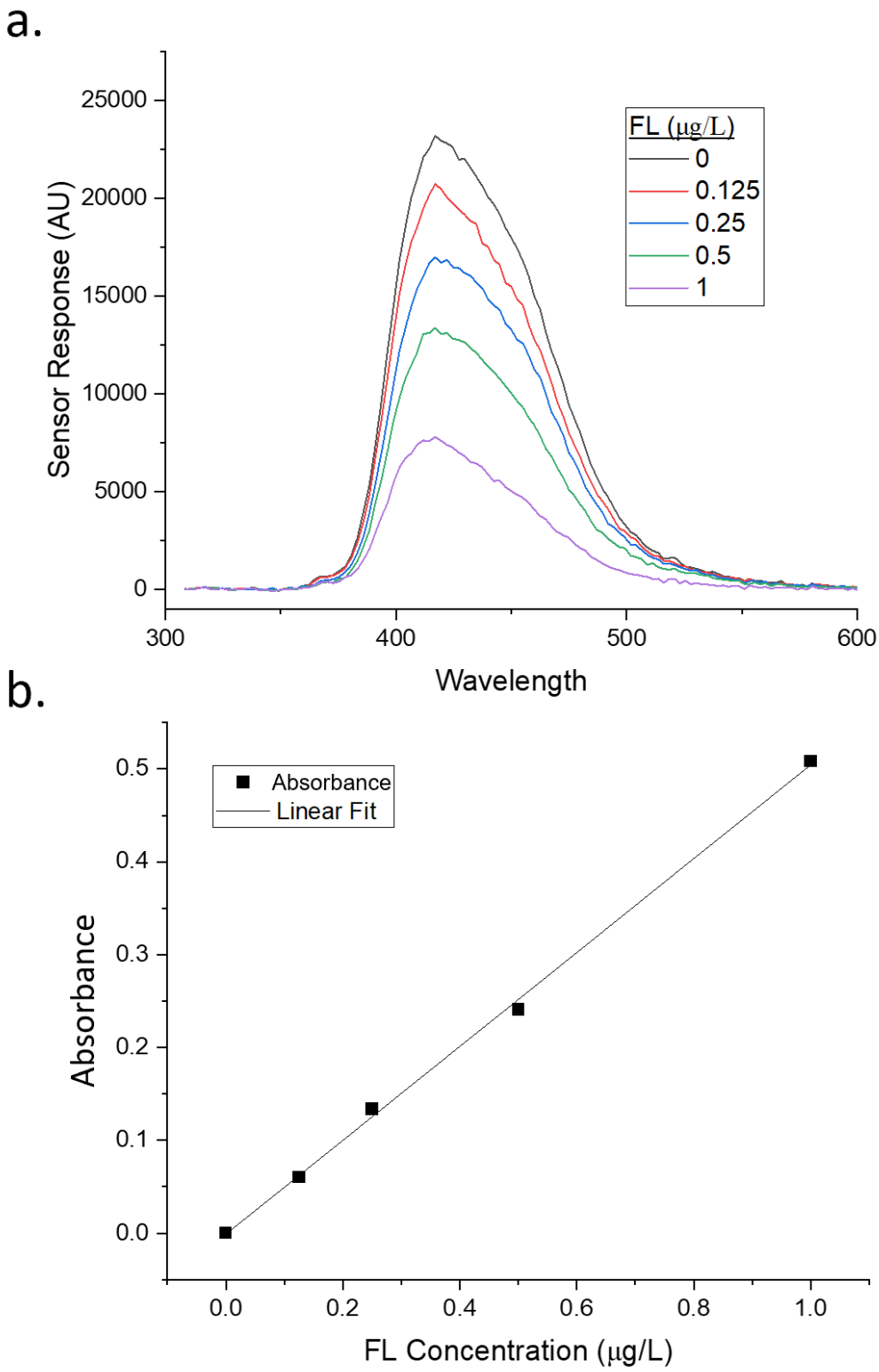

Figure 2-36 Sensor response to increasing concentration of fluorescein (FL) using a 430 nm LED (n = 1). (a) Spectral response of the spectrometer to concentration between 0 μgL^{-1} to 1 μgL^{-1} . (b)

Scatter plot of the calculated absorption for each concentration at 430 nm and a linear fit applied. The linear slope is 0.51, intercept -0.001 and R^2 value of 0.99871.

The overlaid measurement of absorption spectrum of BB3 and the LED emission of the 660 nm LED are shown in Figure 2-37. The peak absorption wavelength of BB3 is measured to be at 654 nm. This is in line with other studies on the absorption spectrum of the dye [325,327]. There is complete overlap of the LED emission and the BB3 absorption spectrum. The peak wavelength emission of the LED is measured to match very close to 654 nm. The absorption wavelength range of BB3 is from between 500 nm to 700 nm and the LED emission wavelength range spanning between 600 and 700 nm.

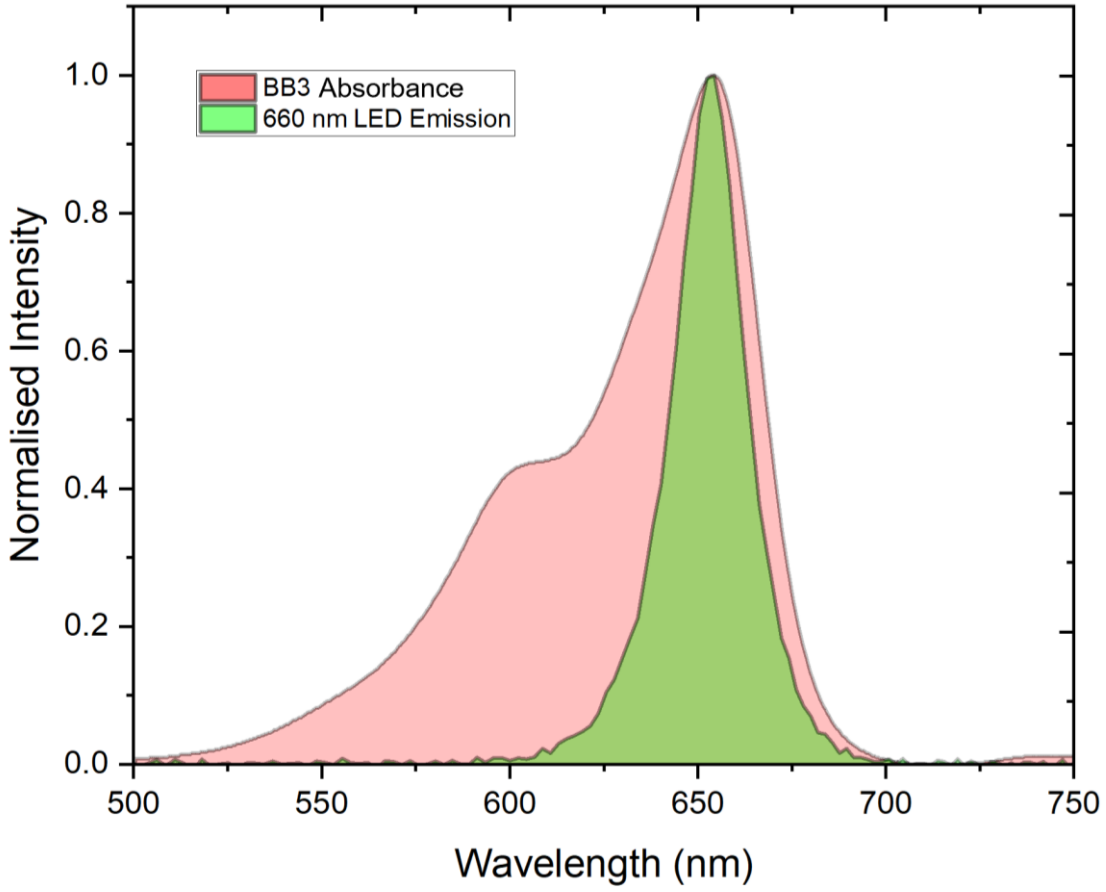

Figure 2-37 Plotted Basic Blue 3 (BB3) absorption and normalised 430 nm LED emission spectra overlap. BB3 absorption spectra measured using Shimadzu UV-1800 UV/Visible Scanning Spectrophotometer. 660 nm LED emission measured using the Hamamatsu C12880MA spectrometer.

The sensor response to the absorption of the 660 nm LED from increasing concentrations of BB3 is presented in Figure 2-38. Figure 2-38a shows the decrease in transmission of the LED emission spectrum as measured by the spectrometer with increasing concentrations of

BB3. The calculated absorption at the pixel corresponding to 654 nm form the spectrometer response is plotted in Figure 2-38b against concentration. From the linear fit applied a line equation gives a slope of 0.43 and an intercept of -0.0008. Good linear correlation between sensor measured absorption and concentration is shown with a R^2 value of 0.99215. A lower sensitivity compared to the previous absorption measurements of the other dyes may be down to the integration time used for the experiment with it set to 0.0001 s. This is the lowest integration time used between the three LEDs and has direct influence on the sensitivity of the system. The integration time was set to avoid saturation of the detector when measuring the LED's emission in DI water. BB3 presents an ideal substitute for the measuring of absorption of Chl-a which has a strong absorption band between 650 and 670 nm [325,326,328]. It is also noted that this can be used to measure the presence of green algae which have an absorption band between 650 and 680 nm [329]. The combination of the 660 nm LED and the absorption measurement using the spectrometer has shown promise for the optical detection of these analytes.

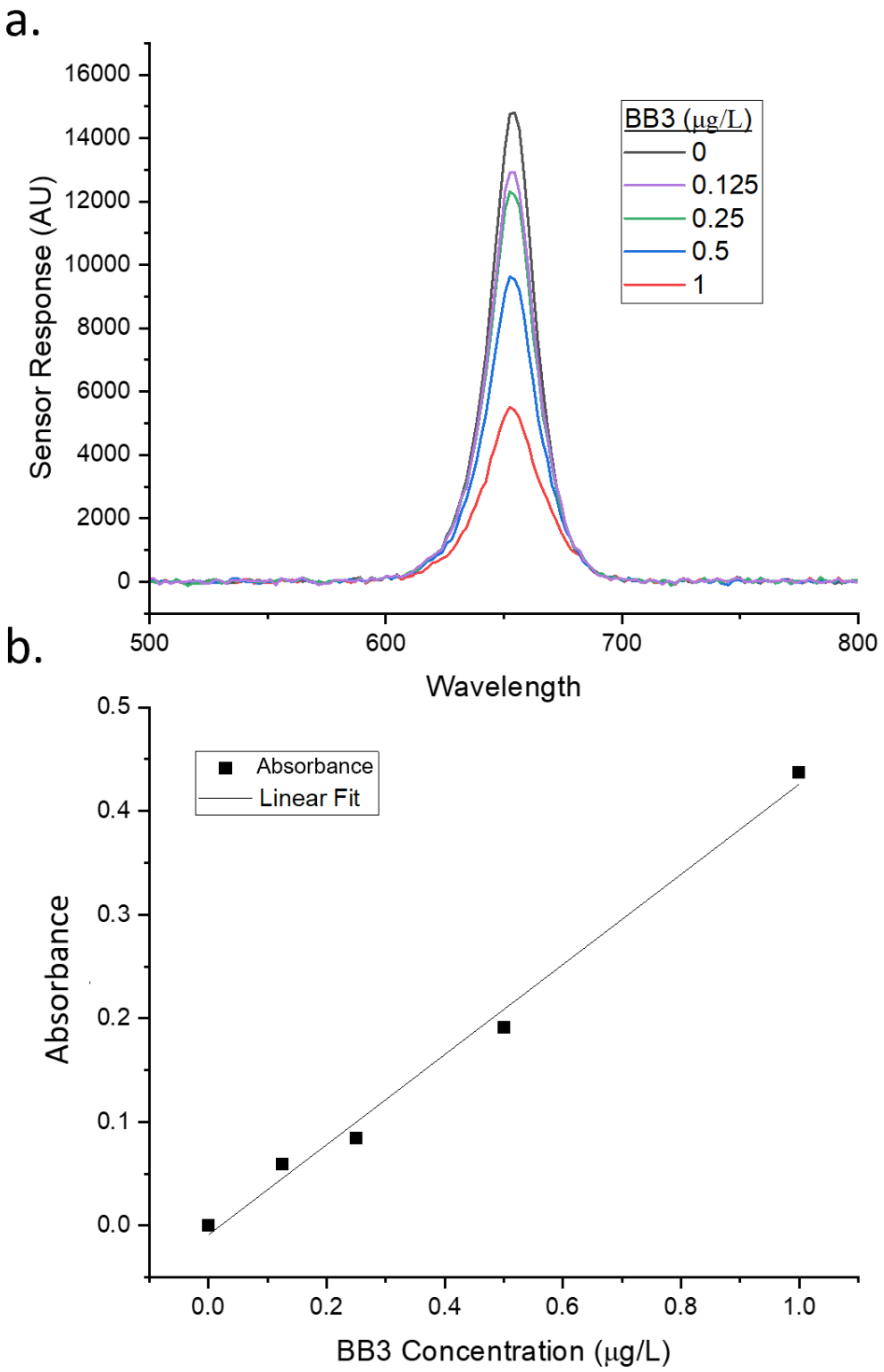

Figure 2-38 Sensor response to increasing concentration of basic blue 3 using a 660 nm LED (n = 1). (a) spectral response of the spectrometer to concentration between 0 μgL^{-1} to 1 μgL^{-1}. (b) Scatter plot of the calculated absorption for each concentration at 654 nm and a linear fit applied. The linear slope is 0.43, intercept -0.009 and R^2 value of 0.99215.

2.3.5.2 **Scatter Measurements**

The sensor response from increasing turbidity concentration using the IR 850 nm LED and spectrometer in scatter mode can be seen in Figure 2-39. There is a clear increase in light scattered with increase in turbidity levels. The detector becomes saturated above 63 NTU showing the limit of detection of the system at the integration time set of 0.2 s.

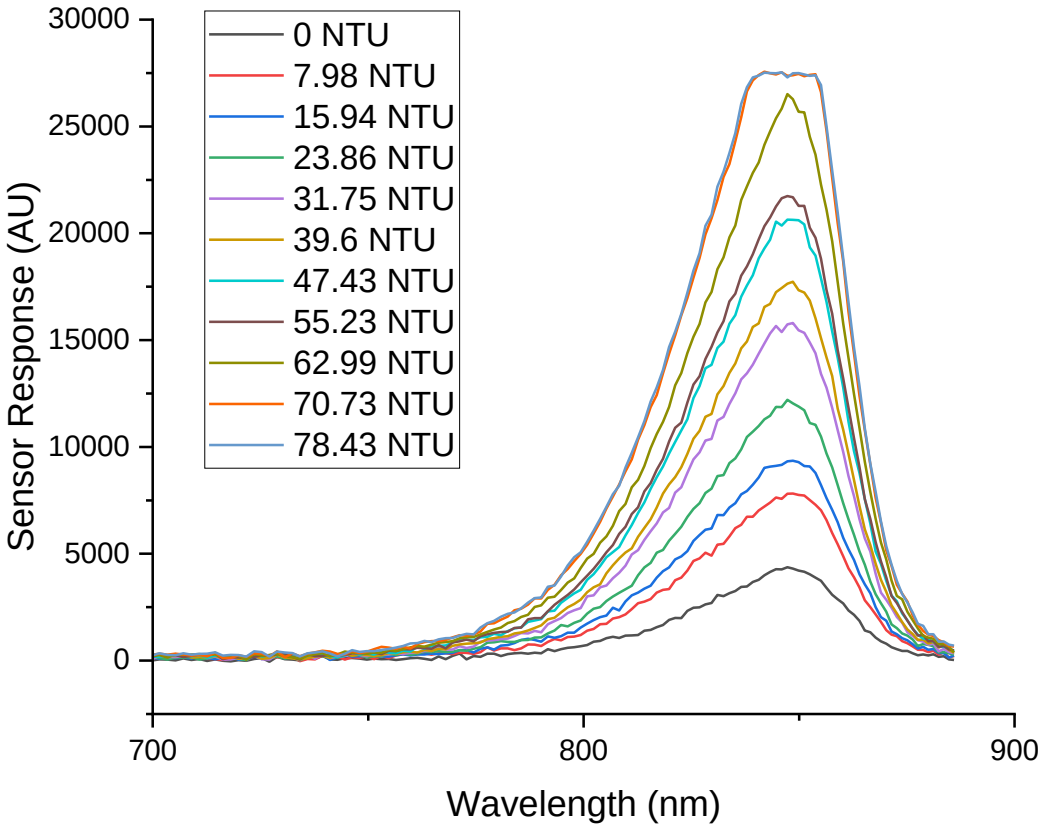

Figure 2-39 Sensor response from the 850 nm LED spectrometer output in scatter mode with increasing turbidity concentrations using turbidity standards in deionised water. A 0.2 s integration time was used for the spectrometer (n = 1).

Figure 2-40 presents the response of the photodiode in the backscatter position to increasing turbidity concentrations using the IR 850 nm LED. For low turbidity values the photodiode response is not fully linear due to low signal being received. With higher turbidity values, from 30 NTU onwards, a clear linear response is seen in the photodiode response up to the highest NTU values of 78 NTU.

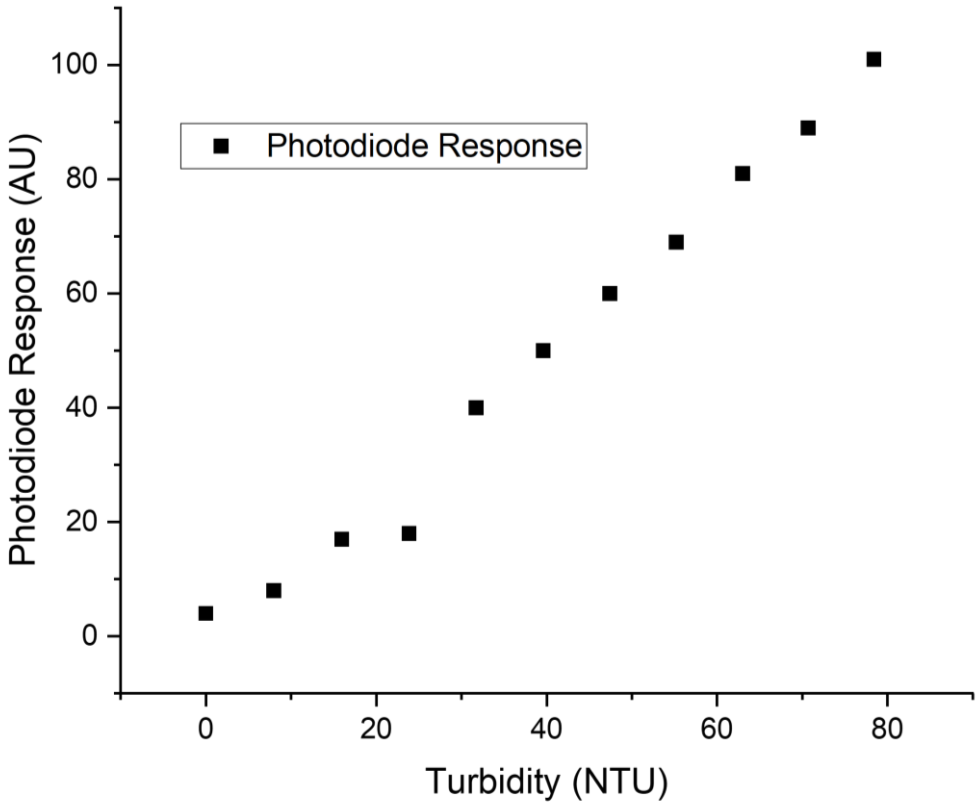

Figure 2-40 Plotted backscatter photodiode response to increasing turbidity concentrations using 850 nm LED. Non-linear response is seen from 0 to 39 NTU due to lower backscatter a lower NTU concentrations with linear response seen at higher turbidity levels (n = 1).

Figure 2-41 presents a combined scatter plot of both the spectrometer's scatter response and the photodiodes backscatter response. The scatter method has shown a linear response at lower turbidity values while the backscatter method displayed linearity at higher NTU ranges. As discussed in Section 1.4.3, the position of the backscatter detectors at 120 degrees provides greater sample volume which allows for higher turbidity values to be measured [88,89,101]. The linear response ranges for both measurement methods are plotted showing an overlap from 40 NTU to 47 NTU. A linear fit is applied to both detector's responses. The spectrometer response has a slope of 336.7 units per NTU value with an intercept of 4353.25 and an R^2 value of 0.99332. The photodiode's response has a slope of 1.3 units per NTU value with an intercept of -1.925 and an R^2 value of 0.99778. Both detectors show good linearity within their ranges of measurement. The scatter method has a much higher slope showing greater sensitivity at lower NTU levels. The backscatter has a much lower sensitivity shown by the slope. However, this demonstrates a method which the backscatter photodiode can be used to extend the limits of detection for turbidity without the need to alter the spectrometers integration time by combining the two methods of scatter and

backscatter measurements. An application of this combination method for extended LOD would be in the event of a sediment resuspension event caused by anthropogenic or storm events [54,330]. A sharp increase of turbidity may surpass the scatter detectors LOD in which case the environment monitoring details would be lost during the high turbidity event. This scenario presents an advantage of incorporating the backscatter photodiode into a deployable environmental sensor design.

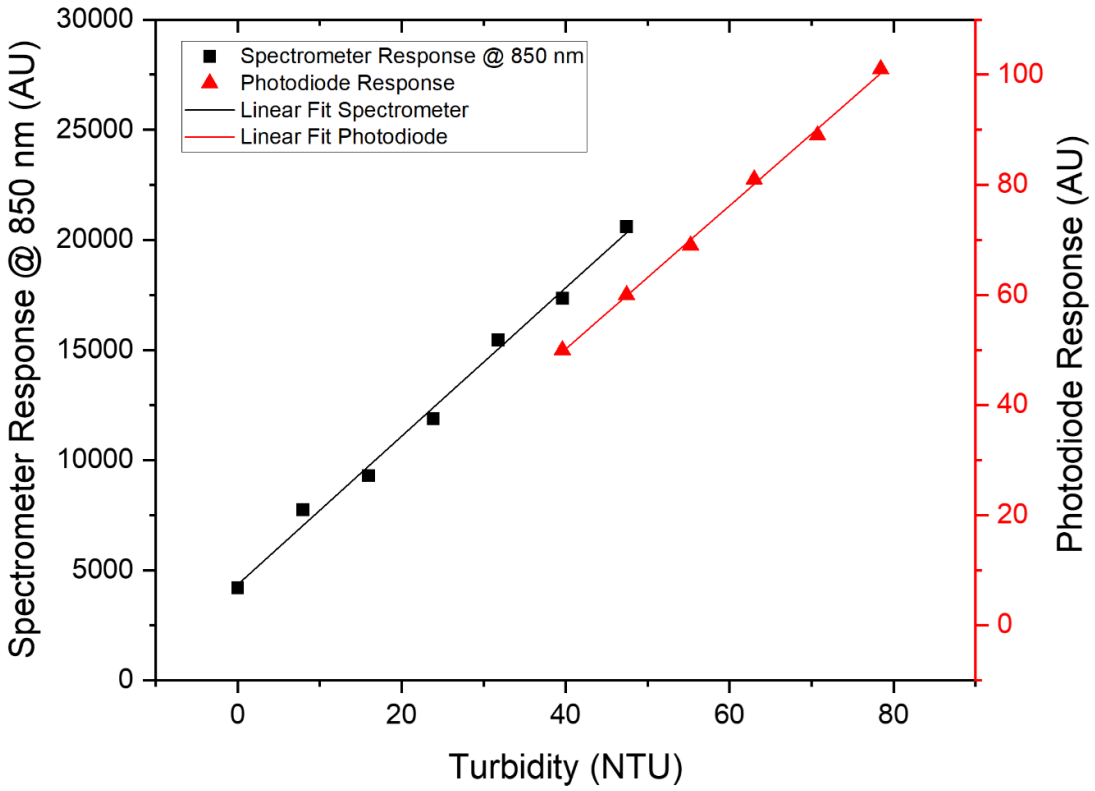

Figure 2-41 Combined scatter plot of spectrometer scatter and photodiode backscatter response to increasing turbidity concentrations between 0 and 80 NTU (n = 1). Spectrometer response is recorded between 0 NTU and 47 NTU. Photodiode response is recorded between 40 NTU and 78 NTU. Linear fit of spectrometer response gives a slope of 336.7, intercept of 4353.25 and a R^2 value of 0.99332. Photodiode response gives a slope of 1.3, intercept of -1.92 and a R^2 value of 0.99778.

2.3.5.3 **Fluorescence Measurements**

Fluorescence Proof of Concept Measurements

Figure 2-42 shows the recorded spectrum of each of the proof-of-concept fluorophores, with an inlay of the visible fluorescence. It was possible using each LED to induce fluorescence in each of the fluorophores tested. Figure 2-42a shows the signal recorded for each LED using quinine sulfate. The fluorescence from the fluorophore was visible to the eye, and it was also possible to record the fluorescence emitted from the fluorophore and spectrally

resolve it using the spectrometer. Quinine sulfate is a broadband fluorescence emitter, fluorescing between approximately 400 – 600 nm. As such there was some overlap between the LED signal and fluorescence signal for LEDs B1 and B2, while for LED B3 the LED and fluorescence signal causing excitation bleed making it not possible to resolve the two signals fully spectrally, although it was still possible to see the fluorescence with the naked eye. Figure 2-42b shows the fluorescence and spectrum recorded for each LED using CFP. Again, in all cases fluorescence was visible seen using as three LEDs. For LED B3 it was once again not possible to spatially resolve the fluorescence signal from the LED signal, however using B1 and B2 there was a small overlap between the LED and fluorescence spectrum, there was sufficient resolution to spectrally resolve the two signals. CFP is a broadband fluorescent maker with a fluorescence spectrum between 410 – 500 nm (FWHM) peaking at 485 nm typically used as a biological marker for physiological processes, visualizing protein localization and detecting transgenic expression in vivo. Figure 2-42c shows visually the fluorescence signal from the diatom algae solution and the fluorescence signal recorded for each LED.

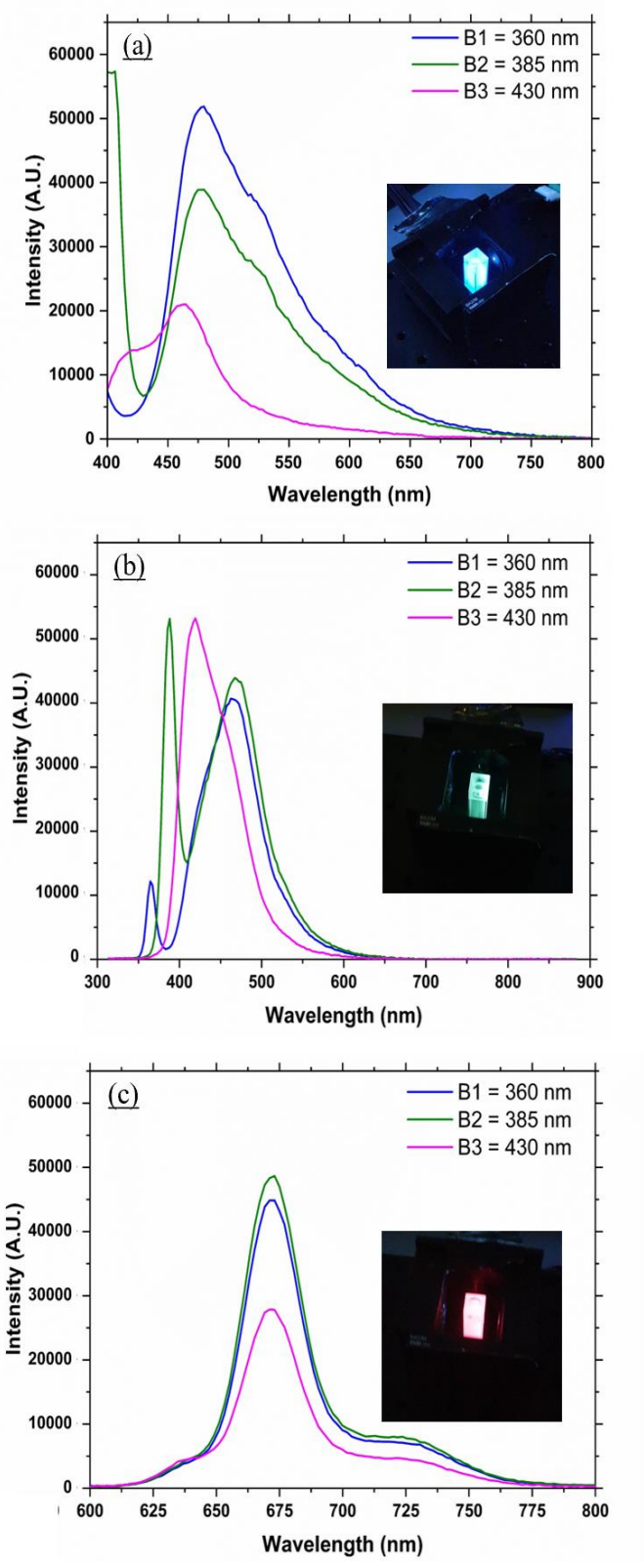

Figure 2-42 (a) Quinine sulfate fluorescence spectrum recorded for each LED with an inlay of the visual fluorescence (n = 1), overlapping of emission and fluorescence seen with B3 causing excitation bleed (b) Cyan fluorescent protein fluorescence spectrum as recorded for each LED with an inlay of the visible fluorescence (n = 1) (c) Chl-a fluorescence spectrum as recorded for each LED with an inlay of the visible fluorescence (n = 1).

Fluorometers that measure in-vivo fluorescence rely on analytical standards for calibration and quality control [325]. This approach is used to ensure reproducibility by using a stable analytical grade standard. Once the devices are calibrated to a given standard, the response can be converted to equivalent standard concentration and conversion factors can be used to infer Chl-a concentration from in-vivo Chl-a measurement [331]. Fluorometers relying on in-vivo measurements, target fluorescence emitted by Chl-a molecule in photosystem II, for which the peak fluorescence emission is approx. 685 nm, although not all Chl-a present is in photosystem II [331]. Standard stability and excitation/emission overlap with Chl-a is thus critical in selecting a suitable standard [325]. For this reason and high solubility in water, Basic Blue 3 (BB3) was selected to benchmark the performance of the fluorometer developed here against a commercial benchtop fluorometer.

Fluorescence Analytical Performance Analysis using Basic Blue 3 Dye

Serial dilutions of BB3 in the 0-1 mg L^{-1} range were used to collect emission scans on both instruments (Figure 2-43a, b) and develop calibration curves (Figure 2-43c, d). This BB3 concentration range and the fluorescence emitted was determined previously, to correspond to the expected fluorescence of Chl-a in the 0.01 to 20 µgL^{-1} range [332]. The benchtop fluorometer was set to the highest sensitivity setting available while the fluorometer developed here used a 2 s integration time. This integration time was optimised to maximise the dynamic range of the instrument and reduce signal-to-noise ratio. While all the BB3 dilutions were successfully detected on the benchtop fluorometer, the CMOS based fluorometer could not detect the dilutions in the low range (i.e., 0.01, 0.02 and 0.05), Figure 2-43, due to a higher signal-to-noise ratio. The calibration curve was thus constructed using the dilutions in the 0.1-1 mg L^{-1} range. To determine the precision and accuracy of the CMOS based fluorometer, a known concentration of BB3 (0.75 mg L^{-1}) was run 10 times on both instruments (Figure 2-43e). Using the developed calibration curves, each run was converted to BB3 concentration (mg L^{-1}). The average concentration was found to be 0.72 ± 0.022 for this device and 0.78 ± 0.0018 for the Jasco fluorometer with a % RSD of 3.004 and 0.23 respectively (Figure 2-43f). Although the Jasco fluorometer demonstrates a higher precision, the % RSD showed by the CMOS fluorometer is within the 5% margin of error acceptable for sensors with environmental applications.

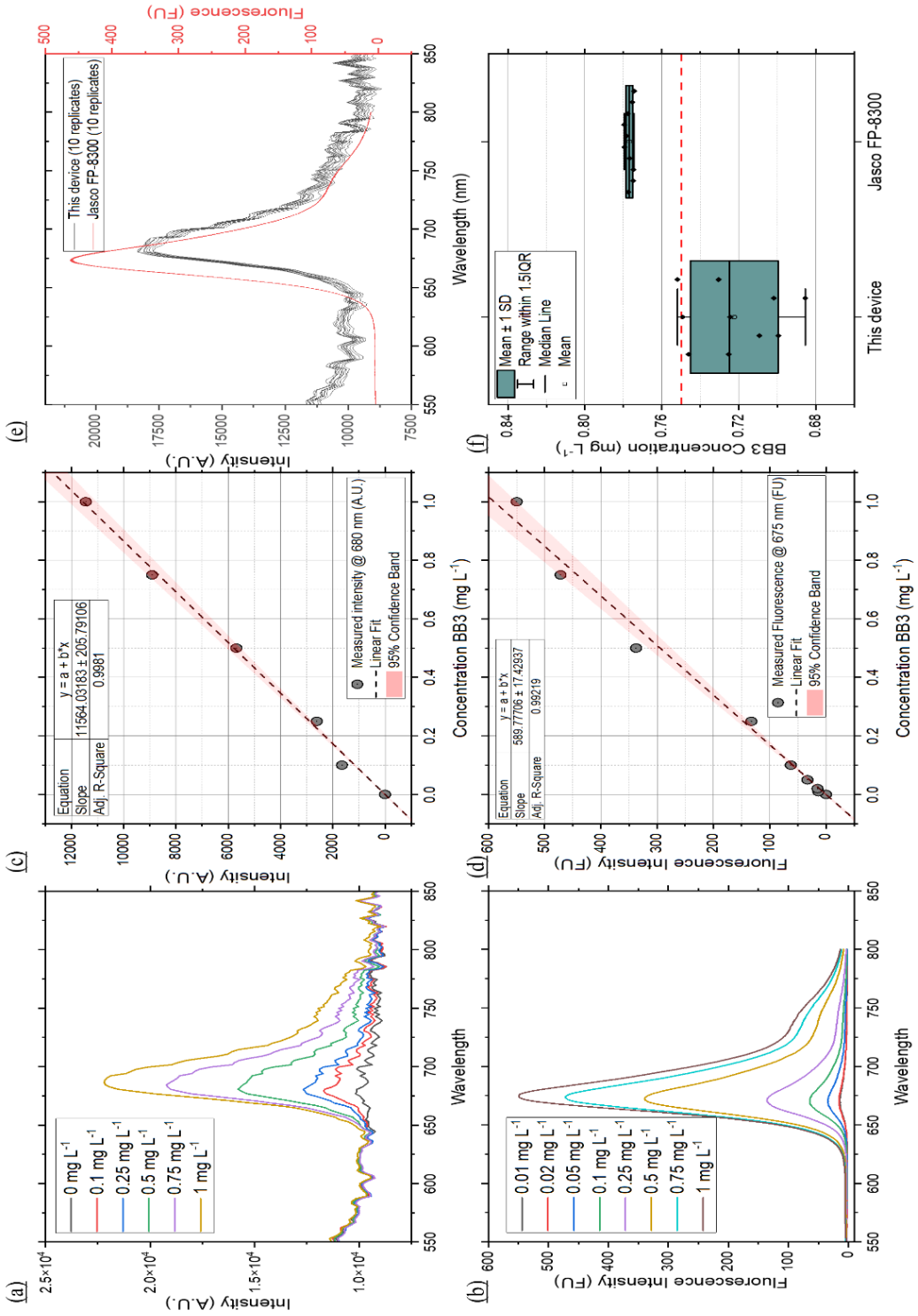

Figure 2-43 Analytical performance with Basic Blue 3 dye (BB3). Emission spectra of serial dilutions of BB3 measured on (a) this device and on (b) the Jasco FP-8300 benchtop fluorometer. Calibration curves for BB3 on (c) this device (λ_{em}=680 nm) and (d) on the Jasco FP-8300 (λ_{em}=675 nm). (e) Ten replica scans (emission spectra) of the same concentration of BB3 (0.75 mg L^{-1}) on both instruments. (f) Box plots following conversion to BB3 (mg L^{-1}) of the 10 replica scans on both instruments, showing precision (mean ± 1 SD) and accuracy (dashed red horizontal line positioned at 0.75 mg L^{-1}) of the two devices. In (a), (c) and (e) an integration time of 2 s was used to collect the emission spectra using LED B2 (λ max=380 nm), in (b), (d) and (e) the sensitivity of the instrument was set to high and slit widths for both the excitation and emission monochromators were set to 5 nm.

Application to extracted Chl-a

Figure 2-44a shows a sample of the Chl-a spectrum using different concentrations of Chl-a extracted in acetone using LED B2 (λ = 380 nm). For each of the three LEDs used in this work it was possible to detect a fluorescence signal for Chl-a concentration between 1 – 20 μg L^{-1}, with LED B2 achieving the highest signal for each concentration and LED B3 (λ = 430 nm) recording the lowest signal intensity. A calibration curve for each LED response was created by taking the peak of the fluorescence signal at 675 nm as recorded by the spectrometer (Figure 2-44a, Table 2-9). Due to the redshift in the fluorescence signal at 20 μg L^{-1} it was excluded from the calibration.

***In-vivo* application**

Figure 2-44b shows a sample of the spectra recorded using LED B2 of the diatom algae. Unlike the previous section these spectra were recorded in-vivo. The measured response is widely used in environmental sensors as a proxy for Chl-a concentration [331]. Fluorescence was successfully detected throughout the diatom algae concentrations with all the LEDs. LED B3 however showed the least change with increasing concentrations and was excluded from the calibration. Collected emission scans for LED B2 and calibration curves for LEDs B1 and B2 are presented in Figure 2-44b while the calibration coefficients are presented in Table 2-9. Similarly, to the extracted Chl-a, LED B2 was the most sensitive to changes in concentration. Globally, Chl concentrations range from 0,01 to 20 μg L^{-1} [332]. In terms of analytical performance, the system can target and successfully quantify Chl-a at environmental concentrations for both in-vivo measurements and combined acetone extraction.

Table 2-9 Calibration slope and R^2 values for acetone extracted Chl-a and in-vivo Chl-a from cultured diatom species Nitzschia ovalis.

LED	**Extracted Chl-a**		***In-vivo* Chl-a**	
	Slope	R^2	Slope	R^2
B1 (λ = 360 nm)	2248.1	0.997	878.39	0.991
B2 (λ = 380 nm)	3265.3	0.994	1498.4	0.995
B3 (λ = 430 nm)	115.03	0.991	ND	ND
ND-not determined				

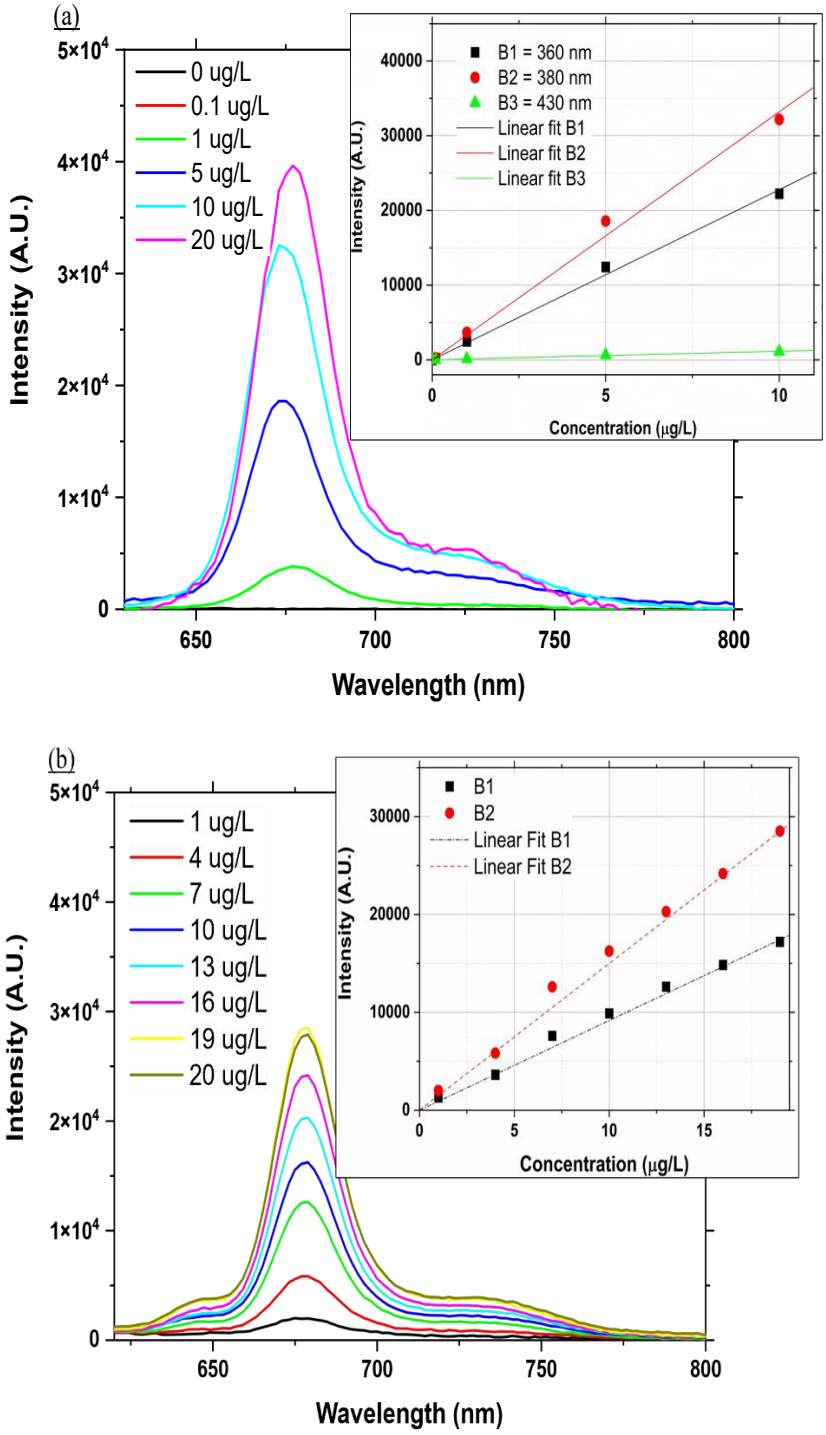

Figure 2-44 (a) Fluorescence spectra of extracted Chl-a in acetone using LED B2 (λ = 380 nm). Chl-a was extracted from laboratory cultures of diatom species Nitzschia ovalis and quantified as described in the Section 2.2.7.3; inset in (a) calibration curve for each LED with extracted Chl-a in acetone using the peak fluorescence emission at 675 nm (n = 3) (b) Fluorescence spectra recorded using LED B2 (λ = 380 nm) of serial dilutions of laboratory drown diatom cultures; inset in (b) calibration curve between in-vivo fluorescence and the diatom concentrations expressed as Chl-a (µg/L) following extraction for LEDs B1 and B2 (n = 3). In both (a) and (b) the Chl-a concentrations were determined as described in the Section 2.2.7.3.

An example of the recorded fluorescence emission spectrum collected for environmental sample is shown in Figure 2-45, between 400 – 850 nm for LEDs B1 and B2. No fluorescence signal was detected for B3; thus, it is not shown. Using the calibration curves developed in the previous section it was possible to calculate the Chl-a concentration by dividing the fluorescence signal peak by the slope of the calibration curve. Using the in-vivo calibration curves developed with laboratory grown diatoms (Figure 2-44b, Table 2-9) a concentration of 3.05 μg L^{-1} was calculated for LED B1 and 3.25 μg L^{-1} for LED B2 respectively. The Chl-a concentration in the sample, following the standard method using filtration and acetone extraction was found to be 2.16 ± 0.24. Such discrepancy is expected as slope coefficients used are for in-vivo Chl-a fluorescence determined with laboratory cultures are expected to be different from environmental mixed populations. In general, the calibration of fluorimeters is carried out on site specific samples due to the large natural variability in the relationship between in-situ fluorescence and extracted Chl-a concentrations. Globally, the slope factor can range from 1 in the Arabian Sea region to greater than 6 in the Southern Ocean province, south of New Zeeland [331]. With the two sources of uncertainty when measuring in-vivo being the variability in the Chl-a specific absorption [333] and the variability in the fluorescence quantum yield [332].

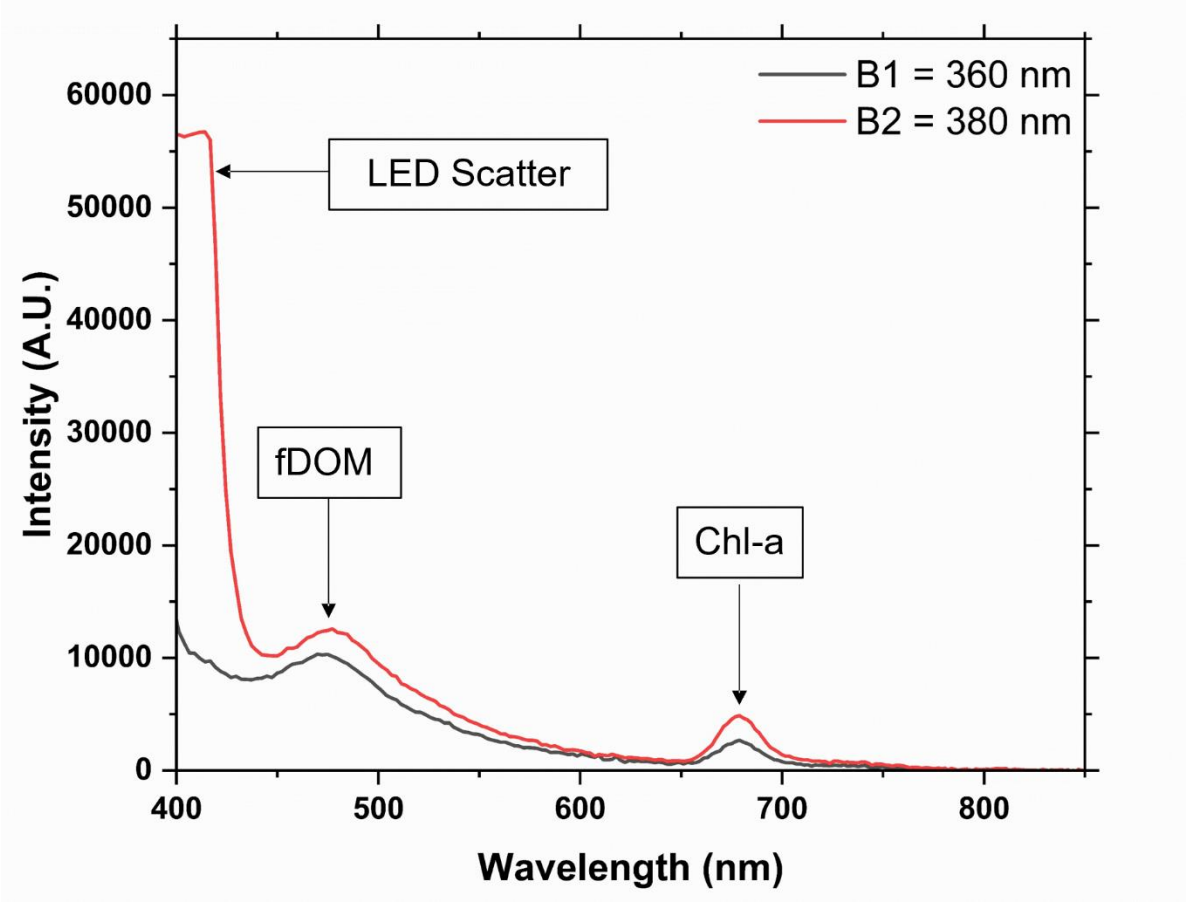

Figure 2-45 Example of fluorescence spectra recorded using LEDs B1 (360 nm) and B2 (380 nm) from an environmental sample. Fluorescence from Chl-a is detected between 650 – 700 nm indicating the presence of algal species in the water. In addition to the Chl a signal an unknown fluorescence signal, believed to be fDOM was also observed between 450 – 600 nm.

The set-up was consistently able to induce and detect fluorescence from all samples tested and does however solve some issues presented such as costing, reliability, and overall footprint, potentially allowing in-situ real time monitoring of environmental events and changes over time. Algal species for example are a vital component of aquatic marine life, serving as the basis of the oceanic food chain. As a species, their environment is threatened by global warming and climate change, and therefore monitoring their levels in oceanic environments may be an important warning mechanism while tracking the impacts of climate change. Should a suitable housing environment be developed this technology may be deployable in marine environments to monitor changes in algal populations at a relatively low-cost.

The experimental work showed that it was possible to detect fluorescence produced by Chl-a samples at expected environmental concentrations and using the calibration curves

quantify those values, making this technology a potentially vital tool for environmental monitoring. Detection capabilities within the μg L^{-1} are essential for real-world application, and similar devices have achieved this range using PMTs [163,334] and PDs [151]. The CMOS mini-spectrometer however has a spectral response range between 340 – 850 nm and a 12 nm spectral resolution. These key features enable spectral deconvolution of overlapping optical signatures and critically, detection of other optical targets within this range. Furthermore, the compact, small design of the CMOS spectrometer enables integration into submersible, in-situ devices where size of electronic components is critical. The C12880MA unit employs a nano-printed reflective concave blazed grating which minimizes the light path and enables the realisation of small, compact detectors. By comparison, a larger light patch is required when diffraction gratings are used in conjunction with CMOS based cameras [302]. The use of LEDs means that the set-up can be flexible in determining the desired excitation wavelength for a particular fluorophore, by simply changing the LED to another wavelength in a plug-and-play manner or designing a multi-wavelength LED electronic board to hold a range of LEDs. The current optical design comprising collimating lenses facilitates the addition of multiple SMD LEDs on the same board thus enabling the detection and quantification of multiple target analytes. The optical components used were kept relatively straight forward by limiting the optics to a collimating and focusing lens, but more sophisticated and complicated components could be incorporated into the design in situations where narrow bands are required or the Stokes shift between the excitation and emission bands are relatively close together.

2.4 Conclusion

The research detailed in this chapter successfully achieves the aim by introducing an electronic and optical benchtop system capable of multiparameter measurements using different optical measurement modes. Central to this system is an eight-LED multispectral light source, complemented by a combination of compact spectrometers and photodiodes. This optical measurement systems displays an advanced and novel measurement system capable of measuring transmittance, absorption, scatter, backscatter, and fluorescence over a spectral wide spectral range from the UV to the IR.

The electronic systems, specifically designed to interface with the chosen sensing components, have been demonstrated to effectively conduct analytical measurements. A notable achievement is reaching Technology Readiness Level 3 (TRL3) as defined in Table 1-6. In terms of performance, the sensor demonstrated proficiency in absorption, transmission, scatter, backscatter, and fluorescence measurements. Its analytical capabilities were validated against a benchtop fluorometer using both analytical standards and environmental samples. Notably, the system could accurately detect and quantify Chl-a extracts both in-vivo from lab-grown cultures and in environmental specimens. A distinct advantage of this system lies in its modular design. The "plug-and-play" nature allows for easy LED replacement or expansion, enabling specificity for various optical parameters. When using multi-LED arrays activated in sequence, the device can effectively scan and record consecutive emission or scatter spectra. The inclusion of spectrometers ensures the resolution of overlapping optical signatures, especially when paired with the sequentially operated LED board.

Given its demonstrated potential, this system is deemed suitable for adaptation into a deployable in-situ device. By leveraging the miniaturised electronic technology of the spectrometers and surface mounted components a significant advantage is presented for the potential to incorporate the detection system into a compact deployable enclosure for in situ sensing. Its design and multiparameter optical measurement capabilities make it a promising tool for accurate, in-field optical measurements of key target analytes.

3 ROBUST DESIGN OF IN SITU OPTICAL SENSOR FOR THE MARINE ENVIRONMENT

3.1 Introduction

The marine environment is a harsh and unforgiving environment for equipment to operate in. Marinisation is a process that factors in the challenges associated with the marine environment into the engineering design of components and equipment intended to operate under these environmental conditions. The environmental and mechanical stresses marine equipment need to endure without failing lead to the need for a robust design approach [199,335]. The concept of robust design was first pioneered by Genichi Taguchi, who defined robustness as "the state where the technology, product, or process performance is minimally sensitive to factors causing variability (either in the manufacturing or user's environment) and aging at the lowest unit manufacturing cost" [336]. Learnings from the comprehensive review of marine materials, mechanical properties, mechanical design, and fabrication method conducted in Section 1.5 will give input into the robustness of the sensor design. These key design inputs need to be incorporated into the sensor design and material selection. The aim of the work presented in this chapter is to integrate the technology into an enclosure which is robust, durable, and able to handle the harshness of the marine environment. to a technology readiness level (TRL) of 5 (see Table 1-7). To achieve this aim, the following objectives must be achieved:

1. An iterative mechanical design and material selection process must be carried out as described in Section 1-3 to optimise the sensor design performance and robustness while maintaining low materials and manufacturing costs. Testing of the sensor prototypes and materials will be conducted at each design iteration to ensure the system is functioning correctly and the design is suitable for the marine environment.

2. An experimental investigation of the materials will be conducted to demonstrate real world performance and suitability for the marine environment in the application of in situ sensors which will provide extensive data and learnings for the reach field and technological development of the next generation of in situ marine sensors

3. Validation experiments will be conducted in the lab using the sensor's different measurement modes (transmittance, fluorescence, and scatter). The optical measurement potential of the sensor will need to be demonstrated for detection of

multiple parameters in the lab (Turbidity, dissolved organic matter, oil and Chl) and validated by using a commercial optical sensor.

3.2 Materials and Methods

The sensor was designed in four distinct sections as shown in Figure 3-1. For each section the optimum materials, manufacturing method were selected as well as the mechanical structure designed. The mechanical designs were made using Autodesk Fusion 360 CAD modelling software.

Sensor Section	Description
Top cap and marine cable	This section facilities access to the internal sections of the sensor and is the interface of the sensor with external hardware using a marine cable for power and communication.
Sensor body	The internal control electronics and frame are housed by the sensor body which encloses the sensor joining the top cap and optical head flanges.
Internal frame	The internal frame is a structural system joining the top and bottom sections of the sensor mechanical and facilitating the mounting of the main control electronics.
Optical Head	The optical head section houses the optical and sensing components of the sensor.

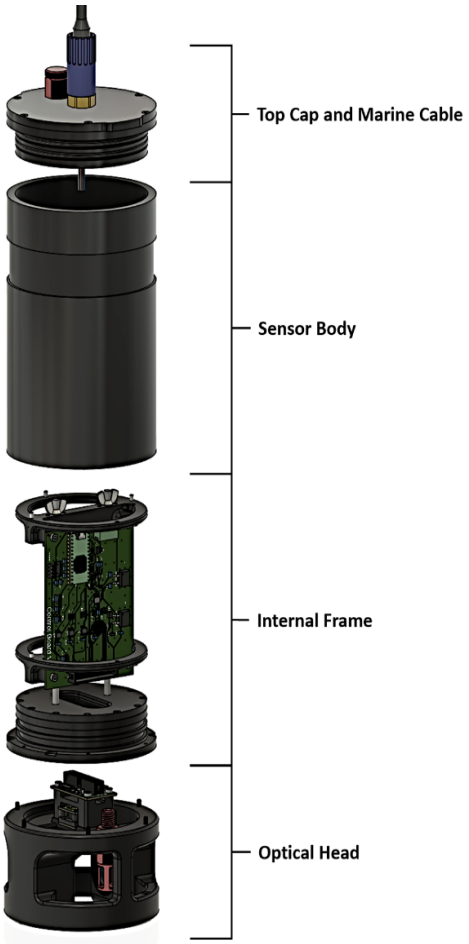

Figure 3-1 Overview of sensor design sections with table of section descriptions and labelled exploded view of sensor sections.

3.2.1 Material and Manufacturing Method

Table 3-1 outlines the materials and manufacturing methods used with the manufacturer and source. For the custom FDM printed components, a Lulzbot Taz6 3D printer with a 0.5 mm nozzle sourced from Farnell Ireland was used. Black RS-Pro PETG 2.85 mm filament was used sourced from Radionics Ltd. Dimensioned drawings and CAD models were supplied to the fabricators for the components which were outsourced.

Table 3-1 Materials and manufacturing method used for each component.

	Component	Material	Manufacturing Method	Manufacturer	Source Link
Top Cap and Marine Cable	Air Pressure Valve	Anodized 6061-T6 Aluminium	Off the Shelf	Blue Robotics	https://bluerobotics.com/
	Bulkhead Connector/Cable Assembly	Brass, chloroprene rubber, ABS	Off the Shelf	MacArtney	https://www.macartney.com/
	Top Cap	Acetal POM-C	CNC Machined	Hubs CNC Machined	https://www.hubs.com/
	Top flange. Press fit water proofing into enclosure using o rings	Anodized 6061-T6 Aluminium	Off the Shelf	Blue Robotics	https://bluerobotics.com/
	O-Rings for Connectors and Flanges	Nitrile Rubber	Off the Shelf	Blue Robotics	https://bluerobotics.com/
	Counter Sunk M3 Fasteners used to bolt the top cap to the flange	316 Stainless Steel	Off the Shelf	Inox Fasteners Ltd	https://www.inox.ie/index.html
Sensor Body	Sensor Body	Acetal POM-C	CNC Machined	P&T Engineering CNC Machined	https://www.ptprecisioneng.com/
Internal Frame	Electronic Tray: Top piece interfaces with top flange, bottom piece for bolting the electronic board onto	PETG	FDM 3D Printed	Custom FDM 3D Printed	-
	Base: Bolts into bottom flange and mounts the two M5 threaded rods as guide rails	PETG	FDM 3D Printed	Custom FDM 3D Printed	-
	M5 Threaded Rods and M3 Counter Sunk Fasteners	316 Stainless Steel	Off the Shelf	Inox Fasteners Ltd	https://www.inox.ie/index.html
Optical Head	Sensor Mounting Tray	PETG	FDM 3D Printed	Custom FDM 3D Printed	-
	Top flange. Press fit water proofing into enclosure using o rings	Anodized 6061-T6 Aluminium	Off the Shelf	Blue Robotics	https://bluerobotics.com/
	Optical Head Main Structure	PA2200 Nylon	SLS 3D Printing	Betalayout SLS 3D Printed	https://eu.beta-layout.com/3d-print/
	M3 and M2 Socket Fasteners	316 Stainless Steel	Off the Shelf	Inox Fasteners Ltd	https://www.inox.ie/index.html

ABS - Acrylonitrile Butadiene Styrene, POM-C - Acetal Copolymer, CNC – Computer Numeric Control, PETG - Polyethylene terephthalate glycol, FDM – Fused Deposition Modelling, SLS – Selective Laser Sintering

3.2.2 **Mechanical System Design**

Figure 3-2 gives an overview of the sensor design. The main features of the design are highlighted in Figure 3-2a. The key dimensions of the sensor unit are shown in Figure 3-2b.

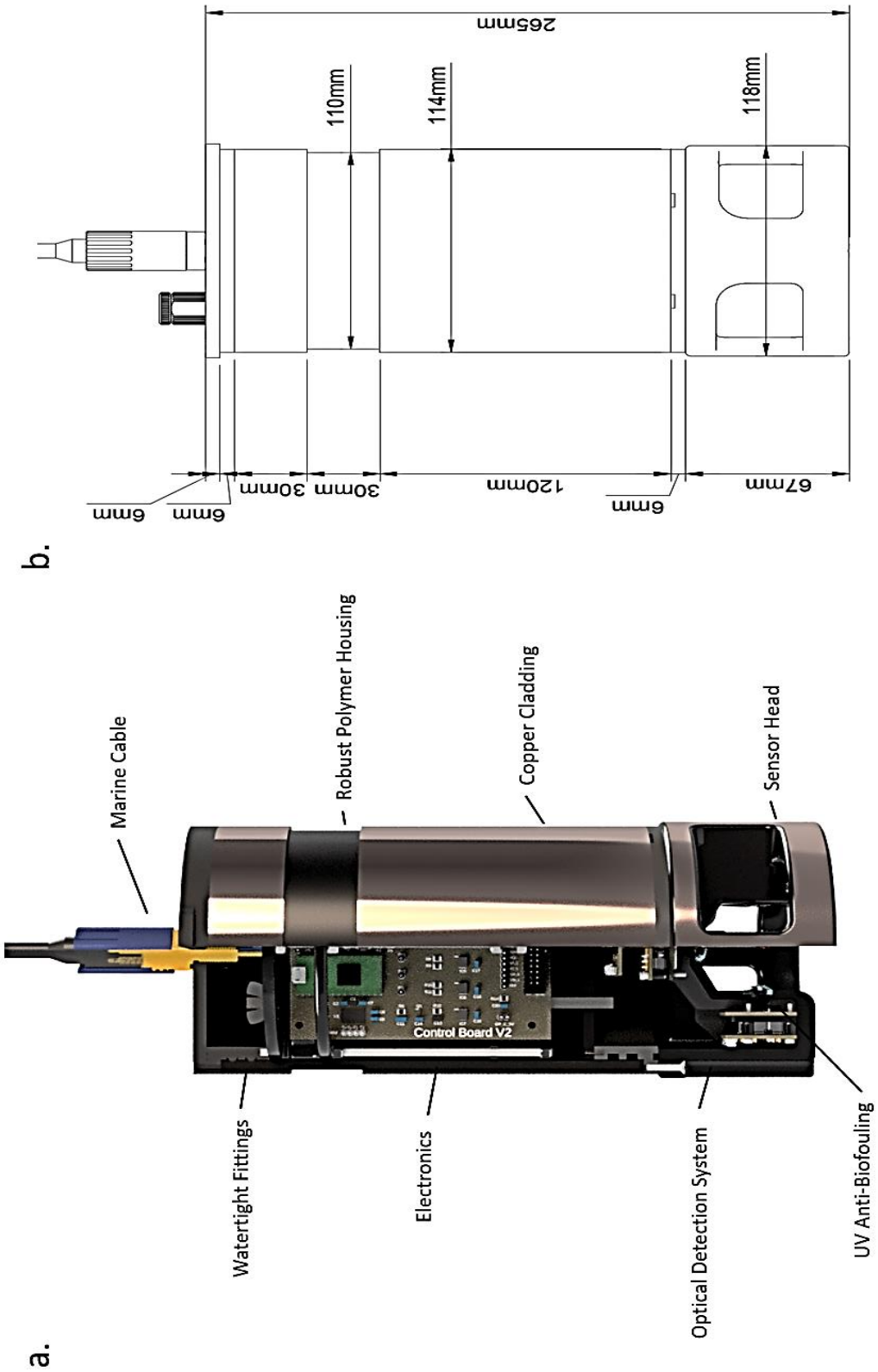

Figure 3-2 Overview design of the optical sensor unit prototype. (a) Labelled CAD Render with quarter-slice view of the sensor unit design. (b) Dimensioned drawing of the sensor unit design.

3.2.2.1 Optical Head and Mounting Structure Design

An overview of the optical head design is presented in Figure 3-3. An exploded view of the optical assembly and internal components is given in Figure 3-3a. The optical setup, orientation of sensing components and key dimensions are shown in Figure 3-3b. The path length between light source and 0-degree position detector was 35 mm. The 90- and 120-degree detectors were positioned 22 mm from the centre point of the path length. The lenses used are outlined in Table 2-1. The light source was positioned 7 mm from the surface of the lens to ensure the light emission from all eight LEDs were distributed evenly across the lens. The 0-degree spectrometer entrance slit is positioned 8 mm from the focusing lens. The entrance slit of the 90-degree detector is positioned 10 mm behind the focusing lens. The photodiode measuring backscatter is positioned 12 mm from the focusing lens.

Two approaches were taken to fabricate the optical head. The first consisted of FDM 3D printing the optical head from PETG using 100% infill to create a watertight seal. To provide additional watertightness the printed optical head was coating in epoxy resin. The epoxy used to waterproof the optical head was XTC-3D™ High Performance 3D Print Coating sourced from Glass Fibre and Resin Supplies and a black dye and silicon thickener were also used to give the correct finish and coat the 3D print. The epoxy coating was left to cure for 24 hrs. The second approach was to leverage more advanced additive manufacturing techniques. SLS 3D printing was selected due to its high-resolution prints and robustness of the print. The material selected was PA2200 Nylon. Post-processing steps were used on the print to ensure the entire structure is completely watertight. The process used for sealing surfaces of the print was infiltration which involved submersing the print in an oil immersion bath to seal any pores in the surfaces where powder may not have fully fused making the print fully airtight and watertight. The optical lenses were fitted to the optical head using epoxy resin. The same method and epoxy as applied as the FDM optical head. The epoxy was applied to the periphery of the lens using a syringe and 20G dispenses needle tip.

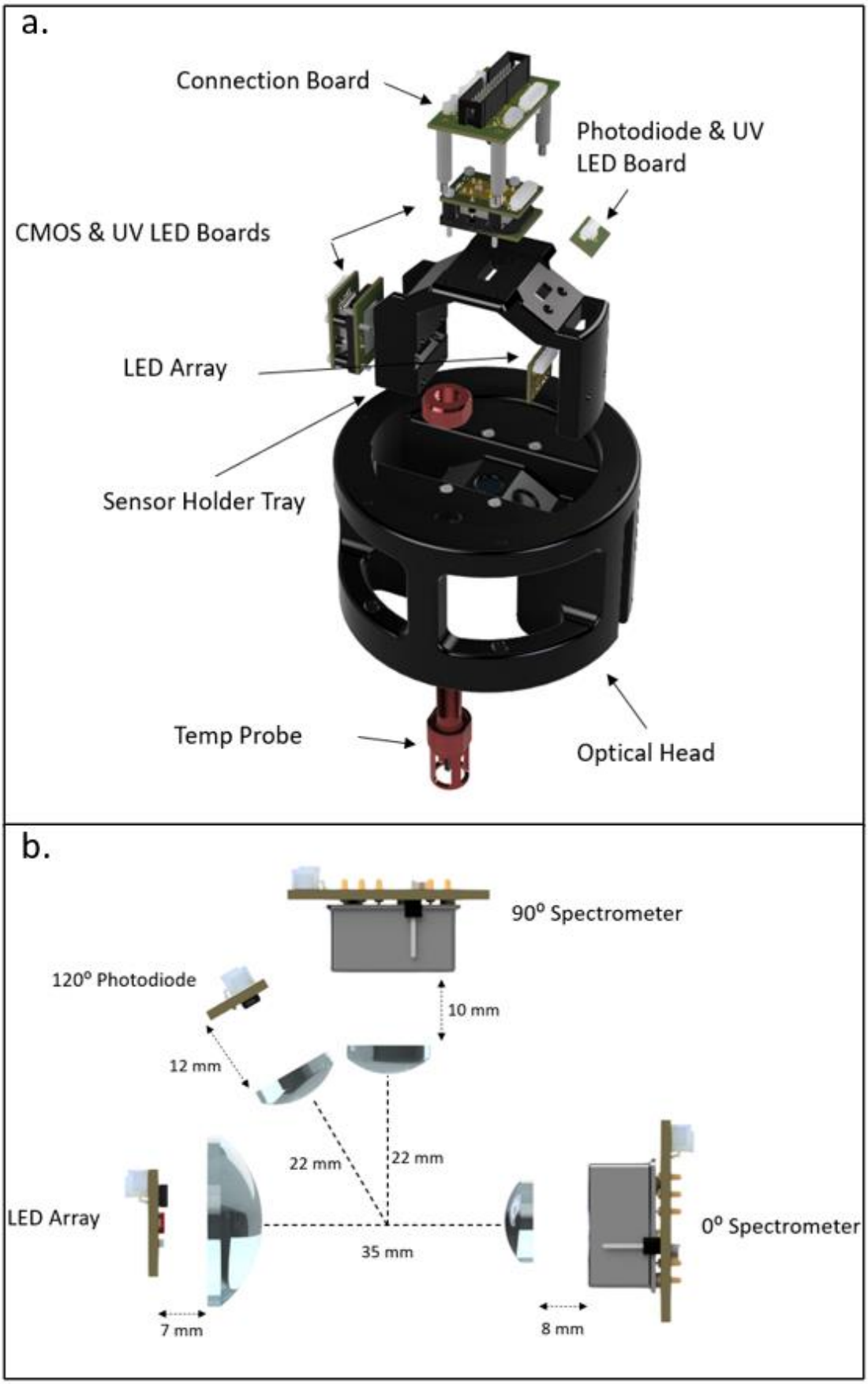

Figure 3-3 (a) Exploded diagram of optical head assembly with labelled components and (b) a labelled and dimensioned render of the optical component positions.

The positioning and instalment method for the temperature probe are presented in Figure 3-4. The probe is positioned 35 mm from the central axis of the optical detectors and is centred in the optical head in the perpendicular axis. The probe is mounted to the optical head using a penetrator and locking nut system. An O-Ring creates a watertight seal interfacing between the probe body and the optical head.

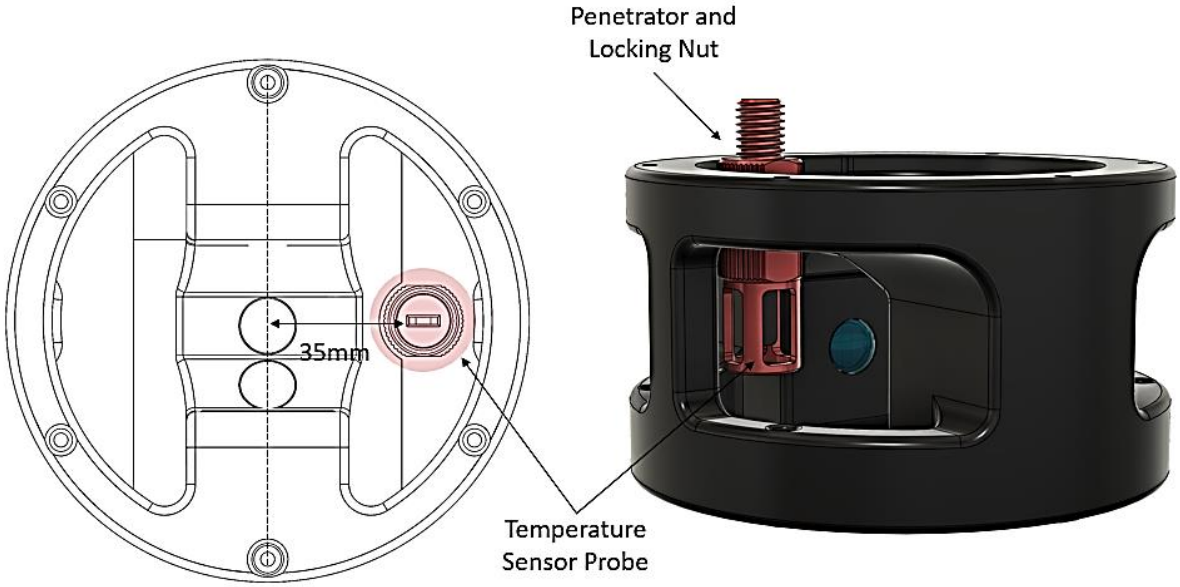

Figure 3-4 Temperature sensor probe fitted to the optical head. On the left of figure, a bottom view of the optical head showing positioning of probe 35 mm from centreline. On the right a CAD Model rendering of the optical head and temperature sensor probe position with label of penetrator and locking nut used to fasten the probe securely.

The design, dimensions and assembly of the electronics mounting tray which is inserted into the optical head (see Figure 3-3) and connection board spacer is shown in Figure 3-5. Figure 3-5a and c present the design of the spacer component which is FDM 3D printed from PETG. The purpose of this component is to position the connection board above the optical mounting tray allowing for connections to be made with components and the central control board in the sensor body. The design of the optical mounting tray and dimensions are seen in Figure 3-5b and d. The sensing components mounted to PCBs are joined to the mounting tray via M2 bolts which bolt to threaded brass inserts on the tray. Figure 3-5e shows the assembled mounting tray, sensing boards, spacer, and connector board. The structure is joined to the optical head via four 30 mm M3 bolts which bolt to four threaded brass inserts inserted into the optical head.

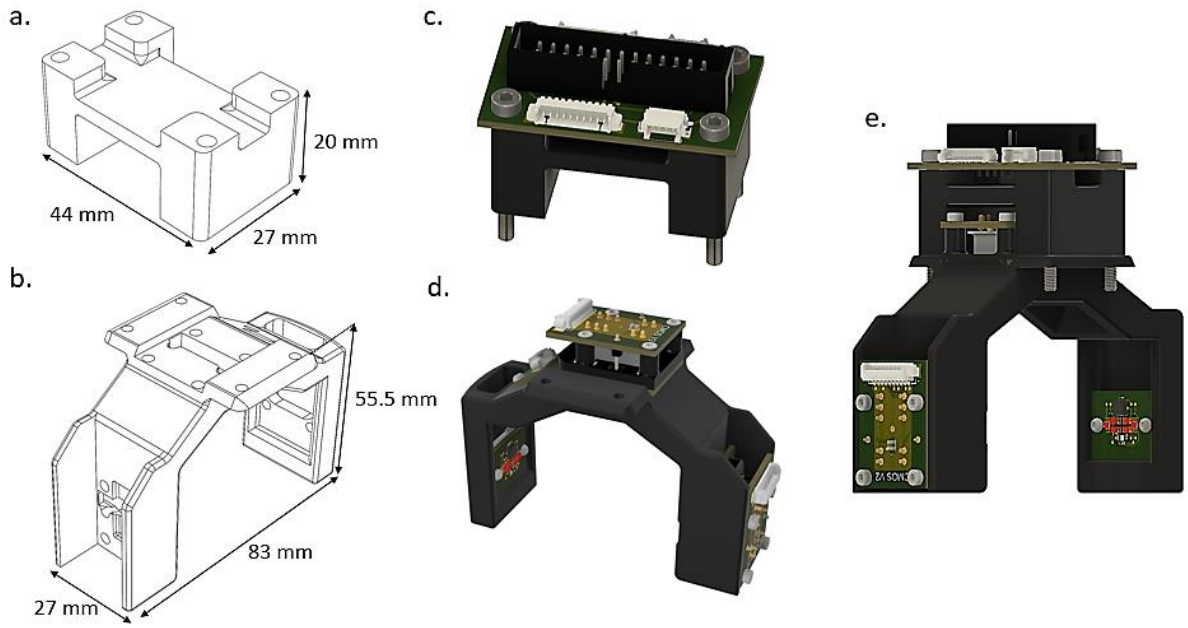

Figure 3-5 Electronic mounting tray and connector board spacer design (a) Dimensioned drawing of connector board spacer (b) Dimensioned drawing of mounting tray. (c) 3D CAD Model Render of spacer and mounted connector board. (d) 3D CAD Model render of mounting tray with sensing components mounted. (e) Assembled mounting tray and spacer with electronics mounted.

The spacer design and dimensions for spacing the spectrometer mounting board and the UV LED board is presented in Figure 3-6. Figure 3-6a gives the dimensions of the spacer with the height of 9 mm which is the required position for the spectrometer entrance slit and UV LEDs to be on the same plane. The assembled stacked boards and spaced are seen in Figure 3-6b. Four M2 20 mm bolts join the stacked boards and bolt into threaded brass inserts in the optical mounting tray.

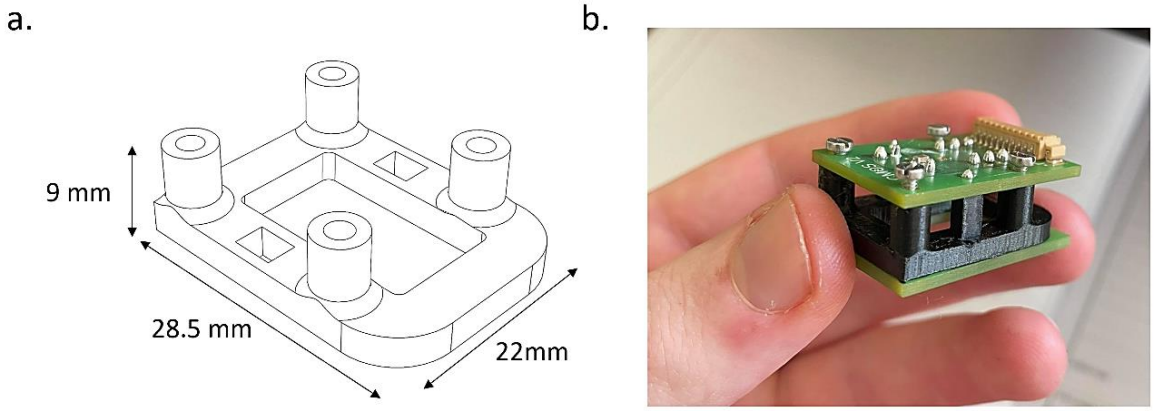

Figure 3-6 Design of spectrometer and UV LED board spacers. (a) Dimensioned drawing of spacer design. (b) Black PLA 3D printed spacer and assembled stacked boards.

3.2.2.2 **Sensor Body Design**

The design and dimensions of the sensor body are presented in Figure 3-7. The inner diameter of 102 mm was chosen to provide a snug fit to insert the 4" O-Ring flanges source from Blue Robotics to create a watertight seal. A 30 mm groove of outside diameter 110 mm is designed to allow clamping equipment to attach the sensor to deployment mounting hardware. The dimensioned drawing and CAD model were supplied to P&T Precision engineering component to CNC design form Acetal POM-C.

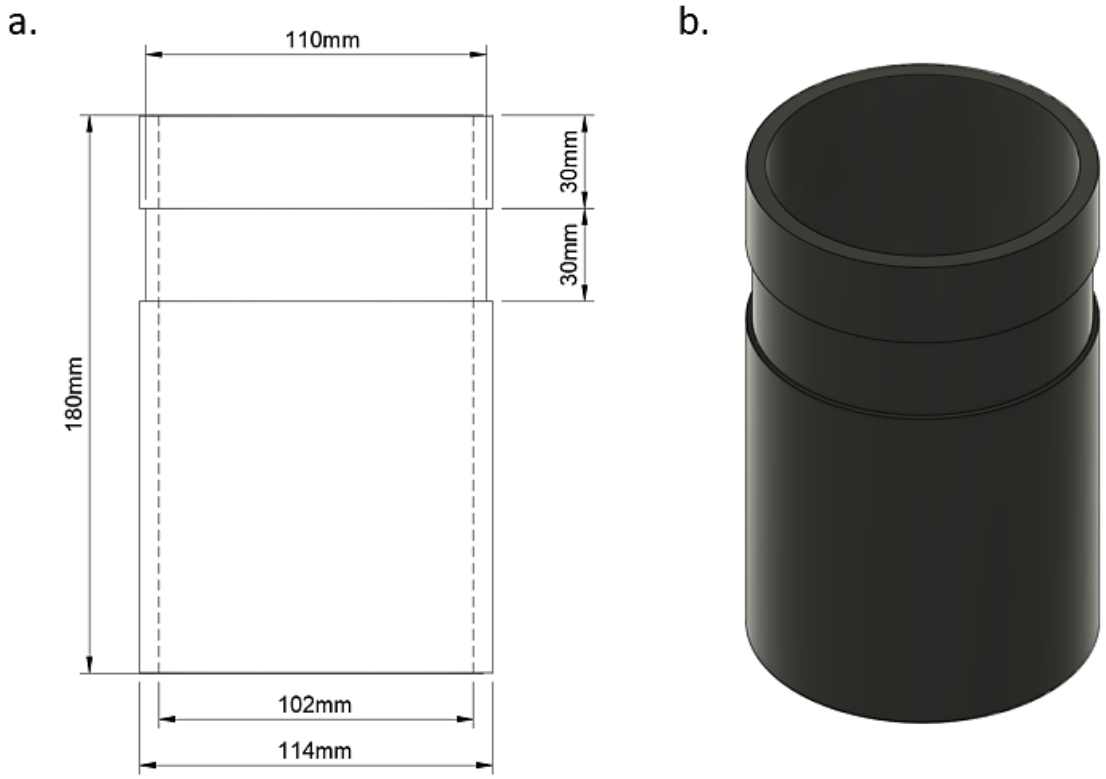

Figure 3-7 Sensor body design (a) Dimensioned drawing of side view of the sensor body. (b) 3D CAD Model rendering of sensor body design.

3.2.2.3 **Top Cap Design**

A labelled diagram of the assembly of the top cap section of the sensor and dimensioned drawing of the top cap are presented in Figure 3-8. Figure 3-8a shows the fitting of the bulkhead connector and pressure valve into the top cap section. Figure 3-8b shows the two holes which need to be drilled into the top cap to insert the bulkhead (11 mm hole) penetrator and the pressure value (10 mm hole) penetrator. Both connectors are secured to the top cap by nylon lock nuts. The top cap is bolted to the flange using 6 countersunk M3 12 mm bolts. A watertight seal is kept between the interface of the top cap and the flange riad a face O-

ring as shown in Figure 3-8a. The flange fits snuggly into the sensor body and two radial O-rings maintain a watertight seal. The dimensioned drawings shown in Figure 3-8b was sent to Hubs Fabricator to CNC machines from 6 mm Acetal POM-C.

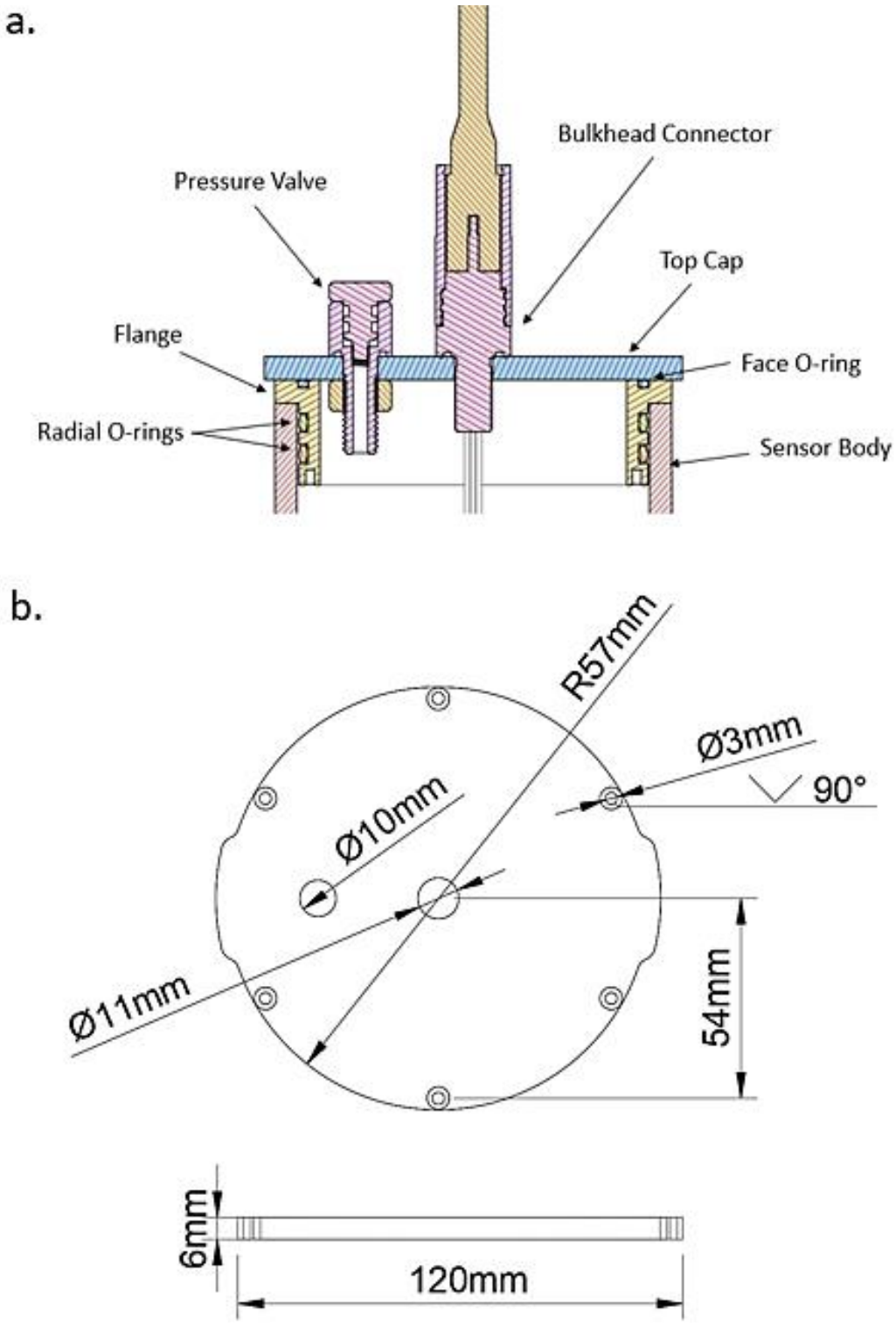

Figure 3-8 Design of the top cap and cable connector. (a) Labelled diagram of a section view of the top section of the sensor showing the valve, connector top cap, flange, and O-ring seals. (b) Dimensioned drawing of top cap design.

3.2.2.4 **Internal Frame Design**

The design of the internal frame is presented in Figure 3-9. The function of the internal frame is to firstly, allow for the electronic control board to be mounted and secondly to provide a central rigid structure to join the top and bottom sections of the sensor together. As seen in the exploded view shown in Figure 3-9a, the connecting drops are joined to a base plate. The base plate is bolted to the bottom flange with 4 M3 counter sunk 12 mm bolts. Two wing nuts join the two flanges via the top plate (shown in Figure 3-9b) which is bolted via 4 countersunk M3 12 mm bolts to the top flange. The connecting rods are M5 threaded stainless steel rods positioned 48 mm apart. Figure 3-9b and c show the assembly of the electronics mounting system. The top and lower plate are spaced 80 mm apart using two plate spacers which the connecting rods fit through. The control PCB is bolted to brass threaded inserts lining up with the top and lower plates using four M3 6 mm bolts. The top plate, lower plate and base plate are all 101 mm in diameter and fit securely into the sensor body. All plates and spacers are FDM 3D printed from PETG with an 80% infill for increased strength.

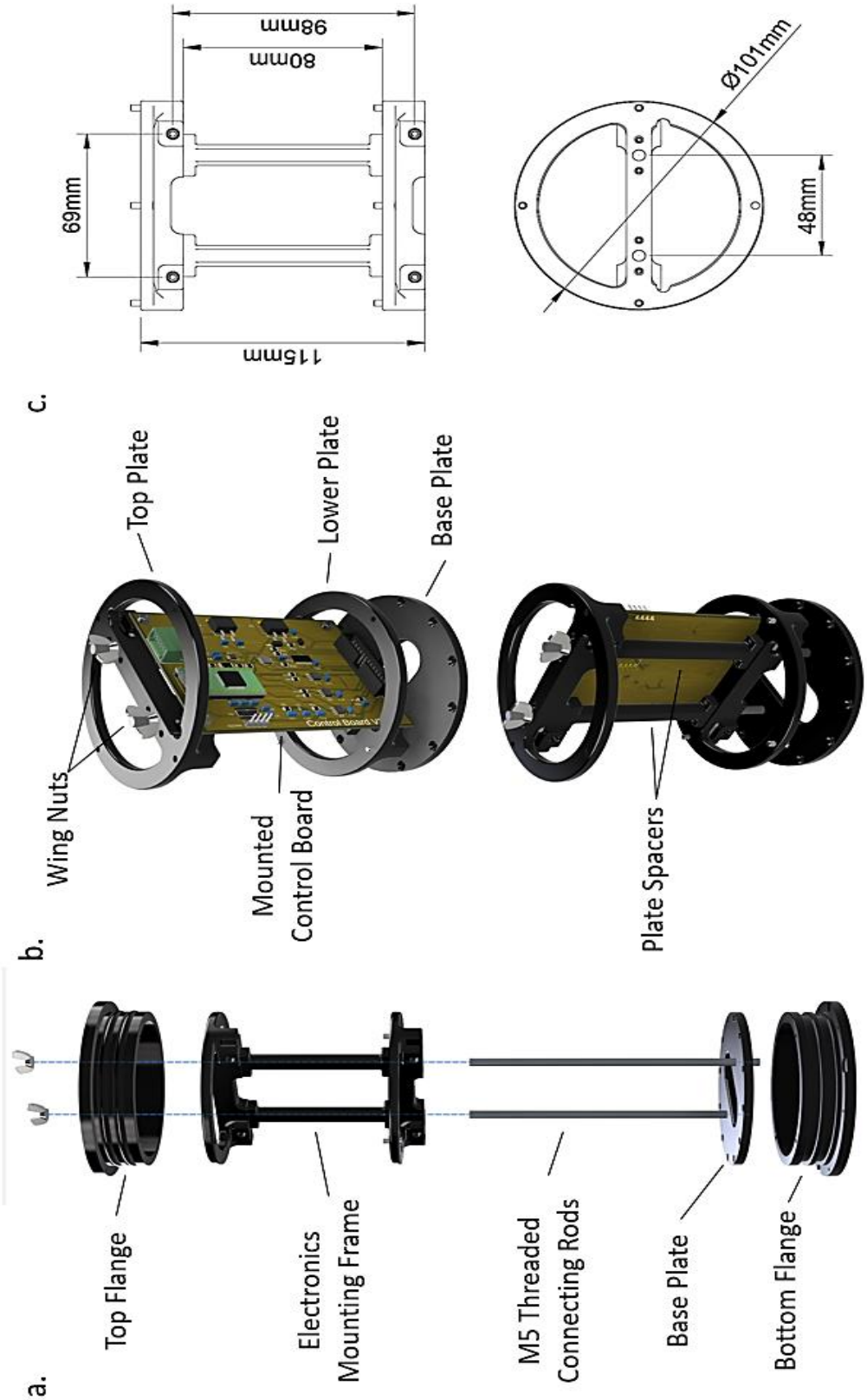

Figure 3-9 Internal frame and electronics mount design with (a) an exploded and labelled view of the internal frame assembly (b) labelled views of internal frame and electronic board mounted and (c) dimensioned drawing of the electronics mounting frame.

3.2.3 Sensor Guard and Ambient Light Reduction Designs

The sensor guard was added to the design to surround and protect the optical head. It also is intended to reduce the ambient light entering the optical detection zone to increase the limits of detection of the fluorescence measurements. The method to reduce ambient light but maintain good flow and avoid water stagnation in the detection zone is based on the work by D'sa et al., (1997) [337]. This method used V-groove geometry with a 30-degree pitch to reduce ambient light while allowing flow through. The design by D'sa et al., can be seen in Figure 3-10.

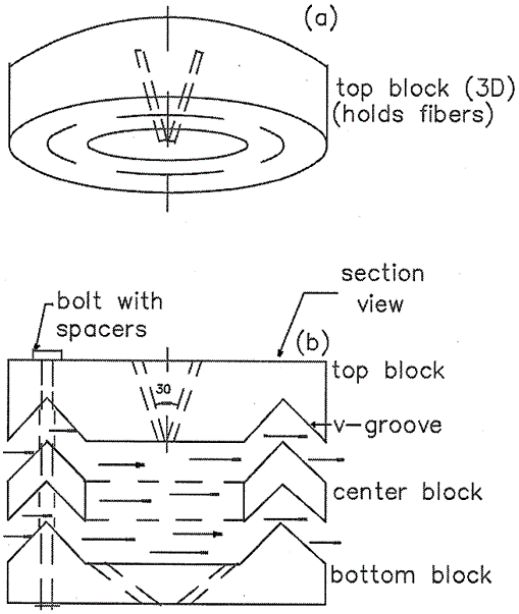

Figure 3-10 Ambient light reduction design by D'sa et al. [337] using 30 degree V-grooves in a cylinder surround the area of detection.

The design of the external sensor guard can be seen in Figure 3-11. Figure 3-11a shows a labelled drawing with dimensions of the guard design and how it mounts to the sensor body. The guard is made in two sections: the guard and the grating cap. Both are FDM 3D printed from PETG. The grating cap is joined to the guard via four 30 mm countersunk stainless-steel bolts which bolt into threaded brass inserts inserted into the base of the guard structure. The guard is bolted to a clamp which joins it to the main sensor body. A 100 mm two-part clamp made from 6061-T6 Aluminum; Type II Anodized material was used which was sourced from Blue Robotics Inc. A total of eight flow channels are included in the guard to allow for horizontal flow across the optical head. The grating cap consists of ten 45-degree V-grooves spaced at 5 mm intervals which were to block the ambient light from beneath but allow vertical flow to the optical head.

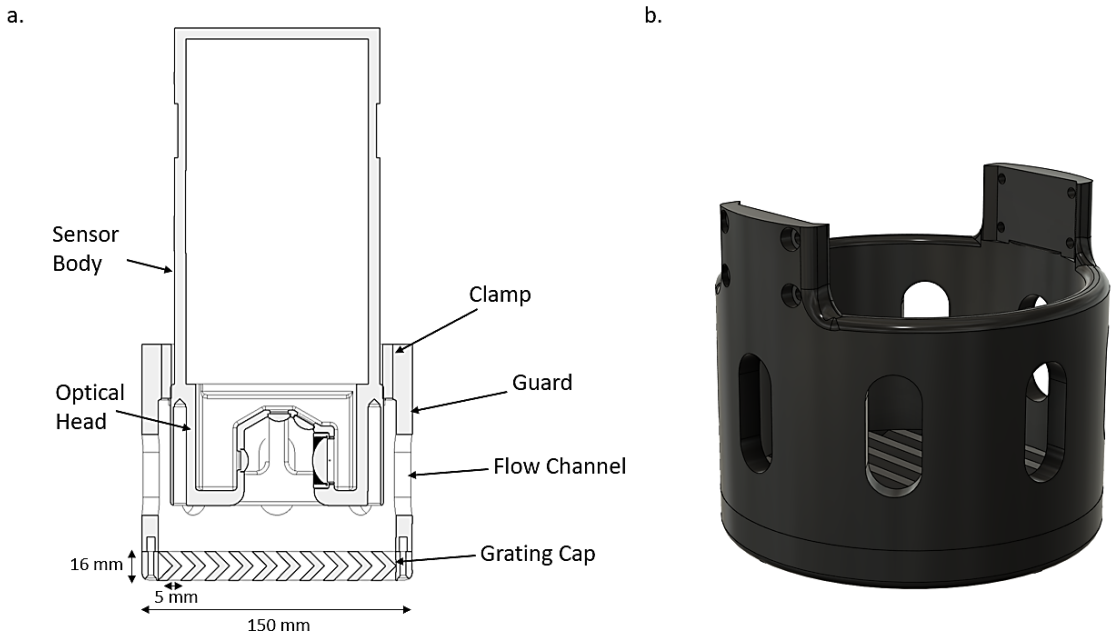

Figure 3-11 External sensor guard design. (a) Labelled diagram of external sensor guard design using 45-degree V grooves (b) 3D CAD model rendering of the sensor guard design.

A second, internal sensor guard, design is shown in Figure 3-12. This design was made to ensure no ambient light effected the fluorescence measurements. Figure 3-12a shows the use of two side walls using a 45-degree groove spaced at 1.7 mm and a 45-degree slant on the bottom section spaced at 3.5 mm. Four holes in the guard design correspond with holes on the optical head which allow the guard to be bolted directly to the optical head. Figure 3-12b and c show the positioning of the guard mounted to the optical head.

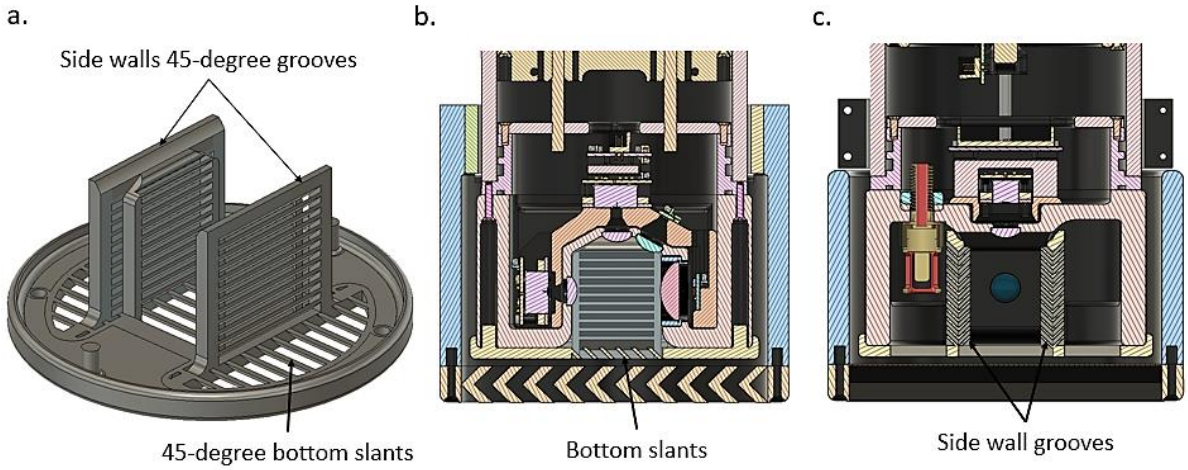

Figure 3-12 Internal sensor guard design (a) Internal guard diagram showing 45 degree side wall grooves spaced 1.7 mm and 45 degree bottom slants spaced 3.5 mm (b) Section side view of internal and external guard fitted to sensor (c) Section front view of internal and external guards fitted to sensor.

3.2.3.1 Testing of Ambient Light Reduction Designs

Tests were carried out both in the lab and in the field to test the effectiveness of the two guard designs and identify what the ideal design and combination of guards would be. The in-lab tests were conducted using a transparent acrylic water tank which allowed the sensor to be fully submerged (see Figure 3-13). The water tank was portable, and the tests were conducted outside to allow for full ambient light conditions to be tested. The datalogger developed (see Section 5.2.2) interfaced with the sensor unit to take readings from the sensor, provide power and store the data for analysis during the tests. A background scan (without the LEDs turning on) using the highest integration time used (4s) in the measurement cycle were taken to measurement the ambient light in the optical detection zone. The combinations of the external guard design and the internal guard attached to the sensor were explored with three scans being made 1) with only the external guard attached 2) with only the internal guard attached and 3) with both the internal guard and the external guard attached to the sensor.

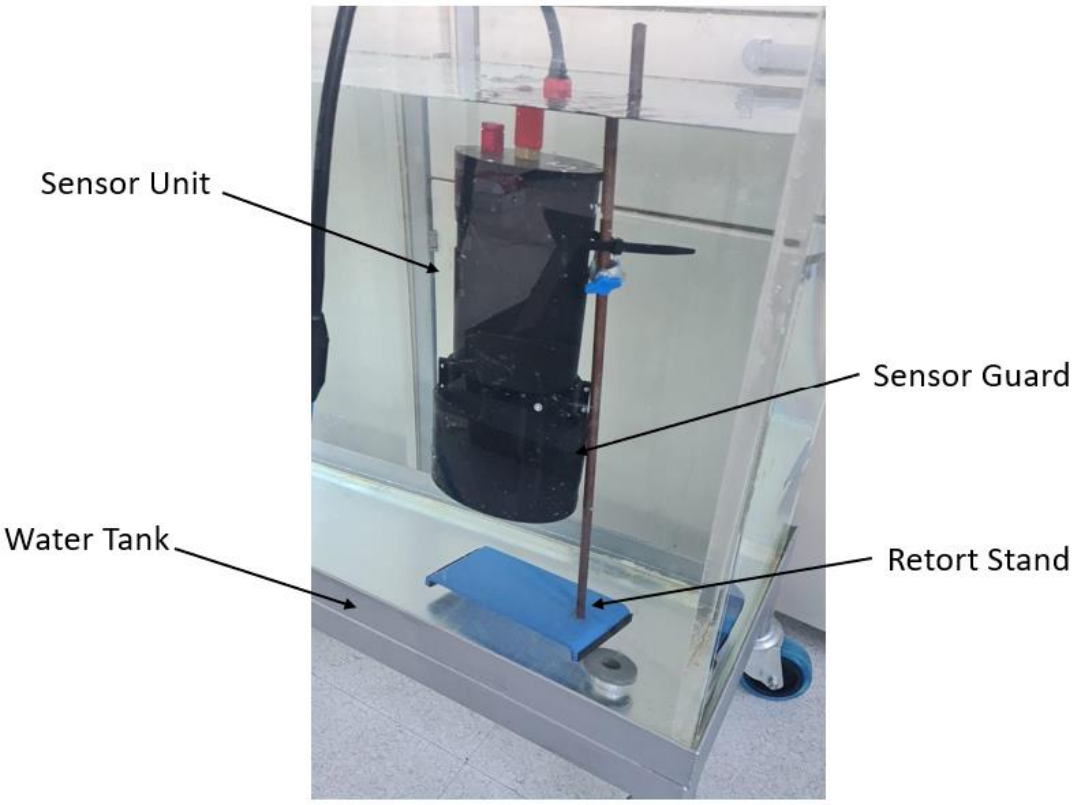

Figure 3-13 Test setup for in lab ambient light block experiment with sun guards on sensor submerged in acrylic water tank.

An environmental experiment was conducted in seawater conditions in Poolbeg Marine Yacht Club, Ringsend, Co. Dublin. The setup consisted of two sensor units (A and B), one with both the internal and external guards attached (A) and the other with only the internal guard (B). An additional commercial sensor (YSI optical sensor) was also deployed to observe the turbidity of the water at the time of testing. Figure 3-14 shows the three sensors attached to a deployment cage which was positioned at a depth of 1m off the side of the marina. This setup allowed for the effectiveness of the addition of the internal guard at reducing ambient light in seawater to be tested. A comparison was made between sensor units A and B in measuring the ambient light at a 4 s integration time.

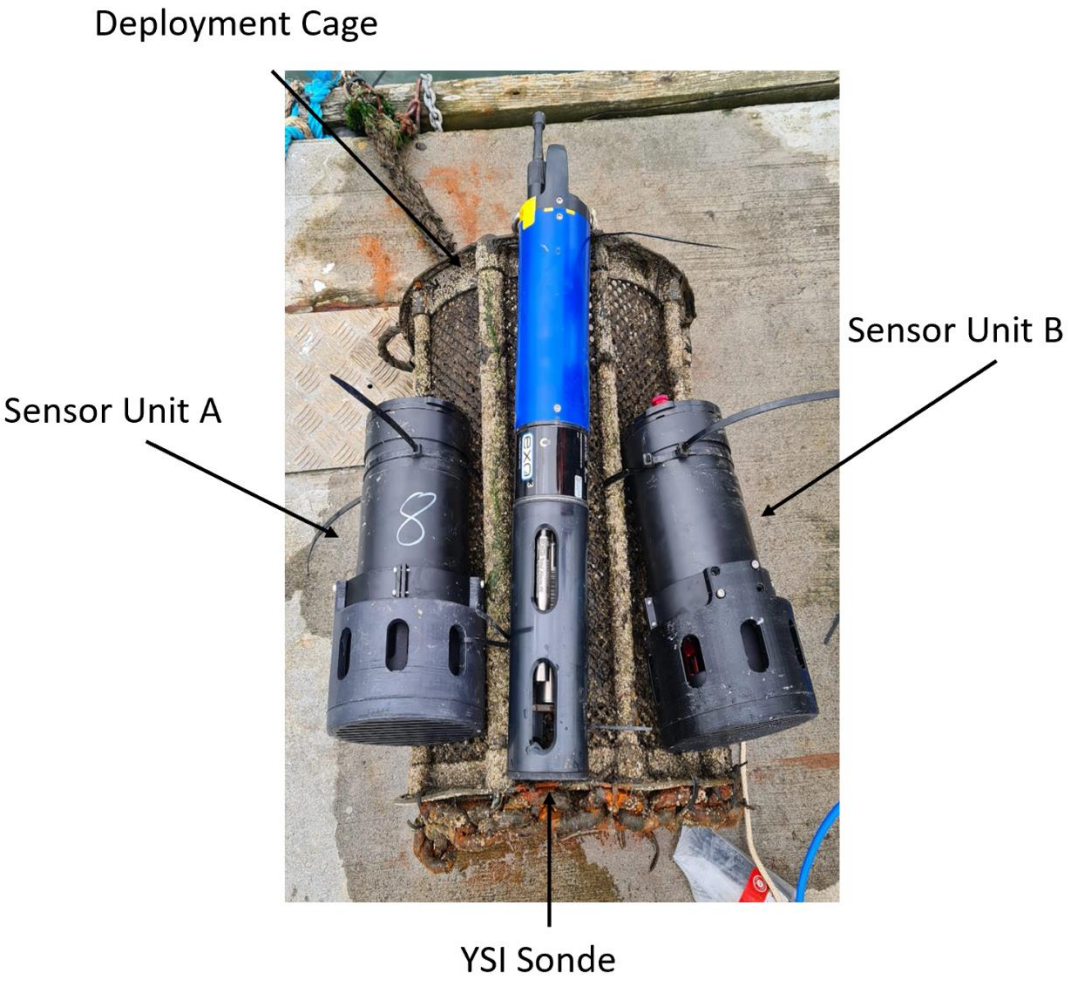

Figure 3-14 Poolbeg Marina guard performance seawater test in situ with two sensors and commercial YSI sensor. Sensor Unit A has both the internal and external guard attached while Sensor Unit B only has the external guard attached.

3.2.4 Testing of Materials and Fouling Prevention Strategies

3.2.4.1 Potential Marinisation Materials for use in the Marine Environment Evaluation

A 12-month study was conducted on the performance of select materials in the marine environment. The purpose of the study was to assess the suitability of the materials for the application of marinisation design for incorporation into the sensor unit design. Table 3-2 outlines the selected materials and their marinisation application. The study was conducted between March 2020 and March 2021. The site location for this study was Poolbeg Marine Yacht Club, Ringsend, Co. Dublin. The site was selected due to it being a dynamic water body location with anthropogenic activity, tidal flush, and freshwater inflow. This study was carried out with the assistance of Mr Adrian Delgado and Dr Chloe Richards, who helped with deployment and took monthly photographs of the material samples.

Table 3-2 Materials, paints and coatings tested for use in sensor design.

Material	Application
Copper	Commonly used my commercial sensors to reduce fouling build up.
Composite	Fibre-glass composite for construction of sensor components.
POM-H	Homo-polymer of POM used for the construction of sensor enclosures.
POM-C	Co-polymer of POM used for the construction of sensor enclosures.
Antifouling Paints	Coatings for reducing biofouling build up on surfaces.
Stainless Steel 316	Marine grade steel used in the construction of marine equipment and sensor enclosures.

Figure 3-15 shows the design of the materials sample holder. Three acrylic panels (240 x 550 mm) were joined by 3D printed brackets using Acrylonitrile Butadiene Styrene (ABS) filament on the Lulzbot Taz 6 printer. The brackets positioned the panels at 120^{o} relative to each other forming the prism structure. On these acrylic sheets material samples were mounted. The sample size was selected to be 100 x 100 mm. Each sample material was tested in triplicate, a sample mounted to each of the three panels in a different position for each panel. The prism structure was placed inside a marine suitable cage to protect the material samples from damage during deployment (Figure 3-15c and d). The key performance indicators (KPIs) for the materials were that 1.) the effect degradation process due to exposure to the marine environment had on the material (see Table 1-4 Chemical

Challenges) and 2.) the rate of biofouling occurring on the material surface (see Table 1-4 Fouling Challenges).

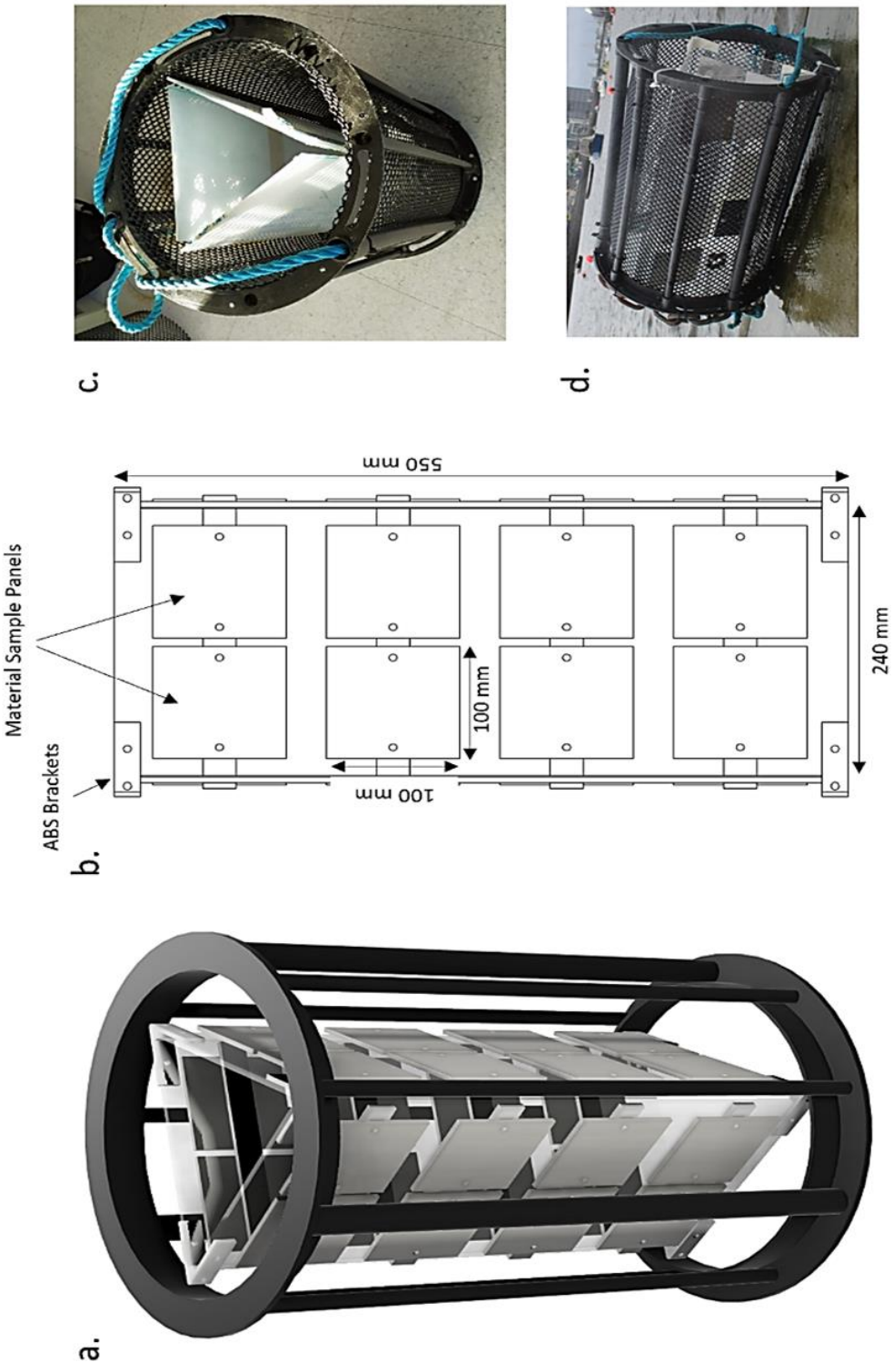

Figure 3-15 Material anti-fouling deployment cage design (a) CAD render view of the prism structure mounted in the deployment cage. (b) labelled diagram of material mounting panel with dimensions. (c) Prism structure inserted into the deployment cage. (d) Deployment cage fitted with the sample materials before deployment.

Following on from the study on materials performance in the marine environment, in field tests were conducted on the sensor in the marine environment. Two sensor prototypes were deployed in Dun Laoghaire harbour, Dublin, Ireland for a total of three week in September 2021 to allow for the sensors' mechanical and fouling performance to be assessed. The sensor performed an anti-fouling cycle using the UV LEDs for 1 minute every 15 min. The KPIs for the sensors during this deployment were:

1. Maintaining mechanical robustness and watertightness as identified in the literature tabulated in Table 1-4 in the mechanical challenges section.

2. Effect of degradation processes as described in Table 1-4 in the chemical challenges section.

3. Prevention of build-up of biological build up on sensor surfaces and optical lenses as described in Table 1-4 in the fouling challenges section.

3.2.4.2 Fouling Prevention Strategies Implemented on Sensor Units

Figure 3-16 shows the external guard and grating cap coated in an antifouling paint. Given the large surface area of the component and the requirement to keep the inlets clear to allow sufficient flow into the optical head, it was deemed necessary to apply additional fouling prevention steps. The antifouling paint which was used was International Trilux 33 which contains Biolux® and copper thiocyanate as fouling prevention biocides. Two coats of the paint were applied with 24 hr dry time between.

Figure 3-16 Sensor outer guard painted with a copper based anti-fouling paint International Trilux 33 to prevent biological growth.

Copper tape is applied to the outside surfaces of the sensor body (see Figure 3-2a). The copper tape used was by 3M with 50 mm width and 0.04 mm foil thickness (component number: T118150) sourced from Radionics Ltd. A layer of duct tape was applied first to the surface of the sensor body before applying the copper tape to provide additional adhesion.

UV light was selected as the fouling prevention method to reduce biological build up forming on the optical lenses in the optical head. The implementation of UV 280 nm peak wavelength LEDs behind each optical lens was described in Section 2.3.2. Figure 3-17 shows the LEDs illuminated on the PCBs. Figure 3-17a shows the two LEDs which are positioned behind the 0- and 90-degree lenses and Figure 3-17b shows the LEDs positioned behind the 120-degree lens. The 280 nm and 310 nm LEDs on the LED array (see Table 2-1) are used for prevention of fouling behind the collimation lens. The UV LEDs are operated at a PWM duty cycle of 75% and an active cycle of on 1 min every 15 min.

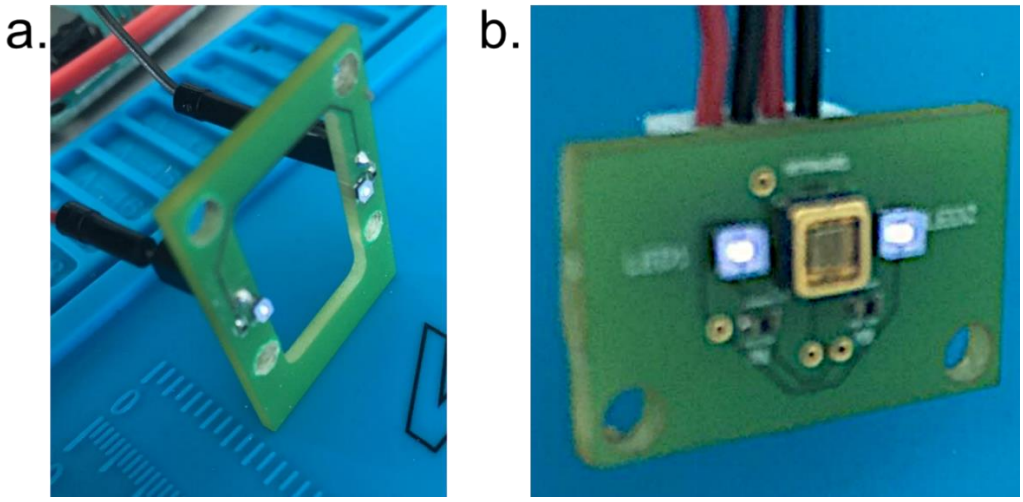

Figure 3-17 280 nm UV LEDs turned on positioned behind the optical lenses of the sensor head for prevention of biological growth on the lens surface exposed to the marine environment (a) the circuit board for the mini-spectrometer lenses (b) the photodiode board with LEDs positioned either side to side behind the lens.

3.2.4.3 Electronics Moisture Damage Prevention

A layer of silicon was applied to the PCBs to provide protection from moisture damage. A conformal silicon spray sourced from Radionics Ltd was used. Two coatings of conformal spray were applied to both sides of the circuit boards with curing time of 24 hrs between coatings. Any electrical contact points were covered with masking tape to avoid impeding connection when connectors to the board are attached.

3.2.5 Sensor Performance Evaluation Experiments

A lab-based study of each mode (transmittance, scatter, and fluorescence) was used to determine the effectiveness of the sensor unit developed in this chapter at measuring marine-based parameters. Turbidity, chlorophyll, dissolved organic matter (DOM) and petroleum were the selected target analytes to demonstrate the sensors measurement capabilities. Lab standards were used as proxies for certain analytes while lab grown diatomic algae were used for the measurement of chlorophyll. An experiment was also conducted to measure fluorescence of algae using a commercial sensor (Hydrocat) to benchmark the performance of the sensor unit by comparing the two sensor's response. The experiments were conducting with the assistance of Dr Louis Free and Mr Adrian Delgado. Throughout the description of the experiments and the results a reference system is used for the LEDs (Table 3-3) on the LED array which were selected in Table 2-8.

Table 3-3 Table of LED reference name and spectral characteristics

LED Reference	**Peak Wavelength Emission (nm)**	**LED Details from** Table 2-8
LED 1	850	Row 9
LED 2	660	Row 8
LED 3	565	Row 7
LED 4	430	Row 6
LED 5	385	Row 5
LED 6	365	Row 4
LED 7	310	Row 3
LED 8	280	Row 2

3.2.5.1 Method for Selecting Suitable Spectrometer Integration Times

The sensitivity of each spectrometer is determined by the set integration time, these values are changed based on the mode of measurement. The three modes used during a measurement scan by the sensor are 1) absorption, 2) scatter and 3) fluorescence. Each required a set series of integration times which the microcontroller configures for each LED in the measurement scan as described in Section 2.2.3 on firmware development. The criteria for selection of integration times for the LEDs for each mode are described below.

Transmittance and Absorption Measurements

Transmittance and absorption results in the lowering of signal as light from the LED is scattered and absorbed by suspended particles in the water. Therefore, the LEDs was configured so be as intense as possible, expecting signals to decrease. Using deionised water, the integration time was adjusted for each LED until the maximum signal is near saturation.

Side Scatter Measurements

The scatter signal is caused by light being scattered by suspended particles in the water. It was expected that the signal will increase up to a certain point as more suspended particles are added to deionised water. Therefore, the integration time was set such that the LED signal is as low as possible with the anticipation that the signal will increase.

Fluorescence Measurements

The fluorescence signal is caused by the absorption of photons and reemission of a photon at a different wavelength, typically longer. Fluorescence signals are typically much less intense that the LED signal, however, can be resolved by using the spectrometer. To configure the fluorescence signal, a solution of the sample with the highest estimated concentration was added to deionised water and the integration times for each LED was adjusted so that the fluorescence signal detected was near saturation. It was noted that it is acceptable if the LED signal saturates if the fluorescence signal can be detected.

3.2.5.2 Turbidity

For the optical measurement of scatter the spectrometer positioned at 90-degrees was used. A volume of 500 mL of deionised water was added to the measurement vessel. Solutions were made of increasing NTU levels using turbidity standards of Reagent CRS-4000 and Reagent CRS-800-100. A total of five turbidity solutions were made with turbidity ranging from 0 – 60 NTU. Spectrums from LEDs 1-6 were recorded at each turbidity concentration three times and the signals were averaged.

3.2.5.3 Quinine Sulfate

Initially to test the optical heads capabilities and potential to measure fluorescence, a quinine sulfate (QS) experiment was conducted. QS was selected due to its close fluorescence output similarity to fluorescence dissolved organic matter (fDOM) [325] and was therefore used as

a proxy. A stock solution of quinine sulfate was prepared using 0.6 mL of H^2SO^4 and mixing it with 200 mL of deionized water. 100 mL of this solution was then taken and mixed with 0.010481 g of quinine sulfate dihydrate to give a stock solution of 100 mg/L. Small amounts of this stock solution were then added to six 500 mL bottles of deionized water for a total of six solution ranging in concentrations from 2 – 620 μg/L.A fluorescence measurement was made using LEDs 4-8 at each concentration using the highest concentration. A calibration curve was then created by taking the peak of the fluorescence.

3.2.5.4 **Petroleum Compounds**

A polycyclic aromatic hydrocarbon naphthalene disulphuric acid (NDSA) was selected as a fluorescence standard for petroleum compounds. A 100 mg/L stock solution of NDSA was prepared in an acidic H_2SO_4 solution. A series of standard solutions in the range of 0 – 0.2 mg/L were prepared from the 100 mg/L stock solution. Each standard solution was run on the sensor, with a background scan performed at 0 mg/L. LED 7 was used to induce fluorescence and fluorescence emission was read at 350 nm.

3.2.5.5 **Chlorophyll A**

To test the sensors fluorescence response to Chl-a lab grown algae were used and the Chl.A extracted (grown and extracted by Mr Adrian Delgado). The extraction process is described in Section 2.2.6.3. A total of six concentrations were tested with a range of 0 μg/L. to 20 μg/L. LEDs 4-7 were selected to induce a fluorescence response with the fluorescence emission measured at 675 nm. A validation study was carried out on the optical head using a HydroCat, a commercially available marine based optical sensor using lab grown algae. The validation study compared the fluorescence signal recorded by the HydroCat with that recorded by the optical head using lab grown algae, with concentrations ranging from 0 – 35 μg/L. Unlike in the previous Chl-a study it was not possible to use the measurement vessel as both the optical head and HydroCat could not fit within it and as such a larger vessel was required to hold both the optical head and HydroCat. Two litres of water were added to the vessel containing the two sensors and algae was added to the water. Due to the large volume of water used in this experiment, large volumes of algae were needed, so the concentrations used were between 0 – 35 μg/L. At each concentration of algae added, a recording using the optical head and HydroCat were made concurrently. To compare the optical head signal with that of the HydroCat, the peak of the fluorescence signal at 680 nm

for LEDs 5 and 6 was plotted as a function of algae concentration and the equation of the line was calculated. The raw signal was then divided by the slope of the line, allowing raw data to be converted to quantitative, and was plotted alongside the HydroCat data.

3.3 Results and Discussion

3.3.1 Fabrication and Assembly of Sensor Prototype

The sensor unit development underwent an iterative design process involving a cycle of design and prototyping phases with multiple units being developed, testing, and redesigned over a period. Figure 3-18 shows the key design and prototyping stages in the sensor development process over a period starting with the initial concept CAD model render and showing physical prototype, redesigns, and final prototype design. With each iteration the design of the sensor was improved and optimised showing the method to be suitable approach for in situ sensor development [289,290].

Figure 3-18 Iterative sensor design progression from first concept CAD model design made in August 2020 to the final sensor prototype version in May 2022.

Key improvements made over the iterative design process to the sensor were:

1. Improved manufacturing approaches were applied to certain components. The optical head fabrication method was changes from FDM 3D printing and epoxy coating (see Figure 3-20) to SLS printing with infiltration waterproofing (see Figure 3-19).

2. Design changes to reduce assembly time and component count. The spacers used for the electronics mounting tray (Figure 3-5a), spectrometer stacked boards (Figure 3-6) and internal frame (Figure 3-9) were 3D printed instead of using off the shelf spacers. These changes reduced the need for additional components and simplified the overall design. The custom design of the components allowed for the exact dimensions required instead of relying of commercially available spacing components.

3. Enhanced optical detection performance. The issue of ambient light affecting the fluorescence measurements was identified through testing and a solution was found in the addition physical light blockers shown in Design Version 4.1 in Figure 3-18. The results of the effect of the sun guard designs are given in Section 3.3.2.

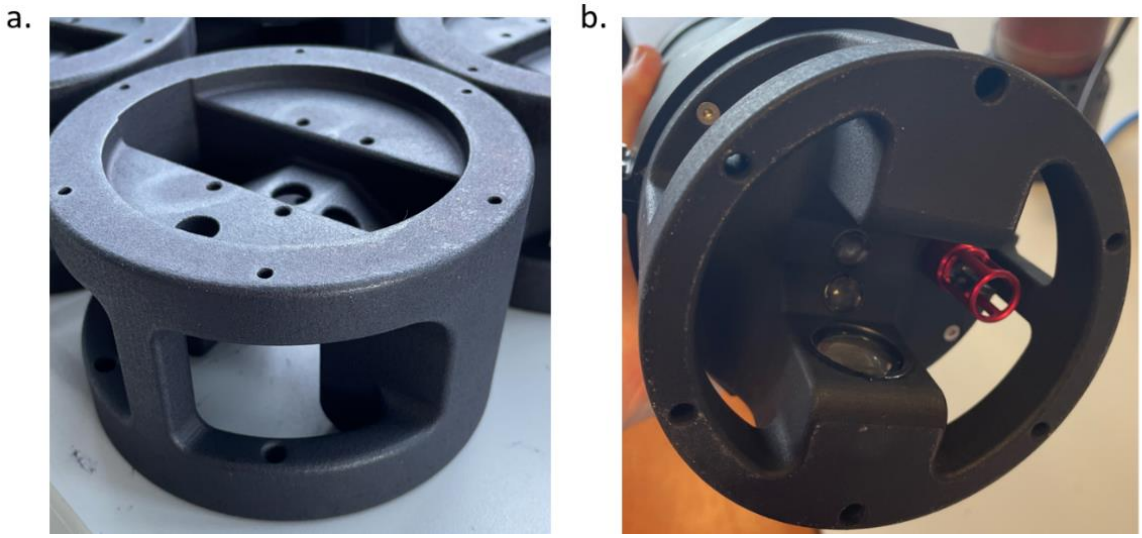

Figure 3-19 (a) SLS 3D printed nylon PA2200 optical head dyed black and infiltration water proofing post processing. (b) Assembled SLS printed optical head with lenses and probe installed.

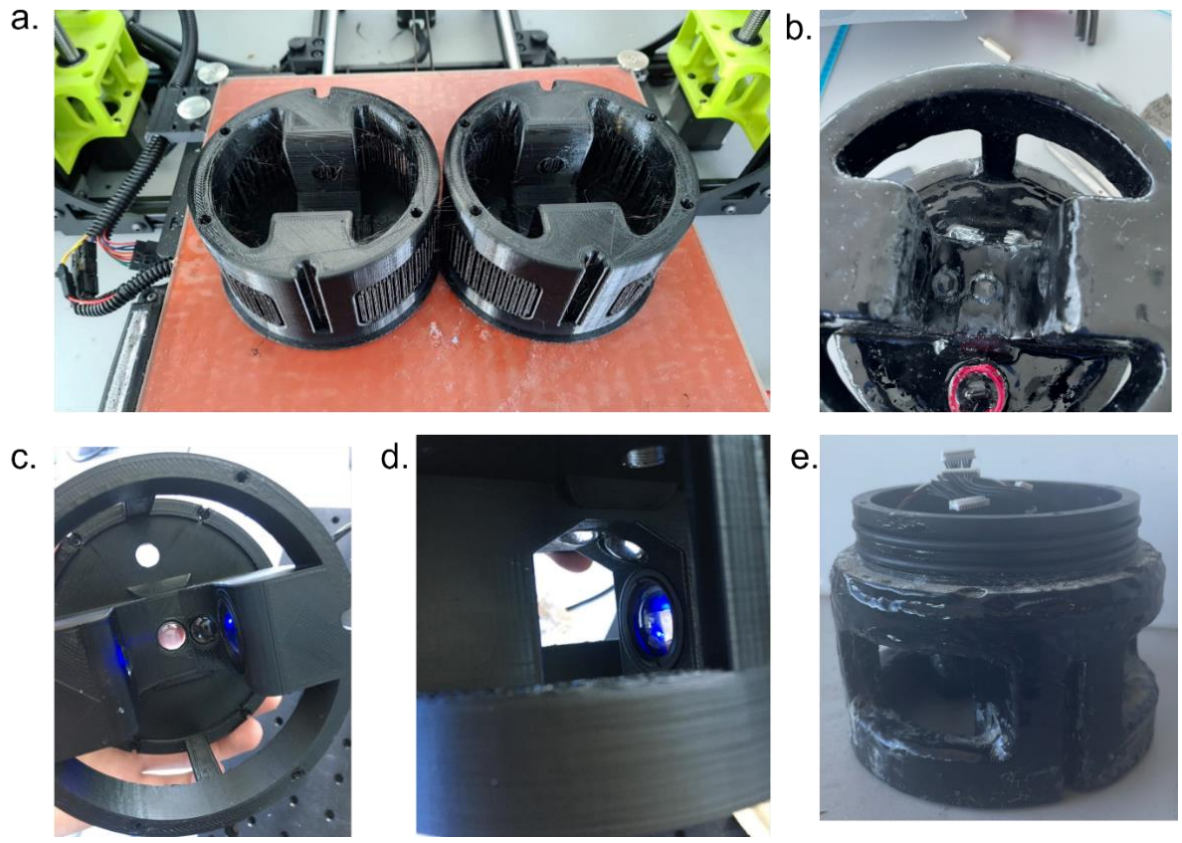

Figure 3-20 FDM 3D printed optical heads (a) two optical heads printed in Lulzbot Taz 6 using PETG filament (b) epoxy coating on outer surface to waterproof 3D print (c) underside view of optical head with lenses fitted (d) side view of optical head with lenses fitted (e) optical head with epoxy coating.

3.3.2 Ambient Light Block Performance

The raw data from the lab testing of the sensor guards can be seen in Figure 3-21 with the three background scans with 4 second integration time overlayed. From the figure it can been seen that the combination of both the internal and the external guard has a significant effect on reducing the ambient light with the individual guards on their own both showing high amounts of saturation of the detector. The dark current effect is removed from the scan be subtracting the average dark signal of the spectrometer (7762) to zero the scans.

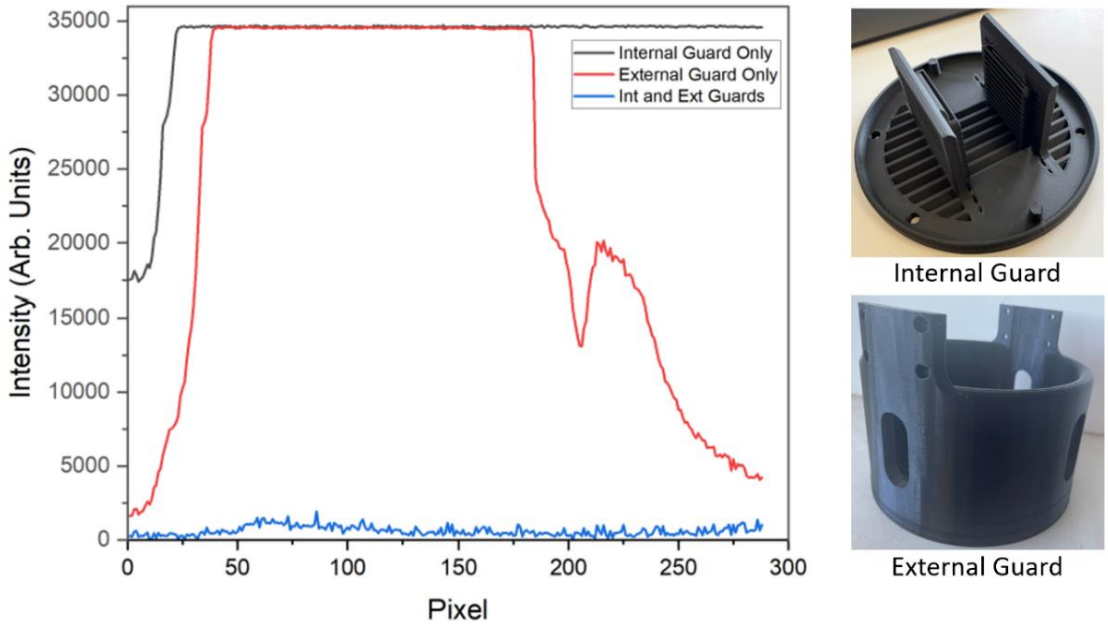

Figure 3-21 Ambient light reduction comparison between the guard combination in sunny conditions. Background scan of ambient light conditions was made using a 4 s integration time of the fluorescence spectrometer in a transparent acrylic tank placed outside of the lab. Scans were taken with the internal and external guard on their own as well both combined. The combination of both guards shows the most significant reduction in ambient light.

The results of the in-field tests conducted off the marine of Poolbeg Yacht Club can be seen in Figure 3-22. Sensor B was only fitted with the external guard while Sensor A was fitted with both the external guard and the internal guard. It can be observed from the two scans overlayed that the combination of the two guards on Sensor A was much more effective at reducing the ambient light while the sensor was deployed in the sea water conditions. This reaffirms the findings from the experiment conducted in the tank in sunny conditions. The combination of an external and internal sensor guard designs provides sufficient ambient light reduction for fluorescence measurements to be conducted as baseline background conditions. The elimination of ambient light will provide greater limits of detection for the optical measurements in the open environment.

Figure 3-23 shows the turbidity values take by the YSI sonde during the deployment. The turbidity value remains around 1 FNU with only a few outliers showing an average to low turbidity level when compared to a previous study of turbidity in the same location Briciu et al. which presents average turbidity of 5.38 NTU [16]. This indicates that high turbidity did not affect the reading by reducing the ambient light significantly at a depth of 1 meter.

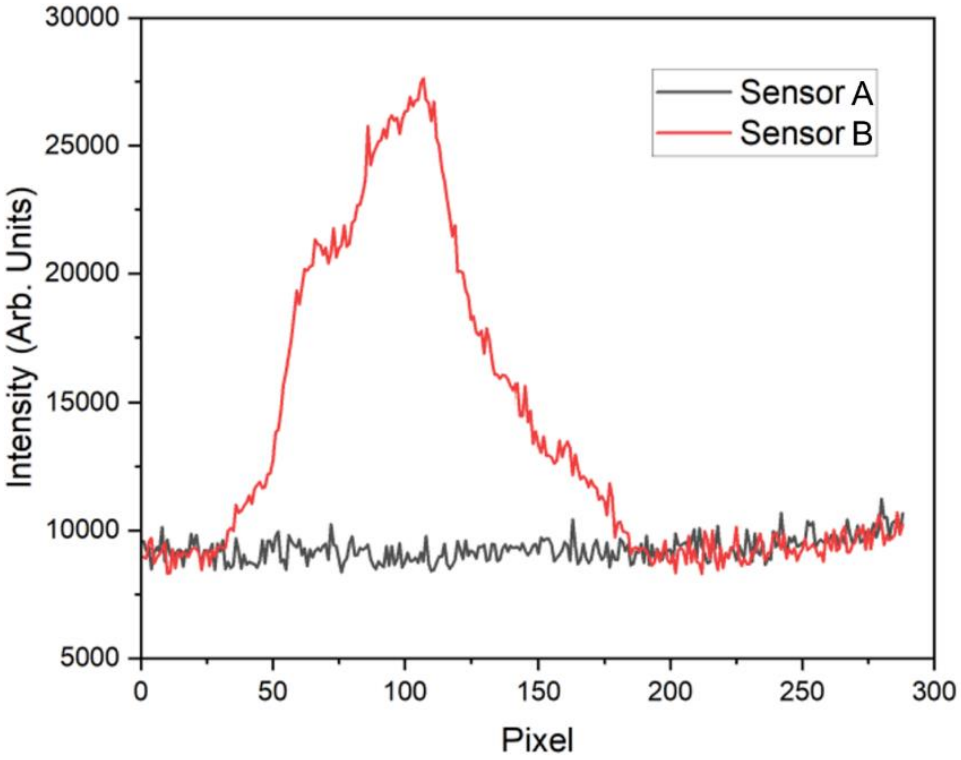

Figure 3-22 Background scan with LEDs turning on taken for comparison between sensors positioned at 1 meter depth in Poolbeg Marina, Co. Dublin. Sensor A has both the internal and external guard attached. Sensor B had only the external guard attached. An integration time of 4 s was used with the fluorescence spectrometer at 90-degrees to the light source. Sensor A shows little ambient light detected while Sensor B shows significant ambient light.

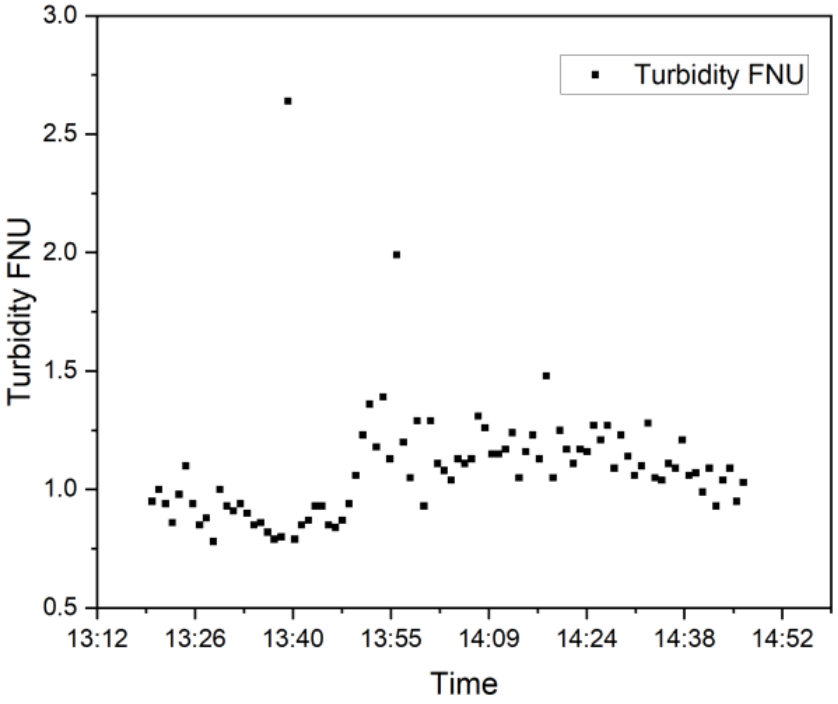

Figure 3-23 Turbidity readings taken by YSI Sonde during the testing of the sensor guards in Poolbeg Marina, Co Dublin showing an average turbidity reading of 1 FNU.

3.3.3 Material and Anti-fouling Performance.

3.3.3.1 Material Anti-Fouling Study in Dublin Port.

Figure 3-24 shows the materials deployment after a 12-month period. The material samples can be seen in Figure 3-24a. Copper and the antifouling paints performed the best with very little macro fouling coverage visible. This is in line with the literature on copper-based materials providing high levels of fouling prevention as well as commercial antifouling paints [274,280]. The composite, polymer and steel panels all have high percentage coverage. This coverage shows additional fouling prevention methods are required in conjunction with the use of these materials if the application is for prolonged exposure to the marine environment.

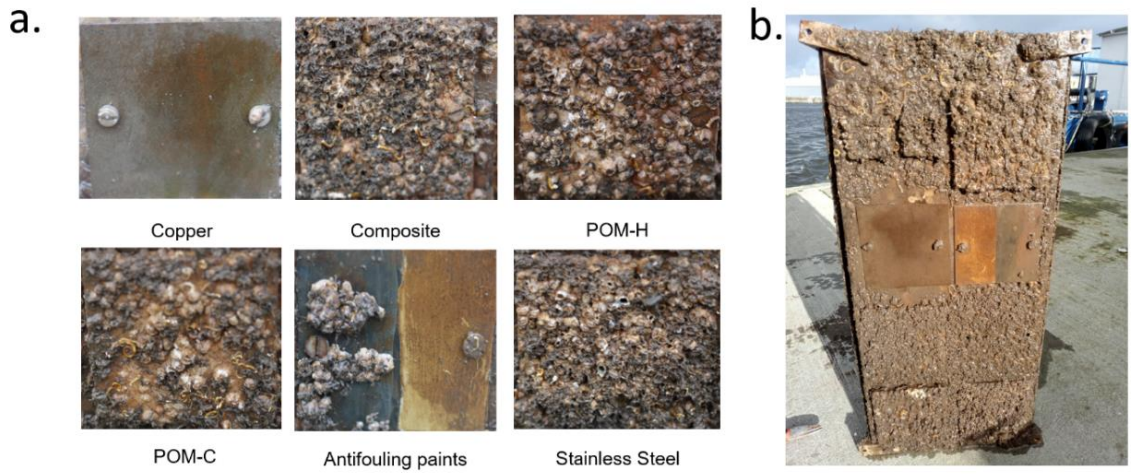

Figure 3-24 Material deployment after 12-month period (a) Sample materials (b) Panel and material samples mounted.

3.3.3.2 Deployment of Sensors in Marine Environment Robustness Performance

Figure 3-25 shows the images of one of the sensors directly after being retrieved from the 3-week long deployment. Applying the KPIs as outlined in Section 3.2.4.1.

1. No mechanical damage was observed on either sensor unit deployed showing a good degree of robustness for longer deployment durations.

2. It was found when opening the sensor bodies that they successfully remained watertight throughout the entire deployment.

3. Figure 3-25a and Figure 3-25e show white powder build up around the stainless-steel fasteners which attach the top cap to the body of the sensor. This could be due to salt build up or a galvanic corrosion acting on the stainless-steel components. Zhang et al 2018 [338] reports the use of a variety of metals and alloy materials used in the sample structure may lead to differences in potential which causes the galvanic corrosion to occur. The stainless-steel 316 fasteners attach the top cap to the 6061-T6 Aluminium flange. To avoid further corrosion, fasteners of the same aluminium allow may need to be incorporated into the design.

4. Figure 3-25c and Figure 3-25d show a build-up of organic matter or slime on the optical head which could be easily wiped off. Figure 3-25f shows the full body of the sensor revealing no build-up of any fouling materials on the areas covered in copper and the oxidation of the copper tape. Figure 3-25b shows a promising result of the optical lenses remaining clear and free of any biofouling build-up which would indicate that the UV LEDs were sufficient in the prevention of biofilms forming on the surface.

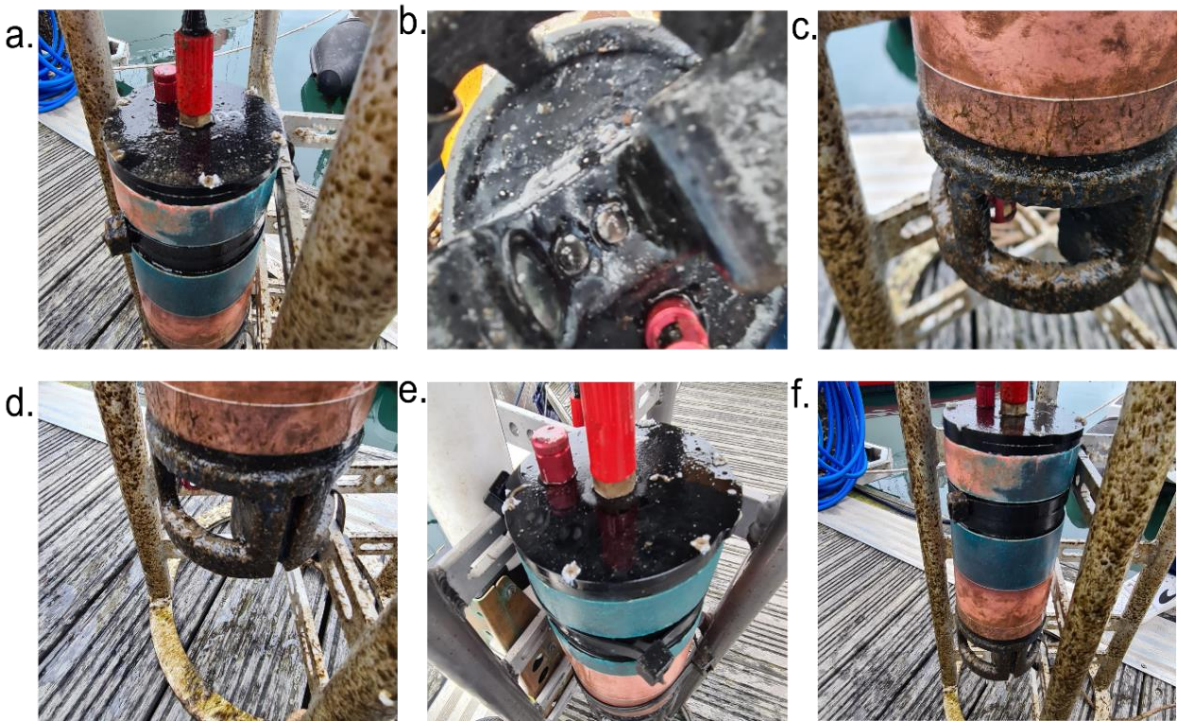

Figure 3-25 Sensor Unit post deployment in Dun Laoghaire, Dublin, Ireland over period of 3 weeks in September 2021 (a) view of top of sensor and marine cable (b) bottom view of the optical head and lenses (c) side view of sensor (d) secondary side view of sensor (e) closer view of top of sensor (f) view of full sensor body.

3.3.4 Sensor Measurement Performance

3.3.4.1 Determination of Suitable Spectrometer Integration Times

The application of the method described in Section 3.2.5.1 gives the results integration times shown in

Table 3-4. The integration times were set up to measure Chl-a fluorescence at a maximum concentration of 20 μg/L.

Table 3-4 Integration times used for each LED in each mode of operation.

LED	Absorption (ms)	Scatter (s)	Fluorescence (s)
LED 1	0.6	0.2	NA
LED 2	0.4	0.1	NA
LED 3	5	1	NA
LED 4	1.5	0.15	4
LED 5	0.02	0.002	2
LED 6	0.02	0.002	3
LED 7	NA	NA	4
LED 8	NA	NA	4

3.3.4.2 Turbidity

Figure 3-26a shows the spectrum of the 850 nm LED as recorded at each of the turbidity concentrations. Starting at 0 NTU, or deionized water, increasing the amount of the turbidity standard present in the sample caused the overall LED signal to increase at all wavelengths. This trend was observed in the spectra of all LEDs used with increasing turbidity.

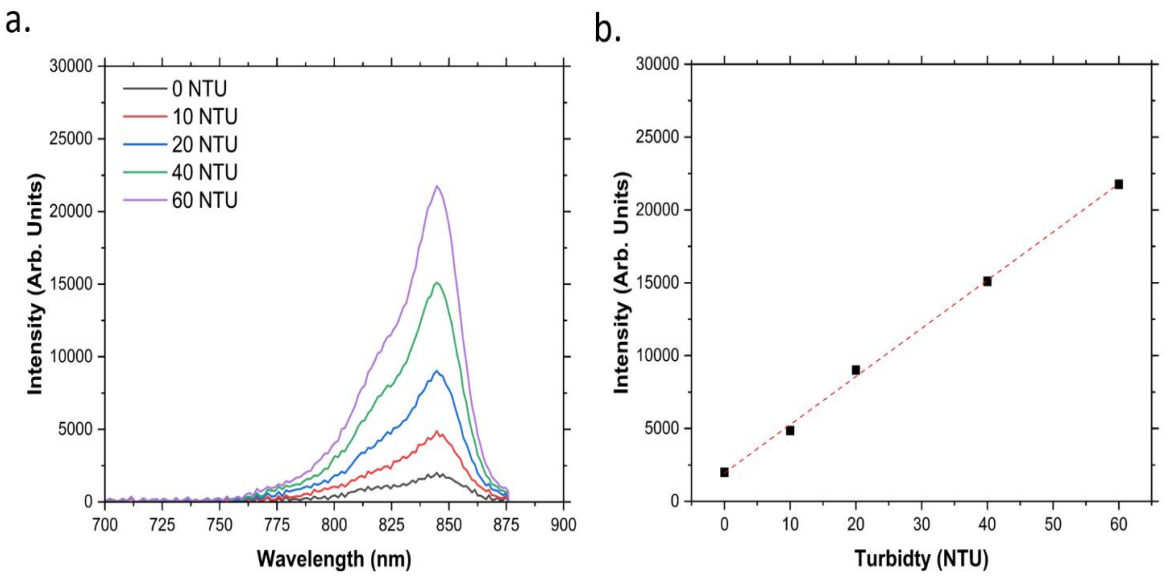

Figure 3-26 (a) Sensor response to increasing levels of NTU, (b) calibration curve generated by taking the peak of the LED signal at 850 nm at each of the NTU concentrations (n = 3). The linear fit, seen in dashed red, gives an equation a slope of 330.68, intercept of 1953.5 and an R^2 value of 0.99855.

Figure 3-26b shows the calibration curve generated by taking the peak of the 850 nm LED at each concentration. The graphs show a strong linear relationship between the intensity of the light measured and turbidity. The equation of the line y = mx + c, was calculated as 330.7 + 1953, with an R^2 value of 0.9986 indicated a strong linear relationship. The large y-intercept value is a result of the non-zero value of the 0 NTU concentration and the peak of the 0 NTU value and the y-intercept are the same at 1953 arb. units.

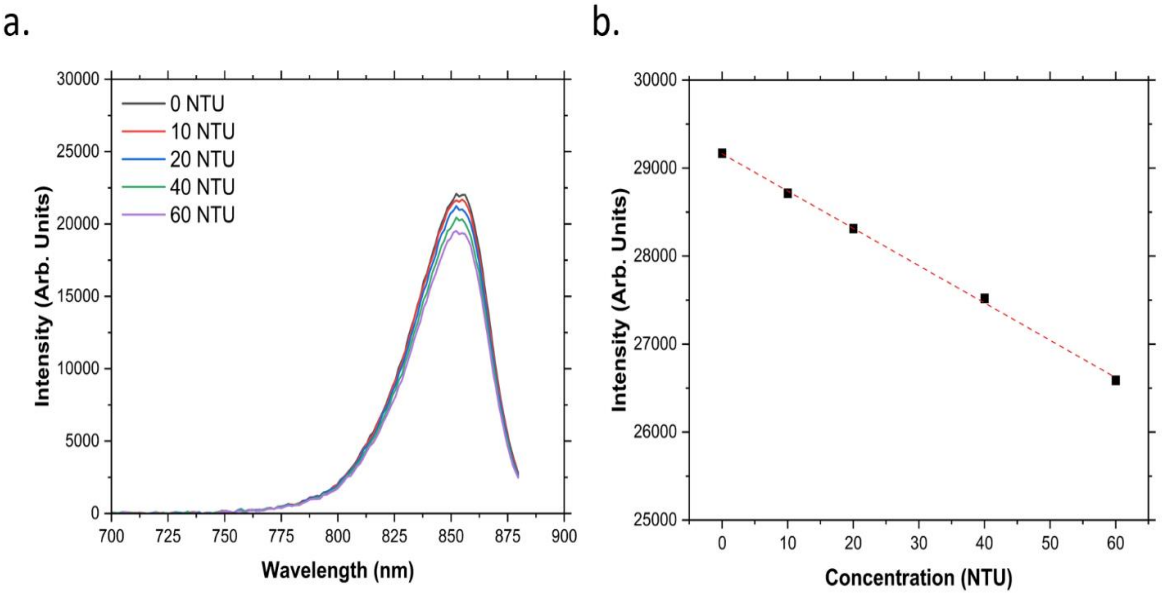

Figure 3-27 (a) Spectrum of the 850 nm LED as recorded at each turbidity concentration after transmitting through the sample. (b) Calibration curve created by taking the peak at 850 nm of each

of the spectra in (a) (n = 3). The linear fit seen in dashed red gives a slope of -42.39, intercept of 29163.4 and an R^2 value of 0.99893.

While not as pronounced as the scattered method, it was still possible to determine the influence of turbidity on transmitted photons as shown Figure 3-27a which shows the 850 nm LED spectrum as recorded at each turbidity concentration. Increasing the turbidity of the sample causes a slight decrease in the intensity of the signal and this affect is seen across all wavelengths measured. A corresponding linear fit was also determined for the transmitted measurements (Figure 3-27b) and was calculated to be -42.3964 + 29163, with the y-intercept having the same value as the 0 NTU measurement, and a corresponding R^2 value of 0.9989.

Although 850 nm is the wavelength specified for optical turbidity standards, photons of all wavelengths are scattered by the particles that are used to make the turbidity standard. As a result, it was possible to create a calibration curve for each LED in the optical head for both scattered and transmitted photons and the corresponding linear equation and R^2 squared values are shown in Table 3-5.

In the case of all LEDs in the optical head, there was a strong linear relationship between the intensity of the light signal detected and the concentration of the turbidity standards as shown by the R^2 values. LED 1, the IR LED, had the greatest linear relationship in both scatter and transmission measurement modes. The relative sensitivity of each LED to the turbidity standard could be determined by the slope of the equation. The general trend observed was that shorter wavelengths tended to be more sensitive to changes in turbidity as indicated by their greater slopes, with the IR 850 nm being the least sensitive wavelength tested. This might suggest that using a more sensitive wavelength may be a better choice for turbidity measurements However, as discussed in Section 1.4.3, IR wavelength ranges are stipulated by both ISO7027 [89] and EPS Method 180.1 [101] for use in determination of turbidity. It is important to understand the matrix effect of multiple species that may be present in a sample and the impact that these will have in the overall output of each LED. These may for example introduce non-linear effects due to absorption and fluorescence [88].

Table 3-5 Calculated linear equations and R^2 values for each LED for scattered and transmitted photons as result of turbidity standards.

LED	Scattered Equation	R^2 value	Transmitted Equation	R^2 value
LED 1	330.86 x + 1953.5	0.9985	-42.794 x +22112	0.9991
LED 2	574.22 x + 302.46	0.9949	-105. 4 x + 25553	0.9965
LED 3	566.47 x + 714.26	0.9964	-120.84 x + 20382	0.9944
LED 4	578.59 x + 639.98	0.9864	-222.7 x + 29002	0.9846
LED 5	605.47 x + 679.41	0.9945	-328.56 x + 25845	0.9667
LED 6	601.42 x + 325.52	0.9983	-326.3 x + 24189	0.9654

Using the LED 1 scatter slope as a sensitivity value gives 330.86 sensor units per NTU. This can be converted to a voltage sensitivity for comparison with other turbidity sensors. Firstly Equation 3-1 is used to calculate the voltage resolution of the MCU's ADC.

$$ADC\ Voltage\ \ Resolution = \frac{V_{max}}{ADC\ Resolution} \qquad 3\text{-}1$$

Where V_{max} is the maximum analog voltage the ADC can read at 3.3 V and ADC resolution is the set resolution of the ADC use which is 2^{16}. This results in an ADC voltage resolution of 50.4 µV. Using the slope from the calibration curve for scatter using LED 1 as Sensitivity, Equation 3-2 can be applied to give sensor resolution in NTU. The resolution in NTU calculated for turbidity is 0.000152 NTU.

$$Sensor\ Resolution\ = \frac{ADC\ Voltage\ Resolution}{Sensitivity} \qquad 3\text{-}2$$

EPS Method 180.1 requires a sensitivity of "a turbidity different of 0.02 NTU or less in waters having less than 1 unit". ISO 7027 specifies a measurement range between 0.05 NTU to 400 NTU. EPS Method 180.1 requires a device have a range of between 0-40 NTU. In the marine environment turbidity in the region of 10 NTU is considered low while a high turbidity level would be 100 NTU and above [339,340]. Table 3-6 gives a comparison between the sensor prototype developed and in situ commercial sensors available for the measurement of turbidity in resolution and measurement range.

Table 3-6 Comparison between sensor developed with other commercial turbidity measuring in situ sensors,

Sensor	Resolution (NTU)	Measurement Range (NTU)	Reference
Sensor developed	0.000152	0-60	-
HydroCAT-EP V2	0.06	0-3000	[341]
Aqua TROLL Turbidity Sensor	0.01	0-1000	[342]
YSI 6136 Turbidity Probe	0.1	0-1000	[343]

The sensor displays relatively good sensitivity within the 0-60 NTU range making it adequate for turbidity measurements in this environment. The range of commercial turbidity sensors is significantly greater with 1000 NTU a standard upper limit. However, as shown in the turbidity experiment conducted on the benchtop prototype in Section 2.3.5.2, the backscatter photodiode can provide additional range to the turbidity measurements of this sensor. Furthermore, the advantage of the spectrometer implemented in the sensor prototype is that the integration time can be dynamic. When greater range is required a lower integration time can be used to extend the side scatter's upper limit of detection, therefore increasing the range of detection. Further work is required to be able to implement this and have the sensor respond to changing environmental event dynamically to maintain greater sensitivity depending on the environmental conditions.

3.3.4.3 **Quinine Sulfate**

Quinine sulfate (QS) solution was selected to test the fluorescence measurement capabilities of the optical head due to it commonly being used as a known standard equivalent to DOM [109]. QS have an excitation range in the UV region between 280 nm and 400 nm and an emission peak wavelength at 480 nm [344]. As shown in Table 1-2, fDOM has correspondingly similar excitation and emission ranges, hence QS can be used as a suitable proxy for fDOM. Figure 3-28a displays an example of the fluorescence emission due to excitation from LEDs 4 to 8 overlaid. In the case of each LED, it was possible to measure the quinine sulfate fluorescence, which has an emission profile between 420 – 500 nm (FWHM) and maximum measured intensity at 465 nm. Although the maximum wavelength of LED 4 is 430 nm, the wavelength range of this LED is broad, and parts of its emission

spectrum were past 400 nm and as a result it did induce fluorescence in the quinine sulfate sample. However, there was a large amount of overlap between the LED spectrum and the fluorescence spectrum, so the LED was excluded from further fluorescence analysis. There was an overlap between the LED and fluorescence signals for LEDs 5 and 6, it was not however enough to interfere with calibration, and these were therefore included in the study. A calibration curve for quinine sulfate was created by taking the peak of the fluorescence signal at 465 nm and plotting it as a function of concentration and is shown in Figure 3-28(b). A strong linear relationship was found for each LED with R^2 values above 0.99 in all cases. The slopes of LEDs 5, 6, 7 were found to be of similar magnitude between 68 - 70, while LED 8 had a lower slope of 39, indicating that LEDs 5, 6 and 7 were more suited for this experiment.

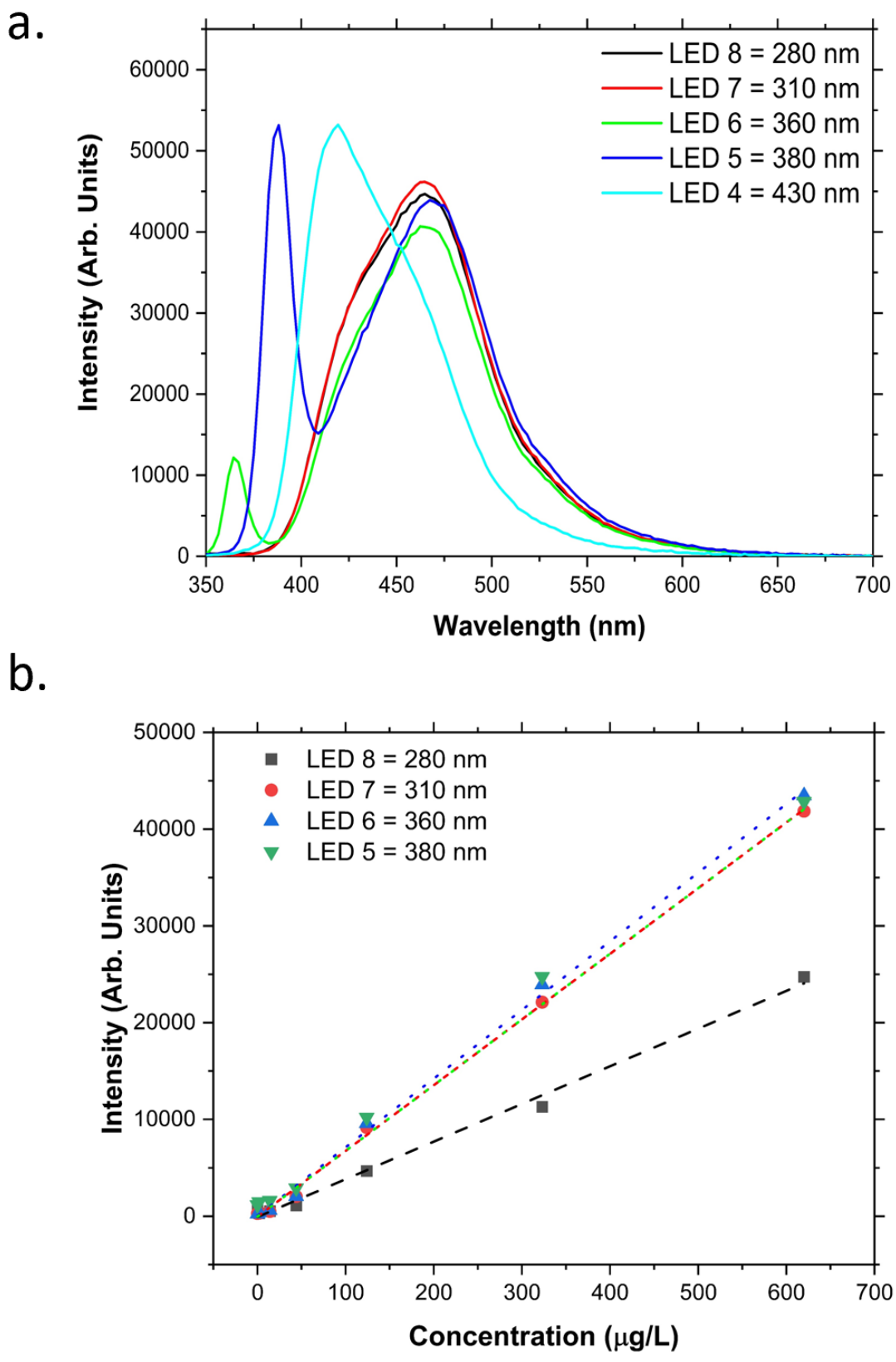

Figure 3-28 (a) Quinine sulfate fluorescence spectra as recorded by LEDs 4 – 8. (b) Calibration curves as a function of quinine sulfate concentration for LEDs 5 – 8. LED 4 was excluded due to its emission spectrum over-lapping with quinine sulfate fluorescence spectrum (n = 3).

A similar calibration curve was created for lower concentrations of quinine sulfate for LEDs 5 and 6 and is shown in Figure 3-29. At these lower concentrations, higher integration times were required to measure the fluorescence signal than in the previous wide concentration study. LED 5 was most sensitive to changes in concentration in this experiment with a slope of 1474.52 and LED 6 had a slope of 635.95. As such, this experiment identified LED 5 with peak emission wavelength of 380 nm as the most suitable LED to use for the detection of fDOM in the environment.

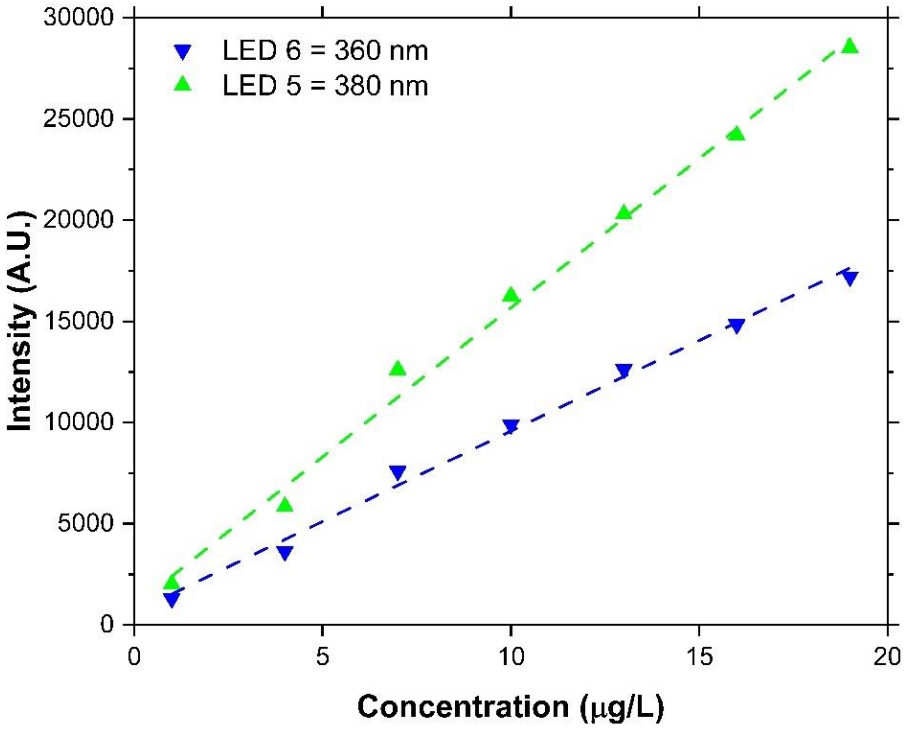

Figure 3-29 Calibration curve of quinine sulfate verses signal strength for excitation light sources LEDs 5 and 6 at low concentrations ranging from 0 – 20 μg/L (n = 3). Emission was measured at 450 nm on the C12880MA spectrometer positioned at 90 degrees to the light source.

3.3.4.4 **Petroleum Compounds**

NDSA, derived from naphthalene, was selected as a proxy fluorescence standard for the measurement of petroleum compounds. NDSA is more soluble in water and allowed for concentration-based fluorescence tests. As discussed in Section 1.3.3, naphthalene is a polycyclic aromatic hydrocarbon composed of two fused benzene rings allowing for fluorescence emission under UV excitation ranges. This allows it to be used as a proxy for oil and petroleum analytes.

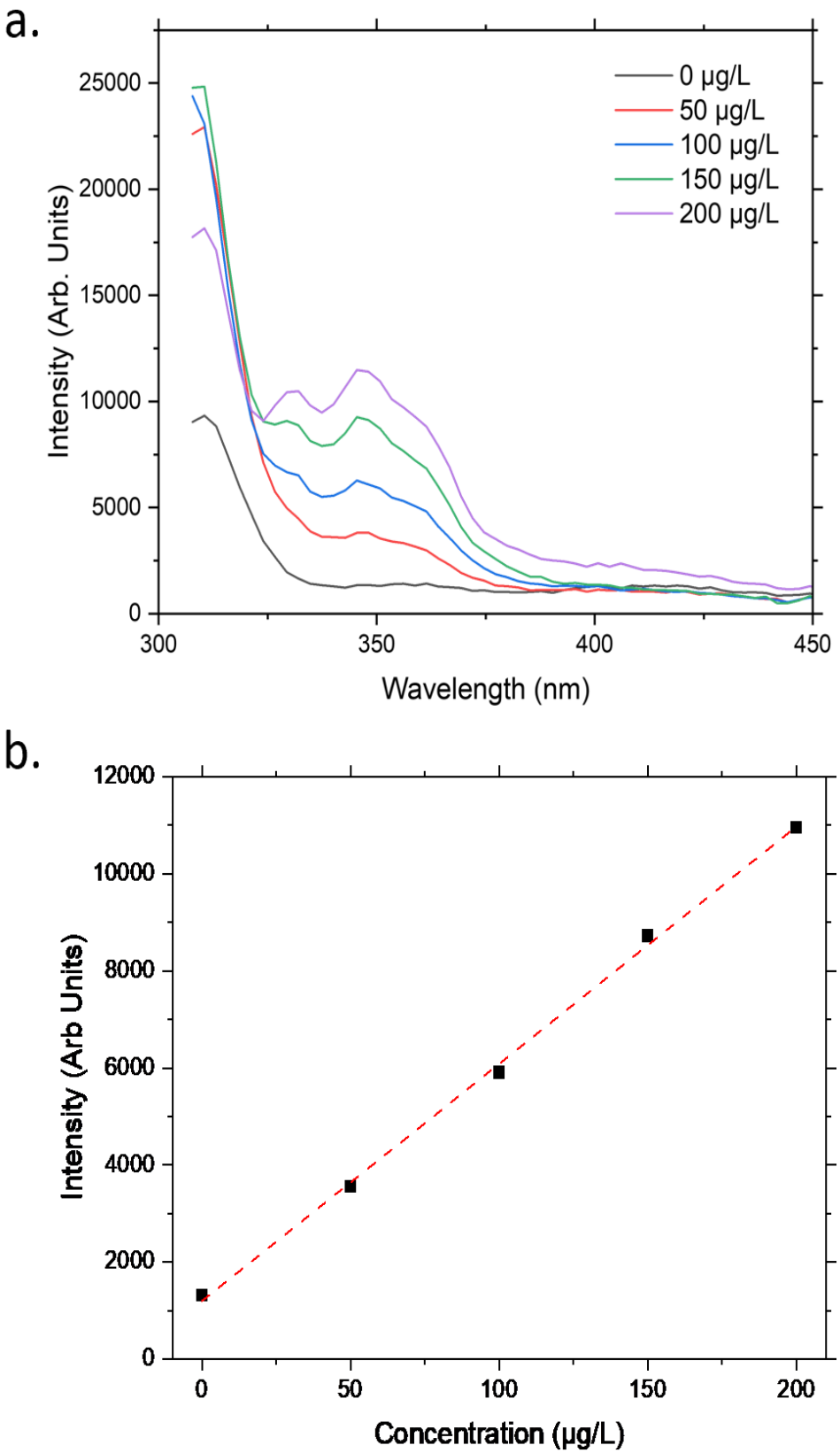

Figure 3-30 (a) Spectrum of the fluorescence emission of NDSA excited by the 310 nm LED for each concentration (0 to 200 µg/L) . (b). Calibration curve created by taking fluorescence intensity at 350 nm of each of the spectra in (a). The linear fit seen in dashed red gives a slope of 48.9, intercept of 1197.86 and an R^2 value of 0.9985.

Figure 3-30 presents the fluorescence response of NDSA with excitation from LED 7 at increasing concentrations. Figure 3-30a shows the spectrometers spectral response to increasing concentrations showing a positive trend in fluorescence intensity with increasing concentrations of NDSA. A scatter plot of the extracted signal intensity at 350 nm against concentration is presented in Figure 3-30b. A strong linear relationship is seen with an R^2 value of 0.9985. A slope of 48.9 would indicate relatively low sensitivity of 48.9 µg/L per AU. A higher integration time can be used to increase this sensitivity depending on LODs required.

3.3.4.5 **Chlorophyll a**

The concentration of chlorophyll measured in the environment can give significant insights into the overall health of the ecosystem in the water column. Chl-a, a component of chlorophyll, fluoresces with a key fluorescence emission wavelength signature as noted in Section 1.3.3. Figure 1-10 shows an excitation range between 280 nm and 450 nm with a unique fluorescence emission spectrum with peak emission at 660 nm. For this reason, Chl-a was selected for the optical sensor's measurement capabilities as a key target analyte for in situ sensors.

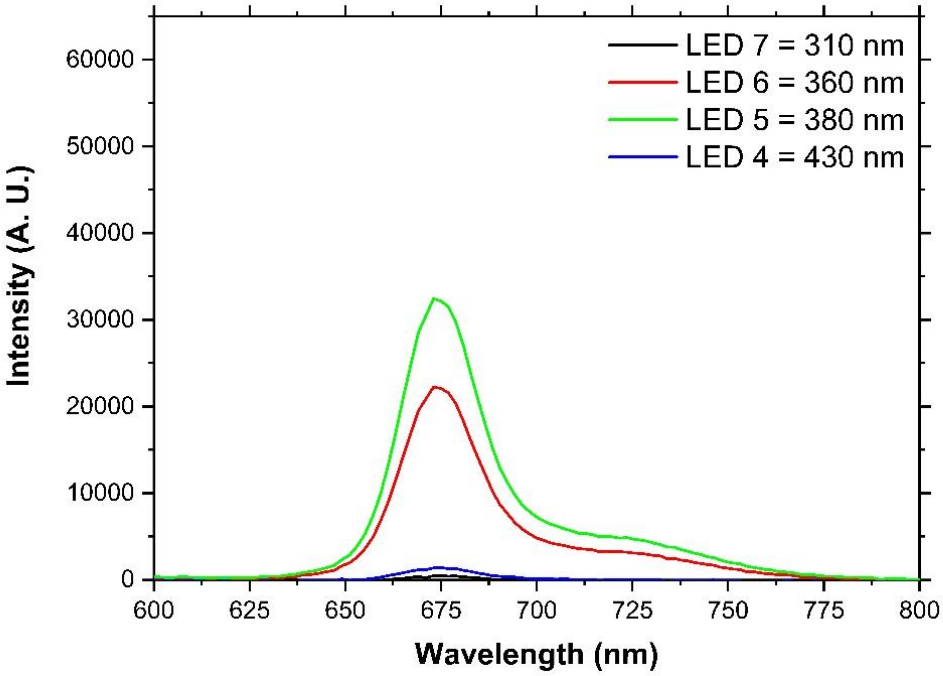

Figure 3-31 Chl-a fluorescence signal spectrum as recorded using LEDs 4 – 7 as excitation light source and measured using the C1880MA mini spectrometer. Measurement taken at 10 µg/L concentration of Chl-a for each LED.

Figure 3-31 shows the fluorescence signal of Chl-a recorded using LEDs 4 – 7. These signals were taken at a concentration of 10 µg/L of Chl-a LEDs 5 and 6 recorded the most intense fluorescence signal, while the fluorescence signal using LEDs 4 and 7 was observed to only just pass the noise threshold at this concentration. LED 8 was also tested but no fluorescence signal was observed at any concentration. This indicates that LEDs 5 and 6 are best suited for in situ fluorescence measurements of Chl-a.

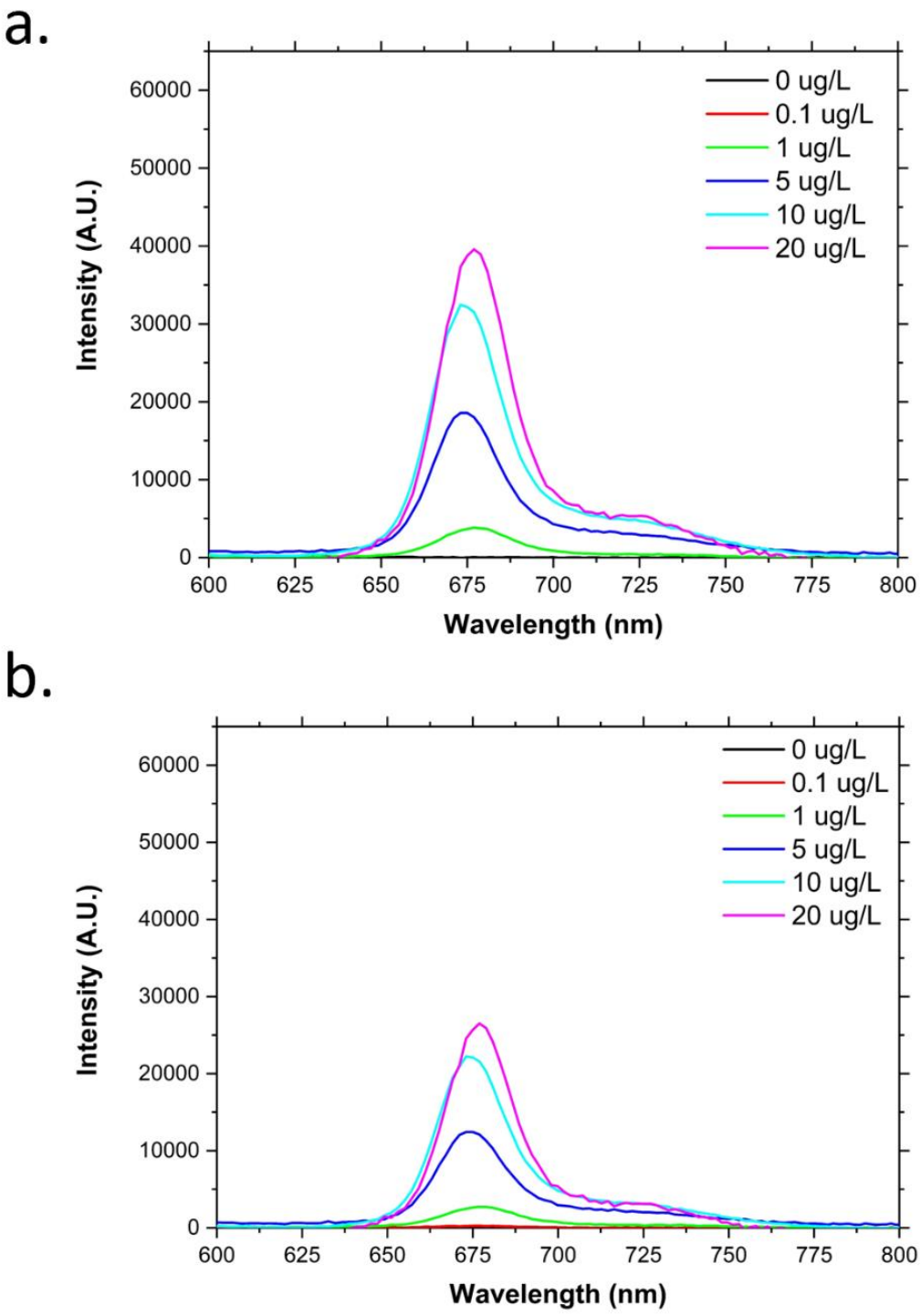

Figure 3-32 Response of sensor measuring Chl-a fluorescence signal as a function of concentration for LED 5 (380 nm) (a) and LED 6 (360 nm) (b). At low concentrations the signal had a linear relationship as a function of concentration, however at 20 µg/L the signal redshifted and was no longer linear.

In Figure 3-32a and b, the Chl-a fluorescence signal of LEDs 5 and 6 at concentration ranging from 0 – 20 µg/L I shown. As can be seen in the figures, at low concentrations (0 – 10 µg/L) the fluorescence increased in a linear fashion, with the peak of the spectrum remaining at 680 nm, however at 20 µg/L the linear relationship broke down at the peak of the fluorescence signal was observed to redshift. Red shift in known to occur in sensor fluorescence measurement at higher concentrations of fluorophore which is occurring with Chl-a for this experiment [345,346]. As such the higher concentration were excluded from the calibration curve. Figure 3-33 shows the Chl-a scatter plot for LED 5 and 6. The scatter plot was created by taking the peak of the fluorescence signal at 680 nm and plotting it as a function of concentration between 0 – 10 µg/L. The linear relationship of both LEDs is high with both above 0.99. LED 5 shows a higher sensitivity compared to LED 6 with slopes of 3282.25 and 2237.79 respectively. This would strongly suggest that LED 5 is the better LED to use to induce fluorescence when measuring Chl-a in situ.

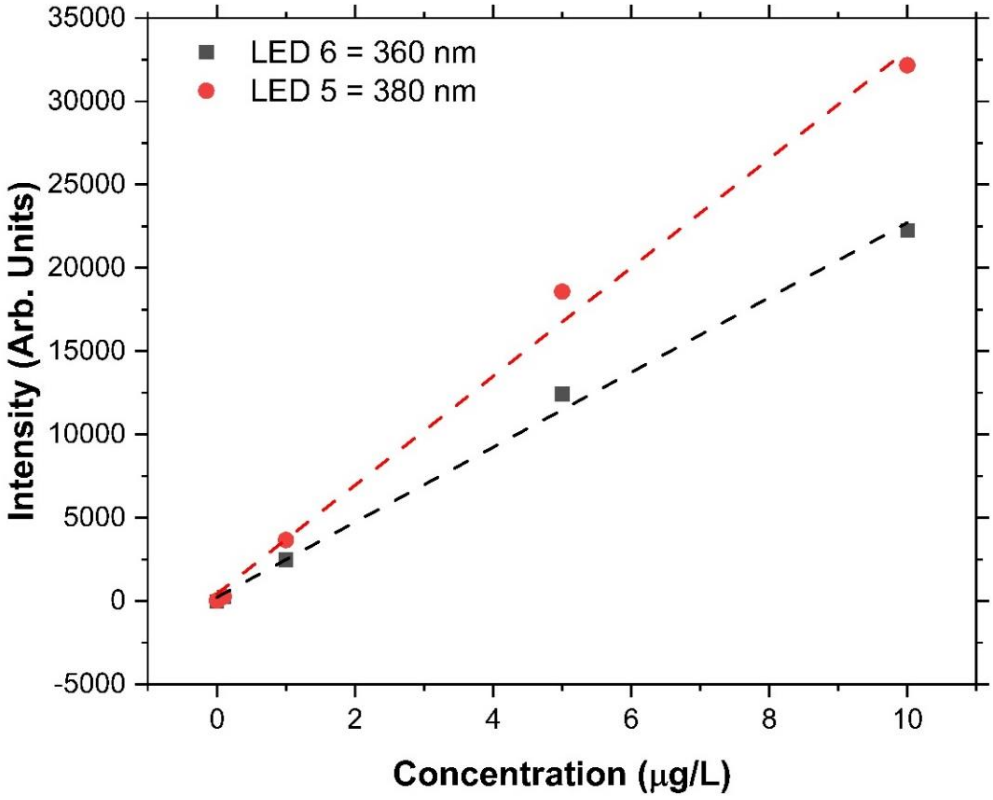

Figure 3-33 Chl-a calibration curve, plotting Chl-a concentration between 0 – 10 µg/L as a function of fluorescence signal strength at 680 nm for LEDs 5 and 6 (n = 3). The linear fit applied to LED 5

gives a slope of 3282.25, intercept of 481.13 and R^2 value of 0.995. The linear fit applied to LED 6 gives a slope of 2237.79, an intercept of 332.3 and an R^2 value of 0.9966.

Figure 3-34 shows the fluorescence signal strength at 680 nm for LEDs 5 as a function of Chl-a concentration between 0 – 35 µg/L, non-linearity and redshift as discussed in the previous section was not observed in this work. These measurements were taken simultaneously with the HydroCat-EP V2. A good linear relationship was established as a function of concentration giving an R^2 value of 0.986.

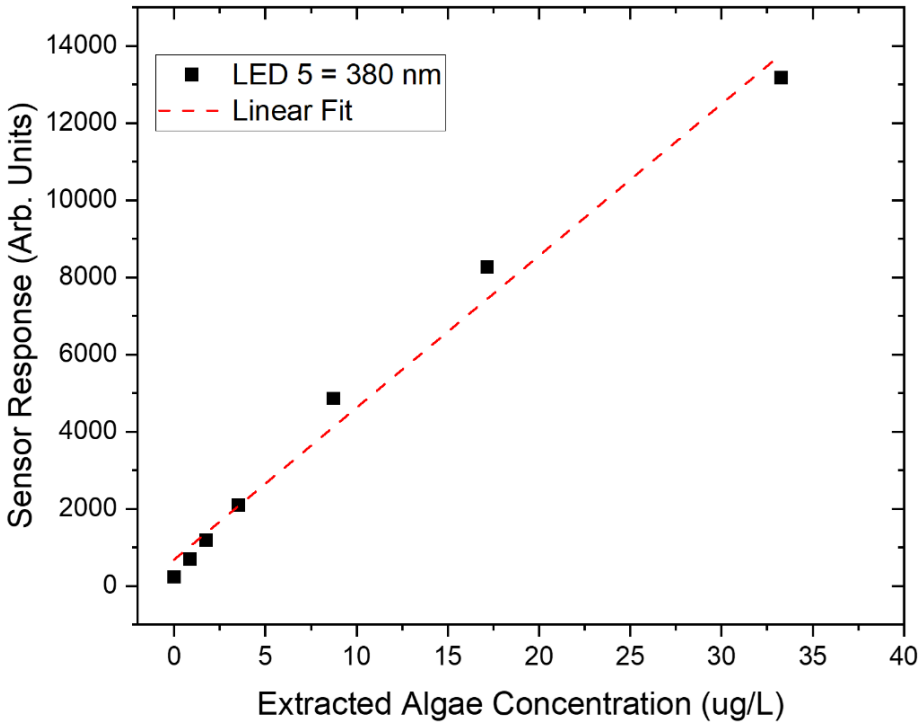

Figure 3-34 Calibration curve plotting Chl-a fluorescence signal strength as a function of concentration for LEDs 5 between 0-35 µg/L. The linear fit applied gave a slope of 393.88, intercept of 682.97 and an R^2 value of 0.986.

The calibration curve generated in Figure 3-34 was applied to convert the raw fluorescence signal from the sensor into a quantitative form and compare the results to a similar signal recorded by the HydroCat.

$$Calilbrated\ Chl\ Reading = \frac{Sensor\ Response\ at\ 680\ nm}{Cal.Curve\ Slope} \qquad 3\text{-}3$$

Equation 3-3 is applied by dividing the raw fluorescence signal by the calculated slopes for each LED. Figure 3-35 shows the comparison in results between LED 5 and the HydroCat.

A high agreement is observed between the commercially available sensor HydroCat reading and the calculated optical head reading from LED 5. This is confirmed by a high correlation coefficient of 0.9995 between the two sensors with a mean absolute error of 0.2826 µg/L and root mean square error of 0.4433 µg/L which are both relatively low.

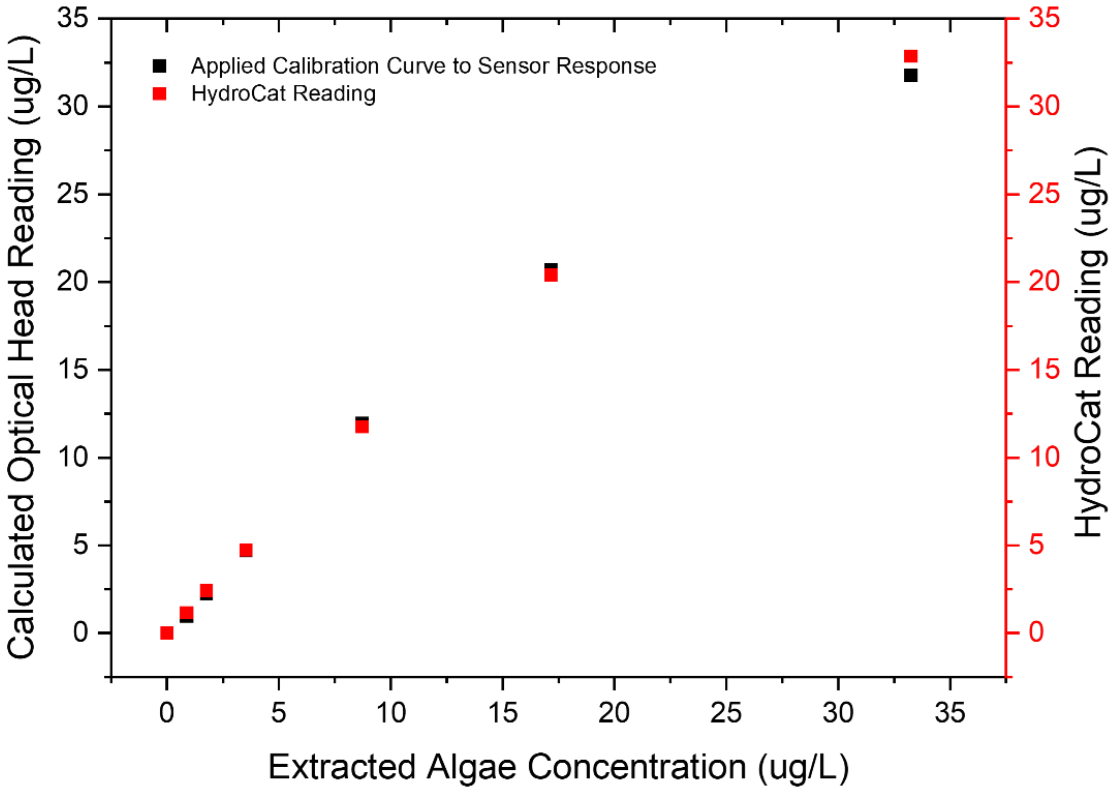

Figure 3-35 Relationship for extracted algae concentration measurement between commercial sensor (HydroCat EP V2) sensor response and the developed optical head's response using LED 5 (380 nm peak excitation) with applied experimentally derived calibration curve with emission measured at 680 nm. Experimental range of testing it set between concentrations of 0 to 35 µg/L with n = 3 for each measurement.

As shown in Section 3.3.4.2, Equation 3-2 can be applied to the slope for LED 5 to convert sensitivity into Chl-a resolution of the sensor between 0 and 35 µg/L. Using the already rederived ADC voltage resolution from Equation 3-1, the resolution of the sensor for fluorescence detection of Chl-a is calculated as 0.00014 µg/L. A tabulated comparison between the sensor prototype and commercially available chlorophyll sensors is presented in Table 3-7. The sensor prototype's resolution is a magnitude of order higher when compared to the other sensors. However, this may be due to the limited range of the calibration curve. Commercial sensors show a good resolution of 0.1 µg/L or lower with measurement ranges of at least 400 µg/L and as high as 1000 µg/L. Again, as with the

turbidity resolution and range, a dynamic integration time could be applied to adapt the range of resolution of the Chl-a fluorescence measurements to increase the sensors detection range.

Table 3-7 Comparison of resolution and measurement range of sensor developed with commercially available chlorophyll in situ sensors.

Sensor	**Resolution (μg/L)**	**Measurement Range (μg/L)**	**Reference**
Sensor developed	0.00014	0-10	-
HydroCAT-EP V2	0.007	0-400	[341]
Aqua TROLL Chlorophyll a Sensor	0.1	0-1000	[347]
YSI 6025 Chlorophyll Sensor	0.1	0-400	[348]

3.4 Conclusion

The work presented in this chapter demonstrates the step-by-step design process taken which involved a thorough investigation of materials and manufacturing methods to achieve an optimal prototype design. Key design advancements were made by applying the iterative design method with testing at each stage identifying areas requiring optimisation. A total of four complete design, prototype and testing iterative cycles were carried out. The materials and prototypes were deployed in the intended environment which provided major insights into their suitability for the marine environment. The findings led to the selection of the most suitable materials for each component included in the sensor design.

The use of engineering polymers POM-C, PA2200 Nylon and PETG allowed for robust components to be manufactured at lower cost using a wide range of manufacturing methods. More advanced geometries could be achieved with additive manufacturing which was required of the optical head design. Marine grade metal materials were used successfully in combination with the polymer materials to provide greater mechanical robustness including 316 stainless steel and 6061-T6 Aluminium. A key finding for future reference is the potential corrosion which was found to occur using stainless steel fasteners with aluminium components in the marine environment.

With fouling growth identified as a major challenge for in situ sensors in the marine environment the strategies implemented in materials and active prevention strategies proved effective in the preliminary experiments. Copper material attached to the outer surface of the enclosure was successful in preventing any fouling build up which was confirmed with the 12 month study showing a high effectiveness. For optical sensors, drift due to fouling is a major challenge. Taking advantage of the latest developments in LED technology applied to the sensors the use of low cost UV LEDs periodically activated during a deployment show great promise in talking this challenge for optical in situ devices. In the preliminary deployment conducted with the sensor, fouling was prevented showing the application of low cost, low power UV LEDs can be applied to the next generation of in situ sensors.

A wide range of manufacturing techniques were applied to the sensor design. The use of the emerging manufacturing technique of additive manufacturing was applied successfully to achieve for more complex geometric designs as was seen in the use of SLS 3D printing

to create the optical head. FDM 3D printing was evaluated to fabricate the optical head however was found to be porous leading to minor leaks in the body which were addressed by coating the print in epoxy which was successful in achieving watertightness. However, the process of applying epoxy to the optical head body was laborious and time consuming which led to a reiteration of the manufacturing method.

A major finding in terms of the sensor's measurement performance in the aquatic environment was that ambient light affected the fluorescence detection more significantly than was previously expected. The optical measurement performance of the sensor was enhanced by the addition of a combination of external and internal sun guards which allow fluorescence measurements in environmental conditions. A learning from this iteration was that it is most critical to assess a developed sensor prototype in the intended environment as soon as is feasible to identify issues of operation outside the lab environment early in the design process to allow for changes to be made.

The in-lab optical performance of the sensor was demonstrated to be capable of measuring multiple parameters with a proficient level of sensitivity and resolution. Target analytes which were identified in Section 1.3 were successfully measured using known standards equivalents in the lab including turbidity, fDOM, oil and chlorophyll. The sensor was demonstrated to have high sensitivity (330.68 AU/NTU) and resolution (0.000152 NTU) in the measurement of turbidity using scatter over a range of 0-60 NTU. The measurement of Chl-a fluorescence was achieved at a sensitivity of 393.88 AU/ μg/L and a resolution of 0.00014 μg/L over a 0-35 μg/L range. This shows the advantage of the novel application of spectrometers and multispectral light source in this design as multiple analytes can be measured without any hardware modifications required. A comparison with commercial sensors for turbidity and Chl-a measurements show the sensor has a very high degree of resolution in detecting the target analytes but measurement ranges need to be increased. The Chl-a measurements of the sensor also compared well with the HydroCat sensor.

Overall, the sensor developed demonstrates a novel technology and design which leverages advances in optical measurement components and manufacturing techniques. Further work is required to explore the optical measurement capabilities of the sensor developed. TRL 4 was achieved with the sensor prototype demonstrated to work at small scall in the intended environment and under laboratory conditions. To achieve a TRL of 7, the sensor design must

demonstrate in the intended environment at pre-commercial scale. The design of the electronics and hardware is complete and ready for scale up to evaluate multiple identical units in the marine environment.

4 SENSOR SCALED-UP PRODUCTION AND PREPARATION FOR IN SITU DEPLOYMENTS

4.1 Introduction

A wide range of in situ monitoring systems (and associated deployment apparatus) for measuring concentrations of various analytes (e.g. nutrients, organic chemicals and metallic elements) have been developed in recent decades [79,288,306,349]. The majority of these systems are still at the laboratory or prototype stage and are yet to be fully developed into commercially available products. The harsh conditions often found in the marine environment can further limit the utility and application of these sensors [350]. There is a gap between sensor prototypes developed in research and ready for market sensor units outside of already established sensor development companies. A one-off prototype can be developed and evaluated to work however does not truly demonstrate a robust sensor design which provides accurate and reliable data in a harsh environment. This requires additional proof of repeatability. Using technology readiness levels (TRLs) (as defined in Table 1-10) as a measure of a prototype's development, TRL 6 demonstrates the full prototype system tested in the relevant environment close to expected performance To do this for small scale prototype developments, multiple prototypes are required to be constructed to extensively test a design in the intended environment. Using the technology readiness level to assess the prototypes performance, the potential of the prototype design being ready for scaling. Further development work is needed; however, the need now is for field deployments, validation and inter-calibration between sensors and other analytical measurement techniques.

The transition from academic based prototype development to commercial or large-scale adoption has been demonstrated to be possible in the marine sensing industry. Argo Float which is a network of floating autonomous measurements devices was initially an international collaboration of industry and academic institutes form the World Ocean Circulation Experiment (WOCE) project conducted in the 1990s [351]. Over 4000 Argo floats are now in operation measuring temperature, salinity and depth profiles in the world's oceans [352,353]. The National Oceanographic Centre (NOC) in Southampton is a leading institute in the field of marine research. Combining academic research affiliated with the University of Southampton with industry production they had developed, testing and commercialised a series of in situ sensors and automated sampling platforms [354]. NOC demonstrate the development process of a microfluidic lab-on-chip (LOC) colorimetric nutrient sensor, making innovative advancements in sensor technology which was

developed in house [355]. These examples show that it is possible to scale up a novel innovation from prototype to commercially viable product.

4.1.1 Defining 'Low-cost' in the Context of Sensor Development

A key factor in scaling a prototype is the incurred cost of materials, fabrication and maintenance [356]. It is important to define 'low-cost' in context of the product being developed. In this case an in-situ marine sensor developed in this work, the cost of materials is the primary source of cost being accounted for with labour costs excluded. Material and fabrication cost are substantially higher the lower the quantity of components being manufactured due to cost scaling [357]. Newly developed 'low-cost' sensors which have been developed by other projects and commercially available sensors can be used as a benchmark to contextualise the costs for this project. According to a review by Wang et al. (2019) [306] optical UV absorption based sensors for nutrient measurements are priced in the region of €10k per sensor. Wang also reports that cost effective fluorimeters have been developed such as that by Leeuw et al. (2013) [116] which can be made for a total cost of $150 USD allowing the sensor to be scaled and deployed in an array for greater spatial resolution. Another fluorometer which was developed and is capable of measuring both chlorophyll-a (Chl-a) and chromophoric dissolved organic matter (CDOM) simultaneously is by Blockstein and Yadid-Pecht (2014) costing less than $500 USD [358]. Matos et al. (2019) [119] reports the development of a turbidity and suspended particle optical measuring prototype for the marine environment which was built as a very low cost using commonly sourced optical components and low cost housing. They were able to build this prototype for around $20 USD. Piermattei et al (2018) [359] in a review of cost effective technologies for the artic ocean, gives a general cost range of typical commercial in situ sensors from between €1000 to €5000 citing sensors like Cyclops-7F Turner Design, ECO FL Wetlabs, SeaPoint, UniLux Chelsea and MicroFlu TriOS. Additionally, more advanced multiparameter commercial sensors such as the EXO YSI can exceed €10,000 [360].

4.1.2 Logistics and Preparation for Low Scale Manufacture

The scaling up of the prototype requires careful planning. The logistics and planning to do so must adhere to real-world factors, i.e., timelines and cost. There are the logistics of: 1) Acquiring all the necessary components and materials. 2) Identifying which components can be fabricated in house or must be outsourced to ensure project deadlines can be met but also

remain within the project budget. 3.) Selecting and communicating with fabricators for the manufacture of custom components to ensure they are fabricated to the required specifications. A top-down design process can be applied to simplify the logistical challenges through the product design being broken down into subsystems [361]. Decomposition of engineering designs or systems into smaller independent sections allows for sections and subsections to be analysed with greater detail [362].

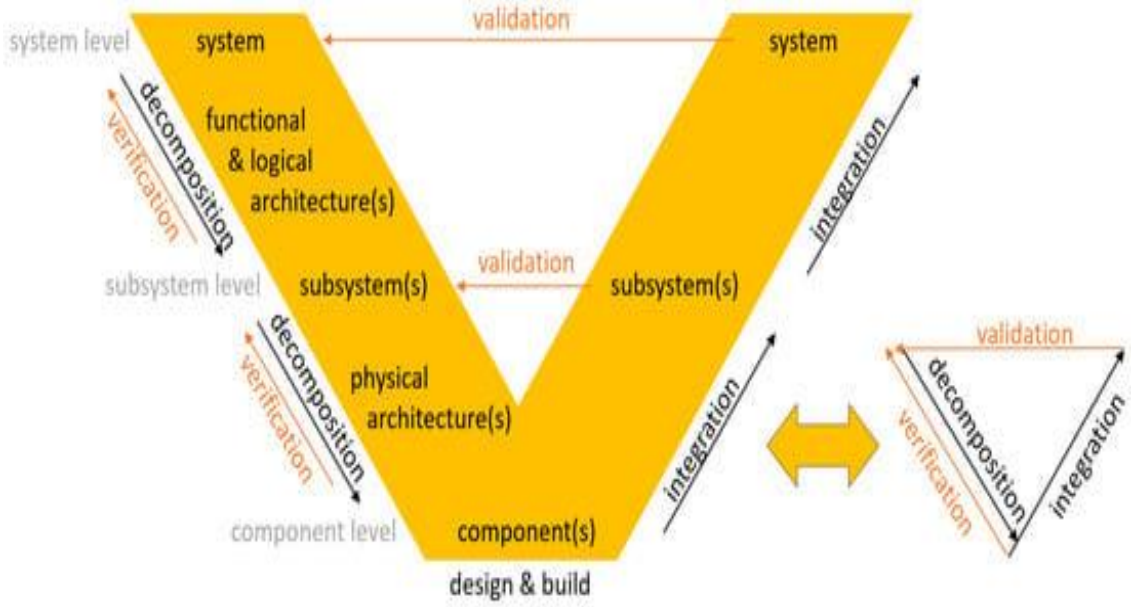

Figure 4-1 Diagram examples of a model-based system engineering approach g known as a "V-Model" adapted from Neumaier, M. et al., (2022) [363].

The 'V-Model' is an engineering design model commonly used in model based system engineering (MBSE) industries [363]. The V-Model (see Figure 4-1) demonstrates a design process consisting of decomposition of a system down to subsystem and components with integration phase following which consists of validation and testing phases bringing the process back to the system level. As well as tackling the logistical challenges of component procurement and fabrication, the V-Model can also be applied to the assembly and testing tasks. Assembling systems in sections is a widely adopted practice in most manufacturing sectors. Production systems use subsystem allocation on assembly lines with a focus of specific tasks to be executed at one or more workstations to efficiently create the final product [364]. Subsystem assembly lines most commonly consist of a straight-line layout however different shapes are used in industry such as parallel line or U-shape line are also used [365,366].

4.1.3 Mitigating Risks and Identifying Failure Points in the Design Phase

Before deploying sensing instrumentation in the field, it is essential to test every subsystem and integrated system correctly to identify any issues and validate the design. Identifying single points of failure (SPOFs) in the sensor design can inform where specific attention must be paid to when testing the functionality of the sensor prototype in preparation for in field deployments. SPOFs are defined as key features or functionalities or the system which if they were the failure the entire system would be non-functioning. SPOF identification gives a good indicator of risk to inform fault management strategies. In 2021, the James Webb telescope was launch by NASA who reported that the entire design had a total of 344 SPOF [367] which outlines the high complexity and risk associated.. This approach allows for risk to be mitigated to ensure the sensor remains durable and functioning for longer periods of deployments.

4.1.4 Calibration and Validation of In Situ Environmental Sensors

There are a series of international standards and guidelines for environmental sensor data validation. ISO 15839:2003 [368] outlines specification and performance tests for the validation of data obtained for water quality from sensors and equipment. Performance parameters are outlined in this ISO document which can be applied to verify the sensor unit's measurement performance in the lab. The key definitions outlining performances parameters for sensors measuring target analytes in water, from ISO 15839, is tabulated in Table 4-1. These parameters must be incorporated into a validation procedure to observe the statical performance of the optical measurement cycle of the sensor. In relationship to the generation of linear calibration curves from in lab known standards for each sensor unit, ISO 8466-1:2021 [369] which relates to the analytical methods of calibration and evaluation with the linear calibration function for water quality measuring devices can be applied. This ISO provides a guide to determining the key statistical parameters of performance outlined in ISO 15839 relating to linearity and calibration. In Table 4-2 the parameters and their outlined determination method as per ISO 8466 are presented.

Table 4-1 Summary of performance parameters for sensors as required in the ISO 15839 [368].

Performance Parameters	**Definitions (EN ISO 15839: 2003)**
Response time	Time interval between the moment when the online sensor/analysing equipment is subjected to an abrupt change in determinant value and the moment when the readings cross the limits of (and remain inside) a band defined by 90% and 110% of the difference between the initial and final value of the abrupt change.
Linearity (range of application)	Condition in which measurements made on calibration solutions (or surrogate tools when standard or certified values are not available) having determinant values spanning the stated range of the on-line sensor have a straight-line relationship with the calibration solution determinant values (or surrogate tools when standard or certified values are not available).
Coefficient of variation	Ratio of the standard deviation of the on-line sensor to the working range of the sensor
Limit of detection (LoD)	Lowest value, significantly greater than zero of a determinant that can be detected.
Limit of quantification (LoQ)	Lowest value of determinant that can be determined with an acceptable level of accuracy and precision.
Repeatability (same day)	Precision under repeatability conditions where independent test results are obtained with the method on identical test items in the same laboratory by the same operator using the same sensor and reagents within short intervals of time (e.g., 24-h).
Day-to-day repeatability	Precision under day-to-day repeatability conditions.
Short time drift	Slope of the regression line derived from a series of measurements carried out on the same calibration solution during laboratory testing and expressed as a percentage of the measurement range over a 24-h period.
Long-time drift	Slope of the regression line derived from a series of differences between reference and measurements values obtained during field testing, expressed as a percentage of the working range over a 24-h period.
Bias (100%-bias=trueness)	Consistent deviation of the measured value from an accepted reference value.
Availability or up-time	Percentage of the full measurement period during which the measurement chain is available for making measurements.
Robustness, memory effect	Temporary or permanent dependence of readings on one or several previous values of the determinant
Robustness, interference	Undesired output signal caused by a property(ies)/substance(s) other than the ones being measured

Table 4-2 Summary of determination methods from ISO 8466-1 [369].

Parameter	Determination method
Linearity	Check for linearity according to ISO 8466-1 using the data set (xi, yi,1) where i=1 to 7.
Coefficient of variation	Calculate the coefficient of variation according to ISO 8466-1 using the data set (xi, yi,1) where i=1 to 7. Express the result as a percentage. It can be compared to coefficients of variation of other on-line sensors.
Limit of detection (LoD)	Calculate the limit of detection as three times the standard deviation of the measurements y1, j for j=1 to 6.
Limit of quantification (LoQ)	Calculate the limit of quantification as ten times the standard deviation of the measurements y1, j for j=1 to 6.

4.1.5 Accounting for Matrix Effects in the Aquatic Environment

Marine and fresh waters can be cocktail of chemical, biological, and physical components. Measuring target analytes optically when in the open environment is much more challenging than under lab conditions. The broad and unpredictable mix of elements in the water column can affect the accuracy and precision of optical measuring devices significantly. For fluorescence, absorption or scatter measurement modes, interference from factors such as temperature, intramolecular deactivation, turbidity and pH [370]. A prominent issue with fluorescence measurements can be caused by high turbidity in the area being sampled [371,372]. By measuring turbidity and fluorescence together this interference can be accounted for and corrected [370].

4.1.6 Aims and Objectives

The primary aim of this chapter is to build the optical sensor developed in Chapter 3 at scale, producing a total of ten replicate units and validate them for in situ deployments. This can be achieved by:

1. The development of a systematic protocol of production for assembling of multiple units in a research laboratory environment at low cost. The focus of this protocol will be on the logistics, procurement and assembly methods required to build the sensor units efficiently and at low cost.

2. The use of protocols to check the quality of systems produced being consistent and deemed robust for deployment. SPOFs of the system must be identified and test protocols developed to ensure the constructed sensor units are robust mechanically and electronically.

3. The optical measurement performance analytically proven to be robust and accurate. Adhering to the ISO 15839: 2003 standard, the sensors must be shown to produce stable and reliable data. The sensors limit of detection (LOD) will be ascertained experimentally for each selected target analyte. Within the LODs for each parameter, a study is required to show other parameters do not interfere significantly to which the calibration curve can be deemed adequate within a region of certainty.

4. The calibration of the sensor units to produce quantifiable real-world data on key target analytes in the marine environment. Chl-a, turbidity and temperature were identified in Section 1.3 as key targets for measurement in the marine environment. Having compared well with the measurements of a commercial sensors in the lab as presented in the Section 3.3.4, the three target analytes are the focus for calibration in this study. With the fabrication of a total of 10 sensor units, each required validation steps to generate calibration curves for both Chl-a and turbidity.

4.2 Materials and Methods

The materials and methods for scaling up assembly of ten sensor unit prototypes, testing the built prototypes and validating the optical measurements are presented in this section. Table 4-3 outlines the details of each of the sensor units built and the version of components used. The version of the sensor enclosure and manufacturing method of the optical head are presented in Section 3.3.1 Likewise, the electronics underwent an iterative design process producing a total of three versions as presented in Section 2.3.2. The sensor units were built in two batches. The first batch of units (units 1-3) built are noted as Design Version 3 in Table 4-3. The second batch consisted of the assembly of the remaining seven sensor units (units 4-7) noted as Design Version 4 in Table 4-3. This division of assembly into batches was done to allow the first three units to inform the assembly process and through testing inform the improvements needed to optimise the remaining sensor units as described in Sections 3.4.1 and 2.3.2. Once tested to be functioning correctly, all ten sensor units were calibrated together.

Table 4-3 Table detailing the build of each sensor unit, manufacturing method and component versions.

Sensor Unit	Design Version	Optical Head Manufacturing Method	Antifouling Prevention Methods	C12880MA Spectrometer Serial No	PCB Version	Firmware Version
Unit 1	3	FDM 3D Printed, Epoxy Coating	Copper tape and UV LEDs	ABS: 20H01762 SCT:20H01763	2	1.2
Unit 2	3	FDM 3D Printed, Epoxy Coating	Copper tape and UV LEDs	ABS: 20H01764 SCT:20H01761	2	1.2
Unit 3	3	FDM 3D Printed, Epoxy Coating	Copper tape and UV LEDs	ABS: 20H01765 SCT:20H01760	2	1.2
Unit 4	4	SLS 3D Printed Infiltration Proofing	UV LEDs	ABS: 2OL00255 SCT:2OL00256	3	1.2
Unit 5	4	SLS 3D Printed Infiltration Proofing	UV LEDs	ABS: 2OL00257 SCT:2OL00258	3	1.2
Unit 6	4	SLS 3D Printed Infiltration Proofing	UV LEDs	ABS: 2OL00259 SCT:2OL00260	3	1.2
Unit 7	4	SLS 3D Printed Infiltration Proofing	UV LEDs	ABS: 2OL00261 SCT:2OL00262	3	1.2
Unit 8	4	SLS 3D Printed Infiltration Proofing	UV LEDs	ABS: 2OL00263 SCT:2OL00264	3	1.2
Unit 9	4	SLS 3D Printed Infiltration Proofing	UV LEDs	ABS: 2OL00265 SCT:2OL00266	3	1.2
Unit 10	4	SLS 3D Printed Infiltration Proofing	UV LEDs	ABS: 2OL00267 SCT:2OL00268	3	1.2

4.2.1 Scale up Assembly of Sensor Units

4.2.1.1 Logistics and Planning for Scaling up Sensor Unit Build

Figure 4-2 outlines the decomposition of the overall system into smaller sections and identifies required fabrication methods. The sensor design was split into three distinct systems which are broken down further into subsystems (description seen in Figure 3-1). The first system was the electronics which consisted of four separate circuits that in the final system all combine to provide the measurement and data output functionalities of the sensor. The fabrication of the electronic circuit boards were all outsourced with the final assembly processes requiring surface mounted (SMD) reflow soldering as well as through hole (THT) component soldering. The soldering processes needed were dependent on the components used on the circuit board. The soldering and assembly of the PCBs was done in house. The second system category was the main body enclosure. Computer numerical control (CNC) machining larger components was not feasible in house, outsourcing was required for both the main enclosure and the top cap. The 3D printed components of the internal frame were outsourced to save additional time. The final category of system is the optical sensor head. This section was the most critical as the assembly influenced the optical measurement setup which needed to be standardised for each sensor unit. The selective lase sintering (SLS) 3D printing of the optical head was outsourced. The insertion of the optical lenses into the optical head was an intricate and delicate process requiring exact assembly steps. The prior knowledge from assembly of previous prototypes meant it was more reliable to assembly this step in-house to ensure the lenses were mounted correctly with a watertight seal.

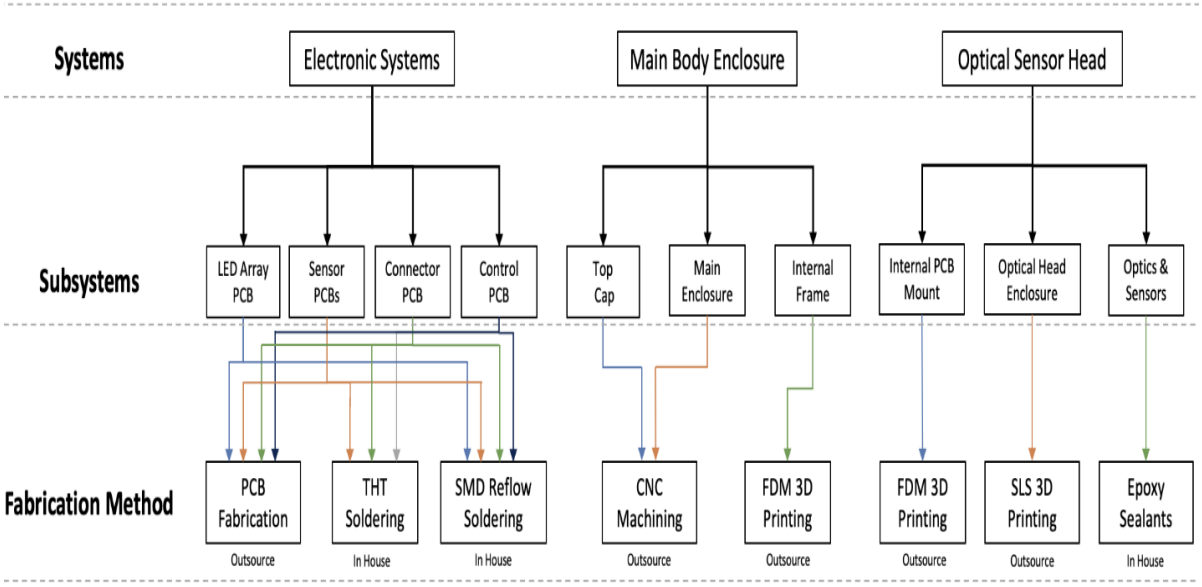

Figure 4-2 Decomposition of sensor design identifying systems, subsystems and assigning fabrication methods required.

Figure 4-3 shows the structured flow diagram of the process of assembly. On the right is the macro view of the full system assembly processes used. Each subsystem was combined in the final assembly of subsystem stage. The fully assemble sensor unit then underwent full testing. The left depicts the micro view of the subsystem assembly process used. This was done for each subsystem outlined in the full system process. Component procurement and outsourced fabrication of components flow into the subsystem assembly task. Component and manufacturing lead times had to be considered before the subsystem assembly step to ensure all components were available. All in-house assembly was done during the assembly step. Once the assembly for the subsystem was carried out, that subsystem was then tested for functionality before being passed to the full system assembly stage.

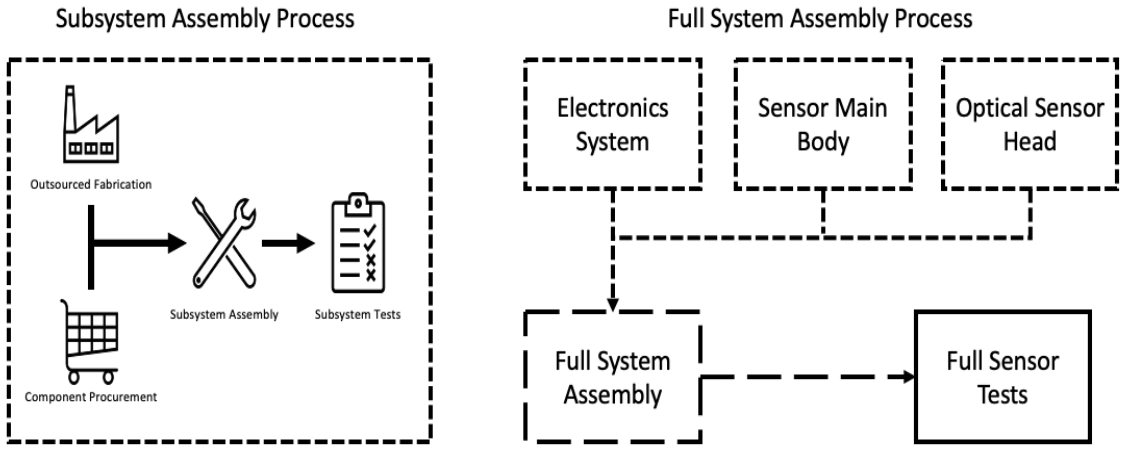

Figure 4-3 Sensor subsystem and full system assembly processes.

4.2.1.2 Scaled Up Assembly of the Sensor Units

The research laboratory the assembly was being carried out in was not designed to facilitate the assembly of multiple prototypes. The lab space as shown in Figure 4-4 was laid out in a more efficient way.

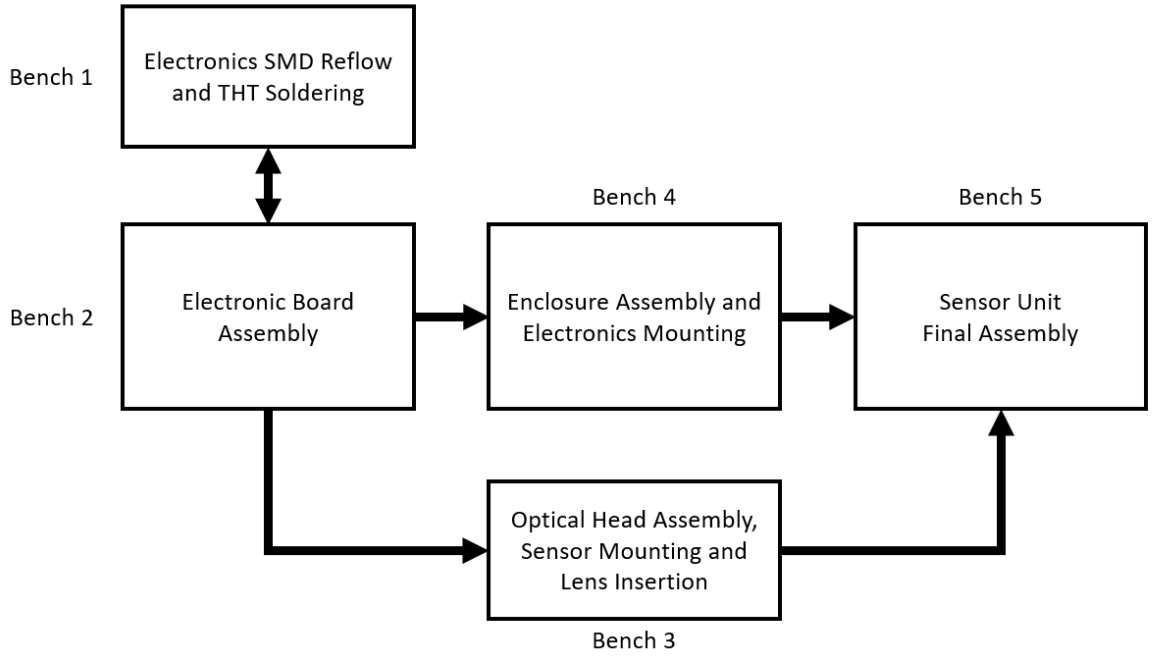

Figure 4-4 Sensor unit assembly line layout with subsystems assembled in stages at allocated benches progressing from Bench 1 to Bench 4 with final assembly of all subsystems done at Bench 5.

The electronics systems were assembled in the first stage moving between Bench 1 and Bench 2. For each sensor unit, eight separate circuit boards were needed. There were two separate stages to soldering the different components to the boards. The first is shown in Figure 4-5 which outlines the reflow soldering processes for soldering the surface mounted components to the main control board. The first step (Figure 4-5a) was to apply the solder paste to the board using a steel stencil with the component pads cut out (supplied by Betalayout with the PCBs). The solder was applied to the pads as shown in Figure 4-5b. The second stage (Figure 4-5c) was component placement, a set of tweezers was used to pick and place the components on their corresponding locations using the PCB design layout as reference. It was ensured that the specific orientation of the component matched the outline on the PCB. The final step in the process is shown in Figure 4-5d which was the reflow soldering. A reflow oven (RK-10590 sourced from Betalayout Ltd) with temperature profile controller was used. Figure 4-5e shows the completed set of surface mounted components soldered to the PCBs.

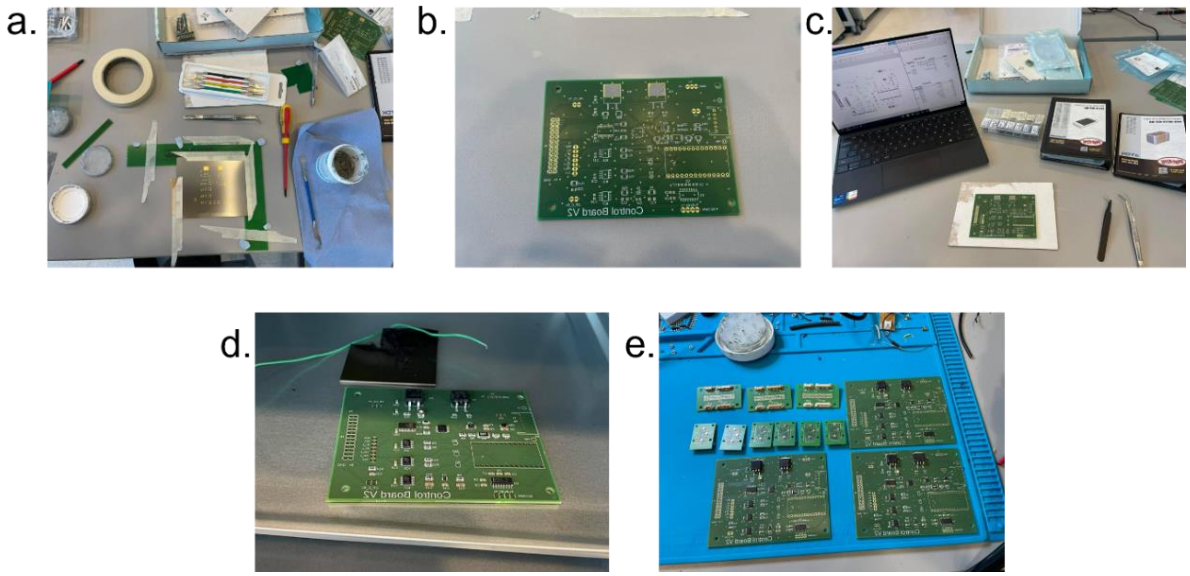

Figure 4-5 Surface mounted components placement and reflow process (a) applying solder paste to board using stencil (b) PCB will solder paste applied (c) component placement d.) components placed and PCB placed in reflow oven for reflow soldering e.) completed reflow soldered surface mount components onto PCBs.

The second stage of the soldering process was to solder the THT components to the boards as outlined in Figure 4-6. This involved hand soldering the components to the board using a soldering iron (Weller WS 81 Analogue Soldering Station 80W sourced from Radionics Ltd). The orientation of each component was considered to ensure correct alignment. Figure 4-6a shows the through hole component soldered to the control board. Figure 4-6b shows how that was done using the soldering iron and vice holder. Figure 4-6c shows the through hole header connectors being soldered to the CMOS spectrometer mounting board. Finally, Figure 4-6d shows the completed set of PCBs. The PCBs were required by the next two subsystem assembly steps and were moved to both Bench 3 and Bench 4.

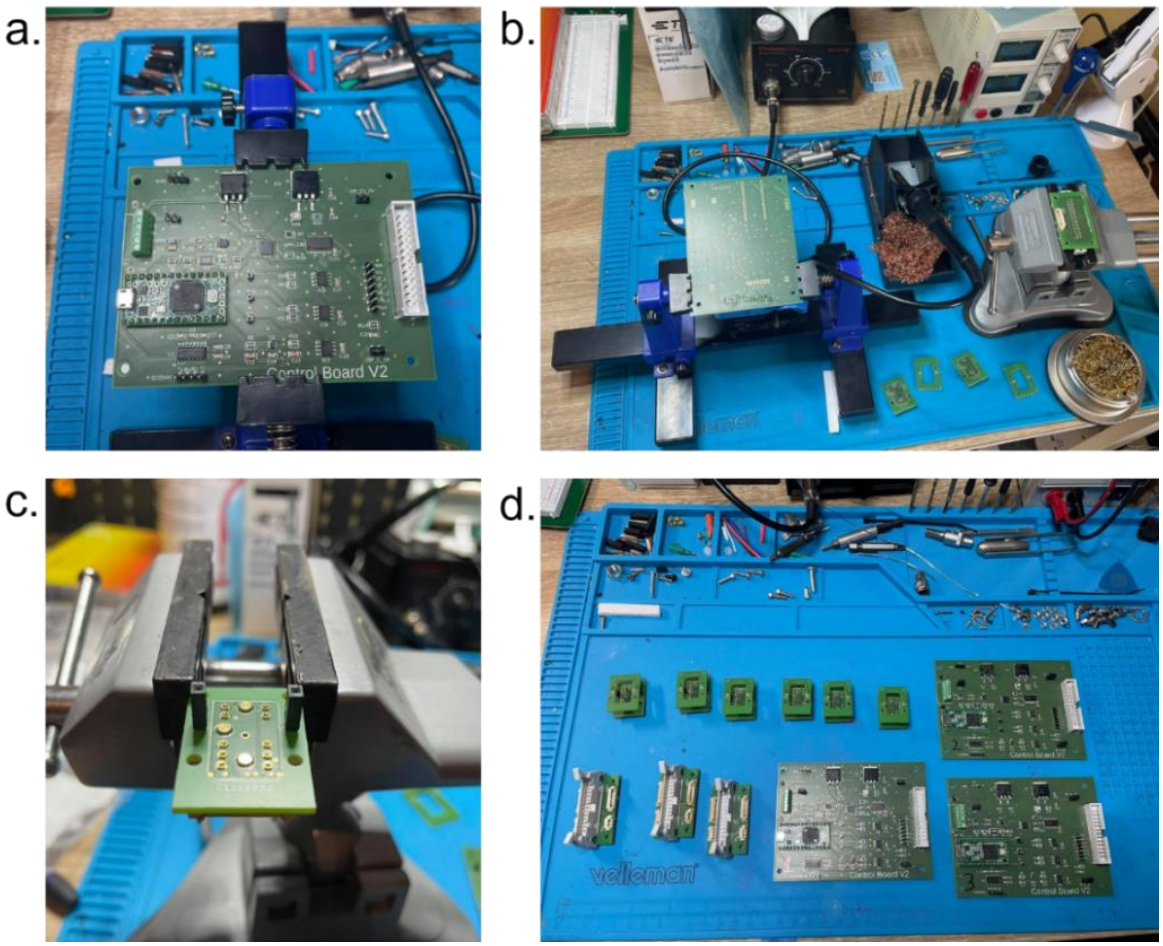

Figure 4-6 Through hole components hand soldered to PCBs (a) THT components solder to main control board d.) Soldering components to boards (c) THT components soldered to CMOS mounting boards d.) Completed PCBs SMD and THT components soldered.

Figure 4-7 shows the subsystems of the sensor with prepared components for Benches 3 and 4 as well as the assembly lines setup in the lab. Two engineering interns assisted with the assembly, Mr. Adam Worthington, and Mr. Harry Beggy; each managed the assembly of a particular subsystem (Figure 4-7c). The optical sensor head was constructed at Bench 3 with the optical lenses inserted into the optical head and the sensor, light source and connector PCBs mounted to the internal mounting platform (Figure 4-7b and e). The main body enclosure was constructed at Bench 4 with the internal structural frame and electronics mounting system constructed (Figure 4-7a and d). The main control electronics were mounted to the frame and the top cap connectors were inserted. Both subsystems from Bench 3 and Bench 4 flow into the final stage at Bench 5. This stage was where all the subsystems were put together to form the completed sensor unit.

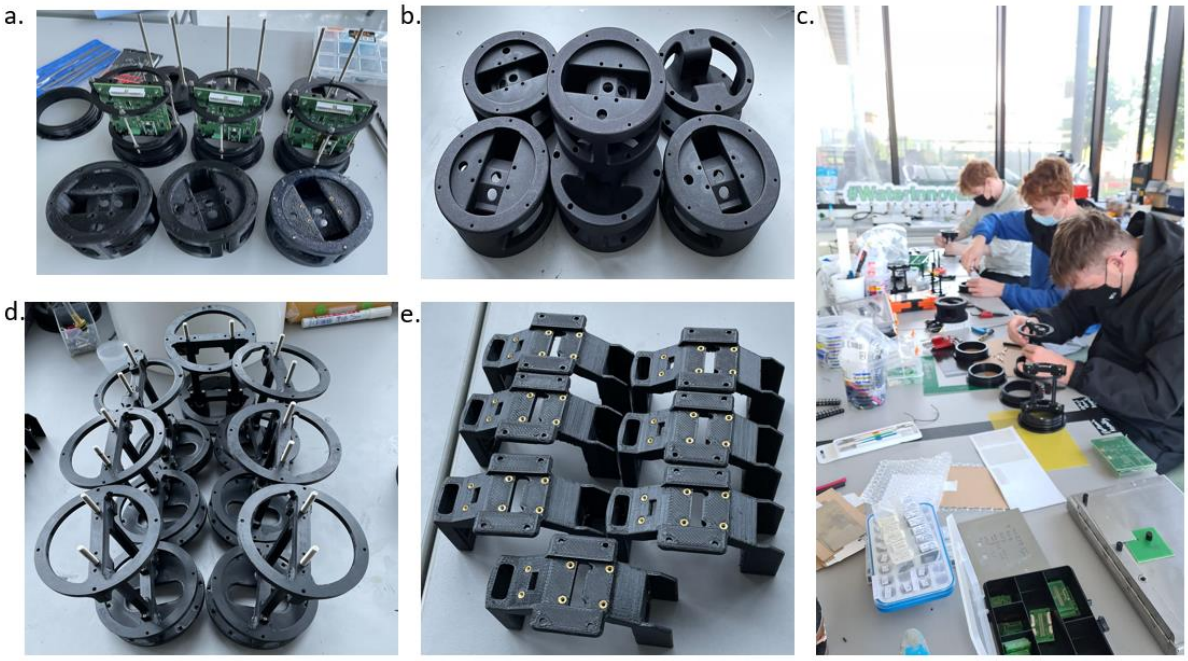

Figure 4-7 Assembly line and stations of sensor unit assembly method (a) mounting controller circuit boards to internal frame structures (b) SLS printed optical heads before optical components are mounted (c) Assembly line in the laboratory with different assembly stations for each subsystem outlined. d.) Internal frames assembled before insertion into the marine sensor enclosure and electronics mounted. e.) Optical electronics mounting tray for optical head before measuring electronics are mounted.

4.2.1.3 Sensor Units Bill of Materials

The bill of materials of the hardware components and fabrication used to construct the enclosure of the sensor units is presented in Table 4-4. The bill of materials for the electronics components and fabrication of the PCBs is shown in Table 4-5.

Table 4-4 Bill of materials of hardware components and fabrication of components for the sensor units.

	Component	Material	Fabricator/Supplier	Quantity	Unit cost (€)	Total Cost (€)
Top Cap	CNC Machined Top Cap	POM-C	3DHubs	1	36.80	36.80
	MCBH6M Subconn connector	Brass/Chloroprene rubber	MacArtney	1	88.23	88.23
	Enclosure Air Valve and Plug	7075-T6 Anodized Aluminum	BlueRobotics	1	10.00	10.00
Sensor Body	Hard Anodized Black 4" O-Ring Flange	6061-T6 Aluminum	BlueRobotics	2	32.13	64.26
	Flange O-Rings Set	Nitrile Rubber (NBR70)	BlueRobotics	2	3.57	7.14
	CNC Machined Enclosure Body	POM-C	P&T Engineering	1	141	141
	FDM 3D Printed Frame Base	PETG	3DHubs	1	8.00	8.00
	FDM 3D Printed Frame Electronics Mounts	PETG	3DHubs	2	8.38	16.76
Optical Head	SLS Printed Optical Head	PA2200 Nylon	BetaLayout, Ireland	1	265.28	265.28
	FDM 3D Printed Sensor Mounting Tray	PETG	3DHubs	1	9.58	9.58
Other	Fasteners	316 Stainless Steel	Inox	-	-	21.80
		Component and fabrication costs as of July 2021		Total Cost		**€668.85**

Table 4-5 Bill of materials of electronic components and fabrication of circuit boards for the sensor units.

	Component	Part number	Supplier	Quantity	Unit cost (€)	Total Cost (€)
Optics	Colimitation Lens	36689	Edmund Optics, UK	1	85.05	85.05
	Plano-convex lens	48668	Edmund Optics, UK	3	70.21	249.00
	Lens Tube	SM1L03	ThorLabs, UK	1	11.95	11.95
Light Source	280 nm LED	XBT-1313-UV-A130-AA280-00	Mouser Electronics, Ireland	7	1.76	12.32
	310 nm LED	CUD1GF1A	Digikey, Ireland	1	7.26	7.26
	360 nm LED	ATS2012UV365	Mouser Electronics, Ireland	1	2.19	2.19
	380 nm LED	ATS2012UV385	Mouser Electronics, Ireland	1	1.56	1.56
	430 nm LED	KP-2012MBC	Farnell, Ireland	1	0.86	0.86
	565 nm LED	SML-LX0805SGC-TR	Mouser Electronics, Ireland	1	0.25	0.25
	660 nm LED	SML-LXF0805SRC-TR	Mouser Electronics, Ireland	1	0.23	0.23
	850 nm LED	VSMY1850X01	Mouser Electronics, Ireland	1	0.71	0.71
Sensors	CMOS, photodetector	C12880MA	Hamamatsu Photonics, UK	2	200	400
	Photodiode	MT03-021	Digikey, Ireland	1	13.16	13.16
	Temperature Probe	CELSIUS-SENSOR-R1-RP	BlueRov-Solutions	1	67.35	67.35
	Current Sensor	INA226AIDGST	Digikey, Ireland	1	2.71	2.71
Electronic Components	Teensy 3.2 Microcontroller	DEV-13736	Digikey, Ireland	1	18.05	18.05
	5V LDO Voltage Regulator	L7805ACD2T-TR	Digikey, Ireland	1	0.49	0.49
	Adjustable LDO Voltage Regulator	LM317D2TR4GOSCT-ND	Digikey, Ireland	1	0.66	0.66
	Op Amp	MCP601	Digikey, Ireland	3	0.31	0.93
	Digital Buffer	MC74VHCT125AD	Digikey, Ireland	1	0.30	0.30
	LED Driver	TLC59116FIPWR	Digikey, Ireland	1	1.92	1.92
	RS-232 to TTL Converter	MAX323	Digikey, Ireland	1	1.20	1.20
	NP Channel MOSFET	NTJD1155LT2G	Digikey, Ireland	1	0.27	0.27
	Power Diode	SBR3U30P1DICT-ND	Digikey, Ireland	1	0.33	0.33
	Connectors	Picoblade/JST XH/IDC	-	-	-	26.61
Custom PCBs	LED Array Board	-	Betalayout, Ireland	1	14.95	14.95
	CMOS Mounting Board	-	Betalayout, Ireland	2	8.11	16.22
	Photodiode Mounting Board	-	Betalayout, Ireland	1	7.98	7.98
	UV LED Mounting Board	-	Betalayout, Ireland	2	8.11	16.22
	Connection Board	-	Betalayout, Ireland	1	15.18	15.18
	Control Board	-	Betalayout, Ireland	1	25.70	25.70
		Component and fabrication costs as of July 2021		Total Cost		€963.24

4.2.2 Sensor Unit Quality Control Test Procedures

The testing procedures which were carried out to verify the subsystems and the full sensor systems were functioning correctly are outlined in this section. The tests were carried out on the subsystems post the assembly step and before the final assembly step. The single points of failure of the system were identified by analysis the resulting effect the failure would have on the overall functionality of the system as a while.

4.2.2.1 Electronic System Tests

The first test conducted on the PCBs after assembly was a visual inspection and continuity test using a multimeter (Fluke 117 Handheld Digital Multimeter sourced from Radionics Ltd). This screening test post soldering was done to ensure no misplaced solder or misconnected pin caused a short. If any solder bridge was found, a soldering iron and solder wick was used to remove the excess solder from the connections. Once this test was completed the boards could receive power without the risk of damaging components.

The second test carried out was to power on the mainboard and uploading test firmware to the microcontroller board. The current draw of the system while idle (not performing any tasks) is 70 mA as known from a known working PCB. The using the multimeter in current measurement mode in series with the benchtop power supply, the current draw of the system was measured., A normal current draw indicates there are no electronic faults in the system. The firmware upload was done via USB connection to a PC computer. A simple program was uploaded initially which outputs a string via the serial port from the microcontroller to the PC. This is read via a serial monitor and displayed on the PC. This test indicated that the microcontroller was functioning correctly and could be uploaded with the sensor test firmware for further testing.

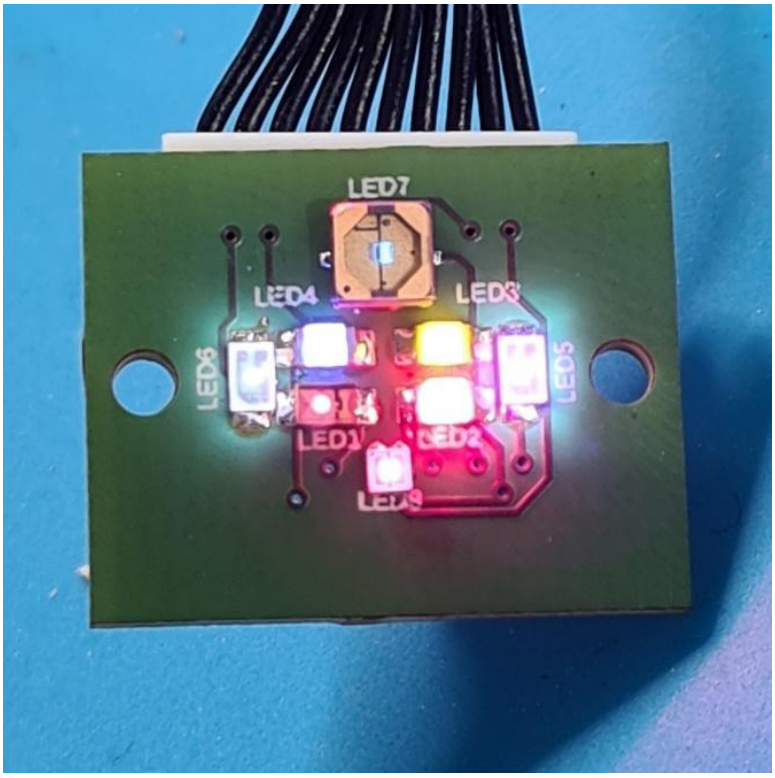

Figure 4-8 Visual inspection of all LEDs functioning correctly using phone camera.

An additional visual inspection was done on the LED Array with all LEDs power on using a known working controller PCB. This was done to ensure that the LEDs were in their correct position and orientation before being placed in the sensor. Figure 4-8 shows power supplied to the LEDs to illuminate them. The wavelength range of the LEDs spanned beyond the visible spectrum so some of the LEDs were not visible with the human eye. A phone camera was used with a wider detection range, to inspect that all the eight LEDs are functioning correctly.

A diagnostic program was written in the firmware using the current monitoring IC on the main controller board (see Section 2.3.2.1). The current measurement was used to validate the onboard current draw of components and the overall system. This was an indicator of whether the system was functioning correctly. The expected current draw of each component was tabulated (see *Table 4-6*) based on a known working system and component manufacturer datasheets. The sensor units diagnostic current draw output was compared to *Table 4-6* to evaluate that all components are operating normally.

Table 4-6 Table of known current draw of each component in system for validation of new sensor unit electronic performance.

Component	Current Draw
LED 1: 280 nm	18.0 mA
LED 2: 310 nm	17.2 mA
LED 3: 365 nm	17.6 mA
LED 4: 385 nm	18.0 mA
LED 5: 430 nm	18.2 mA
LED 6: 565 nm	17.7 mA
LED 7: 660 nm	17.8 mA
LED 8: 880 nm	17.6 mA
UV LEDs on Photodiode Board	32.3 mA
UV LEDs on Spectrometer Board 1	32.7 mA
UV LEDs on Spectrometer Board 2	32.6 mA
Optical Head Sensors Total	18.2 mA

A test program was written to test the functioning of the photodetectors by allowing continuous measurements to be output to a serial monitor on the connected PC (see firmware in Appendix B, Section B.1). The firmware was uploaded to the microcontroller and a series of test measurements in response to difference levels of light was made for each spectrometer and the photodiode. If the photodetector did not respond to different light intensities, there was a fault with either the detector itself, the control circuitry, or the signal processing circuitry. A multimeter was used to measure voltages at the different stages of the circuit while the malfunctioning photodetector was operating to locate the fault.

4.2.2.2 Enclosure Water Tightness Tests

The primary approach for testing the watertightness of a built sensor prototype was to submerge the sensor unit in a body of water for a period and inspect the interior to check if water had penetrated the exterior seals. Figure 4-9 shows the initial tests conducted in the early stages of the sensor unit design to test the viability of the components and housing selected. The unit was left fully submerged in the bucket of water overnight. This test gave a “yes/no” result on whether the housing is or is not watertight.

Figure 4-9 Sensor watertightness test by submersion underwater overnight. Visual inspection of the inside of the sensor housing is conducted post submersion for visual inspection of moisture inside.

A second test to identify the location of leaks was used. An air valve (as described in Section 3.2.2.3) was installed in the top cap (Figure 4-10b). A Mityvac BR-100297 Hand Pump sourced from Blue Robotics Inc was used to pressurise the sensor unit to 50kPa as seen in Figure 4-10a. If leaks were present, they could be detected visually via a stream of bubbles exiting the sensors enclosure while the sensor unit was submerged as seen in Figure 4-10c. If a leak was detected at a specifical location the assembly and seals of the sensor were inspected. Seals were replaced if seen to be visually damaged. A 12 hr pressure test was also conducted to detect minor or slow leaks. The sensor was pressurised to 50 kPa and left for the 12 hrs, a significant drop in pressure after this time would indicate the sensor is not completely airtight.

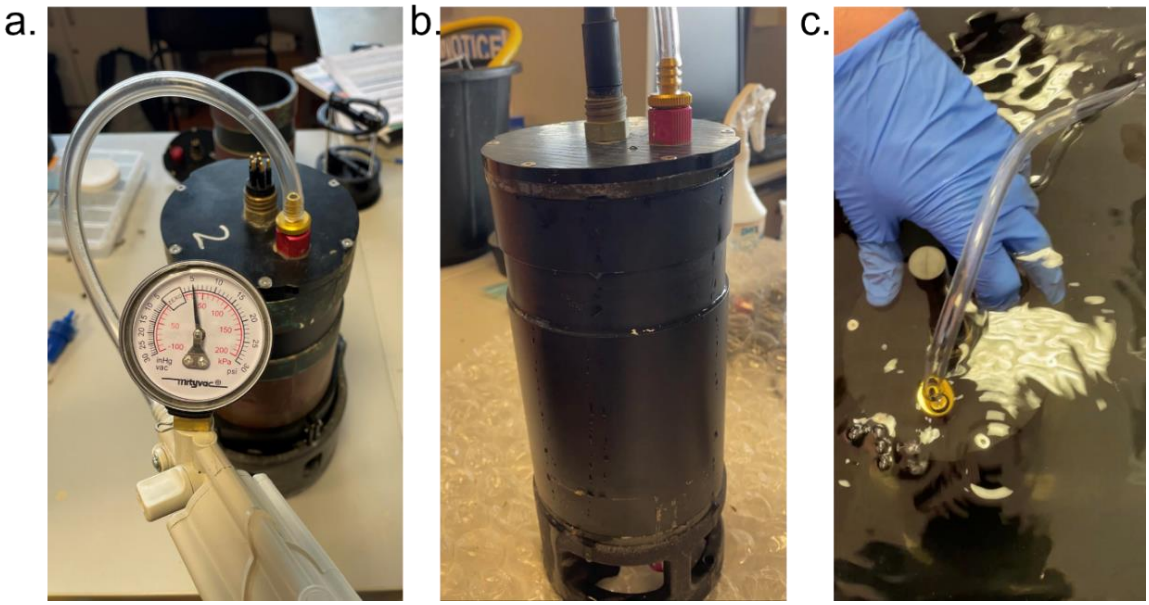

Figure 4-10 Sensor air pressure tests using air pump (a) Pressuring sensor unit to 50 kPa (b) Pressure hose connected to sensor air valve (c) submerged pressure tests to identify leaks via air bubbles.

4.2.3 Validation and Calibration of Sensor Units

The sensor validation experiments were conducted with the assistance of Dr Ciprian Briciu-Burghina and Dr Chloe Richards. They assisted with the preparation of the test analytical solutions. For the validation, calibration and optical performance experiments conducted, Table 4-7 gives the lab standard dyes and reagents used. The integration times used by the spectrometers for the series of experiments in this section were as determined in Section 3.3.4.1 outlined in Table 3-4.

Table 4-7 Lab standards and reagents used for validation experiments.

Standard/Reagent	**Supplier**
Basic Blue 3 (BB3) (CAS: 33203-82-6; 359.89 g/mol; 25 % dye content)	Sigma Aldrich, Ireland
Reagecon CRS-4000-100 (4000 NTU)	Fisher Scientific, UK
Reagecon CRS-800-100 (800 NTU)	Fisher Scientific, UK

For the testing of the sensor units in the lab, a vessel was required to hold the test sample large enough to hold the volume required to submerge the sensors optical head and ambient light block to ensure proper measurement. Figure 4-11 shows a sensor unit placed into the measurement sample holding vessel. The vessel is FDM 3D printed using matte black PLA

filament on the Lulzbot Taz6 3D printer. The vessel can hold up to 1 litre of sample if required.

Figure 4-11 Sensor calibration 1 L vessel, 3D printed with matte black polylactic acid (PLA) 2.85 mm diameter filament with 80% infill on a Lulzbot Taz6 printer.

4.2.3.1 Calibration of C12880MA Spectrometer for each Sensor Unit

The spectrometers used in the sensors were configured for each sensor unit built. As described in Section 2.2.6 each spectrometer unit came with a series of calibration constants which were component specific to calibration the 288 pixels with their respective wavelength output. An excel spreadsheet was setup to allow the conversion to be done automatically by entering the corresponding constants into Equation 2-1 to output the wavelengths for that specific spectrometer unit. Each sensor unit used two spectrometers with the spreadsheet tracking which spectrometers are installed in which sensor units by their serial numbers as seen in Table 4-3. The Figure 4-12 gives a sample of the pixel to wavelength conversion and table of the constants for C12208MA spectrometer 20L00254.

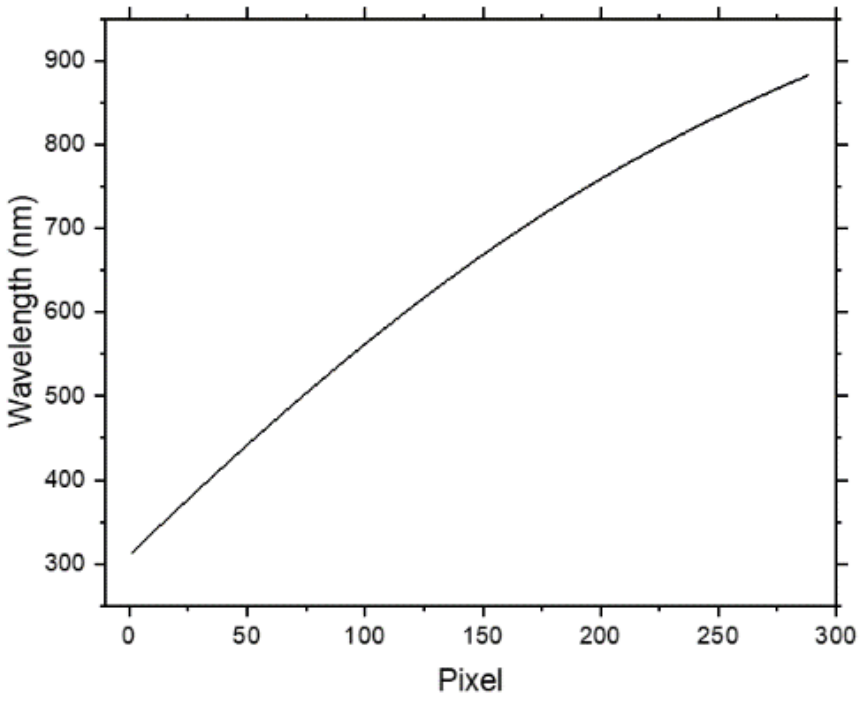

Serial No.	20L00254
A_0	3.104483509E+02
B_1	2.711828349E+00
B_2	-1.469334332E-03
B_3	-4.877979099E-06
B_4	-1.549035209E-09
B_5	2.039666340E-11

Figure 4-12 Sample pixel to wavelength conversion and table of calibration constants for C12880MA spectrometer 20L00254.

4.2.3.2 Sensor Measurement Stability Study

An experiment was conducted to study the sensors optical measurement stability over longer periods. This was done to ensure the LEDs, photodetectors as well as the electronic system recorded the data consistently. An absorption scan and a scatter scan were conducted every 10 min over 2.5 days. The sensor was placed in a dark controlled area where no ambient light or change of conditions would interfere with the sensor readings. In total 330 scans were recorded over this time period, representing a total of 7920 individual spectra. Statistical data analysis was performed on the scatter and absorption signals, except for the IR LED as there was an issue with the signal retrieved and the 280 nm UV LED as this was outside the range of the spectrometer for reliable results. The average and standard deviation for each pixel was calculated, while the standard error and coefficient of variation was calculated for the peak of each LED signal.

4.2.3.3 Interference Turbidity and Fluorescence Experiment

The effect of suspended particles on the fluorescence measurement of Chl-a was investigated with the measurement of three separate concentrations of BB3 dye at high, medium, and low levels of turbidity. The set turbidity levels are 7.14 NTU (Low), 13.74 NTU (Medium) and

26.9 NTU (High). Sensor unit 10 (see Table 4-3) was selected for the experiment. The set region of BB3 fluorescence measurement was between 0 mg/L and 1 mg/L at set measurements points of 0 mg/L, 0.1 mg/L, 0.5 mg/L and 1 mg/L concentrations.

4.2.3.4 Determination of Sensor Unit's Optical Limits of Detection for Target Analytes

The determination of the limits of detection for both Chl-a and turbidity was conducted by serially increasing the concentration of the target analytes in DI water to the point of saturation using the integration times outlined in Table 3-4. The measurement mode used for turbidity measurements is scatter using the 850 nm LED and an integration time of 0.2 s is used for the spectrometer sensitivity. Using BB3 dye as an equivalent for Chl-a, the measurement mode used for the detection of BB3 was fluorescence, using the 380 nm LED and an integration time of 2 s. This gave the lowest and highest point of measurement to outline the limit of detection in both directions for this set series of experiments within the fixed parameters of the set integration times. For turbidity, Reagecon CRS-4000-100 (4000 NTU) and Reagecon CRS-800-100 (800 NTU) turbidity standards were used. The sensor unit selected for testing was sensor unit 10. Using serial dilution of the BB3 to DI water a saturation limit was found. The fluorescence experiment is then repeated with algae diatoms of known concentration within the same limits of detection of the sensor. Using the calibration curve generated from the BB3 response and of the sensor response to the fluorescence from the diatoms, an equivalent comparison was made as a correction factor for the use of BB3 as a stand in equivalent for the calibration of sensors from Chl-a.

4.2.3.5 Calibration Methods for Chlorophyll a

The validation of Chl-a was completed using equivalent BB3 on replicate sensor units. A 100 mg/L BB3 (Stock 1) and 10 mg/L BB3 (Stock 2) stock solution was prepared from BB3 dye in DI water (18 MΩcm-1). Following on from the results of the LOD tests, five BB3 standard solutions in the range of 0 – 1 mg/L were prepared from the 100 mg/L BB3 stock solution (Table 4 8). Each standard solution was run on the sensor unit, with a background scan performed at 0 mg/L. For each concentration of BB3 the measurement was done in triplicate with the sensor output averaged over the three measurements.

Table 4-8 Summary table of volumes added for Basic Blue 3 (BB3) standard solutions used for calibration. Stock 1 = 100 mg/L BB3; Stock 2 = 10 mg/L BB3.

Solution ID	Stock 1 (mL))	Stock 2 (mL)	Concentration (mg/L)
1	0	0	0
2	1	0	0.1
3	2	0	0.2
4	6	0	0.6
5	10	0	1

4.2.3.6 Calibration Methods for Turbidity

The validation of turbidity was completed using standards, Reagecon CRS-4000-100 (4000 NTU) and Reagecon CRS-800-100 (800 NTU) on replicate sensor unit systems as follows. All units (Unit 2 – 10) were validated for turbidity. Five turbidity standard solutions in the range of 0 – 60 NTU were prepared from the 4000 NTU turbidity stock solution (Table 4-9). Each standard solution was run on the sensor, with a background scan performed at 0 NTU. Solutions were read at 850 nm (LED 1) For each turbidity concentration the measurement was done in triplicate with the sensor output averaged over the three measurements.

Table 4-9 Summary table of volumes added for Reagecon standard solutions used for calibration. Stock 1 = 4000 NTU; Stock 2 = 800 NTU.

Solution ID	Stock 1 (mL))	Stock 2 (mL)	Concentration (NTU)
1	0	0	0
2	1.25	0	10
3	2.5	0	20
4	5	0	40
5	7.5	0	60

4.2.3.7 Data collection

Communication software, Arduino and Teensyduino were used to interact with the sensor unit system over USB. Arduino was used to verify communications between the laptop and sensor by navigating to the ‘Serial Monitor’ command in the Tools tab of Arduino. Excel, with COM add-in, Data Streamer, was used to collect fluorescence readings from the sensor unit. The data channels were changed to 288 in the settings tab of the Excel file. The ‘Data Out’ tab was used to control the commands on the sensor unit. The command ‘RB’ was used to record a background signal, with ‘RW3’ being used to run fluorescence, absorption, and scatter signals (n = 3). Data collected was viewed in the ‘Data In’ tab and saved as a CSV file.

4.3 Results and Discussion

The results from the assembly and validation of the ten sensor units are presented in this section. The analysis of the results is conducted with the aim of evaluating the sensor unit's readiness for deployment in the marine environment and to produce robust quantitative data on the selected target analytes.

4.3.1 Fabrication and Assembly of Sensor Units

A total of ten sensor units were assembled successfully. The decision to build the sensor units is two batches allowed significant improvements to be made to the sensor design. The test batch of three sensors were available for testing to inform the design of the remaining sensor units to ensure there were no issues with the design that would have to be modified. By assembling a lower number of sensors first this allowed for improvements to the assembly process to speed up the assembly of the remaining sensor units by making the stages of assembly more efficient. The learnings from the build of the first three sensors were that it was more efficient to break the sensor build into subsystems and assign the task of building each subsystem for all the sensors to a block of time. This meant that the subsystems could be built quicker as more repetition was involved in the process and the final stage of the sensor assembly only consisted of putting the subsystems together. The progress of the assembly process can be seen Figure 4-13. In Figure 4-13a shows the internal frames were constructed from FDM printed components and four M3 and two M5 stainless steel rods and fasteners. A design bottle neck was found with the difficulty of using the M3 steel rods which were complicated to attach the 3D printed electronic mounts at the correct distance. This led to the design change which is described in Section 3.2.2.4. Figure 4-13b shows the assembled internal subsystems of the optical head and the main enclosure with all electronics ready for testing. The remaining seven sensor units were assembled over the course of a month and were completed by the end of August 2021. Figure 4-14 shows the fully assembled sensors lined up on the top of the figure as well as the arranged subsystems for each sensor. The assembly of the seven remaining units was conducted in a single month showing an efficient and streamlined production method was successfully implemented.

Figure 4-13 Assembly of the first three prototype sensor units (units 1-3) as design version 3. (A) FDM 3D Printed internal frames using M3 steel rods as spacers. (B) Assembled internal systems of the sensor.

Figure 4-14 Assembly of final stage design of sensor units. Below are the assembled subsystems ready to be integrated into the full sensor unit. On top is the completed remaining seven sensor units.

4.3.1.1 Cost of Materials

Cost of Electronics and Optics

To produce the PCBs, a fabricator was selected which would produce low cost and high-quality circuit boards with as quick as possible, delivery times. Many fabricators were considered based on the cost, delivery time and quality parameters. Fabricators based in China such as JLCPCB and PCBWay provide quick turnover circuit boards at a very low cost. Operating at a large scale and producing low quantity PCBs in batches with other orders, JLCPCB is able to offer two layered PCBs from $2 [373]. PCBWay offer up to ten 1-2 layer PCBs printed with a 24hr turnover [374]. However, given the timelines required for delivery and import duty costs associated, fabricators from China would be impractical for low scale high quality PCBs. European PCB fabricators are also considered given their closer proximity to Ireland reducing delivery times and import tax issues. Eurocircuits are a large-scale PCB fabricator based in Europe with a production plant located in Germany [375]. They can provide high quality low quantity batches of PCBs. The PCB costs are higher when compared to Chinese fabricators with an order of ten 100 mm x 80 mm PCBs priced at around €15 per PCB [375] compared to $5 price offered by PCBWay [374]. As a compromise and to obtain faster delivery times, Irish based PCB manufactures are considered. ECS Circuits LTD are an Irish based PCB manufacturing company which offer prototype, small batch to medium batch scales as well as PCB design layout assistance. However, the cost per PCB from ECS was too high. Betalayout Ltd are a European PCB manufacturer which are based in county Clare in Ireland. They offer a good compromise between high quality PCBs at lower quantities cost (around €17 per PCB for batch of ten 100 mm x 80 mm sized boards) and delivery times [376].

The bill of materials (BOM) for the electronic and optical components can be seen in Table 4-5. The table of components is broken up into the different categories with components, manufacturer, suppliers, quantity, and costs. The optics section includes the required optical components such as the lenses and mounting components. The primary suppliers of optical components are Newport Corp., Edmund Optics Ltd and Thor Labs Inc. For the collimation and plano-convex fused silica lenses, quotes were obtained from all three suppliers for comparison. For a quote of thirty 12 mm plano-convex lenses and ten 25 mm collimation lenses, Edmund Optics offered the best cost with €71 and €85 per lenses, respectively. Compared to Edmunds, Newport quote was €153 and €168 per lens and Thor Labs offered,

€85 and €97 per lens. The light source section gives the LEDs used on the light source. Many LEDs required were available from Mouser Electronics with specific LED components sourced from both Farnell Ireland and Digikey Ltd. The sensors section gives the photodetectors, temperature probe and current sensing components. Hamamatsu are the manufactures of the C12880MA spectrometer and provided a quote for €200 per spectrometer compared to secondary distributors such as Farnell Ireland with a price of near €400 [377]. The temperature sensor probe manufactured by Blue Robotics Ltd, was sourced from their European distributors BlueRov-Solutions. The additional cost from the European distributor was negated by the import duty on from products from the United States. The electronic components section details the general electronics used for the PCBs. The photodiode, current sensor and electronic components were sourced from Digikey Ltd. The details of the custom PCBs which were fabricated is given in the final section of the table.

Cost of Sensor Enclosure

The fabrication of many of the required components for the enclosure and optical head needed to be outsourced. Fabricators were selected based on quoted cost and delivery times. The main enclosure is the largest component that needed to be fabricated from POM-C. A local fabrication company. P&T Precision Engineering was the only fabricator that was able to offer a quote for the fabrication of the enclosures. The top cap also required POM-C to be machined however due to a smaller size other fabricators were able to give a quote. 3DHubs was selected to machine the top cap due to a lower quote. Additionally, 3DHubs offered FDM 3D printing for the internal frame and optical head sensor mounting components. Due to the complex geometry of the optical head, SLS 3D printing was selected for the fabrication method, Betalayout Ltd were selected to manufacture the optical heads as they also offered post processing procedures to waterproof the components.

The total cost of the enclosure components and materials is shown in Table 4-4. A combination of off the shelf components and custom fabricated components amounted to less than €700 per sensor unit. The sensor design and dimensions are based around certain off the shelf components which allowed the cost to be reduced, primary components that were sourced off the shelf are the 4” O-Ring Flanges that could be sourced from ROV component supplier component Blue Robotics. This strategy for low scale prototype

production allows for high-cost manufacturing of metal components to be avoided and relies on the supply for another larger producer.

Total Cost

The combined cost of the electronics/optical components (Table 4-5) and the hardware components and materials (Table 4-4) amounted to a total material cost of €1632.09 per sensor unit. For the quantity built, custom design and the multiparameter optical measurement capabilities of the sensor this shows a low-cost construction process was achieved. Given the nature of prototype production, there is high cost associated with materials and manufacturing due to lower quantities [356]. With higher minimum order quantities for larger scale product the materials cost to produce the sensors can be reduced significantly [378].

4.3.2 Sensor Units Quality Control Tests

4.3.2.1 Identification of Single Points of Failure of the System

The single points of failure SPOFs were identified to which areas of the design particular attention should be paid to. There were two primary categories of failure points: 1) mechanical failure and 2) electronic malfunction. Table 4-10 outlines the SPOFs of the sensor design and a description of how failure of this components would prevent the sensor from functioning.

Table 4-10 Identification of the sensor's single points of failure.

	SPOF Component	Description
Mechanical SPOFs	Air Valve Penetration	If the watertight interface O-Ring between the air valve penetrator and top cap fails, the sensor's watertightness will be compromised.
	Bulkhead Connector	If the bulkhead connector were damages power and communications to the sensor would be compromised and the O-ring seal with the top cap would allow water to enter the sensor.
	Flanges Face O-Ring	Two flanges are used with two face O-rings interfacing the top cap and the optical head with the flanges. If the O-Ring is compromised water will be able to enter the sensor.
	Flanges Radial O-Rings	The two flanges use two radial O-rings each to interface with the sensor body which if compromised will allow water to enter the sensor.
	Internal Frame	The internal frame is structurally necessary to keep the top and bottom flanges from being pulled out of the sensor body if under tension. If this were to fail the sensor's structure would be compromised.
	Optical Lenses Seals	Four optical lenses are installed in the optical head with epoxy seals interfaces which is not fully seals allow water to enter the sensor.
	Temperature Probe Penetrator	The temperature probe penetrator interfaces with the optical head using a face O-Ring which is fails allows water to enter the system.
Electronic SPOFs	Microcontroller	If the microcontroller were to be damaged the sensor would not be able to function.
	Voltage Regulators	If the voltage regulators were to be damaged the system would not receive the correct power and would not be able to function.
	MAX232 IC	If the serial output from the microcontroller is not converted to RS-232 no communications between sensor and external systems would function.
SPOF – Single Point of Failure, IC – integrated circuit		

4.3.2.2 Analysis of System and Subsystem Quality Control Tests

A test plan, schedule and checklist were drawn up with operation procedures to test each sensor unit with pass/fail criteria. The electronic systems tests allowed for faults caused during the soldering processed to be identified and addressed before permanent damage to the circuit board or sensing component could be done. Shorts were commonly detected after the reflow process with the case being noted as excess solder applied which allowed pints and contacts to be bridged while the solder was in a liquid state. The measurement of the

current draw of the system and components allowed for faults not visible with inspection to be identified. Faults with the LEDs were commonly found due to the polarity of the LED being reversed due to a placement error. The submersion overnight test to identify leaks in the sensor enclosure were successful in identifying which sensors were not watertight. However, the difficulty of identifying the location of leaks in the sensor housing structure led to a design change with the addition of an air valve on the top cap as described in Section 3.2.2.3. The addition of the air valve allowing the sensor to be pressuring was critical in identifying the exact positions of leaks in the sensor enclosure. The most common locations of leaks found while testing the sensors units were the 3D printed optical head, the epoxy surrounding the optical lenses, and the flanges on the top and bottom. All three points were identified as single points of failure, and an increased focus is given to them during testing.

Table 4-11 shows the initial results from the test procedures conducted on the ten sensor units after their construction in September 2021. The sensor units with fails are deemed not fully validated or ready for field deployments. The issues found by the performance tests require addressing and the sensor units will be retested. Initial issues with the electronics systems were found on the circuits boards of sensor 3 and sensor 9 with LEDs not turning on and above normal current draw the issues respectively. Sensor units 3, 5, 7 and 10 all failed the watertightness tests. Sensor 3 leaked after being submerged in a water tank overnight indicating a significant leak while sensor units 5,7 and 10 failed the air pressure test at 50 kPa after a 12-hour period which a slight pressure drop was observed indicated a slow leak either through the optical lenses or the O-ring seals of the housing. Due to either electronic issues or the housing not being deemed watertight the validation of optical configuration could not be carried out on those sensors until the relating issues are resolved.

Table 4-11 Sensor units initial performance tests after construction in September 2021

Sensor unit	Validation of optical configuration	Electronic system test	Water tightness	Testing status
1	Pass	Pass	Pass	Validation Completed
2	Pass	Pass	Pass	Validation Completed
3	Not Yet Tested	Fail	Fail	Validation Not Completed
4	Pass	Pass	Pass	Validation Completed
5	Not Yet Tested	Pass	Fail	Validation Not Completed
6	Pass	Pass	Pass	Validation Completed
7	Not Yet Tested	Pass	Fail	Validation Not Completed
8	Pass	Pass	Pass	Validation Completed
9	Not Yet Tested	Fail	Pass	Validation Not Completed
10	Not Yet Tested	Pass	Fail	Validation Not Completed

4.3.3 Validation and Calibration of Sensor Units Results

4.3.3.1 Sensor Optical Measurement Stability Analysis

Absorption

Figure 4-15 shows an example absorption spectra signal over the 2-and-a-half-day period for each LED. The R LED at 660 nm also must be disregarded at it is saturating in absorption mode. The difference in peak wavelength for each LED was due to different integration times being used and LED emission strengths differing between LED packages on the LED array.

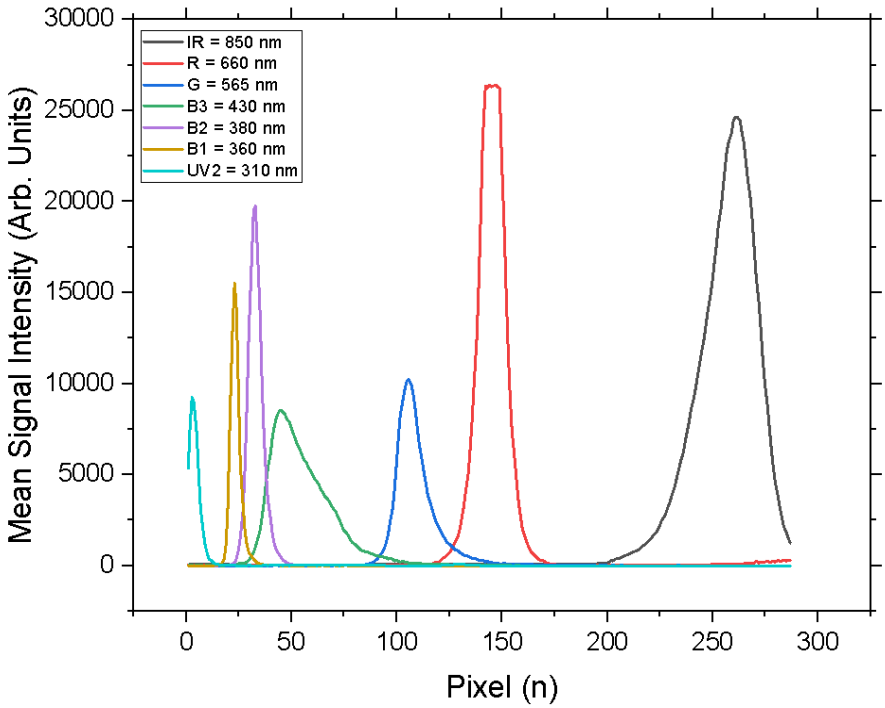

Figure 4-15 Mean absorption signal intensity of each LED averaged over 330 scans.

Table 4-12 shows statistical data calculated at the peak of each LED over the 300 measurements. For each LED the standard error, standard deviation and coefficient of variation were quite small indication that the LEDs and spectrometer are stable and can be relied upon for consistent data in absorption mode. The signals for each LED remain very stable over this period of acquisition of data, indicating good reliability. Figure 4-16 gives the peak wavelength sensor intensity measured over the total period. The standard error, standard deviation, and coefficient of variation for all LEDs are relatively small which indicates the sensor measurements in absorption are highly stable.

Table 4-12 Statistical data calculated at the peak of each LED over 300 measurements in absorption mode.

	IR	G	B3	B2	B1	UV2
Standard Error	8.111	6.570	5.518	12.776	11.724	4.569
Mean Value	24753.5	10286.5	8569.8	19757.4	15483.6	9295.2
Standard Deviation	147.3	119.4	100.2	226.4	213.0	83.0
Coefficient of Variation	0.006	0.012	0.012	0.011	0.014	0.009

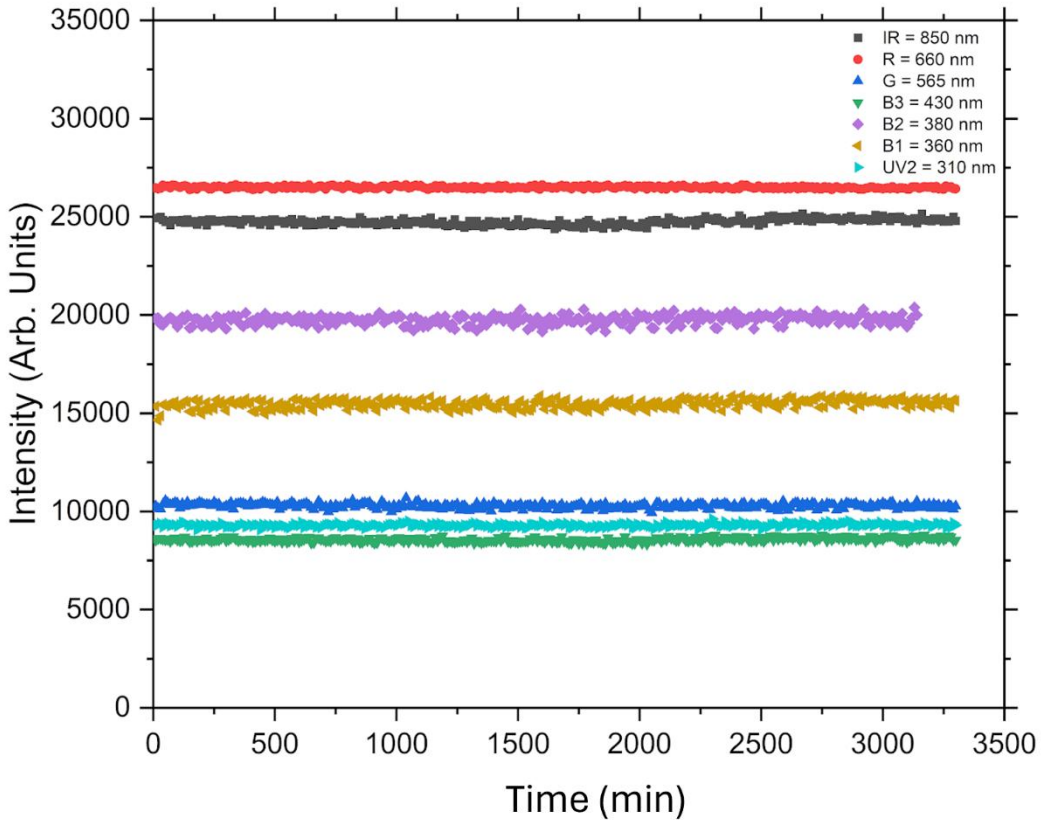

Figure 4-16 Peak signal for each LED in absorption mode over the full course of the data acquisition totally over 330 data points.

Scatter

The same method was applied to the scatter mode measurement which uses the second spectrometer in a 90-degree orientation to the light source. The IR 850 nm LED was not included due to low signal in this measurement mode. Figure 4-17 shows the averaged spectral scans of each LED in scatter mode. There is a disparity between the LED's signal intensities due to the different integration times used as shown in Table 3-4 for scatter measurements.

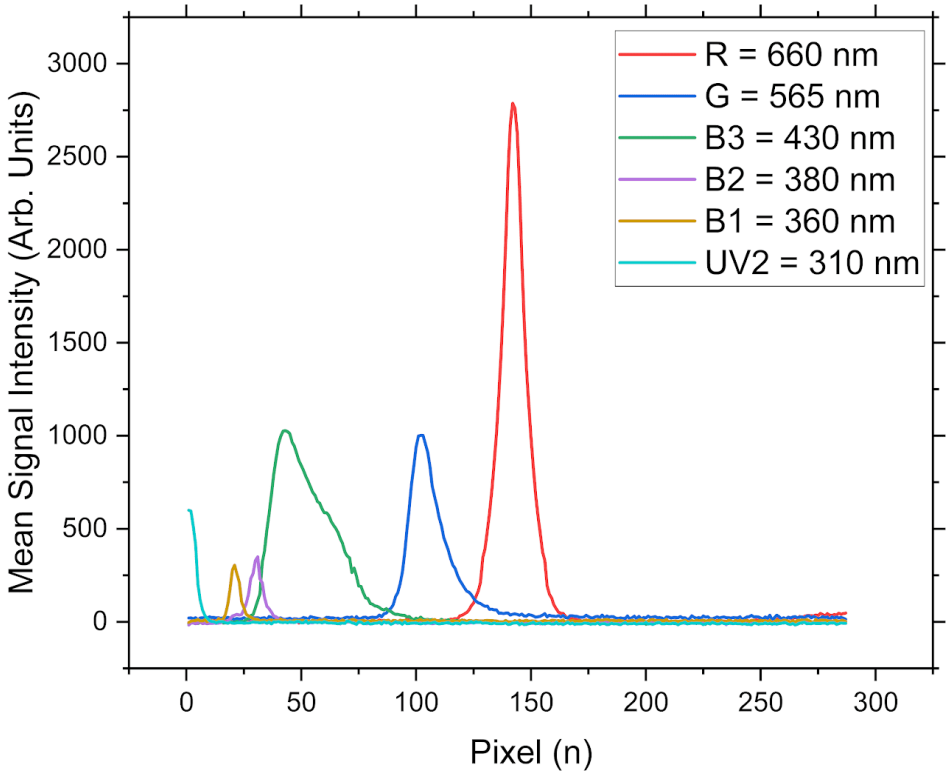

Figure 4-17 Mean scatter signal intensity of each LED spectra recorded by sensor averaged over 330 scans.

Table 4-13 shows the statistical results for the scatter mode measurements over the 2-and-a-half-day period. There is an increase in variation between scatter and absorption however this is due to the lower signal strength measurement by the spectrometer from the LEDs output in scatter mode. The peak intensity for each LED is plotted over the duration of the experiment for scatter mode in Figure 4-18. The signal strength is much lower and closer to the noise floor which increases variance in the results. As the measurement mode relies on particles of scatter to be present to detect a strong signal this baseline measurement is not significant.

Table 4-13 Statistical data calculated at the peak of each LED over 300 measurements in scatter mode.

	R	G	B3	B2	B1	UV2
Standard Error	4.508012	4.571711	2.911876	4.156092	3.5603	4.523243
Mean Value	2822.979	1077.209	1090.4	439.6364	340.9212	629.9394
Standard Deviation	81.89211	83.04925	52.89685	75.49915	64.82914	82.1688
Coefficient of Variation	0.029009	0.077097	0.048511	0.171731	0.190159	0.130439

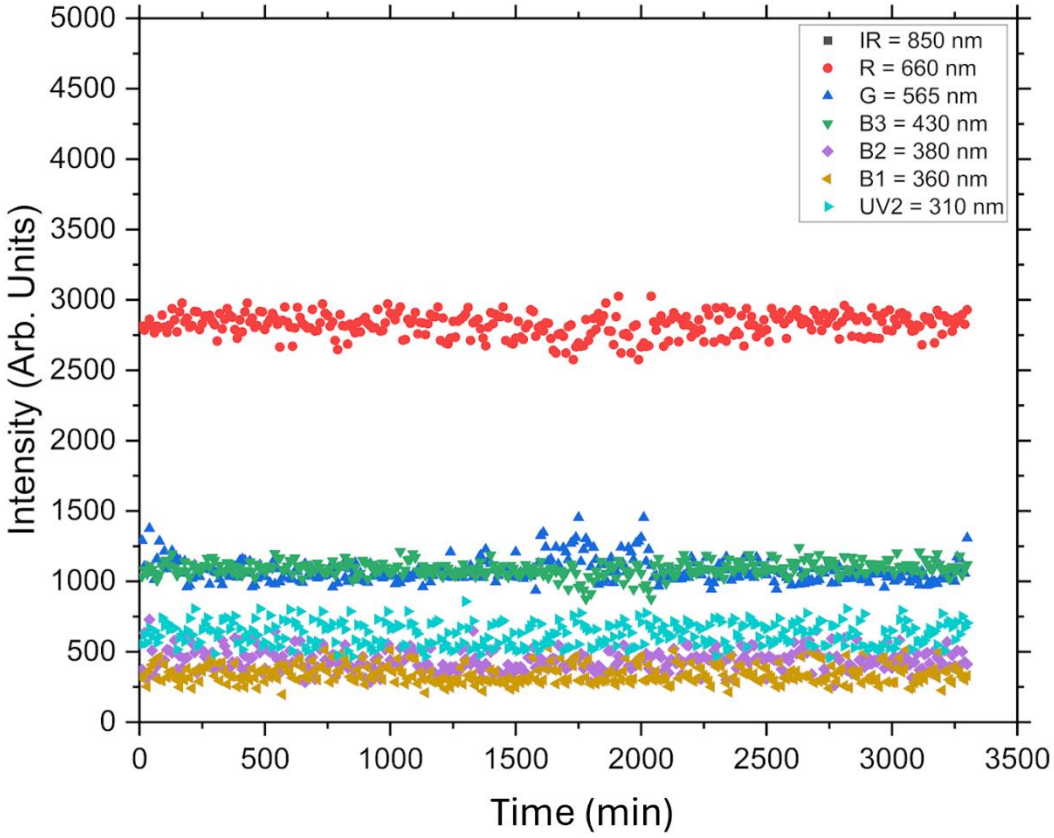

Figure 4-18 Peak signal for each LED in absorption mode over the full course of the data acquisition totally over 330 data points.

4.3.3.2 **Interference Turbidity and Fluorescence Experiment Results**

The three separate fluorescence measurement experiments at different spiked levels of turbidity can be seen in Figure 4-19. Figure 4-19a is the fluorescence measurements at a low turbidity, Figure 4-19b the measurement at medium turbidity and Figure 4-19c is the measurement at a high turbidity level. From Figure 4-19 and Table 4-14 of the data with the

base line subtracted there does not appear to be any clear interference caused by the level of turbidity on the fluorescence measurement.

Table 4-14 Sensor response of increasing concentrations of BB3 with low, medium, and high levels of turbidity. Both turbidity and fluorescence measurements are unaffected by matrix effects.

	Scatter 850 nm				Fluorescence 665 nm		
BB3 (mg/L)	Low	Medium	High		Low	Medium	High
0	11893.67	16372	23671.67		8330.33	8332.667	8478.33
0.1	12188.33	16351	23168.67		11952.67	11611.67	11935
0.5	12063	15984	23126		18479	17384.33	18157.67
1	12035	15407	23395		20000.33	18788.67	19657

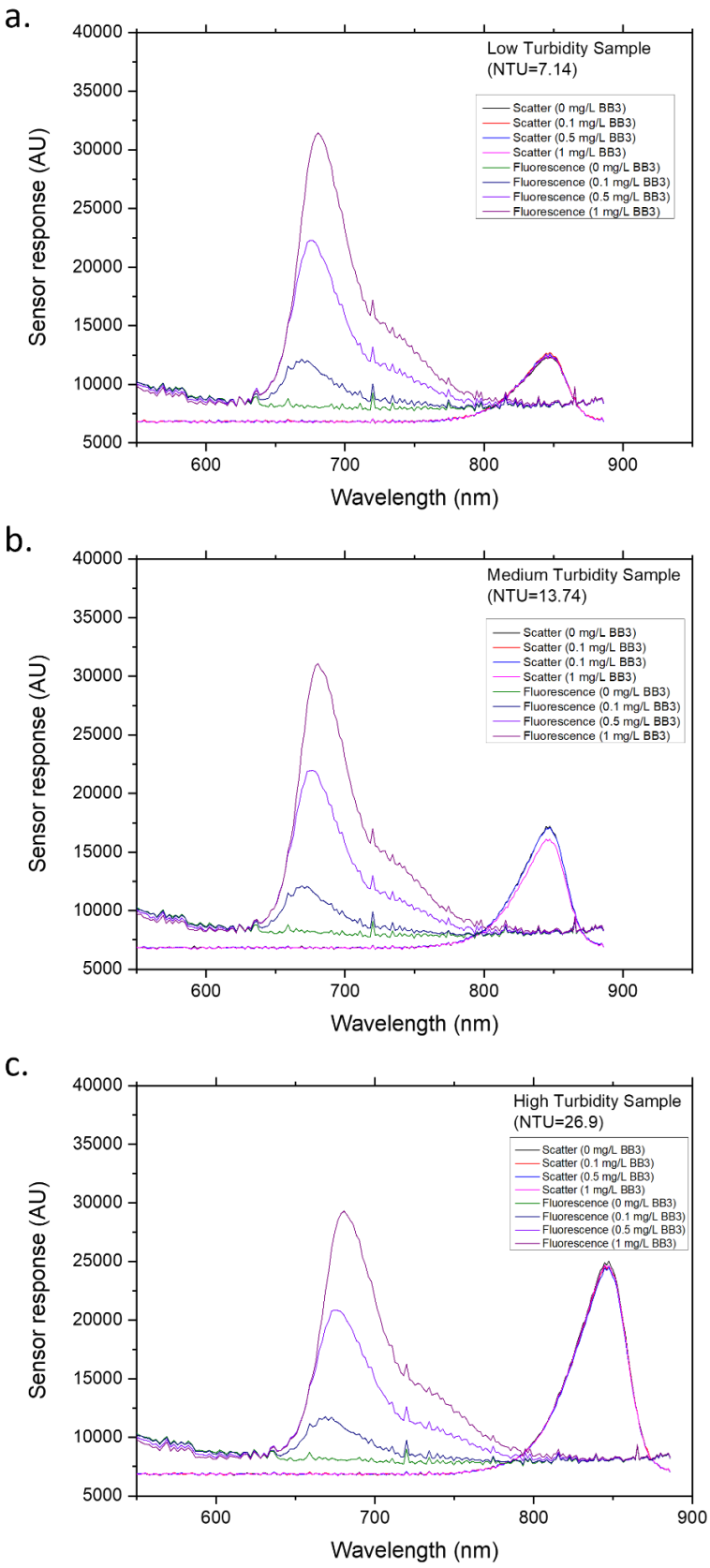

Figure 4-19 Sensor response measuring fluorescence emission of basic blue 3 spiked with low (a), medium (b) and high (c) levels of turbidity. The fluorescence and turbidity spectra measured by the sensor are overlaid. The turbidity measurements remain consistent while the fluorescence measurement at the different concentrations for each turbidity level are unaffected.

4.3.3.3 Determination of Sensor Unit's Optical Limits of Detection for Target Analytes

Figure 4-20 shows the measurement of BB3 fluorescence emission by the sensor over a range of concentrations using the 380 nm LED and a fixed integration time of 2s. Figure 4-20a is the spectral response of fluorescence at the different concentrations. The point of saturation was found at 1 mg/L for this integration time as seen of the spectral response at the peak of the 1.125 mg/L measurement. The sensor response at 1.125 mg/L levels out at the peak wavelength which is an indication of saturations of the system. The fluorescence response measured by the system was plotted as a scatter plot as seen in Figure 4-20b. The sensor response corresponding to the point of 665 nm or the peak fluorescence emission wavelength of BB3 was plotted. A linear fit was applied giving a 0.9987 R^2 value. A slope of 24044.72 sensor units (AU) per 1 mg/L of BB3 was determined from the linear fit and a standard error of 216.47 showing high reliability between the measurement data points and the linear fit applied.

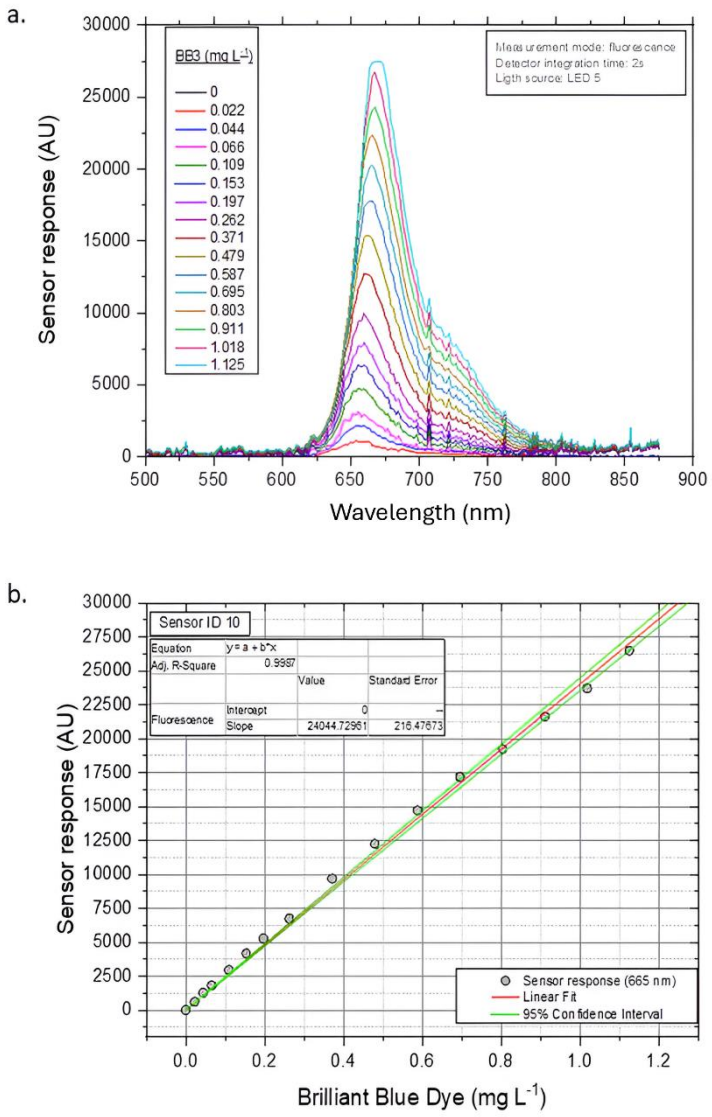

Figure 4-20 Calibration curve for BB3 generated by the spectral measurement of the fluorescence emission taking the sensor response of the pixel intensity corresponding to the peak wavelength of fluorescence emission at 665nm. Excitation light was from a 380 nm LED. Saturation point of detector found at 1.125 mg/L. Conducted on sensor unit 10 (n = 3) with 2 s integration time.

Figure 4-21 shows the sensor response of the measurement of fluorescence from extracted Chl-a form diatoms. The method for extracted is described in Section 2.2.6.3. Using the same measurement setup as with BB3 the saturation point at 59.89 µg/L can be seen from the spectral response on the left. This gives a maximum measurement range of 44.92 µg/L of Chl-a. Figure 4-21b is the linear fit applied to the corresponding 665 nm sensor response. The linear fit at this wavelength produces an R^2 of 0.9958 showing good linearity. The slope of the linear line gives 546.2 sensor response units (AU) for every 1 µg/L of Chl-a. Applying Equation 3-2 shown in Section 3.3.4, the sensor resolution is calculated to be 0.0275 µg/L for this range using the 2 s integration time. A standard error of 14.4725 is shown which

indicates a strong relationship between the measured concentrations and the linear fit. A correction factor can be calculated from the two calibration slopes generated for BB3 and Chl-a by applying Equation 4-1.

$$CF_{BB3\ to\ Chl-a} = \frac{Slope_{Chl-a}}{Slope_{BB3}} \qquad 4\text{-}1$$

Where $CF_{BB3\ to\ Chl-a}$ is the correction factor to convert BB3 calibration to Chl-a equivalence. $Slope_{Chl-a}$ is the slope from the calibration curve generated from extracted Chl-a in AU/ µg/L. $Slope_{BB3}$ is the slope generated from the calibration curve from BB3 in AU/µg/L which gives 240.44 AU/µg/L of BB3. This results in a correction factor of 2.271 which gives for every 1 µg/L of Chl-a is the equivalent to 2.271 µg/L of BB3.

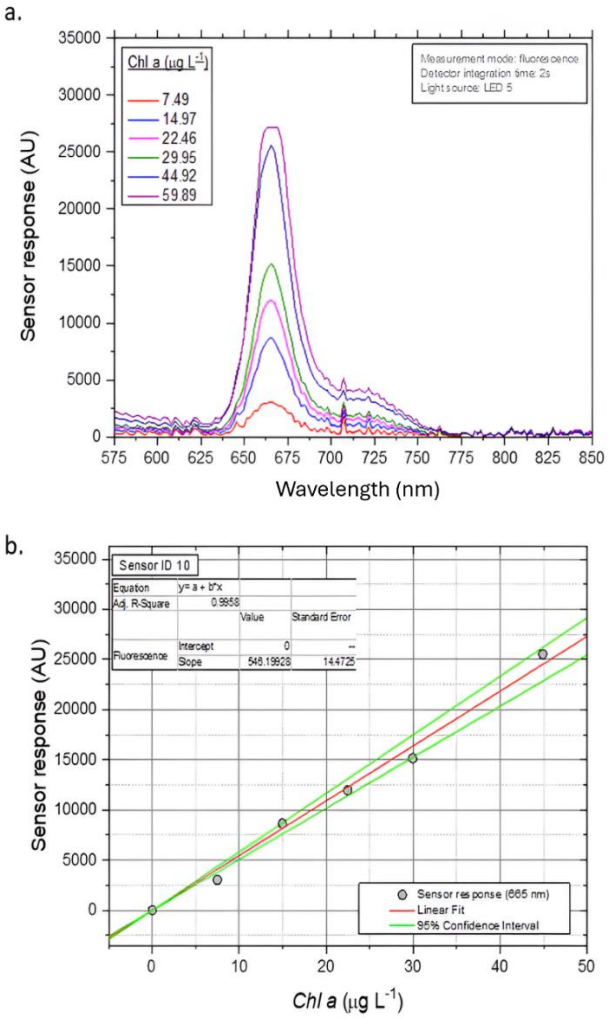

Figure 4-21 Calibration curve for algae diatoms generated by the spectral measurement of the fluorescence emission of Chl-a taking the sensor response of the pixel intensity corresponding to the peak wavelength of fluorescence emission at 665 nm. Correction factor calculated for BB3 standard equivalent. Saturation point of detector found at 59.89 µg/L. Excitation light was from the 380 nm LED. Conducted on sensor unit 10 (n = 3) with 2 s integration time.

The determined limit of detection of the measurement of turbidity using scatter IR can be seen in Figure 4-22. Using turbidity standards, the peak NTU value measured before saturation at the 0.2s integration time was 32.34 NTU as seen by the levelling out of sensor response at the peak wavelength. Figure 4-22b is the scatter plot with linear fit of the sensor response at 850 nm. The linear fit produces an R squared value of 0.99677. The slope of the linear fit is 301.25 sensor response units (AU) for every NTU value. Using Equation 3-2, the sensor resolution is calculated to be 0.00022 NTU within this range using the 0.2 s integration time.

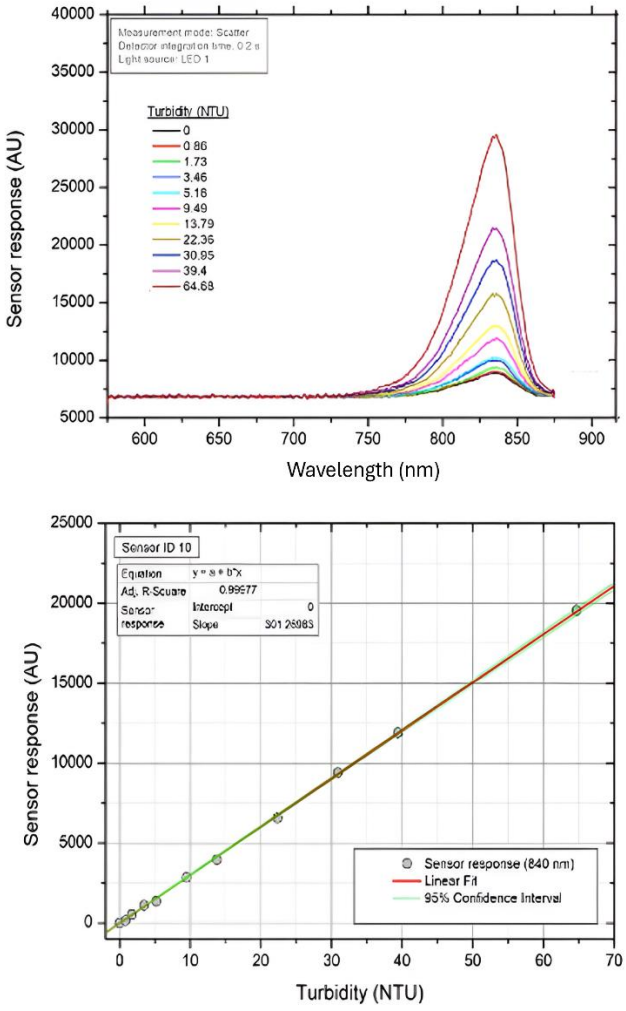

Figure 4-22 Calibration curve for turbidity using NTU standards generated by the spectral measurement of the scatter taking the sensor response of the pixel intensity corresponding to the peak wavelength of scatter emission at 850 nm from the IR LED. The saturation peak was found at 64.68 NTU giving the upper limit of detection. Conducted on sensor unit 10 (n = 3) with 0.2 s integration time.

4.3.3.4 Sensor Units Calibration for Chl-a and Turbidity

For the calibration of the ten sensor units, due to project requirements Unit 1 was unavailable for calibration as it was used as a data output testing platform by the projects industrial partner TechWorks Marine for testing of their data acquisition platform in preparation of in situ deployments.

Chl-a Calibration

The calibration curves generated for Chl-a using BB3 as the equivalent in fluorescence emission for the nine available sensors can be seen in Figure 4-23 including a table of the line equation of the linear fit applied. A good linear relationship is seen for all sensors with R^2 values above 0.99. Unit 2 demonstrated the lowest sensitivity with a slope of 10372 with Unit 3 having a slope of 16719. The design version 4 sensors produced slopes between 18080 and 22764 with unit 10 the outlier with a slope of 15231. This shows variation in slopes between sensors with a number of factors potentially effecting the calibrations. There is a distinction in sensor sensitivity between the design version 3 units (units 2 and 3) and the design version 4 units (units 4-9) with unit 10 being the outlier. Each sensor was assembled by hand including the optical head and electronics which may contribute to variability. Variations in concentrations when mixing solutions may also be a factor in the variability or the distribution of dye in the solution during testing. Each sensor has a unique response in the measurement of fluorescence which will need to be considered when used in producing quantitative data in the marine environment.

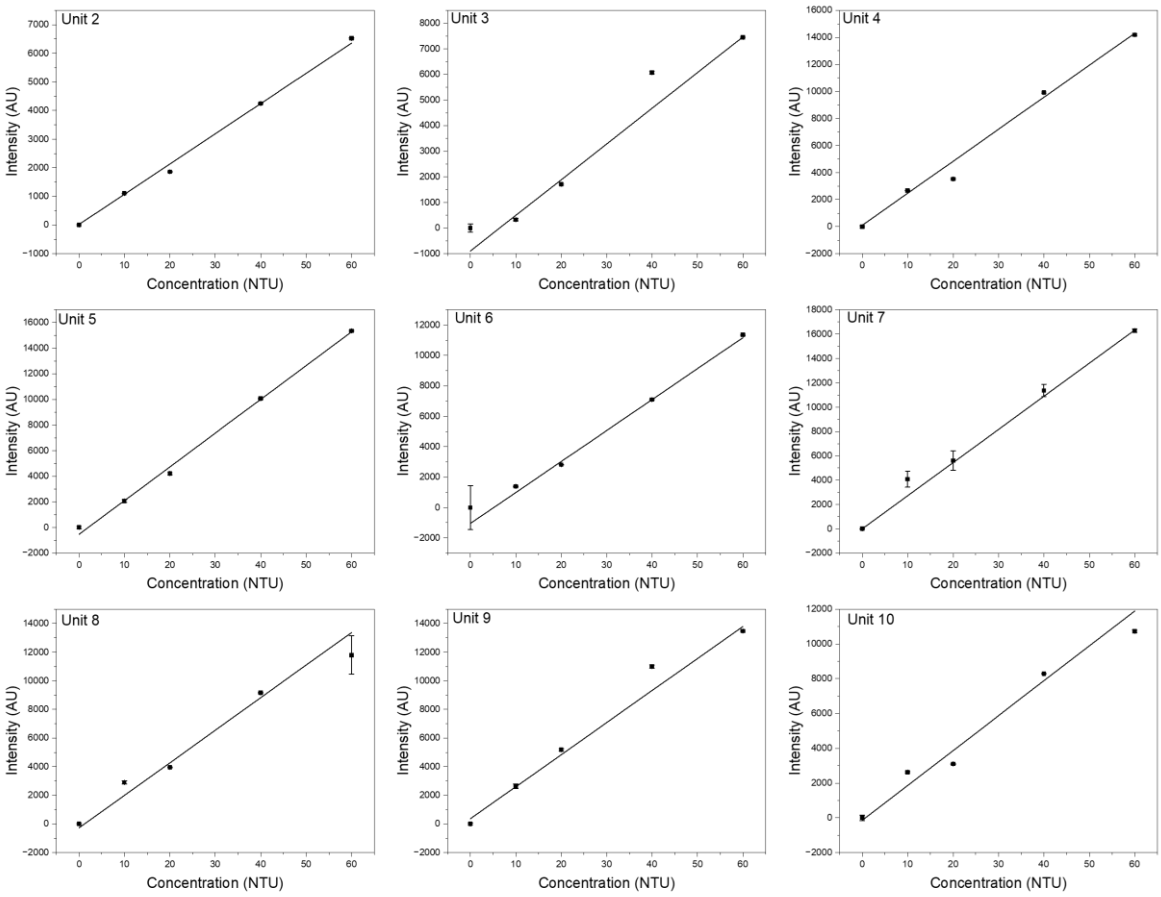

Sensor Unit	Slope	Y-Intercept	R^2 Value
Unit 2	77.074	-92.529	0.9972
Unit 3	98.914	-534.86	0.9636
Unit 4	170.55	-222.85	0.9914
Unit 5	184.59	-459.77	0.9967
Unit 6	136.21	-494.03	0.9918
Unit 7	187.73	+549.3	0.9943
Unit 8	140.6	+380.63	0.9889
Unit 9	164.95	+380.06	0.9848
Unit 10	128.74	+65.38	0.9844

Figure 4-23 Calibration curves generated for Chl-a sensor units 2 to 10 measuring fluorescence of BB3 dye (Chl-a equivalent standard) concentrations between 0 and 1 mg/L (n = 3) with table of linear line equations.

Turbidity Calibration

The calibration curves for turbidity for the nine sensor units can be seen in Figure 4-24. The calibration curves are generated between 0 and 60 NTU for each sensor. A good linear response is seen for all sensor units tested with unit 3 having the lowest R^2 value of 0.9636, all other units are above 0.98. As was the case with the fluorescence BB3 calibration curves, unit 2 demonstrates the lowest sensitivity. There is a distinction between the units built as design version 3 (units 2 and 3) and design version 4 (units 4-10) in sensitivity with units

built as design version 4 showing higher sensitivity in turbidity measurements. Once again, the variability in slopes for each unit may be down to the assembly of the units or human error in making the solutions, or variability in the distribution of suspended particles in the mixture varying the amount of light scattered.

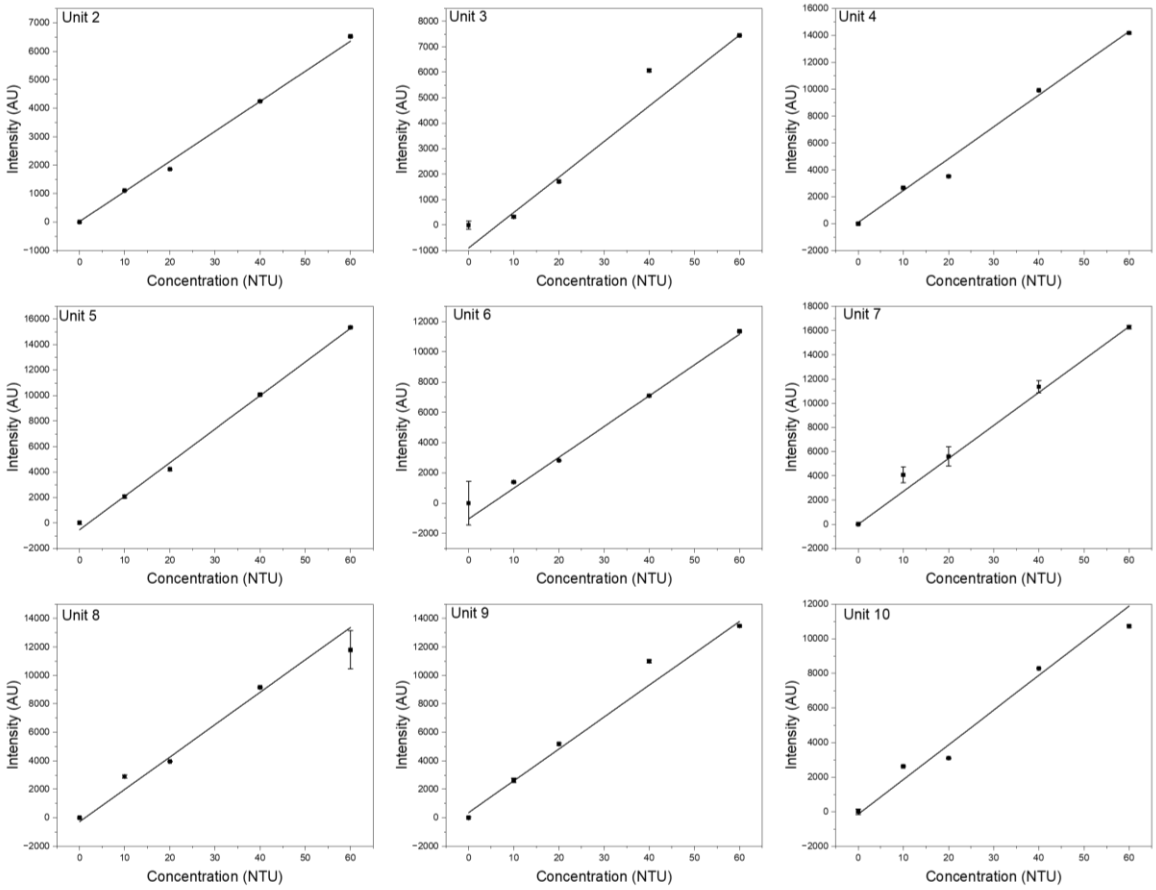

Sensor Unit	Slope	Y-Intercept	R^2 Value
Unit 2	77.074	-92.529	0.9972
Unit 3	98.914	-534.86	0.9636
Unit 4	170.55	-222.85	0.9914
Unit 5	184.59	-459.77	0.9967
Unit 6	136.21	-494.03	0.9918
Unit 7	187.73	+549.3	0.9943
Unit 8	140.6	+380.63	0.9889
Unit 9	164.95	+380.06	0.9848
Unit 10	128.74	+65.38	0.9844

Figure 4-24 Calibration curves generated for turbidity for all sensor unit 2 to 10 over concentration range of 0 - 60 NTU (n = 3) measuring scatter at 90 degrees with 850 nm LED with table of linear fit line equations.

4.4 Conclusion

The aim of the work presented in this chapter was to scale up the assembly of ten sensor units at low cost, test their readiness for in situ deployments and validate the optical measurements to produce robust quantitative data. An efficient prototype production method was developed for the low scale fabrication and assembly of multiple optical sensors in a research laboratory. The sensor units were produced at a low materials cost for small scale product. A systematic testing protocol was developed ensuring checks on each system and subsystem built during assembly to guarantee fully functioning sensor units. The sensor units' optical measurements were validated to provide stable, robust, and calibrated data output for key environmental parameters.

The objective of building multiple sensor units consistently was achieved with an efficient approach to developing a production line to scale up assembly of prototypes. The decomposition of a design into subsystem proved to be highly effective in allowing quick and consistent assembly of full systems. The use of a test batches to assembly first gave key insights into bottlenecks in the assembly process which were modified to make assembly easier for larger batches. Testing each subsystem as the sensor units were being assembled allowed minor flaws to be detected early which saved time overall. The total cost of materials to produce each sensor was €1632.09 with potential to be reduced at larger scale production.

The generation of accurate calibration curve for each individual unit for both turbidity and Chl-a was accomplished with an effective validation protocol. This protocol is applicable for any target analyte the sensor units can optically measure allowing for standardised quantified data to be applied to any sensor unit at scale. This is a novel approach in sensor unit validation which has not been conducted in any known literature as the writer's knowledge. The application of this method can help contribute to scaled up product of lower cost, high resolution next generation in situ sensors for deployment at scale as dense sensor networks while providing uniform data sets from the localised deployment sites. Pre-calibration tests confirmed the sensors measurement stability over extended periods which gives confidence in the electronic optical system design's ability provide dependable data during deployments. The limits of detection of the sensor for both Chl-a and turbidity. Basic blue 3 dye was shown to be a suitable calibration standard for fluorescence of Chl-a allowing

for a less resource intensive calibration process at scale eliminated the need for algae cultures. Turbidity levels were known not to affect fluorescence measurement. The calibration curves generated for all sensors showed a variation between each sensor unit show a unique performance specific to each individual unit built. Table 4-15 shows the sensor unit's performance relative to typical resolution and detection ranges for turbidity and chl-a. The sensor demonstrates a high resolution compared to state of the art requirements. The range is limited due to the calibration requirements however the dynamic capabilities of the spectrometers with use of the integration time being able to be changed allows for the range to be extended for any target analyte. Future work is required to develop the method for adapting the sensor response for calibrated response over a dynamic range.

Table 4-15 Comparison of performance of developed sensor with typical commercial sensor performance for environmental parameters of turbidity and chlorophyll-a.

Developed Sensor Performance			
Environmental Parameter	Resolution	Range of Detection	Reference
Turbidity Chl-a	0.00022 NTU 0.0275 μg/L	0-64.68 NTU 0-44.92 ug/L	- -
Typical Commercial Sensor Performance Ranges			
Environmental Parameter	Resolution	Range of Detection	Reference
Turbidity Chl-a	>0.02 NTU 0.007 – 0.1 μg/L	0-400 NTU 0 – 400 μg/L	[89,101] [341,348]

In summary, the key outcome of this work is a total of ten optical sensors ready to be deployed able to generate accurate environmental data. The sensor units developed highlight a unique and advanced optical sensing approach and are shown to produce precise analytical data of target analytes. The sensors were produced at a low cost which given their potential for multiparameter measurement produce a disruptive technology that could be adopted at large scale to revolutionise the way sensor networks monitor coastal and ocean environments. The methods and protocols for scaled up assembly, testing and validation demonstrated are novel in research level sensor prototyping. There is major potential for application to other research-based sensor design projects to bridge the gap between lab developed prototypes and commercially achievable environmental sensors. To achieve the overall goal of the thesis, the sensors must now be tested in the marine environment through long term deployments to further evaluate their performance and reliability in real-world conditions.

5 DEPLOYMENTS AND DATA ANALYSIS

5.1 Introduction

There is a pressing demand for an increase in operational architectures (autonomous and in situ) at regional and global scales for monitoring coastal and oceanographic zones. Coastal sensor networks for real-time decision support and marine networks for ocean observations, are instrumental in our understanding of waterbodies biochemistry, the impacts of anthropogenic pollutions and what mitigation strategies should be implemented. The high spatial and temporal variability of oceanic signals make monitoring ocean biogeochemistry and biology extremely challenging with long-term trends masked by major short-term natural variability [379]. It is also logistically and economically difficult to cover both short-term and long-term changes in the right locations given the size of the oceanic environment. Regional-to-global in situ oceanic observing networks have been established in response to this challenge such organisations include the Global Ocean Observing System (GOOS) [19], the Ocean Observatories Initiative(OOI) [20] and the U.S Integrated Ocean Observing System(IOOS) [23]. However, using current sensing technologies, the networks must compromise to either have greater spatial coverage limited and lower temporal coverage or vice versa [311]. The requirement for higher spatial and temporal resolution combined has led to a paradigm shift of focus in ocean science and engineering to build lower cost and lower power in situ sensors at larger scales. [13,311].

The main drawback to establishing large scale sensor networks to date has been the capital costs of the sensor units themselves and costs related to deploying and maintaining the sensors in the field, their limitations of detection and length of time they can be deployed for. The average in situ ocean sensor costs in the region of ~$10k which is prohibitive to any national or environmental monitoring body looking to deploy a fleet of sensors to monitor a wider area. The maintenance costs are also steep (up to 80% of deployment costs) given the limitation of the sensors to remain operational in the field for extended periods of time [380]. The nature of the harsh environment the sensors are being placed in required robust materials and design, accurate and reliable electronic sensing components and inherent low scale production numbers cause the price of commercial ocean sensors to be expensive. Reasons for the sensors needing maintenance or to be withdrawn from the field can be anything from reliability issues, component failure, damage to moorings or biofouling build up on the sensor causing drift and reducing accuracy of the instrument [26,380,381]. Limitations of detection can consist of both electrical response capabilities of sensing

components available, and the hardware complexities involved in implementing them, as well as software challenges of implementing algorithms to extract quantitative measurements from raw data within limited ranges. Transmitting data from the sensors to a network while in remote locations (telecommunications, data limits and transmittance ranges) can pose significant logistic challenges in turns of power and range requirements [18]. Another factor which can limit the length of deployment of the sensors is power consumption, especially for remotely deployed sensors which rely on battery power built into the sensor or provided by a buoy or mooring [382].

Scaling up to larger numbers of sensors in a high-density network requires deployment platforms to attach sensors and instruments to provide infrastructure to operate them, provide power and telemetry for data transfer. Many deployment platforms exist for this purpose in different forms and for different locations which are capable of providing 3D spatial resolution at high temporal frequencies which are covered in depth in the following reviews [19,383,384]. State of the art autonomous surface platforms (gliders, floats), AUVs, fixed location moorings, buoys, and the use of boats of opportunity have made deployment of sensors more cost-effective and more practical. This is in part due to the decrease in payloads driven by recent advancements in the miniaturisation of sensing technologies.

5.1.1 Deployment Hardware and Moorings

When deploying in situ, sensors must be fastened securely to ensure they do not drift from the point of measurement. Figure 5-1 below shows examples of different mooring methods and structures. Maintaining a stable position is crucial for the sensor to provide accurate and consistent data on a localised area. High strength clamps, cages, ropes and chains can be used to secure the sensor to a mooring under harsh marine conditions [385]. Clamps and cages (Figure 5-1c and d) directly secure the sensor to provide protection and structural support. These components are fabricated from corrosion resistant, marine grade materials to withstand prolonged exposure to sea water. Ropes and chains also provide a method of attaching sensors to a stable mooring point such as buoy (Figure 5-1b and c), ship or fixed structure such as a harbour wall or jetty (Figure 5-1a). The mooring used in dependent on the location of the measurement site and the depth of the sampling area.

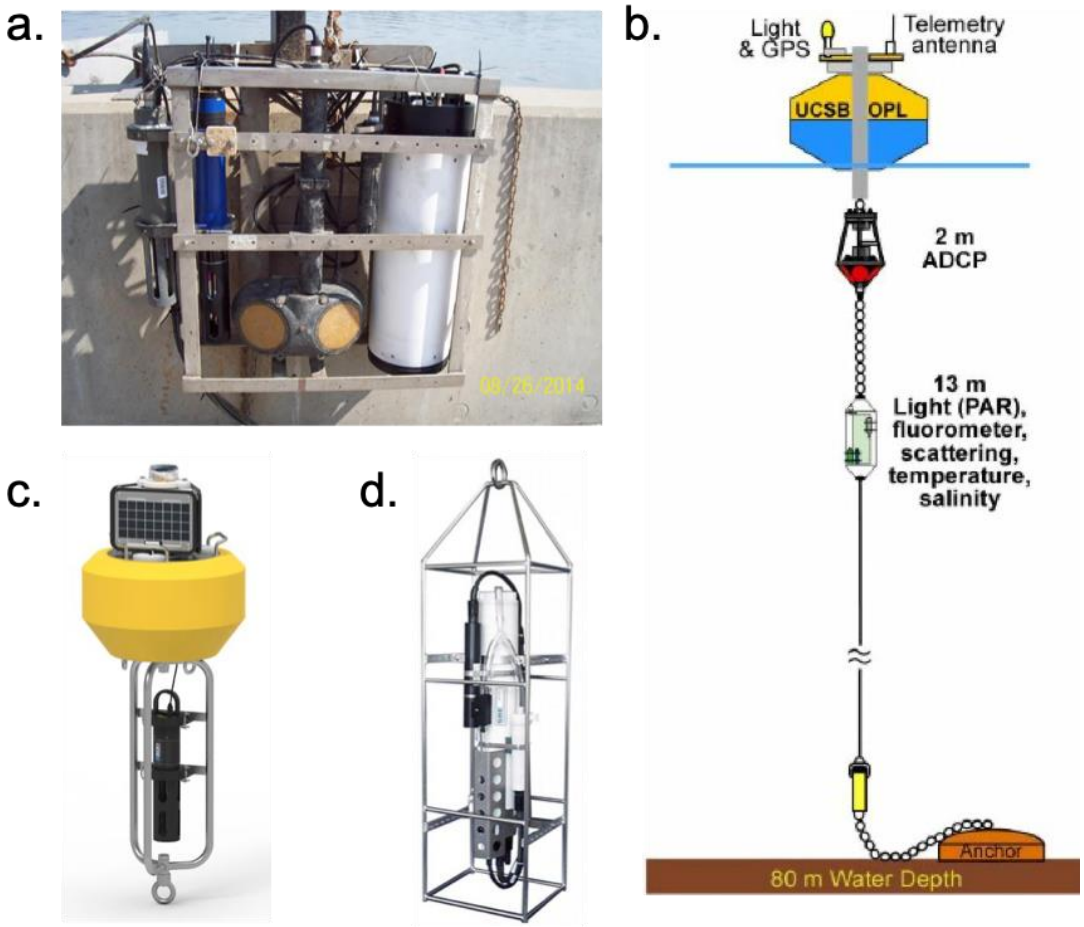

Figure 5-1 Example of sensor mooring systems. (a) Pier mounted enclosure housing multiple sensors [386]. (b) Schematic diagram of a shallow water mooring modified from Benson et al. (2008)[387]. (c) NexSens CB-25 Data Buoy with sensor mounting cage beneath [388]. (d) Stainless steel mounting cage for the SBE 19plus SeaCAT [389].

5.1.2 **Deployment Communication Hardware**

To operate sensors in situ, external hardware is required to interface with the sensor and collect data in the field. Dataloggers are commonly used to retrieve and store data from sensors in the field where access is limited, or timespan of deployments are impractical to remain on site. The datalogger for this application needs to be, portable, able to provide power to the sensor, switch the power on and off to the sensor as well as reliably communicate with the sensor. Commercial datalogging devices are often manufacture specific, use closed hardware that can be modified for custom application and are relatively expensive [390]. There are many examples of researchers developing their own "low-cost" and open source dataloggers taking advantage of inexpensive hardware components [391–393].

Specific cables and connectors are also required for any hardwire connections made between devices in the marine environment [394]. There are two separate categories of connection types for underwater applications: dry-mate and wet-mate (see Figure 5-2). The connection between dry-mate connectors and cables must be made before the assembly is submerged. Whereases, wet-mate connection assemblies allow for connections to be made underwater. The benefit to these types of wet-mate connectors/cables is that they are impervious to moisture while they are connected [395]. It is required for marine cables to have a watertightness rating of IP68 to insure complete isolation of the electrical connections from the environment [396]. Marine cables are durable using robust materials in their construction. Rubber moulded connectors are most commonly used typically made from neoprene or polyurethane [394]. The rubber moulded around the electronic contacts creates a watertight seal between the male and female connectors. The cables can withstand more force, while the integrated strain relief takes additional pressure off the wet-mate connector giving a much more durable and rugged connection [394]. This is done by using a rigid shell or bulkhead assembly which surrounds the rubber body allowing for a strong mechanical coupling [394,397].

Figure 5-2 Examples of dry-mate connectors (on the left) and wet-mate connectors (on the right) sourced from Remouit et al.,2017 [398].

5.1.3 Aims and Objectives

The aim of the work presented in this chapter will be to assess the robustness of the design and capabilities of the built sensors to provide reliable environmental data in situ. This will

be done through multiple deployments of the sensor units in different aquatic environments. The objectives required to achieve this aim are:

1. An assessment of the sensors' power will be conducted, and a method to optimize power usage for longer-term, battery power-dependent deployments will be developed.

2. A large-scale deployment will be conducted using multiple sensor units to be deployed in a total of five different locations across Dublin Bay, Co. Dublin over the course of 3 months. This deployment will be conducted in collaboration with the project's industrial partner TechWorks Marine (TWM). Data integration and management protocols will be required to interface the sensor with TWM's preexisting deployment infrastructure. The outcome of this deployment will give valuable insights into the sensor unit's suitability for long-term deployments in harsh conditions as well as the sensor unit's ability to monitor environmental changes in the marine environment.

3. A second series of deployments in a freshwater environment (Owenmore River, Co. Sligo) will be conducted to explore the versatility of the multispectral measurement capabilities of the sensor design. The development of custom deployment hardware will be required to operate, power, and retrieve the data from the sensor over longer periods while deployed.

5.2 Materials and Methods

5.2.1 Deployment Materials

The cable provided power to the sensor and data communication between the sensor and the external hardware device. Table 5-1 outlines the pin connections required by the sensor to be powered and communicate with external hardware over the RS-232 protocol.

Table 5-1 Table of pin connections from sensor to external hardware.

Pin	Function
1	Ground
2	Reserved
3	Reserved
4	Vin (12v)
5	RS-232 (Tx)
6	RS-232 (Rx)

The components of the cable assembly were, a male bulkhead connection which was attached to the sensor unit, a female cable end connector and the cable itself. MacArtney Underwater Technologies were selected to supply the cable assembly. The MCBH6M Subconn connector, seen in Figure 5-3a, was selected at the bulkhead connector. This mates with the corresponding female cable connector, MCIL6F (Figure 5-3b). A locking sleeve, MCDLS-F, (Figure 5-3d) fitted over the MCIL6F and threaded over the MCBH6M bulkhead to ensure secure connection was maintained. The cable (Power/signal cable - Type 2009/B) selected consisted of two twisted pairs for data communication and two solid core power wires. The cross section of this cable is shown in Figure 5-3c. A custom cable length of 11 m was selected to account for multiple deployment scenarios and setups. The cable configuration matched up with the pin configuration outlined in Table 5-1. The total cost of the cable assembly per sensor was €251.89.

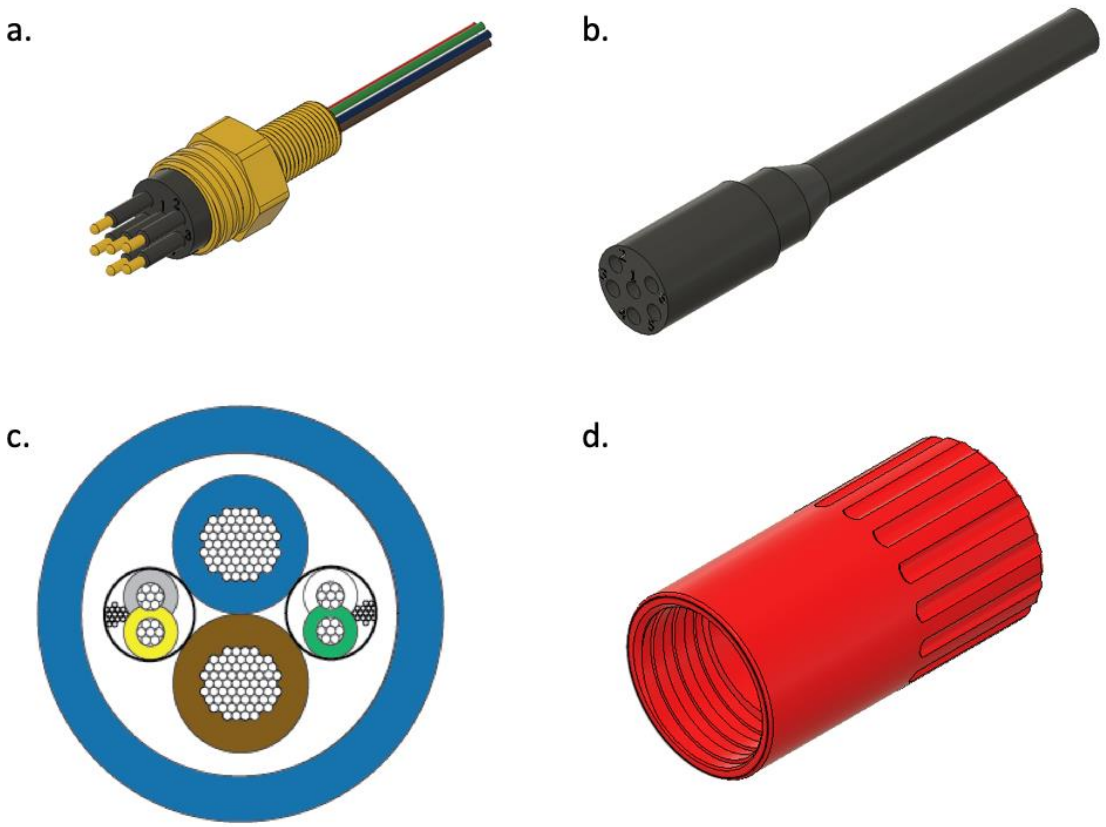

Figure 5-3 Sensor cable component images. (a) MCBH6M Subconn Bulkhead connector. (b) MCIL6F Female Cable connector. (c) Cross section view of type 2009/B Power/signal cable with two twisted pairs and two solid core power wires. (d) MCDLS-F locking sleeve. Images are provided by MacArtney Underwater Technology (https://www.macartney.com).

The components of the datalogger were protected by a watertight enclosure, Raaco Solid sourced from Radionics Ltd. An enclosure to house the delicate electronics was 3D printed from PLA filament on a Creality CR-200B Printer. An Arduino Mega sourced from Radionics Ltd was used as the microcontroller board. An Arduino compatible datalogger shield by Adafruit was used sourced from Digikey Electronics Ltd which allowed for a SD card and a real time clock (RTC) to be interfaced with the Arduino. The Bluetooth transceiver used was the BlueSMiRF Gold board sourced from SparkFun Electronics. This board utilizes the RN-41 Bluetooth module manufactured by Roving Networks which allowed for low power Bluetooth with a transmission range of over 100m. To communicate with the sensor over the serial protocol RS-232 a MAX232 breakout board sourced from SparkFun Electronics was used. This board converted the transistor-transistor logic (TTL) serial output from the Arduino Mega serial port to the RS-232 protocol. A RS Pro 12V lead acid battery with a 24 Ah capacity was sourced from Radionics Ltd. A low side driver N-Channel Mosfet was used to switch power to the sensor via a signal from the Arduino Mega.

Male and female connectors with 6 contacts and waterproof rated were selected to allow connection between the sensor cable and the datalogger. A Binder 680 series 6 contact panel mounted circular female connector was used as the cable connection from the sensor to the datalogger. The male connector was a Binder 680 series 6 contact plug and cable connector. Both were sourced from Radionics Ltd. The complete bill of materials for the datalogger is presented in Table 5-2.

Table 5-2 Bill of materials for datalogger.

Component	Component Number	Supplier	Cost (€)
Arduino Mega 2560 R3	A000067	Radionics Ltd	40.99
Adafruit Datalogger Shield	1141	Digikey Ireland	12.85
BlueSMiRF Gold Bluetooth Modem	WRL-12582	SparkFun Electronics	31.33
MAX3232 Transceiver Board	BOB-11189	SparkFun Electronics	5.99
Vishay 1 A, 100 V, N-Channel Mosfet	IRLD110PBF	Radionics Ltd	1.12
RS PRO 12V T12 Sealed Lead Acid Battery, 24Ah	150-1559	Radionics Ltd	73.15
Verbatim 16 GB SD Card	44082	Radionics Ltd	9.63
RS PRO SPST Rocker Switch	419-750	Radionics Ltd	1.80
Binder 680 Series 6 pin Socket Connector	09-0324-00-06	Radionics Ltd	6.12
Binder 680 Series 6 pin Plug Connector	09-0321-00-06	Radionics Ltd	8.59
Raaco Waterproof Plastic Case, 125 x 275 x 175 mm	136754	Radionics Ltd	17.19
		Total Cost	**208.76**

5.2.2 Datalogger Design

The datalogger enclosure was placed in a more robust protective hard case (52.0 cm length x 41.9 cm width x 19.0 cm height) (see Figure 5-4). Holes were drilled into the protective case and datalogger enclosure to allow for the cable and connectors to be installed. The cable connector was spliced with the MacArtney 2009/B Power/signal cable and connections were made corresponding to the connections outlined in Table 5-1 were made to the datalogger.

Figure 5-4 Datalogger deployment setup. The datalogger and electronics are protected inside a robust case with a large capacity lead acid 12V battery providing power for long durations.

The firmware for the datalogger was written to allow the datalogger to receive commands to set up the deployment which can be seen in Appendix B Section B.4. The firmware was written in C++ using the Arduino IDE. The flow chart of the firmware can be seen in Figure 5-5 showing how the datalogger handled input commands and interfaces with the sensor connected. A deployment cycle was controlled periodically by the datalogger by switching the sensor on and sending the read sequence command ("RW") to the sensor (see Table 5-4 for description of commands used to control sensor). The data was retrieved by the data logger and stored on an onboard SD Card. The data for each measurement cycle was stored on the SD card as a separate text file. The formatting of the text files was as follows: "DXXRXXXX.txt". The "D" represented the current deployment followed by the current deployment number (0-99). The "R" represented the number of readings or measurements taken during that deployment (0-1000).

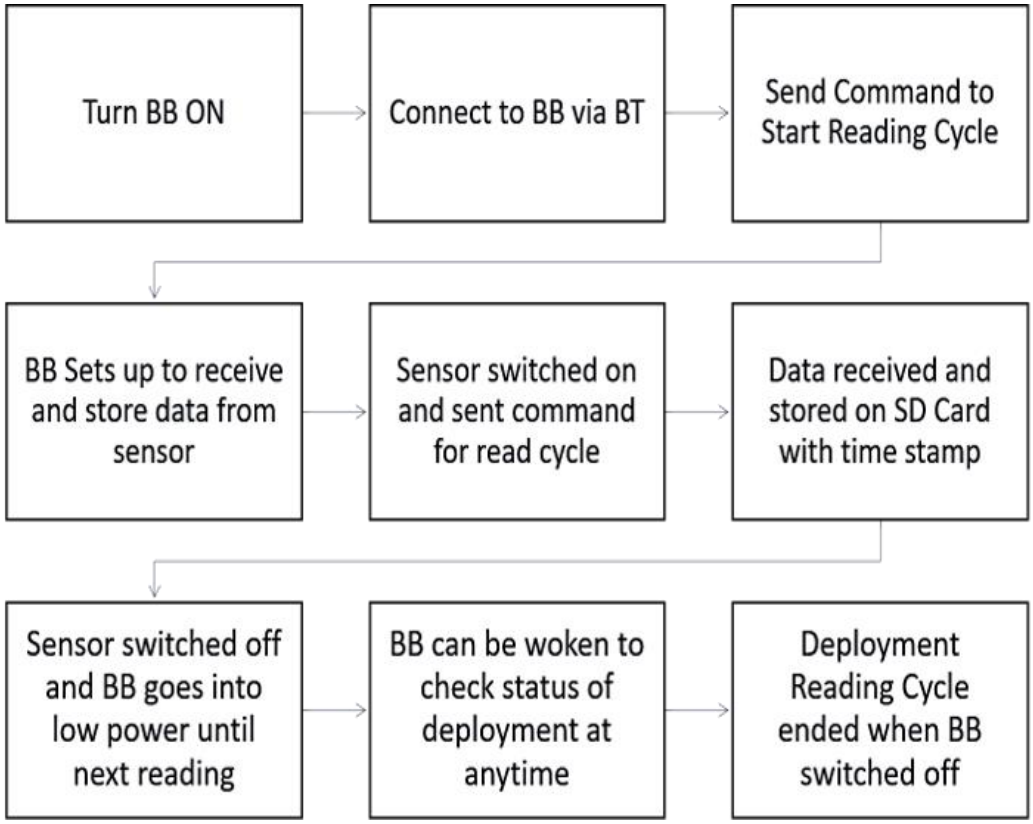

Figure 5-5 Datalogger firmware operational flow diagram. BB or black box refers to the datalogger electronics.

A python script (see Appendix B Section B.3) was written to extract the data from each text file stored on the SD card after the deployment. The program exported the data as a csv file combining all the data from a deployment and sorting it based on timestamp which allowed for analysis of time-based data series. This program extracted the data using key headers and organised the corresponding data into columns. The data points which were extracted are shown in Table 5-3.

Table 5-3 Data points and format of data extracted from datalogger SD card.

Data Point	**Format**
Timestamp	yyyy-mm-dd hh:mm:ss
Battery Voltage	Given in volts
Optical Measurement Response	Specific LED responses from pixel values of the target wavelength as returned by the sensor.
Temperature	Given in degrees Celcius

5.2.3 Sensor Power Management

A power profile of the sensor unit was taken by identifying time-on and power consumption values during the deployment cycle. The time taken by the sensor to perform a full measurement cycle (MC) and anti-fouling cycle (AFC) was measured. The MC is as described in Section 5.2.4.2 and the AFC described in Section 3.2.4.1. The current draw of the system was measured using a Fluke 179 Digital Multimeter.

5.2.4 Data Integration with External Industrial Networks

5.2.4.1 Commands to Operate Sensor during Deployment via External Hardware

A sequence of commands were used which corresponded to the sensor carrying out different functions. This allowed for the timing of the MC and AFC to be controlled by the network controller. The firmware written to operate the sensor in deployment mode can be seen in Appendix B Section B.2.1. Figure 5-6 shows the flow chart of command responses of the sensor when deployed. The "Mini Buoy" (MB) was the external controller built by TWM. The MB controlled power to the sensor and was connected to the sensor via RS-232 serial port. The sensor booted upon switching on power and responded with sensor information and ready status. Once booted the sensor awaits input commands from the controller.

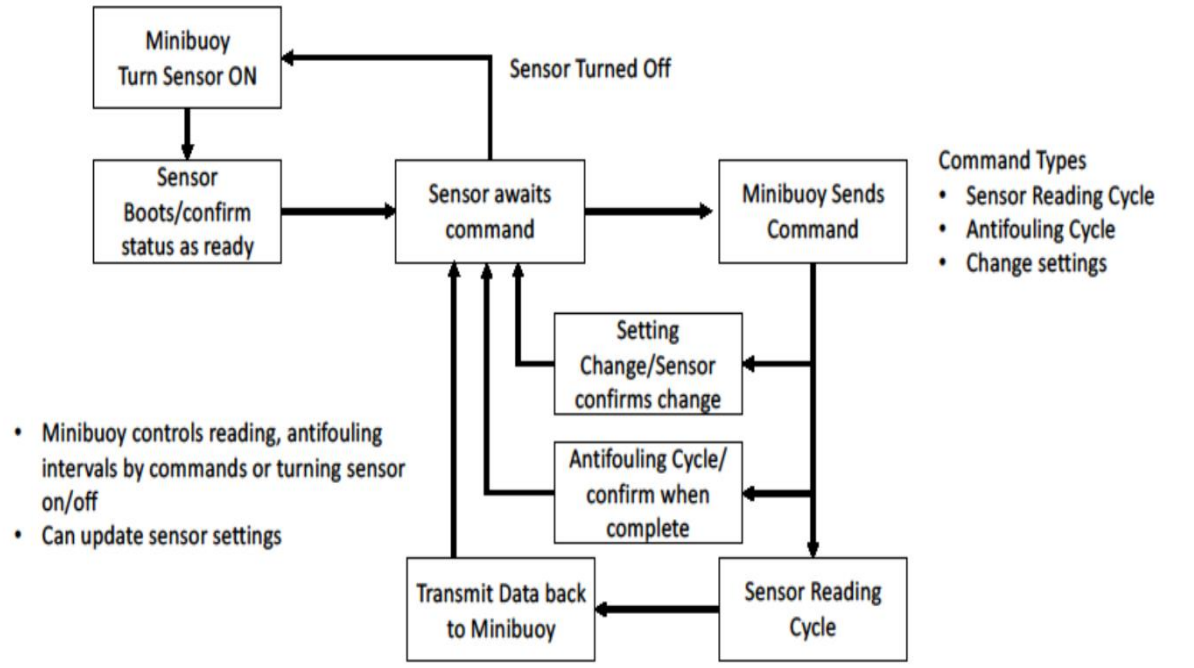

Figure 5-6 Flow chart of sensor firmware operation and sensors response to input commands from external controller/network.

Table 5-4 presents the serial commands used to operate the sensors functions via a serial connection with an external controller. The two main commands used during deployments were the “R” command and the “A” command. The “R” command was used in conjunction with a parameter character which specified which measurement mode the sensor should operate in. Once received the sensor would conduct the measurement and return the data to the external controller. The “A” command initiated the sensor’s antifouling protocol which turned on the UV LEDs at a set PWM duty cycle and for a set length of time as per the settings saved in the sensor’s memory. The settings stored internally on the sensor for integrations times and antifouling parameters could be checked and changed if necessary. The final command which was used was the diagnostic command initiated by sending the character “D”. The sensor was programmed to use the current monitor IC to check the current draw of each sensing component and output the readings to the external hardware for analysis on any faults.

Table 5-4 Serial commands to operate sensor via external hardware.

Command Type	**Serial Command**	**Parameter**	**Value**	**Function**
Sensor Measurement	**R**	**W** – Whole MC **L** – Abs + Sct **F** – Flr **T** – Temp	-	Returns Data from sensor operation
Antifouling Cycle	**A**	-	-	Starts the UV LED antifouling cycle at set PWM duty cycle and time.
Settings Query	**SQ**	-	-	Returns current settings of the sensor
Setting Change	**SC**	**I** + **A**, **S,** or **F** (abs, sct or flr). – Int Time	Array LEDIntTimes[8]	Changes the selected setting parameter with the new value/values
		D – AF Duty Cycle	value % between 0 and 100	
		T – AF Time On	Time in min	
Diagnostics	**D**	-	-	Sensor runs self-diagnostics (on board component current measurements)
MC – measurement cycle (optical measurements and temperature measurements), Abs- absorption measurement, Sct – scatter measurement, Flr- fluorescence measurements, Temp – temperature measurement, UV – Ultraviolet, PWM – pulse width modulation, Int time – integration time of spectrometer, LED – Light Emitting Diode, AF – Antifouling				

5.2.4.2 **Sensor Data Output and Format**

The formatting of the sensors data output from a measurement is shown in Figure 5-7. The measured data was broken in three main sections which are: 1.) the absorption, scatter, and backscatter data, 2.) the fluorescence data and 3.) the temperature data. Indicator phrases and characters were used to indicator the start and end of a measurement, the LED used for the measurement and the measurement mode the data is related to.

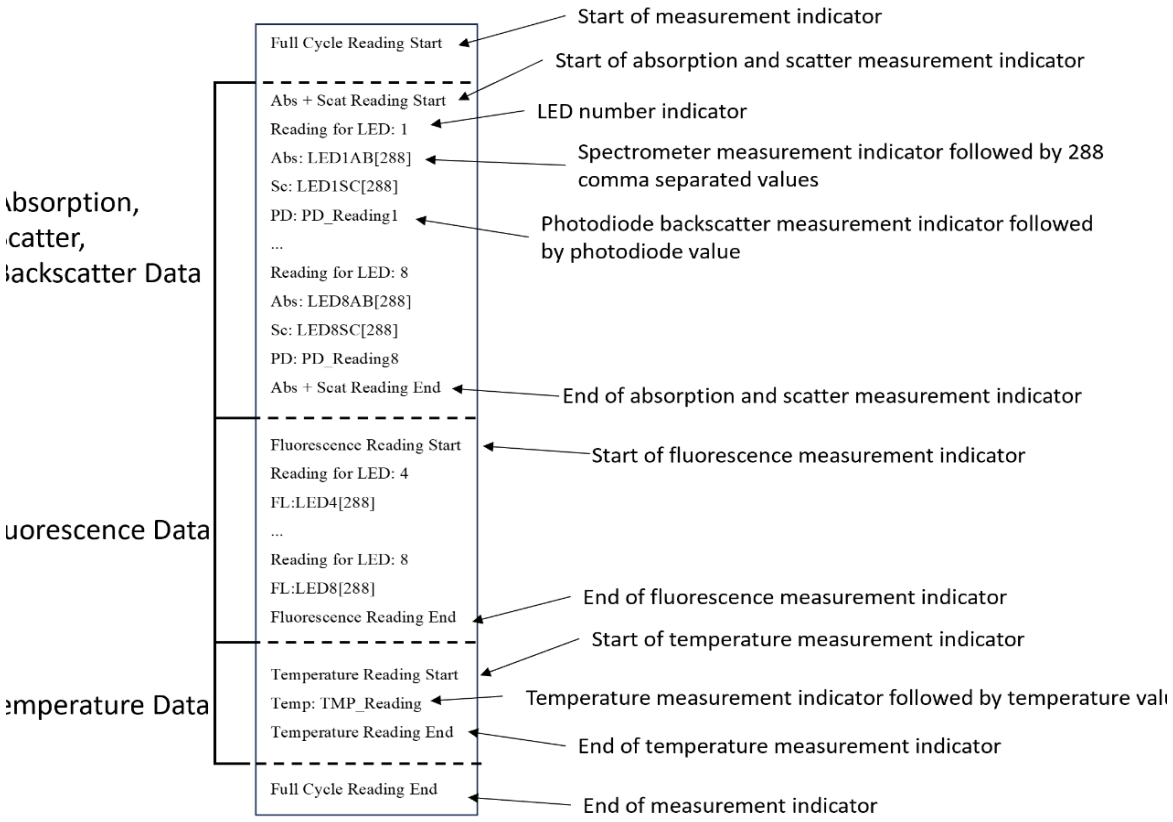

Figure 5-7 Sensor full measurement cycle data output formatting including start and end indicator phrases and structured measurement data from sensor response.

5.2.4.3 **Sensor Raw Data Conversion using Calibration Curves**

Each of the sensors were given a calibration decoder which used the slope of individual systems to retrieve validated signal readings for Chl-a and turbidity which was generated in the work from Section 4.3.3.4. Two data signals were collected per LED by the sensor. The LED was powered on for the raw data signal and powered off for the background data, with the integration time of the spectrometer being constant for each LED. The sensor's fluorescence response was converted to Chl-a concentration by applying Equation 5-1.

$$Chl\ a\ (\mu g\ L^{-1}) = \frac{SR}{Cal\ S\ \times Cal\ BB3} \quad 5\text{-}1$$

Where SR is the sensor response at the Chl-a pixel correspondent to 680 nm from the fluorescence measurement. Cal S is the slope generated by the calibration curve from the sensor's response to BB3 concentrations and Cal BB3 is the correction factor for BB3 to Chl-a concentration conversion derived experimentally in Section 4.3.3.3 Note this relationship is site/season specific, provided here is the ratio found in the laboratory with cultured diatoms, followed by Chl-a extraction.

$$Turbidity\ (\text{NTU}) = \frac{SR}{Cal\ S} \quad 5\text{-}2$$

Equation 5-2 is applied used to normalise the sensor response using the calibration data for turbidity. SR is the sensor response at the pixel value corresponding to 850 nm from the scatter measurement. Cal S is the slope generated from the calibration curve of the sensor in response to concentrations of NTU levels.

$$if(B > SB)\ SR = RSR - B \quad 5\text{-}3$$

$$else\ SR = RSR - SB \quad 5\text{-}4$$

The sensor response (SR) used by equations 5-1 and 5-2 is calculated depending on the logic outcome of equations 5-3 and 5-4. A background measurement (B) is taken by the sensor along with LED measurement (RSR). Additionally, during calibration a sample blank measurement (SB) was taken in the lab. To improve accuracy and ensure the calibration curve slope is valid, the background must be larger than the sample blank measurement to be subtracted from the RSR. Otherwise, the sample blank is used as the reference background. This method accounts for changing ambient light conditions in the environment.

$$if\ (\ (RSR - B) < SB)\ \ return\ 0; \quad 5\text{-}5$$

Equation 5-5 was also applied to the decoder algorithm to avoid negative numbers if the ambient light is severely interfering the sensor and generating negative values which would

be nonsensical. Zero is returned if the sensor response minus the background is still less than the sample blank which indicated the calibration curve would no longer be valid.

5.2.4.4 Network Data Transfer and Storage

Figure 5-8 gives a schematic overview of how data was handled from the sensor with the TWM's infrastructure. The data was immediately transmitted by the sensor over its serial port once acquired and did not store any data beyond a single scan. The output data from the sensor was read and was stored locally on the MB where it underwent a decoding process to quantify data as described in the previous section. During deployments data was transmitted using MQTT as the data broker to AWS DynamoDB for storage and displayed on the TWM's CoastEye platform.

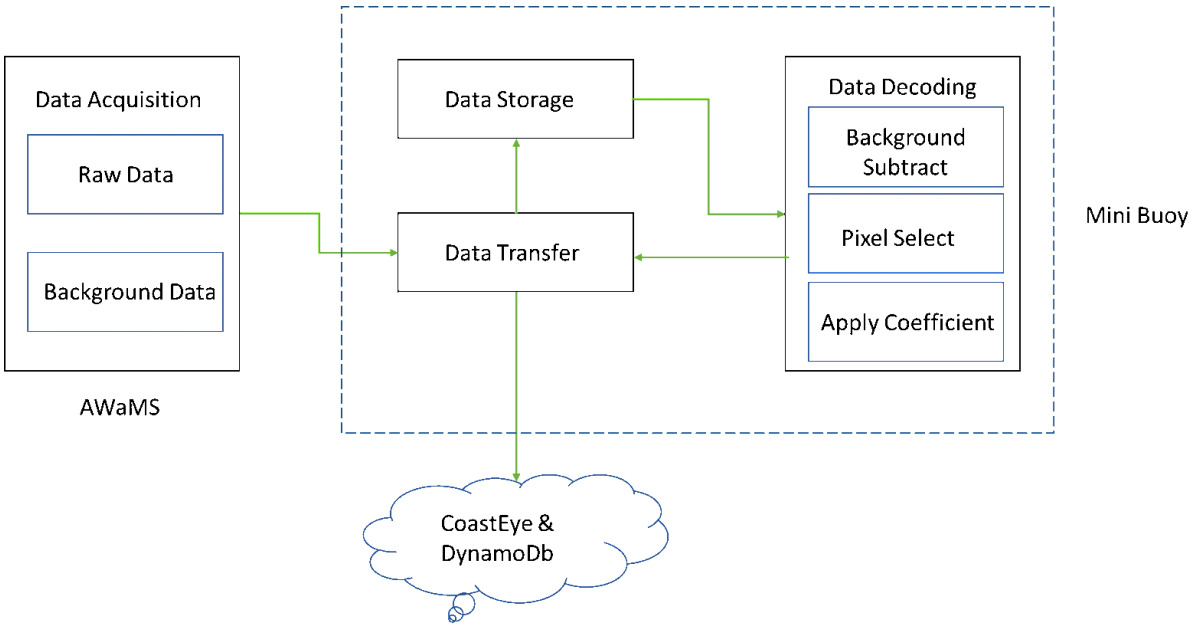

Figure 5-8 Schematic of how the data was handled and manipulated between the sensor and Mini Buoy

The data on the DynamoDB databased was extracted by TWM for use on their CoastEye platform and the raw data was provided to the DCU team in JSON format for analysis. A python script was written using Visual Studio Platform to convert the CSV files with the data in JSON format into usable data files. The code was written with the assistance of Dr Louis Free. The Pandas python library was used to manipulate the data using the corresponding header variables (Table 5-5) in the JSON data. Each subset under the header was then manipulated into a column to allow for the data to analysed using graphing software.

Table 5-5 Headers relating to the JSON conversions of data from the DynamoDB Database.

JSON Header	Data Header Relates To
Timestamp	Time of measurement represented in EPOCH time format
Date	The converted EPOCH timestamp to Y-m-d H:M:S format.
SctLED1	The raw sensor response at 850 nm of the IR LED
bgSctLED1	The raw background sensor response at 850 nm
Turb-NTU	Quantified turbidity measurement from the sensors raw data after the decoding algorithm is applied.
FlrLED5	The raw sensor response at 680 nm from the fluorescence measurement.
bgFlrLED5	The raw background sensor response at 680 nm fluorescence measurement.
Chl-a	Quantified Chl-a measurement from the sensor's raw fluorescence data after decoding algorithm is applied.
Temp	The temperature response from the sensor in degrees Celsius.

5.2.5 Dublin Bay Deployment

For the deployment in Dublin Bay, the sensor was given the acronym AWaMS (Advanced Water Monitoring System) and will be referred to as this in relation to this deployment.

5.2.5.1 Site Locations

Figure 5-9 shows the chosen deployment locations for the five sensors units. Table 5-6 gives the site coordinates of each sensor deployment location. The Howth and Dun Laoghaire locations were positioned inside sheltered harbours. The sensors at Poolbeg and St. Patricks were located at the mouth of the Liffey in brackish water. The Clontarf deployment location was positioned at the estuary of the Liffey.

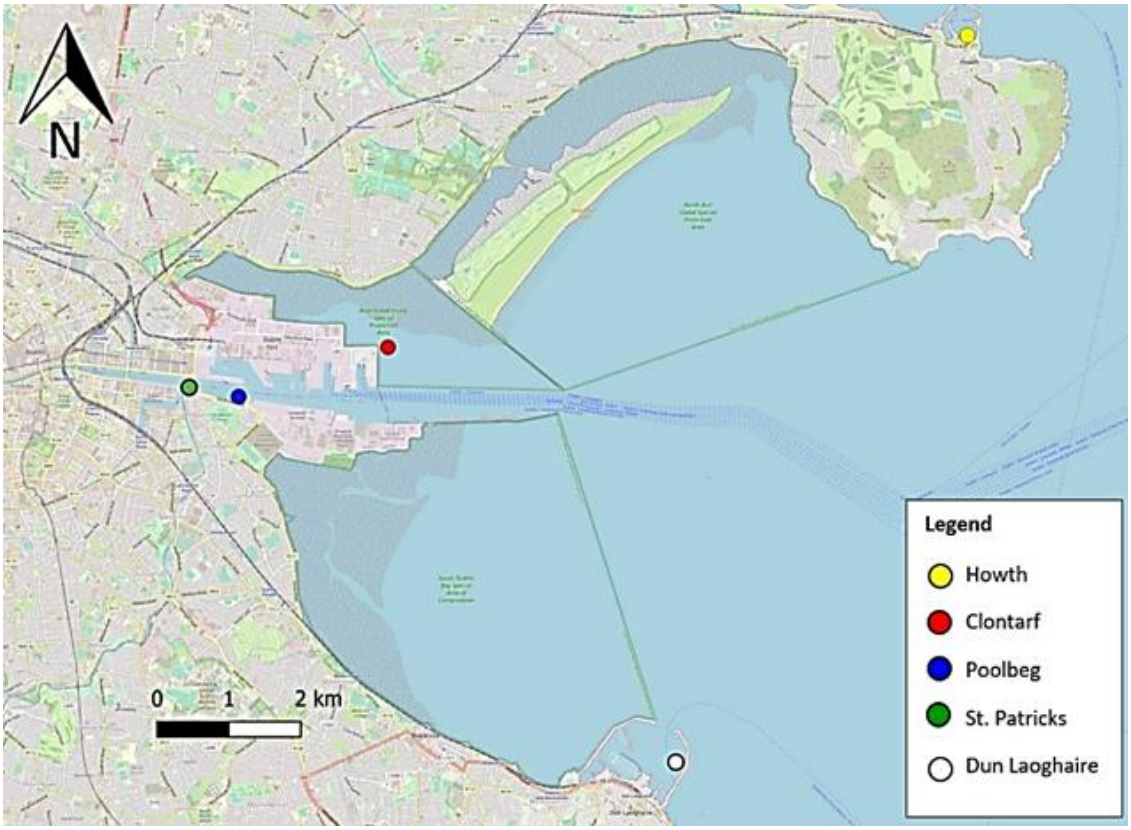

Figure 5-9 Site locations for the deployment of the sensors in Dublin Bay.

Table 5-6 Location and site coordinates of the sensor deployments in Dublin Bay

Site Location	Site Coordinates
Howth:	53°23.3474 N, 006°3.944 W
Clontarf	53°21.018 N, 006°11.202 W
Poolbeg:	53°20.649 N, 006°13.072 W
St. Patrick's	53°20.719 N, 006°13.695 W
Dun Laoghaire	53°17.9122 N, 006°7.5835 W

5.2.5.2 **Deployment Site Setups**

Two separate deployment hardware setups were used to mount the AWaMS in situ depending on the location. The first was the MB which positioned the sensor at a 1-meter depth below the surface underneath the body of the buoy. The second hardware used was a stainless-steel cage structure positioning the AWaMS at a 1-meter depth. The cage was held in place to the mooring using chains and ropes. The AWaMS were clamped to the structures used a series of heavy-duty cable ties. Figure 5-10 shows the deployment setup for the Howth location. The buoy is moored off a pontoon in Howth marina. The deployment setup for the sensor located at Clontarf is shown in Figure 5-11. The data buoy is attached to a mooring buoy. Figure 5-12 shows the deployment setup for the sensor located at Poolbeg

marina. A Seabird HydroCAT-EP and one sensor prototype was deployed on a frame off the side of a pontoon at the Poolbeg Yacht Club marina. The frame was tied to a secure point on the marina and the associated battery, solar panel and components were secured to the same platform. Permission was received from Keith Kelleher, the Marina Manager. The deployment setup for the sensor deployed at St. Patricks Rowing club can be seen in Figure 5-13. The frame was deployed on the western end of the pontoon. Permission was received from John Doyle, the club's Chairperson. Figure 5-14 shows the deployment setup of the sensor deployed in Dun Laoghaire harbour. The AWaMS sensor was deployed using a TWM MB. This was attached to an existing mooring of the National Yacht Club, Dun Laoghaire.

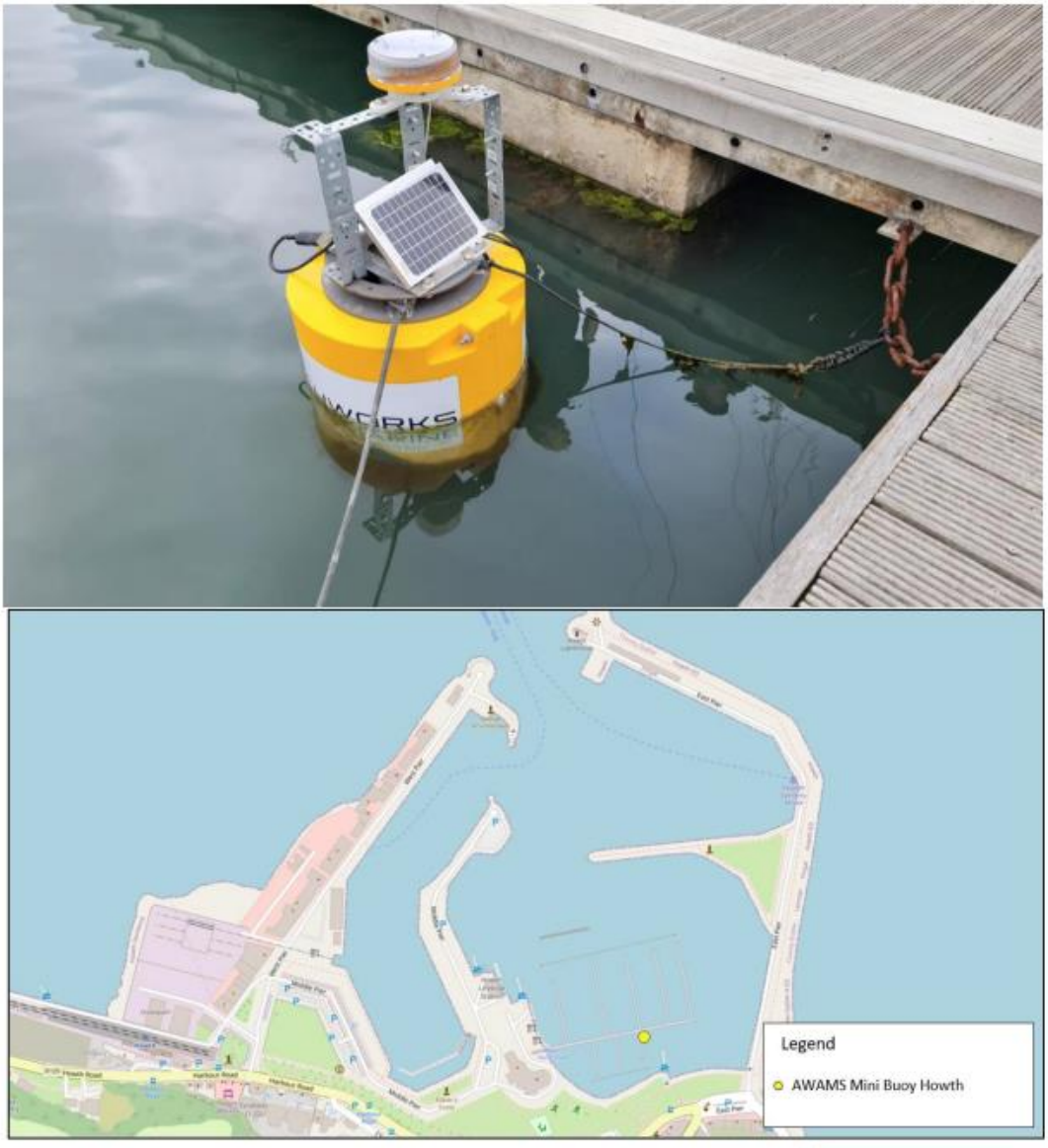

Figure 5-10 Image of Mini Buoy deployed off a pontoon at Howth marina and a map of the deployment location.

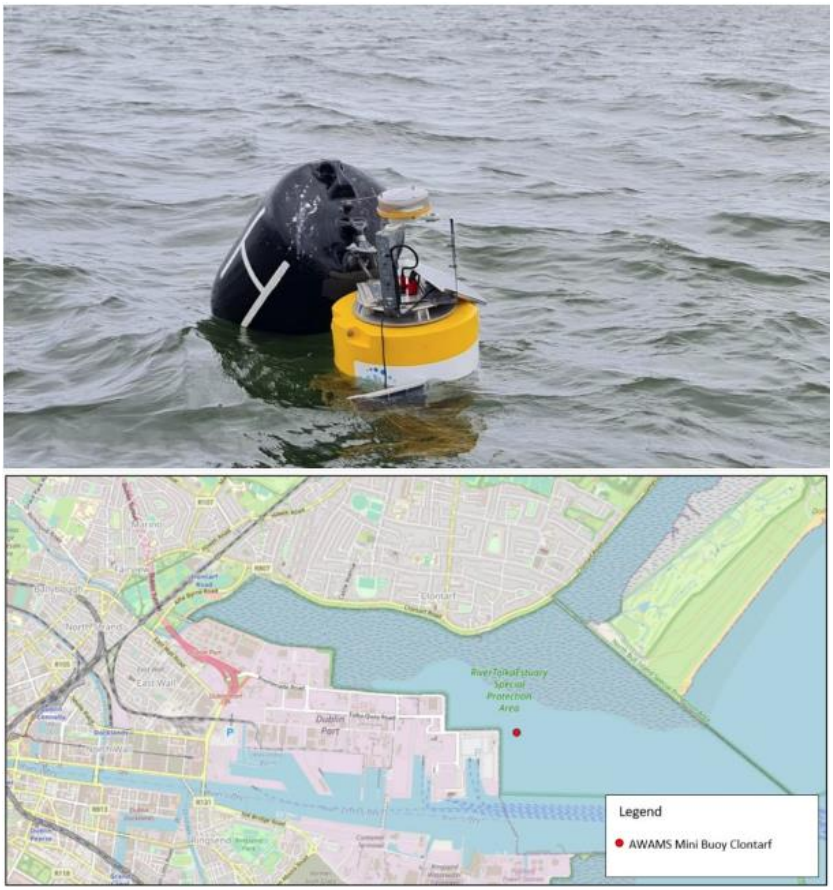

Figure 5-11 Image of Mini Buoy attached to the mooring buoy off Clontarf with damaged solar panel and a map of the deployment location.

Figure 5-12 Image of AWaMS deployed off pontoon at Poolbeg marina and a map of the deployment location.

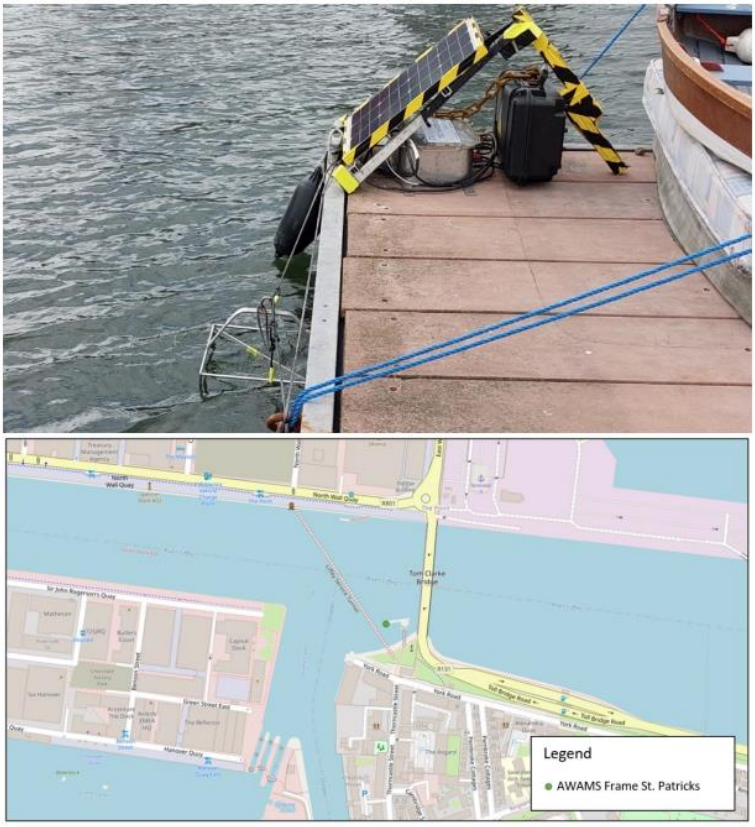

Figure 5-13 Image of the AWaMS Frame at St. Patricks Rowing Club and a map of the deployment location.

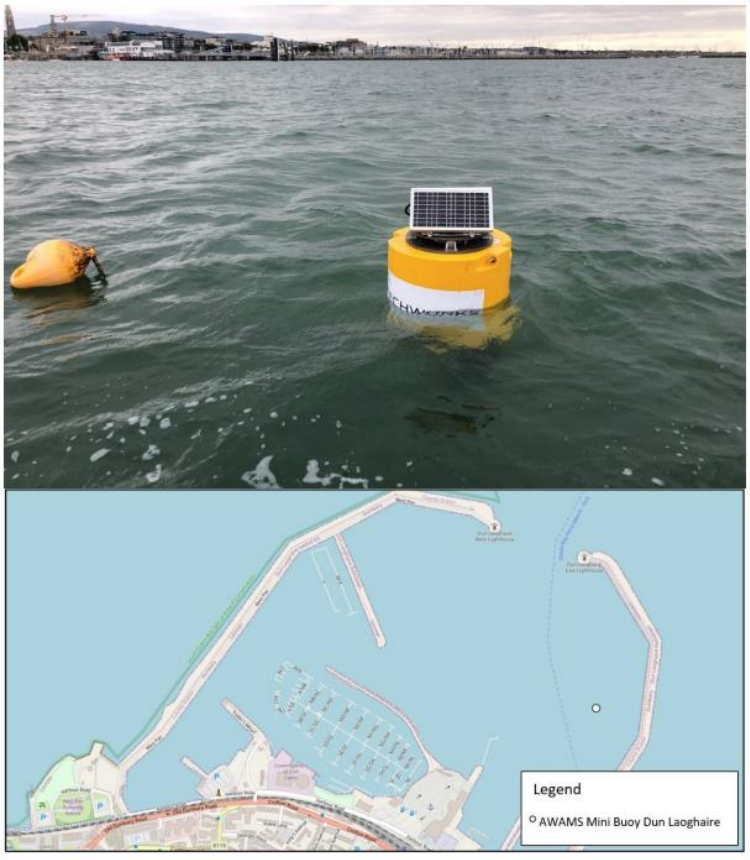

Figure 5-14 Image of the Mini Buoy in Dun Laoghaire Harbour and a map of its location.

5.2.6 Freshwater Deployment

5.2.6.1 Deployment Site Location

The location of the site selected for the freshwater sample deployment can be seen in Figure 5-15. The site was located at 54°08'39.9"N 8°33'07.9"W in the Owenmore River, Co. Sligo. A weather station run by the OPW is located 50 meters up stream of the deployment site at the Owenmore bridge. Sensor Unit 8 was selected for this deployment, see Table 4-3 for details of sensor assembly.

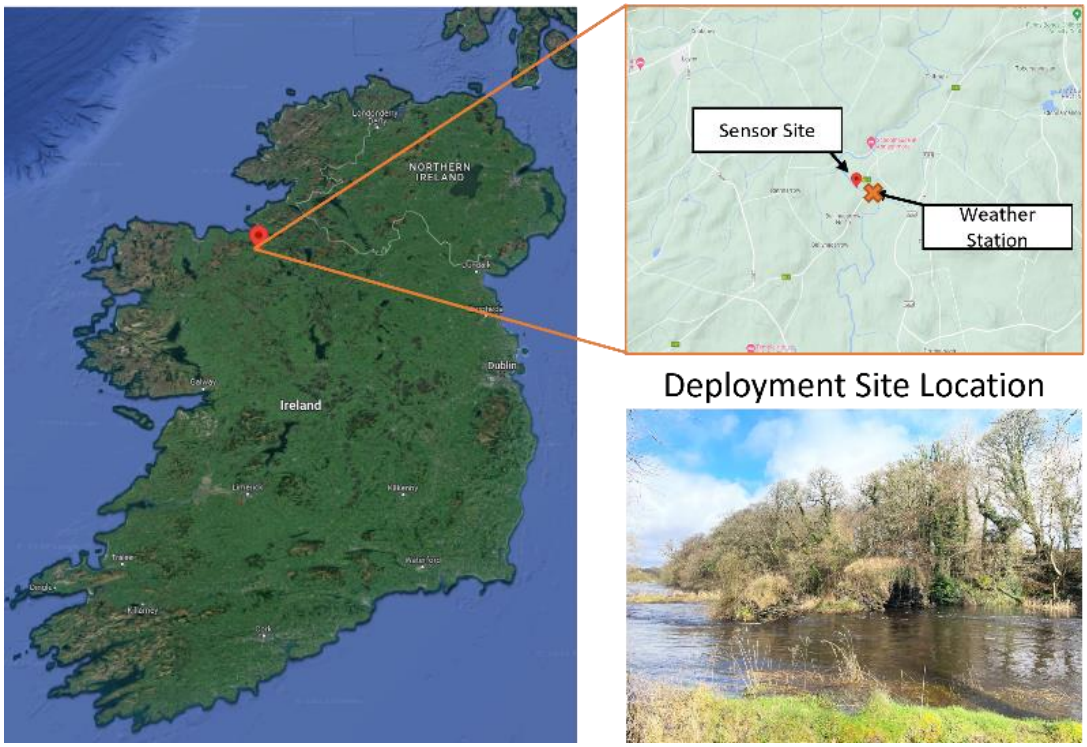

Figure 5-15 Site deployment in the Owenmore River (54°08'39.9"N 8°33'07.9"W). The sensor site is located 50 m downstream from the Owenmore Bridge weather station.

5.2.6.2 Deployment Site Setup

The deployment site setup can be seen in Figure 5-16. The deployments were conducted with the assistance from Mrs Lisa Cronin and Dr Chloe Richards. The DCU sensor and YSI Sonde were attached to stainless-steel cages using a clamps and cable ties. Both cages were anchored to the riverbed using ropes. Both sensors were positioned beside each other, 5 meters from the shoreline to ensure they are in the main flow of the river and remained submerged even at low water levels. Public data on the water level and temperature of the river were retrieved from the OPW for data station 32014 (https://waterlevel.ie/0000032014).

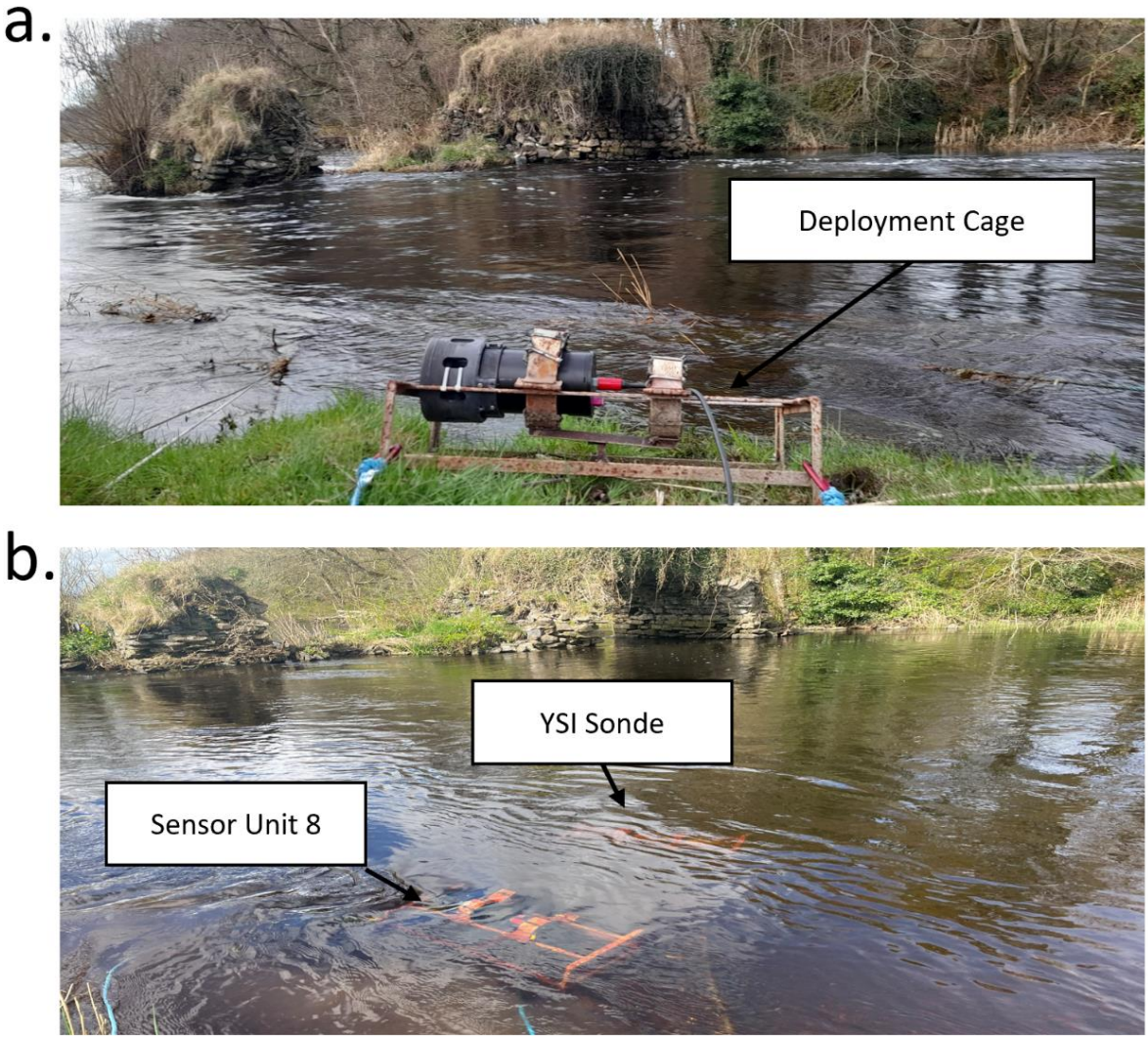

Figure 5-16 Image of the deployment setup. (a) the sensor is deployed attached to a stainless-steel deployment cage (b) Sensor Unit 8 and the YSI Sonde are positioned alongside each other on the riverbed midstream.

A series of deployments were planned, and Unit 8 settings were configured differently each time. The Unit 8 unit was selected for the deployment. The YSI Sonde was fitted with the turbidity measurement probe able to produce turbidity measurements in calibrated NTU values. The following table outlines the sensor system setup for each deployment conducted:

Table 5-7 Owenmore River sensor deployment setup methods.

Deployment Number	Dates of deployments	Method and AWaMS Setup
1	26/03/2023 to 05/04/2023	The 850 nm LED was used for scatter with 0.2s int time and sensor response at corresponding 850nm pixel value was returned by sensor. The 380 nm LED was used for fluorescence with 3 s int time and sensor response at corresponding 450 nm pixel value was returned by sensor.
2	17/04/2023 to 20/04/2023	Int times of fluorescence measurement were adjusted using a water sample taken from river on retrieval of sensor. The scatter measurement was unchanged. The 380 nm LED integration time was reduced to increase the measurement range for fDOM to 0.6 s. Sensor response at pixels corresponding to both 450nm and 680 nm were returned to measure both fDOM and Chl-a from the single fluorescence scan. 430 nm LED was used to measure absorption, 1.8 ms int time was used and corresponding sensor response at 430 nm was returned by sensor. The sensor also returned the temperature measurement.
LED – light emitting diode, Int time – integration time of spectrometer, fDOM – fluorescent dissolved organic matter, Chl-a – chlorophyll a		

5.3 Results and Discussion

5.3.1 System Power Consumption Reduction

5.3.1.1 Power Consumption of Sensor System

With the power profile of the system, methods to reduce to overall power requirements of the system while in operations were evaluated. Methods to reduce the power consumption of the system that were tested are outlined in Table 5-8. The methods were selected based on the following criteria: 1.) Functionality was redundant for the application of measurement or anti-fouling or 2.) being turned off or reduced time-on did not affect performance of the sensor.

Table 5-8 Methods used to reduce the power consumption of the system.

Power Consumption Reduction Method	Description
Reduce processor speed	MCU processor speed was tested at 96 MHz and compared to 24 MHz for reduced power consumption.
Remove unnecessary hardware	Components were switched off when not in use or disabled entirely.
Change AFC frequency	The AFC duty cycle was reduced to less on time.
Sleep Mode	The MCU was put into sleep mode when not in use.

MCU – Microcontroller Unit, LED – Light Emitting Diode, AFC – Anti-fouling Cycle

Table 5-9 shows the measurements of the current draw of the main circuitry blocks of the sensor's electronic systems. The main two power intensive functions the system performs were the MC and AFC. The frequency of the full cycle was set to every 15 min. The power supply was set at 12 V. The MC was measured to last approx. 69 s to complete, and the system drew an average of 100 mA during this time. The AFC lasted 60 s and the system drew an average current amount of 150 mA in total.

Table 5-9 Current draw of main circuitry sections of the sensor electronics system.

Component	Current Draw (mA)
Microcontroller @ 96 MHz speed	50
LEDs (average)	20
AF UV LEDs (PWM 75 %)	100
Sensors	40

AF – Antifouling, UV – Ultraviolet, PWM – Pulse Wide Modulated

Applying Equation 5-6, the charge (Q) in Coulombs, was calculated for each cycle by multiplying the current draw (in Amps) by the duration of time (T). This gave a charge draw of 6.9 C for the MC and 9 C for the AFC.

$$Q = I \times T \tag{5-6}$$

Using Equation 5-7, the total charge (Q) of the sensor was calculated as 15.9 C with Q_1 as the MC charge and Q_2 the AFC charge.

$$Q = Q_1 + Q_2 \tag{5-7}$$

By using the Equation 5-8 below the average current draw (I_{avg}) of the sensor was calculated. At a sampling frequency (F) of every 15 min or 900 s. The average current draw of the system was 0.01767 A or approx. 17.7 mA. Using a 12 V supply this equates to a power consumption of 210 mW.

$$I_{avg} = \frac{Q}{F} \tag{5-8}$$

5.3.1.2 Reduction in Power Consumption

The calculated percentage improvements based on power consumption reduction methods tested (Table 5-8) in decreased power usage are presented in Table 5-10.

Table 5-10 Table of calculated power reduction percentages with applied methods.

Energy Reduction Method	MC Time On & Current Draw				AFC Time On & Current Draw				MC, AFC & System Total Charge			Percentage Charge Reduction %
	MC Time Reduction s	MC Total Time s	MC Current Reduction mA	MC Total Current mA	AFC Time Reduction s	AFC Total Time s	AFC Current Reduction mA	AFC Total Current mA	MC Total Charge C	AFC Total Charge C	System Total Charge C	
Reducing MCU Speed to 24 MHz	0	69	20	80	0	60	20	130	5.52	7.8	13.32	16.23
Disabling the onboard LED	0	69	5	95	0	60	5	145	6.555	8.7	15.255	4.06
Reducing the AFC Duty Cycle to 1:60	0	69	0	100	45	15	0	150	6.9	2.25	9.15	42.45
MCU Sleep Mode during AFC	0	69	0	100	0	60	37	113	6.9	6.78	13.68	13.96
Power off sensors during AFC	0	69	0	100	0	60	40	110	6.9	6.6	13.5	15.09
All Methods Combined	0	69	25	75	45	15	77	73	5.175	1.095	6.27	60.57

MC – Measurement Cycle, AFC – Antifouling Cycle, MCU – Microcontroller Unit, LED – Light Emitting Diode

Reducing the microprocessor speed from 96 MHz to 24 MHz was found to have a 16.23 % reduction on the charge used by the system during the deployment cycle. This reduction is reaffirmed by a study by Wu et al., (2021) [399] who found a significant power consumption reduction with the lowering of a microprocessors processing speed. They study also found a reduction at higher processing speeds due to a reduction of on time required for processing. The study was conducted using a STM32F407 microprocessor which is based on the ARM Cortex M4 as is the processor used on the Teensy 3.2 (MK20DX256). As the microprocessor is not used for any significant processing during the MC or AFC the reduction has no significant effect on the overall performance or on-time of the sensor in carryout it required functions. Further reductions in the CPU speed are possible with the Teensy 3.2 capable of operating at speeds between 2 MHz to 120 MHz However, the USB communication functionality only operates from 24 MHz and above hence why it was selected as the lowest speed for testing. The electronics of the sensor are enclosed within the sensor body, the onboard LED which has the function of indicating the Teensy board is receiving power, was not needed. Disabling this component was found to have a 4.06% reduction of charge used by the system.

The reducing of the AFC duty cycle had a major percentage improvement on the reduction of charge drawn by the system. By reducing the on-time of the UV antifouling LEDs by a factor of 4, over 42% of charge was found to be reduced during the deployment cycle by using a duty cycle of 1:59 instead of 1:14. A study by MacKenzie et al., 2019 [400] reported that duty cycles of 1:30 and 1:60 did reduce biofouling build up. However, the study also found that some growth still occurred at the higher duty cycles. Another study by Whitworth et al. (2022) [401] , using a 280 nm UV light source, found that a duty cycle of 12.5% was required to reduce growth however a duty cycle of 2.5% had an effect and also increased the lifespan of the UV LEDs significantly. The duty cycle of the AFC has a significant effect on the rate of growth of microorganism [212,400,401] but also on the reduction of power consumed. The trade-off between biofouling reduction and prolonged LED life and battery power dependent deployments was considered based on the deployment duration and location.

As described in Section 2.2.3.1, for the AFC, the I2C command to the LED driver is the only required input from the microcontroller board. The LED Driver controlled the PWM signal to the UV LEDs meaning the. microcontroller could enter sleep mode for this duration. In

sleep mode the microcontroller consumed less than 1mA of current. A watchdog timer was used to wake the microcontroller up after the set AFC time of 60 s. A second interrupt was set on the Rx pin of the microcontroller to allow a rising edge from an incoming serial input to also wake the sensor. This was incorporated as a failsafe as the sensor is non-responsive when in sleep mode. A 13.96% reduction was found in the charge used with the original AFC duty cycle of 1:14 was seen. The sensors, (photodetectors and temperature probe) consume 40mA (see Table 5-9) even when not in use. During the AFC they were turned off using a high-side transistor by the MCU as described in Section 2.2.3.1. Turning the sensors off for the duration of the AFC with a duty cycle of 1:14 was found to have a 15.09% reduction of the power consumed over the system total cycle.

The application of all methods combined produced a reduction of charge consumed by the system during the total cycle of 9.63 C or a 60.57% reduction from 15.9 C. The calculated total reduction factored in the compounded effect of methods on other methods such as the reduction of time of the AFC, decrease of the MCU power consumption and the power reduction caused by sensors powered off and the MCU in sleep mode. Applying Equation 5-8 and a sampling frequency of 15 min, this gives an average current consumption of 6.97 mA. Based on a 12 V power supply this equated to 80 mW power consumption with a 130 mW power consumption reduction from the initial operating mode.

Table 5-11 Power consumption comparison between commercial in situ sensors based on a 15 min sampling frequency powered by a 12 V supply.

Sensor Unit	Current Draw (mA)	Time On per Measurement (s)	Avg. Power Consumption (mW)	Fouling Prevention Method	Ref.
SeaBird HydroCAT-EP V2 with Wiper	140	33	61.6	Wiper/Bleach Injection	[341]
YSI EXO3s Multiparameter Sonde (4 Sensors + 1 Central Wiper)	100	4	5.33	Wiper	[402]
Aqua TROLL® 600 Multiparameter Probe	45	5	3	Wiper	[403]

Table 5-11 above shows the comparison between commercially available sensors power consumption with a 15 min sampling frequency. All three commercial sensors have a much

lower average power consumption than the AWaMS. It should be noted the power consumption and times information of the antifouling measures implemented by the sensors were not made available by the suppliers. The measurement times and current draw for each sensor presents the best-case scenario. The time on per measurement times were estimations based on the highest sampling frequency the sensor could operate at. The length of the MC used by AWaMS is drastically longer than the commercial sensors which is contributing to longer time-on and higher power consumption. The AWaMS uses eight LEDs and three separate measurement modes which in total result in a 69 s MC however the measurements can be fine-tuned based on deployment requirements with only necessary measurements being made during the cycle. The integration times required for the fluorescence measurements plus the same length of time to measurement the background is the most significant time period (34 s) used in the MC. Optimising the fluorescence measurements will reduce the power consumption further for future deployments.

5.3.2 Dublin Bay Sensor Deployment

5.3.2.1 Sensor Data Integration Analysis

Each full measurement cycle using all detection modes and LEDs (as produced by the firmware shown in Appendix B Section B.2.1) produced 37kB of data per measurement. Due to this large amount of data per scan the output of the sensor needed to be reduced for the Dublin Bay deployment to be used with TWM's communication infrastructure. The output from the sensor was reduced to only using the LED 1 scatter measurement and fluorescence measurements of LEDs 5-8 (see Table 3-3 for LED details) which. The relating background measurements were included as well as the temperature measurement. The altered firmware for the sensor can be seen in Appendix B Section B.2.2. This reduced the data output from the sensor to 16kB per scan. The raw data from the sensor measurements was stored on board TWM's datalogger via an SD card. The calibration decoder was applied by the datalogger, and the calibrated values of the target parameters were transmitted via the MQTT protocol to the AWS Dynamo DB database. The data retrieved from the sensors was successfully transmitted to the DynamoDB database and was displayed for each sensor on TWM's website CoastEye. Figure 5-17 below shows a screenshot from the CoastEye website of the data from the AWaMS10 sensor deployed at the Clontarf deployment site. The data was retrieved from the DynamoDB database using the python script and was organised for analysis.

Figure 5-17 Screenshot of CoastEye platform showing AWaMS7 data at Clontarf deployment site 15/08/25 - 25/08/2022.

5.3.2.2 **Deployment Data Analysis**

Table 5-12 below tabulates the deployment and recovery times, days deployed, days data collected, and total number of measurements (Chl-a. turbidity and temperature) gathered of each sensor during the deployment in Dublin Bay. The sensor located at Dun Laoghaire collected data for a total of 56 days without failure with a total of 16126 measurements made. The sensors located at Poolbeg and St-Patricks were able to collect data for 38 days (10944 measurements) and 31 days (8928 measurements) respectively. The AWaMS8 was deployed at Poolbeg was accompanied by a commercial sensor the Seabird HydroCAT-EP V2 which collected data on turbidity, Chl-a, and temperature. AWaMS system located in Clontarf was replaced due to a damaged sensor. AWaMS5 was replaced by AWaMS10 on the 16th of August which collected data for a total of 22 days (6336 measurements). The analysis of the issues with the AWaMS system is discussed in Section 5.3.2.4. The sensor deployed in Howth (AWaMS7) collected data for 27 days totally 7776 measurements collected. During this deployment, a total of 50112 measurements were made by the sensors on Chl-a, turbidity, and temperature in five different locations in Dublin Bay.

Table 5-12 Date of deployment and recovery for each of the AWaMS sensors along with their monitoring duration and data collected.

Site Name	Sensor Unit	Deployment (DD/MM/YY)	Recovery (DD/MM/YY)	Duration (days)	Data Collected (days)	Number of Measurements
Howth	AWaMS7	12/08/22	08/09/22	27	27	7776
Clontarf	AWaMS10*	11/08/22	08/09/22	28	22	6336
Poolbeg	AWaMS8**	18/08/22	29/09/22	42	38	10944
St. Pats RC	AWaMS3	18/08/22	29/09/22	42	31	8928
Dun Laoghaire	AWaMS9	15/08/22	27/10/22	73	56	16128

**Replacement sensor for AWaMS5. **Deployed with the SeaBird HydroCAT-EP Sensor. RC – Rowing Club*

Poolbeg Marine Deployment Data

The correlation of the AWaMS unit with the HydroCAT-EP is shown in Figure 5-18, for Chl-a and Figure 5-19 for temperature. From Figure 5-18 it can be seen that no major change in the Chl-a levels in the deployment site occurred with the sampling time period. Spikes in Chl-a levels measured by the HydroCAT match those measured by the AWaMS. One outlier event saw a spike of chl-a occurring on the 23rd of August which was detected by the HydroCAT but not the AWaMS. Figure 5-19 shows a close match between the two sensors' temperature measurements throughout. Interpolation between the two temperature datasets gave a Pearsons correlation coefficient of 0.95 showing high correlation between the two sensors. The data for turbidity from this location returned a value of 0 throughout the deployment period implementation of Equation 5-5. This is a consequence of the calibration decoder and the error associated with measuring the sample blank. When the water is clean, the sensor operates in the noise region of ± 300 AU and would otherwise return slightly negative values. The decoder assigned a value equal to 0 to any negative results. From Figure 5-20 it can be seen from the HydroCAT turbidity measurements that the turbidity levels in the location were incredibly low during the deployment. Figure 5-20 also shows that the raw data (scatter LED 1) closely resembles the response from the HydroCAT-EP sensor.

Implementation of a spike filtration algorithm or a data averaging algorithm of adjacent pixel values would reduce the noise and fix the problem. The low levels of Chl-a and turbidity in the deployment site makes it difficult to draw any significant comparison between the two sensors. The AWaMS system matched the fluorescence measurements of the HydroCAT in the lab-based experiments shown in Section 3.3.4.5 and the is observed to match data for Chl-a, turbidity (at low levels) and temperature as seen from this in situ deployment. This would suggest the measurements of the AWaMS are tentatively deemed valid in the marine environment by comparison with a commercially available in situ sensor.

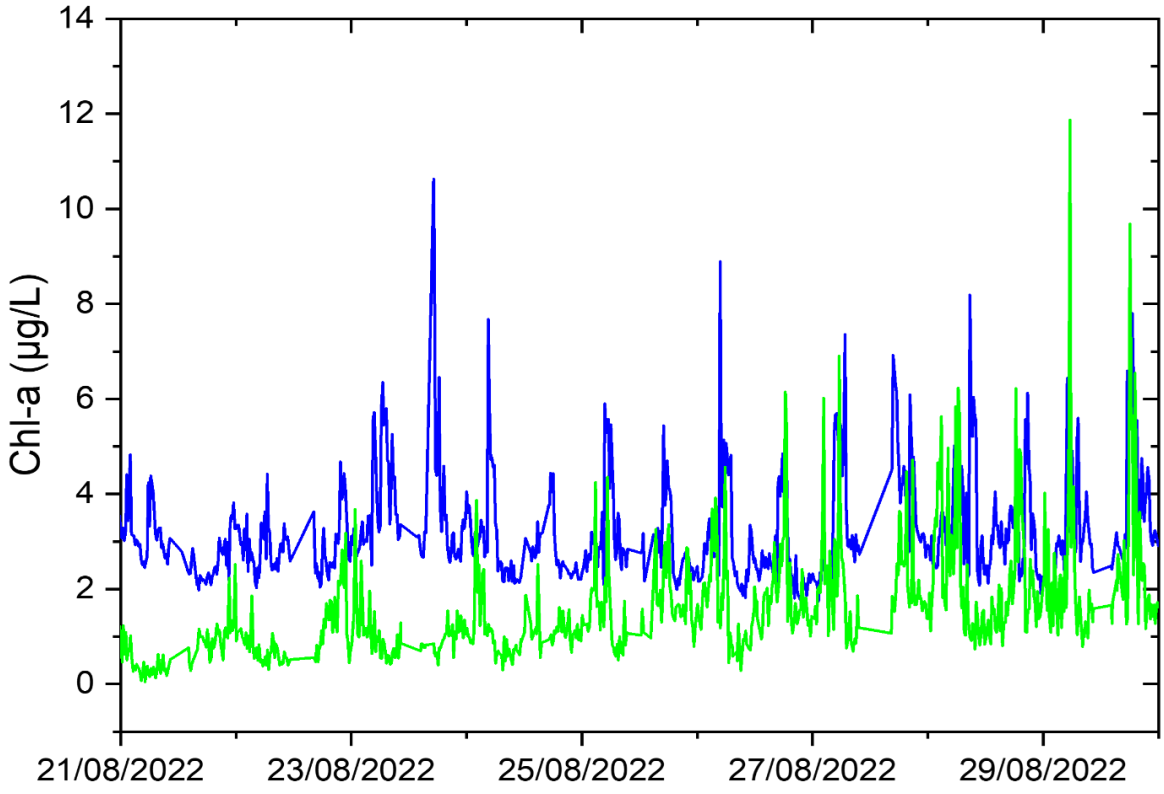

Figure 5-18 Poolbeg deployment Chl-a measurements of AWaMS8 (green) with commercial sensor (HydroCAT-EP)(blue) for comparison of performance between 21/08/2022 and 29/08/2022.

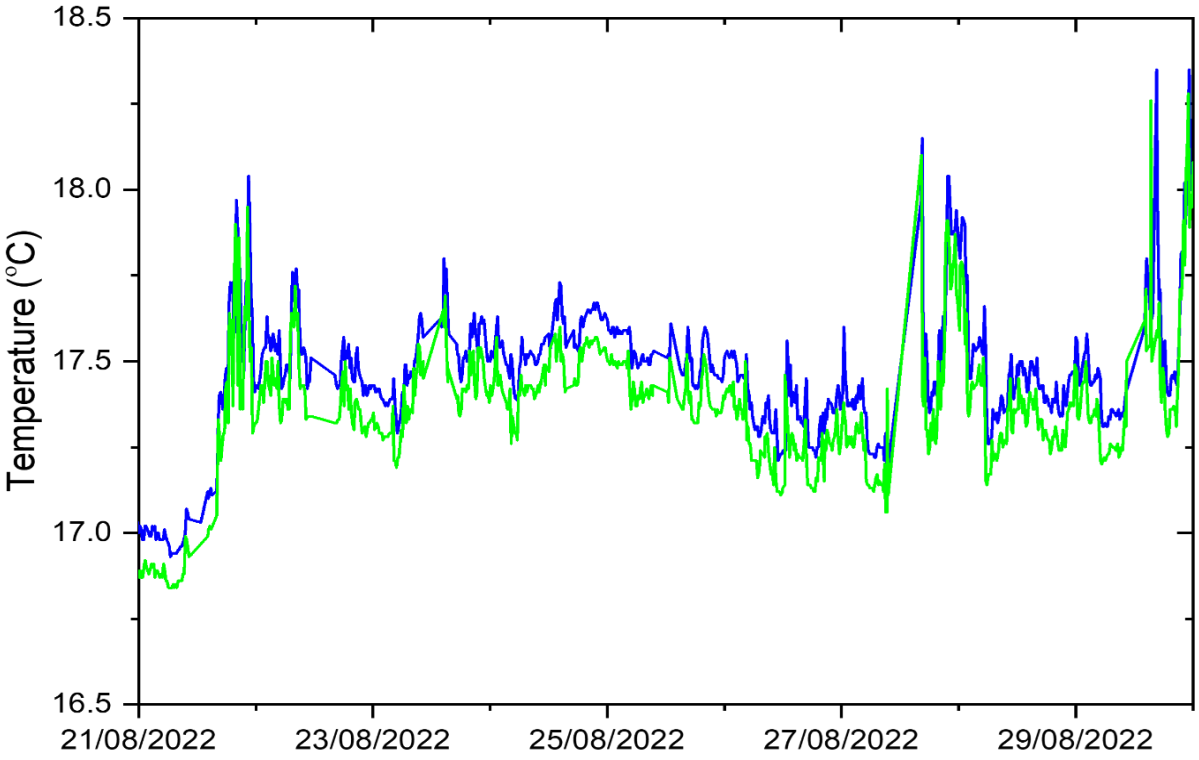

Figure 5-19 Poolbeg deployment temperature measurements of AWaMS8 (green) with commercial sensor (HydroCAT-EP) (blue) for comparison of performance between 21/08/2022 and 29/08/2022.

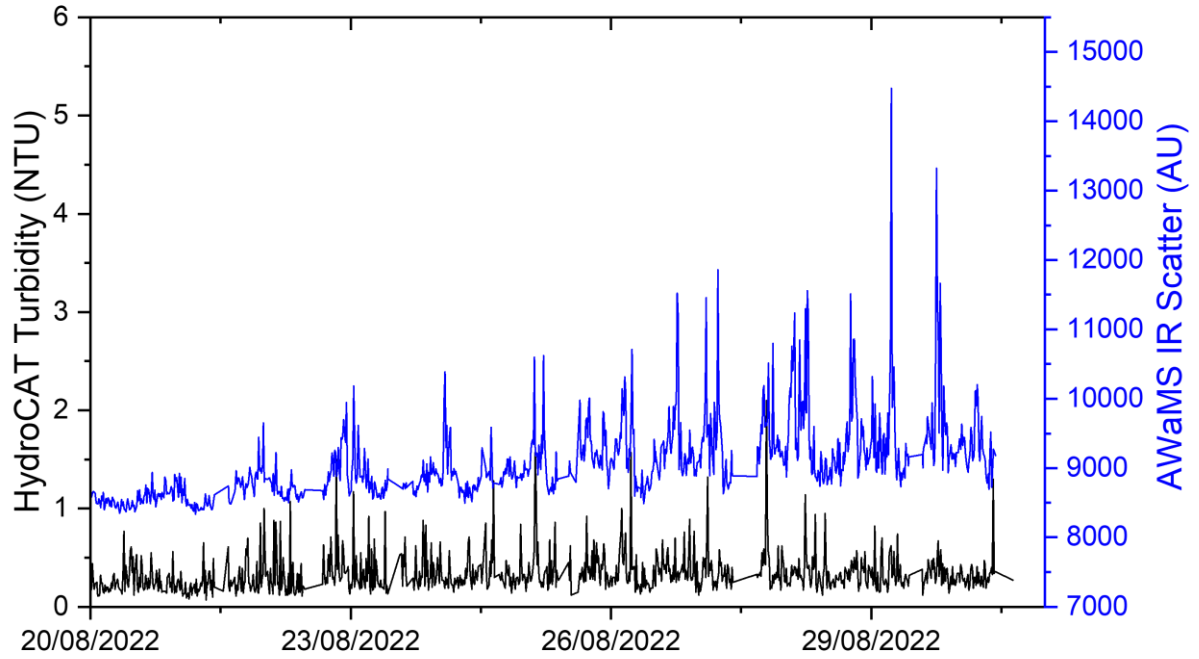

Figure 5-20 Poolbeg deployment turbidity measurements of AWaMS8 (blue) showing raw sensor response of scatter measurement and commercial sensor (HydroCAT-EP) measurements (black) for comparison of performance between 21/08/2022 and 29/08/2022.

Howth Deployment Data

Data from the Howth Deployment is shown in Figure 5-21. A potential primary production event is highlighted which is characterised by an increase in water temperature, turbidity and Chl-a levels [404–407]. With phytoplankton growth, both scatter and fluorescence are increasing and show a good correlation with temperature data. Detection of such events demonstrate that the sensor can distinguish between for example the on-set of an algal bloom (where both Chl-a and turbidity are expected to increase [406]) and a run-off event (where only turbidity is expected to increase [340]). It can be seen for both the turbidity and fluorescence measurement that the decoder algorithm produced zero values for the majority of the deployment. Again, as in the Poolbeg data this would indicate that the sensor was measuring in clean water with low levels of both turbidity and Chl-a.

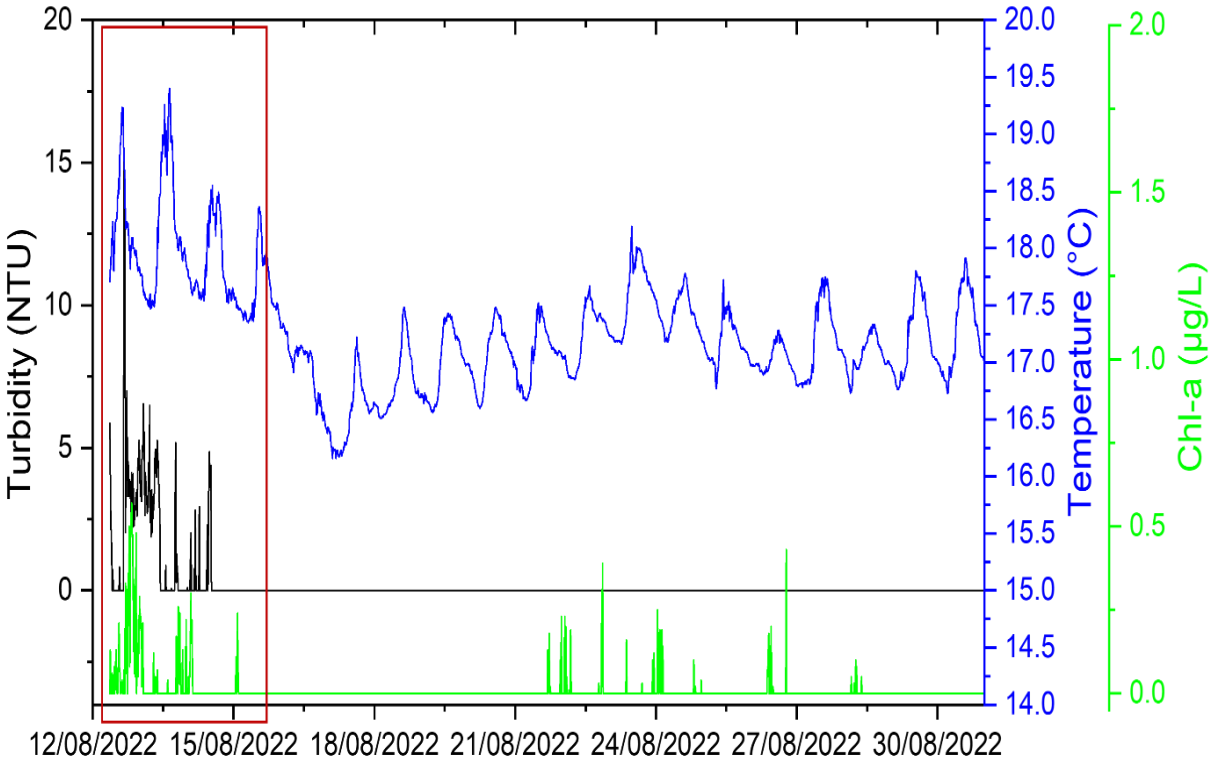

Figure 5-21 Data from AWaMS7 deployed in Howth showing temperature (blue), Chl-a (green) and turbidity (black) between 12/08/2022 and 30/08/2022. Potential primary production event highlighted in a red box with all three parameters spiking over same time period.

Clontarf Deployment Data

Data retrieved from the AWaMS sensor deployed at Clontarf is shown in Figure 5-22. The Chl-a time-series matches closely with the temperature time-series data, and shows a diurnal

cycle driven by tides or sunlight. There are 2 maximum and 2 minimum values (temperature and Chl-a) present over a 24 h period which coincides with the tidal cycle. Temperature increases during the ebb current with a maximum reached at low tide and decreases during the flood current reaching a minimum at high tide. A gradual trend in turbidity is seen from 24/08/2022 until saturation of the detection begins on 27/08/2022. This was caused by a build up a suspended sediment in the water column and is confirmed by images seen in Figure 5-31 taken upon retrieval of the sensor. Figure 5-31 shows significant sediment deposits on the sensor and Figure 5-31b shows a layer of sediment covering the lenses. The turbidity data between the 24th up to the 26th of August before the sensor reached saturation show five clear peaks which all correspond with a low tide in the area. This is shown in Figure 5-23 with the sensor's turbidity measurement plotted against tidal water levels. The tidal level data was obtained from the Irish National Tide Gauge Network (INTGN) [408]. This is a possible explanation and would suggest a build-up of sediment in the sensor's optical detection zone possible cause by lack of flow through the sensor guard.

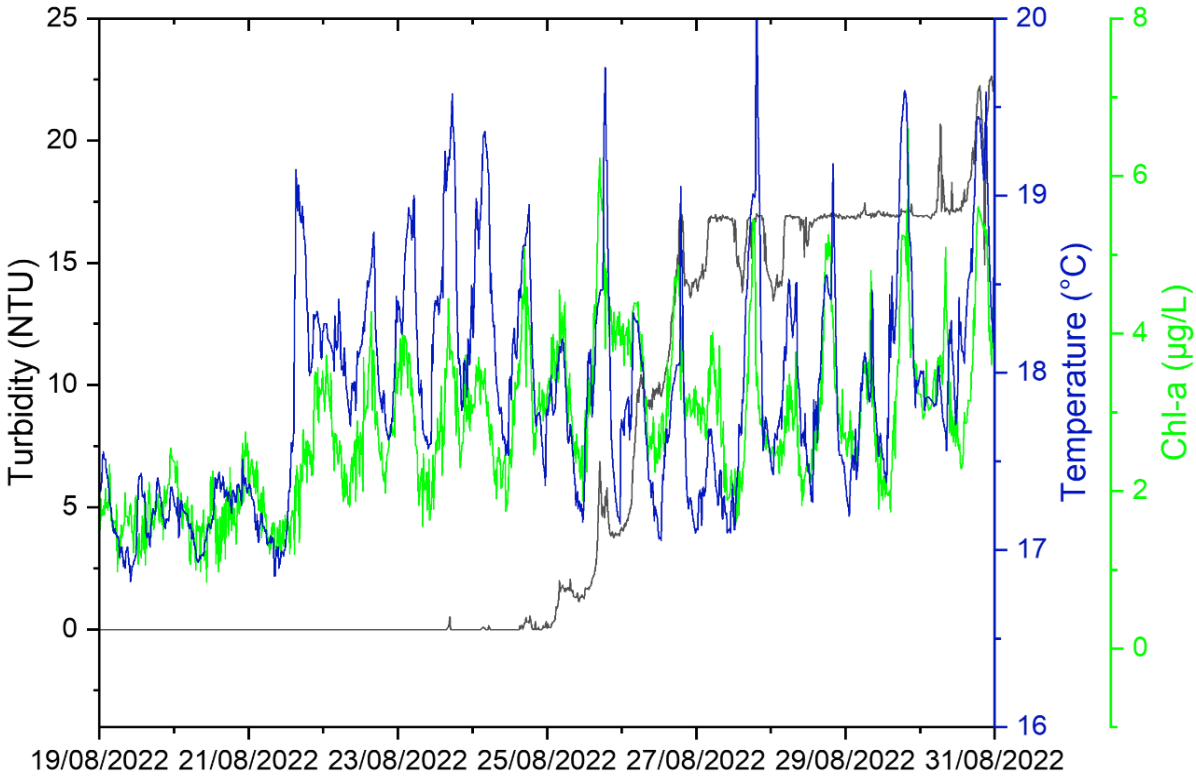

Figure 5-22 Data from AWaMS10 deployed in Clontarf showing temperature (blue), Chl-a (green) and turbidity (black) between 19/08/2022 and 31/08/2022.

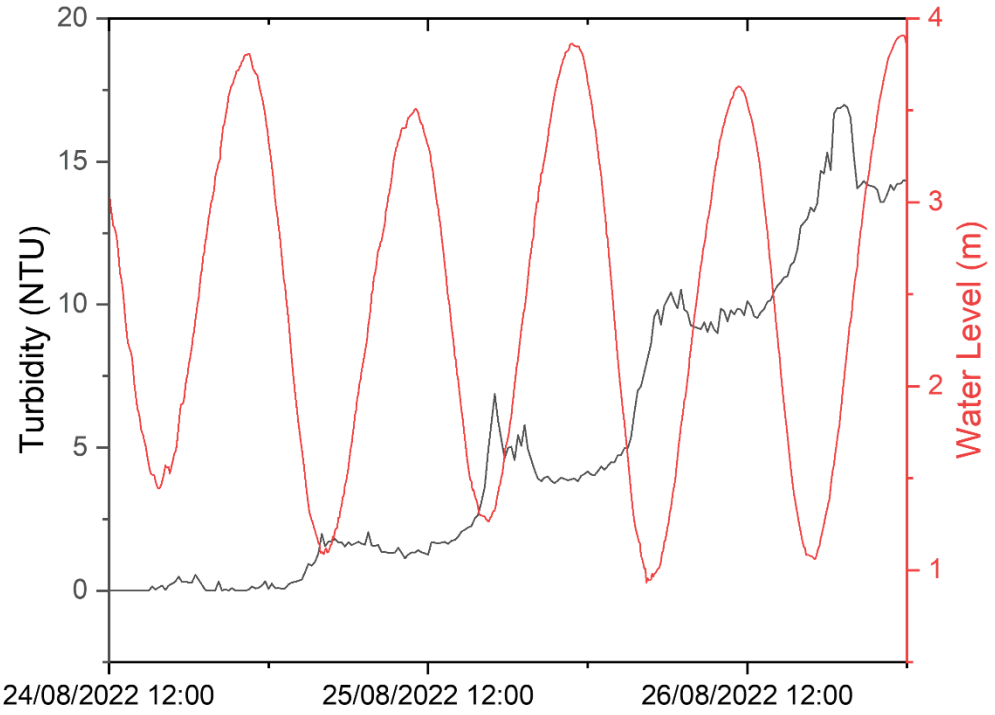

Figure 5-23 Clontarf deployment site data of AWaMS10 turbidity measurements (black) against tidal water level measurement (red) (data obtained from in the Irish National Tide Gauge Network) between 24/08/2022 12:00 and 26/08/2022. Low tides directly correlates with spikes in turbidity measured.

St Patricks Deployment Data

Data coming from the St. Patricks deployment is shown in Figure 5-24. Data is presented from the 30/08/2022 and 20/09/2022. Throughout, there is a significant amount of activity with major spikes in temperature, Chl-a, and turbidity readings from the sensor. A reoccurring event can be seen in all three measurement parameters. The pattern of the event consists of a turbidity spike followed by a significant drop in turbidity and temperature. Such high NTU values are usually present during sediment resuspension events [330,409]. The temperature drop suggests water column mixing of the colder bottom layers with the top warm layers [410,411] and substantiates the resuspension assumption. The data beyond the 6th of September shows a clear upwards trend in turbidity until reaching saturation. As the in deployment in Clontarf, this may be due to a build-up of debris in the optical head and guard structures which can be confirmed on inspection of the sensor unit post deployment as seen in Figure 5-30. Deposits of clay-like mud can be seen in the optical head, inner and outer sensor guard which would have caused the increased scatter.

Figure 5-25 shows the AWaMS sensor response over a shorter period. The data shown is from midnight on the 30th of August to noon on the 1st of September. Within this time there are five distinct resuspension and mixing events labelled a-e. This periodic event may be caused by the tidal activity with the location of the deployment site at the mouth of the river Liffey. Tidal movement would cause a change in the water column as sea water and fresh water mix a low tide [412,413]. It may also be caused by the movement of large shipping vessels in the area who perform a turnabout before docking as was found to be the case by a case study in Dublin Port by Briciu-Burghina et al., (2014) [414]. Marine traffic in ports is known to cause sediment suspension events due to the action of vessel propellers while the vessel is manoeuvring close to the seabed [415]. Peaks of Chl-a are also seen after such events. It is reported by O'Higgins and Wilson (2005) [416] of the impact of the river Liffey discharge of nutrient-rich waters mixing with saline water of the bay caused chlorophyll concentrations to spike.

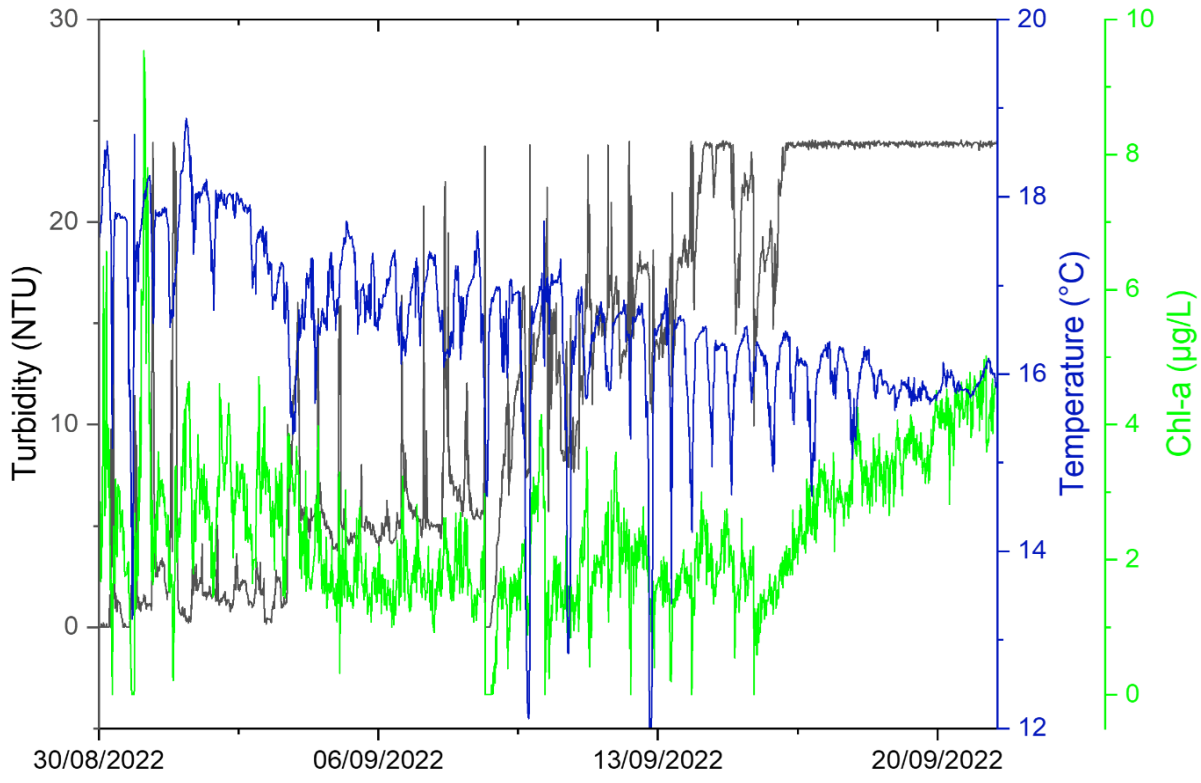

Figure 5-24 Data from AWaMS3 deployed in St Patricks showing temperature (blue), Chl-a (green) and turbidity (black) between 30/08/2022 and 20/09/2022.

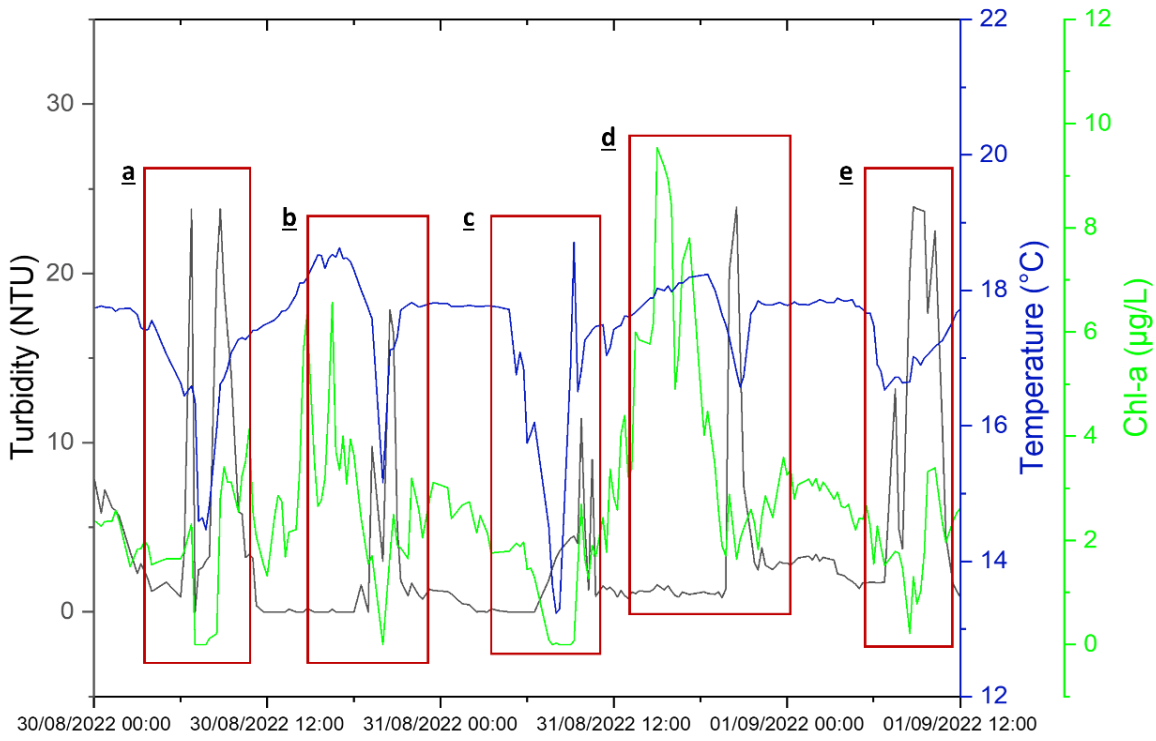

Figure 5-25 AWaMS3 data from St Patricks Rowing Club between 30/08/2022 00:00 and 01/09/2022 12:00 temperature (blue), Chl-a (green) and turbidity (black). Five resuspension and mixing events are highlight occurring at (a) 30th August at 6am, (b) 30th August at 6pm, (c) 31st August 6:30am, (d) 31st August 7:30 pm and (e) 1st September 6:45am.

Dun Laoghaire Harbour Deployment Data

Figure 5-26 shows the data retrieved and organised from the sensor deployed in Dun Laoghaire Harbour. This was the longest in time dataset collected by the AWaMS sensors during the deployment from the 16th of August to the 27th of September 2022. The longer dataset allows for more long-term trends as the site to be observed and shows the AWaMS is capable of longer-term deployments. Similar with Clontarf deployment the Chl-a time-series matches closely the temperature time-series data, and shows a diurnal cycle driven by tides. A spike in turbidity up to 18 NTU can be seen on the 20th of August. This is followed by a spike in Chl-a 2 days later on the 22nd. This may represent the onset of a primary production event [407], phytoplankton bloom [406] with a lag between turbidity seen and Chl-a detected [417,418]. There is a negative trend in temperature measured shows the seasonal transition from warmer to cooler waters moving from summer to autumn months [419]. The water temperature reduces by 2 degrees Celsius over the course of the deployment.

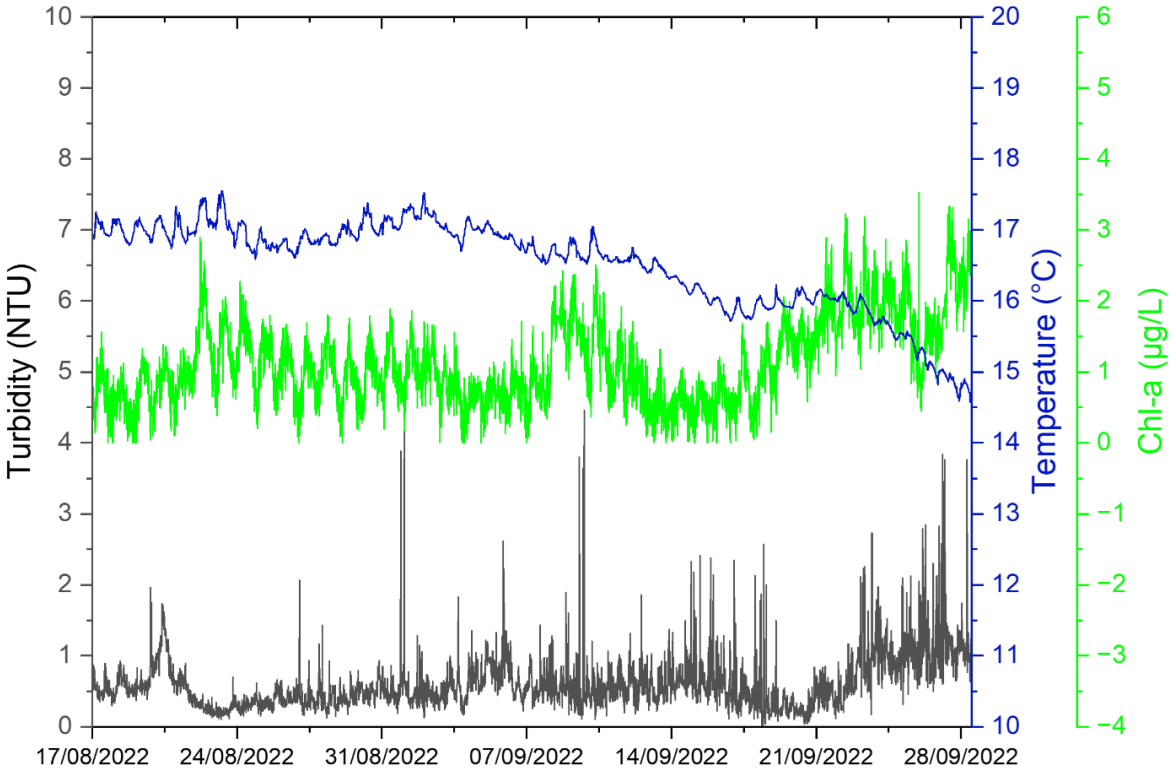

Figure 5-26 Data from AWaMS9 deployed in Dun Laoghaire showing temperature (blue), Chl-a (green) and turbidity (black) between 18/08/2022 and 28/09/2022.

5.3.2.3 Sensor Units Post Deployment Analysis

The long-term marine deployment of the novel sensor unit designs allowed for new information on the sensors design aspects. As seen in this section, the deployment of multiple sensors in different locations for prolonged periods of time produced a wide range of results. Images were taken of the sensors and deployment hardware post while being retrieved by TechWorks Marine. The sensors units were then taken back to the lab to inspect in more detail. The AWaMS units were all intact upon retrieval and remained securely attached to the deployment mounts.

AWaMS7 Post Deployment

AWaMS7 is seen mounted to the deployment hardware post deployment in Howth Harbour after 27 days in Figure 5-27. A thin layer of slime and grass-like or algae macro-fouling growth can be seen on all surfaces, apart from the Trilux 33 painted external sensor guard.

Figure 5-27 Images of post deployment AWaMS7 mounted to Mini Bouy after 27 days deployed at Howth provided by TechWorks Marine. A layer of slime and seaweed growth can be seen on all surfaces except the sensor guard.

Figure 5-28 shows the post deployment images of AWaMS7 upon closer inspection back in the lab. A small amount of moisture was found inside the optical head which caused some minor corrosion of the electronic components, however the sensor remained fully functioning. Figure 5-28a and d show the body and optical head of the sensor with the growth of seaweed, algae and other vegetation on the enclosure body and guard clamp. The sensor's guard is free of fouling due to the anti-fouling paint coating (Figure 5-28a and b). The internal detection area seen in Figure 5-28b shows little fouling inside the optical detection zone and on the lenses. This would support that the UV LED anti-fouling strategy had an effect. The surfaces not receiving the UV light appear to have macro fouling build up occurring.

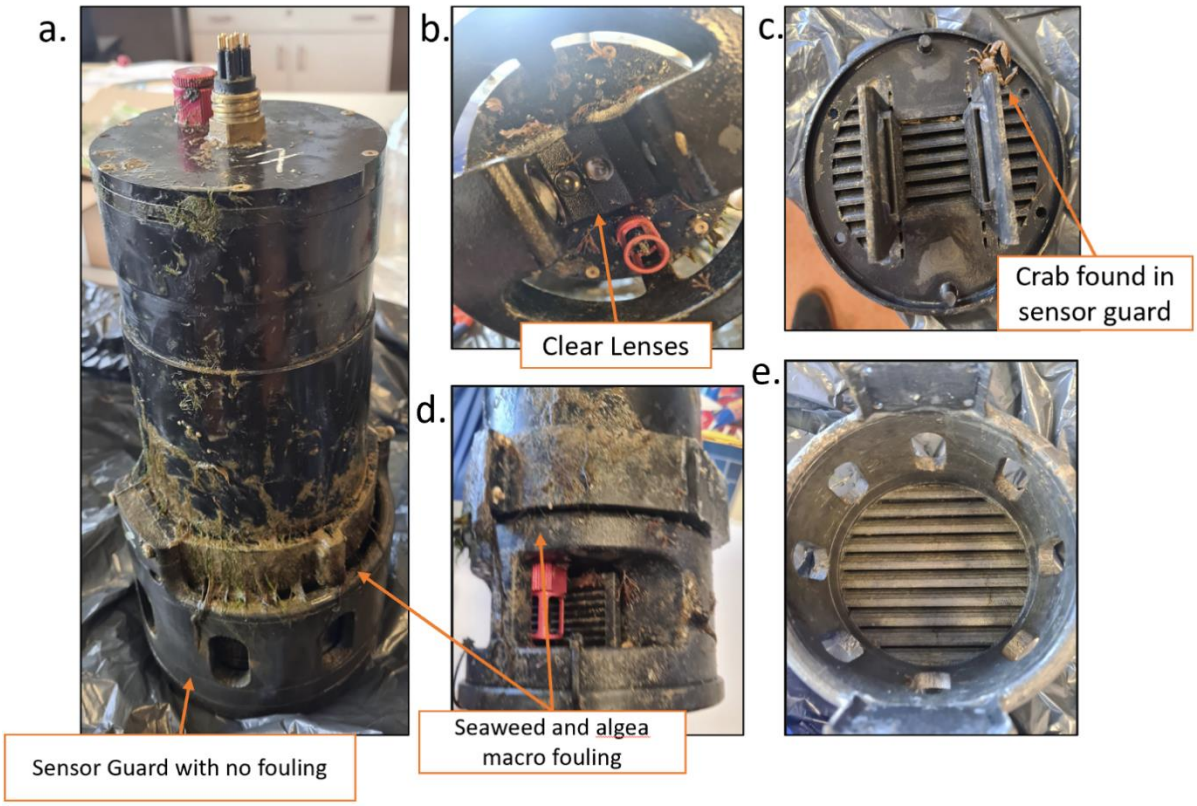

Figure 5-28 Images of AWaMS7 post deployment in lab upon retrieval from Howth Harbour. (a) Full sensor view showing growth of seaweed on the enclosure body and guard clamp but no fouling occurring on the antifouling paint coated sensor guard. (b) Bottom view of optical head showing clear lenses with growth seen outside of the optical detection zone where UV antifouling LEDs had no affect. (c) Top view of the internal guard showing low amounts of sediment and a juvenile crab found inside the guard. (d) View of the optical head showing sediment and seaweed/algae growth on the surfaces. (e) Top view of the external sensor guard showing little debris or biofouling.

AWaMS3 Post Deployment

The images of the AWaMS3 system post deployment can be seen in Figure 5-29 after being deploying in St-Patricks Rowing Club site for 42 days. White deposits are noticed on the top cap section which was also seen in a previous deployment described in Section 3.3.3.2. The primary cause of this is galvanic corrosion with the stainless steel of the fastener interfacing with aluminium flanges causing an electron transfer weakening the aluminium [224]. This will require a design change to prevent with either aluminium fasteners or stainless-steel flanges to be used to avoid the material difference causing galvanic corrosion. The layer of sediment or mud suggests a highly turbulent deployment site which can observed in the data collected by the AWaMS as seen in Figure 5-24. No fouling growth is observed on either the copper tape layer on the sensor body or the sensor guards showing the copper and Trilux 33 antifouling paint was effective. Seaweed growth can be seen on the mounting frame.

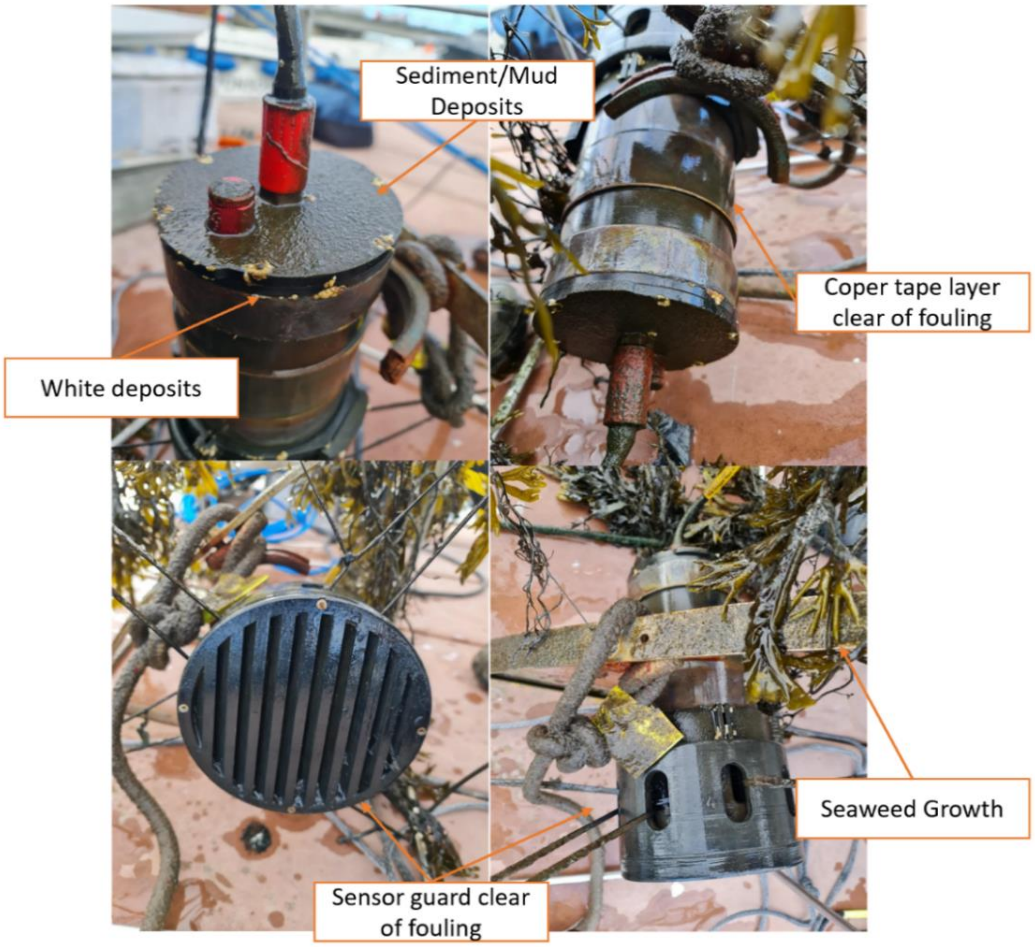

Figure 5-29 Images of post deployment of AWaMS3 deployed at St Patricks Rowing Club for 42 days provided by TechWorks Marine. White deposits can be seen forming around the fasteners on the top cap section. A layer of mud or sediment can be seen deposited on the top cap. The copper tape applied to AWaMS3 shows no signs of fouling growth. Likewise, the sensor guard appears clear of fouling. Seaweed growth can be seen on the deployment cage structure.

Images from a visual inspection of the AWaMS3 after its return to the lab from deployment in St Pats can be seen in Figure 5-30. The sensor was deployed for a total of 42 days. This sensor unit was the only unit with copper tape applied to the enclosure body to prevent fouling. From Figure 5-30a this was highly effective in the prevention of macrofouling build up and the green oxidisation of the copper can be seen. The sensor's external guard is also free of any fouling which was coasted with an anti-fouling copper-based paint. Figure 5-30 b,c,d, and e, all show there was a significant build-up of debris in the guard and optical head. The deployment site is located at the mount of the river Liffey with mixing of sandy and silty mud present. The positioning of the mud deposits all to one side (Figure 5-30c, d, and e) would indicate the flow of the river or tide deposited the mud within the guard structures. This large number of debris would majorly affect the optical measurements of the sensor

unit. This confirms the upward trend of turbidity measurements seen in Figure 5-24 was due to a build-up of debris.

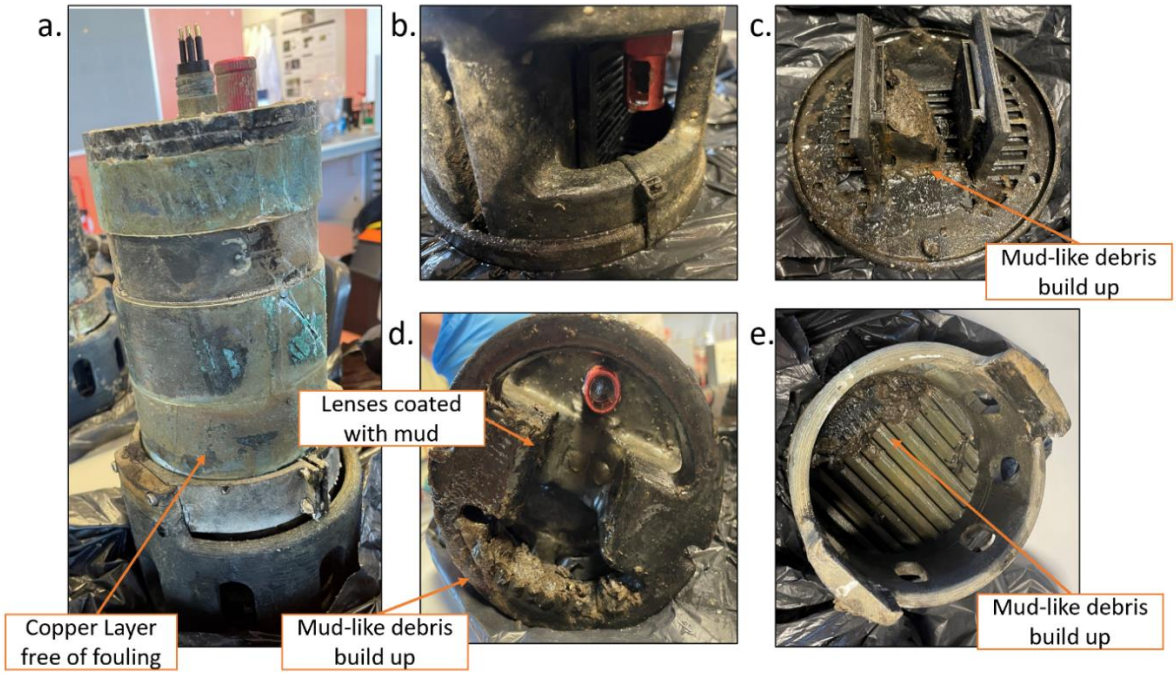

Figure 5-30 Images of AWaMS3 post deployment in lab upon retrieval from St Patricks Rowing Club. (a) Full sensor view showing oxidation of the copper tape on the main enclosure. (b) View of optical head with sediment deposits on surfaces. (c) View on the internal sensor guard with large build-up of debris. (d) Bottom view of optical head showing further deposits of debris and sediment coasting the lenses. (e) Top view of the external sensor guard showing build-up of debris.

AWaMS10 Post Deployment

No post deployment images were taken of AWaMS10 in Clontarf. The AWaMS10 can be seen in Figure 5-31 after its deployment in Clontarf. The system was deployed for 28 days having replaced the AWaMS5 system which failed, failure analysis of this sensor is conducted in Section 5.3.3.3. The sensor collected data for a total of 22 days in total without any electronic or mechanical issues. It was reported by TWM that the Mini-Bouy received damage after a collision with the mooring buoy it was tied to. No damage was identified on the sensor unit due to the impact. Figure 5-31a shows the sensor body with minor fouling of barnacles and seaweed. Figure 5-31c and d show a high amount of sediment settling to on the surfaces of the internal guard and optical head, respectively. Figure 5-31b shows a layer of sediment built up on the lenses. This build-up would explain the positive trend in turbidity seen in the dataset presented in Figure 5-22.

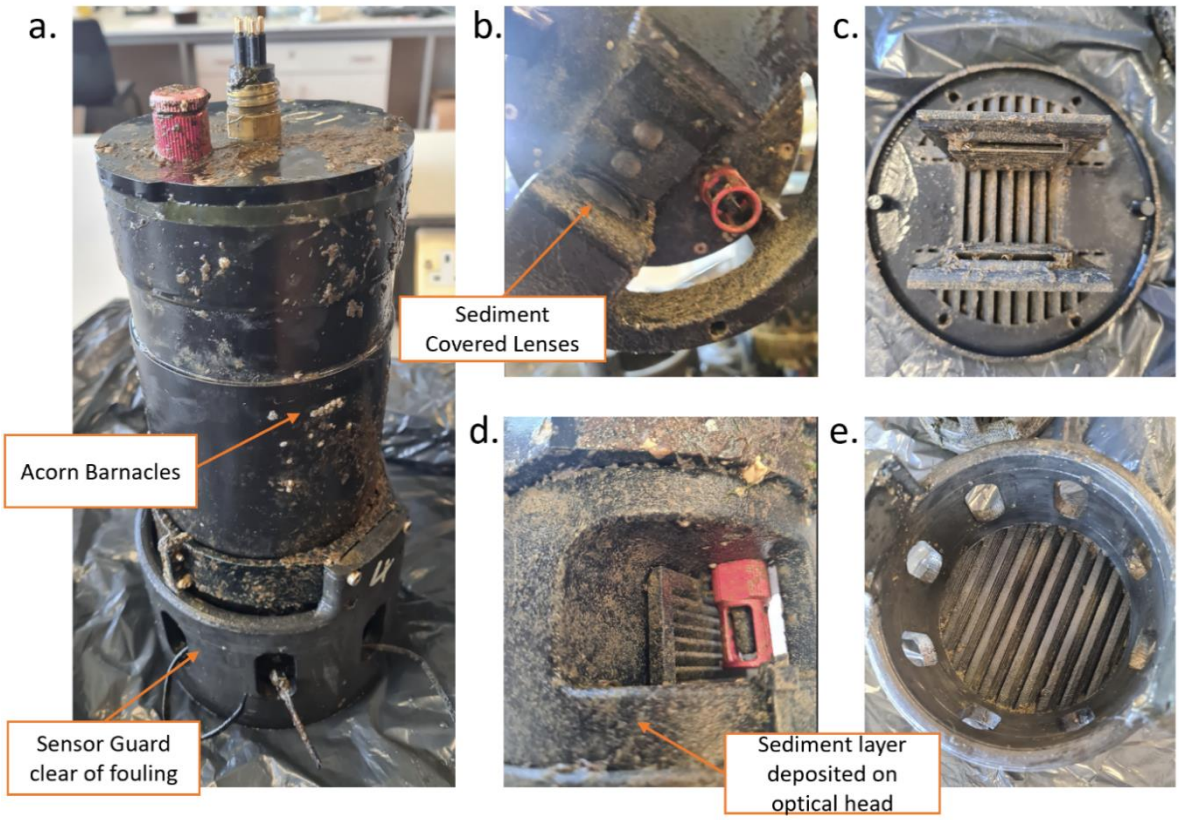

Figure 5-31 5-32 Images of AWaMS10 post deployment in lab upon retrieval Clontarf. (a) Full sensor view showing minor build-up of fouling on the surfaces (b) View of optical head with sediment deposits on lenses and build-up of grasses on internal wall surfaces. (c) View on the internal sensor guard showing deposits of sediment on surfaces (d) View of optical head showing sediment and macrofouling deposited on surfaces (e) Top view of the external sensor guard showing minor amounts of sediment on surfaces.

AWaMS8 Post Deployment

Images of the AWaMS8 sensor and HydroCAT sensor post deployment in Poolbeg Marina can be seen in Figure 5-33. The sensors were deployed for a total of 42 days. The visual inspection of AWaMS8 post deployment in Poolbeg Marine can be seen in Figure 5-34. No leaks or moisture build up were detected inside the sensor housing. Figure 5-34a, b and e show a build-up of macro fouling attached to the enclosure bodies surface. Barnacle and tubeworms can be seen which have adhered to the sensor's surfaces. As with the other sensor units, the guard does not have any fouling occurring on its surface showing the anti-fouling paint had a significant effect. Figure 5-34c and d show that the UV antifouling strategy was also successful as the detection zone and lenses are mostly free of any fouling while the surrounding untreated areas have high amounts of macrofouling from tubeworms.

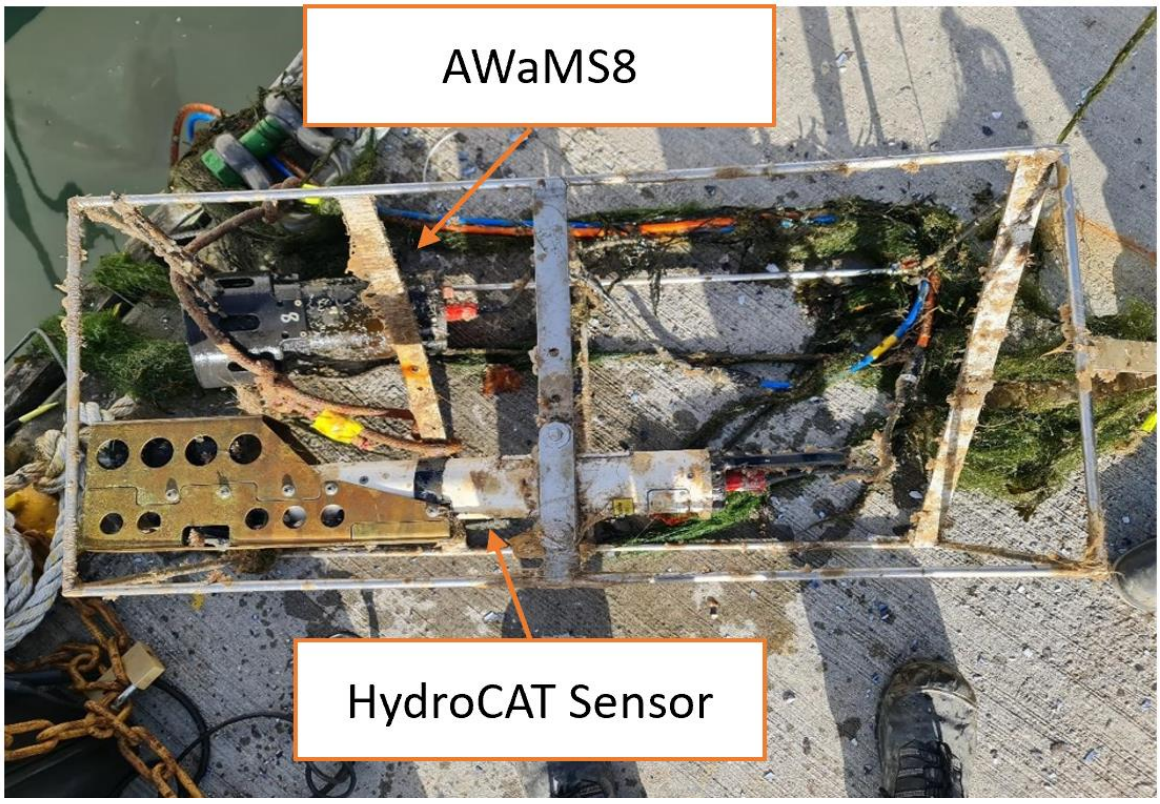

Figure 5-33 Images of post deployment AWaMS8 and HydroCAT-EP sensor mounted to cage deployed in Poolbeg for 42 days provided by TechWorks Marine.

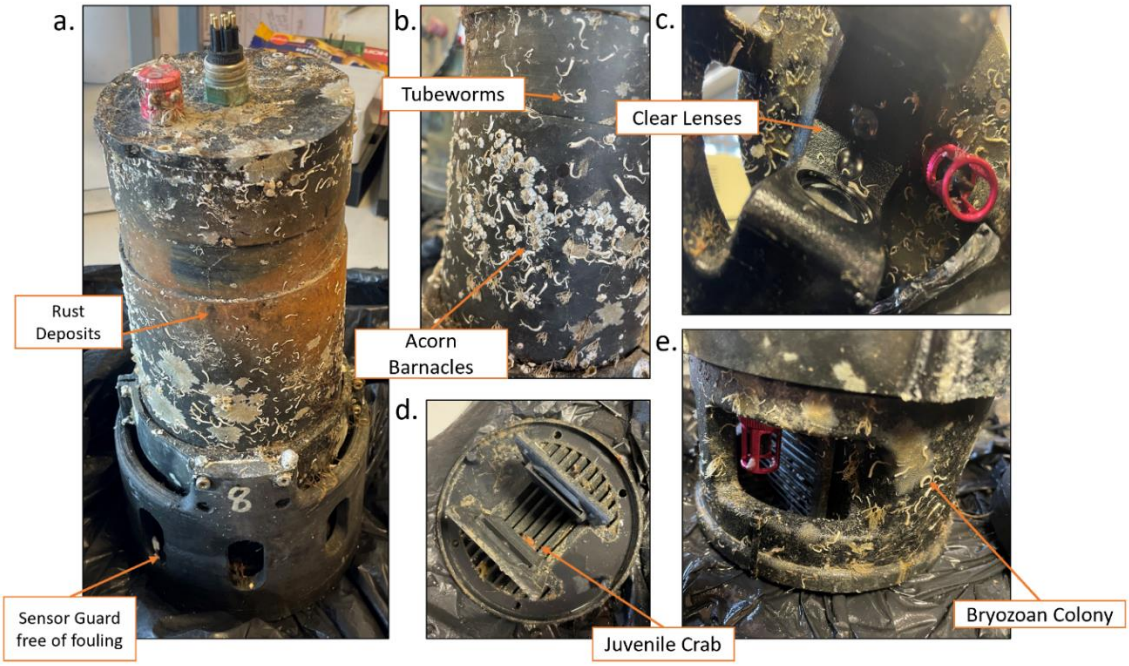

Figure 5-34 5-35 Images of AWaMS8 post deployment in lab upon retrieval Poolbeg Marina. (a) Full sensor view showing macro fouling growth and orange rust deposits (b) Closer view of sensor enclosure showing growth of tubeworms and barnacles on the surface. (c) Bottom view of optical head showing clear lenses with minor fouling around the detection zone. (d) Top view of internal guard showing minor fouling and juvenile crab species (e) View of optical head with build-up of macro fouling on surfaces.

AWaMS8 Post Deployment

The MB with AWaMS9 attached can be seen post deployment in Figure 5-36. The systems were deployed for a total of 72 days. High levels of slime and grass-like seaweed growth can be seen on the body of the Mini-Buoy. Figure 5-37 shows images of AWaMS9 in the lab post retrieval from the Dun Laoghaire Harbour deployment. No leaks or moisture build-ups were detected within the sensor and the unit output data for a total of 56 days. The difference in deployment days and operational days were due to downtime maintenance carried out by TWM on their MB system. A greater amount of macro-fouling can be seen on the body (Figure 5-37a), optical-head (Figure 5-37b), and internal guard (Figure 5-37c and d) compared to the other sensor units. A thick layer of slime, algae, acorn barnacles, tunicates and bryozoan growth can be seen to have formed on all components of the sensor. No discernible growth was found on the external guard except on the contact points between the guard and the mounting clamp (Figure 5-37e). Figure 5-37d shows that the UV anti-fouling cycle kept the lenses clear of any organic matter building up.

Figure 5-36 Images of post deployment of AWaMS9 and Mini Buoy platform deployed in Dun Laoghaire for 73 days provided by TechWorks Marine. High levels of seaweed growth are seen on the Mini Buoy structure.

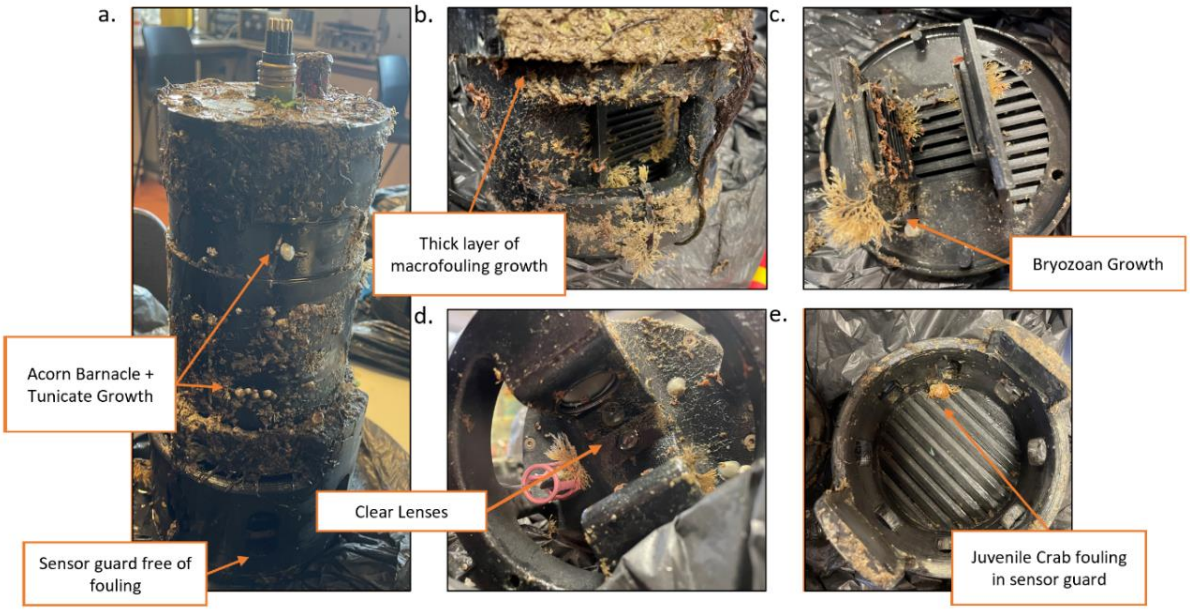

Figure 5-37 Images of AWaMS9 post deployment in lab upon retrieval from Dun Laoghaire Harbour. (a) Full sensor view showing large build-up of fouling on the surfaces. (b) View of optical head with macro fouling on surfaces. (c) Top view of internal guard showing fouling growth. (d) Bottom view of optical head showing clear lenses with build-up of fouling around the detection zone. (e) Top view of the external sensor guard showing minor amounts of fouling with a juvenile crab.

The overall result of this long-term deployment is the sensors demonstrate a robust design capable of remaining operational for months at a time. No discernible damage due to impact or abrasion could be seen to have damaged the sensor units. Apart from AWaMS5, all systems remained watertight throughout with only minor build ups of moisture inside the sensor bodies observed. The galvanic corrosion occurring due to the interface of steel fasteners and the aluminium flanges will need to be addressed. Stainless steel flanges or aluminium fasteners would resolve this issue when used in marine deployments. The antifouling strategies all worked to some degree. The copper tape used on AWaMS3 was effective with no fouling able to occur on the sensor body in contract with the other four sensors which all had some degree of fouling build up on the sensor body. The Trilux 33 antifouling pain applied to the external sensor guard was incredibly effective with not fouling build up occurring on any guard in any deployment site. The UV antifouling LEDs proved a success in the prevention of biological growth occurring in the optical detection zone. The approach however could not prevent sediment from building up and coating the lenses which may solicit the requirement of a physical wiper system for high sediment sites. Additionally, the design of the internal guard for the reduction of ambient light needed to be redesigned to allow additional flow as sediment and fouling is observed to have built up more prominently inside the guard.

5.3.2.4 Sensor Unit Failure Analysis

AWaMS5 which was deployed at the Clontarf site experienced a major breach allow extensive amounts of water to enter the enclosure as seen in Figure 5-38b. The sensor was deployed on the 11th of August 2022. Issues with the data appeared within hours of the deployment as seen on TWM's CoastEye platform. The sensor began returning an 'ovf' (meaning overflow) in place of the temperature value indicating a stack overflow. This suggested that the temperature probe was outputting non-sensical values or out of bounds values. As the temperature probe communicates over a digital protocol (I^2C), moisture damage affected the data more prominently before the entire system failed to operate acting as a warning flag in the data. Moisture sensors inside the sensor housing can be used to more effectively flag an increase of moisture, an example of this design has been done by BlueRobotics for detecting leaks in their ROVs [420]. Figure 5-38 presents a visual inspection of the sensor on its return to the lab to identify the cause. All watertight seals and joins in the sensor were identified as single points of failure. A focus of inspection was put

on the O-rings on the flanges (Figure 5-38c), the face seal O-ring of the flange (Figure 5-38f) and the optical head lens seals (Figure 5-38d and e). The radial O-rings on the top flange were found to have cracking with a visible notch of exposed aluminium seen in Figure 5-38c. Using the air pressure test as described in Section 4.2.2.2, it was found that either the face O-ring of the flange and the top cap or the radial O-rings of the flange and the sensor body (see Figure 3-8 for how the flange O-rings create a watertight seal at both interfaces) did not form a complete seal which allowed a significant amount of air out during pressurisation.

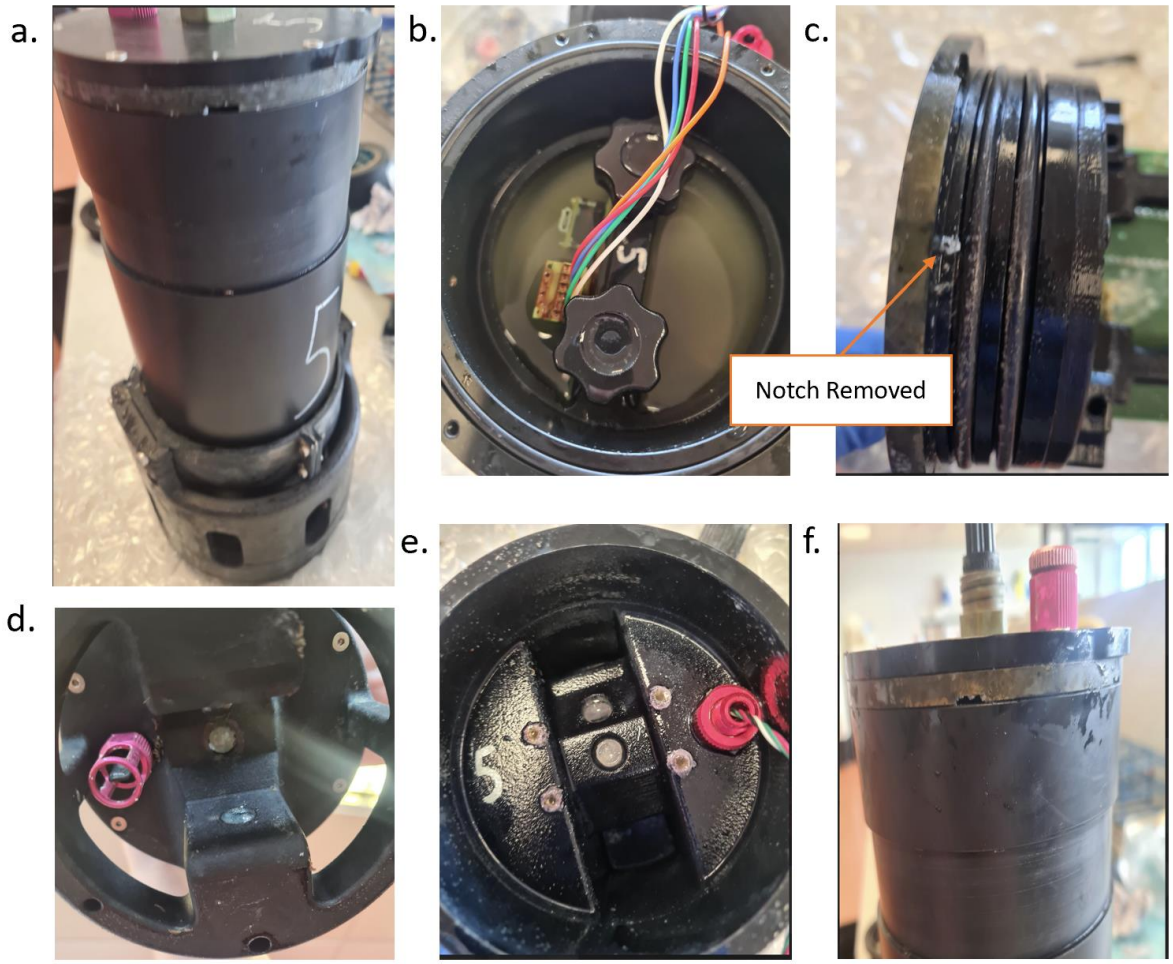

Figure 5-38 Visual inspection images of AWaMS5 which failed while deployed in Clontarf. (a) View of sensor body with no obvious signs of damage. (b) View inside sensor enclosure showing large volume of sea water. (c) View of the top flange and O-Rings with a small silver notch visible in the flange indicating possible damage. (d) Bottom view of the optical head showing no signs of damage. (e) Internal top view inside the optical head showing moisture with white deposits around the brass thread inserts. (e) Inspection image of the top flange showing discolouration of the external surface of the black anodised coating.

The effect of the water damage on the electronics can be seen in Figure 5-39. Any exposed metal connection is damaged by corrosion and oxidation. The silicon coating was applied to the main control board which it can be seen protected some of the electronics (Figure 5-39d and e) however some areas were missed as seen by the areas corroded.

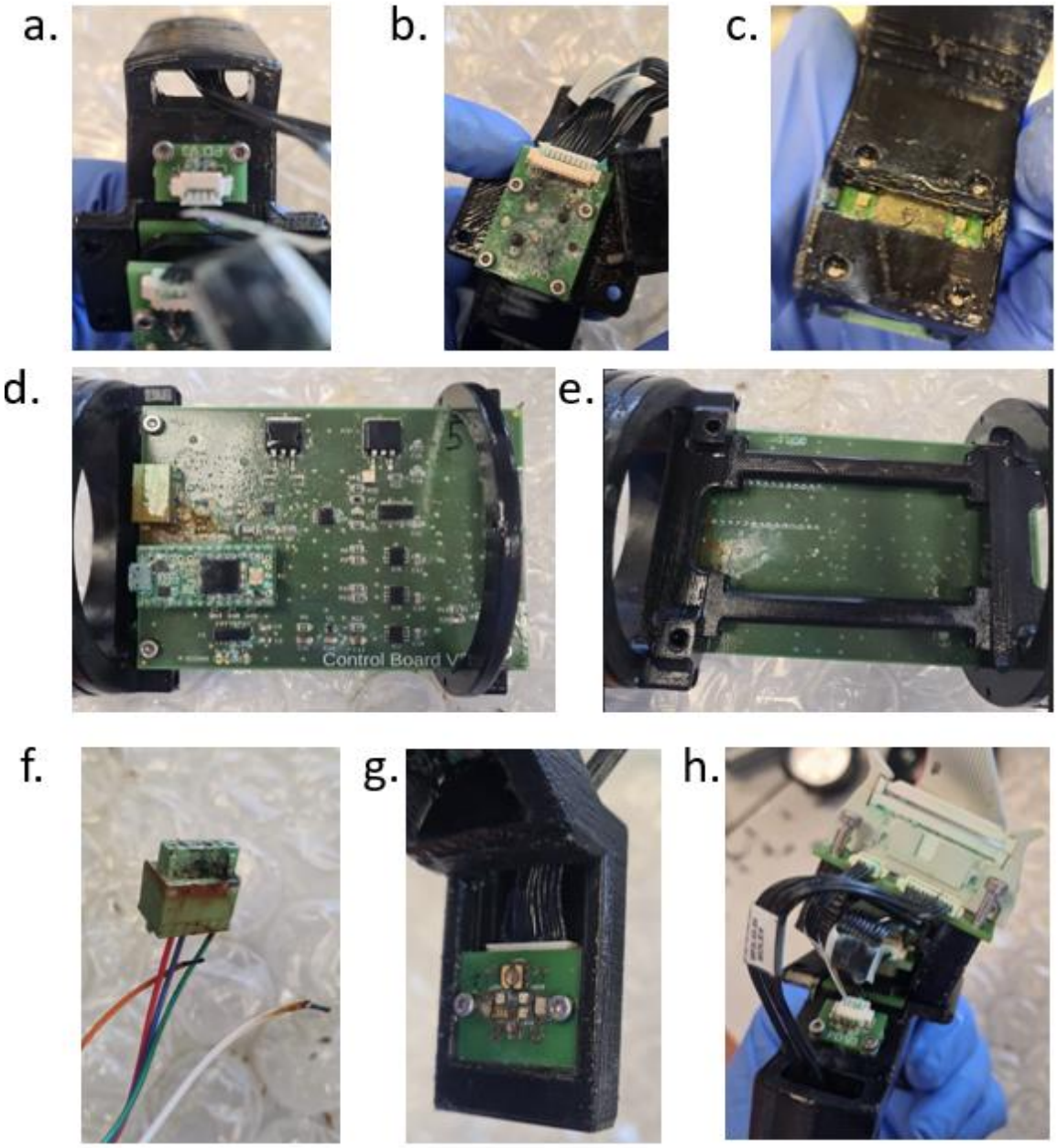

Figure 5-39 Inspection images of the AWaMS5 electronic components after flooding event. (a) image of the photodiode board showing oxidisation of connection pins. (b) View of the mounting board of the spectrometer showing black discolouration and oxidisation of exposed pins. (c) Front view of the spectrometer and UV LED board showing damage to the CMOS spectrometer. (d) Top view of the control board showing oxidation of exposed pins not coated with silicon spray. (e) Bottom view of control board showing minor corrosion of connection pins. (f) View of damaged bulkhead to control board connector. (g) View of LED Array board with oxidised connections. (h)

Side view of electronics mount and connector board showing addition oxidation of copper connections.

Further inspection of the radial O-rings was done as seen in Figure 5-40. Clear cracking can be seen in both O-rings. From the literature there are several causes of degradation of nitrile rubber which results in cracking. Ozone cracking is a common cause highlighted [421–423]. The exposure of rubber to ozone present in the air can cause to oxidative degradation which leads to cracking of the nitrile rubber. Insufficient silicon lubricant applied may have been a contributing factor leading to this. Another causing of cracking is mechanical stress (in tension or compression) [424,425] which deforms the rubber causing microcracking which overtime leads to larger cracks forming. The O-Rings were left on the flanges for a sustained period of time in tension having been constructed in August 2021 and only deployed in August 2022. This prolonged period under mechanical stress may have led to the degradation of the O-rings. In summary, the sensor unit failed due to lack of maintenance. Maintenance of each sensor will need to be conducted pre and post deployments with the O-rings being regularly checked and replaced if needed.

Figure 5-40 Closer inspection of the radial O-rings of AWaMS5 top flange. Cracking can be seen forming in the nitrile-rubber.

5.3.3 Freshwater Sensor Deployment

This deployment was the first test of the sensor units developed in a freshwater environment. The deployments demonstrate the broad capabilities of the design to be used in multiple different aquatic environments.

5.3.3.1 First Deployment in Owenmore River

The data plotted in Figure 5-41 shows the turbidity measurement by the Unit 8 sensor, the YSI Sonde and the water level of the river between the 27th of March and the 4th of April. The datalogger developed was successfully able to operate and power the Unit 8 sensor as well as store the data over the duration of the deployment. Fluorescence measurements to detect fDOM were made by the Unit 8 sensor but the concentrations of fDOM were too high and saturated the detector throughout the deployment. The response from the sensor at 850 nm pixel value for the scatter measurement was converted to NTU values using the calibration curve generated for Unit 8 (see Section 4.3.3.4). From the data the sensor unit matched the readings from the YSI probe closely. From the data supplied by the OPW weather station, it can be seen that the water levels spikes on two occasions. The first which occurs 29th of March caused a spike of turbidity followed by a sharp decreased which in turn was followed by another larger spike of turbidity in both sensors. This event may be in line with a rainfall event with runoff from the land entering the waterway [426,427]. The second high water event does not cause any change in the turbidity values read by either sensor.

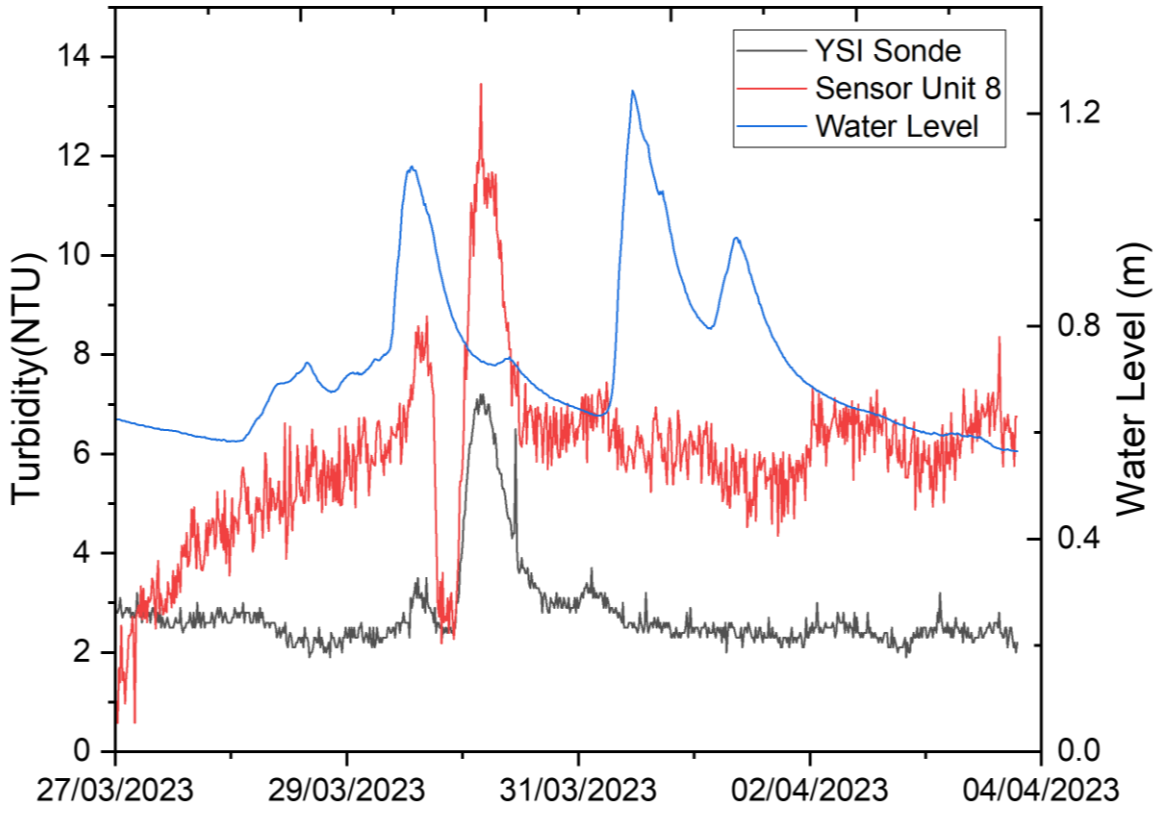

Figure 5-41 Turbidity data from the DCU sensor and the commercial YSI sonde sensor with water levels measured by the weather station upstream overlayed.

5.3.3.2 Second Multiparameter Measurement Deployment in the Owenmore River

The sensor was redeployed on the 17th of April 2023 for a total of three days. The sensor performed a multiparameter measurement cycle using three different LEDs and three different measurement modes. The application of the spectrometer showed its advantages as the integration time for the detection of fDOM in the fluorescence measurement mode was easily altered. Figure 5-42 shows the measurement of the sample taken by the sensor with the new settings. The fluorescence measurement (in red) shows the fluorescence at 450 nm is within the limits of detection of the detector. The addition of the 430 nm LED measurement transmittance is also added (in blue) along with the 850 nm measurement in scatter.

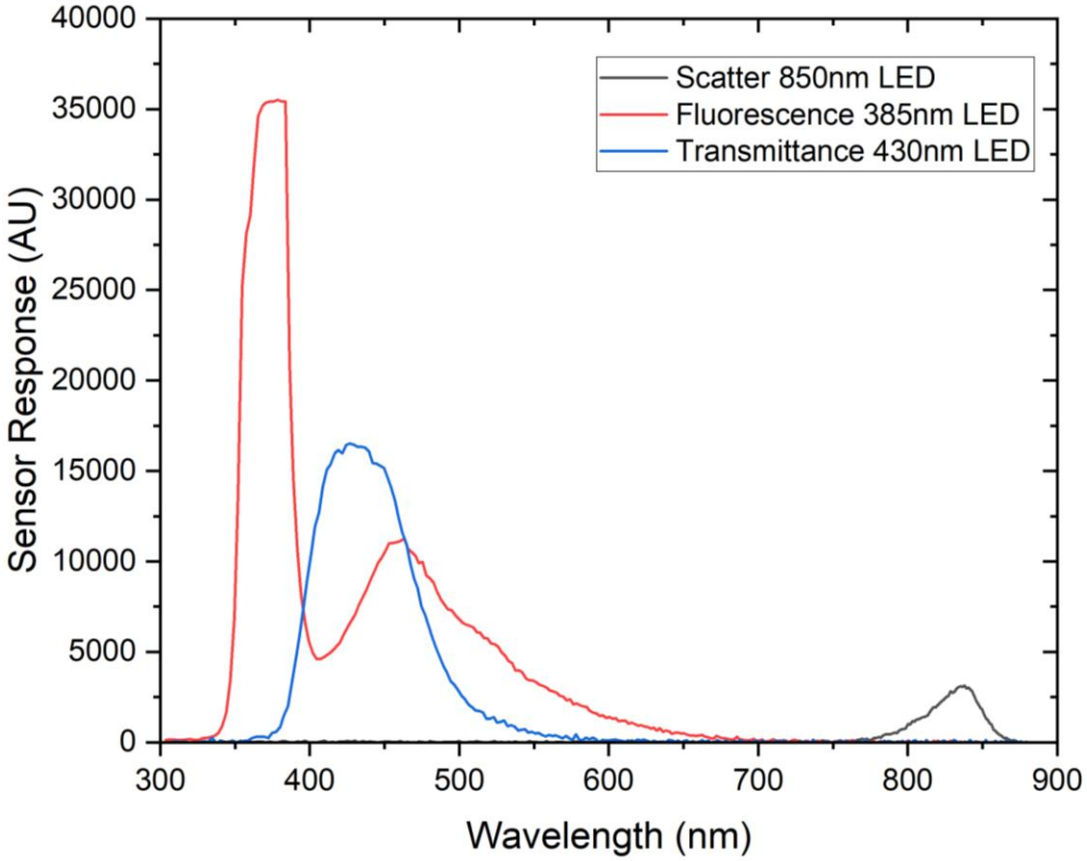

Figure 5-42 A sample measurement taken by the sensor from the sample collected from the Owenmore River with all three measurements overlaid. The black line showing the scattered signal from the 850 nm LED, the red showing the 385 nm LED signal as well as a potential fluorescence peak at 450nm and the blue line showing the 430 nm LED signal transmittance.

The data retrieved from the sensor is plotted in Figure 5-43. Along with the measurement taken by the AWaMS, the water level data was also included. Both the fluorescence response of the sensor at 450 nm and the transmission response at 430 nm show a negative trend. Additionally, the water levels measured during this period also fell by 6 cm. The water levels compared to those measured during the first deployment are lower with no spikes or rainfall events. This would indicate a dry period. There is a slight increase in turbidity levels as seen in the scatter data at 850 nm. There is no change in the sensor's response at 680 nm fluorescence. Periodical temperature measurements correspond to the day and night cycle with peak temperatures recorded after noon and minimum temperature after midnight. Overall, a longer deployment is needed to see any long-term trends or short-term rainfall events.

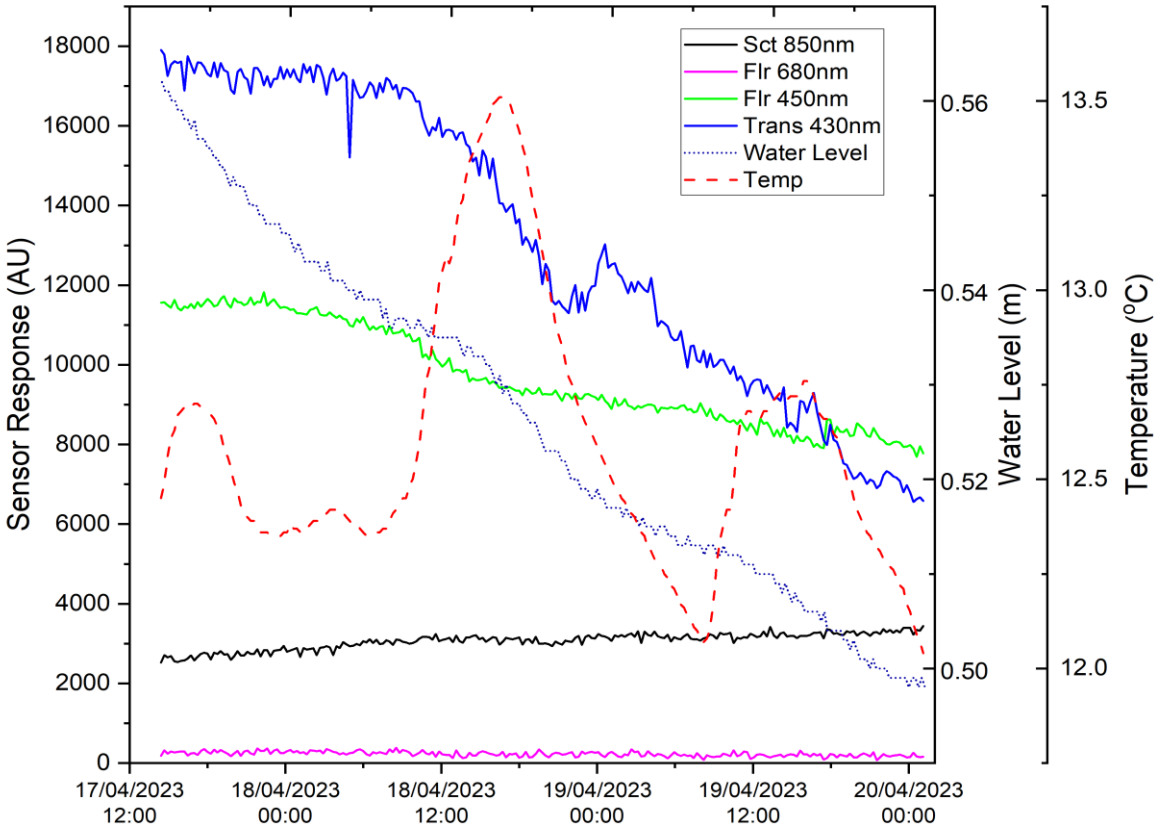

Figure 5-43 Data from the three-day deployment is shown in addition to the temperature measurement from the sensor's temperature probe and the water levels data from the nearby weather station. The signal intensity at 850 nm was used for scatter, for fluorescence 450 nm (fDOM emission) and 680 nm (Chl-a. emission) intensities were plotted and the signal intensity at 430 nm was taken for transmittance.

This setup demonstrates the sensors potential to measure optical response in all three measurement modes (transmittance/absorption, scatter, and fluorescence) using multiple different light sources (UV, Blue and IR LEDs). Two target analytes can be measured in a single fluorescence scan using the spectrometer as shown in the monitoring of both fDOM and Chl-a. This multiparameter measurement ability allows for correlation and trends to be identified between multiple different spectral parameters in the water column. The multiparameter sensor design has significant potential to be expanded even further with the use of the eight LEDs spanning from the UV to the IR able to be measured by two spectrometers and a photodiode in absorption/transmission, scatter/backscatter, and fluorescence modes. The sensor design has been shown to be able to produce data from multiple different parametric perspectives to give a holistic view of the status of the water column being measurement. With further deployments and an expansion of the measurements this would have many applications in aquatic environmental monitoring. This approach is used by remote sensing technologies for the identification of eutrophication processes in coastal regions [428]. Holistic evaluations and multiparametric approaches for water qualities in rivers and freshwater assessments are commonly required in EU states with the Water Framework Directive 2000/60/EC [37] aiming to improve ecological qualities [429]. Further work is required to expand the sensors analytical measurement capabilities and data processing and trend recognition software. Additional deployments are also required to validate the sensors measurement potential be used a multiparametric measurement tool.

5.3.3.3 Datalogger Performance Analysis

Figure 5-44 presents the voltage drop of the battery as measured by the datalogger every 15 min over the course of the deployment. A linear fit is applied to the data which gives a voltage drop of 0.0545 V per day. From the datasheet of the battery, the floating voltage of the battery when fully charged is between 13.5 V and 13.8 V. The cut off voltage the battery can safely operate to is 11.6 V. By applying Equation 5-9 the measured voltage drop of 0.0545 V per day (V_{drop}), 13.4 V as the measured fully charged float voltage (V_{full}) and 11.6 V as the fully discharged voltage (V_{dis}), a total operational time (T) can be calculated as 35 days which highlights the maximum deployment which can be achieved using the datalogger developed.

$$T = \frac{V_{full} - V_{dis}}{V_{drop}} \qquad 5\text{-}9$$

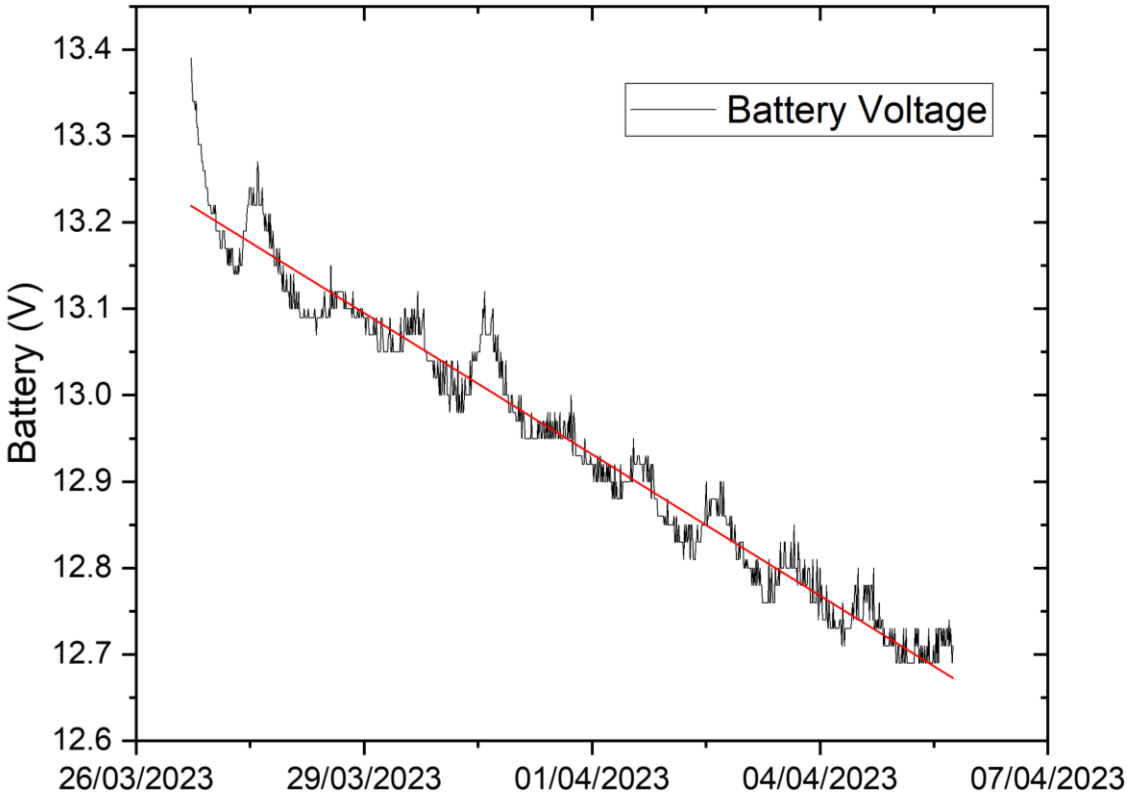

Figure 5-44 Measured battery voltage powering the datalogger and sensor during the deployment in the Owenmore River between 26/03/2023 17:19:40 and 05/04/2023 18:03:42. An applied linear fit to the data (red line) gives a slope of -0.0545 V per day.

The low-cost datalogger functioned sufficiently to allow for long term deployments. The material costs of the datalogger were only €200. The datalogger was able to autonomously operate the sensor, provide power, collect, and store the data. However, a shortcoming of the datalogger was its ability to capture the full spectral scans from the sensor. Data collisions were common, and the sensor had to be reprogramed to provide pixel values at select wavelengths. This can be addressed with more robust software and data handling. A handshake system and error check can be implemented to ensure the data transfer is done correctly in future deployments. As is done with commercial sensors such as the YSI EXO3 Sonde [402] and Aqua TROLL 600 Multiparameter Sonde [403] the datalogging functions and power supply can be built into the sensor itself

5.4 Conclusion

The work presented in this chapter was successful in demonstrating the developed sensor units operating fully, reliably and at scale in the intended environment. The deployments conducted were successful in showing the design to be suitable for long term and repeatable in situ measurements. A unique aspect of the deployment in Dublin Bay was the scale of the deployment in terms of number of sensor units, duration and data generated. This repeated and scaled use of a research developed in situ optical sensor design, to the writer's knowledge, has not been demonstrated in the research field before and contributes to the advancement of new sensing technologies and optical sensor deployment methods. The sensor units throughout the deployments were able to measure multiple environmental events giving key insights into the locations they were deployed in. In all scenarios they compared well with commercial sensors (YSI EXO2 Probe and HydroCAT V2) which cost a magnitude in order more.

The deployment of multiple sensors in multiple locations in Dublin Bay for up to 72 days displayed the robust design and measurement capabilities of the design collecting over 50,000 data points over the duration of the deployment. The AWaMS sensors operated between 27 and 72 days in a marine environment, with only one sensor failure due to a maintenance issue. The necessity of regular maintenance was highlighted. All data from AWaMS was successfully transmitted and stored on the DynamoDB server, showing the designs capabilities with integrating with preexisting industrial hardware systems for sensor network deployments. The sensor deployed in Poolbeg alongside a commercial HydroCAT sensor performed comparable which validated the sensor design to be able to produce valuable environmental data comparable with current state of the art commercial sensors. The sensors provided valuable environmental data, validating their accuracy and reliability. Events like primary production and tidal activity were effectively monitored, underscoring the sensors' utility in detecting key environmental and pollution events. The sensor guard designs, while effective against ambient light, require modification to prevent debris buildup for prolonged deployments in locations with high levels of suspended debris. The implementation of UV LEDs for fouling prevention effectively prevented biofouling on optical lenses in all cases, though additional strategies are needed for high sediment locations to prevent sediment build up.

The deployment of a sensor unit in the Owenmore River displayed the versatility of the sensor's multiparameter measurements to operate in a wide range of different aquatic environments. The first deployment in this location alongside a commercial sensor (YSI) sonde demonstrated the sensor's comparability with a commercial sensor in detecting rainfall associated turbidity events. The second deployment was successful in demonstrating the sensors' multiparameter versatility in measuring fDOM alongside Chl-a, turbidity, and temperature. This initial demonstration of the use of multiple LEDs and multiple optical measurement modes shows potential to be used to provide holistic data of the aquatic environment using technology and measurement approaches not currently used by conventional in situ optical sensors. Future work is required to fully expand on the sensors holistic measurement approach, akin to the strategies applied by remote multiparameter sensing [17,428], to develop trend recognition software algorithms to combine all the optical measurement parameters measurements by the sensor for a whole image of the changing environment.

The development of a low-cost custom datalogger facilitated the ability to do deployments without the need for preexisting infrastructure which allowed the deployment in the Owenmore River to be carried out. The system was built for a total of €210 which is deemed low cost while adding significant value to the sensor design. It was noted that the functionality of the datalogger could be built into the sensor design as is done with other commercial sensors in a future iteration. Independent power and datalogging capabilities would add significant versatility into the sensors' applications. The implemented of power optimisation strategies on the sensor system resulted in a total combined reduction of 60.5% which brought the power usage of the during a deployment cycle of 15-min sampling frequency down to 80mW from 210 mW. This reduction in power allowed for longer deployments when relying on battery power. The analysis of the datalogger built for the Sligo deployments showed the setup had a 33-day deployment time.

In summary, the novel multiparameter optical sensors developed performed beyond expectations. The potential of the measurement technology has been demonstrated in a varied range of aquatic environments. The mechanical design of the sensor proved to be robust for longer term deployments. The optical measurements produced by the sensor units offered good insights in the areas of deployment and a wide range of parameters were shown

to be measured accurately. The sensors unique multiparameter design utilising an advanced optical measurement technology.

6 CONCLUSIONS

The aim of this thesis was to go beyond state of the art in situ sensor which applies the latest advancements in optical measurement components and manufacturing methods to develop a next generation in situ. This was accomplished in the design, build and validate at scale, of a robust, reliable, and relatively low cost multiparameter optical sensor unit. The design leveraged recent developments in optical and electronic technologies, manufacturing methods and materials to address an identified technological and research gap in the field of aquatic environment monitoring. The work was successful in producing a novel next generation multiparameter in situ optical sensor using state of the art optical sensing technologies as well low-cost and robust material selection and manufacturing methods. This work addresses the requirement of low-cost, smart in situ sensors to be used by the next generation of state of the art technologies to achieve greater scale in sensor networks for greater temporal and spatial resolutions in monitoring the aquatic environments.

A total of ten sensor units were produced and tested both analytically in the lab and in situ in the intended environment (Chapters 4 and 5). The sensor design was shown to perform to a high standard analytically using an innovative optical measurement system utilising a unique multispectral light source design, two mini-spectrometers and photodiode in an exact orientation. The optical measurement system was demonstrated to be capable of multiparameter measurements using absorption, transmittance, scatter, backscatter, and fluorescence measurement modes over a UV to IR spectral range (Chapters 2 and 3). The design was taken beyond the prototyping phase to small scall production using an efficient production and validation method in the research lab environment (Chapter 4) showing the possibilities in the research field to bridge the gap between research development and commercial opportunity. The thesis concludes with the validation of the sensor units through multiple deployments in different aquatic environments producing large datasets on the deployment locations and providing valuable insights in the environmental changes (Chapter 5). The sensors were deployed in a total of six separate locations throughout the work of this thesis. A large-scale deployment of five sensors in Dublin Bay in August 2021 to October 2021 showed the robust design able for repeated use in the intended environment over long durations. A separate series of deployments in the Owenmore River in March 2023 to August 2023 displayed the versatility of the sensor design for freshwater applications fully utilising the multiparameter measurement capabilities to identify environmental changes and produce insightful datasets.

In Chapter 1, the need for and role of in situ sensors in monitoring the aquatic environments is outlined. In situ sensors deployed in a network can provide spatial and temporal data at a resolution and accuracy which cannot be achieved and can be combined with other monitoring technologies such as remote sensing and submersible vehicles. The status of state-of-the-art technology in in situ sensors is investigated for both interface-based sensors and wet chemistry systems. The simplicity of interface sensors lend to a lower cost in production and optical interface in situ sensors provide multiparameter measurement capabilities. The outcome of this research gave way to the focus of the thesis being on developing a novel optical in situ sensor capable of multiparameter measurements at low cost which could scale to be deployed in dense sensor networks to provide the resolution of data required to monitor the aquatic environments. A further in-depth review revealed the key target analytes for optical detection that give holistic data into the understanding of environmental conditions and changes over varying temporal ranges. The measurement techniques and sensor technologies to perform these measurements were identified and assessed for their suitability to produce an advanced disruptive measurement technology capable of addressing the requirement of interface-based sensing technology for monitoring the aquatic environment.

In Chapter 2, the investigation and ideation of the concept of an advanced optical multiparameter measurement system were furthered by a proof-of-concept benchtop prototype development. The optimum optical sensing components and configuration were selected and tested analytically through an iterative design process on a benchtop system. A unique multispectral light source was designed and optimised combined with two compact C12880MA mini spectrometers and a board-range photodiode. This setup poses a significant innovation for the application of in situ optical sensors allow wide range multispectral measurements from the UV to the IR which can also be spectrally resolved to provide holistic optical measurement capabilities. The optical detection system was shown be capable of multi-measurement modes using transmittance, absorption, scatter, backscatter, and fluorescence measurements in the quantification of multiple different lab standards and target analytes. The outcome from this chapter was a full proof of concept of the unique and novel design of an optical detection system capable of multiparameter analytical measurements of in lab and field samples. This optical measurement system is unique in its design and has not been produced elsewhere in the research or commercial space for in situ marine sensing. The novelty of this optical measurement system has the potential to be

applied in the next generation of in situ aquatic measurement technologies for state of the art environmental monitoring.

In Chapter 3, the goal of producing a robust deployable sensor with the full integration of the optical measurement system designed in Chapter 2 was achieved by the iterative marinisation design. The iterative design approach allowed for optimisation of the housing design through a cycle of ideation, design, prototyping and testing phases with material selection, material testing, robust mechanical design, and the application of low-cost manufacturing methods. The advancements of additive manufacturing methods including fused deposit modelling and selective laser sintering processes were utilised to achieve more geometrically intricate components such as the optical head design allowed for optimised sensing component placement. Custom component design was also combined with off the shelf components to provide a lower-cost and more practical sensor design using metal-based components such as the O-ring flanges sourced from a larger manufacturer of submersible equipment to save costs in manufacturing. Materials were selected based on their mechanical, fouling prevention and chemical properties for suitability for the intended environment. A compromise between corrosion resistance lower cost polymers and high mechanical strength of metal-based components was made on a component-to-component basis to optimise robustness but reduce overall material and manufacturing costs. The integrated fouling prevention strategies of copper-based materials, antifouling paints and UV light proved to be effective fouling prevention methods as seen in this chapter and presented post deployment in Chapter 5. Through testing a limitation to the sensors fluorescence measurement capability was identified in the form of saturation due to excess ambient light in the open environment. This was addressed by an additional design iteration with an ambient light blocking system developed consisting of two sensor guards, an external and internal design which block all ambient light which through lab and field testing were proved highly effective in reducing ambient light. The sensor design showed promising analytical performance for the quantification of multiple target analytes including quinine sulfate (DOM equivalent), naphthalene (petroleum equivalent) turbidity and chl-a. A calibration curve generated for chl-a measurement comparing closely with a commercial sensor the Hydrocat EP V-2. The sensor in all cases was shown to produce high resolution linear measurements of concentrations of different target analytes showing a promising potential as a in situ monitoring tool. The outcomes of this work were a comprehensive review and recommendations for applicable materials for in situ sensor design for the marine

environment as well as fouling prevention strategies, robust mechanical design of enclosures and electronics integration and manufacturing techniques.

In Chapter 4, the finalised design from Chapter 3 was scaled up to produce multiple sensor units and a method for validating and calibrating the sensor measurement data output. The scaling up of production of the design involved the development of an efficient, low-cost, and streamlined method allowed for the multiple prototype units to be produced in the research lab in a short space of time. This method of scaling up production of a protype environmental sensor has not been seen in the literature according to the writer's knowledge and contributes to a novel development of techniques allowing for higher scale prototype production for testing and evaluating sensor designs. The material and manufacturing costs required to produce the sensors units amounted to €1600 per sensor which presents a major opportunity to reduce the cost of in situ sensors particularly multiparameter interface-based sensors for the increased scaling of sensor networks for monitoring at greater spatial resolutions in larger water bodies such as coastal regions. The validation experiments on the sensor's data output show the system to be stable and able to produce linear responses to concentration-based target analytes. The limits of the detection at fixed spectrometer integration times of the sensor systems were identified for chl-a and turbidity. The sensor's comparative analytical performance against currently available commercial multiparameter sensor is good in terms of sensitivity and resolution (0-44.92 μg/L with a resolution of 0.0275 μg/L for chl-a and for turbidity 0-32.34 NTU with a resolution of 0.0303 NTU). The potential to increase the range of detection was identified with the spectrometer detector's programable integration time allowing for ranges (by increasing or lowering the integration time) to be set based on the environment and expected levels of target analytes. This would give the sensor design a dynamic range in theory with future work required to fully explore this capability. A large-scale calibration process was conducted on each of the ten sensor units for chl-a (using BB3 as equivalent standard) and turbidity. The method developed for the preparation for deployment of multiple sensor units is a novel approach and unique among literature in its scale to produce calibration curve for two separate target analytes for multiple sensors. This method offers a repeatable standardisation of sensor response approach for larger scale sensor development. The developed method is applicable to the next generation of in situ sensors for any measurable optical target analytes in the environment. This gives way to larger numbers of uniform data producing and

interchangeable sensors system to be deployed at scale in denser networks for increasing spatial and temporal monitoring of critical aquatic environments. The calibration curves produced by the sensors also highlight a variance in the sensor's performance highlighting the need for sensor specific calibration to normalised differences in sensor operation.

In Chapter 5, the culmination of all the work presented in the previous chapters in developing, scaling up and preparing multiple sensor units for deployment in the aquatic environment was achieved through the successful deployments of the sensor units in the aquatic environment. The sensors were validated in the intended environment at scale through multiple and repeated long duration deployments in marine, brackish water, and freshwater sites. The data integration of the sensor units was demonstrated to work both with a preexisting infrastructure in the deployments in Dublin Bay and with a custom made datalogger allowing for additional deployments in the Owenmore River. Over 50,000 measurements were made by the five sensors deployed in Dublin Bay over the period of 3 months showing the potential of senso units for large scale deployments to produce high levels of data for monitoring environmental changes. The full measurement cycle of the sensor was found to produce 37 kB of data per scan. This includes all the LEDs cycled for each optical measurement mode (absorption, scatter, and fluorescence) as well as temperature. The sensor output was shown to be able to be optimised on a deployment-to-deployment bases as shown in the Dublin Deployment with the firmware altered to produce targeted datasets focused on the deployment objectives for chl-a, turbidity, and temperature measurements. This adaption of sensor output parameters was also demonstrated with alterations for the freshwater deployment in the Owenmore River with a more expansive dataset output from the sensor utilising the multiparameter measurement capabilities of the sensor for a more expansive optical measurement cycle. Key deployment requirements were also taken into consideration with a limitation found in the sensor's performance due to its high-power requirements during a battery dependent deployment. An extensive assessment of the sensor's power usage was carried out and strategies were implemented to improve the sensors operation efficiency to reduce its power consumption while in deployment mode. The output of this work reduced the overall power usage by over 60% reducing the total operation power requirements from 210 mW to 80 mW. A comparison with commercially available sensor's using the same sample frequency of 15 min show the sensor compared reasonably well with further work required to reduce the power consumption further. A further assessment of the power usage performance of the sensor and datalogger in Sligo concluded the system had a total deployment length of 33 days using a 12 V 24 ah battery.

The sensor's robust design was proven over the multiple long duration deployments with only a single sensor failing due to a maintenance error of the O-rings compromising the water tightness of the system. This was a learning to maintain the O-ring seals on each sensor and replace the O-rings more frequently. However, the sensors proved to be suitable for long term deployments and repeated use, after two years of use during the work presented in this thesis, they are still functioning correctly and being deployed frequently.

This is the first demonstration of a comprehensive approach to developing a novel, beyond state of the art and low-cost in situ sensor technology for the next generation of in situ sensors. The work is demonstrated from idea to scaled up production which is unique within the research field. The iterative design process generated a unique optical sensor design which was proven repeatedly to be a valuable, robust, and reliable environmental monitoring tool. The sensor design has been demonstrated to be suitable for small-scall production and validation offering a methodology to the research field for bridging the gap between academic research based technology developments and full-scale commercial applications. In summary, the contribution of this work is a sensing technology able to address the gap of aquatic environmental monitoring requirements as well as a demonstration of a scaling approach for academic research technology development. The development of the sensor can be furthered in future work with the full potential of the optical measurement capabilities explored. The highlighted potential of the detection system is to produce a fully dynamically changeable in situ, multispectral and multiparameter measuring device. The full commercial scale up of the sensor design can be achieved with further design iterations with larger scale manufacturing design inputs and further in situ deployments to demonstrate the systems potential.

7 REFERENCES

[1] Y. Malhi, J. Franklin, N. Seddon, M. Solan, M.G. Turner, C.B. Field, N. Knowlton, Climate change and ecosystems: threats, opportunities and solutions, Philos. Trans. R. Soc. B Biol. Sci. 375 (2020) 20190104. https://doi.org/10.1098/rstb.2019.0104.

[2] B. Talukder, N. Ganguli, R. Matthew, G.W. vanLoon, K.W. Hipel, J. Orbinski, Climate change-accelerated ocean biodiversity loss & associated planetary health impacts, J. Clim. Change Health. 6 (2022) 100114. https://doi.org/10.1016/j.joclim.2022.100114.

[3] N. MIMURA, Sea-level rise caused by climate change and its implications for society, Proc. Jpn. Acad. Ser. B Phys. Biol. Sci. 89 (2013) 281–301. https://doi.org/10.2183/pjab.89.281.

[4] O. Hoegh-Guldberg, E.S. Poloczanska, W. Skirving, S. Dove, Coral Reef Ecosystems under Climate Change and Ocean Acidification, Front. Mar. Sci. 4 (2017). https://www.frontiersin.org/articles/10.3389/fmars.2017.00158 (accessed September 19, 2023).

[5] V.R. Barros, C.B. Field, D.J. Dokken, M.D. Mastrandrea, K.J. Mach, T.E. Bilir, M. Chatterjee, K.L. Ebi, Y.O. Estrada, R.C. Genova, Climate change 2014 impacts, adaptation, and vulnerability Part B: regional aspects: working group II contribution to the fifth assessment report of the intergovernmental panel on climate change, in: Clim. Change 2014 Impacts Adapt. Vulnerability Part B Reg. Asp. Work. Group II Contrib. Fifth Assess. Rep. Intergov. Panel Clim. Change, Cambridge University Press, 2014: pp. 1–1820.

[6] W.W. Gregg, C.S. Rousseaux, Decadal trends in global pelagic ocean chlorophyll: A new assessment integrating multiple satellites, in situ data, and models., J. Geophys. Res. Oceans. 119 (2014) 5921–5933. https://doi.org/10.1002/2014JC010158.

[7] H.K. Lotze, D.P. Tittensor, A. Bryndum-Buchholz, T.D. Eddy, W.W.L. Cheung, E.D. Galbraith, M. Barange, N. Barrier, D. Bianchi, J.L. Blanchard, L. Bopp, M. Büchner, C.M. Bulman, D.A. Carozza, V. Christensen, M. Coll, J.P. Dunne, E.A. Fulton, S. Jennings, M.C. Jones, S. Mackinson, O. Maury, S. Niiranen, R. Oliveros-Ramos, T. Roy, J.A. Fernandes, J. Schewe, Y.-J. Shin, T.A.M. Silva, J. Steenbeek, C.A. Stock, P. Verley, J. Volkholz, N.D. Walker, B. Worm, Global ensemble projections reveal trophic amplification of ocean biomass declines with climate change, Proc. Natl. Acad. Sci. 116 (2019) 12907–12912. https://doi.org/10.1073/pnas.1900194116.

[8] L. Cheng, J. Abraham, Z. Hausfather, K.E. Trenberth, How fast are the oceans warming?, Science. 363 (2019) 128–129. https://doi.org/10.1126/science.aav7619.

[9] H.-O. Pörtner, D.C. Roberts, H. Adams, C. Adler, P. Aldunce, E. Ali, R.A. Begum, R. Betts, R.B. Kerr, R. Biesbroek, Climate change 2022: Impacts, adaptation and vulnerability, IPCC Sixth Assess. Rep. (2022).

[10] A.N. Tyler, P.D. Hunter, E. Spyrakos, S. Groom, A.M. Constantinescu, J. Kitchen, Developments in Earth observation for the assessment and monitoring of inland, transitional, coastal and shelf-sea waters, Sci. Total Environ. 572 (2016) 1307–1321. https://doi.org/10.1016/J.SCITOTENV.2016.01.020.

[11] T.L. Rosa, A.M. Piecho-Santos, R. Vettor, C. Guedes Soares, Review and Prospects for Autonomous Observing Systems in Vessels of Opportunity, J. Mar. Sci. Eng. 9 (2021) 366. https://doi.org/10.3390/jmse9040366.

[12] M.E. Furlong, D. Paxton, P. Stevenson, M. Pebody, S.D. McPhail, J. Perrett, Autosub Long Range: A long range deep diving AUV for ocean monitoring, 2012 IEEEOES Auton. Underw. Veh. AUV 2012. (2012). https://doi.org/10.1109/AUV.2012.6380737.

[13] G. Mills, G. Fones, A review of in situ/IT methods and sensors for monitoring the marine environment, Sens. Rev. 32 (2012) 17–28. https://doi.org/10.1108/02602281211197116/FULL/PDF.
[14] H. Claustre, K.S. Johnson, Y. Takeshita, Observing the Global Ocean with Biogeochemical-Argo, Annu. Rev. Mar. Sci. 12 (2020) 23–48. https://doi.org/10.1146/annurev-marine-010419-010956.
[15] F. Adamo, F. Attivissimo, C. Guarnieri Calo Carducci, A.M.L. Lanzolla, A Smart Sensor Network for Sea Water Quality Monitoring, IEEE Sens. J. 15 (2015) 2514–2522. https://doi.org/10.1109/JSEN.2014.2360816.
[16] C. Briciu-Burghina, T. Sullivan, J. Chapman, F. Regan, Continuous high-frequency monitoring of estuarine water quality as a decision support tool: a Dublin Port case study, Environ. Monit. Assess. 186 (2014) 5561–5580.
[17] S.W. Bailey, P.J. Werdell, A multi-sensor approach for the on-orbit validation of ocean color satellite data products, Remote Sens. Environ. 102 (2006) 12–23. https://doi.org/10.1016/j.rse.2006.01.015.
[18] G. Xu, Y. Shi, X. Sun, W. Shen, Internet of Things in Marine Environment Monitoring: A Review, Sensors. 19 (2019). https://doi.org/10.3390/S19071711.
[19] C. Whitt, J. Pearlman, B. Polagye, F. Caimi, F. Muller-Karger, A. Copping, H. Spence, S. Madhusudhana, W. Kirkwood, L. Grosjean, B.M. Fiaz, S. Singh, S. Singh, D. Manalang, A.S. Gupta, A. Maguer, J.J.H. Buck, A. Marouchos, M.A. Atmanand, R. Venkatesan, V. Narayanaswamy, P. Testor, E. Douglas, S. de Halleux, S.J. Khalsa, Future Vision for Autonomous Ocean Observations, Front. Mar. Sci. 7 (2020) 697. https://doi.org/10.3389/fmars.2020.00697.
[20] Ocean Observatories Initiative – A new era of oceanography, (n.d.). https://oceanobservatories.org/ (accessed October 25, 2022).
[21] EXPORTS (EXport Processes in the Ocean from Remote Sensing), (n.d.). https://oceanexports.org/ (accessed October 25, 2022).
[22] Biogeochemical Argo | Home, (n.d.). https://biogeochemical-argo.org/ (accessed October 25, 2022).
[23] Home - The U.S. Integrated Ocean Observing System (IOOS), (n.d.). https://ioos.noaa.gov/ (accessed October 25, 2022).
[24] W.F. Directive, Directive 2000/60, EC Eur. Parliam. Counc. Of. 23 (2000) 1.
[25] Marine Strategy Framework Directive 2008/56/EC — European Environment Agency, (n.d.). https://www.eea.europa.eu/policy-documents/2008-56-ec (accessed August 19, 2022).
[26] A. Delgado, C. Briciu-Burghina, F. Regan, Antifouling Strategies for Sensors Used in Water Monitoring: Review and Future Perspectives, Sensors. 21 (2021) 389. https://doi.org/10.3390/s21020389.
[27] M.M. Grand, G.S. Clinton-Bailey, A.D. Beaton, A.M. Schaap, T.H. Johengen, M.N. Tamburri, D.P. Connelly, M.C. Mowlem, E.P. Achterberg, A lab-on-chip phosphate analyzer for long-term In Situ monitoring at fixed observatories: Optimization and performance evaluation in estuarine and oligotrophic coastal waters, Front. Mar. Sci. 4 (2017) 1–16. https://doi.org/10.3389/fmars.2017.00255.
[28] S. Morgan, E. Luy, A. Furlong, V. Sieben, A submersible phosphate analyzer for marine environments based on inlaid microfluidics, Anal. Methods. 14 (2022) 22–33. https://doi.org/10.1039/d1ay01876k.
[29] A.J. Birchill, A.D. Beaton, T. Hull, J. Kaiser, M. Mowlem, R. Pascal, A. Schaap, Y.G. Voynova, C. Williams, M. Palmer, Exploring Ocean Biogeochemistry Using a Lab-on-Chip Phosphate Analyser on an Underwater Glider, Front. Mar. Sci. 8 (2021) 1–18. https://doi.org/10.3389/fmars.2021.698102.

[30] N. Le Bris, P.M. Sarradin, D. Birot, A.M. Alayse-Danet, A new chemical analyzer for in situ measurement of nitrate and total sulfide over hydrothermal vent biological communities, Mar. Chem. 72 (2000) 1–15. https://doi.org/10.1016/S0304-4203(00)00057-8.
[31] G.S. Clinton-Bailey, M.M. Grand, A.D. Beaton, A.M. Nightingale, D.R. Owsianka, G.J. Slavik, D.P. Connelly, C.L. Cardwell, M.C. Mowlem, A Lab-on-Chip Analyzer for in Situ Measurement of Soluble Reactive Phosphate: Improved Phosphate Blue Assay and Application to Fluvial Monitoring, Environ. Sci. Technol. 51 (2017) 9989–9995. https://doi.org/10.1021/acs.est.7b01581.
[32] X. Cao, S.W. Zhang, D.Z. Chu, N. Wu, H.K. Ma, Y. Liu, A design of spectrophotometric microfluidic chip sensor for analyzing silicate in seawater, IOP Conf. Ser. Earth Environ. Sci. 82 (2017). https://doi.org/10.1088/1755-1315/82/1/012080.
[33] F. Geißler, E.P. Achterberg, A.D. Beaton, M.J. Hopwood, J.S. Clarke, A. Mutzberg, M.C. Mowlem, D.P. Connelly, Evaluation of a Ferrozine Based Autonomous in Situ Lab-on-Chip Analyzer for Dissolved Iron Species in Coastal Waters, Front. Mar. Sci. 4 (2017). https://doi.org/10.3389/fmars.2017.00322.
[34] R. Vuillemin, D. Le Roux, P. Dorval, K. Bucas, J.P. Sudreau, M. Hamon, C. Le Gall, P.M. Sarradin, CHEMINI: A new in situ CHEmical MINIaturized analyzer, Deep-Sea Res. Part Oceanogr. Res. Pap. 56 (2009) 1391–1399. https://doi.org/10.1016/j.dsr.2009.02.002.
[35] M. Cuartero, G. Crespo, T. Cherubini, N. Pankratova, F. Confalonieri, F. Massa, M.L. Tercier-Waeber, M. Abdou, J. Schäfer, E. Bakker, In Situ Detection of Macronutrients and Chloride in Seawater by Submersible Electrochemical Sensors, Anal. Chem. 90 (2018) 4702–4710. https://doi.org/10.1021/acs.analchem.7b05299.
[36] F. Edgar Muller-Karger, M. Twardowski, W. Douglas Wilson, Z. Aleck Wang, M. Apm, H. Moustahfid, A. V Mueller, A.P. M Michel, M. Mowlem, B.T. Glazer, T. Aran Mooney, W. Michaels, J.S. McQuillan, J.C. Robidart, J. Churchill, M. Sourisseau, A. Daniel, A. Schaap, S. Monk, K. Friedman, P. Brehmer, Advancing Observation of Ocean Biogeochemistry, Biology, and Ecosystems With Cost-Effective in situ Sensing Technologies, (2019). https://doi.org/10.3389/fmars.2019.00519.
[37] Water Framework Directive (WFD) 2000/60/EC — European Environment Agency, (n.d.). https://www.eea.europa.eu/policy-documents/water-framework-directive-wfd-2000 (accessed August 19, 2022).
[38] EUR-Lex - 32006L0007 - EN - EUR-Lex, (n.d.). https://eur-lex.europa.eu/legal-content/EN/TXT/?uri=CELEX:32006L0007 (accessed August 19, 2022).
[39] EUR-Lex - 31991L0271 - EN - EUR-Lex, (n.d.). https://eur-lex.europa.eu/legal-content/EN/TXT/?uri=celex%3A31991L0271 (accessed August 19, 2022).
[40] C.T. Filstrup, J.A. Downing, Relationship of chlorophyll to phosphorus and nitrogen in nutrient-rich lakes, Inland Waters. 7 (2017) 385–400.
[41] E. Lundsør, L.C. Stige, K. Sørensen, B. Edvardsen, Long-term coastal monitoring data show nutrient-driven reduction in chlorophyll, J. Sea Res. 164 (2020). https://doi.org/10.1016/J.SEARES.2020.101925.
[42] J. Wallace, P. Champagne, G. Hall, Time series relationships between chlorophyll-a, dissolved oxygen, and pH in three facultative wastewater stabilization ponds, Environ. Sci. Water Res. Technol. 2 (2016) 1032–1040. https://doi.org/10.1039/C6EW00202A.
[43] H.A. El-Serehy, H.S. Abdallah, F.A. Al-Misned, R. Irshad, S.A. Al-Farraj, E.S. Almalki, Aquatic ecosystem health and trophic status classification of the Bitter Lakes

along the main connecting link between the Red Sea and the Mediterranean, Saudi J. Biol. Sci. 25 (2018) 204–212. https://doi.org/10.1016/J.SJBS.2017.12.004.
[44] C.S. Roesler, A.H. Barnard, Optical proxy for phytoplankton biomass in the absence of photophysiology: Rethinking the absorption line height, Methods Oceanogr. 7 (2013) 79–94. https://doi.org/10.1016/J.MIO.2013.12.003.
[45] M.J. Behrenfeld, R.T. O'Malley, D.A. Siegel, C.R. McClain, J.L. Sarmiento, G.C. Feldman, A.J. Milligan, P.G. Falkowski, R.M. Letelier, E.S. Boss, Climate-driven trends in contemporary ocean productivity, Nat. 2006 4447120. 444 (2006) 752–755. https://doi.org/10.1038/nature05317.
[46] V. Klemas, Remote sensing of algal blooms: An overview with case studies, J. Coast. Res. 28 (2012) 34–43. https://doi.org/10.2112/JCOASTRES-D-11-00051.1.
[47] H. Haardt, H. Maske, Specific in vivo absorption coefficient of chlorophyll a at 675 nm1, Limnol. Oceanogr. 32 (1987) 608–619. https://doi.org/10.4319/LO.1987.32.3.0608.
[48] L. Zeng, D. Li, Development of in situ sensors for chlorophyll concentration measurement, J. Sens. 2015 (2015). https://doi.org/10.1155/2015/903509.
[49] A.F.B. Omar, M.Z.B. MatJafri, Turbidimeter Design and Analysis: A Review on Optical Fiber Sensors for the Measurement of Water Turbidity, Sensors. 9 (2009) 8311. https://doi.org/10.3390/S91008311.
[50] C. Farrell, F. Hassard, B. Jefferson, T. Leziart, A. Nocker, P. Jarvis, Turbidity composition and the relationship with microbial attachment and UV inactivation efficacy, Sci. Total Environ. 624 (2018) 638–647. https://doi.org/10.1016/J.SCITOTENV.2017.12.173.
[51] E.E. Scott, B.E. Haggard, Natural Characteristics and Human Activity Influence Turbidity and Ion Concentrations in Streams, J. Contemp. Water Res. Educ. 172 (2021) 34–49. https://doi.org/10.1111/J.1936-704X.2021.3353.X.
[52] R. Open Access Citation: Fisher, C. Stark, P. Ridd, R. Jones, Spatial Patterns in Water Quality Changes during Dredging in Tropical Environments, PLoS ONE. 10 (2015) 143309. https://doi.org/10.1371/journal.pone.0143309.
[53] D.M. Lawler, G.E. Petts, I.D.L. Foster, S. Harper, Turbidity dynamics during spring storm events in an urban headwater river system: The Upper Tame, West Midlands, UK, Sci. Total Environ. 360 (2006) 109–126. https://doi.org/10.1016/J.SCITOTENV.2005.08.032.
[54] N. Chen, M.D. Krom, Y. Wu, D. Yu, H. Hong, Storm induced estuarine turbidity maxima and controls on nutrient fluxes across river-estuary-coast continuum, Sci. Total Environ. 628–629 (2018) 1108–1120. https://doi.org/10.1016/J.SCITOTENV.2018.02.060.
[55] W. Ma, T. Huang, X. Li, Z. Zhou, Y. Li, K. Zeng, The Effects of Storm Runoff on Water Quality and the Coping Strategy of a Deep Canyon-Shaped Source Water Reservoir in China, Int. J. Environ. Res. Public. Health. 12 (2015) 7839. https://doi.org/10.3390/IJERPH120707839.
[56] A.J. Welch, S.A. Prahl, M.J.C. van Gemert, Determining the optical properties of turbid media by using the adding–doubling method, Appl. Opt. Vol 32 Issue 4 Pp 559-568. 32 (1993) 559–568. https://doi.org/10.1364/AO.32.000559.
[57] T. Lambert, M.E. Perga, Non-conservative patterns of dissolved organic matter degradation when and where lake water mixes, Aquat. Sci. 81 (2019) 1–13. https://doi.org/10.1007/S00027-019-0662-Z/FIGURES/4.
[58] T.P. Chiu, W.S. Huang, T.C. Chen, Y.L. Yeh, Fluorescence Characteristics of Dissolved Organic Matter (DOM) in Percolation Water and Lateral Seepage Affected

by Soil Solution (S-S) in a Lysimeter Test, Sensors. 19 (2019). https://doi.org/10.3390/S19184016.
[59] K.A. Rodriguez-Avella, M. Baraer, B. Mark, J. McKenzie, L. Somers, Comparing the performance of three methods to assess DOM dynamics within two distinct glacierized watersheds of the tropical Andes, Environ. Pollut. 265 (2020) 115052. https://doi.org/10.1016/J.ENVPOL.2020.115052.
[60] Y. Zhao, K. Song, Z. Wen, L. Li, S. Zang, T. Shao, S. Li, J. Du, Seasonal characterization of CDOM for lakes in semiarid regions of Northeast China using excitation–emission matrix fluorescence and parallel factor analysis (EEM–PARAFAC), Biogeosciences Discuss. 12 (2015) 5725–5756. https://doi.org/10.5194/bgd-12-5725-2015.
[61] M. Peacock, † Duš, M. Materić, D.N. Kothawala, R. Holzinger, M.N. Futter, Understanding Dissolved Organic Matter Reactivity and Composition in Lakes and Streams Using Proton-Transfer-Reaction Mass Spectrometry (PTR-MS), (2018). https://doi.org/10.1021/acs.estlett.8b00529.
[62] A.S. Wymore, B. Rodríguez-Cardona, W.H. Mcdowell, Understanding Dissolved Organic Matter Biogeochemistry Through In Situ Nutrient Manipulations in Stream Ecosystems, J Vis Exp. (2016) 54704. https://doi.org/10.3791/54704.
[63] A.M. Sanseverino, D. Bastviken, I. Sundh, J. Pickova, A. Enrich-Prast, Methane carbon supports aquatic food webs to the fish level, PLoS ONE. 7 (2012). https://doi.org/10.1371/JOURNAL.PONE.0042723.
[64] R. Wolf, J. Heuschele, Water browning influences the behavioral effects of ultraviolet radiation on zooplankton, Front. Ecol. Evol. 6 (2018) 26. https://doi.org/10.3389/FEVO.2018.00026/BIBTEX.
[65] A. Abdelrady, S. Sharma, A. Sefelnasr, M. Kennedy, The Fate of Dissolved Organic Matter (DOM) During Bank Filtration under Different Environmental Conditions: Batch and Column Studies, Water 2018 Vol 10 Page 1730. 10 (2018) 1730. https://doi.org/10.3390/W10121730.
[66] A.M. Hansen, T.E.C. Kraus, B.A. Pellerin, J.A. Fleck, B.D. Downing, B.A. Bergamaschi, Optical properties of dissolved organic matter (DOM): Effects of biological and photolytic degradation, Limnol. Oceanogr. 61 (2016) 1015–1032. https://doi.org/10.1002/LNO.10270.
[67] Z. Asif, Z. Chen, C. An, J. Dong, Environmental Impacts and Challenges Associated with Oil Spills on Shorelines, J. Mar. Sci. Eng. 2022 Vol 10 Page 762. 10 (2022) 762. https://doi.org/10.3390/JMSE10060762.
[68] C.E. Main, H.A. Ruhl, D.O.B. Jones, A. Yool, B. Thornton, D.J. Mayor, Hydrocarbon contamination affects deep-sea benthic oxygen uptake and microbial community composition, Deep Sea Res. Part Oceanogr. Res. Pap. 100 (2015) 79–87. https://doi.org/10.1016/J.DSR.2014.12.008.
[69] J.O. Akinola, O.O. Olawusi-Peters, V.O.E. Akpambang, Ecological hazards of Total petroleum hydrocarbon in brackish water white Shrimp Nematopalaemon hastatus (AURIVILLUS 1898), Egypt. J. Aquat. Res. 45 (2019) 205–210. https://doi.org/10.1016/J.EJAR.2019.07.004.
[70] M. Lichtveld, S. Sherchan, K.B. Gam, R.K. Kwok, C. Mundorf, A. Shankar, L. Soares, The Deepwater Horizon Oil Spill Through the Lens of Human Health and the Ecosystem, Curr. Environ. Health Rep. 3 (2016) 370–378. https://doi.org/10.1007/S40572-016-0119-7/TABLES/1.
[71] R.K. Kwok, A.K. Miller, K.B. Gam, M.D. Curry, S.K. Ramsey, A. Blair, L.S. Engel, D.P. Sandler, Developing Large-Scale Research in Response to an Oil Spill Disaster: a Case Study, (2019). https://doi.org/10.1007/s40572-019-00241-9.

[72] M. Fingas, C.E. Brown, A Review of Oil Spill Remote Sensing, Sensors. 18 (2018). https://doi.org/10.3390/S18010091.
[73] S. Pärt, H. Kankaanpää, J.V. Björkqvist, R. Uiboupin, Oil Spill Detection Using Fluorometric Sensors: Laboratory Validation and Implementation to a FerryBox and a Moored SmartBuoy, Front. Mar. Sci. 8 (2021) 1753. https://doi.org/10.3389/FMARS.2021.778136/BIBTEX.
[74] R.N. Conmy, L. DiPinto, A. Kukulya, O. Garcia-Pineda, G. Graettinger, D. Sundaravadivelu, M. Gloekler, A. Hall, E. Fischell, D. Gomez-Ibanez, Advances in Underwater Oil Plume Detection Capabilities, Int. Oil Spill Conf. Proc. 2021 (2021). https://doi.org/10.7901/2169-3358-2021.1.1141330.
[75] Y. Hou, Y. Li, B. Liu, Y. Liu, T. Wang, Design and Implementation of a Coastal-Mounted Sensor for Oil Film Detection on Seawater, Sens. 2018 Vol 18 Page 70. 18 (2017) 70. https://doi.org/10.3390/S18010070.
[76] M.F. Fingas, K. Yetilmezsoy, M. Bahramian, Development of an Algorithm for Chemically Dispersed Oil Spills, Front. Mar. Sci. 7 (2020) 982. https://doi.org/10.3389/FMARS.2020.600614/BIBTEX.
[77] H.I. Abdel-Shafy, M.S.M. Mansour, A review on polycyclic aromatic hydrocarbons: Source, environmental impact, effect on human health and remediation, Egypt. J. Pet. 25 (2016) 107–123. https://doi.org/10.1016/J.EJPE.2015.03.011.
[78] T. Allsop, L. Zhang, I. Bennion, Detection of organic aromatic compounds in paraffin by a long-period fiber grating optical sensor with optimized sensitivity, Opt. Commun. 191 (2001) 181–190. https://doi.org/10.1016/S0030-4018(01)01131-2.
[79] G. Mills, G. Fones, A review of in situ methods and sensors for monitoring the marine environment, (n.d.). https://doi.org/10.1108/02602281211197116.
[80] Y. Hou, Y. Li, G. Li, M. Xu, Y. Jia, Species Identification and Effects of Aromatic Hydrocarbons on the Fluorescence Spectra of Different Oil Samples in Seawater, (2021). https://doi.org/10.1155/2021/6677219.
[81] W.R. Dawson, M.W. Windsor, Fluorescence Yields of Aromatic Compounds 3251 Fluorescence Yields of Aromatic Compounds, (n.d.). https://pubs.acs.org/sharingguidelines (accessed February 15, 2023).
[82] M. Lo Prejato, D. McKee, C. Mitchell, Inherent Optical Properties-Reflectance Relationships Revisited, J. Geophys. Res. Oceans. 125 (2020) e2020JC016661. https://doi.org/10.1029/2020JC016661.
[83] Y. Fan, W. Li, V.S. Calzado, C. Trees, S. Stamnes, G. Fournier, D. McKee, K. Stamnes, Inferring inherent optical properties and water constituent profiles from apparent optical properties, Opt. Express. 23 (2015) A987–A1009. https://doi.org/10.1364/OE.23.00A987.
[84] J.R.V. Zaneveld, Fifty years of inherent optical properties, Methods Oceanogr. 7 (2013) 3–20. https://doi.org/10.1016/J.MIO.2014.03.002.
[85] S. Pinet, J.-M. Martinez, S. Ouillon, B. Lartiges, R.E. Villar, Variability of apparent and inherent optical properties of sediment-laden waters in large river basins – lessons from in situ measurements and bio-optical modeling, Opt. Express. 25 (2017) A283–A310. https://doi.org/10.1364/OE.25.00A283.
[86] J. Morrow, S. Hooker, C. Booth, G. Bernhard, R. Lind, J. Brown, Advances in Measuring the Apparent Optical Properties (AOPs) of Optically Complex Waters, (2023).
[87] A. Höpe, Chapter 6 - Diffuse Reflectance and Transmittance, in: T.A. Germer, J.C. Zwinkels, B.K. Tsai (Eds.), Exp. Methods Phys. Sci., Academic Press, 2014: pp. 179–219. https://doi.org/10.1016/B978-0-12-386022-4.00006-6.

[88] B.G.B. Kitchener, J. Wainwright, A.J. Parsons, A review of the principles of turbidity measurement, Prog. Phys. Geogr. 41 (2017) 620–642. https://doi.org/10.1177/0309133317726540/ASSET/IMAGES/LARGE/10.1177_0309133317726540-FIG2.JPEG.
[89] ISO - ISO 7027-1:2016 - Water quality — Determination of turbidity — Part 1: Quantitative methods, (n.d.). https://www.iso.org/standard/62801.html (accessed August 18, 2022).
[90] D.A. Bui, P.C. Hauser, Analytical devices based on light-emitting diodes – a review of the state-of-the-art, Anal. Chim. Acta. 853 (2015) 46–58. https://doi.org/10.1016/j.aca.2014.09.044.
[91] B. Kuswandi, Nuriman, J. Huskens, W. Verboom, Optical sensing systems for microfluidic devices: A review, Anal. Chim. Acta. 601 (2007) 141–155. https://doi.org/10.1016/j.aca.2007.08.046.
[92] J. Hodgkinson, R.P. Tatam, Optical gas sensing: a review, Meas. Sci. Technol. 24 (2012) 012004. https://doi.org/10.1088/0957-0233/24/1/012004.
[93] T.G. Mayerhöfer, A.V. Pipa, J. Popp, Beer's Law-Why Integrated Absorbance Depends Linearly on Concentration, ChemPhysChem. 20 (2019) 2748–2753. https://doi.org/10.1002/cphc.201900787.
[94] R.C. Barragán Campos, M. Strojnik, A.R. Rivas, G.G. Torales, F.J.G. Contreras, Optical spectral characterization of leaves for Quercus Resinosa and Magnolifolia species in two senescent states, (2018) 35. https://doi.org/10.1117/12.2321710.
[95] C. Kim, J. Beom Eom, S. Jung, T. Ji, Detection of Organic Compounds in Water by an Optical Absorbance Method, Sensors. 16 (2016) 61. https://doi.org/10.3390/s16010061.
[96] C. Nima, Ø. Frette, B. Hamre, J.J. Stamnes, Y.-C. Chen, K. Sørensen, M. Norli, D. Lu, Q. Xing, D. Muyimbwa, T. Ssenyonga, K.H. Stamnes, S.R. Erga, CDOM Absorption Properties of Natural Water Bodies along Extreme Environmental Gradients, Water. 11 (2019) 1988. https://doi.org/10.3390/w11101988.
[97] R. Röttgers, B.P. Koch, Spectroscopic detection of a ubiquitous dissolved pigment degradation product in subsurface waters of the global ocean, Biogeosciences. 9 (2012) 2585–2596. https://doi.org/10.5194/BG-9-2585-2012.
[98] A.F. Omar, M.Z. MatJafri, Water Quality Measurement using Transmittance and 90° Scattering Techniques through Optical Fiber Sensor, in: 2008 6th Natl. Conf. Telecommun. Technol. 2008 2nd Malays. Conf. Photonics, 2008: pp. 17–21. https://doi.org/10.1109/NCTT.2008.4814227.
[99] H.H. Kleizen, A.B. de Putter, M. van der Beek, S.J. Huynink, Particle concentration, size and turbidity, Filtr. Sep. 32 (1995) 897–901. https://doi.org/10.1016/S0015-1882(97)84175-4.
[100] H. Brumberger, L.C. Anderson, Small-angle x-ray scattering by poly-L-alanine solutions, Biopolymers. 11 (1972) 679–682. https://doi.org/10.1002/bip.1972.360110313.
[101] EPS, Method 180.1: Determination of Turbidity by Nephelometry, 1993. www.epa.gov (accessed October 3, 2022).
[102] L. Wind, W.W. Szymanski, Quantification of scattering corrections to the Beer-Lambert law for transmittance measurements in turbid media, Meas. Sci. Technol. 13 (2002) 270. https://doi.org/10.1088/0957-0233/13/3/306.
[103] T. Oishi, Significant relationship between the backward scattering coefficient of sea water and the scatterance at 120°, Appl. Opt. 29 (1990) 4658. https://doi.org/10.1364/ao.29.004658.

[104] D.R. Dana, R.A. Maffione, Instruments and methods for measuring the backward-scattering coefficient of ocean waters, Appl. Opt. Vol 36 Issue 24 Pp 6057-6067. 36 (1997) 6057–6067. https://doi.org/10.1364/AO.36.006057.
[105] J. Marshall, S. Johnsen, Fluorescence as a means of colour signal enhancement, Philos. Trans. R. Soc. B Biol. Sci. 372 (2017). https://doi.org/10.1098/RSTB.2016.0335.
[106] Granite, Jablonski Diagram | What is it?, Edinb. Instrum. (n.d.). https://www.edinst.com/blog/jablonski-diagram-2/ (accessed December 9, 2023).
[107] H. Franz, V. Jendreizik, Fluorescence Method Development Handbook, in: 2013. https://www.semanticscholar.org/paper/Fluorescence-Method-Development-Handbook-Franz-Jendreizik/320da55f7986dd77c582e26c0e3c705420b7a114 (accessed September 19, 2023).
[108] E. Marcel, B., Collin, S.R., John, J.C., Real-time Coastal Observing Systems for Marine Ecosystem Dynamics and Harmful Algal Blooms: theory, instrumentation and modelling, in: Phytoplankton Fluoresc. Theory Curr. Lit. -Situ Meas. Real-Time Coast. Obs. Syst. Mar. Ecosyst. Dyn. Harmful Algal Blooms, United Nations Educational, Scientific and Cultural Organization, Paris, 2008: pp. 237–280. https://unesdoc.unesco.org/ark:/48223/pf0000160000 (accessed October 12, 2022).
[109] E.M. Carstea, C.L. Popa, A. Baker, J. Bridgeman, In situ fluorescence measurements of dissolved organic matter: A review, Sci. Total Environ. 699 (2020) 134361. https://doi.org/10.1016/J.SCITOTENV.2019.134361.
[110] R.N. Conmy, P.G. Coble, C.E. Del Castillo, Calibration and performance of a new in situ multi-channel fluorometer for measurement of colored dissolved organic matter in the ocean, Cont. Shelf Res. 24 (2004) 431–442. https://doi.org/10.1016/J.CSR.2003.10.010.
[111] R.B. Weisman, S.M. Bachilo, Y. Kadria-Vili, Y.V. Fedotov, D.A. Kravtsov, M.L. Belov, V.A. Gorodnichev, Experimental studies of efficient sensing fluorescence radiation bands to detect oil and petroleum product spills, J. Phys. Conf. Ser. 1399 (2019) 055037. https://doi.org/10.1088/1742-6596/1399/5/055037.
[112] R.N. Conmy, A. Hall, D. Sundaravadivelu, B.A. Schaeffer, A.R. Murray, Fluorescence-estimated oil concentration (Foil) in the Deepwater Horizon subsea oil plume, Mar. Pollut. Bull. 180 (2022) 113808. https://doi.org/10.1016/J.MARPOLBUL.2022.113808.
[113] T. Israsena Na Ayudhya, F.T. Posey, J.C. Tyus, N.N. Dingra, Using a microscale approach to rapidly separate and characterize three photosynthetic pigment species from fern, J. Chem. Educ. 92 (2015) 920–923. https://doi.org/10.1021/ED500344C.
[114] Marine Pollution, (n.d.). https://seos-project.eu//marinepollution/marinepollution-c02-s19-p02.html (accessed May 26, 2023).
[115] M. Shi, J. Ma, K. Zhang, The Impact of Water Temperature on In-Line Turbidity Detection, Water 2022 Vol 14 Page 3720. 14 (2022) 3720. https://doi.org/10.3390/W14223720.
[116] T. Leeuw, E.S. Boss, D.L. Wright, In situ Measurements of Phytoplankton Fluorescence Using Low Cost Electronics, Sens. 2013 Vol 13 Pages 7872-7883. 13 (2013) 7872–7883. https://doi.org/10.3390/S130607872.
[117] K. Murphy, B. Heery, T. Sullivan, D. Zhang, L. Paludetti, K.T. Lau, D. Diamond, E. Costa, N. O'Connor, F. Regan, A low-cost autonomous optical sensor for water quality monitoring, Talanta. 132 (2015) 520–527. https://doi.org/10.1016/J.TALANTA.2014.09.045.
[118] B. Pellerin, B. Bergamaschi, Optical sensors for water quality, in: 2014. https://www.semanticscholar.org/paper/Optical-sensors-for-water-quality-Pellerin-

Bergamaschi/58824391b8944da6ac0b470ff8f323cda9cc6a9b (accessed May 23, 2023).
[119] T. Matos, C.L. Faria, M.S. Martins, R. Henriques, P.A. Gomes, L.M. Goncalves, Development of a cost-effective optical sensor for continuous monitoring of turbidity and suspended particulate matter in marine environment, Sens. Switz. 19 (2019). https://doi.org/10.3390/S19204439.
[120] J.M. Sullivan, M.S. Twardowski, J. Ronald, V. Zaneveld, C.C. Moore, Measuring optical backscattering in water, in: A.A. Kokhanovsky (Ed.), Light Scatt. Rev. 7 Radiat. Transf. Opt. Prop. Atmosphere Underlying Surf., Springer, Berlin, Heidelberg, 2013: pp. 189–224. https://doi.org/10.1007/978-3-642-21907-8_6.
[121] T. Taki, M. Strassburg, Review—Visible LEDs: More than Efficient Light, ECS J. Solid State Sci. Technol. 9 (2020) 015017. https://doi.org/10.1149/2.0402001JSS/XML.
[122] K.B. Mogensen, J.P. Kutter, Optical detection in microfluidic systems, ELECTROPHORESIS. 30 (2009) S92–S100. https://doi.org/10.1002/elps.200900101.
[123] L.E. Shea-Rohwer, J.E. Martin, X. Cai, LED light sources (light for the future), J. Phys. Appl. Phys. 43 (2010) 350301. https://doi.org/10.1088/0022-3727/43/35/350301.
[124] P. Yeh, N. Yeh, C.H. Lee, T.J. Ding, Applications of LEDs in optical sensors and chemical sensing device for detection of biochemicals, heavy metals, and environmental nutrients, Renew. Sustain. Energy Rev. 75 (2017) 461–468. https://doi.org/10.1016/J.RSER.2016.11.011.
[125] AlgaeTorch (Chlorophyll) - bbe moldaenke, (n.d.). https://www.bbe-moldaenke.de/en/products/chlorophyll/details/algaetorch.html (accessed August 8, 2022).
[126] H. Morkoç, Light-Emitting Diodes, in: Nitride Semicond. Devices, Springer Berlin Heidelberg, Berlin, Heidelberg, 1999: pp. 340–378. https://doi.org/10.1007/978-3-642-58562-3_11.
[127] B. Salters, R. Piola, UVC light for antifouling, Mar. Technol. Soc. J. 51 (2017) 59–70. https://doi.org/10.4031/MTSJ.51.2.10.
[128] S. Nakamura, M.S.M. Senoh, T.M.T. Mukai, P-GaN/N-InGaN/N-GaN Double-Heterostructure Blue-Light-Emitting Diodes, Jpn. J. Appl. Phys. 32 (1993) L8. https://doi.org/10.1143/JJAP.32.L8.
[129] Y. Muramoto, M. Kimura, S. Nouda, Development and future of ultraviolet light-emitting diodes: UV-LED will replace the UV lamp, Semicond. Sci. Technol. 29 (2014) 084004. https://doi.org/10.1088/0268-1242/29/8/084004.
[130] D. Feezell, S. Nakamura, Invention, development, and status of the blue light-emitting diode, the enabler of solid-state lighting, Comptes Rendus Phys. 19 (2018) 113–133. https://doi.org/10.1016/j.crhy.2017.12.001.
[131] A.A. Bergh, Blue laser diode (LD) and light emitting diode (LED) applications, Phys. Status Solidi A. 201 (2004) 2740–2754. https://doi.org/10.1002/pssa.200405124.
[132] H. Koizumi, Development and Practical Applications of Blue Light-Emitting Diodes, Engineering. 1 (2015) 167–168. https://doi.org/10.15302/J-ENG-2015064.
[133] R.K. Mondal, S. Adhikari, V. Chatterjee, S. Pal, Recent advances and challenges in AlGaN-based ultra-violet light emitting diode technologies, Mater. Res. Bull. 140 (2021) 111258. https://doi.org/10.1016/j.materresbull.2021.111258.
[134] M. Sobolewski, J. Wojewoda-Budka, Z. Huber, P. Zieba, A. Wierzbicka-Miernik, Solder joints reliability of through hole assemblies with various land and hole design,

Microelectron. Reliab. 125 (2021) 114368. https://doi.org/10.1016/j.microrel.2021.114368.
[135] R.P. Prasad, Introduction to Surface Mount Technology, Surf. Mt. Technol. (1997) 3–50. https://doi.org/10.1007/978-1-4615-4084-7_1.
[136] K.T. Lau, W.S. Yerazunis, R.L. Shepherd, D. Diamond, Quantitative colorimetric analysis of dye mixtures using an optical photometer based on LED array, Sens. Actuators B Chem. 114 (2006) 819–825. https://doi.org/10.1016/J.SNB.2005.07.054.
[137] K. Zhang, S. Timilsina, M. Waguespack, E.M. Kercher, B.Q. Spring, An open-source LED array illumination system for automated multiwell plate cell culture photodynamic therapy experiments, Sci. Rep. 2022 121. 12 (2022) 1–10. https://doi.org/10.1038/s41598-022-22020-7.
[138] R. Setiabudy, M.R. Syahputra, Herlina, The Effect of Surface Mounted Device (SMD) Configuration Array on Light Distribution on LED Lamp, Proc. 2018 Int. Conf. Electr. Eng. Comput. Sci. ICECOS 2018. (2019) 321–326. https://doi.org/10.1109/ICECOS.2018.8605237.
[139] X. Delpueyo, M. Vilaseca, S. Royo, M. Ares, L. Rey-Barroso, F. Sanabria, S. Puig, J. Malvehy, G. Pellacani, F. Noguero, G. Solomita, T. Bosch, Multispectral imaging system based on light-emitting diodes for the detection of melanomas and basal cell carcinomas: a pilot study, J. Biomed. Opt. 22 (2017) 065006. https://doi.org/10.1117/1.JBO.22.6.065006.
[140] M. Brydegaard, Z. Guan, S. Svanberg, Broad-band multispectral microscope for imaging transmission spectroscopy employing an array of light-emitting diodes, Am. J. Phys. 77 (2009) 104–110. https://doi.org/10.1119/1.3027270.
[141] L. Gu, X. Ruan, S. Member, M. Xu, K. Yao, Means of Eliminating Electrolytic Capacitor in AC/DC Power Supplies for LED Lightings, IEEE Trans. POWER Electron. 24 (2009) 1399. https://doi.org/10.1109/TPEL.2009.2016662.
[142] X. Ruan, B. Wang, K. Yao, S. Wang, Letters Optimum Injected Current Harmonics to Minimize Peak-to-Average Ratio of LED Current for Electrolytic Capacitor-Less AC-DC Drivers, IEEE Trans. POWER Electron. 26 (2011). https://doi.org/10.1109/TPEL.2010.2098482.
[143] W. Chen, S.Y.R. Hui, Elimination of an Electrolytic Capacitor in AC/DC Light-Emitting Diode (LED) Driver With High Input Power Factor and Constant Output Current, IEEE Trans. POWER Electron. 27 (2012). https://doi.org/10.1109/TPEL.2010.2103959.
[144] X. Qu, S.-C. Wong, C.K. Tse, Noncascading Structure for Electronic Ballast Design for Multiple LED Lamps With Independent Brightness Control, IEEE Trans. POWER Electron. 25 (2010). https://doi.org/10.1109/TPEL.2009.2028074.
[145] W.-K. Lun, K.H. Loo, S.-C. Tan, Y.M. Lai, C.K. Tse, Bilevel Current Driving Technique for LEDs, IEEE Trans. POWER Electron. 24 (2009). https://doi.org/10.1109/TPEL.2009.2021687.
[146] S.Y.R. Hui, Y.X. Qin, A General Photo-Electro-Thermal Theory for Light Emitting Diode (LED) Systems; A General Photo-Electro-Thermal Theory for Light Emitting Diode (LED) Systems, (2009). https://doi.org/10.1109/APEC.2009.4802712.
[147] H.-T. Chen, S.-C. Tan, R. Hui, Color Variation Reduction of GaN-Based White Light-Emitting Diodes Via Peak-Wavelength Stabilization, IEEE Trans. Power Electron. 29 (2014) 3709. https://doi.org/10.1109/TPEL.2013.2281812.
[148] H. Wong, V. Filip, C.K. Wong, P.S. Chung, Silicon integrated photonics begins to revolutionize, Microelectron. Reliab. 47 (2007) 1–10. https://doi.org/10.1016/J.MICROREL.2006.01.002.

[149] G.E. Moore, Cramming more components onto integrated circuits, Reprinted from Electronics, volume 38, number 8, April 19, 1965, pp.114 ff., IEEE Solid-State Circuits Soc. Newsl. 11 (2009) 33–35. https://doi.org/10.1109/N-SSC.2006.4785860.
[150] B. Heery, C. Briciu-Burghina, D. Zhang, G. Duffy, D. Brabazon, N. O'Connor, F. Regan, ColiSense, today's sample today: A rapid on-site detection of β-d-Glucuronidase activity in surface water as a surrogate for E. coli, Talanta. 148 (2016). https://doi.org/10.1016/j.talanta.2015.10.035.
[151] J.J. Lamb, J.J. Eaton-Rye, M.F. Hohmann-Marriott, An LED-based fluorometer for chlorophyll quantification in the laboratory and in the field, Photosynth. Res. 114 (2012) 59–68. https://doi.org/10.1007/s11120-012-9777-y.
[152] B.G.B. Kitchener, S.D. Dixon, K.O. Howarth, A.J. Parsons, J. Wainwright, M.D. Bateman, J.R. Cooper, G.K. Hargrave, E.J. Long, C.J.M. Hewett, A low-cost bench-top research device for turbidity measurement by radially distributed illumination intensity sensing at multiple wavelengths, HardwareX. 5 (2019) e00052. https://doi.org/10.1016/j.ohx.2019.e00052.
[153] M. Tedetti, P. Joffre, M. Goutx, Development of a field-portable fluorometer based on deep ultraviolet LEDs for the detection of phenanthrene- and tryptophan-like compounds in natural waters, Sens. Actuators B Chem. 182 (2013) 416–423. https://doi.org/10.1016/J.SNB.2013.03.052.
[154] M. Marghany, Chapter 3 - Quantization of Maxwell's equations, in: M. Marghany (Ed.), Synth. Aperture Radar Imaging Mech. Oil Spills, Gulf Professional Publishing, 2020: pp. 41–60. https://doi.org/10.1016/B978-0-12-818111-9.00003-3.
[155] E. Doğanci, Ş. Kaya, A. Aktağ, E. Sarigül Duman, R. Turan, H. Karaçali, E. Yilmaz, Fabrication and characterization of Si-PIN photodiodes, Turk. J. Phys. 43 (2019) 556–562. https://doi.org/10.3906/fiz-1905-16.
[156] R.A. Marques Lameirinhas, J.P. N. Torres, C. P. Correia V. Bernardo, Modelling and Design of a Dual Depletion PIN Photodiode as Temperature Sensor, Sensors. 23 (2023) 4599. https://doi.org/10.3390/s23104599.
[157] A. Beling, J.C. Campbell, Photodetectors, in: H. Venghaus, N. Grote (Eds.), Fibre Opt. Commun. Key Devices, Springer International Publishing, Cham, 2017: pp. 249–290. https://doi.org/10.1007/978-3-319-42367-8_6.
[158] W. Ma, T. Wu, N. Yao, W. Zhou, L. Jiang, Q. Qiu, J. Li, Z. Huang, Bandgap-independent photoconductive detection in two-dimensional Sb2Te3, Commun. Mater. 3 (2022) 1–7. https://doi.org/10.1038/s43246-022-00292-w.
[159] M. Cui, Y. Xu, X. Sun, Z. Wang, H. Gong, X. Chen, T. Hu, Y. Zhang, F. Ren, S. Gu, J. Ye, R. Zhang, Photoconductive and photovoltaic metal-semiconductor-metal κ-Ga2O3 solar-blind detectors with high rejection ratios, J. Phys. Appl. Phys. 55 (2022) 394003. https://doi.org/10.1088/1361-6463/ac7f68.
[160] W. Jung, Op Amp Applications Handbook, Newnes, 2005.
[161] X. Geng, Y. Gao, C. Feng, Y. Guan, A facile and high sensitive micro fluorimeter based on light emitting diode and photodiode, (2017). https://doi.org/10.1016/j.talanta.2017.07.022.
[162] K.-S. Shin, Y.-H. Kim, K.-K. Paek, J.-H. Park, E.-G. Yang, T.-S. Kim, J.-Y. Kang, B.-K. Ju, Characterization of an Integrated Fluorescence-Detection Hybrid Device With Photodiode and Organic Light-Emitting Diode, IEEE ELECTRON DEVICE Lett. 27 (2006). https://doi.org/10.1109/LED.2006.880656.
[163] Y.-H. Shin, M.T. Gutierrez-Wing, J.-W. Choi, A field-deployable and handheld fluorometer for environmental water quality monitoring, Micro Nano Syst. Lett. 6 (2018) 16. https://doi.org/10.1186/s40486-018-0078-x.

[164] M. Brandl, T. Posnicek, R. Preuer, G. Weigelhofer, A Portable Sensor System for Measurement of Fluorescence Indices of Water Samples, IEEE Sens. J. 20 (2020) 9132–9139. https://doi.org/10.1109/JSEN.2020.2988588.
[165] J. Bridgeman, A. Baker, D. Brown, J.B. Boxall, Portable LED fluorescence instrumentation for the rapid assessment of potable water quality, Sci. Total Environ. 524–525 (2015) 338–346. https://doi.org/10.1016/j.scitotenv.2015.04.050.
[166] K. Bürling, M. Hunsche, G. Noga, Use of blue-green and chlorophyll fluorescence measurements for differentiation between nitrogen deficiency and pathogen infection in winter wheat, J. Plant Physiol. 168 (2011) 1641–1648. https://doi.org/10.1016/J.JPLPH.2011.03.016.
[167] H. Yokota, A. Fukasawa, M. Hirano, T. Ide, Low-Light Photodetectors for Fluorescence Microscopy, Appl. Sci. 11 (2021) 2773. https://doi.org/10.3390/app11062773.
[168] S.X. Tao, H.W. Chan, H. Van der Graaf, Secondary Electron Emission Materials for Transmission Dynodes in Novel Photomultipliers: A Review, Materials. 9 (2016) 1017. https://doi.org/10.3390/ma9121017.
[169] P.D. Dahlberg, C.T. Boughter, N.F. Faruk, L. Hong, Y.H. Koh, M.A. Reyer, A. Shaiber, A. Sherani, J. Zhang, J.E. Jureller, A.T. Hammond, A simple approach to spectrally resolved fluorescence and bright field microscopy over select regions of interest, Rev. Sci. Instrum. 87 (2016) 113704. https://doi.org/10.1063/1.4967274.
[170] How Does a Spectrometer Work?, (n.d.). https://bwtek.com/spectrometer-introduction/ (accessed May 17, 2023).
[171] O. Zielinski, N. Rüssmeier, O.D. Ferdinand, M.L. Miranda, J. Wollschläger, Assessing Fluorescent Organic Matter in Natural Waters: Towards In Situ Excitation–Emission Matrix Spectroscopy, Appl. Sci. 2018 Vol 8 Page 2685. 8 (2018) 2685. https://doi.org/10.3390/APP8122685.
[172] K.S. Johnson, L.J. Coletti, In situ ultraviolet spectrophotometry for high resolution and long-term monitoring of nitrate, bromide and bisulfide in the ocean, Deep Sea Res. Part Oceanogr. Res. Pap. 49 (2002) 1291–1305. https://doi.org/10.1016/S0967-0637(02)00020-1.
[173] Z. Yang, T. Albrow-Owen, W. Cai, T. Hasan, Miniaturization of optical spectrometers, Science. 371 (2021). https://doi.org/10.1126/SCIENCE.ABE0722/ASSET/F573C453-1A0B-4A29-B2C3-3A16BC2FCF7A/ASSETS/GRAPHIC/371_ABE0722_FA.JPEG.
[174] E. Ryckeboer, M. Vanslembrouck, R. Baets, R. Bockstaele, Glucose sensing by waveguide-based absorption spectroscopy on a silicon chip, Biomed. Opt. Express Vol 5 Issue 5 Pp 1636-1648. 5 (2014) 1636–1648. https://doi.org/10.1364/BOE.5.001636.
[175] M. Manley, Near-infrared spectroscopy and hyperspectral imaging: non-destructive analysis of biological materials, 43 (2014) 8200–8214. https://doi.org/10.1039/C4CS00062E.
[176] P. Sokołowski, M.S. Wróbel, K. Karpienko, Design and implementation of the driver system for a Hamamatsu C12880MA microspectrometer, Photonics Lett. Pol. 13 (2021) 34–36. https://doi.org/10.4302/PLP.V13I2.1103.
[177] K. Laganovska, A. Zolotarjovs, M. Vázquez, K. Mc Donnell, J. Liepins, H. Ben-Yoav, V. Karitans, K. Smits, Portable low-cost open-source wireless spectrophotometer for fast and reliable measurements, HardwareX. 7 (2020) e00108. https://doi.org/10.1016/J.OHX.2020.E00108.

[178] T.P. Rasmussen, Compact and High Performance Spectrometers based on Novel Transmission Gratings with High Dispersion, Appl. Spectrosc. 70 (2016) 804–809. https://doi.org/10.1177/0003702816638271.
[179] Mini-spectrometer micro series C12880MA | Hamamatsu Photonics, (n.d.). https://www.hamamatsu.com/eu/en/product/optical-sensors/spectrometers/mini-spectrometer/C12880MA.html (accessed August 29, 2022).
[180] G. Horlick, E.G. Codding, Photodiode Arrays for Spectrochemical Measurements, in: D.M. Hercules, G.M. Hieftje, L.R. Snyder, M.A. Evenson (Eds.), Contemp. Top. Anal. Clin. Chem. Vol. 1, Springer US, Boston, MA, 1977: pp. 195–247. https://doi.org/10.1007/978-1-4615-6728-8_4.
[181] M. Nehir, C. Frank, S. Aßmann, E.P. Achterberg, Improving Optical Measurements: Non-Linearity Compensation of Compact Charge-Coupled Device (CCD) Spectrometers, Sensors. 19 (2019) 2833. https://doi.org/10.3390/s19122833.
[182] K. Zhang, P. Burasa, Y. Audet, A novel CMOS spectrometer based on wavelength absorption, Sens. Actuators Phys. 268 (2017) 9–15. https://doi.org/10.1016/j.sna.2017.10.057.
[183] S.B. Sukhavasi, S.B. Sukhavasi, K. Elleithy, S. Abuzneid, A. Elleithy, CMOS Image Sensors in Surveillance System Applications, Sensors. 21 (2021) 488. https://doi.org/10.3390/s21020488.
[184] K.-Y. Zang, Y. Yao, E.-T. Hu, A.-Q. Jiang, Y.-X. Zheng, S.-Y. Wang, H.-B. Zhao, Y.-M. Yang, O. Yoshie, Y.-P. Lee, D.W. Lynch, L.-Y. Chen, A High-Performance Spectrometer with Two Spectral Channels Sharing the Same BSI-CMOS Detector, Sci. Rep. 8 (2018) 12660. https://doi.org/10.1038/s41598-018-31124-y.
[185] D. Litwiller, CCD vs. CMOS: Facts and Fiction, in: 2001. https://www.semanticscholar.org/paper/CCD-vs.-CMOS%3A-Facts-and-Fiction-Litwiller/de6fe1248d29653c3967031e5c47f7160bc39f1a (accessed September 19, 2023).
[186] B. Sutapun, A. Somboonkaew, R. Amarit, S. Chanhorm, Development and Beam-Shape Analysis of an Integrated Fiber-Optic Confocal Probe for High-Precision Central Thickness Measurement of Small-Radius Lenses, Sensors. 15 (2015) 8512–8526. https://doi.org/10.3390/s150408512.
[187] H. Wang, D. Chen, Y. Chen, J. Liu, J. Xu, A. Zhu, F. Long, Development of novel handheld optical fiber dissolved oxygen sensor and its applications, Anal. Chim. Acta. 1200 (2022) 339587. https://doi.org/10.1016/j.aca.2022.339587.
[188] H. Steiner, M. Jakusch, M. Kraft, M. Karlowatz, T. Baumann, R. Niessner, W. Konz, A. Brandenburg, K. Michel, C. Boussard-Plédel, B. Bureau, J. Lucas, Y. Reichlin, A. Katzir, N. Fleischmann, K. Staubmann, R. Allabashi, J.M. Bayona, B. Mizaikoff, *In Situ* Sensing of Volatile Organic Compounds in Groundwater: First Field Tests of a Mid-Infrared Fiber-Optic Sensing System, Appl. Spectrosc. 57 (2003) 607–613.
[189] Flat Windows - Thorlabs, (n.d.). https://www.thorlabs.com/navigation.cfm?guide_id=2367 (accessed August 8, 2022).
[190] M.S. Finch, D.J. Hydes, C.H. Clayson, B. Weigl, J. Dakin, P. Gwilliam, A low power ultra violet spectrophotometer for measurement of nitrate in seawater: introduction, calibration and initial sea trials, Anal. Chim. Acta. 377 (1998) 167–177. https://doi.org/10.1016/S0003-2670(98)00616-3.
[191] M. Eastwood, F. Loya, I. McCubbin, D.W. Wilson, B. Richardson, V. White, A. Mazer, J.I. Rodriguez, E. Urquiza, K. Yee, S. Lundeen, D. Randall, B. Franklin, B.V. Gorp, R. Vargas, P. Mouroulis, C. Sarture, D. Cohen, H. Dierssen, B.-C. Gao, J. Boardman, R.O. Green, Portable Remote Imaging Spectrometer coastal ocean sensor:

design, characteristics, and first flight results, Appl. Opt. Vol 53 Issue 7 Pp 1363-1380. 53 (2014) 1363–1380. https://doi.org/10.1364/AO.53.001363.
[192] R. Schima, S. Krüger, J. Bumberger, M. Paschen, P. Dietrich, T. Goblirsch, Mobile monitoring—open-source based optical sensor system for service-oriented turbidity and dissolved organic matter monitoring, Front. Earth Sci. 7 (2019) 184. https://doi.org/10.3389/FEART.2019.00184/BIBTEX.
[193] Understanding Optical Windows | Edmund Optics, (n.d.). https://www.edmundoptics.com/knowledge-center/application-notes/optics/understanding-optical-windows/ (accessed May 22, 2023).
[194] T. Junge, H. Liborius, T. Mehner, A. Nestler, A. Schubert, T. Lampke, Measurement system based on the Seebeck effect for the determination of temperature and tool wear during turning of aluminum alloys, Procedia CIRP. 93 (2020) 1435–1441. https://doi.org/10.1016/j.procir.2020.03.015.
[195] B. Baker, Chapter 3 - The Right ADC for the Right Application, in: B. Baker (Ed.), Bak. Dozen, Newnes, Burlington, 2005: pp. 65–89. https://doi.org/10.1016/B978-075067819-3/50005-1.
[196] C. Dames, Resistance Temperature Detectors, in: D. Li (Ed.), Encycl. Microfluid. Nanofluidics, Springer US, Boston, MA, 2008: pp. 1782–1790. https://doi.org/10.1007/978-0-387-48998-8_1354.
[197] F. Udrea, S. Santra, J.W. Gardner, CMOS temperature sensors - concepts, state-of-the-art and prospects, in: 2008 Int. Semicond. Conf., 2008: pp. 31–40. https://doi.org/10.1109/SMICND.2008.4703322.
[198] H.B. Mayya, D. Pai, V.M. Kini, P. N H, Effect of Marine Environmental Conditions on Physical and Mechanical Properties of Fiber-Reinforced Composites—A Review, J. Inst. Eng. India Ser. C. 102 (2021) 843–849. https://doi.org/10.1007/s40032-021-00676-w.
[199] R.L. Reuben, Mechanical Properties and Design for Marine Use, in: R.L. Reuben (Ed.), Mater. Mar. Technol., Springer, London, 1994: pp. 19–43. https://doi.org/10.1007/978-1-4471-2011-7_2.
[200] İ. Baylakoğlu, A. Fortier, S. Kyeong, R. Ambat, H.C. Gudla, M.H. Azarian, M.G. Pecht, The detrimental effects of water on electronic devices, E-Prime - Adv. Electr. Eng. Electron. Energy. 1 (2021) 100016. https://doi.org/10.1016/J.PRIME.2021.100016.
[201] M.A. El-Reedy, Chapter 6 - Proactive approach to integrity, in: M.A. El-Reedy (Ed.), Asset Integr. Manag. Offshore Onshore Struct., Gulf Professional Publishing, 2022: pp. 265–345. https://doi.org/10.1016/B978-0-12-824540-8.00006-5.
[202] M. Jimenez-Martinez, Harbor and coastal structures: A review of mechanical fatigue under random wave loading, Heliyon. 7 (2021) e08241. https://doi.org/10.1016/j.heliyon.2021.e08241.
[203] A.S.H. Makhlouf, V. Herrera, E. Muñoz, Chapter 6 - Corrosion and protection of the metallic structures in the petroleum industry due to corrosion and the techniques for protection, in: A.S.H. Makhlouf, M. Aliofkhazraei (Eds.), Handb. Mater. Fail. Anal., Butterworth-Heinemann, 2018: pp. 107–122. https://doi.org/10.1016/B978-0-08-101928-3.00006-9.
[204] R.E. Melchers, Pitting Corrosion of Mild Steel in Marine Immersion EnvironmentPart 1: Maximum Pit Depth, Corrosion. 60 (2004).
[205] B. Valdez, J. Ramirez, A. Eliezer, M. Schorr, R. Ramos, R. Salinas, Corrosion assessment of infrastructure assets in coastal seas, J. Mar. Eng. Technol. 15 (2016) 124–134. https://doi.org/10.1080/20464177.2016.1247635.

[206] A.L. Andrady, A.M. Heikkilä, K.K. Pandey, L.S. Bruckman, C.C. White, M. Zhu, L. Zhu, Effects of UV radiation on natural and synthetic materials, Photochem. Photobiol. Sci. 22 (2023) 1177–1202. https://doi.org/10.1007/s43630-023-00377-6.
[207] A.L. Andrady, S.H. Hamid, X. Hu, A. Torikai, Effects of increased solar ultraviolet radiation on materials, J. Photochem. Photobiol. B. 46 (1998) 96–103. https://doi.org/10.1016/S1011-1344(98)00188-2.
[208] E. Amores, M. Sánchez-Molina, M. Sánchez, Effects of the marine atmosphere on the components of an alkaline water electrolysis cell for hydrogen production, Results Eng. 10 (2021) 100235. https://doi.org/10.1016/j.rineng.2021.100235.
[209] A.L. Andrady, Weathering of polyethylene (LDPE) and enhanced photodegradable polyethylene in the marine environment, J. Appl. Polym. Sci. 39 (1990) 363–370. https://doi.org/10.1002/app.1990.070390213.
[210] P. Liu, X. Zhan, X. Wu, J. Li, H. Wang, S. Gao, Effect of weathering on environmental behavior of microplastics: Properties, sorption and potential risks, Chemosphere. 242 (2020) 125193. https://doi.org/10.1016/j.chemosphere.2019.125193.
[211] Alliance for Coastal Technologies, Biofouling Prevention Technologies for Coastal Sensors / Sensor Platforms, Univ. Md. Cent. Environ. Sci. Workshop Proc. (2003) 23.
[212] A. Delgado, C. Briciu-Burghina, F. Regan, Antifouling Strategies for Sensors Used in Water Monitoring: Review and Future Perspectives, 21 (2021) 389.
[213] Plastics Materials and Processes: A Concise Encyclopedia | Wiley, Wiley.Com. (n.d.). https://www.wiley.com/en-ie/Plastics+Materials+and+Processes%3A+A+Concise+Encyclopedia-p-9780471456032 (accessed July 31, 2023).
[214] Handbook of Polymers - 2nd Edition, (n.d.). https://shop.elsevier.com/books/handbook-of-polymers/wypych/978-1-895198-92-8 (accessed July 31, 2023).
[215] J. Zhu, D. Li, W. Chang, Z. Wang, L. Hu, Y. Zhang, M. Wang, Z. Yang, J. Song, S. Chen, L. Zhang, L. Zhang, In situ marine exposure study on corrosion behaviors of five alloys in coastal waters of western Pacific Ocean, J. Mater. Res. Technol. 9 (2020) 8104–8116. https://doi.org/10.1016/J.JMRT.2020.05.060.
[216] I.V. Gorynin, Titanium alloys for marine application, Mater. Sci. Eng. A. 263 (1999) 112–116. https://doi.org/10.1016/S0921-5093(98)01180-0.
[217] I.V. Gorynin, A.S. Oryshchenko, V.P. Leonov, V.I. Mikhailov, I.A. Schastlivaia, Titanium Application in Marine Engineering and Nuclear-Power Engineering, in: Proc. 13th World Conf. Titan., John Wiley & Sons, Inc., Hoboken, NJ, USA, 2016: pp. 1797–1805. https://doi.org/10.1002/9781119296126.ch302.
[218] Produkte - s::can, (n.d.). https://www.s-can.at/de/produkte/ (accessed August 19, 2022).
[219] OSCAR - TriOS Mess- und Datentechnik, (n.d.). https://www.trios.de/en/oscar.html (accessed August 19, 2022).
[220] Products Archive | Chelsea Technologies, (n.d.). https://chelsea.co.uk/products/ (accessed August 19, 2022).
[221] YSI | Water Quality Sampling and Monitoring Meters and Instruments for dissolved oxygen, pH, turbidity, (n.d.). https://www.ysi.com/ (accessed August 19, 2022).
[222] Fluorometers & Fluorescence Sensors | Turner Designs | United States, (n.d.). https://www.turnerdesigns.com/fluorometers-and-sensors (accessed August 19, 2022).
[223] M. Kutz, Applied Plastics Engineering Handbook: Processing, Materials, and Applications, William Andrew, 2016.

[224] D.A. Shifler, Understanding and Modeling Galvanic Corrosion in Marine Environments, in: OnePetro, 2006. https://dx.doi.org/ (accessed August 9, 2023).
[225] Z. Chen, D. Koleva, K. van Breugel, A review on stray current-induced steel corrosion in infrastructure, Corros. Rev. 35 (2017) 397–423. https://doi.org/10.1515/corrrev-2017-0009.
[226] ISO - ISO 9223:2012 - Corrosion of metals and alloys — Corrosivity of atmospheres — Classification, determination and estimation, (n.d.). https://www.iso.org/standard/53499.html (accessed July 22, 2022).
[227] DNV-RP-B401 Cathodic protection design, DNV. (n.d.). https://www.dnv.com/Default (accessed July 31, 2023).
[228] L.L. Shreir, G.T. Burstein, R.A. Jarman, Corrosion. vol. 2, Corrosion control, 3rd ed, Butterworth-Heinemann, Oxford, 1994.
[229] V.N. Kale, J. Rajesh, T. Maiyalagan, C.W. Lee, RM. Gnanamuthu, Fabrication of Ni–Mg–Ag alloy electrodeposited material on the aluminium surface using anodizing technique and their enhanced corrosion resistance for engineering application, Mater. Chem. Phys. 282 (2022) 125900. https://doi.org/10.1016/j.matchemphys.2022.125900.
[230] R.A. Dickie, F.L. Floyd, Polymeric Materials for Corrosion Control: An Overview, in: Polym. Mater. Corros. Control, American Chemical Society, 1986: pp. 1–16. https://doi.org/10.1021/bk-1986-0322.ch001.
[231] R.B. Seymour, C.E. Carraher, Structure—Property Relationships in Polymers, Springer US, Boston, MA, 1984. https://doi.org/10.1007/978-1-4684-4748-4.
[232] AK Steel 316 Austenitic Stainless steel, (n.d.). https://www.matweb.com/search/DataSheet.aspx?MatGUID=5edc39d3b0fd44efa9fdd90d049c3737&ckck=1 (accessed September 30, 2022).
[233] Metals Handbook Desk Edition, ASM International, 1998. https://doi.org/10.31399/asm.hb.mhde2.9781627081993.
[234] Titanium, Ti, (n.d.). https://www.matweb.com/search/DataSheet.aspx?MatGUID=66a15d609a3f4c829cb6ad08f0dafc01&ckck=1 (accessed September 30, 2022).
[235] Overview of materials for Acetal Copolymer, Unreinforced, (n.d.). https://www.matweb.com/search/DataSheet.aspx?MatGUID=c3039ef87c9245448cdebe961b19a54c (accessed September 30, 2022).
[236] Overview of materials for Polyetheretherketone, Unreinforced, (n.d.). https://www.matweb.com/search/DataSheet.aspx?MatGUID=2164cacabcde4391a596640d553b2ebe&ckck=1 (accessed August 1, 2023).
[237] Aluminum 6061-T6; 6061-T651, (n.d.). https://www.matweb.com/search/DataSheet.aspx?MatGUID=b8d536e0b9b54bd7b69e4124d8f1d20a&ckck=1 (accessed September 30, 2022).
[238] ASM Specialty Handbook: Aluminum and Aluminum Alloys, ASM Int. (n.d.). https://www.asminternational.org/asm-specialty-handbook-aluminum-and-aluminum-alloys/results/-/journal_content/56/06610G/PUBLICATION/ (accessed August 1, 2023).
[239] S. Kalpakjian, S.R. Schmid, Manufacturing Engineering and Technology, Prentice Hall, 2010.
[240] S. Haridy, I. Alsyouf, M. Shamsuzzaman, Effective X-bar & R Chart for Monitoring Aluminum Extrusion Process, in: 2019. https://www.semanticscholar.org/paper/Effective-X-bar-%26-R-Chart-for-Monitoring-Aluminum-Haridy-Alsyouf/3fb83cda5e8d3e3045b7b2c0fa24556c1f5cd6ff (accessed August 1, 2023).

[241] DeGarmo's Materials and Processes in Manufacturing, 13th Edition | Wiley, Wiley.Com. (n.d.). https://www.wiley.com/en-ie/DeGarmo%27s+Materials+and+Processes+in+Manufacturing%2C+13th+Edition-p-9781119492825 (accessed August 1, 2023).
[242] V. Songmene, I. Zaghbani, G. Kientzy, Machining and Machinability of Tool Steels: Effects of Lubrication and Machining Conditions on Tool Wear and Tool Life Data, Procedia CIRP. 77 (2018) 505–508. https://doi.org/10.1016/J.PROCIR.2018.08.252.
[243] A.B. Strong, Plastics: Materials and Processing, Pearson Prentice Hall, 2006.
[244] J.S. Mohammed, Applications of 3D printing technologies in oceanography, Methods Oceanogr. 17 (2016). https://doi.org/10.1016/j.mio.2016.08.001.
[245] Machines | Free Full-Text | Possible Applications of Additive Manufacturing Technologies in Shipbuilding: A Review, (n.d.). https://www.mdpi.com/2075-1702/8/4/84 (accessed August 1, 2023).
[246] Y. Ni, R. Ji, K. Long, T. Bu, K. Chen, S. Zhuang, A review of 3D-printed sensors, Appl. Spectrosc. Rev. 52 (2017) 623–652. https://doi.org/10.1080/05704928.2017.1287082.
[247] D.T. Pham, S.S. Dimov, Rapid Prototyping Processes, in: D.T. Pham, S.S. Dimov (Eds.), Rapid Manuf. Technol. Appl. Rapid Prototyp. Rapid Tool., Springer, London, 2001: pp. 19–42. https://doi.org/10.1007/978-1-4471-0703-3_2.
[248] T. Matos, V. Pinto, P. Sousa, M. Martins, E. Fernández, R. Henriques, L.M. Gonçalves, Design and In Situ Validation of Low-Cost and Easy to Apply Anti-Biofouling Techniques for Oceanographic Continuous Monitoring with Optical Instruments, Sensors. 23 (2023) 605. https://doi.org/10.3390/s23020605.
[249] B. Orzeł, K. Stecuła, Comparison of 3D Printout Quality from FDM and MSLA Technology in Unit Production, Symmetry. 14 (2022) 910. https://doi.org/10.3390/sym14050910.
[250] A. Jandyal, I. Chaturvedi, I. Wazir, A. Raina, M.I. Ul Haq, 3D printing – A review of processes, materials and applications in industry 4.0, Sustain. Oper. Comput. 3 (2022) 33–42. https://doi.org/10.1016/J.SUSOC.2021.09.004.
[251] K. Szykiedans, W. Credo, Mechanical Properties of FDM and SLA Low-cost 3-D Prints, Procedia Eng. 136 (2016) 257–262. https://doi.org/10.1016/j.proeng.2016.01.207.
[252] Y.A. Gueche, N.M. Sanchez-Ballester, S. Cailleaux, B. Bataille, I. Soulairol, Selective Laser Sintering (SLS), a New Chapter in the Production of Solid Oral Forms (SOFs) by 3D Printing, Pharmaceutics. 13 (2021) 1212. https://doi.org/10.3390/pharmaceutics13081212.
[253] N.A. Charoo, S.F. Barakh Ali, E.M. Mohamed, M.A. Kuttolamadom, T. Ozkan, M.A. Khan, Z. Rahman, Selective laser sintering 3D printing – an overview of the technology and pharmaceutical applications, Https://Doi.Org/10.1080/03639045.2020.1764027. 46 (2020) 869–877. https://doi.org/10.1080/03639045.2020.1764027.
[254] A. Kafle, E. Luis, R. Silwal, H.M. Pan, P.L. Shrestha, A.K. Bastola, 3D/4D Printing of Polymers: Fused Deposition Modelling (FDM), Selective Laser Sintering (SLS), and Stereolithography (SLA), Polymers. 13 (2021) 3101. https://doi.org/10.3390/polym13183101.
[255] F.M. Mwema, E.T. Akinlabi, Basics of Fused Deposition Modelling (FDM), Fused Depos. Model. (2020) 1–15. https://doi.org/10.1007/978-3-030-48259-6_1.
[256] J.W. Stansbury, M.J. Idacavage, 3D printing with polymers: Challenges among expanding options and opportunities, Dent. Mater. Off. Publ. Acad. Dent. Mater. 32 (2016) 54–64. https://doi.org/10.1016/j.dental.2015.09.018.

[257] K.L. Mittal, A. Pizzi, Handbook of Sealant Technology, CRC Press, 2009.
[258] D.A. Willistein, An Introduction to Optical Window Design, 2006.
[259] T. Newswander, R.A. Paquin, Materials for Optical Systems, in: Handb. Optomech. Eng., CRC Press, 2017: pp. 53–87. https://doi.org/10.4324/9781315153247-3.
[260] Watertight Enclosure for ROV/AUV (6" Series), Blue Robot. (n.d.). https://bluerobotics.com/store/watertight-enclosures/6-series/wte6-asm-r1/ (accessed August 9, 2023).
[261] V. Petrovic, J. Vicente Haro Gonzalez, O. Jordá Ferrando, J. Delgado Gordillo, J. Ramón Blasco Puchades, L. Portolés Griñan, Additive layered manufacturing: sectors of industrial application shown through case studies, Int. J. Prod. Res. 49 (2011) 1061–1079. https://doi.org/10.1080/00207540903479786.
[262] B. Vayre, F. Vignat, F. Villeneuve, Designing for Additive Manufacturing, Procedia CIRP. 3 (2012) 632–637. https://doi.org/10.1016/j.procir.2012.07.108.
[263] T.D. Ngo, A. Kashani, G. Imbalzano, K.T.Q. Nguyen, D. Hui, Additive manufacturing (3D printing): A review of materials, methods, applications and challenges, Compos. Part B Eng. 143 (2018) 172–196. https://doi.org/10.1016/j.compositesb.2018.02.012.
[264] S. Morales-Planas, J. Minguella-Canela, J. Lluma-Fuentes, J.A. Travieso-Rodriguez, A.-A. García-Granada, Multi Jet Fusion PA12 Manufacturing Parameters for Watertightness, Strength and Tolerances, Materials. 11 (2018) 1472. https://doi.org/10.3390/ma11081472.
[265] H. Agrawaal, J.E. Thompson, Additive manufacturing (3D printing) for analytical chemistry, Talanta Open. 3 (2021) 100036. https://doi.org/10.1016/j.talo.2021.100036.
[266] R. Ambat, S.G. Jensen, P. Møller, Corrosion Reliability of Electronic Systems, ECS Trans. 6 (2008) 17–28. https://doi.org/10.1149/1.2900650/XML.
[267] IPC HDBK-830A-2013, Guidelines for Design, Selection and Application of Conformal Coatings, IPC Stand. (n.d.).
[268] J.J. Licari, Chemistry and Properties of Polymer Coatings, Coat. Mater. Electron. Appl. (2003) 65–200. https://doi.org/10.1016/B978-081551492-3.50004-0.
[269] P.E. Tomlins, & L. Zou, Surface Insulation Resistance and the Properties of Conformal Coatings, National Physical Laboratory, Middlesex, U.K, 2000. http://eprintspublications.npl.co.uk/1594/ (accessed October 18, 2022).
[270] E.A. Kosasih, A. Zikri, M.I. Dzaky, Water vapor desorption from silica gel in a combined drying and double-condenser compression refrigeration system, Heliyon. 8 (2022) e09757. https://doi.org/10.1016/j.heliyon.2022.e09757.
[271] Y. Li, C. Ning, Latest research progress of marine microbiological corrosion and bio-fouling, and new approaches of marine anti-corrosion and anti-fouling, Bioact. Mater. 4 (2019) 189–195. https://doi.org/10.1016/j.bioactmat.2019.04.003.
[272] A. Kerr, M.J. Cowling, C.M. Beveridge, M.J. Smith, A.C.S. Parr, R.M. Head, J. Davenport, T. Hodgkiess, The early stages of marine biofouling and its effect on two types of optical sensors, Environ. Int. 24 (1998) 331–343. https://doi.org/10.1016/S0160-4120(98)00011-7.
[273] L. Delauney, C. Compère, M. Lehaitre, C. Compare, M. Lehaitre, C. Compère, M. Lehaitre, Biofouling protection for marine environmental sensors, Ocean Sci. 6 (2010) 503–511. https://doi.org/10.5194/os-6-503-2010.
[274] A. Delgado, C. Briciu-Burghina, F. Regan, Antifouling Strategies for Sensors Used in Water Monitoring: Review and Future Perspectives, Sens. 2021 Vol 21 Page 389. 21 (2021) 389. https://doi.org/10.3390/S21020389.

[275] A. Whelan, F. Regan, Antifouling strategies for marine and riverine sensors, J. Environ. Monit. 8 (2006) 880–886. https://doi.org/10.1039/B603289C.
[276] J. Bak, S.D. Ladefoged, M. Tvede, T. Begovic, A. Gregersen, Dose requirements for UVC disinfection of catheter biofilms, Https://Doi.Org/10.1080/08927010802716623. 25 (2010) 289–296. https://doi.org/10.1080/08927010802716623.
[277] N. Bloecher, T. Solvang, O. Floerl, Efficacy testing of novel antifouling systems for marine sensors, Ocean Eng. 240 (2021) 109983. https://doi.org/10.1016/j.oceaneng.2021.109983.
[278] Copper Nickels : Seawater Corrosion Resistance and Antifouling, (n.d.). https://www.copper.org/applications/marine/cuni/properties/corrosion/corrosion_resistance_and_antifouling.html (accessed August 9, 2023).
[279] E. Almeida, T.C. Diamantino, O. de Sousa, Marine paints: The particular case of antifouling paints, Prog. Org. Coat. 59 (2007) 2–20. https://doi.org/10.1016/j.porgcoat.2007.01.017.
[280] S.J. Brooks, M. Waldock, Copper Biocides in the Marine Environment, in: T. Arai, H. Harino, M. Ohji, W.J. Langston (Eds.), Ecotoxicol. Antifouling Biocides, Springer Japan, Tokyo, 2009: pp. 413–428. https://doi.org/10.1007/978-4-431-85709-9_24.
[281] P. Hu, Q. Xie, C. Ma, G. Zhang, Silicone-Based Fouling-Release Coatings for Marine Antifouling, Langmuir. 36 (2020) 2170–2183. https://doi.org/10.1021/acs.langmuir.9b03926.
[282] Y. Bhoj, M. Tharmavaram, D. Rawtani, A comprehensive approach to antifouling strategies in desalination, marine environment, and wastewater treatment, Chem. Phys. Impact. 2 (2021) 100008. https://doi.org/10.1016/j.chphi.2020.100008.
[283] R. Wanka, J. Koc, J. Clarke, K.Z. Hunsucker, G.W. Swain, N. Aldred, J.A. Finlay, A.S. Clare, A. Rosenhahn, Sol–Gel-Based Hybrid Materials as Antifouling and Fouling-Release Coatings for Marine Applications, ACS Appl. Mater. Interfaces. 12 (2020) 53286–53296. https://doi.org/10.1021/acsami.0c15288.
[284] M.R. Detty, R. Ciriminna, F.V. Bright, M. Pagliaro, Environmentally Benign Sol–Gel Antifouling and Foul-Releasing Coatings, Acc. Chem. Res. 47 (2014) 678–687. https://doi.org/10.1021/ar400240n.
[285] C. Richards, C. Briciu-Burghina, M.R. Jacobs, A. Barrett, F. Regan, Assessment of Antifouling Potential of Novel Transparent Sol Gel Coatings for Application in the Marine Environment, Molecules. 24 (2019) 2983. https://doi.org/10.3390/molecules24162983.
[286] Foul Free at Folger Pinnacle - AML Oceanographic Case Study, (n.d.). https://amloceanographic.com/blog/post/foul-free-folger-pinnacle (accessed August 2, 2023).
[287] 10 Tips to Prevent Biofouling on Water Quality Instruments, (n.d.).
[288] C. Briciu-Burghina, S. Power, A. Delgado, F. Regan, Sensors for Coastal and Ocean Monitoring, Annu. Rev. Anal. Chem. 16 (2023) 451–469. https://doi.org/10.1146/annurev-anchem-091922-085746.
[289] N. Ramachandran, N.A. Langrana, L.I. Steinberg, V.R. Jamalabad, Initial Design Strategies for Iterative Design, 4 (1992) 159–169.
[290] S.B. Wachter, J. Agutter, N. Syroid, F. Drews, M.B. Weinger, D. Westenskow, The employment of an iterative design process to develop a pulmonary graphical display, J. Am. Med. Inform. Assoc. 10 (2003) 363–372. https://doi.org/10.1197/JAMIA.M1207/2/JAMIAM1207.F07.JPEG.

[291] ISO - ISO 16290:2013 - Space systems — Definition of the Technology Readiness Levels (TRLs) and their criteria of assessment, (n.d.). https://www.iso.org/standard/56064.html (accessed August 12, 2022).
[292] (PDF) A REVIEW OF TECHNOLOGY READINESS LEVEL (TRL) IN DEVELOPING COMMAND AND CONTROL SYSTEM FOR MARITIME OPERATIONS, (n.d.). https://www.researchgate.net/publication/348034972_A_REVIEW_OF_TECHNOLOGY_READINESS_LEVEL_TRL_IN_DEVELOPING_COMMAND_AND_CONTROL_SYSTEM_FOR_MARITIME_OPERATIONS (accessed August 12, 2022).
[293] Z. Yang, T. Albrow-Owen, W. Cai, T. Hasan, Miniaturization of optical spectrometers., Science. 371 (2021). https://doi.org/10.1126/science.abe0722.
[294] A. Delgado, C. Briciu-Burghina, F. Regan, Antifouling strategies for sensors used in water monitoring: Review and future perspectives, Sens. Switz. 21 (2021) 1–25. https://doi.org/10.3390/s21020389.
[295] A.U. Alam, D. Clyne, M.J. Deen, A Low-Cost Multi-Parameter Water Quality Monitoring System, Sensors. 21 (2021) 3775. https://doi.org/10.3390/s21113775.
[296] X. Wang, L. Sun, Y. Shi, Research on a Miniature Multiparameter Water Quality Sensor Chip and a System with a Temperature Compensation Function, J. Sens. 2020 (2020) e8897916. https://doi.org/10.1155/2020/8897916.
[297] R. Zhang, Z. Wang, X. Li, Z. She, B. Wang, Water Quality Sampling and Multi-Parameter Monitoring System Based on Multi-Rotor UAV Implementation, Water. 15 (2023) 2129. https://doi.org/10.3390/w15112129.
[298] M. Yoshida, T. Horiuchi, Y. Nagasawa, In situ multi-excitation chlorophyll fluorometer for phytoplankton measurements: Technologies and applications beyond conventional fluorometers, in: Ocean. MTSIEEE KONA, 2011: pp. 1–4. https://doi.org/10.23919/OCEANS.2011.6107049.
[299] Y. Pan, L. Qiu, A Submersible in-Situ Highly Sensitive Chlorophyll Fluorescence Detection System, IOP Conf. Ser. Mater. Sci. Eng. 677 (2019) 022065. https://doi.org/10.1088/1757-899X/677/2/022065.
[300] R.I. Chowdhury, K.A. Wahid, K. Nugent, H. Baulch, Design and Development of Low-Cost, Portable, and Smart Chlorophyll-A Sensor, IEEE Sens. J. 20 (2020) 7362–7371. https://doi.org/10.1109/JSEN.2020.2978758.
[301] R. Bullis, J. Coker, J. Belding, A. De Groodt, D.W. Mitchell, N. Velazquez, A. Bell, J. Hall, W.A. Gunderson, J.E.C. Gunderson, The Fluorino: A Low-Cost, Arduino-Controlled Fluorometer, J. Chem. Educ. 98 (2021) 3892–3897. https://doi.org/10.1021/acs.jchemed.1c00876.
[302] W.R.F. Silva, W.T. Suarez, C. Reis, V.B. dos Santos, F.A. Carvalho, E.L. Reis, F.C. Vicentini, Multifunctional Webcam Spectrophotometer for Performing Analytical Determination and Measurements of Emission, Absorption, and Fluorescence Spectra, J. Chem. Educ. 98 (2021) 1442–1447. https://doi.org/10.1021/acs.jchemed.0c01085.
[303] E.K.N. da Silva, V.B. dos Santos, I.S. Resque, C.A. Neves, S.G.C. Moreira, M. de O.K. Franco, W.T. Suarez, A fluorescence digital image-based method using a 3D-printed platform and a UV-LED chamber made of polyacid lactic for quinine quantification in beverages, Microchem. J. 157 (2020) 104986. https://doi.org/10.1016/j.microc.2020.104986.
[304] K. Laganovska, A. Zolotarjovs, M. Vázquez, K. Mc Donnell, J. Liepins, H. Ben-Yoav, V. Karitans, K. Smits, Portable low-cost open-source wireless spectrophotometer for fast and reliable measurements, HardwareX. 7 (2020) e00108. https://doi.org/10.1016/j.ohx.2020.e00108.

[305] L.A.Jr. Porter, C.A. Chapman, J.A. Alaniz, Simple and Inexpensive 3D Printed Filter Fluorometer Designs: User-Friendly Instrument Models for Laboratory Learning and Outreach Activities, J. Chem. Educ. 94 (2017) 105–111. https://doi.org/10.1021/acs.jchemed.6b00495.
[306] Z.A. Wang, H. Moustahfid, A.V. Mueller, A.P.M. Michel, M. Mowlem, B.T. Glazer, T.A. Mooney, W. Michaels, J.S. McQuillan, J.C. Robidart, J. Churchill, M. Sourisseau, A. Daniel, A. Schaap, S. Monk, K. Friedman, P. Brehmer, Advancing Observation of Ocean Biogeochemistry, Biology, and Ecosystems With Cost-Effective in situ Sensing Technologies, Front. Mar. Sci. 6 (2019). https://www.frontiersin.org/articles/10.3389/fmars.2019.00519 (accessed August 15, 2023).
[307] K.R. Murphy, C.A. Stedmon, T.D. Waite, G.M. Ruiz, Distinguishing between terrestrial and autochthonous organic matter sources in marine environments using fluorescence spectroscopy, Mar. Chem. 108 (2008) 40–58. https://doi.org/10.1016/j.marchem.2007.10.003.
[308] L. Jørgensen, C.A. Stedmon, T. Kragh, S. Markager, M. Middelboe, M. Søndergaard, Global trends in the fluorescence characteristics and distribution of marine dissolved organic matter, Mar. Chem. 126 (2011) 139–148. https://doi.org/10.1016/j.marchem.2011.05.002.
[309] J.C. Campbell, 8 - Advances in photodetectors, in: I.P. Kaminow, T. Li, A.E. Willner (Eds.), Opt. Fiber Telecommun. V Fifth Ed., Academic Press, Burlington, 2008: pp. 221–268. https://doi.org/10.1016/B978-0-12-374171-4.00008-3.
[310] J. Shalf, The future of computing beyond Moores Law, Philos. Trans. R. Soc. A. 378 (2020). https://doi.org/10.1098/RSTA.2019.0061.
[311] Z.A. Wang, H. Moustahfid, A. V. Mueller, A.P.M. Michel, M. Mowlem, B.T. Glazer, T.A. Mooney, W. Michaels, J.S. McQuillan, J.C. Robidart, J. Churchill, M. Sourisseau, A. Daniel, A. Schaap, S. Monk, K. Friedman, P. Brehmer, Advancing Observation of Ocean Biogeochemistry, Biology, and Ecosystems With Cost-Effective in situ Sensing Technologies, Front. Mar. Sci. 6 (2019) 519. https://doi.org/10.3389/FMARS.2019.00519/BIBTEX.
[312] T.P. Bean, N. Greenwood, R. Beckett, L. Biermann, J.P. Bignell, J.L. Brant, G.H. Copp, M.J. Devlin, S. Dye, S.W. Feist, L. Fernand, D. Foden, K. Hyder, C.M. Jenkins, J. van der Kooij, S. Kröger, S. Kupschus, C. Leech, K.S. Leonard, C.P. Lynam, B.P. Lyons, T. Maes, E.E.M. Nicolaus, S.J. Malcolm, P. McIlwaine, N.D. Merchant, L. Paltriguera, D.J. Pearce, S.G. Pitois, P.D. Stebbing, B. Townhill, S. Ware, O. Williams, D. Righton, a review of the tools used for marine monitoring in the UK: Combining historic and contemporary methods with modeling and socioeconomics to fulfill legislative needs and scientific ambitions, Front. Mar. Sci. 4 (2017) 263. https://doi.org/10.3389/FMARS.2017.00263/BIBTEX.
[313] GitHub - open-eio/arduino-microspec: Arduino firmware for Hamamatsu C12880 microspectrometer, (n.d.). https://github.com/open-eio/arduino-microspec (accessed September 7, 2022).
[314] GitHub - MajenkoLibraries/TLC59116: Arduino library to control the TLC59116 PWM LED Driver chips., (n.d.). https://github.com/MajenkoLibraries/TLC59116 (accessed September 7, 2022).
[315] GitHub - jarzebski/Arduino-INA226: INA226 Bi-directional Current/Power Monitor Arduino Librar, (n.d.). https://github.com/jarzebski/Arduino-INA226 (accessed September 7, 2022).
[316] E.: H. Rai, ed., The Measurement of photosynthetic pigments in freshwater and standardization of methods, Schweizerbart Science Publishers, Stuttgart, Germany,

1980.
http://www.schweizerbart.de//publications/detail/isbn/9783510470129/Archiv_Ergebnisse_d_Limnol_Heft_14.
[317] ISO 22013:2021(en), Marine environment sensor performance — Specifications, testing and reporting — General requirements, (n.d.). https://www.iso.org/obp/ui/#iso:std:iso:22013:ed-1:v1:en (accessed July 20, 2022).
[318] Teensy 3.2 & 3.1: New Features, (n.d.). https://www.pjrc.com/teensy/teensy31.html (accessed August 29, 2022).
[319] J.J. Creelman, E.A. Luy, G.C.H. Beland, C. Sonnichsen, V.J. Sieben, Simultaneous Absorbance and Fluorescence Measurements Using an Inlaid Microfluidic Approach, Sensors. 21 (2021) 6250. https://doi.org/10.3390/s21186250.
[320] W.M. Madani, R. Seoudi, Improving the fluorescent properties of polyacrylic acid by adding a mixture of (silver nanoparticles/rhodamine B), J. Umm Al-Qura Univ. Appl. Sci. (2023). https://doi.org/10.1007/s43994-023-00041-w.
[321] A. Kathiravan, V. Anbazhagan, M.A. Jhonsi, R. Renganathan, Fluorescence Quenching of Xanthene Dyes by TiO2, Z. Für Phys. Chem. 221 (2007) 941–948. https://doi.org/10.1524/zpch.2007.221.7.941.
[322] R. Rossano, N. Ungaro, A. D'Ambrosio, G.M. Liuzzi, P. Riccio, Extracting and purifying R-phycoerythrin from Mediterranean red algae Corallina elongata Ellis & Solander, J. Biotechnol. 101 (2003) 289–293. https://doi.org/10.1016/S0168-1656(03)00002-6.
[323] Y. Fujita, S. Shimura, Phycoerythrin of the marine blue-green alga Trichodesmium thiebautii, Plant Cell Physiol. 15 (1974) 939–942. https://doi.org/10.1093/oxfordjournals.pcp.a075083.
[324] F. Le Guern, V. Mussard, A. Gaucher, M. Rottman, D. Prim, Fluorescein Derivatives as Fluorescent Probes for pH Monitoring along Recent Biological Applications, Int. J. Mol. Sci. 21 (2020) 9217. https://doi.org/10.3390/ijms21239217.
[325] A. Earp, C. Hanson, P. Ralph, V. Brando, S. Allen, M. Baird, L. Clementson, P. Daniel, A. Dekker, P. Fearns, J. Parslow, P. Strutton, P. Thompson, M. Underwood, S. Weeks, M. Doblin, Review of fluorescent standards for calibration of in situ fluorometers: Recommendations applied in coastal and ocean observing programs, Opt. Express. 19 (2011) 26768–82. https://doi.org/10.1364/OE.19.026768.
[326] L. Guidi, M. Tattini, M. Landi, How Does Chloroplast Protect Chlorophyll Against Excessive Light?, in: 2017. https://doi.org/10.5772/67887.
[327] M. Hossain, A. Deb, Z. Sultan, A. Shaikh, M. Chowdhury, M. Sarker, Synthesis and Application of Graphene Oxide (GO) for Removal of Cationic Dyes from Tannery Effluents, Text. Leather Rev. 3 (2020). https://doi.org/10.31881/TLR.2020.12.
[328] R. van Grondelle, E. Boeker, Limits on Natural Photosynthesis, J. Phys. Chem. B. 121 (2017) 7229–7234. https://doi.org/10.1021/acs.jpcb.7b03024.
[329] F. Lefèvre, A. Chalifour, L. Yu, V. Chodavarapu, P. Juneau, R. Izquierdo, Algal fluorescence sensor integrated into a microfluidic chip for water pollutant detection, Lab. Chip. 12 (2012) 787–793. https://doi.org/10.1039/C2LC20998E.
[330] R. Valipour, L. Boegman, D. Bouffard, Y.R. Rao, Sediment resuspension mechanisms and their contributions to high-turbidity events in a large lake, Limnol. Oceanogr. 62 (2017) 1045–1065. https://doi.org/10.1002/lno.10485.
[331] C. Roesler, J. Uitz, H. Claustre, E. Boss, X. Xing, E. Organelli, N. Briggs, A. Bricaud, C. Schmechtig, A. Poteau, F. D'Ortenzio, J. Ras, S. Drapeau, N. Haëntjens, M. Barbieux, Recommendations for obtaining unbiased chlorophyll estimates from in situ chlorophyll fluorometers: A global analysis of WET Labs ECO sensors, Limnol. Oceanogr. Methods. 15 (2017) 572–585. https://doi.org/10.1002/lom3.10185.

[332] T.L. Richardson, E. Lawrenz, J.L. Pinckney, R.C. Guajardo, E.A. Walker, H.W. Paerl, H.L. MacIntyre, Spectral fluorometric characterization of phytoplankton community composition using the Algae Online Analyser, Water Res. 44 (2010) 2461–2472. https://doi.org/10.1016/j.watres.2010.01.012.
[333] A. Bricaud, A. Morel, L. Prieur, Optical efficiency factors of some phytoplankters1, Limnol. Oceanogr. 28 (1983) 816–832. https://doi.org/10.4319/lo.1983.28.5.0816.
[334] Z. Wang, W. Liu, Y. Zhang, W. Sima, J. Liu, A novel submersible phytoplankton fluorometer with multi-wavelength light emitting diode array as excitation source, in: Light-Emit. Diode Mater. Devices II, SPIE, 2007: pp. 231–237. https://doi.org/10.1117/12.754626.
[335] G.Z. Forristall, C.K. Cooper, Metocean Extreme and Operating Conditions, in: M.R. Dhanak, N.I. Xiros (Eds.), Springer Handb. Ocean Eng., Springer International Publishing, Cham, 2016: pp. 47–76. https://doi.org/10.1007/978-3-319-16649-0_3.
[336] D. Stewardson, Robust Engineering, Taguchi G, Chowdhury S, Taguchi S, McGraw-Hill, New York, 2000. Hard-Bound, Number of pages: 241. ISBN 0 07 134782 8, Qual. Reliab. Eng. Int. 17 (2001) 141–142. https://doi.org/10.1002/QRE.382.
[337] E.J. Dsa, S.E. Lohrenz, V.L. Asper, R.A. Walters, Time Series Measurements of Chlorophyll Fluorescence in the Oceanic Bottom Boundary Layer With a Multisensor Fiber-Optic Fluorometer, J. Atmospheric Ocean. Technol. 14 (1997) 889–896.
[338] H. Zhang, Study on the Influence of Galvanic Corrosion on Ship Structural Materials, IOP Conf. Ser. Earth Environ. Sci. 252 (2019) 022015. https://doi.org/10.1088/1755-1315/252/2/022015.
[339] C. Newport, O. Padget, T.B. de Perera, High turbidity levels alter coral reef fish movement in a foraging task, Sci. Rep. 11 (2021) 5976. https://doi.org/10.1038/s41598-021-84814-5.
[340] S.W. Effler, A.R. Prestigiacomo, F. Peng, K.B. Bulygina, D.G. Smith, Resolution of Turbidity Patterns from Runoff Events in a Water Supply Reservoir, and the Advantages of In Situ Beam Attenuation Measurements, Lake Reserv. Manag. 22 (2006) 79–93. https://doi.org/10.1080/07438140609353886.
[341] HydroCAT-EP V2 | Sea-Bird Scientific - Overview | Sea-Bird, (n.d.). https://www.seabird.com/moored/hydrocat-ep-v2/family?productCategoryId=62331495701 (accessed September 5, 2023).
[342] Turbidity Sensor | Aqua TROLL Multiparameter Sondes, (n.d.). https://in-situ.com/en/aqua-troll-turbidity-sensor (accessed September 23, 2023).
[343] 6136 Turbidity Sensor | ysi.com, (n.d.). https://www.ysi.com/accessory/id-6136/6136-turbidity-sensor (accessed September 23, 2023).
[344] A.S. Kristoffersen, S.R. Erga, B. Hamre, Ø. Frette, Testing Fluorescence Lifetime Standards using Two-Photon Excitation and Time-Domain Instrumentation: Fluorescein, Quinine Sulfate and Green Fluorescent Protein, J. Fluoresc. 28 (2018) 1065–1073. https://doi.org/10.1007/S10895-018-2270-Z.
[345] D.M. Uriza-Prias, A. Méndez-Blas, J.F. Rivas-Silva, Redshift of Excitation Wavelength Caused by the Concentration of L-Tryptophan in Water: A Theoretical and Experimental Study, Open J. Phys. Chem. 11 (2021) 87–105. https://doi.org/10.4236/ojpc.2021.112005.
[346] O. Divya, A.K. Mishra, Understanding the concept of concentration-dependent red-shift in synchronous fluorescence spectra: Prediction of lambda(SFS)(max) and optimization of Deltalambda for synchronous fluorescence scan, Anal. Chim. Acta. 630 (2008) 47–56. https://doi.org/10.1016/j.aca.2008.09.056.
[347] Aqua TROLL Chlorophyll a Sensor - In-Situ, (n.d.). https://in-situ.com/en/aqua-troll-chlorophyll-a-sensor (accessed September 24, 2023).

[348] 6025 Chlorophyll Sensor | ysi.com, (n.d.). https://www.ysi.com/accessory/id-6025/6025-chlorophyll-sensor (accessed September 24, 2023).
[349] A.A. Fernandez-Jaramillo, C. Duarte-Galvan, L.M. Contreras-Medina, I. Torres-Pacheco, R. de J. Romero-Troncoso, R.G. Guevara-Gonzalez, J.R. Millan-Almaraz, Instrumentation in developing chlorophyll fluorescence biosensing: A review, Sens. Switz. 12 (2012) 11853–11869. https://doi.org/10.3390/S120911853.
[350] A.M. Skålvik, C. Saetre, K.-E. Frøysa, R.N. Bjørk, A. Tengberg, Challenges, limitations, and measurement strategies to ensure data quality in deep-sea sensors, Front. Mar. Sci. 10 (2023). https://doi.org/10.3389/fmars.2023.1152236.
[351] V. Gouretski, World Ocean Circulation Experiment – Argo Global Hydrographic Climatology, Ocean Sci. 14 (2018) 1127–1146. https://doi.org/10.5194/os-14-1127-2018.
[352] D. Roemmich, M. Belbéoch, H. Freeland, S. Garzoli, W.J. Gould, F. Grant, M. Ignaszewski, B. King, B. Klein, P.-Y. Le Traon, K. Mork, W.B. Owens, S. Pouliquen, M. Ravichandran, S. Riser, A. Sterl, T. Suga, M.-S. Suk, P. Sutton, V. Thierry, P. Vélez-Belchí, S. Wijffels, J. Xu, Argo: The Challenge of Continuing 10 Years of Progress, Oceanography. 22 (2009) 46–55. https://doi.org/10.5670/oceanog.2009.65.
[353] W. Walczowski, M. Merchel, D. Rak, P. Wieczorek, I. Goszczko, Argo floats in the southern Baltic Sea, Oceanologia. 62 (2020) 478–488. https://doi.org/10.1016/j.oceano.2020.07.001.
[354] R. Comunian, M. Morrison, R. Ajit, Knowledge and Business Engagement Networks in Academic Maritime Research: A Case Study of the University of Southampton, J. Marit. Res. 12 (2015) 3–12.
[355] A.D. Beaton, A.M. Schaap, R. Pascal, R. Hanz, U. Martincic, C.L. Cardwell, A. Morris, G. Clinton-Bailey, K. Saw, S.E. Hartman, M.C. Mowlem, Lab-on-Chip for In Situ Analysis of Nutrients in the Deep Sea, ACS Sens. 7 (2022) 89–98. https://doi.org/10.1021/acssensors.1c01685.
[356] E.J. Christie, D.D. Jensen, R.T. Buckley, D.A. Menefee, K.K. Ziegler, K.L. Wood, R.H. Crawford, Prototyping Strategies: Literature Review and Identification of Critical Variables, in: 2012: p. 25.1091.1-25.1091.22. https://peer.asee.org/prototyping-strategies-literature-review-and-identification-of-critical-variables (accessed August 23, 2023).
[357] M. Relich, I. Nielsen, A. Gola, Reducing the Total Product Cost at the Product Design Stage, Appl. Sci. 12 (2022) 1921. https://doi.org/10.3390/app12041921.
[358] L. Blockstein, O. Yadid-Pecht, Lensless Miniature Portable Fluorometer for Measurement of Chlorophyll and CDOM in Water Using Fluorescence Contact Imaging, IEEE Photonics J. 6 (2014). https://doi.org/10.1109/JPHOT.2014.2326665.
[359] V. Piermattei, A. Madonia, S. Bonamano, R. Martellucci, G. Bruzzone, R. Ferretti, A. Odetti, M. Azzaro, G. Zappalà, M. Marcelli, Cost-Effective Technologies to Study the Arctic Ocean Environment, Sensors. 18 (2018) 2257. https://doi.org/10.3390/s18072257.
[360] J.A Busch, J. Engel, O. Zielinski, A. Friedrichs, Review of State of the Art in Affordable Fluorescence Sensors. D2.2 Work Package 2 Crowdsourcing Technologies for the Monitoring of the Colour, Transparency & Fluorescence of the Sea., Citclops, n.d. http://www.1000001labs.org/wp-content/uploads/2013/09/Review-of-the-state-of-the-art-in-affordable-fluorescence-sensors.pdf (accessed August 15, 2023).
[361] A. Vergnano, F. Gherardini, F. Leali, The Systematic Design of Industrial Products through Design Archetypes: An Application on Mechanical Transmissions, Appl. Sci. 10 (2020) 2277. https://doi.org/10.3390/app10072277.

[362] An intelligent decomposition approach for coupled engineering systems | Multidisciplinary Analysis Optimization Conferences, (n.d.). https://arc.aiaa.org/doi/abs/10.2514/6.1992-4821 (accessed August 16, 2023).
[363] M. Neumaier, S. Kranemann, B. Kazmeier, S. Rudolph, Automated Piping in an Airbus A320 Landing Gear Bay Using Graph-Based Design Languages, Aerospace. 9 (2022) 140. https://doi.org/10.3390/aerospace9030140.
[364] A. Dolgui, F. Sgarbossa, M. Simonetto, International Journal of Production Research ISSN: (Print) (Online) Journal homepage: https://www.tandfonline.com/loi/tprs20 Design and management of assembly systems 4.0: systematic literature review and research agenda Design and management of assembly systems 4.0: systematic literature review and research agenda, Int. J. Prod. Res. 60 (2021) 184–210. https://doi.org/10.1080/00207543.2021.1990433.
[365] J.M. Nilakantan, S.G. Ponnambalam, Robotic U-shaped assembly line balancing using particle swarm optimization, Http://Dx.Doi.Org/10.1080/0305215X.2014.998664. 48 (2015) 231–252. https://doi.org/10.1080/0305215X.2014.998664.
[366] D. Battini, M. Faccio, A. Persona, F. Sgarbossa, New methodological framework to improve productivity and ergonomics in assembly system design, Int. J. Ind. Ergon. 41 (2011) 30–42. https://doi.org/10.1016/J.ERGON.2010.12.001.
[367] G. Currin, James Webb Telescope Has 344 Single-Point Failures. Here Are 5 Critical Elements of the Mission., (2021). https://interestingengineering.com/science/james-webb-has-344-single-point-failures-here-are-the-5-most-critical-elements (accessed August 16, 2023).
[368] 14:00-17:00, ISO 15839:2003, ISO. (n.d.). https://www.iso.org/standard/28740.html (accessed August 22, 2023).
[369] 14:00-17:00, ISO 8466-1:2021, ISO. (n.d.). https://www.iso.org/standard/77139.html (accessed August 22, 2023).
[370] C.-L. Ng, Y.-J. Ng, Q.-Q. Chen, H.F. Hemond, Corrections for matrix effects on fluorescence measurement of a multi-platform optical sensor, Water Pract. Technol. 11 (2016) 644–660. https://doi.org/10.2166/wpt.2016.069.
[371] F.W.J. Teale, Fluorescence Depolarization by Light-Scattering in Turbid Solutions, Photochem. Photobiol. 10 (1969) 363–374. https://doi.org/10.1111/j.1751-1097.1969.tb05701.x.
[372] M.G. Müller, I. Georgakoudi, Q. Zhang, J. Wu, M.S. Feld, Intrinsic fluorescence spectroscopy in turbid media: disentangling effects of scattering and absorption, Appl. Opt. 40 (2001) 4633–4646. https://doi.org/10.1364/AO.40.004633.
[373] PCB Prototype & PCB Fabrication Manufacturer - JLCPCB, (n.d.). https://jlcpcb.com/?from=VG_PCBA&gclid=Cj0KCQjwrfymBhCTARIsADXTabmOGBdd7Yvd3UZguOAEYhLMSpo_z9DLYBIGhr2-9ZEeeYPScLv-06gaAmemEALw_wcB (accessed August 18, 2023).
[374] China PCB Prototype & Fabrication Manufacturer - PCB Prototype the Easy Way, (n.d.). https://www.pcbway.com/ (accessed August 18, 2023).
[375] PCB & PCBA prototypes and small series “right first time” - Eurocircuits, (n.d.). https://www.eurocircuits.com/ (accessed August 18, 2023).
[376] Your PCB specialist | Beta LAYOUT Ltd., (n.d.). https://eu.beta-layout.com/ (accessed August 18, 2023).
[377] C12880MA - Spectrometer, 340 to 850nm, 10 Pins, (n.d.). https://ie.farnell.com/hamamatsu/c12880ma/image-sensor-module-10-pins/dp/3134750 (accessed August 19, 2023).

[378] B.R.D.L. Gala, P.P. Zirena, A.Y. Arredondo, Product redesigning, cost reduction, component substitution, and their influence in value management in micro and small enterprises, Manag. Sci. Lett. (2020) 1277–1286. https://doi.org/10.5267/j.msl.2019.11.030.
[379] R. Lampitt, P. Favali, C.R. Barnes, M.J. Church, M.F. Cronin, K.L. Hill, Y. Kaneda, D.M. Karl, A.H. Knap, M.J. McPhaden, K.A. Nittis, I.G. Priede, J.-F. Rolin, U. Send, C.-C. Teng, T.W. Trull, D.W.R. Wallace, R.A. Weller, In Situ Sustained Eulerian Observatories, (2010) 354–363. https://doi.org/10.5270/OCEANOBS09.PP.27.
[380] Y. Xiaofan, L. Cherkasova, T.T. Tajanašimuni´, T. Rosing, Optimizing Sensor Deployment and Maintenance Costs for Large-Scale Environmental Monitoring, (n.d.).
[381] J.S. Pearlman, M. Bushnell, A.R. Sastri asastri, uvicca R. James Christian, B. Jjh, A.R. Sastri, J.R. Christian, E.P. Achterberg, D. Atamanchuk, J.J. H Buck, P. Bresnahan, P.J. Duke, W. Evans, S.F. Gonski, B. Johnson, S. Kim Juniper, S. Mihaly, L.A. Miller, M. Morley, D. Murphy, S. Nakaoka, T. Ono, G. Parker, K. Simpson, T. Tsunoda, Perspectives on in situ Sensors for Ocean Acidification Research, (2019). https://doi.org/10.3389/fmars.2019.00653.
[382] J. Ma, T. Kodama, A. Daniel, M. Biogeochemistry, A. Laës-Huon, C. Barus, A.D. Beaton, D. Blandfort, N. Guigues, M. Knockaert, D. Munaron, I. Salter, E.S. Malcolm Woodward, N. Greenwood, E.P. Achterberg, Toward a Harmonization for Using in situ Nutrient Sensors in the Marine Environment, (2020). https://doi.org/10.3389/fmars.2019.00773.
[383] C. Albaladejo, P. Sánchez, A. Iborra, F. Soto, J.A. López, R. Torres, Wireless sensor networks for oceanographic monitoring: A systematic review, Sensors. 10 (2010) 6948–6968. https://doi.org/10.3390/s100706948.
[384] F. Chai, K.S. Johnson, H. Claustre, X. Xing, Y. Wang, E. Boss, S. Riser, K. Fennel, O. Schofield, A. Sutton, Monitoring ocean biogeochemistry with autonomous platforms, Nat. Rev. Earth Environ. 1 (2020) 315–326. https://doi.org/10.1038/s43017-020-0053-y.
[385] R. Venkatesan, K. Ramesh, A. Kishor, N. Vedachalam, M.A. Atmanand, Best Practices for the Ocean Moored Observatories, Front. Mar. Sci. 5 (2018). https://www.frontiersin.org/articles/10.3389/fmars.2018.00469 (accessed August 1, 2023).
[386] Field Deployment Guide: Aquatic Sensors Workgroup of the Methods and Data Comparability Board, (n.d.). https://acwi.gov/methods/sensors/field_deploy/index.html (accessed August 26, 2023).
[387] B. Benson, G. Chang, F. Spada, D. Manov, R. Kastner, Real-Time Telemetry Options for Ocean Observing Systems, (2008).
[388] NexSens CB-25 Data Buoy, (n.d.). https://www.fondriest.com/nexsens-cb-25-data-buoy.htm (accessed August 26, 2023).
[389] SBE 19plus V2 SeaCAT Profiler CTD | Sea-Bird Scientific - Overview | Sea-Bird, (n.d.). https://www.seabird.com/sbe-19plus-v2-seacat-profiler-ctd/product?id=60761421596 (accessed August 26, 2023).
[390] R. Hut, U. Wollschläger, C. Udell, J.S. Horsburgh, J. Caraballo, M. Ramírez, A.K. Aufdenkampe, D.B. Arscott, S.G. Damiano, Low-Cost, Open-Source, and Low-Power: But What to Do With the Data?, (2019). https://doi.org/10.3389/feart.2019.00067.
[391] G.M. Spinelli, Z.L. Gottesman, A low-cost Arduino-based datalogger with cellular modem and FTP communication for irrigation water use monitoring to enable access

to CropManage, HardwareX. 6 (2019) e00066. https://doi.org/10.1016/J.OHX.2019.E00066.
[392] P.A. Beddows, E.K. Mallon, Cave pearl data logger: A flexible arduino-based logging platform for long-term monitoring in harsh environments, Sens. Switz. 18 (2018). https://doi.org/10.3390/S18020530.
[393] E. Baker, Open source data logger for low-cost environmental monitoring, Biodivers. Data J. 2 (2014) 1059. https://doi.org/10.3897/BDJ.2.E1059.
[394] W. Song, W. Cui, An Overview of Underwater Connectors, J. Mar. Sci. Eng. 9 (2021) 813. https://doi.org/10.3390/jmse9080813.
[395] Review of Electrical Connectors for Underwater Applications | IEEE Journals & Magazine | IEEE Xplore, (n.d.). https://ieeexplore.ieee.org/abstract/document/8048605?casa_token=xTC5RrKlRwgAAAAA:DWWFiky8sThe4aXE7bW3nkdRWWHw9U8dbSVBawlUk9GVS-mHYgZ8_hhA8LSr16hYgzgh3aW9 (accessed August 1, 2023).
[396] IEC 60529:1989+AMD1:1999+AMD2:2013 CSV | IEC Webstore | water management, smart city, rural electrification, (n.d.). https://webstore.iec.ch/publication/2452&preview (accessed July 20, 2022).
[397] H. Painter, J. Flynn, Current and Future Wet-Mate Connector Technology Developments for Scientific Seabed Observatory Applications, in: OCEANS 2006, 2006: pp. 1–6. https://doi.org/10.1109/OCEANS.2006.306829.
[398] F. Rémouit, P. Ruiz-Minguela, J. Engström, Review of Electrical Connectors for Underwater Applications, IEEE J. Ocean. Eng. 43 (2018) 1037–1047. https://doi.org/10.1109/JOE.2017.2745598.
[399] H. Wu, C. Chen, K. Weng, An Energy-Efficient Strategy for Microcontrollers, Appl. Sci. 11 (2021) 2581. https://doi.org/10.3390/app11062581.
[400] A.F. MacKenzie, E.A. Maltby, N. Harper, C. Bueley, D. Olender, R.C. Wyeth, Periodic ultraviolet-C illumination for marine sensor antifouling, Biofouling. 35 (2019) 483–493. https://doi.org/10.1080/08927014.2019.1616698.
[401] P. Whitworth, N. Aldred, K.J. Reynolds, J. Plummer, P.W. Duke, A.S. Clare, Importance of Duration, Duty-Cycling and Thresholds for the Implementation of Ultraviolet C in Marine Biofouling Control, Front. Mar. Sci. 8 (2022). https://www.frontiersin.org/articles/10.3389/fmars.2021.809011 (accessed September 5, 2023).
[402] YSI EXO3s Multiparameter Water Quality Batteryless Sonde | ysi.com, (n.d.). https://www.ysi.com/exo3s (accessed September 5, 2023).
[403] Aqua TROLL 600 Multiparameter Sonde - In-Situ, (n.d.). https://in-situ.com/en/aqua-troll-600-multiparameter-sonde (accessed September 27, 2023).
[404] M.W. Matthews, Chapter 6 - Bio-optical Modeling of Phytoplankton Chlorophyll-a, in: D.R. Mishra, I. Ogashawara, A.A. Gitelson (Eds.), Bio-Opt. Model. Remote Sens. Inland Waters, Elsevier, 2017: pp. 157–188. https://doi.org/10.1016/B978-0-12-804644-9.00006-9.
[405] G.-C. Gong, F.-K. Shiah, K.-K. Liu, Y.-H. Wen, Ming-Hsin Liang, Spatial and temporal variation of chlorophyll a, primary productivity and chemical hydrography in the southern East China Sea, Cont. Shelf Res. 20 (2000) 411–436. https://doi.org/10.1016/S0278-4343(99)00079-5.
[406] M. Rome, R.E. Beighley, T. Faber, Sensor-based detection of algal blooms for public health advisories and long-term monitoring, Sci. Total Environ. 767 (2021) 144984. https://doi.org/10.1016/j.scitotenv.2021.144984.
[407] A.M. Lewandowska, P. Breithaupt, H. Hillebrand, H.-G. Hoppe, K. Jürgens, U. Sommer, Responses of primary productivity to increased temperature and

phytoplankton diversity, J. Sea Res. 72 (2012) 87–93. https://doi.org/10.1016/j.seares.2011.10.003.
[408] Irish National Tide Gauge Network - data.gov.ie, (n.d.). https://data.gov.ie/dataset/irish-national-tide-gauge-network (accessed September 6, 2023).
[409] M. Grifoll, P. Cerralbo, J. Guillén, M. Espino, L.B. Hansen, A. Sánchez-Arcilla, Characterization of bottom sediment resuspension events observed in a micro-tidal bay, Ocean Sci. 15 (2019) 307–319. https://doi.org/10.5194/os-15-307-2019.
[410] J.N. Moum, W.D. Smyth, Upper Ocean Mixing☆, in: J.K. Cochran, H.J. Bokuniewicz, P.L. Yager (Eds.), Encycl. Ocean Sci. Third Ed., Academic Press, Oxford, 2019: pp. 71–79. https://doi.org/10.1016/B978-0-12-409548-9.11573-8.
[411] J. Sprintall, M.F. Cronin, Upper Ocean Vertical Structure, in: J.H. Steele (Ed.), Encycl. Ocean Sci. Second Ed., Academic Press, Oxford, 2009: pp. 217–224. https://doi.org/10.1016/B978-012374473-9.00627-5.
[412] H. Wang, Y. Jia, C. Ji, W. Jiang, C. Bian, Internal tide-induced turbulent mixing and suspended sediment transport at the bottom boundary layer of the South China Sea slope, J. Mar. Syst. 230 (2022) 103723. https://doi.org/10.1016/j.jmarsys.2022.103723.
[413] G.P. Allen, J.C. Salomon, P. Bassoullet, Y. Du Penhoat, C. de Grandpré, Effects of tides on mixing and suspended sediment transport in macrotidal estuaries, Sediment. Geol. 26 (1980) 69–90. https://doi.org/10.1016/0037-0738(80)90006-8.
[414] C. Briciu-Burghina, T. Sullivan, J. Chapman, F. Regan, No Title, 186 (2014) 5561–5580. https://doi.org/10.1007/S10661-014-3803-9.
[415] A. Guarnieri, S. Saremi, A. Pedroncini, J.H. Jensen, S. Torretta, M. Vaccari, C. Vincenzi, Effects of marine traffic on sediment erosion and accumulation in ports: a new model-based methodology, Ocean Sci. 17 (2021) 411–430. https://doi.org/10.5194/os-17-411-2021.
[416] T.G. O'Higgins, J.G. Wilson, Impact of the river Liffey discharge on nutrient and chlorophyll concentrations in the Liffey estuary and Dublin Bay (Irish Sea), Estuar. Coast. Shelf Sci. 64 (2005) 323–334. https://doi.org/10.1016/j.ecss.2005.02.025.
[417] C. Zhao, J. Maerz, R. Hofmeister, R. Röttgers, K. Wirtz, R. Riethmüller, C. Schrum, Characterizing the vertical distribution of chlorophyll a in the German Bight, Cont. Shelf Res. 175 (2019) 127–146. https://doi.org/10.1016/j.csr.2019.01.012.
[418] M. F-Pedrera Balsells, M. Grifoll, M. Fernández-Tejedor, M. Espino, Short-Term Response of Chlorophyll a Concentration Due to Intense Wind and Freshwater Peak Episodes in Estuaries: The Case of Fangar Bay (Ebro Delta), Water. 13 (2021) 701. https://doi.org/10.3390/w13050701.
[419] F. de L.L. de Amorim, K.H. Wiltshire, P. Lemke, K. Carstens, S. Peters, J. Rick, L. Gimenez, M. Scharfe, Investigation of marine temperature changes across temporal and spatial Gradients: Providing a fundament for studies on the effects of warming on marine ecosystem function and biodiversity, Prog. Oceanogr. 216 (2023) 103080. https://doi.org/10.1016/j.pocean.2023.103080.
[420] SOS Leak Sensor, Blue Robot. (n.d.). https://bluerobotics.com/store/sensors-cameras/leak-sensor/sos-leak-sensor/ (accessed September 28, 2023).
[421] T. Nakagawa, T. Toya, M. Oyama, Ozone Resistance of Highly Saturated Nitrile Rubber (HNBR), J. Elastomers Plast. 24 (1992) 240–261. https://doi.org/10.1177/009524439202400307.
[422] C. Treib, K. Loos, M. Johlitz, A. Lion, Ozone ageing: experimental methods on pristine and protected natural rubber, Contin. Mech. Thermodyn. 34 (2022) 1563–1577. https://doi.org/10.1007/s00161-022-01148-x.

[423] G.J. Lake, The determination of threshold strain of rubber in ozone resistance tests, Polym. Test. 11 (1992) 117–137. https://doi.org/10.1016/0142-9418(92)90042-A.
[424] B.N. Cassenti, A. Staroselsky, Deformation and stability of compressible rubber O-rings, Int. J. Mech. Mater. Eng. 12 (2017) 5. https://doi.org/10.1186/s40712-017-0072-8.
[425] A. Kömmling, M. Jaunich, P. Pourmand, D. Wolff, M. Hedenqvist, Analysis of O-Ring Seal Failure under Static Conditions and Determination of End-of-Lifetime Criterion, Polymers. 11 (2019) 1251. https://doi.org/10.3390/polym11081251.
[426] S. Jian, C. Yin, Y. Wang, X. Yu, Y. Li, The Possible Incoming Runoff Under Extreme Rainfall Event in the Fenhe River Basin, Front. Environ. Sci. 10 (2022). https://www.frontiersin.org/articles/10.3389/fenvs.2022.812351 (accessed September 9, 2023).
[427] G. Göransson, M. Larson, D. Bendz, Variation in turbidity with precipitation and flow in a regulated river system – river Göta Älv, SW Sweden, Hydrol. Earth Syst. Sci. 17 (2013) 2529–2542. https://doi.org/10.5194/hess-17-2529-2013.
[428] A. Lefebvre, D. Devreker, First Comprehensive Quantitative Multi-Parameter Assessment of the Eutrophication Status from Coastal to Marine French Waters in the English Channel, the Celtic Sea, the Bay of Biscay, and the Mediterranean Sea, J. Mar. Sci. Eng. 8 (2020) 561. https://doi.org/10.3390/jmse8080561.
[429] A. Barbosa-Vasconcelos, Â. Mendes, F. Martins, E. Lopes, A. Machado, A.A. Bordalo, P. Vaz-Pires, N. Vieira, P. Martins da Costa, L.J. Bessa, River water analysis using a multiparametric approach: Portuguese river as a case study, J. Water Health. 16 (2018) 991–1006. https://doi.org/10.2166/wh.2018.047.

APPENDICES

Appendix A Sensor Electronic Design Schematics

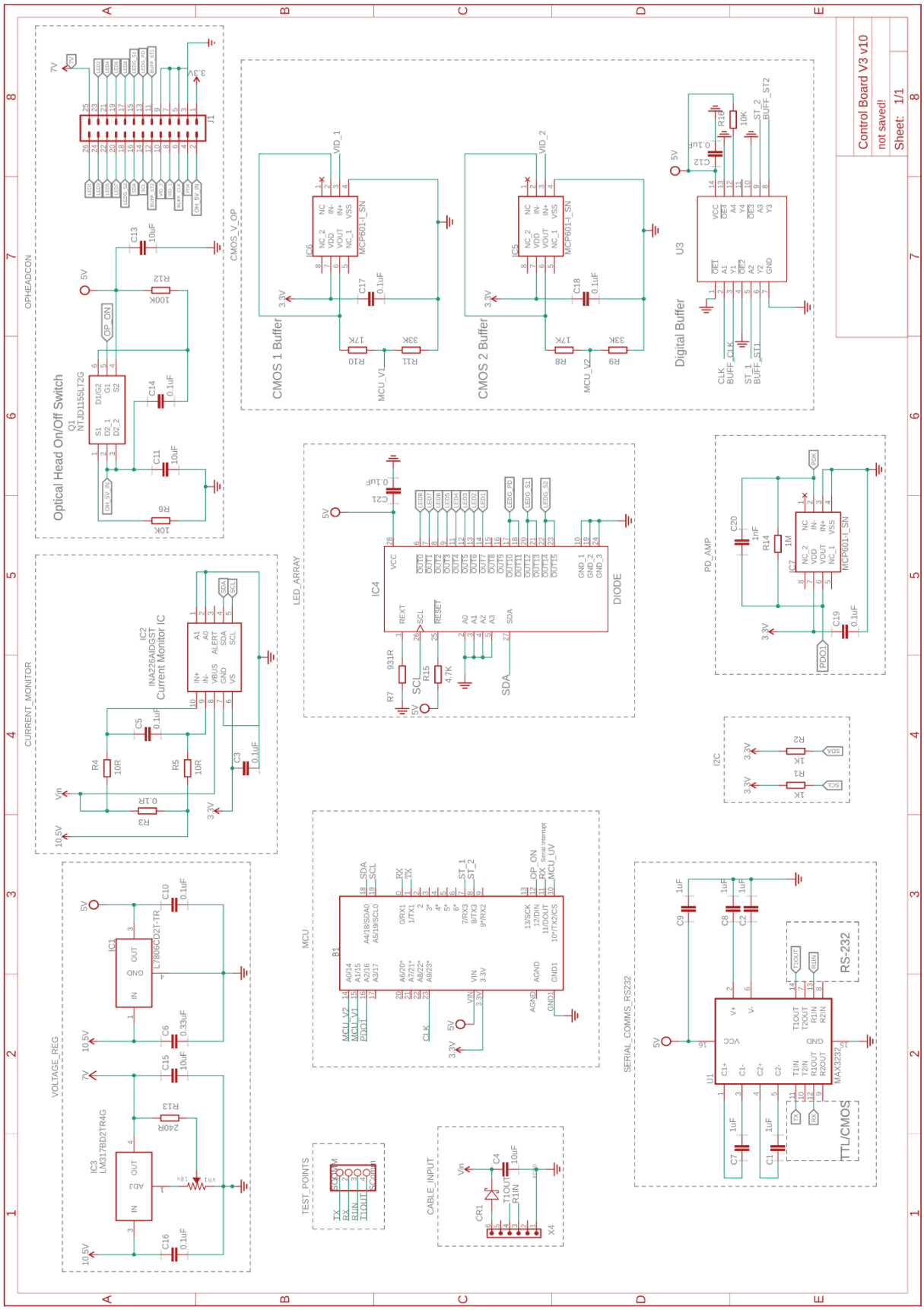

Figure A-1 Schematic design of the final version sensor control board printed circuit board.

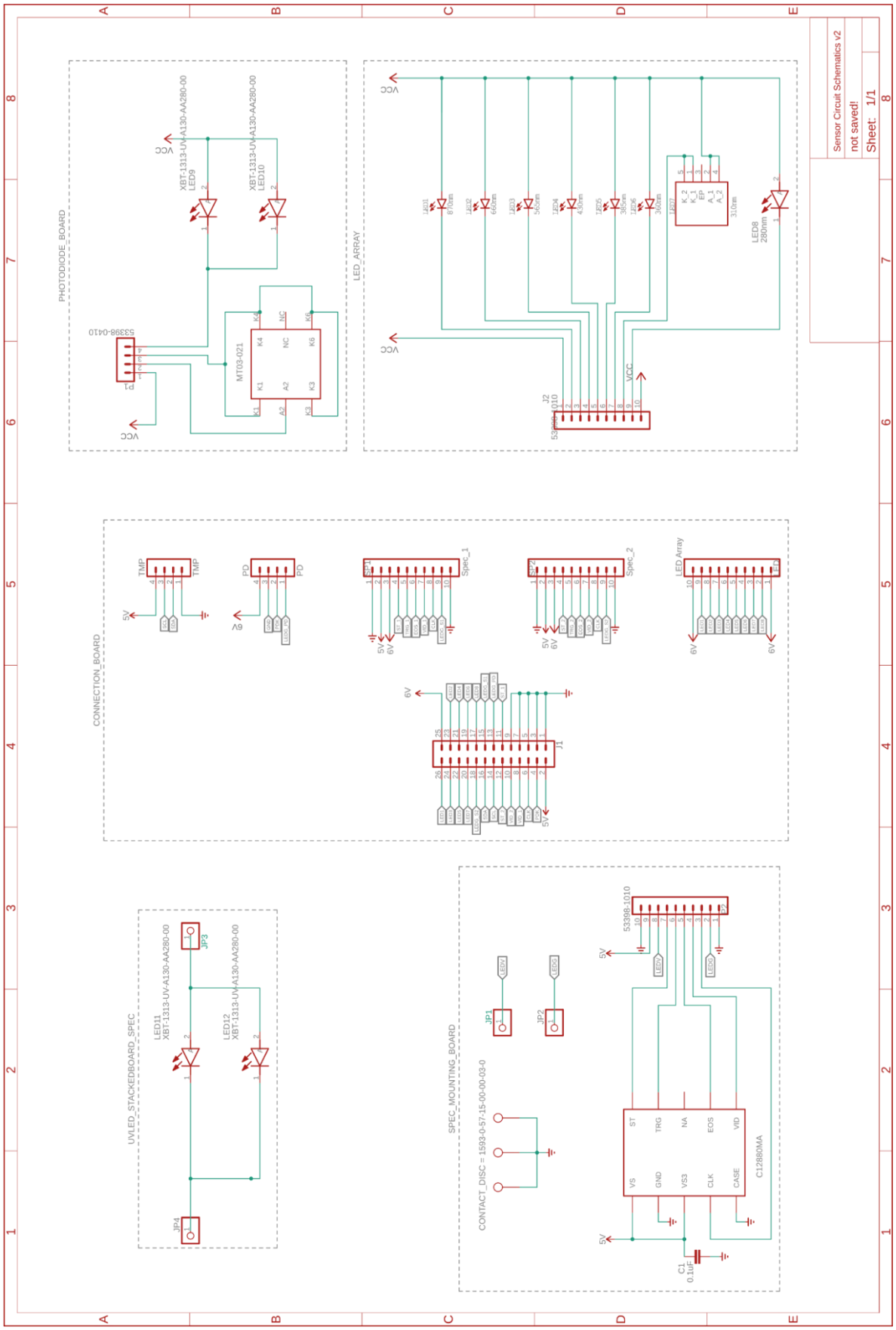

Figure A-2 Schematic design of final version of the connector, LED array, photodiode, spectrometer mounting, and UV LED stacked circuit boards used in the sensor.

Appendix B Software and Firmware Code

B.1 Benchtop Electronics Testing Firmware

```
//Libraries Included
/*****************************************************************************
******/
//Teensy Sleep Mode Library
#include <Snooze.h>
#include <SnoozeBlock.h>

//ADC Libraries
#if defined(CORE_TEENSY)
#include <ADC.h> /* https://github.com/pedvide/ADC */
#else
#include <elapsedMillis.h>
#endif


//I2C Library
#include <Wire.h>

//Spectrometer Library
#include "C12880MA.h"

//Temp Sensor Library
#include "TMP_TSYS01.h"

//Current Monitor Library
#include "INA.h"


//LED Driver
#include "LD_TLC59116.h"
LD_TLC59116 ledDriver(0);

/*****************************************************************************
******/
//Sleep Mode
SnoozeDigital digital;
SnoozeBlock config_teensy32(digital);
#define sleepInterruptPin 11

/*****************************************************************************
******/
//mySerial Comms
#define mySerial Serial        // Communicatge with USB
//#define mySerial Serial1       // Hardware mySerial, communicate with RX,TX bins (0,1)
to other microcontroller
#define SERIAL_TX           1 // Serial transmission
#define SERIAL_RX           0 // Serial receiving
```

```
#define BAUDRATE        9600 // 2000000 works likely also

// Variables for main loop
char   inBuff[] = "----------------";
int    bytesread;

/*************************************************************************
******/
//Low Power Control
#define headSwt 12   //set high to turn optical sensors on

boolean headOn = false; //only turn on when needed: when spectrometers/temp sensors are
required
/*************************************************************************
******/

/*************************************************************************
******/

//Current Monitor Sensor
INA226 ina;
bool CU_ON = false;
void CS_Setup() {
  ina.begin();

  // Configure INA226
  ina.configure(INA226_AVERAGES_16,              INA226_BUS_CONV_TIME_140US,
INA226_SHUNT_CONV_TIME_140US, INA226_MODE_SHUNT_BUS_CONT);

  // Calibrate INA226. Rshunt = 0.01 ohm, Max excepted current = 4A
  ina.calibrate(0.12, 0.3);
}


/*************************************************************************
******/
//UV Antifouling
const int PWM_Pins[8] = {0, 1, 10, 11, 12, 13, 14, 15}; //sensor UV LEDs, LED 310nm and
280nm on Array
const double dc_p = 0.75;
const int pwm_Res = 255;
const int duty_cycle = pwm_Res * dc_p; //duty cycle of the PWM

void UV_ON(String on) {
  if (on == '1') {
    mySerial.println("Antifouling UV LEDs ON");
    for (int i = 0; i < 8; i++) {
      ledDriver.analogWrite(PWM_Pins[i], duty_cycle);
    }
  }
```

```
  else {
    mySerial.println("Antifouling UV LEDs OFF");
    for (int i = 0; i < 8; i++) {
      ledDriver.analogWrite(PWM_Pins[i], 0);
    }
  }
}

/**********************************************************************
******/

// LED Array
const int ledHigh = 255;
const int ledLow = 0;


const int LED[8] = {7, 6, 5, 4, 3, 2, 1, 0};
//850nm,660nm,565nm,430nm,385nm,365nm,310nm,280nm

//Cycle through LEDs in Array
void LEDArrayTest(String sLED) {
  if (sLED == 'T') { //cycle through LEDs and test current
    float bgI = 0; //background current
    float fI = 0; //whole current with LED on
    float ledI = 0; //LED current

    mySerial.println("LED Array Test");
    for (int i = 0; i < 8; i++) {
      //Take Current Reading before LED is turned on
      bgI = ina.readShuntCurrent();
      ledDriver.analogWrite(LED[i], ledHigh);
      delay(100);
      //Take Current Reading While LEd is on
      fI = ina.readShuntCurrent();
      //Subtract background from current with LED on and convert to mA
      ledI = (fI - bgI) * 1000;

      mySerial.print("LED "); mySerial.print(i + 1);
      mySerial.println(" Current: "); mySerial.print(ledI); mySerial.println("mA");

      ledDriver.analogWrite(LED[i - 1], ledLow);
      delay(100);
      if (i == 7) ledDriver.analogWrite(LED[7], ledLow);
    }
  }

  if (sLED == 'A') { // turn all LEDs on
    mySerial.println("LED Array Test");
    for (int i = 0; i < 8; i++) {
      ledDriver.analogWrite(LED[i], ledHigh);
```

```
    }
    ledDriver.analogWrite(LED[7], ledHigh);
  }

  else if (sLED == 'N')
  {
    mySerial.println("LEDs OFF");
    for (int i = 0; i < 8; i++) {
      ledDriver.analogWrite(LED[i], ledLow);
    }
  }
  else {
    int iLED = sLED.toInt();
    mySerial.print("LED " + sLED); mySerial.println(" ON");
    for (int i = 0; i < 8; i++) {
      if ( i == iLED - 1) ledDriver.analogWrite(LED[i], ledHigh);
      //else digitalWrite(LED[i],LOW);
    }
  }
}

/**********************************************************************
******/

//Spectrometer
#define SPEC_CLK        23

//Spec 1: 20D00472

#define SPEC_TRG         11
#define SPEC_ST1         7
#define SPEC_VIDEO1       15


//Spec 2: 20D00473

#define SPEC_TRG        11
#define SPEC_ST2        8
#define SPEC_VIDEO2      14
//IC
bool contSpec = false;
int CMOS_ON = 0;

uint16_t data[C12880_NUM_CHANNELS];
uint16_t data2[C12880_NUM_CHANNELS];
C12880_Class spec1(SPEC_TRG, SPEC_ST1, SPEC_CLK, SPEC_VIDEO1);
C12880_Class spec2(SPEC_TRG, SPEC_ST2, SPEC_CLK, SPEC_VIDEO2);


// Function to calculate corresponding wavelengths for spectrometer coefficients
```

```
float integrationTimes1[8] = {2.3, 0.25, 4, 0.78, 0.023, 0.04, 2, 4}; //default int times for each LED 880nm -> 280nm


//WATER
//float integrationTimes2[8] = {0.01,0.001,0.012,0.003,0.0001,0.0001,0.001,0.01}; //default int times for each LED 880nm -> 280nm

//AIR
float integrationTimes2[8] = {0.017, 0.003, 0.002, 0.001, 0.00001, 0.00001, 0.0005, 0.001}; //default int times for each LED 880nm -> 280nm


float integ_time1 = 0.01;
float integ_time2 = 0.01;

void specBegin() {
  spec1.begin();
  spec2.begin();
  spec1.set_integration_time(integ_time1);
  spec2.set_integration_time(integ_time2);

  pinMode(SPEC_CLK, OUTPUT);
  pinMode(SPEC_ST1, OUTPUT);
  pinMode(SPEC_ST2, OUTPUT);
  digitalWrite(SPEC_CLK, LOW);
  digitalWrite(SPEC_ST1, LOW);
  digitalWrite(SPEC_ST2, LOW);


}

/*************************************************************************
******/


//Photodiode
bool PD_ON = false;
const int PDInput = A2;
//int PD1 = 0;
int PD_120 = 0;
//Runing Average variables
const int numReadings = 25;
int readings[numReadings];      // the readings from the analog input
int readIndex = 0;              // the index of the current reading
int total = 0;                  // the running total
int average = 0;                // the average
```

```
/*************************************************************************
******/
//Temperature Sensor
bool TMP_ON = false;
TSYS01 tempSensor;
float tempC = 0;
/*************************************************************************
******/


/*************************************************************************
******/


//Timers
unsigned long waits;
unsigned long seconds;

void componentSetup() {
  specBegin();
  CS_Setup();
  ledDriver.begin();
  Wire.begin();
  analogReadResolution(16);
  tempSensor.init();



  //pinMode(SERIAL_TX,      OUTPUT);
  //pinMode(SERIAL_RX,      INPUT);
  pinMode(headSwt,        OUTPUT);

  pinMode(LED_BUILTIN,     OUTPUT);

  digital.pinMode(sleepInterruptPin, INPUT, FALLING);//pin, mode, type


  digitalWrite(LED_BUILTIN,     HIGH);
  digitalWriteFast(headSwt,     LOW);

  //digitalWriteFast(SERIAL_TX,   LOW);

  contSpec = false;
  PD_ON = false;
  TMP_ON = false;
}

/*************************************************************************
******/
```

```
void setup() {
  while (millis() < 3000);
  mySerial.begin(BAUDRATE);
  mySerial.setTimeout(1);                    // Serial read timeout
  printHelp();
#if defined(CORE_TEENSY)
#endif
  componentSetup();

}

/************************************************************************
******/
int period = 100;
unsigned long time_now = 0;
bool bg_Scan = false;
String bg_spec, bg_led;


void loop() {

  SerialRead();
  if (millis() >= time_now + period) {
    time_now += period;
    if (PD_ON == true) PDread();
    if (TMP_ON == true) TMPread();
    if (contSpec == true) SpecR(CMOS_ON);
    if (bg_Scan == true) specCL(bg_spec.toInt(), bg_led.toInt());
    if (CU_ON == true) aveCurr();
    SerialRead();
  }
}
/************************************************************************
******/
//Serial Interface
/************************************************************************
******/
//Loop Serial Read Function
void SerialRead() {
  if (mySerial.available()) {
    bytesread = mySerial.readBytesUntil('\n', inBuff, 16); // Read from serial until CR is read
or timeout exceeded
    inBuff[bytesread] = '\0';
    String instruction = String(inBuff);
    processInstruction(instruction);
  }
}

//Print User Interface to Serial Monitor
```

```
/*************************************************************************
******/
void printHelp() {
  mySerial.println("      Optical Sensor Controller");
  mySerial.println("=========================================");
  mySerial.println("Turn optical head on/off.....O + 1..ON..O + 0..OFF");
  mySerial.println("=========================================");
  mySerial.println("Turn UV LEDs on/off.....U + 1..ON..U + 0..OFF");
  mySerial.println("=========================================");
  mySerial.println("LED Array Test.....LT");
  mySerial.println("All LEDs ON.....LA");
  mySerial.println("Select LED ON.....L1,L2...L8");
  mySerial.println("Turn LEDs Off.....LN");
  mySerial.println("=========================================");
  mySerial.println("Set CMOS Integration Time.....SI + 1 or 2 + Int Time");
  mySerial.println("Request Reading from CMOS.....SR + 1 or 2");
  mySerial.println("Calibrate Spectrometer Int Times.....SC + 1 or 2");
  mySerial.println("Full Cycle Spectrometer Read.....SF + 1 or 2");
  mySerial.println("");
  mySerial.println("Set CMOS in Continous Reading Mode.....C + 1 or 2");
  mySerial.println("Both CMOS in continous mode.....C + A");
  mySerial.println("CMOS continous mode with background removed...C + D + 1 or 2
(CMOS) + 1 to 8 (LED)");
  mySerial.println("Turn Continous Mode Off.....C");
  mySerial.println("=========================================");
  mySerial.println("Request Reading from Photodiode.....PR");
  mySerial.println("Continous Reading from Photodiode...PC");
  mySerial.println("=========================================");
  mySerial.println("Request Reading from Temp Sensor.....TR");
  mySerial.println("Continous Reading from Temp Sensor...TC");
  mySerial.println("=========================================");
  mySerial.println("Read current monitor.....I");
  mySerial.println("Current Monitor continous mode...IC");
  mySerial.println("=========================================");
  mySerial.println("");
}

/*************************************************************************
******/
//Function to process user input

void processInstruction(String instruction) {
  String value    = "0.01";
  String command2    = "o";
  String value2 = "0.01";
  String command  = "o";



  int instructionLength = instruction.length();
```

```
if (instructionLength > 0) {
  command = instruction.substring(0, 1);
}
if (instructionLength > 1) {
  value = instruction.substring(1, 2);
}
if (instructionLength > 2) {
  command2 = instruction.substring(2, 3);
}
if (instructionLength > 3) {
  value2 = instruction.substring(3, instructionLength);
}

//Sleep Mode

if (command == 'Z') {
  mySerial.println("Going to Sleep...");
  delay(200);
  Snooze.deepSleep( config_teensy32 );
}
//Current Monitor

if (command == 'I') {
  if (value == 'C') {
    CU_ON = true;
  }
  else {
    CurrRead(); CU_ON = false;
  }
}

if (command == 'T') {
  if (value == 'C') {
    if (command2 == '1') {
      TMP_ON = true;
      mySerial.println("Temp Sensor Continous Mode On");
    }

    else {
      TMP_ON = false;
      mySerial.println("Temp Sensor Continous Mode OFF");
    }
  }

  else if (value == 'R') {
    TMPread();
  }
}

if (command == 'P') {
```

```
  if (value == 'C') {
    if (command2 == '1') {
      PD_ON = true;
      mySerial.println("Phododiode Continous Mode On");
    }

    else {
      PD_ON = false;
      mySerial.println("Phododiode Continous Mode OFF");
    }
  }

  else if (value == 'R') {
    PDread();
  }
}

if (command == 'O') {
  if (value == '1') {
    mySerial.println("Optical Head Sensors ON");
    digitalWrite(headSwt, HIGH);

  }
  else if (value == '0') {
    mySerial.println("Optical Head Sensors OFF");
    digitalWrite(headSwt, LOW);

  }

}

if (command == 'U') {
  UV_ON(value);
}


if (command == 'C') {
  if (value == '1') {
    CMOS_ON = 1;
    contSpec = true;
    mySerial.println("Spec 1 Cont Mode");
  }
  else if (value == '2') {
    CMOS_ON = 2;
    contSpec = true;
    mySerial.println("Spec 2 Cont Mode");
  }

  else if (value == 'A') {
    CMOS_ON = 3;
```

```
      contSpec = true;
      mySerial.println("Spec 1 and 2 Cont Mode");
    }

    else if (value == 'D') {
      bg_Scan = true;
      bg_spec = command2;
      bg_led = value2;
      mySerial.print("Minus Background CMOS Scan, CMOS:  "); mySerial.print(bg_spec);
mySerial.print(" LED: "); mySerial.println(bg_led);

    }


    else {
      contSpec = false;  bg_Scan = false; CMOS_ON = 0;
      mySerial.println("Continous Mode OFF");
    }
  }

  //LED Controls
  if (command == 'L') {
    LEDArrayTest(value);
  }


  //Spectrometer Commands
  if (command == 'S') {
    //Read from Spectrometer
    if (value == 'R') {
      if (command2 == '1') {
        mySerial.println("CMOS 1 Readout");
        spec1.read_into(data);
        for (int i = 0; i < C12880_NUM_CHANNELS; i++) {
          mySerial.print(data[i]);
          mySerial.print(',');
          if (i == 286) mySerial.println(' ');
        }
      }
      else if (command2 == '2') {
        mySerial.println("CMOS 2 Readout");
        spec2.read_into(data);
        for (int i = 0; i < C12880_NUM_CHANNELS; i++) {
          mySerial.print(data[i]);
          mySerial.print(',');
          if (i == 286) mySerial.println(' ');
        }
      }
    }
    //Set Integration Time
```

```
  else if ( value == 'I') {
    if (command2 == '1') {
      mySerial.println(" Set S1 Int Time to: " + value2);
      integ_time1 = value2.toFloat();
      spec1.set_integration_time(integ_time1);
      if ((integ_time1 < 0.0) || (integ_time1 > 9999.99)) {
        mySerial.println("Integration time out of valid Range");
      }
    }

    if (command2 == '2') {
      mySerial.println(" Set S2 Int Time to: " + value2);
      integ_time2 = value2.toFloat();
      spec2.set_integration_time(integ_time2);
      if ((integ_time2 < 0.0) || (integ_time2 > 9999.99)) {
        mySerial.println("Integration time out of valid Range");
      }
    }
  }

  else if ( value == 'C') {
    if (command2 == '1') {
      mySerial.println(" Calibrate CMOS: 1");
      cmosCal(1);

    }
    else if (command2 == '2') {
      mySerial.println(" Calibrate CMOS: 2");
      cmosCal(2);
    }

  }
  else if ( value == 'F') {
    if (command2 == '1') {
      mySerial.println(" Full Spectrum Read CMOS: 1");
      fullSpec(1);

    }
    else if (command2 == '2') {
      mySerial.println(" Full Spectrum Read CMOS: 2");
      fullSpec(2);
    }

    else if (command2 == 'A') {
      mySerial.println(" Full Spectrum Read");
      fullSpec(3);
    }

  }
```

```
    else if ( value == 'V') {
      mySerial.print("LED Variance Check, CMOS:     "); mySerial.print(command2);
mySerial.print(" LED: "); mySerial.println(value2);
      ledVar(command2.toInt(), value2.toInt());

    }

  }
  if (command == 'M') {
    mySerial.println(" ");
    printHelp();
    mySerial.println(" ");
    mySerial.println(" ");
    mySerial.println(" ");
    mySerial.println(" ");
  }
  else { // invalid input, display status
    // printHelp();
  } // end if else switch
}


/**************************************************************************
******/
//Spectrometer Functions
/**************************************************************************
******/

void SpecR(int spec) {
  if (spec == 1) {
    spec1.read_into(data);
    for (int i = 0; i < C12880_NUM_CHANNELS; i++) {
      mySerial.println(data[i]);
    }
  }
  else if (spec == 2) {
    spec2.read_into(data);
    for (int i = 0; i < C12880_NUM_CHANNELS; i++) {
      mySerial.println(data[i]);
    }
  }
  else {
    spec1.read_into(data);
    spec2.read_into(data2);
    for (int i = 0; i < C12880_NUM_CHANNELS; i++) {
      mySerial.print(data[i]); mySerial.print(","); mySerial.println(data2[i]);
    }
  }
}
```

```
/*************************************************************************
******/
//Calibration Function
// Range to be between 50 and 60 thousand bits

const int upperLimit = 61000; //highest data point should be lower than this limit
const int lowerLimit = 550000; //lower data point should be higher than this limit

void cmosCal(int spec) {
  int led = 1;
  int i = 0;
  boolean Calibrated = false;
  int dataPoint = 0;
  uint16_t max = 0;


  if (spec == 1) {
    mySerial.println("Calibrating Second Spectrometer");

    for (i = 0; i < 8; i++) { //For loop to cycle through LED array (8 in total)
      led = i;
      for (int j = 0; j < 8; j++) {              //Sets the current LED HIGH, turns the others off
        if ( j == led) ledDriver.analogWrite(LED[led], ledHigh);
        else ledDriver.analogWrite(LED[led], ledLow);
      }

      mySerial.print("Calibrating LED: "); mySerial.println(led + 1);

      while (Calibrated == false) {                        //While loop to check if cmos response is
within set range response, exits when response is inside the set range
        delay(10);
        spec1.set_integration_time(integrationTimes1[led]); //set new int time
        delay(1);
        spec1.read_into(data);
        delay(1);//Read in data
        /* for (int i = 0; i < C12880_NUM_CHANNELS; i++){
          mySerial.println(data[i]);
          }*/
        delay(1);

        max = 0;
        for (int k = 0; k < C12880_NUM_CHANNELS; k++) { //Loop through the data to find
maximum value
          delay(1);
          if (data[k] > max) {
            max = data[k]; dataPoint = k;
          }

        }
        if (max > upperLimit) {
```

```
        integrationTimes1[led] = integrationTimes1[led] - 0.00001; Calibrated = false;  //if max is over limit
        //mySerial.println(integrationTimes2[led],5); mySerial.print("Upper Limit Exceeded: "); mySerial.println(max); mySerial.println("Data point max located at: "); mySerial.println(dataPoint);
       }


       else if (max < lowerLimit) {
        integrationTimes1[led] = integrationTimes1[led] + 0.00001; Calibrated = false; //if max is under limit
        //mySerial.println(integrationTimes1[led],4); mySerial.print("Lower Limit Exceeded: ");mySerial.println(max); mySerial.println("Data point max located at: "); mySerial.println(dataPoint);
       }

       else if (max < upperLimit && max > lowerLimit) {
         Calibrated = true; //mySerial.println("Calibrated!!!");
       } //if max within limit


     }
     Calibrated = false;

   }
   mySerial.println("Spectrometer 1 Calibrated");
   for (int i = 0; i < 8; i++) {
    ledDriver.analogWrite(LED[i], ledLow);
   }
  }

  else if ( spec == 2) {
   mySerial.println("Calibrating Second Spectrometer");

   for (i = 0; i < 8; i++) { //For loop to cycle through LED array (8 in total)
    led = i;
    for (int j = 0; j < 8; j++) {              //Sets the current LED HIGH, turns the others off
     if ( j == led) ledDriver.analogWrite(LED[led], ledHigh);
     else ledDriver.analogWrite(LED[j], ledLow);
    }

    mySerial.print("Calibrating LED: "); mySerial.println(led + 1);

    while (Calibrated == false) {                    //While loop to check if cmos response is within set range response, exits when response is inside the set range
      delay(10);
      spec2.set_integration_time(integrationTimes2[led]); //set new int time
      delay(1);
      spec2.read_into(data);
      delay(1);//Read in data
```

```
      /*for (int i = 0; i < C12880_NUM_CHANNELS; i++){
        mySerial.println(data[i]);
        }*/
      delay(1);

      max = 0;
      for (int k = 0; k < C12880_NUM_CHANNELS; k++) { //Loop through the data to find maximum value

        if (data[k] > max) {
          max = data[k]; dataPoint = k;
        }

      }
      if (max > upperLimit) {
        integrationTimes2[led] = integrationTimes2[led] - 0.00001; Calibrated = false;  //if max is over limit
        mySerial.println(integrationTimes2[led], 5); mySerial.print("Upper Limit Exceeded: "); mySerial.println(max); mySerial.println("Data point max located at: "); mySerial.println(dataPoint);
      }


      else if (max < lowerLimit) {
        integrationTimes2[led] = integrationTimes2[led] + 0.00001; Calibrated = false; //if max is under limit
        mySerial.println(integrationTimes2[led], 5); mySerial.print("Lower Limit Exceeded: "); mySerial.println(max); mySerial.println("Data point max located at: "); mySerial.println(dataPoint);
      }

      else if (max < upperLimit && max > lowerLimit) {
        Calibrated = true; //mySerial.println("Calibrated!!!");
      } //if max within limit


    }
    Calibrated = false;

  }
  mySerial.println("Spectrometer 2 Calibrated");
  for (int i = 0; i < 8; i++) {
    ledDriver.analogWrite(LED[i], ledLow);
  }
 }
}

/*****************************************************************************
******/
```

```
//Cycle through each led/ assign corresponding int time/ take background reading/ take reading with led on/ minus background from data/ print
uint16_t background[C12880_NUM_CHANNELS];

void fullSpec(int spec) {
  int i;
  int led;
  if (spec == 1) {
    for (i = 0; i < 8; i++) { //cycle through 8 LEDs
      led = i;
      //Set Int Time
      delay(10);
      spec1.set_integration_time(integrationTimes1[led]); //set new int time
      delay(1);
      //Take background reading
      spec1.read_into(background);
      delay(1);//Read in data

      //Turn LED on
      for (int j = 0; j < 8; j++) {              //Sets the current LED HIGH, turns the others off
        if ( j == led) ledDriver.analogWrite(LED[j], ledHigh);
      }
      //Take actual reading
      spec1.read_into(data);
      delay(1);//Read in data
      for (int i = 0; i < 8; i++) {
        ledDriver.analogWrite(LED[i], ledLow);
      }
      //Print data minus background
      mySerial.print("Reading for LED: "); mySerial.println(led + 1);
      for (int i = 0; i < C12880_NUM_CHANNELS; i++) {
        mySerial.print(data[i] - background[i]);
        mySerial.print(' ');
        if (i == 286) mySerial.println(' ');

      }
    }

  }
  else if (spec == 2) {
    for (i = 0; i < 8; i++) { //cycle through 8 LEDs
      led = i;
      //Set Int Time
      delay(10);
      spec2.set_integration_time(integrationTimes2[led]); //set new int time
      delay(1);
      //Take background reading
      spec2.read_into(background);
      delay(1);//Read in data
```

```
    //Turn LED on
    for (int j = 0; j < 8; j++) {              //Sets the current LED HIGH, turns the others off
      if ( j == led) ledDriver.analogWrite(LED[led], ledHigh);
      else ledDriver.analogWrite(LED[j], ledLow);
    }
    //Take actual reading
    spec2.read_into(data);
    delay(1);//Read in data
    for (int i = 0; i < 8; i++) {
      ledDriver.analogWrite(LED[i], ledLow);
    }
    //Print data minus background
    mySerial.print("Reading for LED: "); mySerial.println(led + 1);
    for (int i = 0; i < C12880_NUM_CHANNELS; i++) {
      mySerial.print(data[i] - background[i]);
      mySerial.print(' ');
      if (i == 286) mySerial.println(' ');

    }
  }
}
//Return two CMOS readings at the same time

else if (spec == 3) {
  //Set Up data storage arrays for second cmos
  uint16_t background2[C12880_NUM_CHANNELS];
  uint16_t data2[C12880_NUM_CHANNELS];


  for (i = 0; i < 8; i++) { //cycle through 8 LEDs
    led = i;
    //Set Int Time
    delay(10);
    spec1.set_integration_time(integrationTimes1[led]);
    delay(1);
    spec2.set_integration_time(integrationTimes2[led]); //set new int time
    delay(1);
    //Take background reading
    spec1.read_into(background);
    delay(1);
    spec2.read_into(background2);
    delay(1);//Read in data

    //Turn LED on
    for (int j = 0; j < 8; j++) {              //Sets the current LED HIGH, turns the others off
      if ( j == led) ledDriver.analogWrite(LED[led], ledHigh);
      else ledDriver.analogWrite(LED[j], ledLow);
    }
    //Take actual reading
    spec1.read_into(data);
```

```
      delay(1);
      spec2.read_into(data2);
      delay(1);//Read in data
      for (int i = 0; i < 8; i++) {
        ledDriver.analogWrite(LED[i], ledLow);
      }
      //Print data minus background
      mySerial.print("Reading for LED: "); mySerial.println(led + 1);
      mySerial.print(" CMOS 1 "); mySerial.println(" CMOS 2");
      mySerial.println("------------------");

      for (int i = 0; i < C12880_NUM_CHANNELS; i++) {
        mySerial.print("      "); mySerial.print(data[i] - background[i]); mySerial.print(" , ");
mySerial.println(data2[i] - background2[i]);

      }
    }
  }
}

/**********************************************************************
******/
//continous spectrometer with led, minus dark

void specCL(int spec, int led) {
  led = led - 1; //convert for led pin array
  if (spec == 1) { // function using spec 1
    ledDriver.analogWrite(LED[led], ledLow);
    spec1.read_into(background);
    delay(1);//Read in data
    ledDriver.analogWrite(LED[led], ledHigh);
    delay(1);
    spec1.read_into(data);
    for (int i = 0; i < C12880_NUM_CHANNELS; i++) {
      mySerial.println(data[i] - background[i]);
    }

  }
  else if (spec == 2) { // function using spec 2
    ledDriver.analogWrite(LED[led], ledLow);
    spec2.read_into(background);
    delay(1);//Read in data
    ledDriver.analogWrite(LED[led], ledHigh);
    delay(1);
    spec2.read_into(data);
    for (int i = 0; i < C12880_NUM_CHANNELS; i++) {
      mySerial.println(data[i] - background[i]);
    }

  }
```

```
}
/**********************************************************************
******/
//LED Variance Check
void ledVar(int spec, int led) {
  led = led - 1; //convert for led pin array
  uint16_t curr_val = 0;
  uint16_t prev_val = 0;
  uint16_t highest = 0;
  int wavelength = 0;
  int samples = 100;

  if (spec == 1) { // function using spec 1
    spec1.set_integration_time(integrationTimes1[led]);
    for (int k = 0; k < samples; k++) {
      spec1.read_into(background);
      delay(1);
      ledDriver.analogWrite(LED[led], ledHigh);
      delay(3);
      spec1.read_into(data);
      for (int i = 0; i < C12880_NUM_CHANNELS; i++) {
        curr_val = data[i] - background[i];
        if (curr_val > prev_val) {
          highest = curr_val;
          wavelength = i;
          prev_val = curr_val;
        }

      }

      mySerial.print(highest); mySerial.print(","); mySerial.println(wavelength);
      ledDriver.analogWrite(LED[led], ledLow);
      delay(50);
    }

  }
  else if (spec == 2) { // function using spec 1
    spec2.set_integration_time(integrationTimes2[led]);
    for (int k = 0; k < samples; k++) {
      spec2.read_into(background);
      delay(1);
      ledDriver.analogWrite(LED[led], ledHigh);
      delay(3);
      spec2.read_into(data);
      for (int i = 0; i < C12880_NUM_CHANNELS; i++) {
        curr_val = data[i] - background[i];
        if (curr_val > prev_val) {
          highest = curr_val;
          wavelength = i;
```

```
        prev_val = curr_val;
       }

     }
     mySerial.print(highest); mySerial.print(","); mySerial.println(wavelength);
     ledDriver.analogWrite(LED[led], ledLow);
     delay(50);
    }

  }

}
/**************************************************************************
******/
//Photodiode Functions
/**************************************************************************
******/
//Function to read averaged photodiode

void PDread() {
  int PD1 = 0;

  PD_120 = 0;

  for (int i = 0; i < numReadings; i++) {
    PD1 = PD1 + analogRead(PDInput);
    waits = millis();
    while (millis() < waits + 5) {}
  }
  PD1 = PD1 / numReadings;

  mySerial.println(PD1);
  PD_120 = PD1;
}


void PDreadCycle() {}

/**************************************************************************
******/
//I2C function to read temperature sensor
/**************************************************************************
******/
void TMPread() {

  tempSensor.read();

  tempC = tempSensor.temperature();
  mySerial.println(tempC, 3);
}
```

```
/*************************************************************************
******/
//I2C function to read current sensor
/*************************************************************************
******/
void CurrRead() {
  mySerial.print("Bus voltage:   ");
  mySerial.print(ina.readBusVoltage(), 5);
  mySerial.println(" V");

  mySerial.print("Bus power:     ");
  mySerial.print(ina.readBusPower(), 5);
  mySerial.println(" W");


  mySerial.print("Shunt voltage: ");
  mySerial.print(ina.readShuntVoltage(), 5);
  mySerial.println(" V");

  mySerial.print("Shunt current: ");
  mySerial.print(ina.readShuntCurrent(), 5);
  mySerial.println(" A");
  mySerial.println("");
}

//take average current measurment
void aveCurr() {

  float PD1 = 0;


  for (int i = 0; i < numReadings; i++) {
    PD1 = PD1 + ina.readShuntCurrent();
    waits = millis();
    while (millis() < waits + 5) {}
  }
  PD1 = PD1 / numReadings;

  mySerial.println((PD1 * 1000), 5);
}
```

B.2 Sensor Deployment Firmware

B.2.1 Sensor Deployment Firmware Full Scan Measurements

B.2.2 Sensor Firmware for Deployment in Owenmore River, Co Sligo

```
// Sensor Firmware for deployment in Owenmore River to measure fDOM, Turbidity, Chl-a, and Temperature
// Code Written by Sean Power, Dublin City University, 23/03/2023

// Calibration Values for Sensor 9
// Turbidity Calibration Values
const int pixelT = 260;
const float TurbSlope = 171.09;
const float sampleBlankTurb = 3207;

// Chlorophyll Calibration Values
const int pixelC = 154;
const float ChlSlope = 18.164;
const float sampleBlankChl = 86.67;
const float BB3Conv = 22.71;

// Other Pixel Values
const int pixelCDOM = 60;
const int pixelLED5 = 50;

// Libraries Included
// Including necessary libraries for various functionalities
#include <Snooze.h>
#include <SnoozeBlock.h>
#include <Wire.h>
#include <EEPROM.h>
#include "C12880MA.h"
#include "TMP_TSYS01.h"
#include "INA.h"
#include "LD_TLC59116.h"

// Including specific libraries based on the core definition
#if defined(CORE_TEENSY)
   #include <ADC.h> // ADC library for Teensy
#else
   #include <elapsedMillis.h> // Fallback to elapsedMillis if not on Teensy
#endif

// Sensor Information
// Various information related to the sensor
const int SensorSerialNo = 10;
double FirmwareVersion = 1.4;
String CMOS2_Serial = "2OL00267"; // Absorption Serial Number
String CMOS1_Serial = "2OL00268"; // Fluorescence + Scatter Serial Number
```

```
// Sleep Mode Configuration
// Configuration for sleep mode of the Teensy microcontroller
SnoozeDigital digital;
SnoozeTimer timer;
SnoozeBlock config_teensy32(digital, timer);
#define sleepInterruptPin 11
#define headSwt 12

// Serial Communication Configuration
// Configurations related to serial communication
#define mySerial Serial1
#define SERIAL_TX 1
#define SERIAL_RX 0
#define BAUDRATE 9600

char inBuff[] = "------------------------------------------------------------";
int bytesread;

// Current Monitor Sensor Configuration
// Setup for the Current Monitor Sensor
INA226 ina;
bool CU_ON = false;

void CS_Setup() {
  ina.begin();
  ina.configure(INA226_AVERAGES_16,              INA226_BUS_CONV_TIME_140US,
INA226_SHUNT_CONV_TIME_140US, INA226_MODE_SHUNT_BUS_CONT);
  ina.calibrate(0.12, 0.3);
}

// UV Antifouling Configuration
// Configuration for the UV antifouling
const int PWM_Pins[8] = {0, 1, 10, 11, 12, 13, 14, 15};
float dc_p;
int pwm_Res = 255;
unsigned int AF_Length;

// LED Array Configuration
// Configuration for the LED array used in the sensor
const int LED[8] = {7, 6, 5, 4, 3, 2, 1, 0};

// Spectrometer Configuration
// Configuration for the spectrometer used in the sensor
#define SPEC_CLK 23
#define SPEC_TRG 11
#define SPEC_ST1 7
#define SPEC_VIDEO1 15
#define SPEC_ST2 8
#define SPEC_VIDEO2 14
```

```
bool contSpec = false;
int CMOS_ON = 0;

C12880_Class spec1(SPEC_TRG, SPEC_ST1, SPEC_CLK, SPEC_VIDEO1);
C12880_Class spec2(SPEC_TRG, SPEC_ST2, SPEC_CLK, SPEC_VIDEO2);

float integrationTimesA[8];
float integrationTimesS[8];
float integrationTimesF[8];

void specBegin() {
  spec1.begin();
  spec2.begin();
}


/*****************************************************************************
******/
// Photodiode Configuration
// Configuration and variables for Photodiode operations.
bool PD_ON = false; // Variable to check if Photodiode is ON or OFF
const int PDInput = A2; // Assigning the analog pin A2 for Photodiode input
int PD_120 = 0; // Variable to store some Photodiode value

// Running Average Variables
// Variables for calculating the running average.
const int numReadings = 25; // Number of readings to consider for average
int readings[numReadings]; // Array to store the readings from the analog input
int readIndex = 0; // Index of the current reading
int total = 0; // Variable to store the running total
int average = 0; // Variable to store the average of readings

// Temperature Sensor Configuration
// Configuration and variables for Temperature Sensor operations.
bool TMP_ON = false; // Variable to check if Temperature Sensor is ON or OFF
TSYS01 tempSensor; // Object for Temperature Sensor operations
float tempC = 0; // Variable to store temperature in Celsius

// EEPROM Functions
// Functions for handling EEPROM operations.

// EEPROM Addresses
// Defined constants for EEPROM addresses.
const int absorbInts = 0;
const int scatterInts = 32;
const int flourInts = 64;
const int AF_dutyCycle = 96;
const int AF_cycleLength = 100;

// Sensor Query Function
```

```
// Function to query the sensor and print out the current integration times
// and antifouling cycle parameters from the EEPROM.
void sensorQuery() {
  // Print Sensor Details
  printSensorDetails();

  // Get and Print Current Absorption Integration Times
  EEPROM.get(absorbInts, integrationTimesA);
  mySerial.print("Current Absorption Int Times are: ");
  for (int i = 0; i < 8; i++) {
    mySerial.print(integrationTimesA[i], 6);
    if (i != 7) mySerial.print(',');
  }
  mySerial.println();

  // Get and Print Current Scatter Integration Times
  EEPROM.get(scatterInts, integrationTimesS);
  mySerial.print("Current Scatter Int Times are: ");
  for (int i = 0; i < 8; i++) {
    mySerial.print(integrationTimesS[i], 6);
    if (i != 7) mySerial.print(',');
  }
  mySerial.println();

  // Get and Print Current Fluorescence Integration Times
  EEPROM.get(flourInts, integrationTimesF);
  mySerial.print("Current Fluorescence Int Times are: ");
  for (int i = 0; i < 8; i++) {
    mySerial.print(integrationTimesF[i], 6);
    if (i != 7) mySerial.print(',');
  }
  mySerial.println();

  // Get and Print Current Antifouling Duty Cycle
  EEPROM.get(AF_dutyCycle, dc_p);
  mySerial.print("Current antifouling duty cycle is: ");
  mySerial.println(dc_p);

  // Get and Print Current Antifouling Cycle Length
  EEPROM.get(AF_cycleLength, AF_Length);
  mySerial.print("Current antifouling cycle length is: ");
  mySerial.println(AF_Length);
}

// Sensor Change Function
// This function is responsible for changing sensor settings based on the provided values.
void sensorChange(String value3, String value4, String value5) {
  // If the first value is "I", change integration times.
  if (value3 == "I") {
    if (value4 == "A") {
```

```
      for (int i = 0; i < value5.length(); i++) {
        integrationTimesA[i] = getValue(value5, ',', i).toFloat();
      }
      EEPROM.put(absorbInts, integrationTimesA);
    } else if (value4 == "S") {
      for (int i = 0; i < value5.length(); i++) {
        integrationTimesS[i] = getValue(value5, ',', i).toFloat();
      }
      EEPROM.put(scatterInts, integrationTimesS);
    } else if (value4 == "F") {
      for (int i = 0; i < value5.length(); i++) {
        integrationTimesF[i] = getValue(value5, ',', i).toFloat();
      }
      EEPROM.put(flourInts, integrationTimesF);
    } else {
      mySerial.println("No matching command found for integration time settings change");
    }
  }
  // If the first value is "D", change the duty cycle.
  else if (value3 == "D") {
    EEPROM.put(AF_dutyCycle, value4.toFloat());
  }
  // If the first value is "T", change the cycle length.
  else if (value3 == "T") {
    EEPROM.put(AF_cycleLength, value4.toInt());
  }
  // If no matching command found, print an error message.
  else {
    mySerial.println("No matching command found for settings change");
  }
}
// Get Value Function
// This function retrieves a value from a comma-separated string based on the given index.
String getValue(String data, char separator, int index) {
  int found = 0;
  int strIndex[] = {0, -1};
  int maxIndex = data.length();

  for (int i = 0; i <= maxIndex && found <= index; i++) {
    if (data.charAt(i) == separator || i == maxIndex) {
      found++;
      strIndex[0] = strIndex[1] + 1;
      strIndex[1] = (i == maxIndex) ? i + 1 : i;
    }
  }
  // Return the found value, or an empty string if not found.
  return found > index ? data.substring(strIndex[0], strIndex[1]) : "";
}

// Component Setup Function
```

```
// This function initializes various components of the system.
void componentSetup() {
  // Begin various components and set initial configurations.
  specBegin();
  CS_Setup();
  ledDriver.begin();
  Wire.begin();
  analogReadResolution(16);
  tempSensor.init();
  pinMode(headSwt, OUTPUT);

  // Set initial states for pins and variables.
  digital.pinMode(sleepInterruptPin, INPUT, FALLING); // pin, mode, type
  digitalWriteFast(headSwt, LOW);
  contSpec = false;
  PD_ON = false;
  TMP_ON = false;
}

// Setup Function
// This function initializes the system.
void setup() {
  // Wait for the serial communication to be established.
  while (!mySerial) {
    ;
  }

  // Begin serial communication with the defined baud rate and set timeout.
  mySerial.begin(BAUDRATE);
  mySerial.setTimeout(1);

  // Call the component setup function to initialize various components.
  componentSetup();

  // Print the sensor details.
  printSensorDetails();

  // Notify that the sensor is ready.
  mySerial.println("Sensor Ready");
}

// Main Loop Function
// This function continuously checks for serial input and processes it.
void loop() {
  // Call the SerialRead function to check for and process serial input.
  SerialRead();
}

// Serial Interface Section
```

```
// Serial Read Function
// This function checks for available serial input and processes it.
void SerialRead() {
  // Check if serial input is available.
  if (mySerial.available()) {
    // Read from serial until a newline character is read or timeout is exceeded.
    bytesread = mySerial.readBytesUntil('\n', inBuff, 64);

    // Terminate the input buffer string.
    inBuff[bytesread] = '\0';

    // Convert the input buffer to a string for processing.
    String instruction = String(inBuff);

    // Process the received instruction.
    processInstruction(instruction);
  }
}

// Print Sensor Details Function
// This function prints the details of the sensor to the serial monitor.
void printSensorDetails() {
  mySerial.print("Sensor No: DCUS");
  mySerial.println(SensorSerialNo);
  mySerial.print("Baud Rate: ");
  mySerial.println(BAUDRATE);
  mySerial.print("Firmware Version: ");
  mySerial.println(FirmwareVersion);
  mySerial.print("CMOS 1 Serial No: ");
  mySerial.println(CMOS1_Serial);
  mySerial.print("CMOS 2 Serial No: ");
  mySerial.println(CMOS2_Serial);
}

// Process Instruction Function
// This function processes the instruction received from the serial monitor.
void processInstruction(String instruction) {
  // Initialization of variables to store various parts of the instruction.
  String value1 = "0"; // Outlines overall command branch (R, A, S, D)
  String value2 = "0"; // Second identifier for R and S (R -> W, L, F, T, B)(S -> Q, C) Adding
RB for background scan
  String value3 = "0"; // Third identifier for SC (I, F, D, T)
  String value4 = "0"; // Fourth indication for SCI (1 or 2) or Value or array of values for SC
  String value5 = "0"; // Fourth indication for SCI (1 or 2) or Value or array of values for SC

  int instructionLength = instruction.length();

  // Assign values based on the length and content of the instruction.
  if (instructionLength > 0) value1 = instruction.substring(0, 1);
  if (instructionLength > 1) value2 = instruction.substring(1, 2);
```

```
  if (instructionLength > 2) value3 = instruction.substring(2, 3);
  if (value3 == "F" or value3 == "D" or value3 == "T") value4 = instruction.substring(3,
instructionLength);
  else if (instructionLength > 4) value4 = instruction.substring(3, 4);
  if (instructionLength > 4) value5 = instruction.substring(4, instructionLength);

  // Sensor Reading Cycle
  if (value1 == "R") {
    // Full reading cycle
    if (value2 == "W") deployScan();
    // Command not recognized
    else mySerial.println("No matching command found for Sensor Reading Cycle");
  }
  // Antifouling Cycle
  else if (value1 == "A") {
    mySerial.println("Antifouling Cycle Start");
    antiFoulingProgram();
    mySerial.println("Antifouling Cycle End");
  }
  // Settings
  else if (value1 == "S") {
    // Query Current Settings
    if (value2 == "Q") {
      mySerial.println("Sensor Settings: ");
      sensorQuery();
    }
    // Change Settings
    else if (value2 == "C") {
      mySerial.println("Change Sensor Settings");
      sensorChange(value3, value4, value5);
    }
    // Command not recognized
    else mySerial.println("No matching command found for Settings");
  }
  // Diagnostics
  else if (value1 == "D") diagnosticProgram();
  // Command not recognized
  else mySerial.println("No matching command found");
}

// Diagnostic Program function
void diagnosticProgram() {
  // Initialize current variables
  float bgI = 0; // Background current
  float fI = 0;  // Current with device on
  float ledI = 0; // LED current measurement

  // Start the LED driver
  ledDriver.begin();
```

```
  // Perform LED Array Check
  mySerial.println("LED Array Current Measurement");

  // Turn on the head switch
  digitalWriteFast(headSwt, HIGH);
  delay(10);

  // Loop through each LED to measure current
  for (int i = 0; i < 8; i++) {
    // Take Current Reading before LED is turned on
    bgI = ina.readShuntCurrent();

    // Turn on the LED
    ledDriver.analogWrite(LED[i], ledHigh);
    delay(100);

    // Take Current Reading While LED is on
    fI = ina.readShuntCurrent();

    // Calculate LED current and convert to mA
    ledI = (fI - bgI) * 1000;

    // Output the current of each LED
    mySerial.print("LED ");
    mySerial.print(i + 1);
    mySerial.print(" Current: ");
    mySerial.print(ledI);
    mySerial.println("mA");

    // Turn off the previous LED
    ledDriver.analogWrite(LED[i - 1], ledLow);
    delay(100);
  }

  // Ensure the last LED is turned off
  ledDriver.analogWrite(LED[7], ledLow);
  delay(100);

  // Perform UV LEDs Check for different boards
  mySerial.println("UV LED Current Measurement");
  checkUVLEDCurrent();

  // Perform Optical Head Sensor Check
  mySerial.println("Optical Head Current Measurement");
  checkOpticalHeadCurrent();

  // Perform Idle Check
  mySerial.println("System Power Measurement");
  checkSystemPower();
}
```

```
// Helper function to check UV LED current for different boards
void checkUVLEDCurrent() {
    float bgI, fI, ledI;
  // ... Other necessary UV LEDs checks

  // Example for PD Board
  bgI = ina.readShuntCurrent();
  ledDriver.analogWrite(PWM_Pins[2], ledHigh);
  ledDriver.analogWrite(PWM_Pins[3], ledHigh);
  delay(100);

  fI = ina.readShuntCurrent();
  ledI = (fI - bgI) * 1000;

  ledDriver.analogWrite(PWM_Pins[2], ledLow);
  ledDriver.analogWrite(PWM_Pins[3], ledLow);

  mySerial.print("UV LEDs PD Board ");
  mySerial.print(" Current: ");
  mySerial.print(ledI);
  mySerial.println("mA");
  delay(100);
}

// Helper function to check Optical Head current
void checkOpticalHeadCurrent() {
    float bgI, fI, ledI;

  digitalWriteFast(headSwt, LOW);
  delay(100);
  bgI = ina.readShuntCurrent();
  digitalWriteFast(headSwt, HIGH);
  delay(100);

  fI = ina.readShuntCurrent();
  ledI = (fI - bgI) * 1000;
  digitalWriteFast(headSwt, LOW);

  mySerial.print("Optical Head ");
  mySerial.print(" Current: ");
  mySerial.print(ledI);
  mySerial.println("mA");
}

// Helper function to check System Power
void checkSystemPower() {
  // Output bus voltage
  mySerial.print("Bus voltage:   ");
  mySerial.print(ina.readBusVoltage(), 5);
```

```
  mySerial.println(" V");

  // Output bus power
  mySerial.print("Bus power:     ");
  mySerial.print(ina.readBusPower(), 5);
  mySe
rial.println(" W");

  // Output shunt voltage
  mySerial.print("Shunt voltage: ");
  mySerial.print(ina.readShuntVoltage(), 5);
  mySerial.println(" V");

  // Output shunt current
  mySerial.print("Shunt current: ");
  mySerial.print(ina.readShuntCurrent(), 5);
  mySerial.println(" A");
}

//Reading measruement from temperature sensor
void temp() {
  mySerial.println("Temperature Reading Start");
  digitalWriteFast(headSwt, HIGH);
  tempSensor.read();
  tempC = tempSensor.temperature();
  mySerial.println(tempC, 3);
  digitalWriteFast(headSwt, LOW);
  mySerial.println("Temperature Reading End");
}

//Reading measruement from photodiode sensor
int PDread() {
  int PD1 = 0;

  for (int i = 0; i < numReadings; i++) {
    PD1 = PD1 + analogRead(PDInput);
    waits = millis();
    while (millis() < waits + 5) {}
  }
  PD1 = PD1 / numReadings;

  return PD1;

}

//UV LEDs for Antifouling cycle
void antiFoulingProgram() {
  unsigned long AF_interval;
  unsigned long current_time;
  AF_interval = EEPROM.get(AF_cycleLength, AF_Length) * 60000;
```

```
  UV_ON();

  current_time = millis();
  while (millis() < current_time + 1000) {
    SerialRead();
  }

  timer.setTimer(AF_interval); // milliseconds
  Snooze.deepSleep(config_teensy32);
  UV_OFF();
  current_time = millis();
  while (millis() < current_time + 1000) {
    SerialRead();
  }
  mySerial.flush();

}

//Turn UV LEDs ON
void UV_ON() {
  EEPROM.get(AF_dutyCycle, dc_p);
  int duty_cycle = pwm_Res * (dc_p / 100); //duty cycle of the PWM
  for (int i = 0; i < 8; i++) {
    ledDriver.analogWrite(PWM_Pins[i], duty_cycle);
  }
}

//Turn UV LEDs OFF
void UV_OFF() {
  for (int i = 0; i < 8; i++) {
    ledDriver.analogWrite(PWM_Pins[i], 0);
  }
}


//Measurement Cycle
void deployScan() {
  mySerial.println("Calibrated Data Reading Start");

  //digitalWriteFast(headSwt,     HIGH);
  //Set Up data storage arrays absorbtion and scatter
  uint16_t backgroundF[C12880_NUM_CHANNELS];
  uint16_t dataF[C12880_NUM_CHANNELS];

  uint16_t backgroundS[C12880_NUM_CHANNELS];
  uint16_t dataS[C12880_NUM_CHANNELS];

  uint16_t backgroundA[C12880_NUM_CHANNELS];
  uint16_t dataA[C12880_NUM_CHANNELS];
```

```
  //Introduce dummy scan to discharge CMOS 1
  uint16_t dummy[C12880_NUM_CHANNELS];


/*************************************************************************
**********************/
  //Turbidity Scan//

/*************************************************************************
**********************/
  digitalWriteFast(headSwt, HIGH);
  int led = 0;
  EEPROM.get(scatterInts, integrationTimesS);
  spec1.set_integration_time(integrationTimesS[led]);
  delay(1);
  spec1.read_into(dummy);
  delay(5);

  for (int j = 0; j < 8; j++) { //Sets the current LED HIGH, turns the others off
    if (j == led) ledDriver.analogWrite(LED[led], ledHigh);
    else ledDriver.analogWrite(LED[j], ledLow);
  }
  delay(5);
  spec1.read_into(dataS);
  delay(5);

  for (int i = 0; i < 8; i++) {
    ledDriver.analogWrite(LED[i], ledLow);
  }

  delay(5);
  spec1.read_into(backgroundS);
  delay(5);
  digitalWriteFast(headSwt, LOW);
  //Print Scan

/*************************************************************************
**********************/
  mySerial.println("Turbidity Reading");
  mySerial.println("**********");
  mySerial.println("Scan with LED On");

  printData(dataS);

  mySerial.print("Turb value at pixel ");
  mySerial.print(pixelT);
  mySerial.print(" is: ");
  mySerial.println(dataS[pixelT]);
  mySerial.println(" ");
```

```
  mySerial.println("Background Scan");
  printBlanks();
  printData(backgroundS);

  mySerial.print("Turb BG value at pixel ");
  mySerial.print(pixelT);
  mySerial.print(" is: ");
  mySerial.println(backgroundS[pixelT]);
  mySerial.println("******************");
  printBlanks();


/*************************************************************************
**********************/
  //Flr Scan//

/*************************************************************************
**********************/
  digitalWriteFast(headSwt, HIGH);
  led = 4;
  EEPROM.get(flourInts, integrationTimesF);
  spec1.set_integration_time(integrationTimesF[led]);
  delay(1);
  spec1.read_into(dummy);
  delay(5);

  for (int j = 0; j < 8; j++) { //Sets the current LED HIGH, turns the others off
    if (j == led) ledDriver.analogWrite(LED[led], ledHigh);
    else ledDriver.analogWrite(LED[j], ledLow);
  }
  spec1.read_into(dataF);
  delay(5);

  for (int i = 0; i < 8; i++) {
    ledDriver.analogWrite(LED[i], ledLow);
  }

  spec1.read_into(backgroundF);
  delay(5);
  digitalWriteFast(headSwt, LOW);
  delay(10);
  //Print Scan

/*************************************************************************
**********************/
  mySerial.println("Chl Reading");
  mySerial.println("******************");
  mySerial.println("Scan with LED On");
  // printBlanks();
```

```
  printData(dataF);
  printBlanks();

  mySerial.print("CHL value at pixel ");
  mySerial.print(pixelC);
  mySerial.print(" is: ");
  mySerial.println(dataF[pixelC]);
  printBlanks();
  mySerial.print("CDOM value at pixel ");
  mySerial.print(pixelCDOM);
  mySerial.print(" is: ");
  mySerial.println(dataF[pixelCDOM]);
  mySerial.println("******************");
  printBlanks();
  //Background

  mySerial.println("******************");
  printBlanks();
  mySerial.println("Background Scan Flr");
  printData(backgroundF);

  mySerial.print("CHL BG value at pixel ");
  mySerial.print(pixelC);
  mySerial.print(" is: ");
  mySerial.print(backgroundF[pixelC]);
  printBlanks();
  mySerial.print("FLR CDOM BG value at pixel ");
  mySerial.print(pixelCDOM);
  mySerial.print(" is: ");
  mySerial.println(backgroundF[pixelCDOM]);
  mySerial.println("******************");
  printBlanks();


//*************************************************************************
*//
  //Absorbtion//
  led = 3;
  digitalWriteFast(headSwt, HIGH);
  EEPROM.get(absorbInts, integrationTimesA);
  spec2.set_integration_time(integrationTimesA[led]);
  delay(5);

  for (int j = 0; j < 8; j++) { //Sets the current LED HIGH, turns the others off
    if (j == led) ledDriver.analogWrite(LED[led], ledHigh);
    else ledDriver.analogWrite(LED[j], ledLow);
  }
  spec2.read_into(dummy);
  delay(10);
  spec2.read_into(dataA);
```

```
  delay(5);

  for (int i = 0; i < 8; i++) {
    ledDriver.analogWrite(LED[i], ledLow);
  }
  delay(5);
  spec2.read_into(backgroundA);
  delay(5);

  digitalWriteFast(headSwt, LOW);
  delay(10);

//*************************************************************************
*//
  //Absorbtion//

//*************************************************************************
*//
  mySerial.println("CDOM Scan Abs");
  mySerial.println("*****************");
  printBlanks();
  mySerial.println("Scan with LED On");

  printData(dataA);

  mySerial.print("Abs CDOM value at pixel ");
  mySerial.print(pixelLED5);
  mySerial.print(" is: ");
  mySerial.println(dataA[pixelLED5]);
  printBlanks();

  mySerial.println("Background Scan Abs");

  printData(backgroundA);

  mySerial.print("Abs CDOM BG value at pixel ");
  mySerial.print(pixelLED5);
  mySerial.print(" is: ");
  mySerial.println(backgroundA[pixelLED5]);
  mySerial.println("*****************");
  printBlanks();

  double Turb, Chl, CDOM_Flr, CDOM_Abs;

  Turb = dataS[pixelT] - backgroundS[pixelT];
  Chl = dataF[pixelC] - backgroundF[pixelC];
  CDOM_Flr = dataF[pixelCDOM] - backgroundF[pixelCDOM];
  CDOM_Abs = dataA[pixelLED5] - backgroundA[pixelLED5];
  tempSensor.read();
  tempC = tempSensor.temperature();
```

```
  mySerial.println("Turb Chl CDOM Flr  CDOM Abs Temp");
  mySerial.print(Turb, 0);
  mySerial.print(",");
  mySerial.print(Chl, 0);
  mySerial.print(",");
  mySerial.print(CDOM_Flr, 0);
  mySerial.print(",");
  mySerial.print(CDOM_Abs, 0);
  mySerial.print(",");
  mySerial.print(tempC, 2);
  mySerial.println(" ");
  mySerial.println("******************");
  printBlanks();

  mySerial.println("Calibrated Reading End");
  digitalWriteFast(headSwt, LOW);
}

//Print a line of 288 blank values
void printBlanks() {
  for (int i = 0; i < C12880_NUM_CHANNELS; i++) {
    mySerial.print(" ");
    if (i != C12880_NUM_CHANNELS - 1) mySerial.print(" ");
    else mySerial.println(" ");
  }
  mySerial.flush();
}

//Print spectromter values
void printData(uint16_t data[]) {
  for (int i = 0; i < C12880_NUM_CHANNELS; i++) {
    mySerial.print(data[i]);
    if (i != C12880_NUM_CHANNELS - 1) mySerial.print(",");
    else mySerial.println(" ");
  }
  mySerial.flush();
}
```

B.2.3 Sensor Deployment Firmware Reduced Data for Dublin Bay Deployment

```
// Sensor Firmware for deployment in Owenmore River to measure fDOM, Turbidity, Chl-a, and Temperature
// Code Written by Sean Power, Dublin City University, 16/07/2022

//Sensor Firmware for Dublin Bay Deployment reducing data produced by reducing LEDs used in scans
//No absorption, only LED 1 for Turbidity Scatter, LEDs 5 to 8 for FLR


//Libraries Included
```

```
/*************************************************************************
******/
//Teensy Sleep Mode Library
#include <Snooze.h>
#include <SnoozeBlock.h>

//ADC Libraries
#if defined(CORE_TEENSY)
#include <ADC.h> /* https://github.com/pedvide/ADC */
#else
#include <elapsedMillis.h>
#endif


//I2C Library
#include <Wire.h>

//Spectrometer Library
#include "C12880MA.h"

//Temp Sensor Library
#include "TMP_TSYS01.h"

//Current Monitor Library
#include "INA.h"


//LED Driver
#include "LD_TLC59116.h"
LD_TLC59116 ledDriver(0);


//EEPROM Library
#include <EEPROM.h>


/*************************************************************************
******/
//Sensor Info

const int SensorSerialNo = 3;
double FirmwareVersion =   1.2;

String CMOS2_Serial = "2OL00267"; //Absorbtion
String CMOS1_Serial = "2OL002648"; //Flourescemce + Scatter


/*************************************************************************
******/
//Sleep Mode
```

```
SnoozeDigital digital;
SnoozeTimer timer;
SnoozeBlock config_teensy32(digital, timer);
#define sleepInterruptPin 11

#define headSwt 12


/*************************************************************************
******/
//mySerial Comms
#define mySerial Serial        // Comms with USB

//#define mySerial Serial1       // Hardware mySerial, communicate with RX,TX bins (0,1)
to other microcontroller
#define SERIAL_TX            1 // Serial transmission
#define SERIAL_RX            0 // Serial receiving
#define BAUDRATE          9600

// Variables for main loop
char   inBuff[] = "------------------------------------------------------------";
int    bytesread;

/*************************************************************************
******/

//Current Monitor Sensor
INA226 ina;
bool CU_ON = false;
void CS_Setup(){
   ina.begin();

  // Configure INA226
  ina.configure(INA226_AVERAGES_16,              INA226_BUS_CONV_TIME_140US,
INA226_SHUNT_CONV_TIME_140US, INA226_MODE_SHUNT_BUS_CONT);

  // Calibrate INA226. Rshunt = 0.01 ohm, Max excepted current = 4A
  ina.calibrate(0.12, 0.3);
  }

/*************************************************************************
******/
//UV Antifouling
const int PWM_Pins[8] = {0,1,10,11,12,13,14,15}; //sensor UV LEDs, LED 310nm and
280nm on Array
float dc_p;
int pwm_Res = 255;
unsigned int AF_Length;
```

```
/*************************************************************************
******/

// LED Array
const int ledHigh = 255;
const int ledLow = 0;

const int LED[8] = {7,6,5,4,3,2,1,0};
//850nm,660nm,565nm,430nm,385nm,365nm,310nm,280nm

/*************************************************************************
******/

//Spectrometer
#define SPEC_CLK 23

//Spec 1: 20D00472
#define SPEC_TRG 11
#define SPEC_ST1 7
#define SPEC_VIDEO1 15

//Spec 2: 20D00473
#define SPEC_TRG 11
#define SPEC_ST2 8
#define SPEC_VIDEO2 14
//IC
bool contSpec = false;
int CMOS_ON = 0;

C12880_Class spec1(SPEC_TRG,SPEC_ST1,SPEC_CLK,SPEC_VIDEO1); //Scatter and
Flourescence
C12880_Class spec2(SPEC_TRG,SPEC_ST2,SPEC_CLK,SPEC_VIDEO2); //Absorbtion

//integration times sets (Absorbtion -> CMOS 2  Scatter, Flourecence -> CMOS 1)

//Int Time Set values are stored in MCU EEPROM memory

//CMOS 2 Absorbtion Int Set
float integrationTimesA[8];

//CMOS 1 Scatter Int Set
float integrationTimesS[8];

//CMOS 1 Flourescense Int Set
float integrationTimesF[8];

void specBegin(){
  spec1.begin();
  spec2.begin();
  }
```

```
/*************************************************************************
******/
//Photodiode
bool PD_ON = false;
const int PDInput = A2;
//int PD1 = 0;
int PD_120 = 0;
//Runing Average variables
const int numReadings = 25;
int readings[numReadings];      // the readings from the analog input
int readIndex = 0;              // the index of the current reading
int total = 0;                  // the running total
int average = 0;                // the average


/*************************************************************************
******/
//Temperature Sensor
bool TMP_ON = false;
TSYS01 tempSensor;
float tempC = 0;
/*************************************************************************
******/
//EEPROM Functions

//addresses
const int absorbInts = 0;
const int scatterInts = 32;
const int flourInts = 64;
const int AF_dutyCycle = 96;
const int AF_cycleLength = 100;

/*unsigned int AF_cycleLength = flourInts  + sizeof(integrationTimesF);
unsigned int AF_dutyCycle = AF_cycleLength  + sizeof(AF_Length);*/

void sensorQuery(){

    //Serial.println( "Read custom object from EEPROM: " );
    //Print Sensor Serial Number First

    printSensorDetails();

    EEPROM.get( absorbInts, integrationTimesA);
    mySerial.print("Current Absorbtion Int Times are: ");
     for(int i = 0; i < 8; i++){
     mySerial.print(integrationTimesA[i],6); if(i != 7)mySerial.print(',');}
     mySerial.println("");
```

```
      EEPROM.get( scatterInts, integrationTimesS);
    mySerial.print("Current Scatter Int Times are: ");
      for(int i = 0; i < 8; i++){
      mySerial.print(integrationTimesS[i],6);if(i != 7) mySerial.print(',');}
      mySerial.println("");

      EEPROM.get(flourInts, integrationTimesF);
    mySerial.print("Current Flourescence Int Times are: ");
      for(int i = 0; i < 8; i++){
      mySerial.print(integrationTimesF[i],6); if(i != 7) mySerial.print(',');}
      mySerial.println("");

     EEPROM.get( AF_dutyCycle, dc_p);
    mySerial.print("Current antifouling duty cycle is: "); mySerial.println(dc_p);

      EEPROM.get( AF_cycleLength, AF_Length);
    mySerial.print("Current antifouling cycle length is: "); mySerial.println(AF_Length);
  }

 void  sensorChange(String value3, String value4, String value5){
if(value3 == "I"){
  if(value4 == "A"){
    for(int i = 0; i < value5.length();i++){
      integrationTimesA[i] = getValue(value5,',', i).toFloat();
      }
    EEPROM.put(absorbInts, integrationTimesA);
    }

  else if(value4 == "S"){
     for(int i = 0; i < value5.length();i++){
      integrationTimesS[i] = getValue(value5,',', i).toFloat();
      }
    EEPROM.put(scatterInts, integrationTimesS);
      }
  else if(value4 == "F"){
       for(int i = 0; i < value5.length();i++){
         integrationTimesF[i] = getValue(value5,',', i).toFloat();
      }
    EEPROM.put( flourInts, integrationTimesF);
      }
   else {mySerial.println("No matching command found for integration time settings
change");}
  }
else if(value3 == "D"){
     EEPROM.put( AF_dutyCycle, value4.toFloat());
    }

else if(value3 == "T"){
       EEPROM.put( AF_cycleLength, value4.toInt());
       }
```

```
else {mySerial.println("No matching command found for settings change");}
 }


// String  var = getValue( StringVar, ',', 2); // if  a,4,D,r  would return D
String getValue(String data, char separator, int index)
{
    int found = 0;
    int strIndex[] = { 0, -1 };
    int maxIndex = data.length();

    for (int i = 0; i <= maxIndex && found <= index; i++) {
        if (data.charAt(i) == separator || i == maxIndex) {
            found++;
            strIndex[0] = strIndex[1] + 1;
            strIndex[1] = (i == maxIndex) ? i+1 : i;
        }
    }
    return found > index ? data.substring(strIndex[0], strIndex[1]) : "";
}  // END
/**************************************************************************
******/

//Timers
unsigned long waits;
unsigned long seconds;

void componentSetup(){
  specBegin();
  CS_Setup();
  ledDriver.begin();
  Wire.begin();
  analogReadResolution(16);
  tempSensor.init();
  pinMode(headSwt,        OUTPUT);
  digital.pinMode(sleepInterruptPin, INPUT, FALLING);//pin, mode, type
  digitalWriteFast(headSwt,     LOW);

  contSpec = false;
  PD_ON = false;
  TMP_ON = false;
  }

/**************************************************************************
******/

void setup() {
  while (!mySerial) {;}
  mySerial.begin(BAUDRATE);
  mySerial.setTimeout(1);
```

```
  componentSetup();
  printSensorDetails();
  mySerial.println("Sensor Ready");
}

/**************************************************************************
******/


void loop() {

  SerialRead();

}

/**************************************************************************
******/
//Serial Interface
/**************************************************************************
******/
//Loop Serial Read Function
void SerialRead(){
       if (mySerial.available()) {
      bytesread=mySerial.readBytesUntil('\n', inBuff, 64); // Read from serial until CR is read
or timeout exceeded
      inBuff[bytesread]='\0';
      String instruction = String(inBuff);
      processInstruction(instruction);
    }
  }


//Print User Interface to Serial Monitor
/**************************************************************************
******/
void printSensorDetails() {
  mySerial.print("Sensor No: DCUS");     mySerial.println(SensorSerialNo);
  mySerial.print("Baud Rate: ");        mySerial.println(BAUDRATE);
  mySerial.print("Firmware Version: "); mySerial.println(FirmwareVersion);
  mySerial.print("CMOS 1 Serial No: "); mySerial.println(CMOS1_Serial);
  mySerial.print("CMOS 2 Serial No: "); mySerial.println(CMOS2_Serial);
}

// Process Instruction
void processInstruction(String instruction){
  String value1 = "0"; //outlines overall command branch (R,A,S,D)
  String value2 = "0"; //second identifier for R and S (R -> W,L,F,T,B)(S -> Q,C) Adding
RB for background scan
  String value3 = "0"; //Third identifier for SC (I,F,D,T)
  String value4 = "0";  //Fourth indication for SCI (1 or 2) or Value or array of values for SC
```

```
  String value5 = "0";  //Fourth indication for SCI (1 or 2) or Value or array of values for SC


  int instructionLength = instruction.length();
  if (instructionLength > 0) {   value1 = instruction.substring(0,1); }


  if (instructionLength > 1) {   value2 = instruction.substring(1,2); }

  if (instructionLength > 2) {   value3 = instruction.substring(2,3); }


  if(value3 == "F" or value3 == "D" or value3 == "T") {value4 =
instruction.substring(3,instructionLength);}
  else if(instructionLength > 4) { value4 = instruction.substring(3,4); }

  if (instructionLength > 4) {   value5 = instruction.substring(4,instructionLength); }

//Sensor Reading Cycle
  if(value1 == "R"){
    //Full reading cycle
    if(value2 == "W"){
     // mySerial.println("Full Cycle Reading Start");
      fullReading();
      }

    //Absorbtion + Scatter Reading
    else if(value2 == "L"){
      //mySerial.println("Abs + Scat Reading Start");
      Ab_Sc();
      }

    //Flourescence Reading
    else if(value2 == "F"){
     // mySerial.println("Abs + Scat Reading Start");
      flour();}

    //Temperature Reading
    else if(value2 == "T"){
      //mySerial.println("Abs + Scat Reading Start");
      temp();
      }
         //Background Scan
    else if(value2 == "B"){
      BGscan();
      }


    //Command not recognised
    else{mySerial.println("No matching command found for Sensor Reading Cycle");}
```

```
    }

//Antifouling Cycle
  else if(value1 == "A"){
    mySerial.println("Antifouling Cycle Start");
    antiFoulingProgram();
    mySerial.println("Antifouling Cycle End");
    }

//Settings
  else if(value1 == "S"){
     //Query Current Settings
    if(value2 == "Q"){
      mySerial.println("Sensor Settings: ");
      sensorQuery();}

    //Change Settings
    else if(value2 == "C"){
      mySerial.println("Change Sensor Settings");
      //mySerial.print(value3); mySerial.print(value4); mySerial.println(value5);
      sensorChange(value3,value4,value5);
      }

    //Command not recognised
    else{mySerial.println("No matching command found for Settings");}

    }

//Diagnostics

  else if(value1 == "D"){
    diagnosticProgram();
    }

//Command not recognised
  else { mySerial.println("No matching command found");}

  }

 void diagnosticProgram(){
    float bgI = 0; //background current
    float fI = 0; //current with device on
    float ledI = 0; //Current measurement
    ledDriver.begin();

  //LED Array Check
    mySerial.println("LED Array Current Measurement");
    digitalWriteFast(headSwt,     HIGH);
    delay(10);
    for(int i = 0; i<8; i++){
```

```
    //Take Current Reading before LED is turned on
        bgI = ina.readShuntCurrent();
   ledDriver.analogWrite(LED[i], ledHigh);
   delay(100);
   //Take Current Reading While LEd is on
        fI = ina.readShuntCurrent();
   //Subtract background from current with LED on and convert to mA
     ledI = (fI-bgI)*1000;

   mySerial.print("LED "); mySerial.print(i+1);
   mySerial.println(" Current: "); mySerial.print(ledI); mySerial.println("mA");

   ledDriver.analogWrite(LED[i-1], ledLow);
   delay(100);
   if(i == 7) ledDriver.analogWrite(LED[7], ledLow);
     }
delay(100);
  //UV LEDs Check
  //LEDs to check are the two on the PD and 2 CMOS boards 10 + 11 on PD board, 12 + 13
on CMOS 1, 14 + 15 on CMOS 2
   mySerial.println("UV LED Current Measurement");

     bgI = ina.readShuntCurrent();
     ledDriver.analogWrite(PWM_Pins[2], ledHigh); ledDriver.analogWrite(PWM_Pins[3],
ledHigh);
     delay(100);

     fI = ina.readShuntCurrent();
     ledI = (fI-bgI)*1000;

     ledDriver.analogWrite(PWM_Pins[2], ledLow); ledDriver.analogWrite(PWM_Pins[3],
ledLow);

     mySerial.print("UV LEDs PD Board ");
     mySerial.print(" Current: "); mySerial.print(ledI); mySerial.println("mA");
     delay(100);

     bgI = ina.readShuntCurrent();
     ledDriver.analogWrite(PWM_Pins[4], ledHigh); ledDriver.analogWrite(PWM_Pins[5],
ledHigh);
     delay(100);

     fI = ina.readShuntCurrent();
     ledI = (fI-bgI)*1000;

     ledDriver.analogWrite(PWM_Pins[4], ledLow); ledDriver.analogWrite(PWM_Pins[5],
ledLow);

     mySerial.print("UV LEDs CMOS Board 1 ");
     mySerial.print(" Current: "); mySerial.print(ledI); mySerial.println("mA");
```

```
    delay(100);


    bgI = ina.readShuntCurrent();
    ledDriver.analogWrite(PWM_Pins[6], ledHigh); ledDriver.analogWrite(PWM_Pins[7],
ledHigh);
    delay(100);

    fI = ina.readShuntCurrent();
    ledI = (fI-bgI)*1000;

    ledDriver.analogWrite(PWM_Pins[6], ledLow); ledDriver.analogWrite(PWM_Pins[7],
ledLow);

    mySerial.print("UV LEDs CMOS Board 2 ");
    mySerial.print(" Current: "); mySerial.print(ledI); mySerial.println("mA");
    delay(100);


  //Optical Head Sensor Check
   mySerial.println("Optical Head Current Measurement");

    digitalWriteFast(headSwt,    LOW);
    delay(100);
    bgI = ina.readShuntCurrent();
    digitalWriteFast(headSwt,    HIGH);
    delay(100);

    fI = ina.readShuntCurrent();
    ledI = (fI-bgI)*1000;
    digitalWriteFast(headSwt,    LOW);


    mySerial.print("Optical Head ");
    mySerial.print(" Current: "); mySerial.print(ledI); mySerial.println("mA");



  //Idle Check
  mySerial.println("System Power Measurement");
  mySerial.print("Bus voltage:   ");
  mySerial.print(ina.readBusVoltage(), 5);
  mySerial.println(" V");

  mySerial.print("Bus power:    ");
  mySerial.print(ina.readBusPower(), 5);
  mySerial.println(" W");


  mySerial.print("Shunt voltage: ");
```

```
  mySerial.print(ina.readShuntVoltage(), 5);
  mySerial.println(" V");

  mySerial.print("Shunt current: ");
  mySerial.print(ina.readShuntCurrent(), 5);
  mySerial.println(" A");
  mySerial.println("");

 }

 void fullReading(){
  mySerial.println("Full Cycle Reading Start");
  //BGscan();
  Ab_Sc();
  flour();
  delay(10);
  temp();
  delay(100);
  mySerial.println("Full Cycle Reading End");
  }


//Removing Absorption and all but LED 1 scatter
 void Ab_Sc(){
    digitalWriteFast(headSwt,     HIGH);
    mySerial.println("Scat Reading Start");

    uint16_t dataS[C12880_NUM_CHANNELS];

    //Introduce dummy scan to discharge CMOS 1
    uint16_t dummy[C12880_NUM_CHANNELS];

    int photoDiodeBackground;
    int photoDiodeData;

   // EEPROM.get( absorbInts, integrationTimesA);
    EEPROM.get( scatterInts, integrationTimesS);
    spec1.set_integration_time(integrationTimesS[0]);
    delay(1);
    spec1.read_into(dummy);
    //delay(10);
    //spec2.read_into(dummy);
    delay(10);


    spec1.set_integration_time(integrationTimesS[0]);

    spec1.read_into(backgroundS);

    //Turn LED on
```

```
  for(int j = 0; j<8; j++){                  //Sets the current LED HIGH, turns the others off
  if( j == 0) ledDriver.analogWrite(LED[0], ledHigh);
  else ledDriver.analogWrite(LED[j], ledLow);
     }

  //Take actual reading
  spec1.read_into(dataS);
  //delay(1);
  photoDiodeData = PDread();

  delay(1);//Read in data
   for(int i = 0; i<8; i++){
     ledDriver.analogWrite(LED[i], ledLow);
     }

  delay(10);
  //Print data minus background
  mySerial.print("Reading for LED: "); mySerial.println(0 + 1);


   mySerial.print("Sct: ");
   mySerial.print("Int time: "); mySerial.println(integrationTimesS[0],6);
   delay(100);
  for (int i = 0; i < C12880_NUM_CHANNELS; i++){
  mySerial.print(dataS[i]);
  if(i != C12880_NUM_CHANNELS-1) mySerial.print(","); else mySerial.println(" ");
  delay(5);
     }


   mySerial.print("Sct BG: ");
   mySerial.print("Int time: "); mySerial.println(integrationTimesS[0],6);
  for (int i = 0; i < C12880_NUM_CHANNELS; i++){
  mySerial.print(backgroundS[i]);
  if(i != C12880_NUM_CHANNELS-1) mySerial.print(","); else mySerial.println(" ");
  delay(5);
     }

  mySerial.println("Scat Reading End");
  digitalWriteFast(headSwt,     LOW);

 }


void flour(){
  mySerial.println("Fluorescence Reading Start");
  digitalWriteFast(headSwt,     HIGH);

     //Set Up data storage arrays absorbtion and scatter
  uint16_t backgroundF[C12880_NUM_CHANNELS];
```

```
  uint16_t dataF[C12880_NUM_CHANNELS];

  //Introduce dummy scan to discharge CMOS 1
  uint16_t dummy[C12880_NUM_CHANNELS];

  EEPROM.get( flourInts, integrationTimesF);
  spec1.set_integration_time(integrationTimesF[4]);
  delay(1);
  spec1.read_into(dummy);
  delay(10);

    for(int i = 4; i<8; i++){ //cycle through 8 LEDs
  int led = i;
 //Set Int Time
  delay(1);
  spec1.set_integration_time(integrationTimesF[led]);

  delay(1);
  ////Take background reading
  spec1.read_into(backgroundF);
  delay(1);
  //Turn LED on
  for(int j = 0; j<8; j++){                 //Sets the current LED HIGH, turns the others off
  if( j == led) ledDriver.analogWrite(LED[led], ledHigh);
  else ledDriver.analogWrite(LED[j], ledLow);
     }
   delay(1);
  //Take actual reading
  spec1.read_into(dataF);
  delay(1);

   for(int i = 0; i<8; i++){
     ledDriver.analogWrite(LED[i], ledLow);
     }
  //Print data minus background
  mySerial.print("Reading for LED: "); mySerial.println(led + 1);
  mySerial.print("Flr: ");
  mySerial.print("Int time: "); mySerial.println(integrationTimesF[i],6);

  for (int i = 0; i < C12880_NUM_CHANNELS; i++){
  //mySerial.print(dataF[i] - backgroundF[i]); if(i != C12880_NUM_CHANNELS-1)
mySerial.print(","); else mySerial.println(" ");
  mySerial.print(dataF[i]); if(i != C12880_NUM_CHANNELS-1) mySerial.print(","); else
mySerial.println(" ");
     }
   mySerial.println(" ");

       //Background of FLR LED Reading
  mySerial.print("Flr BG: ");
```

```
   mySerial.print("Int time: "); mySerial.println(integrationTimesF[i],6);

    for (int i = 0; i < C12880_NUM_CHANNELS; i++){
   mySerial.print(backgroundF[i]);          if(i          !=          C12880_NUM_CHANNELS-1)
mySerial.print(","); else mySerial.println(" ");
       }
    mySerial.println(" ");

     }

   mySerial.println("Fluorescence Reading End");
   digitalWriteFast(headSwt,     LOW);

  }

 void BGscan(){
     mySerial.println("Background Reading Start");
   digitalWriteFast(headSwt,     HIGH);

       //Set Up data storage arrays absorbtion and scatter
   uint16_t backgroundF[C12880_NUM_CHANNELS];
   uint16_t backgroundA[C12880_NUM_CHANNELS];
   uint16_t backgroundS[C12880_NUM_CHANNELS];

   EEPROM.get( absorbInts, integrationTimesA);
   EEPROM.get( scatterInts, integrationTimesS);
   EEPROM.get(flourInts, integrationTimesF);
    mySerial.println("Background Reading for ABS and SCT");
   for(int i = 0; i<8; i++){ //cycle through 8 LEDs
   int led = i;
   for(int i = 0; i<8; i++) ledDriver.analogWrite(LED[i], ledLow);
 //Set Int Time
   delay(10);
   spec2.set_integration_time(integrationTimesA[led]); //set new int time
   delay(10);
   spec1.set_integration_time(integrationTimesS[led]);

   delay(10);
   spec2.read_into(backgroundA);
   delay(10);
   //Take background reading
   spec1.read_into(backgroundS);

   delay(10);

   //Print data minus background
   mySerial.print("Background reading for LED: "); mySerial.println(led + 1);


//Flipped order of abs and sct
```

```
    mySerial.print("Abs BG: ");
    mySerial.print("Int time: "); mySerial.println(integrationTimesA[i],6);
    for (int i = 0; i < C12880_NUM_CHANNELS; i++){
    mySerial.print(backgroundA[i]);          if(i          !=          C12880_NUM_CHANNELS-1)
mySerial.print(","); else mySerial.println(" ");
    delay(5);
        }

     delay(200); ///////delay between sct and abs
     mySerial.print("Sct BG: ");
     mySerial.print("Int time: "); mySerial.println(integrationTimesS[i],6);
     delay(100);
    for (int i = 0; i < C12880_NUM_CHANNELS; i++){
    mySerial.print(backgroundS[i]);
    if(i != C12880_NUM_CHANNELS-1) mySerial.print(","); else mySerial.println(" ");
    delay(5);
        }

      }


    //CMOS 1 Flr BG Scan
       for(int i = 3; i<8; i++){ //cycle through 8 LEDs
    int led = i;
  //Set Int Time
    //delay(1);
    spec1.set_integration_time(integrationTimesF[led]);
     for(int i = 0; i<8; i++) ledDriver.analogWrite(LED[i], ledLow);

   delay(1);
    //Take background reading
    spec1.read_into(backgroundF);
    delay(1);

    //Print data minus background
    mySerial.print("Reading for LED: "); mySerial.println(led + 1);
    mySerial.print("Flr BG: ");
    mySerial.print("Int time: "); mySerial.println(integrationTimesF[i],6);

    for (int i = 0; i < C12880_NUM_CHANNELS; i++){
    mySerial.print(backgroundF[i]);          if(i          !=          C12880_NUM_CHANNELS-1)
mySerial.print(","); else mySerial.println(" ");
    delay(5);
        }
     mySerial.println(" ");
      }

    mySerial.println("Background Reading End");
    digitalWriteFast(headSwt,     LOW);
  }
```

```
 void temp(){
     mySerial.println("Temperature Reading Start");
     digitalWriteFast(headSwt,     HIGH);
     tempSensor.read();
     tempC = tempSensor.temperature();
     mySerial.println(tempC,3);
     digitalWriteFast(headSwt,     LOW);
     mySerial.println("Temperature Reading End");
  }

int PDread(){
   int PD1 = 0;

   for(int i = 0; i < numReadings; i++){
     PD1 = PD1 + analogRead(PDInput);
     waits = millis();
     while (millis() < waits + 5) {}
   }
   PD1 = PD1/numReadings;

   return PD1;


   }


void antiFoulingProgram(){
     unsigned long AF_interval;
     unsigned long current_time;
     AF_interval = EEPROM.get(AF_cycleLength,AF_Length) * 60000;
     UV_ON();

     current_time = millis();
     while(millis() < current_time + 1000){
       SerialRead();
       }

     timer.setTimer(AF_interval);// milliseconds
     Snooze.deepSleep( config_teensy32 );
     UV_OFF();
     current_time = millis();
     while(millis() < current_time + 1000){
       SerialRead();
       }
    mySerial.flush();

  }

void UV_ON(){
   EEPROM.get( AF_dutyCycle, dc_p);
```

```
   int duty_cycle = pwm_Res * (dc_p/100); //duty cycle of the PWM
   for(int i = 0; i<8; i++){
   ledDriver.analogWrite(PWM_Pins[i],duty_cycle);
     }
  }

void UV_OFF(){
        for(int i = 0; i<8; i++){
   ledDriver.analogWrite(PWM_Pins[i],0);
      }
     }
```

B.3 Dublin Bay Deployment Data Retrieval & Sorting Software

```
//Code written to organise Dublin Bay deployment data from AWS Dynamo DB provided by TechWorks Marine, extract data from JSON format and organise into excel columns for analysis.
//Code written by Sean Power and Louis Free, Dublin City University

import pandas as pd
import csv
import json
import matplotlib.pyplot as plt
import datetime
import fnmatch

KEYWORD = 'AWAMS1'

headers = ['Timestamp', 'Date', 'SctLED1', 'bgSctLED1', 'Turb-NTU',
          'FlrLED5', 'bgFlrLED5', 'Chl-A', 'Temp']

data = pd.DataFrame(columns = headers)

def add_to_DataFrame(ts,t,s,bgs,tur,f,bgf,c,tmp):
    global data
    data = data.append({'Timestamp':ts,'Date':t, 'SctLED1':s,
                    'bgSctLED1':bgs, 'Turb-NTU':tur,'FlrLED5':f,
                    'bgFlrLED5':bgf, 'Chl-A':c, 'Temp':tmp},
ignore_index=True)

def extract(pload, index, end)->str:
    return(pload[index].split(':')[1][2:len([1])-end])

def data_values(payload, data):
    timestamp = int(extract(payload,11,3))
    time = datetime.datetime.fromtimestamp(timestamp).strftime('%Y-%m-%d
%H:%M:%S')
    sctLED1 = int(extract(payload,5,2))
    bgsctLED1 = int(extract(payload,7,2))
    TurbNTU = float(extract(payload,9,4))
```

```
    FlrLED5 = int(extract(payload,4,2))
    bgFlrLED5 = int(extract(payload,8,2))
    ChlA = float(extract(payload,6,2))
    temp = float(extract(payload,6,2))
    add_to_DataFrame(timestamp,time,sctLED1,bgsctLED1,TurbNTU,FlrLED5,bgFlrL
ED5,ChlA,temp)
    #print(data)


def sort(p):
    if KEYWORD in p:
        p = p.split(',')
        data_values(p,data)

for i in range(1,11):
    if i < 10:
        df = pd.read_csv(f"MB100{i}-1656637200_1666054800.csv")
    else:
        df = pd.read_csv(f"MB10{i}-1656637200_1666054800.csv")
    payload = df['Payload']#[0].split(',')

    for p in payload:
        sort(p)
    if i < 10:
        data.to_excel(f'MB00{i}.xlsx')
    else:
        data.to_excel(f'MB0{i}.xlsx')
```

B.4 Datalogger Sensor Operation Firmware

```
//Code written for Datalogger using Arduino Mega, adafruit datalogger, BlueSmirf BT Transceiver to control DCU Optical Sensor.
//Code written by Sean Power, Dublin City University
//Changes made to stop sensor reading cycle repeating and tidying up syntax of output to make more usable. Add in string identifier to catch sensor start up

//Include Libraries
/* ------------------------------------------------- */
//SD Card Storage Libraries
#include <SPI.h>
#include <SD.h>

//EEPROM Library
#include <EEPROM.h>

//Sleep Mode Library
#include <Sleep_n0m1.h>

//RTC Library
#include "RTClib.h"
```

```
/* ---------------------------------------------------- */
//Variables
/* ---------------------------------------------------- */
//Variable String to flag end of sensor reading
String stopFlag = "Sensor Ready";
int startOK = 0; //when true command can be sent to sensor.
//Function to waiting until stopFlag found before sending a command to the sensor
int Contains(String s, String search) {
  int max = s.length() - search.length();
  int lgsearch = search.length();

  for (int i = 0; i <= max; i++) {
    if (s.substring(i, i + lgsearch) == search) return 1;
  }

  return 0;
}


//General Variables
//Voltage Divider Resistor Values 220k, 110k
const int battV = A7; //voltage divider to monitor battery capacity flag before 10.8Vs

//EEPROM Storage Variables
unsigned int n; //counter for the read files
unsigned int m; //counter for deployment
const int readCntAdrs = 0; //address of read counter, reset to 0 each deployment setting
const int dplyCntAdrs = 5; //address for deployment, increments each deployment.

//RTC Variables
RTC_PCF8523 rtc;
int Year, Month, Day, Hour, Minute, Second;
int lastY, lastM, lastD, lastH, lastMin, lastS;

//SD CARD Variables
const int chipSelect = 10;
File myFile;
char file[50];
char lastFile[50];
char* diaFile = "diaFile.txt";

//Sleep Mode Variables
Sleep sleep;

unsigned long sleepDeviceTime = 900000; //Period between readings 900000 is 15 mins
unsigned long sleepUVTime = 60000; //Period between readings 60000 is 1 min

boolean UVTime = false;

//Sensor Control Variables
```

```
const int sensorSwitch = 5; //pin to turn mosfet power switch on to power sensor

//commands to sensor
//char fullReadCMD[2] = ; //whole reading cycle
String sensorCommand;

bool blackBoxStatusB = false;
bool blackBoxDataB = false;
bool fullReadingB = false;
bool deploymentB = false;

bool snglReading = false;

bool sPassthrough = false;

// Comms Variables
#define btSerial    Serial //Serial port for BT comms
#define btBaudRate  115200 //BT Baud Rate
//btBuffer Read Variables
char   btInBuff[64]; //reading sensor data buffer
int    btBytesRead;
int bytesPerReading;

//Comms for sensor are on main Serial
#define sSerial    Serial2 //Serial port for BT comms
#define mainBaudRate 9600 //Baud rate of Sensor

//main serial buffer read variables
char   inBuff[1727]; //reading sensor data buffer
int    bytesread;

double RWbytes = 100;
int Dbytes = 100;

//Reading timeouts
double readTimeOut = 3000;
unsigned long started_waiting_at;
int serialCounter = 0;
bool timeout = false;

unsigned long sensorStartDelay = 6000;

/* ------------------------------------------------- */
//Functions
/* ------------------------------------------------- */

//EEPROM Functions
void setCrntDplymtFile() {
  EEPROM.get(readCntAdrs, n);
  EEPROM.get(dplyCntAdrs, m);
```

```
  snprintf(file, sizeof(file), "D%02dR%04d.txt", m, n);
  btSerial.print("New File: "); btSerial.println(file);
}

void setLastCrntDplymtFile() {
  int N;
  int M;
  EEPROM.get(readCntAdrs, n);
  EEPROM.get(dplyCntAdrs, m);

  Serial.print("lastY: "); Serial.println(lastY);
  if (n == 0) N = 0;
  else N = n - 1;
  if (m == 0) M = 0;
  else M = m - 1;

  snprintf(lastFile, sizeof(lastFile), "D%02dR%04d.txt", M, N);

  Serial.print("Last File: "); Serial.println(lastFile);
}


void resetN() {
  EEPROM.put(readCntAdrs, 0);
  EEPROM.get(readCntAdrs, n);
  Serial.print("N = "); Serial.println(n);
}

void resetM() {
  EEPROM.put(dplyCntAdrs, 0);
  EEPROM.get(dplyCntAdrs, m);
  Serial.print("M = "); Serial.println(m);
}


//RTC Functions

void rtcBegin() {
  if (! rtc.begin()) {
    btSerial.println("Couldn't find RTC");
    btSerial.flush();
    abort();
  }

  //rtc.adjust(DateTime(F(__DATE__), F(__TIME__)));

}


String rtcTimeStamp() {
```

```
  char message[120];
  DateTime timestamp = rtc.now();
  Year = timestamp.year();
  Month = timestamp.month();
  Day = timestamp.day();
  Hour = timestamp.hour();
  Minute = timestamp.minute();
  Second = timestamp.second();

  sprintf(message, "%d-%d-%d %02d:%02d:%02d", Month, Day, Year, Hour, Minute,
Second);

  return message;
}

//SD CARD Functions
void SDcardSetup() {
  pinMode(SS, OUTPUT); //SPI pin

  //Initilise SD Card
  if (!SD.begin(chipSelect)) {
    btSerial.println("initialization failed!");
    return;
  }
  btSerial.println("initialization done.");
}

void writeSDcard(String input, int ln, String command) {

  if (command == "RW")myFile = SD.open(file, FILE_WRITE);
  else if (command == "D") myFile = SD.open(diaFile, FILE_WRITE);

  if (myFile) {
    myFile.print(input);
    if (ln == 1) {
      myFile.println(" ");
    }
    // close the file:
    myFile.close();
  }
  else {    // if the file didn't open, print an error:
    btSerial.print("error opening "); btSerial.println(myFile);
  }

}

void readSDcard(String command) {
  if (command == "RW") {
    setLastCrntDplymtFile();
    btSerial.println(lastFile);
```

```
    myFile = SD.open(lastFile);
  }

  else if (command == "D") {
    myFile = SD.open(diaFile);
  }

  if (myFile) {
    btSerial.println(lastFile);

    // read from the file until there's nothing else in it:
    while (myFile.available()) {
      btSerial.write(myFile.read());
    }
    // close the file:
    myFile.close();
  }

  else {
    // if the file didn't open, print an error:
    btSerial.println("error opening test.txt");
  }

}

// Sensor Control Functions
void SensorControlSetup() {
  pinMode(sensorSwitch, OUTPUT);
  digitalWrite(sensorSwitch, LOW);
}

//Comms Functions

void commSetUp() {
  sSerial.begin(mainBaudRate);
  sSerial.setTimeout(5000);
  while (!sSerial) {
    ;
  }
  btSerial.begin(btBaudRate);
  while (!btSerial) {
    ;
  }
  btSerial.println("Starting BT Serial");
}

#include <avr/power.h>

void lowPowerSetup() {
```

```
  for (int i = 0; i <= 53; i++) {
    pinMode(i, OUTPUT);
    digitalWrite(i, LOW);
  }

  power_usart3_disable();
  power_usart1_disable();
}

//Setup Function
void deviceSetup() {
  commSetUp();
  lowPowerSetup();
  SensorControlSetup();
  SDcardSetup();
  rtcBegin();

}

int UVCounter = 0;
void setup() {
  deviceSetup();
  deploymentB = true;
}

//static unsigned long timeLastInput = 0;
//unsigned long now;
const long TIME_OUT =  4500L;


String command;
int idleTime = 10000;
unsigned long time_now = 0;

void loop() {

  btSerialRead();


  if (fullReadingB == true) {
    deploymentB = true;
    snglReading = true;
    fullReading();
    snglReading = false;
    deploymentB = false;
  }

  else if (blackBoxDataB == true) {

    blackBoxData();
```

```
  }
  else if (blackBoxStatusB == true) {
    deploymentB = true;
    blackBoxStatus();
    deploymentB = false;
  }

  else if (deploymentB == true) {

    deployment();

  }

  else if (sPassthrough == true) {

    if (sSerial.available()) {      // If anything comes in Serial (USB),
      btSerial.write(sSerial.read());   // read it and send it out Serial1 (pins 0 & 1)
    }

    if (btSerial.available()) {
      char stopSPT = 'x';
      char inChar = (char)btSerial.read();// If anything comes in Serial1 (pins 0 & 1)
      if (inChar == stopSPT) {
        btSerial.println("Stopped Serial Passthrough");
        digitalWrite(sensorSwitch, LOW);
        sPassthrough = false;
      }
      else sSerial.write(inChar);
    }

  }
}

void btSerialRead() {
  if (btSerial.available()) {
    btBytesRead = btSerial.readBytesUntil('\n', btInBuff, 64); // Read from serial until CR is
read or timeout exceeded
    btInBuff[btBytesRead] = '\0';
    String instruction = String(btInBuff);
    btSerial.println(String(btInBuff));
    processInstruction(instruction);
  }
}

void sensorSerialRead() {
  startOK = 0;
  while (startOK == 0) {
    if (sSerial.available()) {
```

```
    bytesread = sSerial.readBytesUntil('\n', inBuff, 1727); // Read from serial until CR is read or timeout exceeded
    inBuff[bytesread] = '\0';
    btSerial.println(String(inBuff));
    startOK = Contains(String(inBuff), stopFlag);
   }
  }
  startOK = 0;
}

//process commands sent from BT device
void processInstruction(String instruction) {
  //commands to operate sensor will be the same as the commands being sent to the sensor
  // RW, RL, RF, RT, D, A, SQ
  String value1 = "0"; //outlines overall command branch (R,A,S,D)
  String value2 = "0"; //second identifier for R and S (R -> W,L,F,T)(S -> Q,C)
  String value3 = "0"; //Third identifier for SC (I,F,D,T)
  String value4 = "0";  //Fourth indication for SCI (1 or 2) or Value or array of values for SC
  String value5 = "0";  //Fourth indication for SCI (1 or 2) or Value or array of values for SC

  int instructionLength = instruction.length();
  if (instructionLength > 0) {
   value1 = instruction.substring(0, 1);
  }


  if (instructionLength > 1) {
   value2 = instruction.substring(1, 2);
  }

  if (instructionLength > 2) {
   value3 = instruction.substring(2, 3);
  }


  if (value3 == "F" or value3 == "D" or value3 == "T") {
   value4 = instruction.substring(3, instructionLength);
  }
  else if (instructionLength > 4) {
   value4 = instruction.substring(3, 4);
  }

  if (instructionLength > 4) {
   value5 = instruction.substring(4, instructionLength);
  }

  //Black Box Commands
  //notated by starting with B

  if (value1 == "B") {
```

```
  //Black Box Status check
  //will give battery capacisty, deployment info, RTC time check
  if (value2 == "S") {
    btSerial.println("Check Black Box Status");
    //blackBoxStatus();
    blackBoxStatusB = true;
    blackBoxDataB = false;
    fullReadingB = false;
    deploymentB = false;
  }

  //request data stored on sd card
  else if (value2 == "R") {
    btSerial.println("Retrieving data from SD storage");
    //blackBoxData();
    blackBoxDataB = true;
    blackBoxStatusB = false;
    fullReadingB = false;
    deploymentB = false;

  }
  //Command not recognised
  else {
    btSerial.println("No matching command found for Black Box");
  }
}

//Sensor Commands
//Sensor Reading Cycle
else if (value1 == "R") {
  //Full reading cycle
  if (value2 == "W") {
    btSerial.println("Full Cycle Reading Start");
    EEPROM.get( readCntAdrs, n); //get current deployment number

    writeSDcard("Deployment: ", 0, "RW" ); writeSDcard(String(n), 1, "RW");
    //fullReading();
    fullReadingB = true;
    blackBoxDataB = false;
    blackBoxStatusB = false;
    deploymentB = false;
  }

  //Command not recognised
  else {
    btSerial.println("No matching command found for Sensor Reading Cycle");
  }
}

else if (value1 == "N") {
```

```
  resetN();
  btSerial.println("Read Number Reset to 0");
 }
 else if (value1 == "M") {
  resetM();
  btSerial.println("Deployment Number Reset to 0");
 }

 //Deployment Mode with continous readings perdiodically
 else if (value1 == "F") {
  deploymentB = true;
  fullReadingB = false;
  blackBoxDataB = false;
  blackBoxStatusB = false;
  resetN();
  EEPROM.get(dplyCntAdrs, m);
  m++;
  EEPROM.put(dplyCntAdrs, m);
  btSerial.println("Deployment Cycle Started");
 }

 else if (value1 == "Z") {
  deploymentB = false;
  fullReadingB = false;
  blackBoxDataB = false;
  blackBoxStatusB = false;
  btSerial.println("Deployment Stopped");
 }


 else if (value1 == "P") {
  sPassthrough = !sPassthrough;

  if (sPassthrough == true) {
    btSerial.println("Passthrough to Sensor Enabled");
    digitalWrite(sensorSwitch, HIGH);
    //turn on sensor for passthrough to work
  }

  else
  { btSerial.println("Passthrough to Sensor Disabled");
    digitalWrite(sensorSwitch, LOW);
  }
 }

 //check RTC Functions
 else if (value1 == "T") {
  btSerial.println(rtcTimeStamp());
 }
```

```
  else if (value1 == "S") {
    Serial.println("Device going to sleep");
    btSerial.println(rtcTimeStamp());
    delay(5);
    deviceSleep(sleepDeviceTime);
    delay(5);
    btSerial.println(rtcTimeStamp());
    Serial.println("Device awake");
  }
  //UV MODDE
  else if (value1 == "U") {

    uvMode();

  }
  //Command not recognised
  else {
    btSerial.println("No matching command found");
  }
}

void uvMode() {
  btSerial.println("Starting UV Mode");
  digitalWrite(sensorSwitch, HIGH);
  delay(1000);
  sSerial.write("A"); sSerial.write("\n");
  sSerial.flush();
  delay(10);
  btSerial.println(rtcTimeStamp());
  delay(5);
  deviceSleep(sleepUVTime);
  delay(5);
  btSerial.println(rtcTimeStamp());
  btSerial.println("Device awake");
  digitalWrite(sensorSwitch, LOW);
}

void deployment() {
  fullReading();

  UVCounter++;
  if (UVCounter > 3) {
    UVCounter = 0;
    UVTime = true;
    uvMode();
  }
  btSerial.print("UV Counter at: ");  btSerial.println(UVCounter);

  btSerial.println("Entering Idle Mode");
  time_now = millis();
```

```
  if (UVTime == true) {
    UVTime = false;

    btSerial.println(rtcTimeStamp());
    delay(5);
    btSerial.println(sleepDeviceTime - sleepUVTime);
    deviceSleep(sleepDeviceTime - sleepUVTime);
    delay(5);
    btSerial.println(rtcTimeStamp());
    btSerial.println("Device awake");
  }
  else deviceSleep(sleepDeviceTime);

  /*
    while (millis() < time_now + sleepTime) {
    btSerialRead();
    if (deploymentB == false) break;
    }*/

  btSerial.println("End of Idle Mode");
}

void fullReading() {
  btSerial.println("Full Reading Cycle Started");
  //Set up file name
  if (snglReading == true) {
    m++;
    EEPROM.put(dplyCntAdrs, m);
  }
  else {
    n++; //interate
    EEPROM.put(readCntAdrs, n);
  }
  setCrntDplymtFile();
  btSerial.print("File name for data to be stored: "); btSerial.println(file);
  //Turn on Sensor
  digitalWrite(sensorSwitch, HIGH);
  btSerialRead();
  sensorSerialRead();
  btSerial.print("Timestamp: ");  btSerial.println(rtcTimeStamp());
  writeSDcard("Timestamp: ", 0, "RW" ); writeSDcard(rtcTimeStamp(), 1, "RW");
  writeSDcard("Battery: ", 0, "RW" ); writeSDcard(String(readBattery()), 1, "RW");
  sSerial.write("RW\n");
  sSerial.flush();
  delay(100);

  int ln;
  command = "RW";
  bytesPerReading = 0;
  bytesread = 0;
```

```
  //Reading response into text file on SD card
  while (bytesPerReading < 32000) {
    unsigned long now = millis();
    static unsigned long timeLastInput = now;
    btSerialRead();
    if (deploymentB == false) break;
    if (sSerial.available()) {
      bytesread = sSerial.readBytesUntil('\n', inBuff, 2727); // Read from serial until CR is
read or timeout exceeded
      timeLastInput = now;
      inBuff[bytesread] = '\0';

      if (bytesread < 2727) {
        ln = 1;
      }//btSerial.println(bytesread);}
      else ln = 0;

      bytesPerReading = bytesPerReading + bytesread;
      writeSDcard(inBuff, ln, command);

      // btSerial.print("Byte Count: "); btSerial.println(bytesPerReading);
      btSerial.println(String(inBuff));

    }

    if (now - timeLastInput > TIME_OUT) {
      btSerial.println("Time out");
      //btSerial.print("now - timeLastInput "); btSerial.println(now - timeLastInput);
      break;
    }
  }

  bytesPerReading = 0;

  //Catch when read cycle is complete
  btSerial.println("Flag end of Sensor Reading Cycle");

  //Turn off sensor and enter sleep mode for set period
  digitalWrite(sensorSwitch, LOW);

  fullReadingB = false;
  /* sleep.pwrDownMode(); //set sleep mode
    sleep.sleepDelay(sleepTime); //sleep for: sleepTime*/
  //Repeat until command breaks cycle or BB switched off

}

void diagnosticProgram() {
  btSerial.print("File name for diagnostics to be stored: "); btSerial.println(diaFile);
```

```
  //Turn on Sensor
  btSerialRead();
  digitalWrite(sensorSwitch, HIGH);
  delay(100);
  /*btSerial.println("Wait Start");
      started_waiting_at = millis();
      while(millis() < started_waiting_at + sensorStartDelay){
       //sSerial.read();
     btSerialRead();
     if(deploymentB == false) break;
    }
    btSerial.println("Wait Stop");
    sSerial.flush();

    writeSDcard("Timestamp: ", 0, "D" ); writeSDcard(rtcTimeStamp(),1,"D");
  */
  sensorSerialRead();
  sSerial.write("D\n");


  delay(100);


  int ln;
  command = "D";
  bytesPerReading = 0;
  bytesread = 0;

  while (bytesPerReading < 570) {
    unsigned long now = millis();
    static unsigned long timeLastInput = now;
    btSerialRead();
    if (deploymentB == false) break;
    if (sSerial.available()) {
      bytesread = sSerial.readBytesUntil('\n', inBuff, 988); // Read from serial until CR is read
or timeout exceeded
      timeLastInput = now;
      inBuff[bytesread] = '\0';

      if (bytesread < 988) {
        ln = 1;
      } //btSerial.println(bytesread);}
      else ln = 0;

      bytesPerReading = bytesPerReading + bytesread;
      writeSDcard(inBuff, ln, command);

      // btSerial.print("Byte Count: "); btSerial.println(bytesPerReading);
      btSerial.println(String(inBuff));
```

```
    }

    if (now - timeLastInput > TIME_OUT) {
      btSerial.println("Time out");
      //btSerial.print("now - timeLastInput "); btSerial.println(now - timeLastInput);
      break;
    }
  }
  //Catch when read cycle is complete
  btSerial.println("Flag end of Sensor Reading Cycle");

  //Turn off sensor and enter sleep mode for set period
  digitalWrite(sensorSwitch, LOW);
  blackBoxStatusB = false;
}

void blackBoxData() {
  btSerial.println("Black Box Data Start");
  btSerial.println("Retrieving Last Deployment Reading");
  readSDcard("RW");

  btSerial.println("Diagnostic Reading");
  readSDcard("D");
  blackBoxDataB = false;
}

void blackBoxStatus() {
  btSerial.println("Black Box Status Start");
  //Check status of BB and Sensor
  EEPROM.get(readCntAdrs, n);
  btSerial.print("Current Deployment is: "); btSerial.println(n);

  btSerial.print("Current file is: "); btSerial.println(file);
  btSerial.print("Battery Voltage: "); btSerial.print(readBattery());  btSerial.println("V");
  //sensor wake up sequence
  //Set up file name
  diagnosticProgram();
}

float readBattery() {
  int inputVoltage = analogRead(battV);
  float batteryV = inputVoltage * (5.00 / 1023.00) * 3.5;
  return batteryV;
}

void deviceSleep(long sleepTime) {

  sleep.pwrDownMode(); //set sleep mode
  //sleep.sleepPinInterrupt(intPin, LOW);
  sleep.sleepDelay(sleepTime); //sleep for: sleepTime
```

```
}
void printDirectory(File dir, int numTabs) {
  // Begin at the start of the directory
  dir.rewindDirectory();

  while (true) {
    File entry =  dir.openNextFile();
    if (! entry) {
      // no more files
      //Serial.println("**nomorefiles**");
      break;
    }
    for (uint8_t i = 0; i < numTabs; i++) {
      btSerial.print('\t');   // we'll have a nice indentation
    }
    // Print the 8.3 name
    btSerial.print(entry.name());
    // Recurse for directories, otherwise print the file size
    if (entry.isDirectory()) {
      btSerial.println("/");
      printDirectory(entry, numTabs + 1);
    } else {
      // files have sizes, directories do not
      btSerial.print("\t\t");
      btSerial.println(entry.size(), DEC);
    }
    entry.close();
  }
}
```

B.5 Sligo Deployment Data Sorting Software

```
import os
import csv
import re

# define folder path containing text files
folder_path = '/Users/seanpower/Documents/Sligo Data/seanssensordata220423'

# define regular expression pattern to match sensor data
data_pattern = r"Turb Chl CDOM Flr CDOM Abs Temp\s+(\d+),(\d+),(\d+),(\d+),([\d.]+)"


# define regular expression pattern to match timestamp
timestamp_pattern = r"Timestamp: (\d+-\d+-\d+ \d+:\d+:\d+)"

# define regular expression pattern to match battery voltage
battery_pattern = r"Battery: (\d+\.\d+)"

# define CSV header
```

```
header = ['Timestamp', 'Turb', 'Chl', 'CDOM Flr', 'CDOM Abs', 'Temp', 'Battery']

# initialize list to store extracted values
data = []

# get list of filenames sorted by filename
filenames = sorted(os.listdir(folder_path))

# loop through all text files in the folder in order
for filename in filenames:
    if filename.endswith('.TXT'):
        filepath = os.path.join(folder_path, filename)
        with open(filepath, 'r') as f:
            # read text file contents
            print(filename)
            contents = f.read()

            # extract timestamp using regular expression pattern
            timestamp_match = re.search(timestamp_pattern, contents)
            if timestamp_match:
                print("timestamp match")
                timestamp = timestamp_match.group(1)

            # extract battery voltage using regular expression pattern
            battery_match = re.search(battery_pattern, contents)
            if battery_match:
                print("battery match")
                battery = battery_match.group(1)

            # extract sensor data using regular expression pattern
            data_match = re.search(data_pattern, contents)
            if data_match:
                print("data match")
                turb, chl, cdom_flr, cdom_abs, temp = data_match.groups()


                data.append([timestamp, turb, chl, cdom_flr, cdom_abs, temp, battery])

# write extracted values to CSV file
with open('SligoData.csv', 'w', newline='') as f:
    writer = csv.writer(f)
    writer.writerow(header)
    writer.writerows(data)

print('Done.')
```